Galactic archæology in the Gaia era : unveiling the formation of the Milky Way with extremely metal-poor stars Informations

Federico Sestito

UNIVERSITÉ DE STRASBOURG

ÉCOLE DOCTORALE 182

[UMR 7550]

Observatoire astronomique de Strasbourg

THÈSE présentée par :

[Federico SESTITO]

soutenue le : **19 Novembre 2020**

pour obtenir le grade de : **Docteur de l'université de Strasbourg**

Discipline/ Spécialité : Astrophysique

Galactic Archæology in the Gaia era: unveiling the formation of the Milky Way with extremely metal-poor stars

THÈSE dirigée par :

[Monsieur MARTIN Nicolas]	Docteur, Observatoire Astronomique de Strasbourg
[Madame STARKENBURG Else]	Docteur, Kapteyn Institute, Groningen

RAPPORTEURS :

[Madame LIND Karin]	Docteur, Department of Astronomy, Stockholm University
[Monsieur RIX Hans-Walter]	Professeur, Max Planck Institut für Astronomie, Heidelberg

---

AUTRES MEMBRES DU JURY :

[Monsieur FAMAEY Benoit]	Docteur, Observatoire Astronomique de Strasbourg
[Monsieur IBATA Rodrigo]	Docteur, Observatoire Astronomique de Strasbourg
[Monsieur MARTIN Nicolas]	Docteur, Observatoire Astronomique de Strasbourg
[Madame STARKENBURG Else]	Docteur, Kapteyn Institute, Groningen

Contents

List of Publications

First author publications

- Authors: **Sestito, F.**, Buck, T., Starkenburg, E., Martin, N. F., Navarro, J. F., Venn, K. A., Obreja, A., Jablonka, P., Maccio, A.. **Exploring the origin of low-metallicity stars in Milky Way-like galaxies with the NIHAO-UHD simulations**, submitted to MNRAS, arXiv:2009.14207.
- Authors: **Sestito, F.**, Martin, N. F., Starkenburg, E., Arentsen, A., Ibata, R. A., Longeard, N., Kielty, C., Youakim, K., Venn, K. A., Aguado, D. S., Carlberg, R. G., González Hernández, J. I., Hill, V., Jablonka, P., Kordopatis, G., Malhan, K., Navarro, J. F., Sánchez-Janssen, R., Thomas, G., Tolstoy, E., Wilson, T. G., Palicio, P. A., Bialek, S., Garcia-Dias, R., Lucchesi, R., North, P., Osorio, Y., Patrick, L. R., and Peralta de Arriba, L.. **The Pristine survey X: a large population of low-metallicity stars permeates the Galactic disc**, 2020, MNRAS, 497, L7.
- Authors: **Sestito, F.**, Longeard, N., Martin, N. F., Starkenburg, E., Fouesneau, M., González Hernández, J. I., Arentsen, A., Ibata, R., Aguado, D. S., Carlberg, R. G., Jablonka, P., Navarro, J. F., Tolstoy, E., and Venn, K. A. **Tracing the formation of the Milky Way through ultra metal-poor stars**, 2019, MNRAS, 484, 2166.

Co-author publications

- Authors: Caffau, E., Bonifacio, P., Sbordone, L., Matas Pinto, A. M., François, P., Jablonka, P., Lardo, C., Martin, N. F., Starkenburg, E., Aguado, D., González-Hernández, J. I., Venn, K., Mashonkina, L., and **Sestito, F.**. **The Pristine survey XI: the FORS2 sample**, 2020, MNRAS, 493, 4677.
- Authors: Venn, K. A., Kielty, C. L., **Sestito, F.**, Starkenburg, E., Martin, N., Aguado, D. S., Arentsen, A., Bonifacio, P., Caffau, E., Hill, V., Jablonka, P., Lardo, C., Mashonkina, L., Navarro, J. F., Sneden, C., Thomas, G., Youakim, K., González-Hernández, J. I., Sánchez Janssen, R., Carlberg, R., and Malhan, K.. **Pristine IX: CFHT ESPaDOnS Spectroscopic Analysis of 115 Bright Metal-Poor Candidate Stars**, 2020, MNRAS, 492, 3241.

- Authors: Arentsen, A., Starkenburg, E., Martin, N. F., Hill, V., Ibata, R., Kunder, A., Schultheis, M., Venn, K. A., Zucker, D. B., Aguado, D., Carlberg, R., González Hernández, J. I., Lardo, C., Longeard, N., Malhan, K., Navarro, J. F., Sánchez-Janssen, R., **Sestito, F.**, Thomas, G., Youakim, K., Lewis, G. F., Simpson, J. D., and Wan, Z.. **The Pristine Inner Galaxy Survey (PIGS) I: Tracing the kinematics of metal-poor stars in the Galactic bulge**, 2020, MNRAS, 491, L11.

- Authors: Youakim, K., Starkenburg, E., Martin, N. F., Matijevič, G., Aguado, D. S., Allende Prieto, C., Arentsen, A., Bonifacio, P., Carlberg, R. G., González Hernández, J. I., Hill, V., Kordopatis, G., Lardo, C., Navarro, J. F., Jablonka, P., Sánchez Janssen, R., **Sestito, F.**, Thomas, G. F., and Venn, K.. **Pristine VIII. - The metallicity distribution function of the Milky Way halo down to the extremely metal-poor regime**, 2020, MNRAS, 492, 4986.

- Authors: Aguado, D. S., Youakim, K., González Hernández, J. I., Allende Prieto, C., Starkenburg, E., Martin, N., Bonifacio, P., Arentsen, A., Caffau, E., Peralta de Arriba, L., **Sestito, F.**, Garcia-Dias, R., Fantin, N., Hill, V., Jablonca, P., Jahandar, F., Kielty, C., Longeard, N., Lucchesi, R., Sánchez-Janssen, R., Osorio, Y., Palicio, P. A., Tolstoy, E., Wilson, T. G., Coté, P., Kordopatis, G., Lardo, C., Navarro, J. F., Thomas, G. F., and Venn, K.. **The Pristine Survey - VI. The first three years of medium-resolution follow-up spectroscopy of Pristine EMP star candidates**, 2020, MNRAS, 490, 2241.

- Authors: Bonifacio, P., Caffau, E., **Sestito, F.**, Lardo, C., Martin, N. F., Starkenburg, E., Sbordone, L., François, P., Jablonka, P., Henden, A. A., Salvadori, S., González Hernández, J. I., Aguado, D. S., Hill, V., Venn, K., Navarro, J. F., Arentsen, A., Sanchez-Janssen, R., and Carlberg, R. **The Pristine survey - V. A bright star sample observed with SOPHIE**, 2019, MNRAS, 487, 3797.

- Authors: Starkenburg, E., Aguado, D. S., Bonifacio, P., Caffau, E., Jablonka, P., Lardo, C., Martin, N., Sánchez-Janssen, R., **Sestito, F.**, Venn, K. A., Youakim, K., Allende Prieto, C., Arentsen, A., Gentile, M., González Hernández, J. I., Kielty, C., Koppelman, H. H., Longeard, N., Tolstoy, E., Carlberg, R. G., Coté, P., Fouesneau, M., Hill, V., McConnachie, A. W., and Navarro, J. F.. **The Pristine survey IV: approaching the Galactic metallicity floor with the discovery of an ultra-metal-poor star**, 2018, MNRAS, 481, 3838.

Publications from conferences

- Authors: **Sestito, F.**, Martin, N., and Starkenburg, E.. **Tracing the formation of the Milky Way through ultra metal-poor stars**, SF2A-2019: Proceedings of the Annual meeting of the French Society of Astronomy and Astrophysics. Eds.: P. Di Matteo, O. Creevey, A. Crida, G. Kordopatis, J. Malzac, J.-B. Marquette, M. N'Diaye, O. Venot, 2019, pp.153-155.

- Authors: **Sestito, F.**, Martin, N., and Starkenburg, E.. **Tracing the formation of the Milky Way through ultra metal-poor stars**, 53rd ESLAB Symposium: The Gaia Universe, held 8-12 April, 2019 at ESTEC/ESA, Noordwijk, The Netherlands. eslab53, id.47.

CHAPTER

1 Introduction: where does Galactic Archæology (or Palæontology) stand?

One of the goals of Astronomy and Astrophysics is to understand the formation of the first structures in the early Universe and their physical properties, and this embraces several open questions. For instance, on the formation of the first stars: how to form stars starting from a chemically pristine composition of the gas, their mass distribution, how the first stars polluted and ionised the interstellar medium and triggered the formation of the next generation of stars, the physics of supernovae and the subsequent formation of heavy elements. Then the formation of larger structures: how do galaxies form, the distribution in size and mass of the first galaxies, the amount of their stellar, gaseous and dark matter content, the dichotomy between dwarf galaxies and globular clusters and their relation with the chemical content of the gas and the dark matter distribution. There are two ways to answer these questions. One is to observe at high redshift and, therefore, look back in time, when the Universe was a few billions of years old. The other way is to look at the chemistry and kinematics of stars formed in the early Universe that are still living and observable nowadays in the Milky Way and its satellites. This latter field is the so-called Galactic Archæology or Palæontology. Since these stars formed in the early and unpolluted Universe, they must be low-mass, and among the oldest and most metal-poor. From their chemical abundances it is possible to reconstruct the fossil record of the first generation of stars and their formation sites, while the dynamics of the most metal-poor stars might carry the imprints of the assembly and accretion history of the Milky Way. The following introduction focuses on the general properties of the most metal-poor stars, the Pristine survey as leading the investigation of this population of stars, the revolution started with the Gaia satellite and the synergy with ground-based surveys. The following chapters are a collection of works developed during my PhD, and they focus on the dynamical study of the most metal-poor stars using both observations (Chapters 2 and 3) and high-resolution cosmological simulations (Chapter 4).

1.1 The oldest and most metal-poor stars as witnesses of the early Universe

This Section will describe the main properties of the most metal-poor stars, in particular their importance, the expectations on where to find them, and a summary of the most important surveys of metal-poor stars, which will be followed by a Section describing one of the most efficient photometric survey hunting for the most metal-poor stars, the Pristine survey.

First, let's summarise the taxonomy of the metal-poor stars introduced by Beers & Christlieb (2005) and based on the content of metals in the stellar atmosphere.

1.1.1 What does it mean to be very/extremely/ultra (...) metal-poor?

Beers & Christlieb (2005) proposed a new nomenclature to better distinguish how much a star is lacking in metals. First, defining the metallicity as:

$$[\mathrm{Fe/H}] = \log_{10}\left(\frac{N_{\mathrm{Fe}}}{N_{\mathrm{H}}}\right)_{\star} - \log_{10}\left(\frac{N_{\mathrm{Fe}}}{N_{\mathrm{H}}}\right)_{\odot}, \tag{1.1}$$

where N_X is the number of atoms of a given species, Equation 1.1 provides the ratio between the number of the metal atoms and the atoms of hydrogen for a star relative to the Sun. Because the abundance of Iron is strongly related to the total content of metals, as a first order, [Fe/H] = [M/H]. With this definition, Beers & Christlieb (2005) proposed the nomenclature listed in Table 1.1.

Table 1.1: Nomenclature of the stars based on the metallicity as proposed in Beers & Christlieb (2005).

[Fe/H]	Term	Acronym
$> +0.5$	Super metal-rich	SMR
~ 0.0	Solar	–
< -1.0	Metal-poor	MP
< -2.0	Very metal-poor	VMP
< -3.0	Extremely metal-poor	EMP
< -4.0	Ultra metal-poor	UMP
< -5.0	Hyper metal-poor	HMP
< -6.0	Mega metal-poor	MMP

Beers & Christlieb (2005) also provided a subclassification of the metal-poor stars into groups based on the abundance of Carbon and neutron-capture elements, such as Europium and Barium. Neutron-capture elements can be divided into two main groups according to the timescale of the nuclear reactions in which they were produced. If this timescale is much shorter than the time needed by the β^--decay[1], as in the case of the core-collapse phase of the supernovae and the subsequent nucleosynthesis, then rapid-process (hereafter r-process) elements are formed. Other environments and phenomena with energies

[1] β^--decay is the nuclear process from which a neutron decays into a proton, an electron, and an electron antineutrino, i.e., $\mathrm{n} \rightarrow \mathrm{p} + \mathrm{e}^- + \overline{\nu}_{\mathrm{e}}$

and densities capable of producing r-process elements are neutrino-driven winds in supernovae, collapsars, binary neutron star mergers, and even neutron-rich regions in the early Universe according to inhomogeneous cosmological models (Kajino et al., 2019, and references therein). On the contrary, if the timescale for their synthesis is much larger than the β^--decay, as in the stellar atmosphere of asymptotic giant branch stars (AGB), then these elements are named slow-process (hereafter s-process) elements. Both Europium and Barium are formed in r- and s-process nuclear reactions, with the former that is mostly formed with r-processes. A ratio of the abundances of these two elements, [Ba/Eu] can help to better distinguish what was the main channel that formed the neutron-capture elements in a given metal-poor star. In particular, the most metal-poor stars with r-process enhancement and weak s-process elements are thought to be among the oldest objects, and formed within 300 Myr after the formation of the first stars (e.g., Frebel & Norris, 2015; Hill et al., 2017; Ji & Frebel, 2018).

It has been observed that a large fraction of the most metal-poor stars are enriched in Carbon, e.g., 15 – 20 per cent in the VMP regime and 40 per cent in the EMP regime (Yong et al., 2013; Lee et al., 2013; Placco et al., 2014). This large fraction of Carbon enhanced stars might be related to stellar processes in the early Universe (proceeding differently than nowadays because of a lack of metals in their atmospheres), or to binarity. If the carbonicity is coupled with abundance of neutron-capture elements, it can provide an excellent tool to unveil the origin of the progenitor of that particular metal-poor star and to have an overview of the physical processes in a metal-devoid environment. Multiple scenarios have been proposed to explain the enhancement in Carbon. For instance, mass-exchange in a binary system: if the companion reached the asymptotic giant branch, it would pollute the atmosphere of the CEMP star with Carbon and s-process elements. On the other hand, CEMP stars not enhanced in s-process elements are likely to be single stars (Starkenburg et al., 2014) in which the Carbon has been produced in the progenitor. Massive and rapidly rotating UMP stars in the early Universe (Meynet et al., 2006, 2010), or faint supernovae (Tominaga et al., 2014), can produce high quantity of Carbon. Arentsen et al. (2019) showed that a fraction of the CEMP stars with no enhancement in s-process are in a binary system and open to the possibility that multiple scenarios can produce such feature. Therefore, a subclassification based on carbonicity coupled with neutron-capture elements might help to distinguish the progenitor of these metal-poor stars. Table 1.2 reports the subclassification of the metal-poor based on Europium, Barium, and Carbon as introduced by Beers & Christlieb (2005).

Table 1.2: Definition of the metal-poor subclasses as proposed in Beers & Christlieb (2005).

Term	Properties
Neutron-capture-rich stars	
r-I	$0.3 \leq$ [Eu/Fe] ≤ 1.0 and [Ba/Eu] < 0.0
r-II	$0.3 \leq$ [Eu/Fe] > 1.0 and [Ba/Eu] < 0.0
s	[Ba/Fe] > 1.0 and [Ba/Eu] > 0.5
r/s	$0.0 <$ [Ba/Eu] < 0.5
Carbon Enhanced metal-poor stars	
CEMP	[C/Fe] > 1.0
CEMP-r	[C/Fe] > 1.0 and [Eu/Fe] > 1.0
CEMP-s	[C/Fe] > 1.0, [Ba/Fe] > 1.0, and [Ba/Eu] > 0.5
CEMP-no	[C/Fe] > 1.0 and $0.0 <$ [Ba/Fe] < 0.0

1.1.2 Why metal-poor stars are important?

Stars with low abundances of metals can provide precious information and open a window on the early Universe. As the early Universe expanded, and the decoupling between radiation and matter produced the Cosmic Microwave Background (CMB), the temperature of the baryons decreased until the first recombination happened, producing the lightest elements, such as Hydrogen, Helium, and a small amount of Lithium. Measuring the Lithium in the most metal-poor stars can provide an estimate of its primordial abundance, and therefore we can better infer the content of the baryons and the baryon to photon ratio in the early Universe.

The composition of these chemically pristine stars is also helpful for inferring the properties of the first stars and how they polluted the interstellar medium (ISM). The first stars, also called Population III stars, are the necessary channels to form for the first time the elements heavier than Lithium, and contribute to polluting the ISM with their ejecta and supernovae. The upper and lower limits of the mass and the distribution of the first stars, i.e., the initial mass function of these objects, are still open questions in physics and astronomy. Several authors point out that first stars should be more massive than the most massive stars we can find nowadays, spanning a range between few tens to few thousands of solar masses (e.g., Omukai & Palla, 2001; Bromm et al., 2002; Stacy et al., 2010; Loeb, 2010). The main reason for such massive stars is the lack of an efficient coolant in the ISM. Star forming regions in the early Universe were composed of Hydrogen, Helium, Lithium, and molecular Hydrogen, with the latter component playing the role of the main coolant. With the absence of metals[2], the temperature and density in star forming regions of the early Universe are higher than those we can expect at the present day. This allows to form such massive protostellar object with a balance between the radiation and the gravitational force (e.g., Loeb, 2010, and references therein). More recent studies (e.g., Greif et al., 2011; Stacy et al., 2016; Hirano & Bromm, 2017; Vorobyov et al., 2018) show that it is possible to form first stars with a lower mass of about $\sim 0.1\,M_\odot$ thanks to turbulence and fragmentation. A massive forming first star can induce instabilities in its circumstellar disk, and the subsequent fragmentation will produce the ideal conditions in temperature and density to form low-mass stars, as shown

[2] In Astronomy, the metals are all the chemical elements heavier than Helium.

in Figure 1.1. Therefore, these authors open up the scenario that low-mass, and therefore unpolluted, first stars are still present and possibly observable in the present Universe. The subsequent generations also contain a lot of information about the first stars and it is possible to trace the elements produced in the explosions of the first supernovae, since it is reasonably thought that the ISM has been polluted by few supernovae explosions.

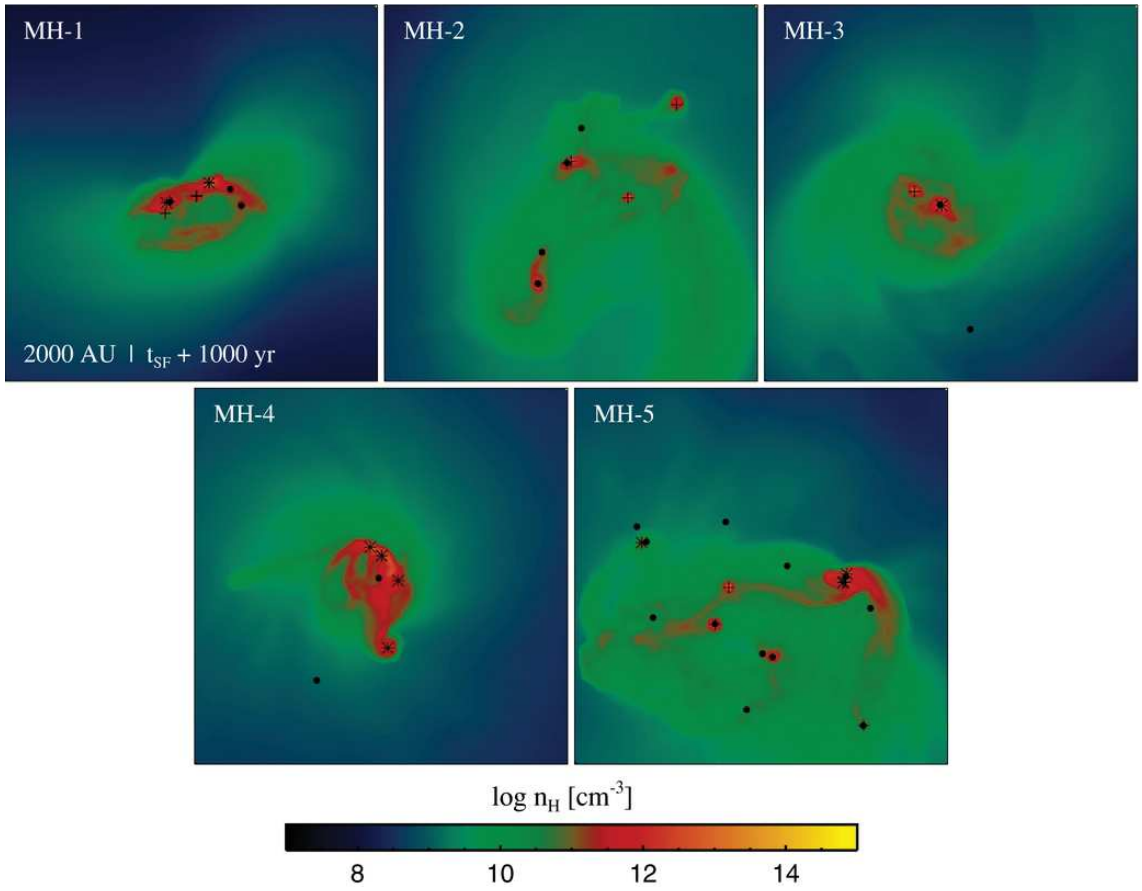

Figure 1.1: First stars formation from Greif et al. (2011). The star forming regions is fragmented and the formation of low-mass first stars is allowed. Protostars with masses below 1 $M_\odot$, between 1 $M_\odot$ and 3 $M_\odot$, and above 3 $M_\odot$ are denoted by black dots, crosses, and asterisks, respectively. Each panel has a size of $2000 \times 2000\,AU^2$ and represents a different halo simulation, colour-coded by the neutral hydrogen density. Fragmentation and cooling mechanisms play a crucial role in the formation of low-mass Population III stars.

The spatial and kinematical distributions of the most metal-poor stars are also informative on the formation and evolution of galaxies, either large galaxies, such as the Milky Way and Andromeda, or also dwarf galaxies. Together with their chemistry, the study of the most metal-poor stars can better characterise the properties of their formation sites.

Historically, metal-poor stars have been observed to shed light on the formation and structure of the Milky Way. For instance, Baade (1946, 1951) studied metal-poor RR Lyrae stars to better characterise the shape and the stellar distribution of the inner region of the Galaxy, since the study of the morphology of the Milky Way was still in its pioneering phase. The RR Lyrae are a class of periodic variables on the horizontal branch and, thanks to the

precise relation between the pulsation period and their luminosity, they can be used as standard candles for the determination of distances across the Galaxy. Another historical example about metal-poor stars as tracers of the early assembly of the Milky Way was investigated by Eggen et al. (1962). They computed eccentricities and angular momenta from the velocity vectors of 221 dwarf stars. The sample was composed of stars at various metallicities. Eggen et al. (1962) found that the metal-poor population has a large ultraviolet excess explainable with their lack of metals in the atmosphere, hence these two quantities correlate. Moreover, coupling these stellar atmospheric properties with kinematics, Eggen et al. (1962) found that the ultraviolet excess, hence the metallicity, is well correlated with the eccentricity. In particular, the authors pointed out that the metal-poor stars (larger UV excess) have larger eccentricities and small angular momenta, while the metal-rich population have small eccentricities and large angular momenta, due to their circular orbits. Eggen et al. (1962) concluded that the difference in the kinematical properties of the two population are strictly connected to the formation of the Milky Way. For instance, the collapse of the material that formed the proto-galaxy was moving radially inward bringing the first stars (the most metal-poor) and the gas with the same high-eccentricity orbits. As the cosmic time passes, in 0.1 Gyr, the stellar and gaseous orbits decoupled, with the latter component forming a disk and circularising its motion. As the gas settled and heated, the metal-rich population formed with low-eccentric orbits.

As it will be introduced in the following Sections, nowadays we can benefit from a much larger sample of metal-poor stars and the combination of chemical and kinematical information will shed lights on the assembly and evolution of out Milky Way. This information can be complemented by state-of-the-art cosmological simulation to better interpret the observational results.

1.1.3 Where to find the most metal-poor stars?

In the last two decades, several theoretical studies investigated where the most metal-poor stars are expected to be observed (e.g., White & Springel, 2000; Brook et al., 2007; Salvadori et al., 2010; Tumlinson, 2010; Starkenburg et al., 2017a; El-Badry et al., 2018) to better understand the assembly history of the Milky Way, and galaxies in general. White & Springel (2000) with high-resolution zoom-in numerical simulations predicted that the oldest population are centrally concentrated, finding that the ~ 60 per cent are distributed within the 10 kpc from the centre of the simulated galaxy. White & Springel (2000) also pointed out that the age does not necessarily correlate with metallicity, showing that low metallicity stars can be found in younger and isolated dwarf galaxies. With this picture, they reported that only 16 per cent of the low-metallicity stars populate the inner 10 kpc of the simulated galaxy, and the majority is distributed in the outer halo and satellites. Brook et al. (2007) used cosmological chemodynamical SPH simulations of Milky Way-analog galaxies to investigate the spatial distribution of Population III stars at both high-redshift and nowadays. Similarly to White & Springel (2000), they found that the distribution of the metal-free population differs from the oldest population. For instance, the latter is more concentrated in the bulge region, while the former is distributed through the halo of the simulated MW-analogs. Moreover, metal-free stars continue to form until redshift $z \sim 4$, i.e., ~ 2 Gyr after the Big Bang, in case of chemically isolated satellites.

Starkenburg et al. (2017a) used the APOSTLE Local Group simulations in order to predict where the most metal-poor and the oldest stars can be observed. The APOSTLE simulations set (Sawala et al., 2016; Fattahi et al., 2016) is composed of 12 halo pairs selected from the DOVE cosmological volume (Jenkins, 2013). These simulations reproduce the Local Group's main galaxies in their distance, their relative velocity, both radial and tangential, their total mass, and they are sufficiently isolated by smaller haloes. Starkenburg et al. (2017a) defined the oldest stars as the objects formed < 0.8 Gyr after the Big Bang (redshift $z > 6.9$), and the most metal-poor stars with [Fe/H] < -2.5. The authors decomposed the simulated galaxies into an inner region with $R \leq 15$ kpc from the galactic centre and the outer region with $15\,\text{kpc} < R \leq 100\,\text{kpc}$. They interestingly found that the majority of the oldest stars have a metallicity [Fe/H] ≤ -2.0, and hence are VMP, with a small tail reaching [Fe/H] < -1.0. While looking at the distribution in age of the most metal-poor stars, they found that 50 per cent have formed within 1.1 Gyr after the Big Bang and 90 per cent of them have formed within 2.4 Gyr. These results, shown in Figure 1.2, are in agreement in both the inner and outer regions of the simulated galaxies. Starkenburg et al. (2017a) also pointed out that the oldest stars are concentrated in the inner region of the galaxies, although in the outskirt the population is still old. Also the outer region of the galaxies, together with the satellites and the inner region, are ideal places to look for the most metal-poor stars. El-Badry et al. (2018) analysed the FIRE cosmological simulations (Hopkins et al., 2014; Wetzel et al., 2016). Other than the age and metallicity distribution of the oldest and most metal-poor stars, in agreement with Starkenburg et al. (2017a), El-Badry et al. (2018) analysed also their spatial and kinematical distribution. They found that the majority of the oldest stars are accreted during the hierarchical assembly, i.e., ex-situ, and distributed in a pressure-supported fashion, i.e., a non-rotating spheroid. The in-situ counterpart, formed in the inner part of the galaxy, have been driven outwards either by bursty star formation and by variation in the gravitational potential across cosmic time. The kinematical distribution of the stars from El-Badry et al. (2018) is shown Figure 1.2, while the schematic illustration of the assembly of the simulated galaxies is shown in Figure 1.3.

The aforementioned works agree that it is likely to find the most metal-poor stars, and also the oldest, distributed in a pressure-supported spheroid, i.e., the halo, in the inner region of the Galaxy, i.e., the bulge, and in dwarf satellites. Since the halo intersects the disk, the spheroidal distribution will also allow for some of these oldest stars to transit through the disk region, or even resemble the kinematics of the younger and more metal-rich population. In case of the latter kind of motion, one should expect to find, approximately, the same number of progrades and retrogrades. So far, cosmological simulations and observational surveys were focusing on their global and predominant distribution, while in the following Chapters (see also Sestito et al., 2019, 2020a,b), I will investigate the detection of a population of low-metallicity stars confined to the Milky Way disk. In particular, this population is largely favouring the prograde motion, hard to reconcile with a non-rotating spheroidal distribution.

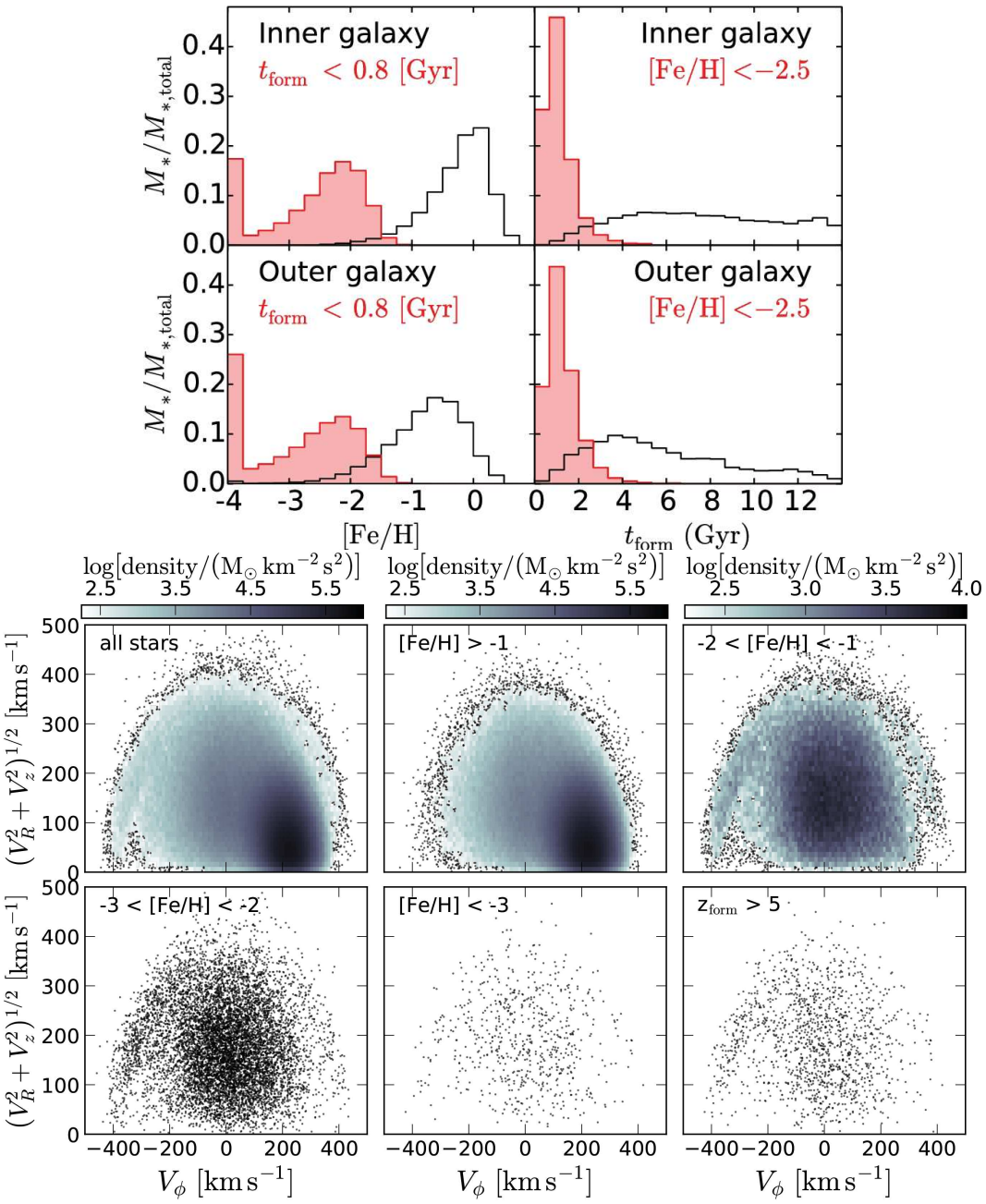

Figure 1.2: Distribution in age, metallicity and velocity of the most metal-poor and oldest stars. Top panels from Starkenburg et al. (2017a): on the left, the metallicity distribution of the oldest stars ($t_{form} < 0.8$ Gyr) in the inner and outer regions of the simulated galaxies in the APOSTLE simulations. On the right, distribution in the formation time for the most metal-poor stars ([Fe/H] < -2.5). These panels clearly show how the majority of the oldest stars are distributed in the VMP regime, and the majority of the most metal-poor stars were formed within 3 Gyr. Bottom panels from El-Badry et al. (2018): kinematical distribution in the rotational component of the velocity v_ϕ vs. the sum of the radial and vertical components $(v_R^2+v_z^2)^{1/2}$. Stars have been divided into metallicity bins, while the bottom right panel shows the stars formed at redshift $z > 5$. The most metal-poor and the oldest stars are distributed in a non-rotating spheroid, while at higher metallicity, there is a high density peak coincident with the disk ($v_\phi \sim 200\,\mathrm{km\,s^{-1}}, (v_R^2+v_z^2)^{1/2} \leq 100\,\mathrm{km\,s^{-1}}$).

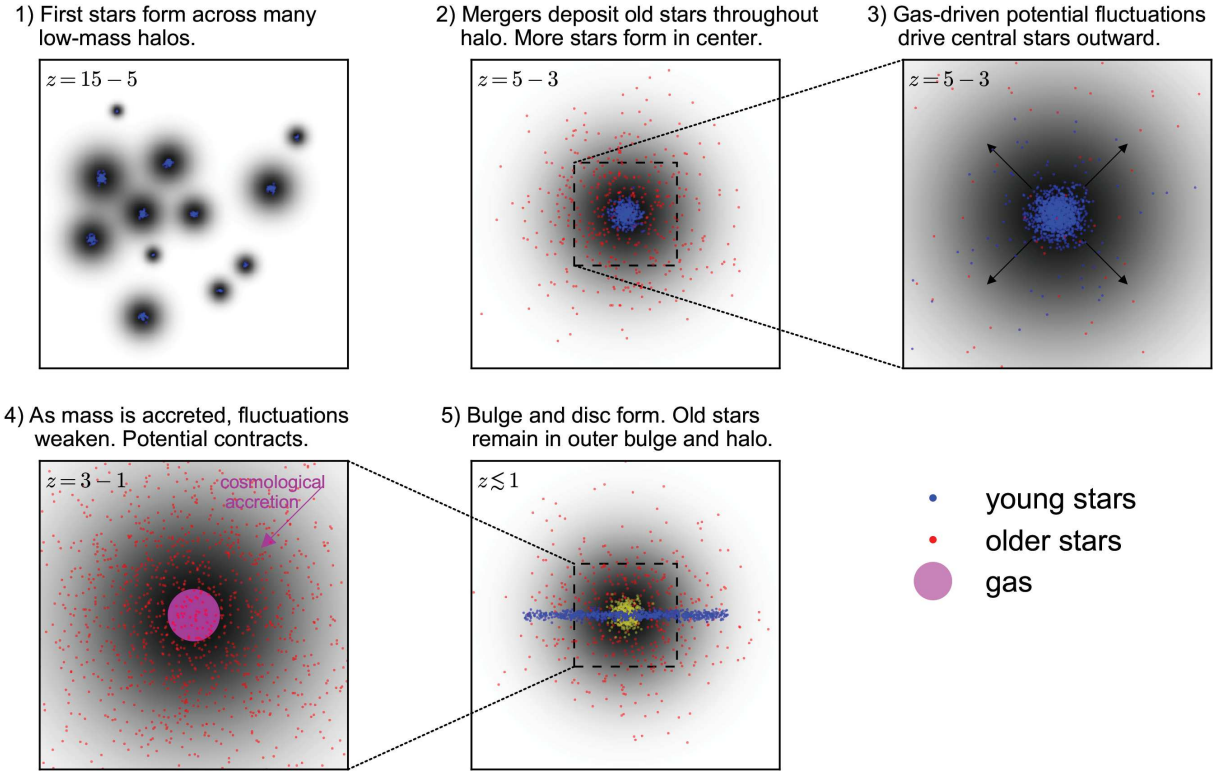

Figure 1.3: Sketch of the assembly of the galaxies and the subsequent stellar distribution as discussed in El-Badry et al. (2018). At very high redshift ($z > 5$, panel 1), the first stars are forming in the low-mass haloes, and then merging to form the proto-galaxy ($3 < z < 5$, panel 2) and depositing the stars in the inner region. Energetic gas-driven processes are moving the stars outwards, while younger stars are forming ($3 < z < 5$, panel 3). After the potential settled ($1 < z < 3$, panel 4), the bulge and disk formed ($z < 1$, panel 5), while the oldest and most metal-poor stars are distributed in the bulge and halo.

1.1.4 How to find the most metal-poor stars?

By definition, metal-poor stars have a low content of metals in their atmospheric composition, and therefore the lower the metallicity, the weaker the iron lines in the spectra. However, it is possible to infer the metallicity from the Ca II H and K lines (3968, 3933Å). This doublet has been demonstrated to be an excellent proxy for the Iron content and sufficiently strong to be well measured in the most metal-poor stars. In this subsection, I will report on the methods and results of some of the most important surveys used for the discovery of the most metal-poor stars while, in the following Section, I will describe in depth the Pristine survey (Starkenburg et al., 2017b), that I am a member of.

One of the pioneering surveys hunting for these rare and metal-devoid objects was the HK survey (Beers et al., 1985), based on a combination of objective-prism plates and a narrow filter centred on the Ca H&K doublet, capable of reaching magnitudes of $B \sim 15.5$. The HK survey started to cover an area of ~ 1940 deg^2 in the southern hemisphere using a total of 80 photographic plates. The HK survey found a heterogeneous ensemble of celestial objects, with the majority of these being hot stars (A and B types) and sun-like stars with strong Ca H&K lines (G and K types). The minority of this ensemble ($\sim$ 1800 objects), that are objects

with weak Ca lines, have been selected to be metal-poor candidates. A subsequent spectroscopic follow-up campaign revealed that this subsample is composed of a large variety of objects, and not only metal-poor stars (Beers et al., 1985). For instance, symbiotic stars, cataclysmic variables, subdwarf O stars, white dwarfs, K and M Ca II emission line stars, and even extragalactic objects such as Seyfert galaxies. The final number of confirmed very metal-poor stars ([Fe/H] ≤ -2.0) was 134, out of a starting sample of 1800 objects. To point out the rarity of stars as the metallicity decreases, they found only 5 stars with [Fe/H] ≤ -3.5, of which only one is ultra metal-poor ([Fe/H] ≤ -4.0). The continuation of this survey (e.g., Beers et al., 1992, 1999) extended the sample to a few thousand stars in the VMP regime, while in the UMP, the number remained lower than 10.

A second important survey leading the discovery of metal-deficient stars is the Hamburg/ESO survey (HES) covering ~ 6700 deg^2 in the southern high Galactic latitude sky (Christlieb et al., 2002, 2008). HES combines the line strengths of the Calcium doublet inferred from objective-prism and broad band colours, such as $(B-V)$, to provide a more efficient selection of the metal-poor candidates. Moreover, HES was reaching 2 magnitudes fainter than the HK and, together, the total volume searched for the most metal-poor stars was increased by a factor of 10 (Christlieb et al., 2008). An interesting result, also summarised in Beers & Christlieb (2005) and confirmed by later studies (Arentsen et al., 2019, and references therein), is that as the metallicity decreases the carbonicity rapidly increases. The HES survey has been useful to map various regions of our Galaxy, since the number of metal-poor stars greatly increased. From their chemo-dynamical investigation (Beers et al., 2017), they discovered the presence of a population of metal-deficient stars ([Fe/H] > 2.5) in the Solar neighbourhood, with similar kinematics to the more metal-rich population of the disk. A population of stars confined to the disk of the Milky Way, although with lower metallicities, will be analysed in depth in the following Chapters (see also Sestito et al., 2019, 2020a). Beers et al. (2017) also proposed new candidates members for the Helmi stream (Helmi et al., 1999) and the tidal debris of ωCen globular cluster (see also Dinescu, 2002; Meza et al., 2005; Navarro et al., 2011).

The SkyMapper Southern Survey, among various Galactic and extragalactic scientific goals, is hunting for the most metal-poor stars in the southern hemisphere (Keller et al., 2007; Da Costa et al., 2019) with high efficiency. Thanks to a combination of medium-band filters, SkyMapper can provide a better selection of metal-poor candidates among the more metal-rich population, and provides an estimate of the photometric metallicities. This combination, showed in Figure 1.4, is composed of a temperature sensitive colour $(g-i)$ and a quantity sensitive to the metallicity absorption, namely $m = v - g - 1.5(g-i)$, in which the v filter is covering the Ca doublet region of the stellar spectrum. As shown in Figure 1.4, the most metal-poor stars are well separated from the more metal-rich population. The spectral range that is covered by the v filter is shown in comparison to the Pristine narrow-band Ca H&K filter in Figure 1.6. The spectroscopic follow-up provided the confirmation of the high efficiency of the SkyMapper Southern Survey in selecting the most metal-poor stars (Da Costa et al., 2019). In numbers, ~ 19 per cent of stars with photometric metallicity [Fe/H] ≤ -2.0 has a confirmed spectroscopic metallicity of [Fe/H] ≤ -3.0, while only ~ 7 per cent is not VMP, i.e., [Fe/H] > -2.0. As an example, this survey discovered the most Iron-poor star known SMSS J031300.36$-$670839.3 (Keller et al., 2014; Nordlander et al., 2017) with [Fe/H] < -6.5 and a large abundance of Carbon $A(C) \sim 6$.

To underline how rare the most metal-poor stars are, after 35 years from the first HK sur-

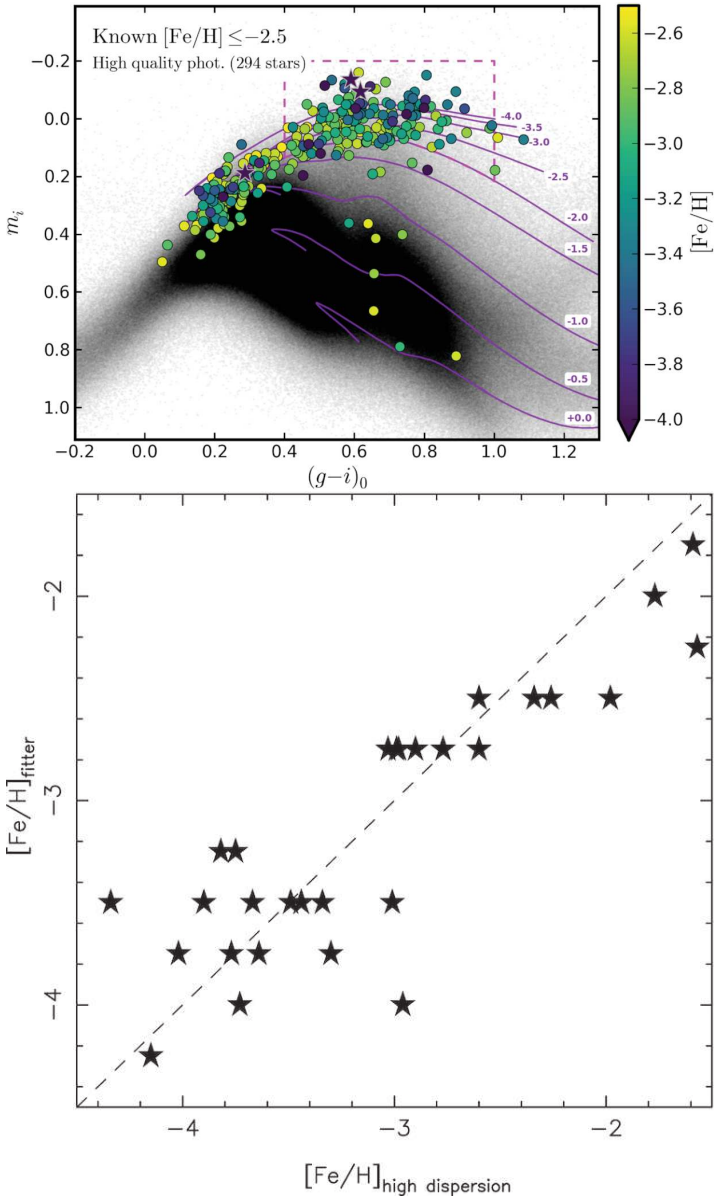

Figure 1.4: SkyMapper Southern Survey. Top panel: photometric selection of metal-poor star candidates from Da Costa et al. (2019). Known low-metallicity stars ([Fe/H] ≤ −2.5) have been colour-coded with their spectroscopic metallicity, while isochrones from the Dartmouth Stellar Evolution Database (Dotter et al., 2008) are shown with blue lines from metallicity from the solar to the UMP regime with a step of 0.5 dex and ages of 12.5 Gyr. The horizontal axis is temperature sensitive, while the vertical axis, that is defined to be $m = v - g - 1.5(g - i)$, is a proxy for metallicity. The most metal-poor stars are populating the region of this space close to the very metal-poor isochrones. Only a small fraction of the sample is dispersed in the higher metallicity region. Bottom panel: the high correlation between the high-resolution spectroscopic metallicity and the photometric ones inferred by the SkyMapper Survey (Da Costa et al., 2019).

vey investigation, only 42 stars in the ultra metal-poor regime have been discovered taking into account all the surveys (Sestito et al., 2019). Moreover, Youakim et al. (2017) estimate that, if we observe 800 random halo stars in the magnitude range of $14 < V < 18$ mag, only 1 is likely to be extremely metal-poor. As a matter of fact, one of the largest spctroscopic surveys, the Sloan Digital Sky Survey (SDSS, York et al., 2000), only discovered serendipitously a few UMPs (e.g., Caffau et al., 2011; Aguado et al., 2018a,b), although scanning the entire Sky. For instance, thanks to SDSS, the most metal-poor star known has been discovered (Caffau et al., 2011). Hence, if we want to build a large statistical sample of the most metal-poor, an extremely efficient selection of the candidates is crucial. In the following Section, the Pristine survey, one of the most high-efficiency surveys hunting for the most metal-poor stars, will be described in depth.

1.2 Hunting for the most metal-poor stars with the Pristine survey

The Pristine survey (Starkenburg et al., 2017b) is hunting for the most metal-poor stars in the Milky Way, and it is a photometric survey based on a narrow-band filter centred in the Ca H&K doublet, a proxy for metallicity. The Pristine filter is mounted on the MegaCam instrument at the Canada-France-Hawaii Telescope (CFHT), and therefore looking towards the North sky. The Pristine survey has been observing the sky and covering up to ~ 5000 deg^2. The projection of the Pristine footprint together with the map of the observed Milky Way is shown in Figure 1.5.

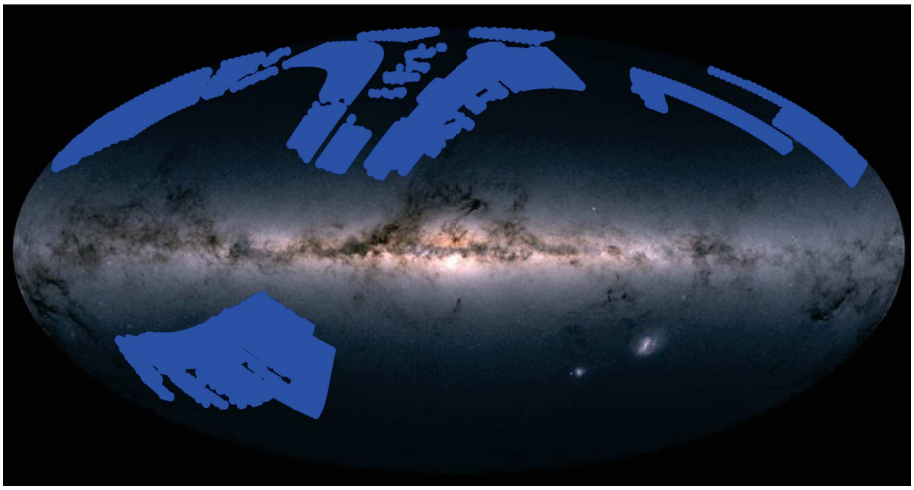

Figure 1.5: The Pristine footprint. The footprint of the Pristine survey (blue dots) is superposed to the Galaxy map provided by Gaia Data Processing and Analysis Consortium (DPAC). The Pristine survey is targeting the most metal-poor stars towards the direction of the Milky Way halo. For the Gaia DPAC, credit to: A. Moitinho / A. F. Silva / M. Barros / C. Barata, University of Lisbon, Portugal; H. Savietto, Fork Research, Portugal.

Discovering very metal-poor stars with narrow-band photometry is very efficient for various reasons. There is no need for a preselection of the targets, all the objects in a field of view are observed (modulo some chip gaps). Also, the integration time is much smaller compared to spectroscopic methods, and good weather conditions are not required.

The dependence of the Ca H&K equivalent width on surface gravity is much weaker in the very metal-poor regime than for metal-rich stars. Therefore the Ca doublet can be used as a good estimator of metallicity for these pristine stars. Figure 1.6 shows the behaviour of Ca H&K lines from synthetic spectra as a function of the effective temperature, surface gravity, and temperature. The higher the metallicity, the broader the Ca H&K absorption lines.

As shown in the bottom panel of Figure 1.6, in the spectral region around Ca H&K lines, C and N bands can be present and responsible for affecting the measurement of the metallicity. However, it has been shown (Starkenburg et al., 2017b), that the Pristine filter is so narrow that the inferred photometric metallicities are far less biased by the carbon and nitrogen bands compared to other broader band filters (e.g., the v filter from the SkyMapper Southern Survey Da Costa et al., 2019). However, a more quantitative analysis of the dependency and bias on the Carbon in Pristine filter is under development.

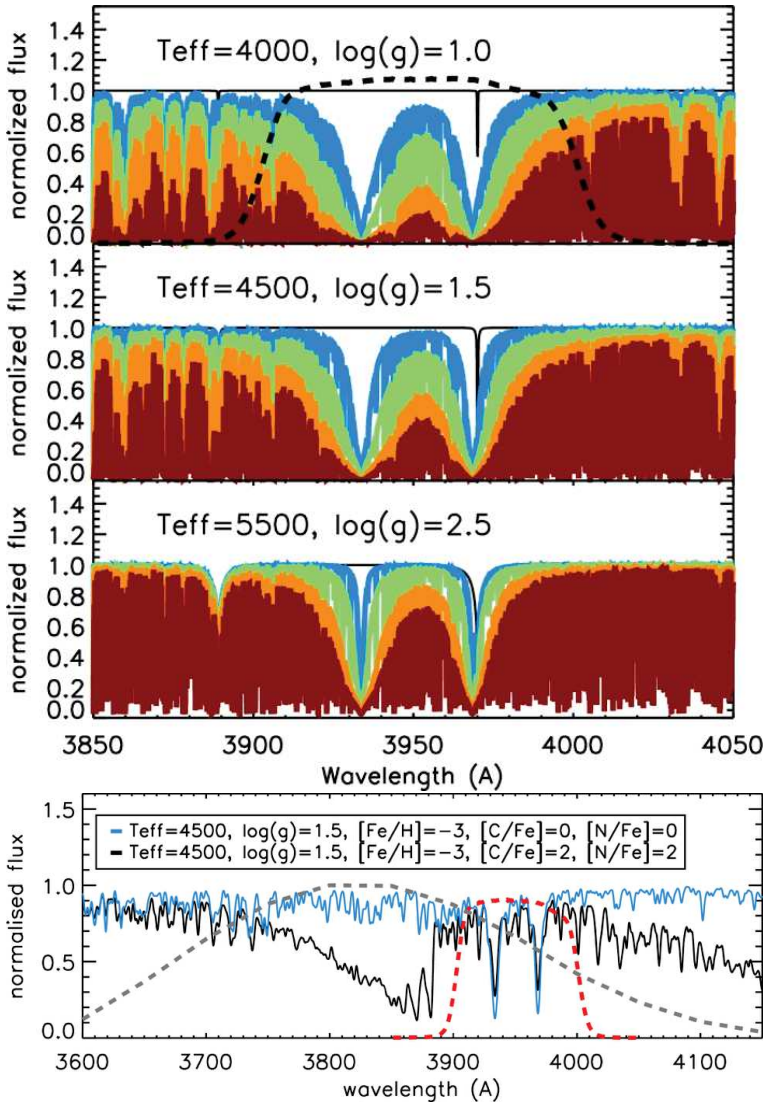

Figure 1.6: The Pristine Ca H&K filter. Top three panels: Synthetic stellar spectra with metallicity [Fe/H] = 0.0 (red), [Fe/H] = −1.0 (orange), [Fe/H] = −2.0 (green), [Fe/H] = −3.0 (blue), and no metals (black) for stars with different effective temperature and surface gravity. In the top panel, the Pristine filter is marked with a dashed line. Bottom panel: Comparison of the Pristine filter (red) and the SkyMapper v filter (gray). Overplotted two synthetic spectra of extremely metal-poor stars at the same effective temperature and surface gravity, but different Carbon and Nitrogen enhancement. The enrichment of Carbon and Nitrogen produces two absorption bands visible in the black spectrum. The Pristine filter, with its narrow design, is much less biased by these absorption features compared to a broader v filter. Figure from Starkenburg et al. (2017b)

1.2.1 The photometric metallicity calibration

In order to measure photometric metallicities, the Pristine filter is coupled with broad-band photometry (e.g., SDSS, APASS, Gaia DR2 etc.). A first investigation of the feasibility of deriving the photometric metallicity was done using synthetic spectra generated with Model Atmospheres in Radiative and Convective Scheme (MARCS, Gustafsson et al., 2008) and TURBOSPECTRUM (Plez, 2012) and attempting to find a colour-colour space capable of disentangling the stars according to their metallicity. This diagram is shown in Figure 1.7. The horizontal axis, the $(g-i)$ colour from SDSS (York et al., 2000), is temperature sensitive, while the vertical axis, sensitive to the absorption lines, is composed of a combination of the Ca H&K filter, the SDSS g filter, and a multiple of $(g-i)$. As shown in the left panel of Figure 1.7, the very metal-poor synthetic stars are well separated from their metal-rich counterpart. Moreover, the metallicity calibration in the very metal-poor regime at fixed effective temperature weakly depends on the surface gravity compared to the more metal-rich synthetic stars.

Then, a calibration with real objects observed at the CFHT with MegaCam was performed selecting stars overlapping with the SDSS footprint. For this step, the selected stars compre-

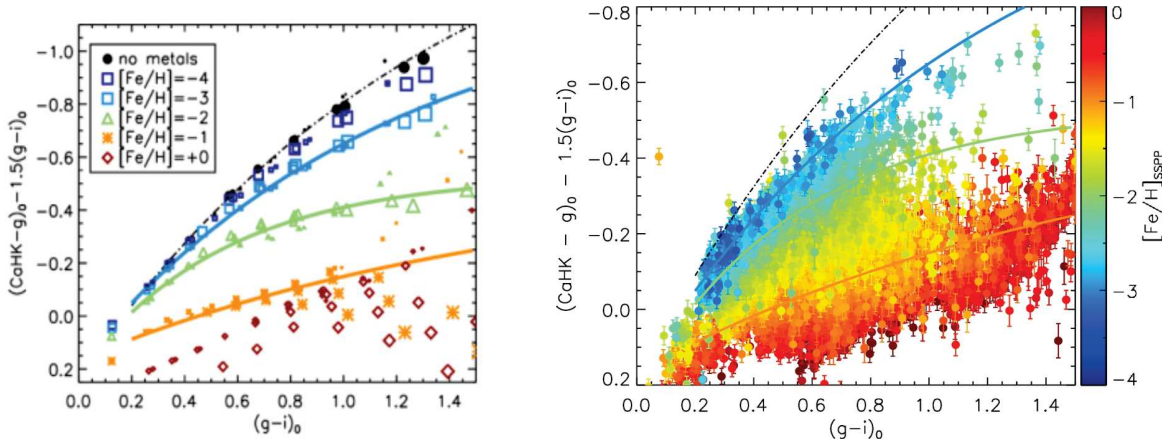

Figure 1.7: The Pristine colour-colour diagram. Left panel: Photometry extracted from syntheticstellar spectra at different metallicity, effective temperature, and surface gravity in the Pristine colour-colour diagram. Right panel: Overlapping of the stars in the Pristine footprint and SDSS/SEGUE plotted in the Pristine colour-colour diagram. In both panels, the solid lines represent the curve fitting of the photometric metallicity colour-coded as the markers. The colour $(g-i)$ is a proxy of the effective temperature, while the vertical axis is an indicator of the metallicity. Figure from Starkenburg et al. (2017b).

hend the sample with $ugriz$ photometry and measured spectroscopic metallicities from the SDSS/SEGUE (Yanny et al., 2009; Eisenstein et al., 2011) survey (see right panel of Figure 1.7). The latter is a spectroscopic survey providing metallicities and stellar parameters from spectroscopy, reaching an overlap of about $\sim 18{,}000$ stars. To better calibrate the Pristine photometric metallicities, several cleaning steps are applied to the SDSS/SEGUE sample as described in Starkenburg et al. (2017b). The first step is to remove stars with large uncertainties on the metallicity, δ[Fe/H] ≥ 0.2, and on the radial velocity, $\delta v_r \geq 10\,\mathrm{km\,s^{-1}}$. A second cut was applied to stars with signal-to-noise ratio below 25 in the spectral range [4000, 8000]Å. Then, non-point sources identified by SDSS and by the Cambridge Astronomical Survey Unit pipeline (CASU, Irwin & Lewis, 2001) have been removed from the SDSS/SEGUE sample to improve the Pristine colour-colour metallicity calibration. A removal of variable objects present in Pan-STARRS1 (Chambers et al., 2016) is needed for a better calibration. White dwarfs are also contaminating the sample, therefore a photometric cut has been applied to remove these degenerate objects, selecting stars with $(u-g)_0 \geq 0.6$ mag. In this era of large and all-sky surveys, it is possible to cross-match data between the various surveys and retrieve much easily information on the nature of the targets, and, therefore, the removal of contaminants from the metal-poor candidate list is far more efficient than in the past. For comparison, back in the years of the HK survey, the majority of the observed metal-poor candidates were contaminants, such as hot stars, variables and cataclysmic objects, white dwarfs, emission line stars, etc.

Now that the sample is filtered, the colour-colour space in Figure 1.7 is pixelated with a width of 0.025 mag. As described in Starkenburg et al. (2017b), for each bin or pixel, an average of the metallicity with a 2σ clipping is performed. This latter procedure is needed to better remove possible contaminants still present after the previous cleaning steps. Because extremely metal-poor stars are rare objects, some regions of the Pristine colour-colour dia-

gram are not populated. Therefore, the photometric metallicity of empty pixels has been put equal to the nearest bins. According to Starkenburg et al. (2017b), the photometric metallicities produced by the SDSS calibration can reach an accuracy of ~ 0.2 dex down to the extremely metal-poor regime, while the calibration starts to saturate in the ultra metal-poor regime. The latter issue does not implicate the failure of the Pristine survey in the discovery of ultra metal-poor stars (see Section 1.2.3), while it suggests a suboptimal calibration at this metallicity regime. Once the Pristine space is calibrated and the photometric metallicities are calculated over a footprint of ~ 5000 deg^2 (see 1.5), then the most promising candidates was spectroscopically followed-up.

1.2.2 The spectroscopic follow-up

Once stars in the Pristine footprint are observed with the Ca H&K filter and assigned a photometric metallicity, the most metal-poor stars are spectroscopically followed-up with low-, medium-, or high-resolutions spectrographs, according to their magnitudes. Fainter objects are spectroscopically follow-up with low- and medium-resolution spectrographs. While spectra of bright targets are acquired with high-resolution facilities. For instance, these latter targets have been observed at CFHT with ESPaDOnS, at VLT with UVES, at OHP with SOPHIE, and at CAHA with CAFÉ and then analysed by Caffau et al. (2017), Bonifacio et al. (2019) (see appendix A), Venn et al. (2020) (see appendix B), and Caffau et al. (2020).

Aguado et al. (2019) show the results of a 3-year medium-resolution spectroscopic campaign with a sample of 1007 very metal-poor candidates. The stars have been observed, at least with a signal to noise ratio of about 25, with IDS ($R \sim 3300$) at the Isaac Newton Telescope, with ISIS ($R \sim 2400$) at the William Herschel Telescope, and with EFOSC2 ($R \sim 900$) at the New Technology Telescope. The spectra have been analysed using `FERRE` (Allende Prieto et al., 2006), providing the metallicity and the carbon abundance.

Defining the success rate as the ratio between the number of stars with spectroscopic [Fe/H] below a certain value, $N([\mathrm{Fe/H}]_{spec} < X)$, and the number of stars with photometric [Fe/H] below the same value, Youakim et al. (2017) and Aguado et al. (2019) show that the success rate for the Pristine survey is 23 per cent for [Fe/H] ≤ -3.0, and 56 per cent for [Fe/H] ≤ -2.5. The comparison between the photometric and the spectroscopic metallicity for the stars presented in Aguado et al. (2019) is shown in Figure 1.8.

Then from a first spectroscopic investigation, the most promising metal-poor stars are observed using high-resolution spectrographs, as in the case of Pristine_221.8781 + 9.7844 (Starkenburg et al., 2018) described in the following subsection.

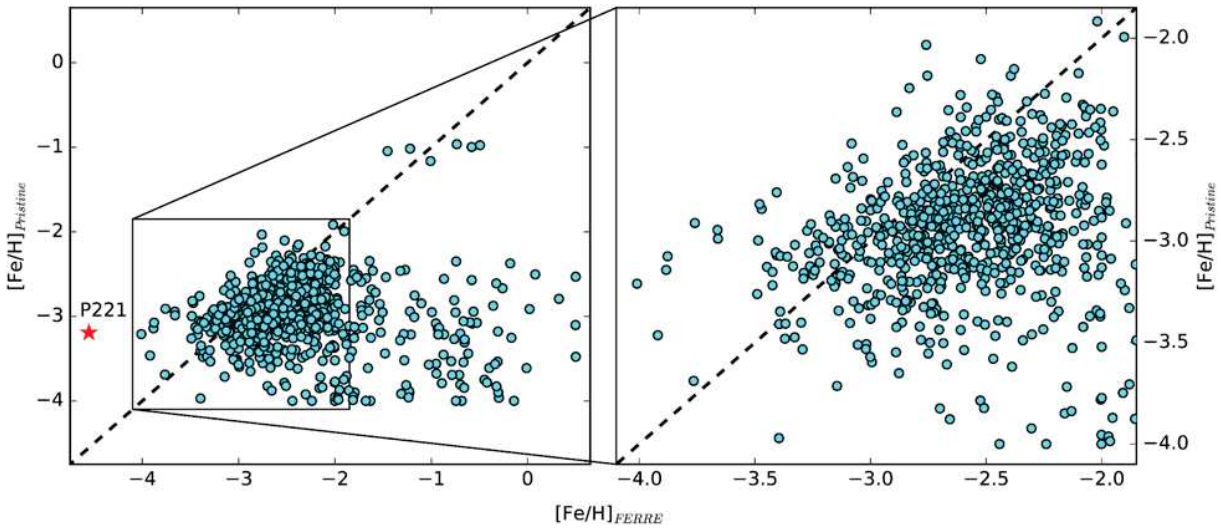

Figure 1.8: Photometric vs. spectroscopic metallicity from Aguado et al. (2019). The spectroscopic metallicity inferred with FERRE on the horizontal axis are compared to the photometric metallicity from Pristine for the sample of 1007 very metal-poor candidates. The right panel is a zoom on the most crowded region of the left panel. Pristine_221.8781 + 9.7844, an ultra metal-poor star discovered by the Pristine collaboration (see Section 1.2.3), is marked with a star. This comparison displays the high efficiency of the Pristine survey in selecting very metal-poor stars with photometry.

1.2.3 One of the most metal-poor star: Pristine_221.8781 + 9.7844

As previously described, the Pristine survey is hunting for the most metal-poor stars in the Milky Way. The finding of the most metal-poor stars can also be instructive to better understand the mechanisms that produced the observable amount of elements in the stars, starting from a mixture of Hydrogen, Helium, and Lithium in the early Universe. The Pristine survey was able to discover so far one star in the ultra metal-poor regime ([Fe/H] ≤ -4.0), called Pristine_221.8781 + 9.7844 (Starkenburg et al., 2018). The star was spectroscopically followed-up at medium-resolution with the WHT using ISIS (R$\sim$ 2400) and at high-resolution at ESO/Very Large Telescope with UVES (R$\sim$ 30000). The analysis of the high-resolution spectra was conducted using four different and independent techniques in order to better quantify the different sources of uncertainties and systematics, and to provide robust measurements of the chemical abundances, crucial in this regime of metallicity. Very briefly, the methods consist in the use of FERRE (Allende Prieto et al., 2006), of MyGIsFOS (Sbordone et al., 2014), two codes that are fitting the spectral lines given a stellar grid of synthetic spectra. The third and the fourth are DAOSPEC (Stetson & Pancino, 2008) and IRAF (Tody, 1986, 1993), which use the classical equivalent width approach. While the analysis of the medium-resolution spectra was done using FERRE only.

In the ultra metal-poor regime, the estimation of the stellar parameters and abundances is a difficult problem and, even with high-resolution spectra, it is not trivial to break the dwarf/giant degeneracy. Anticipating on Section 1.3, thanks to the parallax provided by Gaia DR2, it was possible to break the aforementioned degeneracy for Pristine_221.8781 + 9.7844. The inference of the distance from the parallax suggests that the star cannot be a dwarf, as also shown in Sestito et al. (2019). With this information, the spectroscopic analysis found

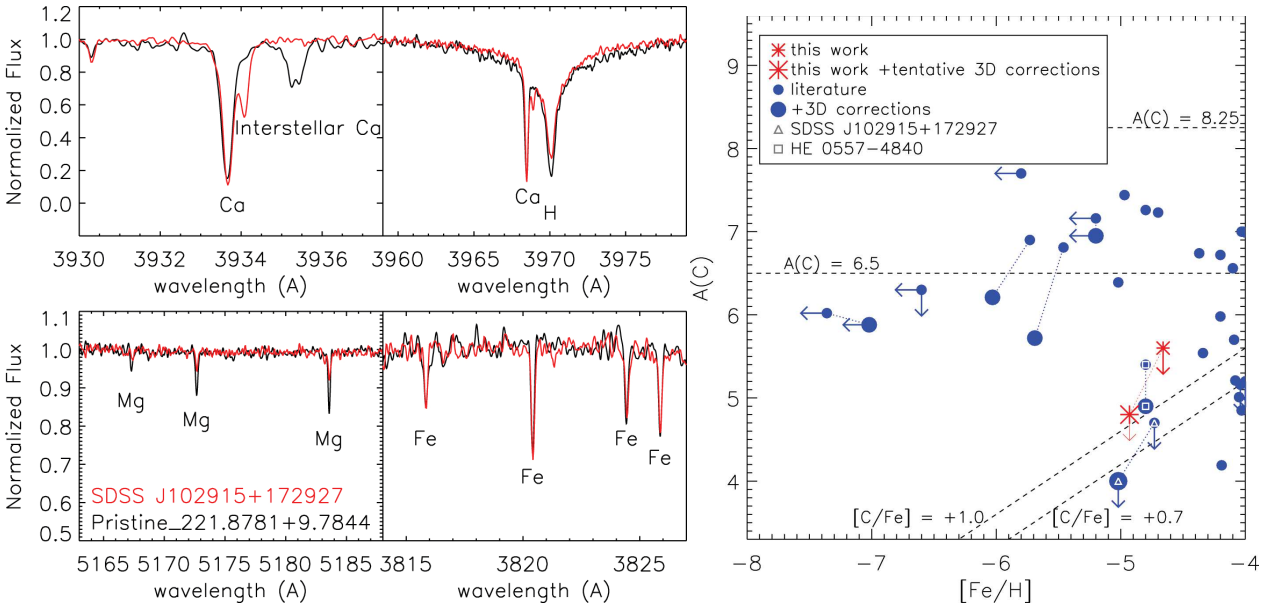

Figure 1.9: Pristine_221.8781 + 9.7844 vs. other UMP stars. Left panels: comparison between the spectra of Pristine_221.8781 + 9.7844 (black line) and of the Caffau star (SDSS J102915+172927, red line). Examples of Iron, Magnesium, and Calcium lines are shown. These panels clearly show the similarity between the two stars, and the ultra metal-poor nature of Pristine_221.8781 + 9.7844. Right panel: Carbon abundance vs. [Fe/H] for the UMPs. Tentative 3D corrections to the spectroscopic analysis has been provided for a subsample of the UMP (Starkenburg et al., 2018). The low Carbon abundance of Pristine_221.8781+9.7844, together with its low [Fe/H], places this star as one of the most metal-poor known. All the panels are from Starkenburg et al. (2018).

that Pristine_221.8781 + 9.7844 has [Fe/H] = −4.66 ± 0.13, with an upper limit for the Carbon abundance of $A(C) = 5.6$, a very unusual low Carbon abundance for this regime of metallicity (Starkenburg et al., 2018). The combination of these values place this star as one of the most metal-poor star known, similarly to the Caffau star (SDSS J102915+172927, Caffau et al., 2011). The comparison between the spectra of the two stars is shown on the left panels of Figure 1.9. The right panel of Figure 1.9 reports the abundance of Carbon as a function of the metallicity for the ultra metal-poor stars, as shown in the work of Starkenburg et al. (2018). To be noted, in this particular metal-poor regime, the total metallicity can differ from the abundance of Iron ([Fe/H]), and therefore a star, such as Pristine_221.8781+9.7844 ([Fe/H] = −4.66), can be more metal-poor than a star at [Fe/H] ≤ −6.5, i.e., SMSS J031300.36−670839.3 (Nordlander et al., 2017). In the UMP regime, the majority of the stars is rich in Carbon, and new discoveries such as Pristine_221.8781 + 9.7844 can put more constraints on the multiple channels of the formation of elements and cooling mechanisms in the early Universe.

1.2.4 Other projects within the Pristine survey

The Pristine survey has a high efficiency in finding new very metal-poor stars, and it allows to investigate different regions of the Galaxy. Therefore, the scientific outcome of the Pristine survey is broad. As shown in Longeard et al. (2018, 2020), the Pristine survey is very efficient

in finding possible members of dwarf galaxies, since it is possible to efficiently select candidate members using the reliable photometric metallicities. Dwarf galaxies are interesting for various reasons, we can learn from them about the low-mass end of galaxy formation (e.g., Koposov et al., 2009), they are ideal places to test the cosmological standard model ΛCDM since they are thought to be dark matter dominated (e.g., Bullock & Boylan-Kolchin, 2017), and understanding their formation might also shed lights on the formation of other structures, for instance globular clusters (e.g., Willman & Strader, 2012).

Additionally, Arentsen et al. (2020) has shown that the Pristine survey will provide a better view of the very metal-poor tail of the Milky Way bulge, that it is important to better disentangle the multiple structures, such as the inner halo, the bar, and the disk, overlapping in the very few kpc at the centre of the Milky Way and connect them with the formation and evolution history of the Galaxy.

Starkenburg et al. (2019) pointed out that the coupling of the Pristine CaH&K filter and the SDSS ugr filters can also be used as a powerful tool to map the outer Milky Way halo finding Blue Horizontal Branch stars (BHBs). BHBs are excellent standard candles, and with their reliable distances they are ideal to constrain the size of the Galaxy and its gravitational potential, that is strictly linked to the dark matter content, and also better identify substructures, such as streams. From Starkenburg et al. (2019), it turns out that the Pristine CaH&K filter coupled with the broad band photometry, in particular with the u filter, it is an ideal diagnostic to discern the BHBs from the blue straggle (BS) stars, fainter and more compact objects that can contaminate the sample of BHB candidates.

Youakim et al. (2020) studied the metallicity distribution function (MDF) of the halo down to the EMP regime, which is very helpful to dissect the Galactic structures at different radii, and also to have an estimate on the number of globular clusters compared to the field population. This latter result shows that the lack of globular cluster in the extremely metal-poor regime is not caused by statistical undersampling, but rather points to a likely physical mechanism that prohibits extremely metal-poor GCs from forming or surviving.

1.3 The revolution of Gaia DR2

The Gaia satellite is a mission of the European Space Agency (ESA) with the aim of creating, for the very first time, a precise multidimensional map of the Milky Way consisting of more than one billion sources. Thanks to the astrometric and photometric data from this satellite, it is possible to better constrain the physical properties of the Galaxy, especially with the synergy of large spectroscopic surveys that are providing the chemical abundances of the stars. Chemodynamical studies can provide precious insights not only into the present composition of the Milky Way, but it would help to unveil the formation and the evolution of the Galaxy.

The Gaia telescope, placed at the second Lagrangian point of the Sun-Earth orbit, is scanning the whole sky measuring the photometry, the astrometry, and inferring stellar parameters of celestial objects, such as the asteroids in the Solar system, the stars in the Milky Way, and it is capable to reach extragalactic sources, e.g., quasars. In this work, the second data release of Gaia (hereafter Gaia DR2) was used to infer the distance and the orbital parameters of very metal-poor stars, using both the photometric and astrometric information from the Gaia catalogue.

1.3.1 Gaia DR2 contents

The Gaia DR2 catalogue was built on the data collected between the 25th July 2014 and the 23rd May 2016, spanning a period of 22 months of observations and it was released on the 25th April 2018. The main parameters that are used in the work of this thesis are the position on the sky, the right ascension (α) and the declination (δ), the astrometric parallax (ϖ), the proper motions in right ascension and declination (μ_α, μ_δ), the photometry (G, BP, and RP), and all the uncertainties on these quantities. Table 1.3 contains the number of sources for which Gaia DR2 provides the parameters, and it also shows a useful comparison with the first data release (Gaia DR1) in order to understand the improvement between the two releases. For instance, in Gaia DR2, the number of sources with measured coordinates, proper motions, and parallax (5-parameters sources) has increased by a factor 650 with respect to Gaia DR1. And for only 21.3 per cent of the sources, the parallax and the proper motion are not provided, vs. 99.8 per cent for Gaia DR1. As new products in Gaia DR2, that are absent in Gaia DR1, there are the photometry in the BP and RP bands, the effective temperature ($T_{\rm eff}$), the extinction and reddening (A_G and E(BP−RP)), the radial velocity among others, as listed in Table 1.3. All the quantities and information extractable from Gaia DR2, especially when combined with data from ground-based surveys, are contributing to improve our knowledge of the Milky Way. It is now possible to dissect the various structures that are composing the Galaxy, i.e., the thin and thick disk, the halo and the bulge, to discover accreted structures, to build a 3D map of the extinction, to better understand the Milky Way gravitational potential and the dark matter content, to better understand the stellar evolution and the physics related to it, a larger census of small objects in the Solar system etc. Moreover, large surveys can benefit from Gaia improving their selection with the accurate photometric and astrometric information.

Table 1.3: Gaia DR2 vs. DR1 outcome.

Parameters	Gaia DR2	Gaia DR1
Total number of sources	1,692,919,135	1,142,679,769
Number of 5-parameters sources ($\alpha, \delta, \mu_\alpha, \mu_\delta, \varpi$)	1,331,909,727	2,057,050
Number of 2-parameters only sources (α, δ)	361,009,408	1,140,622,719
Sources with mean G magnitude	1,692,919,135	1,142,679,769
Sources with mean BP-band photometry	1,381,964,755	0
Sources with mean RP-band photometry	1,383,551,713	0
Sources with radial velocities	7,224,631	0
Variable sources	550,737	3,194
Known asteroids with epoch data	14,099	0
Gaia-CRF sources	556,869	2,191
Effective temperatures (T_{eff})	161,497,595	0
Extinction (A_G) and reddening (E(BP−RP))	87,733,672	0
Sources with radius and luminosity	76,956,778	0

1.3.2 Gaia DR2 photometry

Gaia DR2 (Evans et al., 2018) provides the G photometric band for all the sources, while for ~ 80 per cent of them also lists the photometry in the BP and RP bands. The top-left panel of Figure 1.10 shows the transmissivity of the three Gaia bands as a function of the wavelength. As shown, the G band is a broad filter covering the spectral range between [330, 1050] nm, while the BP and RP bands are respectively covering [330, 680] nm and [630, 1050] nm. A combination of these passbands can be used as a temperature indicator (i.e. BP − RP). The other panels in Figure 1.10 show the typical uncertainty in the three Gaia passbands as a function of the magnitude. In the G band, the typical uncertainties in the bright region $G \sim$ 13 mag is around 1 millimag, while it reaches few tens of millimag at $G \sim 20$ mag. In the BP and RP bands, the the typical uncertainties at $G \sim 13$ mag is around a few millimag, while it reaches ~ 200 millimag at $G \sim 20$ mag.

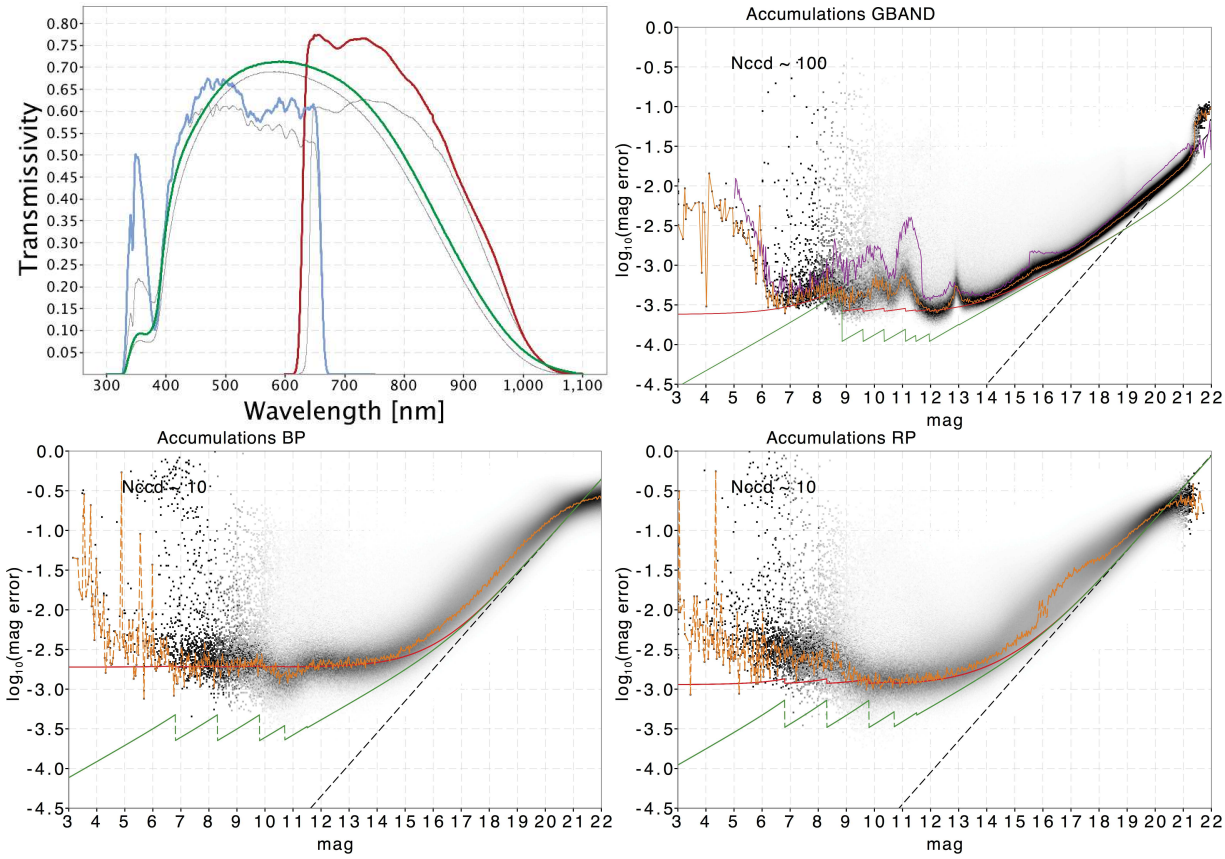

Figure 1.10: Gaia passbands properties. Top left panel: the observed transmissivity curve for the G (orange), BP (blue), and RP (red) filters is shown as a function of the wavelength. Grey lines show the theoretical expectation for the transmissivity curve. Top right and bottom panels: the error on the Gaia filters as a function of the magnitude. The errors are shown in logarithmic scale. Figure from Evans et al. (2018).

1.3.3 Gaia DR2 astrometric solutions

Gaia DR2 provides five astrometric parameters such as the position in the Sky (α, δ), the proper motion (μ_α, μ_δ), and the parallax (ϖ) for ~ 79 per cent of the sources as shown by Lindegren et al. (2018). All of these astrometric parameters are the key ingredients to infer the distances and the orbits of the stars.

Thanks to the accuracy of Gaia DR2, we are now living in the era where the uncertainty on the data are dominated by systematics and offsets, especially for bright targets. Therefore, when deriving other physical quantities, such as the distance and the orbital parameters, the systematics and offsets on the astrometric solutions must be taken into account. A good test bed for the offset of the parallax is to measure such quantity for a sample of quasars. The quasars are extragalactic and far objects, meaning that the parallax should be consistent with zero. In case of systematics and offsets, we should expect that the parallax, for instance, is distributed around the value of the offset, also including negative values. Lindegren et al. (2018) inferred the offset from quasars to be $\varpi_0 = -0.029$ mas.

Another issue to take into account is the possible negative values for the parallax, therefore one does not simply invert the parallax to calculate the distance. As shown by Bailer-Jones (2015); Bailer-Jones et al. (2018), even though the parallax measurement has a gaussian distribution (see left panel of Figure 1.11), when we represent it as a function of the distance, the obtained distribution is not symmetric anymore (see right panel of Figure 1.11), this is clearly visible when the relative uncertainty is higher than the 20 per cent, $\sigma_\varpi/\varpi > 0.2$. For this reason, it is not advised to invert the parallax, but a Bayesian approach is mandatory.

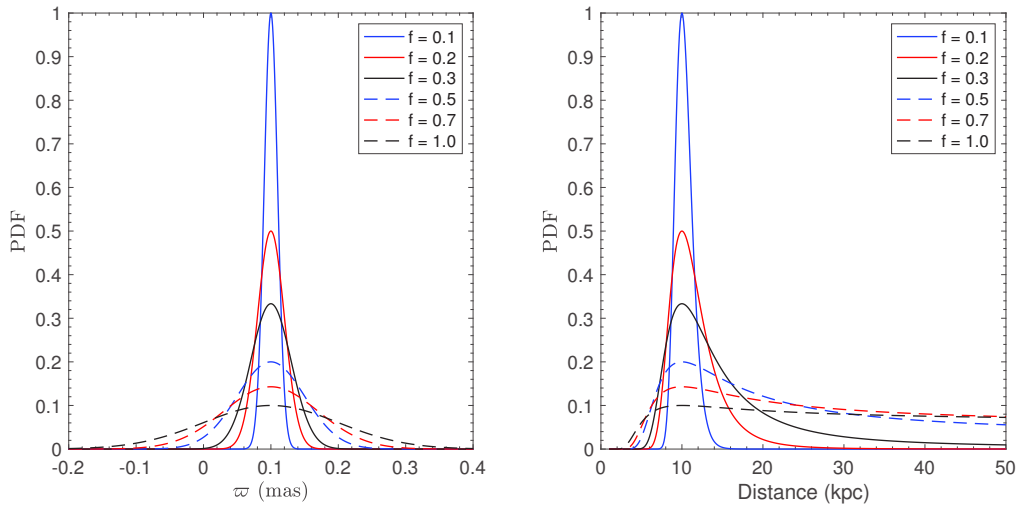

Figure 1.11: Left panel: Gaussian distribution function of the parallax for fixed value of $\varpi = 0.1$ mas and different values of the relative uncertainty $f = 0.1, 0.2, 0.3, 0.5, 0.7, 1.0$. Right panel: Distribution function of the measurement of the parallax as a function of the distance. The values of parallax and relative uncertainties are the same as in the left panel. A large relative uncertainty ($f > 0.1$) produces an asymmetric distribution in distance. For higher relative uncertainties, the distribution displays a flat behaviour towards large distances. Figure similar to Bailer-Jones (2015).

Such a Bayesian approach is fully described in Bailer-Jones (2015), and considers the

probability distribution function PDF, or the posterior $P(r)$, to have a star at a certain distance given the parallax. The posterior is the product between the likelihood, that is the probability to have that parallax given a model and uncertainty on the parallax $L(\varpi|\sigma_\varpi, M)$, and the prior, that is the probability to have a certain model $P(M)$. The prior on the model, as an example, could take into account the expected distribution of stars in the Milky Way, and it reflects our knowledge and ignorance on a physical process. A Bayesian approach to infer distances has been used in this work (see Chapters 2 and 3), for our purposes the posterior takes into account also the photometric and parallax data from Gaia DR2 in the likelihood, while the knowledge on the age distribution of the very metal-poor stars together with the density distribution of the stars in the Milky Way has been inserted in the prior. Using these photometric and astrometric data in a Bayesian context allows to better constrain the distance, especially in cases in which the parallax has a negative value or its relative uncertainty is large. To infer the distance with a precise and accurate method is essential to better understand the nature of the observed objects, e.g., measure the effective temperature and surface gravity, and to obtain reliable orbital parameters.

1.3.4 The outcomes of the revolution

The synergy between ground-based spectroscopic surveys and the Gaia satellite is producing an unprecedented chemo-dynamical decomposition of the Milky Way. For instance, it is possible to identify new structures in the Milky Way and satellites accreted into our Galaxy. Probably the most famous accretion event, after the Sagittarius dwarf galaxy, is the so-called Gaia-Enceladus-Sausage (GES), an accreted satellite comparable in size and mass with the Small Magellanic Cloud ($M \sim 6 \times 10^8$ M$_\odot$ Belokurov et al., 2018; Haywood et al., 2018; Helmi et al., 2018). The discovery of this accreted structure started with Gaia DR1, from which Belokurov et al. (2018) found a mildly retrograde structure in the velocity space. Helmi et al. (2018), in order to probe the kinematical and chemical properties of Gaia-Enceladus-Sausage, selected stars in common between Gaia DR2 (for the kinematics) and APOGEE (for the chemistry and radail velocities, Abolfathi et al., 2018). The analysed sample of stars inhabits the sphere with a radius of 5 kpc centred in the Sun. From the kinematical side of the analysis, Helmi et al. (2018) found the presence in the inner halo of a structure with slightly retrograde mean rotational motion (see top panels of Figure 1.12). While, thanks to APOGEE, Helmi et al. (2018) found a large spread in metallicity, meaning GES formed stars in multiple bursts, and that the [α/H] of its more metal-rich tail is lower than that of the MW thick disk (see bottom panels of Figure 1.12), implying a lower star formation rate than the Galactic thick disk. From the star formation rate and the kinematics, Helmi et al. (2018) found that the progenitor of GES has a mass of $M \sim 6 \times 10^8$ M$_\odot$ and it has been accreted 8 – 11 Gyr ago. Before Gaia, the work of identifying new structures in the Milky Way was a difficult task, although a hint of a new structure, and most probably related to GES, was detected by Meza et al. (2005) and then confirmed by Navarro et al. (2011) using an heterogeneous sample of stars in the solar neighbourhood. Meza et al. (2005); Navarro et al. (2011) also proposed that ωCen is a debris of the discovered accreted structure.

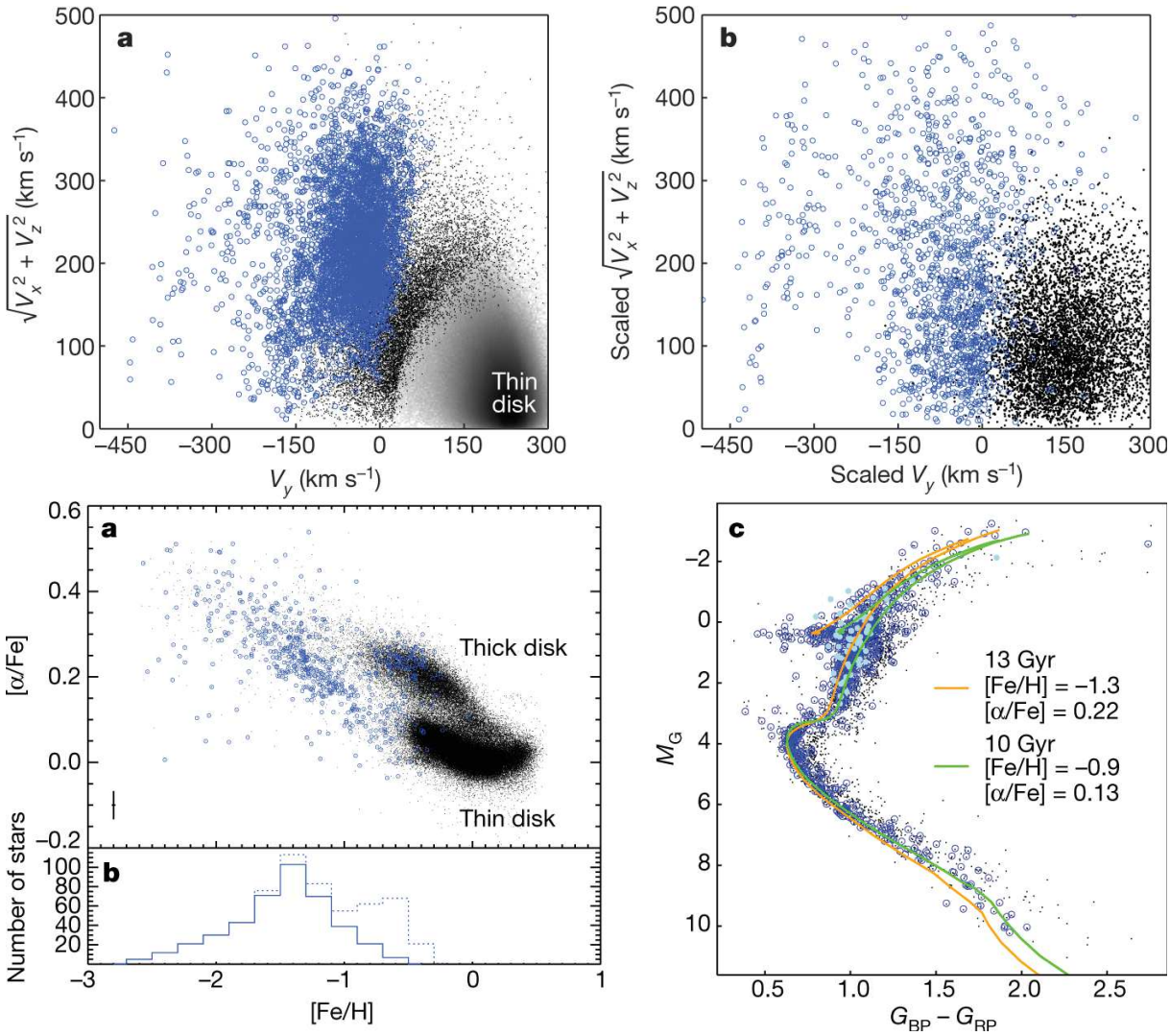

Figure 1.12: The chemodynamical properties of Gaia-Enceladus-Sausage (GES) from Helmi et al. (2018). Top panels: velocity space of the Solar neighbourhood, the gray shaded markers denote the disk, halo stars are represented with black points, while the blue circles denote the GES structure as in Helmi et al. (2018). The right top panel is the same but using a simulation that is able to reproduce the thick disk and the accreted GES feature. Bottom panels: a) chemical abundance of α-elements as a function of metallicity for the GES (blue circles) and the disk+halo (black dots). To be noted, the separation between GES and the disk. GES markers in the thick disk region are contaminants from the latter that have similar kinematics of GES. b) the metallicity distribution of GES without (with) the contaminants shown with the solid (dashed) line. c) comparison in the HRD between the GES (blue circles) and the halo in the Solar neighbourhood (black dots), superimposed metal-poor isochrones are shown with solid lines.

As a second example for this already started revolution in Galactic Archæology, there is the discovery of another accreted structure, the so called Gaia-Sequoia (Barbá et al., 2019). Thanks to the synergy between Gaia DR2, the DECam Plane Survey (DECaPS, Schlafly et al., 2018), and the VISTA Variables in the VLáctea Extended Survey (VVVX, Minniti et al., 2018), Barbá et al. (2019) analysed the properties of Gaia-Sequoia, a large structure discovered towards the bulge with a [Fe/H] $= -1.5 \pm 0.3$. They propose two scenarios for the nature of this structure, the first is that Gaia-Sequoia is one of the largest globular cluster in the Milky Way, with a size comparable or larger than ωCen, alternatively the observed structure is the core of a new more extended dwarf galaxy. Monty et al. (2020) reanalysing the chemodynamical properties of a sample of Gaia-Sequoia candidates found that this structure can be kinematically divided into two subgroups, one with low-energy orbits and one with higher orbital energy, meaning that the first subgroup is more confined in the inner part of the Galaxy, while the second is more dispersed in the nearby halo. Both Gaia-Enceladus-Sausage and Gaia-Sequoia are well summarised and discussed in Myeong et al. (2019). Figure 1.13 from Monty et al. (2020) shows that the two accreted structures inhabit two different regions of the action space (for an introduction on the action space and the action momentum vector, see Figure 1.15 and Section 1.3.7).

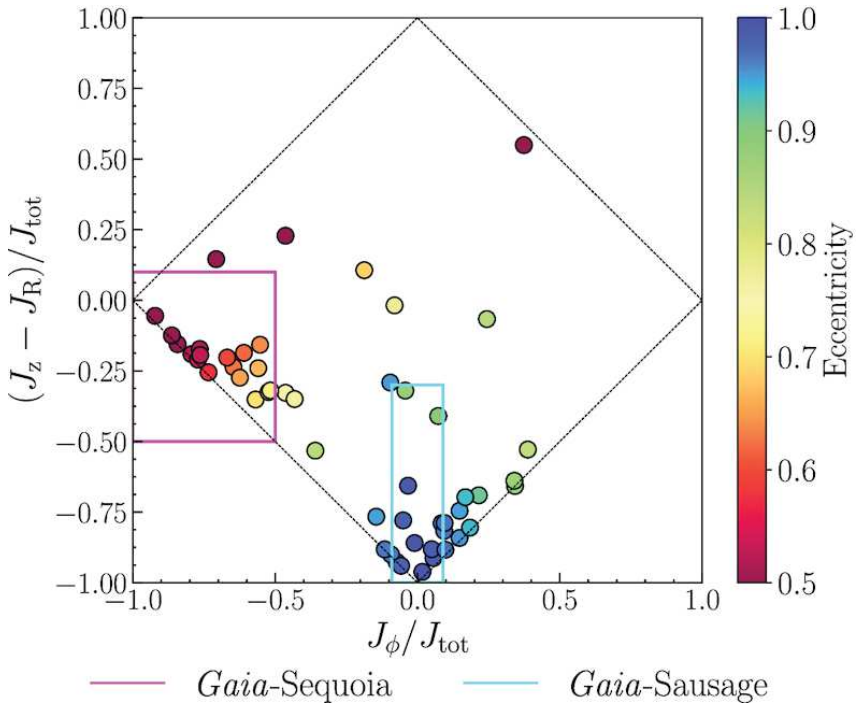

Figure 1.13: The dynamical properties of Gaia-Enceladus-Sausage and Gaia-Sequoia in the action space from Monty et al. (2020). Anticipating Section 1.3.7, the action space is useful to disentangle the structure in the Milky Way with different kinematics. The abscissa is a proxy for the rotational motion, while the vertical axis is a proxy of the vertical and radial motion. Stars in the In the action space, the two accreted structures, Gaia-Enceladus-Sausage (GES, in the cyan box) and Sequoia (in the magenta box), inhabit two different regions meaning different motion. GES is slowly rotating with high eccentricity (> 0.7), while the stars in Sequoia have higher retrograde rotational orbits and lower eccentricities (< 0.7).

Precise astrometry and photometry from Gaia DR2 have also been crucial in developing new algorithms to efficiently find new structures. As an example, Malhan & Ibata (2018) developed STREAMFINDER, a powerful tool to detect dynamically cold and thin stellar stream structures hidden in the Gaia DR2 footprint. The discovery of new structures and the characterisation of the halo stellar distribution can better constrain the Milky Way potential (Malhan & Ibata, 2019).

1.3.5 The Pristine survey meets Gaia DR2

Before Gaia DR2, the metal-poor candidates from the Pristine survey were selected estimating the photometric metallicity by coupling the metallicity-sensitive Pristine narrow-band Ca HK filter with the SDSS broad band photometry. In principle, it is possible to recalibrate the Pristine survey selection using Gaia DR2 G, BP, and RP photometry, and to create a new large sample of metal-poor candidates. This calibration is underway and two main options are on the table, one is to use the precious information that the parallax from Gaia DR2 can provide as in Bonifacio et al. (2019) and the second is to apply the same procedure described in Section 1.2.1. The left panel of Figure 1.14 shows the first attempt for the calibration of the Pristine space using Gaia passbands. The horizontal axis, $(BP-RP)_0$ is a proxy for the temperature, while the vertical axis is sensitive to metallicity. As shown in Figure 1.14, the first attempt in the calibration of the Pristine space with Gaia DR2 is promising since the most metal-poor stars are well separated from the more metal-rich ones.

SDSS provided an exquisite photometry reflecting in an efficient selection of very metal-poor candidates, but limited to magnitudes fainter than $V \sim 14.5$ mag. While with Gaia DR2, it is now possible to extend the calibration of the Pristine space towards a magnitude of 10 in the V band, where the Pristine narrow band Ca HK filter starts to saturate. A tentative calibration of the Pristine space for exploring bright magnitudes before Gaia DR2 has been put in place using APASS gri photometry (Henden et al., 2018). The use of the APASS filters resulted in a suboptimal selection of the most metal-poor stars, clearly improved by the exquisite Gaia DR2 photometry, as discussed in Bonifacio et al. (2019) and displayed in the right panels of Figure 1.14.

Bright stars are particularly useful when dealing with weaker spectral lines, because we can study them with higher spectroscopic resolution and precision than fainter objects. This is well described in Bonifacio et al. (2019) and Venn et al. (2020). Taken together with the fainter sample of metal-poor stars in the Pristine survey, we are aiming to cover all Galaxy environments, including the halo (e.g., Youakim et al., 2020), the disk (e.g., Sestito et al., 2020a), and the bulge (e.g., Arentsen et al., 2020). A high-resolution spectroscopic follow-up of these new bright extremely metal-poor candidates, selected with Pristine+Gaia DR2, is underway with the échelle spectrographs at the CAHA telescope (CAFÉ), at the CFHT (ESPaDOnS), and at GEMINI (GHOST).

The improvements that Gaia DR2 provides do not stop with the recalibration of the Pristine photometric metallicity towards brighter magnitudes, but, thanks to the astrometric solutions, it is possible to infer the kinematical parameters of these rare objects, as shown in Sestito et al. (2019, 2020a, see also Chapters 2 and 3 and Section 1.3.7).

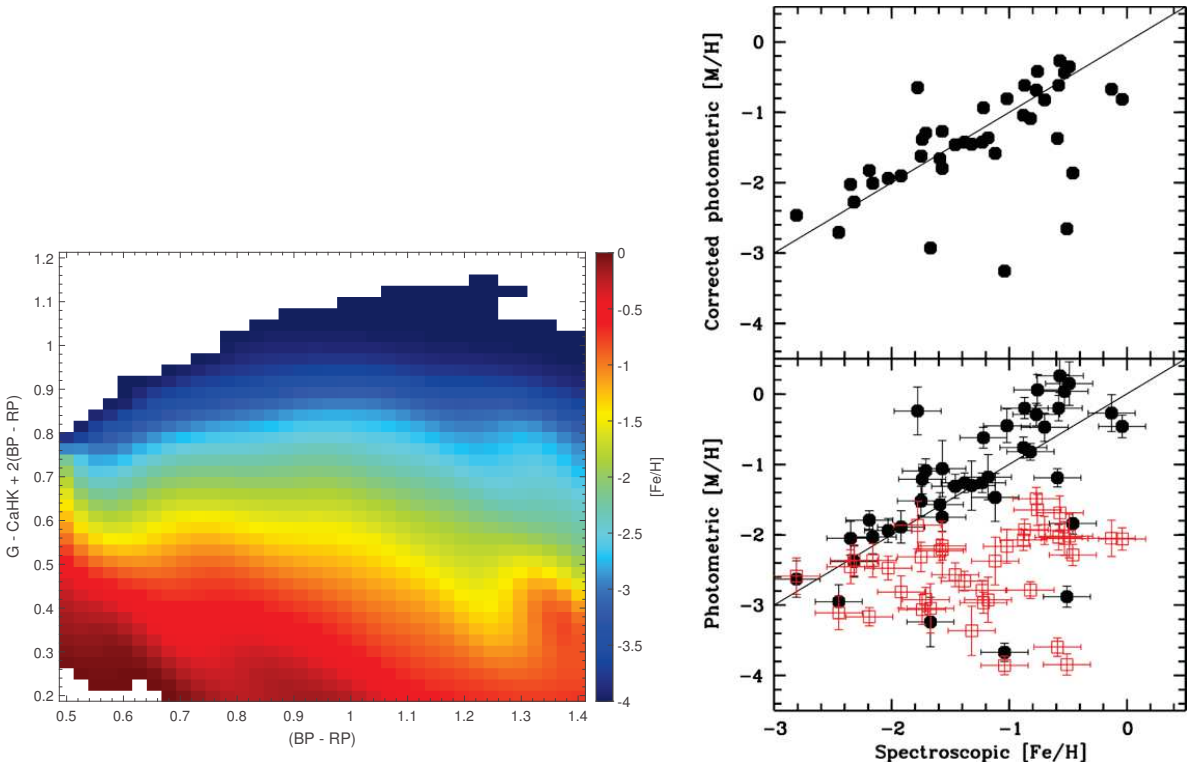

Figure 1.14: Left panel: The calibration of the Pristine space with Gaia DR2 passbands. The horizontal axis, $(BP - RP)$, is a proxy for the effective temperature. The lower the colour, the higher the effective temperature. The vertical axis is a metallicity sensitive. The space has been pixelated, and in each bin, the median metallicity has been calculated. The selection of metal-poor candidates is promising with the Gaia photometry, the most metal-poor stars are well separated from the more metal-rich population. Right panels: The comparison of the spectroscopic metallicity vs. the photometric inference for the bright very metal-poor candidates (Bonifacio et al., 2019). In the bottom panel a comparison between the APASS+Pristine metallicity calibration in red and the estimated metallicity from Gaia DR2+Pristine in black (Bonifacio et al., 2019). Thanks to Gaia, the photometric metallicity determination in the bright end of the Pristine survey has been largely improved compared to APASS, as visible in the bottom panel.

1.3.6 Complementing Gaia with multi-object spectroscopy: a unique window on the early Galaxy

The exquisite information provided by Gaia satellite can be complemented by large ground-based surveys for a deeper and unprecedented chemo-dynamical study of our Galaxy. For instance, quantities such as chemical abundances, stellar parameters, and radial velocity for objects too faint for the Gaia RVS spectrometer, can be easily accessed by ground-based surveys. One of the large ground-based surveys that will play a crucial role in Galactic Archæology is WEAVE (WHT Enhanced Area Velocity Explorer, Dalton et al., 2012). WEAVE is based on a new multi-object fiber spectrograph at the WHT telescope and it will see first light early 2021. WEAVE is divided into several sub-surveys covering different topics and observing the Milky Way and extragalactic objects. Regarding the Milky Way, WEAVE will dissect the stellar disk, the stellar halo, other structures such as the stellar streams and clusters. WEAVE will also investigate into the very metal-poor tail of the Galaxy and the poorly understood phases of stellar evolution, e.g., massive stars, variable stars, stellar ejecta, etc. It will perform integral field spectroscopy of nearby galaxies and dwarf galaxies, and it will spectroscopically follow-up extragalactic targets studied in the radio wavelength, such as from the Low-Frequency Array (LOFAR, van Haarlem et al., 2013).

Of particular interest is the synergy between the Galactic Archæology WEAVE sub-survey and the Pristine survey, bringing a wealth of data on the very metal-poor tail of the Milky Way. The memorandum of understanding between the two surveys will let the Pristine survey selects the most metal-poor targets to be observed using ~ 2 per cent of the fibres of WEAVE. Taking into account the success rates of the Pristine survey in their selection of metal-poor candidates, and the window function of WEAVE, Pristine+WEAVE is expecting to discovery approximately ~ 8000 new extremely metal-poor stars of which ~ 100 should be ultra metal-poor (Aguado et al., 2019), improving the current number (42 UMPs) of this latter and rarest sample. As also mentioned in Section 1.2.3, the spectroscopic analysis of the most metal-poor stars is a hard task, therefore the Pristine team is developing an ad hoc pipeline, well tailored to very metal-poor stars, to optimise the extraction of the information from the WEAVE spectra. The chemical analysis from the Pristine+WEAVE spectra will be complemented by the kinematical information extractable from Gaia to efficiently characterise the various regions of the Milky Way.

Similarly to WEAVE that will cover the Northern hemisphere, the 4 m Multi-Object Spectroscopic Telescope (4MOST, de Jong et al., 2019) will be operative in very near future, and it will be able to observe ~ 2400 objects simultaneously. 4MOST will cover the Southern hemisphere, complementing WEAVE. 4MOST will also play a crucial role in the study of the Milky Way and the Magellanic Clouds. All of these surveys will provide important constraints on the structure of the Milky Way, on the merging and accretion events happened during the Galaxy's history, and they will explore the very metal-poor tail of already discovered merging events, such as Gaia-Enceladus-Sausage (e.g., Belokurov et al., 2018; Haywood et al., 2018; Helmi et al., 2018, see Section 1.3.4) and Gaia-Sequoia (e.g., Barbá et al., 2019, see Section 1.3.4), but also including new discoveries.

1.3.7 A friendly introduction to action-angle variables

Thanks to the exquisite astrometric dataset of Gaia DR2 in synergy with ground-based spectroscopic information, it is possible to infer the distances and the orbital parameters of the

stars. Chapters 2 and 3 discuss the kinematical analysis of the most pristine stars from the ultra metal-poor ([Fe/H] ≤ -4.0) to the very metal-poor regime ([Fe/H] ≤ -2.0), while a more in-depth description on the choice of the parameters for the inference of the kinematical parameters is presented in Appendix C.

There are several physical quantities that are helpful in the kinematical analysis of stars, namely the maximum and the minimum distance from the Galactic centre called the apocentre and pericentre, respectively, the maximum height from the plane, the eccentricity of the orbit, the velocity and position vectors, the energy and the angular momentum, and the action-angle variables. These latter physical quantities are very helpful in describing the motion and disentangle structures with different orbits, since they are constant of the motion. These quantities will be used in the following Chapters as the core of the kinematical analysis and, since they might be used only by a niche of researchers, a friendly introduction follows.

When we are dealing with a physical system, not necessarily in Astronomy, it is possible to describe it using the Hamiltonian formalism (Hamilton, 1834, 1835; Goldstein, 1950; Landau & Lifshitz, 1969). With this formalism, the time evolution of the system can be defined using the Hamiltonian equation:

$$\frac{d\mathbf{p}}{dt} = -\frac{\partial \mathscr{H}}{\partial \mathbf{q}}, \quad \frac{d\mathbf{q}}{dt} = +\frac{\partial \mathscr{H}}{\partial \mathbf{p}} \tag{1.2}$$

where $(\mathbf{q}, \mathbf{p})$ are canonical variables (such as position and its momentum) and $\mathscr{H} = \mathscr{H}(\mathbf{q}, \mathbf{p}, t)$ is the Hamiltonian function that describes the energy of the system. By construction, it depends on the canonical variables and on time. It can be more convenient to replace the position and the momentum with a new set of canonical variables, the angle and its momentum $(\mathbf{\Theta}, \mathbf{J})$, also called the action, in order to easily describe the motion. Sometimes the couple of the angle and the action (the momentum) is called action-angle variables. The relation between the previous canonical variables $(\mathbf{q}, \mathbf{p})$ and the momentum of the action-angle variables is the following:

$$J_k \equiv \oint p_k dq_k. \tag{1.3}$$

Since $(\mathbf{\Theta}, \mathbf{J})$ are canonical coordinates, their Poisson brackets[3] have to satisfy:

$$\{\Theta_i, J_j\} = \delta_{ij} \tag{1.4}$$

with δ_{ij} as the Kronecker delta.

One of the characteristics of the action momentum vector is that the integration in Equation 1.3 does not depend on the choice of the path, and therefore the action is a constant of the motion. This means that the new Hamiltonian function $\mathscr{W}$, written with the new set of canonical variables, depends only on the action momentum $\mathscr{W} = \mathscr{W}(\mathbf{J})$ and it has to satisfy:

$$\frac{d\mathbf{J}}{dt} = -\frac{\partial \mathscr{W}}{\partial \mathbf{\Theta}} = 0, \quad \frac{d\mathbf{\Theta}}{dt} = +\frac{\partial \mathscr{W}}{\partial \mathbf{J}}. \tag{1.5}$$

[3] given two functions $f(\mathbf{q}, \mathbf{p}, t)$ and $g(\mathbf{q}, \mathbf{p}, t)$ the Poisson brackets are:

$$\{f, g\} \equiv \sum_{i=1}^{N} \left(\frac{\partial f}{\partial q_i} \frac{\partial g}{\partial p_i} - \frac{\partial f}{\partial p_i} \frac{\partial g}{\partial q_i} \right)$$

This implies that the action momentum vector can be used to describe the orbit of a particle and to discriminate between different kinds of motion, while the angles, i.e., the coordinates, are informative on the position of the particle within the given orbit. In Astronomy, the action momentum vector can be used to identify the orbits of the stars and to clearly see if a given star is confined to the disk or venture far in the halo. With a large sample of stars, and possibly coupling their kinematics with their chemistry, it is possible to identify accreted structures (Binney & Tremaine, 2008). A first use of the action-angle variables has been already reported in Section 1.3.4 as regards the discovery of Gaia-Enceladus-Sausage. In the following Chapters, the actions are largely used to better analyse the kinematics of the most metal-poor stars.

Usually the action-angle variables are shown in cylindrical coordinates, (J_r, J_ϕ, J_z), since they can better describe the motion in presence of rotation and of a disk. $\mathbf{J}$ is expressed in units of $\mathrm{kpc} \cdot \mathrm{km\,s^{-1}}$, where the azimuthal component of the action momentum is usually equivalent to the vertical component of the angular momentum ($J_\phi \equiv L_z$). Broadly speaking, J_ϕ, J_r, and J_z are proxies of the motion in the rotational, the radial, and the vertical component, respectively. Hence, stars confined to the Galactic plane, and therefore with a small motion on the vertical direction, have small J_z, stars with a prograde (retrograde) orbits have positive (negative) values of J_ϕ, while the greater the eccentricity, the greater the radial component of the action momentum J_r.

A friendly and digestible summary plot of the actions spaces is sketched in Figure 1.15. The left panel helps for the interpretation of the results described in Chapters 2 (Sestito et al., 2019) and 3 (Sestito et al., 2020a), in which the action space used is generated from J_z and J_ϕ. In this space, the axes are normalised by the corresponding values for the Sun (see Appendix C), assumed to have a prograde circular orbit in the disk. Hence stars that do not venture far out of the Milky Way plane have low values of J_z, and these are marked by blue, red, and black dots. Blue and red markers are prograde and retrograde stars with low eccentric orbits, respectively, while black dots represent stars with high eccentricities and likely to be confined to the disk both with prograde ($J_\phi/J_{\phi,\odot} > 0$) and retrograde ($J_\phi/J_{\phi,\odot} < 0$) motion. Magenta markers represent stars with halo-like orbits, hence large J_z. The right panel illustrates the use of the action momentum $\mathbf{J}$ as in Chapter 4 (Sestito et al., 2020b). A different action space has been used for a comparison between simulated galaxies and the observed Milky Way. Since the simulated galaxies have different sizes and masses, and therefore gravitational potentials, than the Milky Way, the comparison has to be done normalising the axes to the norm of the action momentum vector J_{TOT}. Also in Chapter 4, I have explored the action space using all the action components. Hence the abscissa is the normalised azimuthal component of the action momentum, i.e., J_ϕ/J_{TOT}, while the ordinate takes into account the difference between the vertical and the radial component of the action vector, i.e., $(J_z - J_r)/J_{TOT}$. The same colour-code has been applied as in the left panel, hence prograde (blue dots) and retrograde (red dots) planar stars are at the extreme right and left of this space, respectively. This means that the majority of the motion is concentrated in the azimuthal component, hence small J_z and J_r, and so their difference. The stars with high eccentricity likely confined to the plane, hence large J_r and small J_z, are located in the bottom region of this space (black dots). Halo-like stars populate the remaining part of the space (magenta dots).

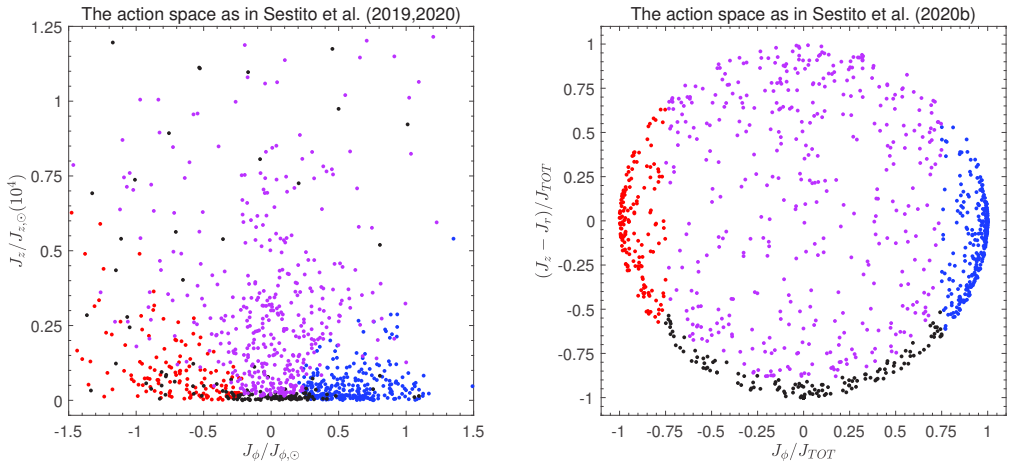

Figure 1.15: Action Space Sketch for the low-metallicity stars/star particles ([Fe/H] ≤ -2.5). Left panel: the azimuthal component vs. the vertical component of the action, J_ϕ vs. J_z as in Sestito et al. (2019, 2020a). The stars that remain confined to the disk possess low values of J_z. Out of these sample of planar stars, the ones with lower eccentricity and prograde (positive J_ϕ) motion are denoted by blue dots, while their retrograde counterparts (negative J_ϕ) are denoted by red dots. High eccentricity planar stars are denoted by black markers, both prograde and retrograde. Stars with halo-like orbits are displayed in magenta. The axes are both normalised by the action components of the Sun, assumed to have a circular prograde orbit in the MW plane. Right panel: action space as in (Sestito et al. 2020b, in prep.) using all the action components. The horizontal axis is the azimuthal component J_ϕ, while the vertical axis shows the difference between the vertical and the radial component of the action. Both axes are normalised by the norm of the action J_{TOT}. Star particles are colour-coded as in the left panel.

1.3.8 In the following Chapters

The following Chapters will investigate the kinematics of the most metal-poor stars of the Milky Way. I will start in Chapter 2 by describing the orbital information of all the ultra metal-poor stars, thought to be among the oldest objects in our Galaxy, and therefore tracers of the infant Universe and of the assembly of the galaxies. In particular, I will focus on a peculiar population confined to the Milky Way plane. In Chapter 3, I will extend the analysis to the very metal-poor stars discovered by the Pristine (Starkenburg et al., 2017b; Aguado et al., 2019) and the LAMOST (Cui et al., 2012; Li et al., 2018) surveys. This sample will be essential to bridge the gap between the metallicity region in which the disk was already discovered and the ultra metal-poor regime from Sestito et al. (2019). Moreover, the size of the sample is needed to reach statistically robust results. Both the works in Chapter 2 and 3 use the precious synergy between ground-based surveys and the Gaia satellite. In particular, the exquisite astrometric and photometric data from Gaia DR2 are coupled with metallicity and radial velocity of the other surveys to infer distances, stellar parameters, and precious kinematical information. Chapter 4 investigates the origin of the most metal-poor stars, also focusing on the presence of these stars in the disk region, thanks to the use of one of the most high-resolution cosmological simulations, the NIHAO-UHD suite (Buck et al., 2020). All the Chapters pose new interesting questions on the formation and evolution of the Galaxy.

CHAPTER

2 Tracing the formation of the Milky Way through ultra metal-poor stars.

This Chapter contains the published paper Sestito et al. (2019), in which I have conducted the analysis of the kinematical properties of all the 42 ultra metal-poor stars ([Fe/H] ≤ -4.0) present in the literature. For this work, I have developed a bayesian inference tool to measure precise and accurate distances, using both observational data and theoretical models for estimating the posterior probability function. As concern the observational information, hence the likelihood, this method requires the exquisite photometric data in the G, BP, and RP bands and the parallax from Gaia DR2, with their uncertainties. From the theoretical side, thus the prior, I use ultra metal-poor isochrones from MIST (Dotter, 2016; Choi et al., 2016) with age ≥ 11 Gyr, a model that describes the density distribution of stars in the Galaxy, and a Salpeter Initial Mass Function. As output, this bayesian inference estimates the probability distribution function for the distance and the stellar parameters, such as the effective temperature and the surface gravities. This latter quantities, estimated independently by the spectra, can be very useful for spectroscopic analyses, as shown in Venn et al. (2020) and Appendix B.

Then using the radial velocities from high-resolution spectroscopy, the exquisite proper motion from Gaia DR2, and `Galpy`, the kinematical properties have been extracted. Surprisingly, a large fraction of the UMPs, i.e., ~ 26 per cent (11 UMPs), is confined to the disk with a maximum excursion of 3 kpc from the plane. 10 out of 11 of these stars with planar orbits are in prograde motion, and largely exceeding the expectations from a non-rotating spheroid, in which an equal number of prograde and retrograde stars is expected to be found. Also, this sample of prograde planar stars spans a wide range of eccentricities, and as an example, the most metal-poor star known has a quasi-circular prograde orbit. With this work, three scenarios have been proposed to explain the results. Briefly, the first scenario is that these planars stars have been brought in by the building blocks that formed the disk of the Milky Way, the second scenario invokes the presence of merging events that deposited the stars in a co-planar fashion, and the last one is the formation of these UMPs in an unpolluted reservoir of gas in the Milky Way disk.

Monthly Notices
of the
ROYAL ASTRONOMICAL SOCIETY

MNRAS **484,** 2166–2180 (2019) doi:10.1093/mnras/stz043
Advance Access publication 2019 January 9

Tracing the formation of the Milky Way through ultra metal-poor stars

Federico Sestito,[1,2★] Nicolas Longeard,[1] Nicolas F. Martin,[1,3] Else Starkenburg,[2] Morgan Fouesneau,[3] Jonay I. González Hernández,[4,5] Anke Arentsen,[2] Rodrigo Ibata,[1] David S. Aguado,[6] Raymond G. Carlberg,[7] Pascale Jablonka,[8,9] Julio F. Navarro,[10] Eline Tolstoy[11] and Kim A. Venn[10]

[1]*Observatoire astronomique de Strasbourg, CNRS, UMR 7550, F-67000 Strasbourg, France*
[2]*Leibniz Institute for Astrophysics Potsdam (AIP), An der Sternwarte 16, D-14482 Potsdam, Germany*
[3]*Max-Planck-Institut für Astronomie, Königstuhl 17, D-69117 Heidelberg, Germany*
[4]*Instituto de Astrofisica de Canarias, Vía Láctea, E-38205 La Laguna, Spain*
[5]*Departamento de Astrofísica, Universidad de La Laguna, Tenerife, E-38206 La Laguna, Spain*
[6]*Institute of Astronomy, University of Cambridge, Madingley Road, CB3 0HA Cambridge, UK*
[7]*Department of Astronomy and Astrophysics, University of Toronto, Toronto, ON M5S 3H4, Canada*
[8]*GEPI, Observatoire de Paris, Université PSL, CNRS, Place Jules Janssen, F-92190 Meudon, France*
[9]*Institute of Physics, Laboratoire d'astrophysique, École Polytechnique Fédérale de Lausanne (EPFL), Observatoire, CH-1290 Versoix, Switzerland*
[10]*Department of Physics and Astronomy, University of Victoria, PO Box 3055, STN CSC, Victoria BC V8W 3P6, Canada*
[11]*Kapteyn Astronomical Institute, University of Groningen, Landleven 12, NL-9747AD Groningen, the Netherlands*

Accepted 2018 December 24. Received 2018 December 20; in original form 2018 November 7

ABSTRACT

We use *Gaia DR2* astrometric and photometric data, published radial velocities and MESA models to infer distances, orbits, surface gravities, and effective temperatures for all ultra metal-poor stars ([Fe/H] < -4.0 dex) available in the literature. Assuming that these stars are old (> 11 Gyr) and that they are expected to belong to the Milky Way halo, we find that these 42 stars (18 dwarf stars and 24 giants or sub-giants) are currently within $\sim$20 kpc of the Sun and that they map a wide variety of orbits. A large fraction of those stars remains confined to the inner parts of the halo and was likely formed or accreted early on in the history of the Milky Way, while others have larger apocentres (> 30 kpc), hinting at later accretion from dwarf galaxies. Of particular interest, we find evidence that a significant fraction of all known UMP stars ($\sim$26 per cent) are on prograde orbits confined within 3 kpc of the Milky Way plane ($J_z < 100$ km s^{-1} kpc). One intriguing interpretation is that these stars belonged to the massive building block(s) of the proto-Milky Way that formed the backbone of the Milky Way disc. Alternatively, they might have formed in the early disc and have been dynamically heated, or have been brought into the Milky Way by one or more accretion events whose orbit was dragged into the plane by dynamical friction before disruption. The combination of the exquisite *Gaia DR2* data and surveys of the very metal-poor sky opens an exciting era in which we can trace the very early formation of the Milky Way.

Key words: stars: distances – Galaxy: abundances – Galaxy: disc – Galaxy: evolution – Galaxy: formation – Galaxy: halo.

1 INTRODUCTION

Ultra metal-poor (UMP) stars, defined to have [Fe/H][1] < -4 dex (Beers & Christlieb 2005), are extremely rare objects located mainly in the Milky Way (MW) halo. Because they are ultra metal-poor, also relative to their neighbourhood, it is assumed that they formed from relative pristine gas shortly after the big bang (e.g. Freeman & Bland-Hawthorn 2002). As such, they belong to the earliest generations of stars formed in the Universe (Karlsson, Bromm & Bland-Hawthorn 2013). Because they are old, observable UMPs must be low-mass stars, however the minimum metallicity at which low-mass stars can form is still an open question (see Greif 2015; and references therein). The search for, and study of, stars with the lowest metallicities are therefore important topics to answer

★ E-mail: federico.sestito@astro.unistra.fr
[1][Fe/H] $= \log(N_{Fe}/N_H)_\star - \log(N_{Fe}/N_H)_\odot$, with N_X= the number density of element X.

questions on the masses of the first generation of stars and the universality of the initial mass function (IMF), as well as on the early formation stages of galaxies and the first supernovae (e.g. Frebel & Norris 2015; and references therein). Careful studies over many decades have allowed us to build up a catalogue of 42 UMP stars throughout the Galaxy. Many of these stars were discovered in survey programs that were or are dedicated to finding metal-poor stars using some special pre-selection through prism techniques (e.g. the HK and HES surveys; Beers, Preston & Shectman 1985; Christlieb, Wisotzki & Graßhoff 2002) or narrow-band photometry (such as for instance the SkyMapper and Pristine survey programmes; Starkenburg et al. 2017a; Wolf et al. 2018). Others were discovered in blind but very large spectroscopic surveys such as SDSS/SEGUE/BOSS (York et al. 2000; Yanny et al. 2009; Eisenstein et al. 2011) or LAMOST (Cui et al. 2012).

From the analysis of cosmological simulations, predictions can be made for the present-day distribution of such stars in MW-like galaxies. Since these predictions have been shown to be influenced by the physics implemented in these simulations, we can use the present-day distribution to constrain the physical processes of early star formation. For instance, a comparison between the simulations of Starkenburg et al. (2017b) and El-Badry et al. (2018) indicates a clear sensitivity of the present-day distribution on the conditions applied for star formation and the modelling of the ISM.

In an effort to refine the comparison with models and unveil the phase-space properties of these rare stars, we combine the exquisite *Gaia DR2* astrometry and photometry (Gaia Collaboration 2018) with models of UMP stars (MESA isochrones and luminosity functions; Paxton et al. 2011; Choi et al. 2016; Dotter 2016; waps.cfa.harvard.edu/MIST) to infer the distance, stellar properties, and orbits of all 42 known UMP stars.

This paper is organized as follows: Section 2 explains how we put our sample together while Section 3 presents our statistical framework to infer the distance, effective temperature, surface gravity, and orbit of each star in the sample using the *Gaia DR2* information (parallax, proper motion, and *G*, *BP*, and *RP* photometry). The results for the full sample are presented in Section 4 and we discuss the implications of the derived orbits in Section 5 before concluding in Section 6. We refer readers who are interested in the results for individual stars to Appendix A (available Online), in which each star is discussed separately.

2 DATA

We compile the list of all known ultra metal-poor ([Fe/H] < -4.0 dex), hyper metal-poor ([Fe/H] < -5.0 dex), and mega metal-poor ([Fe/H] < -6.0 dex) stars from the literature building from the Joint Institute of Nuclear Astrophysics catalogue (Abohalima & Frebel 2017), supplemented by all relevant discoveries. The literature properties for these stars are listed in Table 1. We crossmatch this list with the *Gaia DR2* catalogue[2] (Gaia Collaboration 2018) in order to obtain the stars' photometric and astrometric information. This is listed in Table 2.

Some stars were studied in more than one literary source, with different methods involving 1D or 3D models and considering the stellar atmosphere at Local Thermodynamic Equilibrium (LTE) or non-LTE, leading to dissimilar results on metallicity and stellar parameters. In this paper, when multiple results are available, we report in Table 1 preferentially results including 3D stellar atmosphere and/or involving non-LTE modelling. If all results are in 1D LTE, we favour the most recent results.

When the UMP stars are recognized to be in binary systems and the orbital parameters are known (see Table 1), the reported radial velocity is the systemic value that is corrected for the binary orbital motion around the centre of mass.

Assuming that all stars in our sample are distant, we consider that all the extinction is in the foreground. Therefore, all stars are de-reddened using the Schlegel, Finkbeiner & Davis (1998) extinction map as listed in Table 1 and the Marigo et al. (2008) coefficients for the Gaia filters based on Evans et al. (2018), i.e.

$$G_0 = G - 2.664E(B-V), \tag{1}$$

$$BP_0 = BP - 3.311E(B-V), \tag{2}$$

$$RP_0 = RP - 2.021E(B-V). \tag{3}$$

Extinction values remain small in most cases (Table 1).

We assume that the distance between the Sun and the Galactic centre is 8.0 kpc, that the Local Standard of Rest circular velocity is $V_c = 239\,\mathrm{km\,s^{-1}}$, and that the peculiar motion of the Sun is ($U_0 = 11.10\,\mathrm{km\,s^{-1}}$, $V_0 + V_c = 251.24\,\mathrm{km\,s^{-1}}$, $W_0 = 7.25\,\mathrm{km\,s^{-1}}$) as described in Schönrich, Binney & Dehnen (2010).

3 INFERRING THE PROPERTIES OF STARS IN THE UMP SAMPLE

3.1 Distance inference

It is ill advised to calculate the distance to a star by simply inverting the parallax measurement (Bailer-Jones 2015), especially for large relative measurement uncertainties (e.g. $\delta\varpi/\varpi > 0.2$) and negative parallaxes. Therefore, we infer the probability distribution function (PDF) of the heliocentric distance to a star by combining its photometric and astrometric data with a sensible MW stellar density prior. Following Bayes' rule (Sharma 2017), the posterior probability of having a star at a certain distance given its observables $\boldsymbol{\Theta}$ (e.g. photometry, metallicity, parallax) and a model $\mathcal{M}$ is characterized by its likelihood $\mathcal{L}(\boldsymbol{\Theta}|\mathcal{M})$ and the prior $\mathcal{P}(\mathcal{M})$. The likelihood gives the probability of the set of observables $\boldsymbol{\Theta}$ given model $\mathcal{M}$, whereas the prior represents the knowledge of the model used for the representation of a phenomenon. With these notations,

$$\mathcal{P}(\mathcal{M}|\boldsymbol{\Theta}) \propto \mathcal{L}(\boldsymbol{\Theta}|\mathcal{M})\mathcal{P}(\mathcal{M}). \tag{4}$$

In this work, the model parameters are $\mathcal{M} = \{\mu = 5\log(r) - 5, A\}$, with μ the distance modulus of the star, r the distance to the star, and A its age. The observables $\boldsymbol{\Theta}$ can be split into the Gaia photometric observables $\boldsymbol{\Theta}_{\rm phot} = \{G_0, BP_0, RP_0, \delta_G, \delta_{BP}, \delta_{RP}\}$ and the Gaia astrometric (parallax) observables $\boldsymbol{\Theta}_{\rm astrom} = \{\varpi, \delta_\varpi\}$, with δx the uncertainty associated with measurement x. Assuming that the photometric and astrometric information on the star are independent, equation (4) becomes

$$\mathcal{P}(\mathcal{M}|\boldsymbol{\Theta}) \propto \mathcal{L}_{\rm phot}(\boldsymbol{\Theta}_{\rm phot}|\mathcal{M})\mathcal{L}_{\rm astrom}(\boldsymbol{\Theta}_\varpi|\mathcal{M})\mathcal{P}(\mathcal{M}). \tag{5}$$

[2] https://gea.esac.esa.int/archive/

Table 1. Physical parameters of the analysed UMPs found in literature. [Fe/H], [C/Fe], v_r, $T_{\rm lit}$, log(g)$_{\rm lit}$ are from the articles listed in the column References. v_r and the binarity flag denoted with *a* are from Arentsen et al. (2018), the v_r values for binary systems denoted with *a* are the systemic radial velocities corrected for the binary orbital motion. v_r values for stars that are not known to be in a binary system and from the compilation of Arentsen et al. (2018) are calculated with a weighted average of all the v_r measurements. $E(B-V)$ is from Schlegel et al. (1998). In case the star is in a binary system, the binarity flag is equal to Y, while stars labelled with N are not in a binary system or the binarity is not known.

Identifier	α_{J2000} (deg)	δ_{J2000} (deg)	[Fe/H] (dex)	$\delta_{[Fe/H]}$ (dex)	[C/Fe] (dex)	$\delta_{[C/Fe]}$ (dex)	v_r (km s^{-1})	δ_{v_r} (km s^{-1})	$T_{\rm lit}$ (K)	$\delta_{T_{\rm lit}}$ (K)	log(g)$_{\rm lit}$ (dex)	$\delta_{\log(g)_{\rm lit}}$ (dex)	E(B-V) (mag)	Binarity	References
HE 0020−1741	5.6869167	−17.4080944	−4.05	–	1.4	–	93.06	0.83	4630.0	150	0.95	0.3	0.021	N	Placco et al. (2016)
SDSS J0023+0307	5.80834363858	3.13284420892	<−6.6	–	<2.0	–	−195.5	1.0	6140	132	4.8	0.6	0.028	N	Aguado et al. (2018b)
HE 0044−3755	11.6508144643	−37.6593210379	−4.19	–	−0.3	–	48.3	2.5	4800	100	1.5	0.1	0.010	N	Cayrel et al. (2004)
HE 0057−5959	14.9749409617	−59.7249294278	−4.08	–	0.86	–	375.64a	1.00	5257	–	2.65	–	0.016	N	Norris et al. (2007), Norris et al. (2013)
HE 0107−5240	17.3714810637	−52.4095009821	−5.5	0.2	3.85	–	46.0a	2.0	5100	150	2.2	0.3	0.011	Ya	Christlieb et al. (2004)
HE 0134−1519	24.2724039774	−15.0729979538	−4.0	0.2	1.00	0.26	244	1	5500	100	3.2	0.3	0.016	N	Hansen et al. (2015)
SDSS J014036.21+234458.1	25.1509195676	23.7495011637	−4.0	0.3	1.1	0.3	−197a	1	5703	100	4.7	0.3	0.114	Ya	Yong et al. (2013)
BD+44 493	36.7072451683	44.9629239592	−4.3	0.2	1.2	0.2	−150.14	0.63	5430	150	3.4	0.3	0.079	N	Ito et al. (2013)
HE 0233−0343	39.1241380137	−3.50167460698	−4.7	0.2	3.48	0.24	64	1	6300	100	3.4	0.3	0.022	N	Hansen et al. (2015)
BPS CS 22963−0004	44.1940476203	−4.85483952327	−4.09	0.15	0.40	0.23	292.4	0.2	5060	42	2.15	0.16	0.045	N	Roederer et al. (2014)
SDSS J030444.98+391021.1	46.1874375223	39.1725764233	−4.0	0.2	0.7	–	87	8	5859	13	5.0	0.5	0.111	N	Aguado et al. (2017b)
SMSS J031300.36−670839.3	48.2515614545	−67.1442601577	<−6.53	–	4.5	0.2	298.5a	0.5	5125	–	2.3	–	0.032	N	Keller et al. (2014), Nordlander et al. (2017)
HE 0330+0148	53.158696449	1.96666957231	−4.0	0.1	2.6	–	−33.6a	1.0	4100	200	5.2	0.1	0.094	Y	Plez, Cohen & Meléndez (2005)
HE 0557−4840	89.6636087844	−48.6658029727	−4.8	0.2	1.65	–	211.9	0.8	4900	100	2.2	0.3	0.037	N	Norris et al. (2007)
SDSS J081554.26+472947.5	123.976115075	47.4965559814	<−5.8	–	>5.0	–	−95	23	6215	82	4.7	0.5	0.063	N	Aguado et al. (2018a)
SDSS J092912.32+023817.0	142.301366238	2.63806158906	−4.97	–	<3.91	–	388.3	10.4	5894	–	3.7	–	0.053	Y	Bonifacio et al. (2015), Caffau et al. (2016)
SDSS J094708.27+461010.0	146.784471294	46.1694746754	−4.1	0.2	1.0	0.4	−5	12	5858	73	5.0	0.5	0.013	N	Aguado et al. (2017a)
HE 1012−1540	153.722814524	−15.9314366402	−4.17	0.16	2.2	–	225.8a	0.5	5230	32	2.65	0.2	0.061	N	Roederer et al. (2014)
SDSS J102915+172927	157.313121378	17.4910907404	−4.99	0.06	<0.7	–	−35	4	5850	100	4.0	0.2	0.023	N	Caffau et al. (2011)
SDSS J103402.70+070116.6	158.511301205	7.02129528322	−4.01	0.14	–	–	153	3	6270	–	4.0	–	0.02	N	Bonifacio et al. (2018)
SDSS J103556.11+064143.9	158.983818359	6.6955582264	<−5	–	3.08	–	−45	6	6262	–	4	–	0.024	N	Bonifacio et al. (2015)
SDSS J105519.28+232234.0	163.830333515	23.3761158455	−4.00	0.07	<0.7	–	62	4	6232	28	4.9	0.1	0.015	N	Aguado et al. (2017b)
SDSS J120441.38+120111.5	181.172452065	12.019865284	−4.34	0.05	<1.45	–	51	3	5917	–	3	–	0.024	N	Placco et al. (2015)
SDSS J124719.46−034152.4	191.831114232	−3.69791795379	−4.11	0.18	<1.61	–	84	6	6332	–	4	–	0.022	N	Caffau et al. (2013b)
LAMOST J125346.09+075343.1	193.44189217	7.89526036289	−4.02	0.06	1.59	–	78.0	0.4	6030	135	3.65	0.16	0.025	N	Li et al. (2015)
SDSS J131326.89−001941.4	198.3620349838832	−0.3281488686298	−4.7	0.2	2.8	0.3	268	4	5525	106	3.6	0.5	0.024	Y	Allende Prieto et al. (2015), Frebel et al. (2015), Aguado et al. (2017b)
HE 1310−0536	198.379940261	−5.87014820763	−4.2	0.2	2.36	0.23	113.2	1.7	5000	100	1.9	0.3	0.037	N	Hansen et al. (2015)
HE 1327−2326	202.524748159	−23.6971386187	−5.96	–	3.78	–	64.4a	1.3	6200	100	3.7	0.3	0.066	N	Frebel et al. (2008)
HE 1424−0241	216.668044499	−2.90763517546	−4.05	–	<0.63	–	59.8	0.6	5260	–	2.66	–	0.055	N	Norris et al. (2013), Cohen et al. (2008)
SDSS J144256.37−001542.7	220.734907425	−0.26188939275	−4.09	0.21	<1.59	–	225	9	5850	–	4	–	0.036	N	Caffau et al. (2013a)
Pristine221.8781+9.7844	221.878064787	9.78436859397	−4.66	0.13	<1.76	–	−149.0	0.5	5792	100	3.5	0.5	0.020	N	Starkenburg et al. (2018)
SDSS J164234.48+443004.9	250.643694345	44.5013644484	−4.0	0.2	0.55	0.0	−136	4	6280	150	5.0	0.3	0.011	N	Aguado et al. (2016)
SDSS J173403.91+644633.0	263.516273652	64.7758235012	−4.3	0.2	3.1	0.2	−258	13	6183	78	5.0	0.5	0.028	N	Aguado et al. (2017a)
SDSS J174259.67+253135.8	265.748669215	25.526636261	−4.8	0.07	3.6	0.2	−221.93	10.00	6345	–	4	–	0.055	N	Bonifacio et al. (2015)
2MASS J18082002−5104378	272.083464041	−51.0771900644	−4.07	0.07	<0.5	–	16.54	0.12	5440	100	3.0	0.2	0.101	Y	Meléndez et al. (2016) Schlaufman et al. (2018)
BPS CS 22891−0200	293.829490257	−61.7067706698	−4.06	0.15	–	–	131	10	4490	33	0.5	0.1	0.068	N	Roederer et al. (2014)
BPS CS 22885−0096	305.213220651	−39.8917320574	−4.21	0.07	–	–	−248	10	4580	34	0.75	0.15	0.048	N	Roederer et al. (2014)
BPS CS 22950−0046	305.368323431	−13.2760006492	−4.12	0.14	–	–	111	10	4380	32	0.5	0.1	0.054	N	Roederer et al. (2014)
BPS CS 30336−0049	311.348055352	−28.7099758468	−4.04	0.09	−0.28	0.31	−236.6	0.8	4827	100	1.5	0.2	0.054	N	Lai et al. (2008)
HE 2139−5432	325.676864649	−54.3119357441	−4.02	–	–	–	105a	3	5457	44	2.0	0.2	0.017	Ya	Norris et al. (2013)
HE 2239−5019	340.611864594	−50.0669213083	−4.2	0.2	<1.7	–	368.7	0.5	6100	100	3.5	0.3	0.010	N	Hansen et al. (2015)
HE 2323−0256	351.62419731	−2.66612144628	−4.38	0.15	–	–	−125.8a	0.3	4630	34	0.95	0.13	0.043	N	Roederer et al. (2014)

3.1.1 $\mathcal{L}_{\rm phot}(\boldsymbol{\Theta}_{\rm phot}|\mathcal{M})$

In order to determine the photometric likelihood of a given star for a chosen μ and A, we rely on the isochrone models from the MESA/MIST library (Paxton et al. 2011; Choi et al. 2016; Dotter 2016), as they are the only set of publicly available isochrones that reach the lowest metallicity ([Fe/H] $= -4.0$ dex) and is therefore the most appropriate for our study.

Any isochrone, $\mathcal{I}$, of a given age, A, associated with a luminosity function[3] $\Phi(M_G|A)$, predicts the density distribution triplet of absolute magnitudes $p(M_G, M_{BP}, M_{RP}|\mathcal{I}, \Phi)$ in

[3]This associated luminosity function, Φ, assumes a Salpeter IMF (Salpeter 1955). The choice of the IMF is not very sensitive for the type of stars we analyse.

Table 2. Gaia properties of the stars. Coordinates at J2015.5, the dereddened G_0, BP_0, and RP_0 magnitudes, proper motion μ_α, μ_δ, and the parallax ϖ for the analysed sample of UMPs (https://gea.esac.esa.int/archive/ Gaia Collaboration 2016, 2018) are listed. G_0, BP_0, and RP_0 magnitudes are dereddened using the Schlegel et al. (1998) extinction map. The parallaxes ϖ are not corrected for the offset $\varpi_0 = -0.029$ mas.

Identifier	$\alpha_{J2015.5}$ (deg)	$\delta_{J2015.5}$ (deg)	Gaia id	G_0 (mag)	δ_G (mag)	BP_0 (mag)	δ_{BP} (mag)	RP_0 (mag)	δ_{RP} (mag)	μ_α (mas yr^{-1})	δ_{μ_α} (mas yr^{-1})	μ_δ (mas yr^{-1})	δ_{μ_δ} (mas yr^{-1})	ϖ (mas)	δ_ϖ (mas)
HE 0020−1741	5.68699047742	−17.40811466246	2367173119271988480	12.5609	0.00017	13.0699	0.0010	11.9040	0.0006	14.424	0.064	−4.546	0.043	0.1456	0.0384
SDSS J0023+0307	5.80835977813	3.132743082	2548541852945056896	17.5638	0.001	17.7947	0.0074	17.1246	0.0074	3.743	0.318	−13.912	0.187	0.2697	0.1406
HE 0044−3755	11.65089731416	−37.65935345272	5000753194373767424	11.6633	0.0003	12.1427	0.0009	11.0310	0.0009	15.234	0.061	−7.529	0.041	0.2152	0.0344
HE 0057−5959	14.97496136508	− 59.72497472878	4903905598859396480	15.0507	0.0004	15.3857	0.0025	14.5292	0.0025	2.389	0.042	−10.522	0.041	0.1982	0.0254
HE 0107−5240	17.37149810186	−52.40951706252	4927204800008334464	14.9334	0.0003	15.3232	0.0019	14.3638	0.0019	2.414	0.033	−3.735	0.035	0.0789	0.0258
HE 0134−1519	24.27251527664	−15.07304490506	2453397508316944128	14.2270	0.0003	14.5501	0.0022	13.7181	0.0022	24.961	0.056	−10.905	0.039	0.3454	0.0299
SDSS J014036.21+234458.1	25.15092436121	23.74940873996	290930261314166528	15.0495	0.0006	15.3423	0.0034	14.5750	0.0034	1.019	0.176	−21.466	0.091	1.0482	0.0562
BD+44 493	36.70796538815	44.96278519908	341511064663637376	8.6424	0.0005	8.9634	0.0016	8.1758	0.0016	118.359	0.141	−32.229	0.105	4.7595	0.0660
HE 0233−0343	39.12435352835	−3.50172027632	2495327693479473408	15.2126	0.0005	15.4433	0.0027	14.8029	0.0027	49.962	0.073	−10.607	0.072	0.7925	0.0545
BPS CS 22963−0004	44.1941414394	−4.85485100336	5184426749232471808	14.6906	0.0005	14.9991	0.0024	14.1973	0.0024	21.712	0.058	−2.666	0.059	0.2220	0.0364
SDSS J030444.98+391021.1	46.18743595787	39.17249343121	142874251765330944	17.0085	0.0019	17.3215	0.0088	16.5085	0.0088	−0.282	0.336	−19.276	0.241	0.0752	0.1929
SMSS J031300.36−670839.3	48.25163934361	−67.14425547143	4671418400651900544	14.4342	0.0003	14.8379	0.0018	13.8545	0.0018	7.027	0.032	1.088	0.03	0.0981	0.0162
HE 0330+0148	53.15953261866	1.96344241611	3265069670684495744	13.0859	0.0004	13.8664	0.0032	12.2728	0.0032	194.093	0.453	−749.533	0.499	12.7174	0.2106
HE 0557−4840	89.66361346726	−48.66579980934	4794791782906532608	15.0976	0.0004	15.5156	0.0028	14.4984	0.0028	0.718	0.043	0.735	0.044	0.0389	0.0207
SDSS J081554.26+472947.5	123.97602487635	47.49645166114	931227322991970560	16.5417	0.0006	16.8056	0.0057	16.1052	0.0057	−14.154	0.135	−24.229	0.09	0.4441	0.0837
SDSS J092912.32+023817.0	142.30134736257	2.63804791153	3844818546870217728	17.8302	0.0023	18.1360	0.0316	17.3618	0.0316	−4.379	0.342	−3.177	0.364	0.1276	0.1872
SDSS J094708.27+461010.0	146.78455769932	46.16940656739	821637654725909760	18.7343	0.0021	19.0195	0.0221	18.2783	0.0221	13.898	0.317	−15.819	0.332	0.1989	0.2299
HE 1012−1540	153.7223563828	−15.93131552666	3751852536639575808	13.7019	0.0004	14.0084	0.0033	13.2135	0.0033	−102.32	0.046	28.13	0.04	2.5417	0.0280
SDSS J102915+172927	157.31307233934	17.49107327845	3890626773968983296	16.4857	0.0013	16.7665	0.0062	15.9976	0.0062	−10.863	0.146	−4.056	0.113	0.7337	0.0780
SDSS J103402.70+070116.6	158.51126738928	7.02126631404	3862721340654330112	17.1906	0.0018	17.4051	0.0227	16.7943	0.0063	−7.795	0.236	−6.728	0.291	0.2874	0.1367
SDSS J103556.11+064143.9	158.98383317025	6.69554785085	3862507691800855040	18.3472	0.0034	18.6230	0.0197	17.9584	0.0197	3.416	0.403	−2.41	0.369	−0.3912	0.3163
SDSS J105519.28+232234.0	163.83036912138	23.37606935407	3989873022818570240	17.5182	0.0025	17.7015	0.0317	17.1298	0.0317	7.591	0.291	−10.798	0.324	0.5909	0.1821
SDSS J120441.38+120111.5	181.17245380263	12.01984412118	3919025342543602176	16.0270	0.0005	16.3239	0.0043	15.5497	0.0043	0.395	0.11	−4.915	0.067	0.2454	0.0656
SDSS J124719.46−034152.4	191.83107728926	−3.69791015204	3681866216349964288	18.1908	0.0016	18.3958	0.0118	17.7716	0.0118	−8.562	0.439	1.812	0.226	0.3075	0.2098
LAMOST J125346.09+075343.1	193.44198364753	7.895007511	3733768078624022016	12.2280	0.0002	12.4603	0.0011	11.8239	0.0011	21.045	0.082	−58.727	0.049	1.4053	0.0378
SDSS J131326.89−001941.4	198.36201866349555	−0.32817714440715445	3687441358777986688	16.3560	0.0010	16.7237	0.0058	15.8183	0.0710	−3.790	0.160	−6.567	0.078	0.2976	0.0972
HE 1310−0536	198.37991838382	−5.8701554707	3635533208672382592	14.0256	0.0004	14.5363	0.0021	13.3649	0.0021	−5.054	0.053	−1.687	0.042	0.0078	0.0342
HE 1327−2326	202.52450119109	−23.69694272263	6194815228636688768	13.2115	0.0004	13.4500	0.0019	12.8012	0.0019	−52.524	0.04	45.498	0.035	0.8879	0.0235
HE 1424−0241	216.66802803117	−2.90764744641	3643332182086977792	15.0437	0.0007	15.3934	0.0046	14.5017	0.0046	−3.82	0.087	−2.85	0.066	0.1152	0.0469
SDSS J144256.37−001542.7	220.73490626598	−0.26186035888	3651420563283262208	17.5635	0.0023	17.8216	0.0277	17.1364	0.0277	−0.269	0.315	6.743	0.396	−0.3910	0.2981
Pristine221.8781+9.7844	221.87803086877	9.78436834556	1174522686140620672	16.1846	0.0009	16.4688	0.0053	15.7060	0.0053	−7.763	0.110	−0.058	0.116	0.1187	0.0940
SDSS J164234.48+443004.9	250.643641407	44.50138608236	1405755062407483520	17.4658	0.0012	17.6987	0.0112	17.0356	0.0112	−8.769	0.149	5.025	0.244	0.3122	0.0906
SDSS J173403.91+644633.0	263.51630029934	64.77581642801	1632736765377141632	19.1198	0.0038	19.3849	0.0465	18.7074	0.0465	2.638	0.44	−1.643	0.553	−0.1052	0.2702
SDSS J174259.67+253135.8	265.74864014534	25.52658646063	4581822389265279232	18.5115	0.0022	18.7628	0.0248	18.0991	0.0248	−6.093	0.248	−11.567	0.292	−0.1628	0.1870
2MASS J18082002−5104378	272.08342547713	−51.07724449784	6702907209758894848	11.4880	0.0003	11.7853	0.0024	11.0119	0.0024	−5.627	0.068	−12.643	0.058	1.6775	0.0397
BPS CS 22891−0200	293.82944462026	−61.70676742367	6445220927325014016	13.4478	0.0003	13.9306	0.0017	12.8053	0.0017	−5.024	0.053	0.754	0.036	0.1135	0.0342
BPS CS 22885−0096	305.21319576813	−39.89176180812	6692925538259931136	12.9385	0.0003	13.3482	0.0017	12.3514	0.0017	−4.434	0.038	−6.91	0.028	0.1708	0.0247
BPS CS 22950−0046	305.36833037469	−13.27600846442	6876806419780834048	13.7403	0.0002	14.2631	0.0011	13.0627	0.0011	1.57	0.045	−1.815	0.028	0.0587	0.0270
BPS CS 30336−0049	311.34804708033	−28.71001086007	6795730493933072128	13.5803	0.0002	14.0740	0.0013	12.9283	0.0013	−1.685	0.038	−8.132	0.027	0.0418	0.0227
HE 2139−5432	325.676883449	−54.31195504869	6461736966363075200	14.9386	0.0003	15.2991	0.0017	14.4000	0.0017	2.547	0.046	−4.484	0.041	−0.0067	0.0298
HE 2239−5019	340.61191653735	−50.06702317874	6513870718215626112	15.6038	0.0007	15.8336	0.0034	15.2107	0.0034	7.744	0.054	−23.66	0.076	0.2200	0.0545
HE 2323−0256	351.6242048175	−2.66612932812	2634585342263017984	13.9922	0.0004	14.4286	0.0031	13.3832	0.0031	1.742	0.062	−1.831	0.048	0.0038	0.0359

the Gaia photometric bands. After computing the likelihood $p(\mathbf{\Theta}_{\rm phot}|M_G, M_{BP}, M_{RP}, \mu)$, of these predictions shifted to a distance modulus μ, against the observed photometric properties of the star, $\mathcal{L}_{\rm phot}$ results from the marginalization along that isochrone:

$$\begin{aligned}\mathcal{L}_{\rm phot}(\mathbf{\Theta}_{\rm phot}|\mu, A, \Phi) &= \int_{\mathcal{I}} p(\mathbf{\Theta}_{\rm phot}|M_G, M_{BP}, M_{RP}, \mu) \\ &\times p(M_G, M_{BP}, M_{RP}|\mathcal{I}, \Phi) p(\mathcal{I}|A) d\mathcal{I}, \end{aligned} \quad (6)$$

with

$$\begin{aligned} p(\mathbf{\Theta}_{\rm phot}|M_G, M_{BP}, M_{RP}, \mu) &= \mathcal{N}(G_0|M_G + \mu, \delta_G^2 + 0.01^2) \\ &\times \mathcal{N}((BP-RP)_0|M_{BP} - M_{RP}, \delta_{BP}^2 + \delta_{RP}^2 + 2\times 0.01^2) \end{aligned} \quad (7)$$

and $\mathcal{N}(x|m, s^2)$ the value of a Gaussian function of mean m and variance s^2 taken on x. In equation (7), a systematic uncertainty of 0.01 mag is added to the photometric uncertainties in each band to represent the uncertainties on the models.

For most stars, we expect to find two peaks in $\mathcal{L}_{\rm phot}(\mathbf{\Theta}_{\rm phot}|\mathcal{M})$, corresponding to the dwarf and giant solutions but stars close to the main sequence turnoff naturally yield a PDF with a single peak.

3.1.2 $\mathcal{L}_{\rm astrom}(\mathbf{\Theta}_\varpi|\mathcal{M})$

Gaia DR2 provides us with a parallax ϖ and its uncertainty δ_ϖ, which is instrumental in breaking the dwarf/giant distance degeneracy for most stars. The astrometric likelihood is trivially

defined as

$$\mathcal{L}_{\rm astrom}(\varpi\,|\delta_\varpi, r) = \frac{1}{\sqrt{2\pi}\delta_\varpi}\exp\left(-\frac{1}{2}\left(\frac{\varpi-\varpi_0-r^{-1}}{\delta_\varpi}\right)^2\right). \quad (8)$$

Here, $\varpi_0 = -0.029$ mas is the parallax zero-point offset measured by Lindegren et al. (2018).

Even in cases for which the parallax is small and the associated uncertainties are large, the Gaia data are often informative enough to rule out a nearby (dwarf) solution.

3.1.3 $\mathcal{P}(\mathcal{M})$

Prior on the distance and position $(r|\ell, b)$ — The prior on the distance and position to the star folds in our knowledge of the distribution of UMP stars around the MW. Since we expect those stars to be among the oldest stars of the MW and (likely) accreted, we first assume a halo profile. In particular, we use the RR Lyrae density power-law profile inferred by Hernitschek et al. (2018), $\rho(r) \propto r^{-3.4}$, since RR Lyrae stars are also expected to be old halo tracers.

From this stellar density profile, the probability density to have a star at distance r from the Sun along the line of sight described by Galactic coordinates (ℓ, b) is

$$\mathcal{P}_{\rm H}(r|\ell, b) = \rho_0 r^2\left(\frac{D_{\rm GC}(r|\ell, b)}{r_0}\right)^{-3.4}. \quad (9)$$

In this equation, $D_{\rm GC}(r|\ell, b)$ is the distance of the star to the Galactic centre, while ρ_0 and r_0 are reference values for the density and the scalelength of the halo. For this work, the specific values of ρ_0 and r_0 will not affect the result because they will be simplified during the normalization of the posterior PDF.

Anticipating the results described in Section 4, we find that, even when using a pure halo prior, ∼26 per cent of our sample remains confined to the MW plane and the distance inference for a small number of stars yields unrealistic (unbound) orbits. Hence we repeat the analysis described with a mixture of a thick disc and a halo prior to investigate if, and how, the choice of the prior affects our results. This alternative MW prior is defined as

$$\mathcal{P}_{\rm DH}(r|\ell, b) = \eta\mathcal{P}_{\rm D,norm}(r|\ell, b) + (1-\eta)\mathcal{P}_{\rm H,norm}(r|\ell, b), \quad (10)$$

with $\eta = 1/2$ the mixture coefficient, $\mathcal{P}_{\rm H,norm}(r|\ell, b)$ the normalized halo prior expressed in equation (9), and $\mathcal{P}_{\rm D,norm}(r|\ell, b)$ the normalized thick disc prior defined by Binney & Tremaine (2008):

$$\mathcal{P}_{\rm D}(r|\ell, b) = \frac{r^2\Sigma_{\rm T}}{2z_{\rm T}}\exp\left(-\frac{D_{\rm GC}(r, \ell, b)}{D_{\rm T}} - \frac{|z|}{z_{\rm T}}\right), \quad (11)$$

with $\Sigma_{\rm T} = 268.648\,{\rm M}_\odot\,{\rm pc}^{-2}$ the disc surface density, $D_{\rm T} = 2$ kpc the radial scalelength for the density and $z_{\rm T} = 0.9$ kpc the vertical scalelength (Bland-Hawthorn & Gerhard 2016).

Prior on the age A, $\mathcal{P}(A)$ — There is no well defined age constraint for UMP stars, but they are usually assumed to be very old (Starkenburg et al. 2017b). Hence we assume that all the stars studied here were formed at least 11.2 Gyr ago ($\log(A/{\rm yr}) = 10.05$). Beyond this age, we assume a uniform prior on $\log(A)$ until 14.1 Gyr ($\log(A/{\rm yr}) = 10.15$), which is the maximum value of the isochrone grid.

Finally, $\mathcal{P}(\mathcal{M}) = \mathcal{P}(r|\ell, b)\mathcal{P}(A)$.

3.1.4 *Posterior PDF on distance* r

So far, $\mathcal{M} = \{\mu, A\}$ but we aim to infer the PDF on the distance modulus (or the distance) to the star alone. In order to do so, we simply marginalize over the age:

$$P(r = 10^{(\mu+5)/5}|\boldsymbol{\Theta}) = \int \mathcal{P}(\mathcal{M}|\boldsymbol{\Theta})dA, \quad (12)$$

assuming $\mu \geq 0$ mag ($r \geq 10$ pc).

3.2 Effective temperature and surface gravity inference

For each point of the theoretical isochrones $\mathcal{I}(A, \mu)$ corresponds a value of the surface gravity, $\log(g)$, and a value of the effective temperature, $T_{\rm eff}$. Marginalizing the likelihood and prior over distance modulus and age instead of over the isochrone as in equation (6), we can find the posterior probability as a function of $\log(g)$ and $T_{\rm eff}$. In detail,

$$\mathcal{P}(\log(g), T_{\rm eff}|\boldsymbol{\Theta}) = \iint \mathrm{P}(\boldsymbol{\Theta}|\log(g), T_{\rm eff}, \mathcal{I}(A), \mu) \times \Phi(M(\log(g), T_{\rm eff}, A))\mathcal{P}(r, \ell, b)\mathcal{L}_{\rm astrom}(\varpi\,|r(\mu), \delta_\varpi)\,{\rm d}A\,{\rm d}\mu. \quad (13)$$

3.3 Orbital inference

Gaia DR2 provides proper motions in right ascension and declination with their associated uncertainties and covariance. Combining this with the distance inferred through our analysis, we can calculate the velocity vector PDF $P(\boldsymbol{v}) = P(v_r, v_\alpha, v_\delta)$ for all 42 stars in our UMPs sample. This PDF, in turn, allows us to determine the properties of the orbit of the stars for a given choice of Galactic potential. We rely on the `galpy`[4] package (Bovy 2015) and choose their *MWPotential14*, which is a MW gravitational potential composed of a power law, exponentially cut-off bulge, a Miyamoto Nagai Potential disc, and a Navarro, Frenk & White (1997) dark matter halo. A more massive halo is chosen for this analysis, with a mass of $1.2 \cdot 10^{12}\,{\rm M}_\odot$ compatible with the value from Bland-Hawthorn & Gerhard (2016; versus $0.8 \cdot 10^{12}\,{\rm M}_\odot$ for the halo used in *MWPotential14*).

For each star, we perform a thousand random drawings from the position, distance, radial velocity, and proper motion PDFs. In the case of the two components of the proper motion (μ_α, μ_δ), we consider their correlation given by the coefficients in *Gaia DR2*, drawing randomly these two parameters according to a multivariate Gaussian function that takes into account the correlation. The possible correlation between coordinates and proper motions is not taken into account because it does not affect our result. For each drawing, we integrate this starting phase-space position backwards and forwards for 2 Gyr and extract the apocentre, $r_{\rm apo}$, pericentre, $r_{\rm peri}$, eccentricity, ε, energy E, the angular momentum L of the resulting orbit (note that in this frame of reference, $L_z > 0$ means a prograde orbit), and the action-angle vector $(J_r, J_\phi = L_z, J_z$, where the units are in km s^{-1} kpc).

4 RESULTS

Tables 3 and 4 summarize the results of the analysis and list the inferred stellar and orbital properties for all stars, respectively. In cases for which the (distance) PDF is double-peaked, we report the two solutions along with their fractional probability.

Fig. 1 shows the colour-magnitude diagram (CMD) and the temperature-surface gravity diagram for our UMP sample, plot-

[4] http://github.com/jobovy/galpy

Table 3. Inferred stellar parameters for the stars in the sample. Distances D, effective temperatures T_{eff} and surface gravities log(g) obtained in this work for the UMPs sample. If a second peak in the PDF is present, an estimate of the subtended area around the two peaks within $\pm 3\sigma$ is shown (Area= $\int_{d_1-3\sigma}^{d_1+3\sigma} P(r)\mathrm{d}r$). The column *Prior* indicates the MW prior used for inferring the parameters (i.e. H means halo prior, D+H indicates the disc+halo prior).

Identifier	D (kpc)	δ_D (kpc)	T_{eff} (K)	$\delta_{T_{eff}}$ (K)	log(g) (dex)	$\delta_{\log(g)}$ (dex)	Area	Prior
HE 0020−1741	10.3	0.4	4774	20	1.05	0.05		H
	10.3	0.4	4774	20	1.05	0.05		D+H
SDSS J0023+0307	2.710	0.139	6116	66	4.6	0.1	88%	H
	11.03	0.73	6047	146	3.4	0.1	12%	H
	2.693	0.136	6108	65	4.6	0.1	99.6%	D+H
	11.02	0.74	6050	154	3.4	0.1	0.4%	D+H
HE 0044−3755	5.70	0.25	4852	22	1.2	0.1		H
	5.65	0.26	4863	23	1.2	0.1		D+H
HE 0057−5959	6.80	0.71	5483	42	2.7	0.1		H
	6.50	0.72	5501	44	2.7	0.1		D+H
HE 0107−5240	14.3	1.0	5141	32	1.9	0.1		H
	14.2	1.0	5141	32	1.9	0.1		D+H
HE 0134−1519	3.75	0.33	5572	90	2.9	0.1		H
	3.61	0.30	5589	37	2.9	0.1		D+H
SDSS J014036.21+234458.1	0.762	0.022	5963	41	4.6	0.1		H
	0.761	0.022	5962	40	4.6	0.1		D+H
BD+44 493	0.211	0.003	5789	19	3.2	0.1		H
	0.211	0.003	5794	20	3.2	0.1		D+H
HE 0233−0343	1.090	0.043	6331	47	4.5	0.1		H
	1.088	0.043	6327	47	4.5	0.1		D+H
BPS CS 22963−0004	4.47	0.42	5589	42	2.9	0.1		H
	4.36	0.39	5601	43	3.0	0.1		D+H
SDSS J030444.98+391021.1	14.9	1.3	5547	39	2.8	0.1	99%	H
	1.505	0.071	5649	68	4.7	0.1	1%	H
	14.3	2.5	5548	74	2.8	0.2	79%	D+H
	1.503	0.071	5648	68	4.7	0.1	21%	D+H
SMSS J031300.36−670839.3	12.0	0.8	5111	31	1.8	0.1		H
	12.1	0.8	5111	32	1.8	0.1		D+H
HE 0330+0148	0.075	0.001	4454	1	5.0	0.1		H
	0.075	0.001	4460	1	5.0	0.1		D+H
HE 0557−4840	20.0	1.3	5017	28	1.6	0.1		H
	20.0	1.3	5018	30	1.6	0.1		D+H
SDSS J081554.26+472947.5	1.591	0.067	6034	56	4.6	0.1		H
	1.588	0.066	6031	56	4.6	0.1		D+H
SDSS J092912.32+023817.0	15.6	2.6	5708	124	3.1	0.2	68%	H
	2.398	0.205	5775	122	4.7	0.1	32%	H
	2.367	0.198	5756	120	4.7	0.1	95%	D+H
	15.5	2.6	5713	125	3.1	0.2	5%	D+H
SDSS J094708.27+461010.0	3.84	0.30	5854	110	4.7	0.1	82%	H
	21.9	2.0	5801	118	3.2	0.1	18%	H
	3.76	0.28	5823	55	4.7	0.1	98%	D+H
	21.9	2.0	5802	120	3.2	0.1	2%	D+H
HE 1012−1540	0.384	0.004	5872	16	4.7	0.1		H
	0.384	0.004	5870	16	4.7	0.1		D+H
SDSS J102915+172927	1.281	0.051	5764	57	4.7	0.1		H
	1.278	0.050	5761	56	4.7	0.1		D+H
SDSS J103402.70+070116.6	2.79	0.26	6366	110	4.5	0.1	89%	H
	8.28	0.64	6333	211	3.6	0.1	11%	H
	2.75	0.25	6330	110	4.5	0.1	99.4%	D+H
	8.18	0.65	6320	200	3.6	0.1	0.6%	D+H
SDSS J103556.11+064143.9	3.97	0.35	6144	110	4.6	0.1	67%	H
	15.6	1.2	6072	168	3.5	0.1	33%	H
	3.88	0.32	6114	106	4.6	0.1	95.5%	D+H
	15.6	1.2	6073	175	3.5	0.1	0.5%	D+H
SDSS J105519.28+232234.0	3.49	0.45	6452	147	4.5	0.1	96%	H
	8.84	0.94	6581	248	3.8	0.2	4%	H
	3.30	0.39	6387	138	4.5	0.1	99.7%	D+H
	8.79	0.99	6606	257	3.8	0.2	0.3%	D+H
SDSS J120441.38+120111.5	7.03	0.54	5679	56	3.1	0.1		H
	6.96	0.53	5686	59	3.1	0.1		D+H

Table 3 – *continued*

Identifier	D (kpc)	δ_D (kpc)	$T_{\rm eff}$ (K)	$\delta_{T_{\rm eff}}$ (K)	log(g) (dex)	$\delta_{\log(g)}$ (dex)	Area	Prior
SDSS J124719.46−034152.4	4.17	0.32	6296	92	4.5	0.1	92%	H
	13.5	1.0	6256	196	3.6	0.1	8%	H
	4.09	0.30	6273	90	4.5	0.1	99%	D+H
	13.4	1.0	6263	205	3.6	0.1	1%	D+H
LAMOST J125346.09+075343.1	0.766	0.016	6598	52	3.8	0.1		H
	0.766	0.016	6608	52	3.8	0.1		D+H
SDSS J131326.89−001941.4	8.59	2.86	5649	171	3.1	0.3	99.96%	H
	1.765	0.248	6278	171	4.5	0.1	0.04%	H
	8.07	2.70	5687	185	3.1	0.3	96.85%	D+H
	1.707	0.227	6237	164	4.6	0.1	3.15%	D+H
HE 1310−0536	20.6	0.9	4788	20	1.0	0.1		H
	20.6	0.9	4764	21	1.0	0.1		D+H
HE 1327−2326	1.212	0.024	6581	52	3.8	0.1		H
	1.212	0.024	6591	51	3.8	0.1		D+H
HE 1424−0241	10.3	1.0	5308	40	2.3	0.1		H
	10.3	1.0	5308	40	2.3	0.1		D+H
SDSS J144256.37−001542.7	11.3	1.0	5993	165	3.4	0.1	87%	H
	2.683	0.266	6104	128	4.6	0.1	13%	H
	2.634	0.249	6079	124	4.6	0.1	84%	D+H
	11.3	1.0	5998	172	3.4	0.1	16%	D+H
Pristine221.8781+9.7844	7.36	0.55	5700	63	3.1	0.1		H
	7.28	0.52	5710	65	3.1	0.1		D+H
SDSS J164234.48+443004.9	2.66	0.16	6149	77	4.6	0.1	99%	H
	10.2	0.7	6126	163	3.5	0.1	1%	H
	2.64	0.16	6140	76	4.6	0.1	99.95%	D+H
	10.1	0.7	6148	172	3.5	0.1	0.05%	D+H
SDSS J173403.91+644633.0	5.46	1.02	6094	233	4.6	0.1	86%	H
	21.8	3.0	6131	297	3.5	0.2	14%	H
	5.05	0.79	5992	208	4.6	0.1	97%	D+H
	21.7	3.0	6134	302	3.5	0.2	3%	D+H
SDSS J174259.67+253135.8	4.46	0.52	6194	145	4.6	0.1	63%	H
	16.6	1.4	6115	198	3.5	0.1	37%	H
	4.34	0.48	6162	140	4.6	0.1	94%	D+H
	16.5	1.4	6118	206	3.5	0.1	6%	D+H
2MASS J18082002−5104378	0.647	0.012	6124	44	3.5	0.1		H
	0.647	0.012	6133	44	3.5	0.1		D+H
BPS CS 22891−0200	14.7	0.5	4789	2	1.2	0.1		H
	13.6	0.6	4836	22	1.2	0.1		D+H
BPS CS 22885−0096	6.65	0.22	5068	16	1.7	0.1		H
	6.61	0.38	5070	27	1.7	0.1		D+H
BPS CS 22950−0046	19.1	0.3	<4780	–	<1.0	–		H
	19.1	0.3	<4780	–	<1.0	–		D+H
BPS CS 30336−0049	15.5	0.7	4809	20	1.1	0.1		H
	15.5	0.7	4802	21	1.1	0.1		D+H
HE 2139−5432	11.0	0.9	5259	34	2.1	0.1		H
	11.0	0.9	5259	34	2.1	0.1		D+H
HE 2239−5019	4.19	0.28	6195	179	3.5	0.1		H
	4.13	0.16	6411	100	3.6	0.1		D+H
HE 2323−0256	14.2	0.6	4937	22	1.4	0.1		H
	14.2	0.6	4937	22	1.4	0.1		D+H

ted with three isochrones that cover the age range we considered ($\log(A/\mathrm{yr}) = 10.05, 10.10, 10.15$). For stars for which the dwarf/giant degeneracy is not broken, we show both solutions connected by a dot–dashed line, where the least probable solution is marked with a dot–dashed ellipse. Only results using a MW halo prior are shown here. As we can see, from the CMD plot (left-hand panel of Fig. 1), the method overall works well, except for the HE 0330+0148 ($(BP - RP)_0 \approx 1.6$ mag) that lays outside the colour range of the available set of isochrones. This special case is discussed in more detail in section A13 (available Online). The distances and stellar parameters lead to the conclusion that 18 stars (∼43 per cent) are in the main sequence phase, and the other 24 are in the subgiant/giant phase (∼57 per cent). This is of course a result of the observing strategies of the multiple surveys that led to the discovery of these stars.

Table 4. Inferred orbital parameters of the stars in the sample. Position (X,Y,Z), the apocentre and pericentre distances in the galactocentric frame, the velocity (U,V,W) in the heliocentric frame, the eccentricity $\varepsilon = (r_{\rm apo} - r_{\rm peri})/(r_{\rm apo} + r_{\rm peri})$ of the orbit, the z-component of the angular momentum, the energy and the kind of orbit (IH = inner halo with $r_{\rm apo} < 30$ kpc, OH = outer halo with $r_{\rm apo} > 30$ kpc, P = close to the MW plane, S = possible Sgr stream member, ω = possible ωCen member) are listed. For the unbound orbits, all the orbital parameters and the kind of orbit are denoted by NB.

Identifier	X (kpc)	Y (kpc)	Z (kpc)	U (km s^{-1})	V (km s^{-1})	W (km s^{-1})	Apo (kpc)	Peri (kpc)	ε	L_z (km s^{-1} kpc)	E (km^2 s^{-2})	Orbit
HE 0020−1741	$7.909^{+0.0}_{-0.0}$	$1.84^{+0.0}_{-0.0}$	$-8.846^{+0.0}_{-0.0}$	$-428.7^{+0.0}_{-0.0}$	$-446.4^{+0.0}_{-0.0}$	$-192.2^{+0.0}_{-0.0}$	$295.8^{+0.0}_{-0.0}$	$12.0^{+0.0}_{-0.0}$	$0.92^{+0.0}_{-0.0}$	$-2311.5^{+0.0}_{-0.0}$	$63046.1^{+0.0}_{-0.0}$	IH
SDSS J0023+0307	$8.456^{+0.039}_{-0.026}$	$1.311^{+0.113}_{-0.075}$	$-2.375^{+0.133}_{-0.199}$	$76.8^{+3.9}_{-5.2}$	$-251.2^{+8.6}_{-12.9}$	$69.2^{+8.1}_{-5.4}$	$9.8^{+0.0}_{-0.0}$	$0.6^{+0.1}_{-0.1}$	$0.88^{+0.03}_{-0.04}$	$108.2^{+97.9}_{-65.3}$	$-68950.0^{+0.0}_{-0.0}$	IH
	NB	NB	NB	NB	NB	NB	NB	NB	NB	NB	NB	NB
HE 0044−3755	$7.353^{+0.028}_{-0.036}$	$-0.824^{+0.036}_{-0.045}$	$-5.61^{+0.246}_{-0.308}$	$-235.9^{+11.0}_{-12.9}$	$-397.1^{+17.8}_{-22.0}$	$-18.1^{+2.5}_{-2.9}$	$21.8^{+4.6}_{-3.0}$	$4.5^{+0.7}_{-0.7}$	$0.66^{+0.01}_{-0.01}$	$-885.7^{+102.1}_{-134.0}$	$-35273.2^{+6822.9}_{-5458.3}$	IH
HE 0057−5959	$6.077^{+0.187}_{-0.22}$	$-3.206^{+0.312}_{-0.367}$	$-5.839^{+0.568}_{-0.668}$	$206.5^{+10.9}_{-9.8}$	$-456.5^{+26.5}_{-29.9}$	$-129.0^{+20.5}_{-19.4}$	$31.3^{+10.2}_{-5.9}$	$9.0^{+0.4}_{-0.3}$	$0.56^{+0.07}_{-0.06}$	$-1947.5^{+229.5}_{-256.5}$	$-20642.9^{+9464.8}_{-6625.3}$	OH
HE 0107−5240	$5.255^{+0.167}_{-0.191}$	$-5.497^{+0.334}_{-0.382}$	$-12.877^{+0.782}_{-0.894}$	$12.5^{+2.4}_{-2.0}$	$-294.3^{+18.3}_{-19.5}$	$77.2^{+8.7}_{-7.7}$	$15.9^{+1.0}_{-0.9}$	$3.2^{+1.5}_{-1.0}$	$0.66^{+0.08}_{-0.1}$	$-354.3^{+98.9}_{-105.5}$	$-46879.6^{+3604.2}_{-3604.2}$	IH
HE 0134−1519	$9.025^{+0.103}_{-0.082}$	$0.244^{+0.025}_{-0.019}$	$-3.679^{+0.291}_{-0.369}$	$-302.5^{+18.8}_{-23.8}$	$-416.8^{+34.1}_{-43.2}$	$-197.1^{+3.7}_{-3.3}$	$70.2^{+49.3}_{-20.7}$	$4.1^{+5.9}_{-0.6}$	$0.87^{+0.02}_{-0.07}$	$-1555.1^{+313.6}_{-425.6}$	$2196.4^{+16677.9}_{-10006.7}$	OH
SDSS J014036.21+234458.1	$8.447^{+0.023}_{-0.025}$	$0.414^{+0.021}_{-0.023}$	$-0.473^{+0.027}_{-0.024}$	$132.8^{+3.6}_{-3.6}$	$-153.5^{+3.6}_{-4.3}$	$61.5^{+4.2}_{-4.7}$	$11.4^{+0.2}_{-0.1}$	$2.5^{+0.1}_{-0.1}$	$0.64^{+0.02}_{-0.02}$	$884.9^{+29.2}_{-30.8}$	$-61399.9^{+465.4}_{-413.7}$	P
BD+44 493	$8.157^{+0.005}_{-0.005}$	$0.131^{+0.004}_{-0.004}$	$-0.054^{+0.002}_{-0.002}$	$30.6^{+2.4}_{-2.6}$	$-184.5^{+2.7}_{-2.8}$	$51.8^{+0.4}_{-0.4}$	$8.3^{+0.0}_{-0.0}$	$1.5^{+0.2}_{-0.1}$	$0.69^{+0.01}_{-0.03}$	$549.6^{+21.8}_{-22.6}$	$-76078.3^{+236.5}_{-236.5}$	P
HE 0233−0343	$8.62^{+0.04}_{-0.04}$	$0.063^{+0.004}_{-0.004}$	$-0.913^{+0.061}_{-0.056}$	$-175.5^{+9.0}_{-8.6}$	$-209.8^{+13.8}_{-13.3}$	$27.5^{+5.0}_{-5.2}$	$11.9^{+0.5}_{-0.4}$	$1.0^{+0.3}_{-0.3}$	$0.85^{+0.04}_{-0.05}$	$344.6^{+119.0}_{-114.2}$	$-62501.0^{+1475.7}_{-1248.6}$	P
BPS CS 22963−0004	$10.739^{+0.268}_{-0.231}$	$-0.087^{+0.007}_{-0.008}$	$-3.62^{+0.304}_{-0.352}$	$-421.8^{+20.9}_{-24.0}$	$-359.1^{+29.5}_{-34.1}$	$-39.2^{+19.1}_{-16.6}$	$155.8^{+183.4}_{-55.0}$	$3.0^{+8.7}_{-1.1}$	$0.96^{+0.0}_{-0.01}$	$-1134.0^{+337.8}_{-391.2}$	$25397.6^{+15195.6}_{-11396.7}$	OH
SDSS J030444.98+391021.1	NB	NB	NB	NB	NB	NB	NB	NB	NB	NB	NB	NB
	$9.24^{+0.063}_{-0.059}$	$0.735^{+0.037}_{-0.035}$	$-0.435^{+0.021}_{-0.022}$	$-77.0^{+6.6}_{-7.0}$	$-33.8^{+5.1}_{-5.8}$	$-139.9^{+6.8}_{-6.1}$	$16.5^{+1.1}_{-1.0}$	$7.9^{+0.1}_{-0.1}$	$0.35^{+0.03}_{-0.03}$	$1960.2^{+38.6}_{-47.4}$	$-40260.6^{+1798.9}_{-1574.0}$	IH
SMSS J031300.36−670839.3	$5.821^{+0.134}_{-0.16}$	$-8.413^{+0.516}_{-0.619}$	$-8.566^{+0.526}_{-0.631}$	$-218.6^{+18.4}_{-19.5}$	$-459.4^{+16.2}_{-18.2}$	$-32.7^{+12.9}_{-12.2}$	$40.4^{+14.7}_{-7.8}$	$5.8^{+1.5}_{-1.5}$	$0.76^{+0.02}_{-0.01}$	$519.6^{+227.0}_{-176.6}$	$-14038.7^{+9814.5}_{-7633.5}$	OH
HE 0330+0148	$8.055^{+0.002}_{-0.002}$	$-0.003^{+0.0}_{-0.0}$	$-0.049^{+0.002}_{-0.002}$	$106.0^{+8.6}_{-9.1}$	$-240.9^{+9.1}_{-11.1}$	$-71.1^{+8.1}_{-8.1}$	$9.0^{+0.6}_{-0.0}$	$0.5^{+0.3}_{-0.2}$	$0.89^{+0.04}_{-0.06}$	$83.2^{+73.0}_{-89.8}$	$-72495.6^{+717.6}_{-717.6}$	P
HE 0557−4840	$12.281^{+0.27}_{-0.254}$	$-17.142^{+1.012}_{-1.075}$	$-9.58^{+0.566}_{-0.601}$	$-110.0^{+5.3}_{-5.9}$	$-203.0^{+2.8}_{-3.1}$	$-32.5^{+6.1}_{-4.4}$	$23.4^{+1.2}_{-1.1}$	$8.2^{+0.9}_{-0.7}$	$0.48^{+0.02}_{-0.03}$	$2273.1^{+186.3}_{-165.6}$	$-29646.0^{+2020.2}_{-2272.7}$	IH
SDSS J081554.26+472947.5	$9.332^{+0.082}_{-0.091}$	$0.185^{+0.011}_{-0.013}$	$0.892^{+0.055}_{-0.061}$	$-12.2^{+18.0}_{-18.0}$	$-176.1^{+12.1}_{-9.9}$	$-156.2^{+12.6}_{-15.2}$	$9.7^{+0.2}_{-0.2}$	$5.0^{+0.5}_{-0.5}$	$0.32^{+0.04}_{-0.03}$	$705.3^{+101.9}_{-92.2}$	$-59940.5^{+2067.3}_{-1447.1}$	IH
SDSS J092912.32+023817.0	$9.225^{+0.165}_{-0.064}$	$-1.502^{+0.203}_{-0.078}$	$1.401^{+0.189}_{-0.073}$	$-218.9^{+9.2}_{-5.2}$	$-275.2^{+13.3}_{-7.8}$	$178.3^{+1.6}_{-2.4}$	$23.5^{+2.6}_{-1.4}$	$2.7^{+0.3}_{-0.1}$	$0.79^{+0.04}_{-0.02}$	$91.4^{+71.5}_{-48.8}$	$-33988.5^{+3752.4}_{-2170.6}$	IH/S
	$16.138^{+0.072}_{-0.234}$	$-9.971^{+0.088}_{-0.287}$	$9.303^{+0.082}_{-6.944}$	$-321.7^{+9.5}_{-43.6}$	$-447.3^{+4.7}_{-35.4}$	$-102.6^{+1.1}_{-40.7}$	$193.7^{+17.6}_{-11.8}$	$21.1^{+0.1}_{-0.4}$	$0.8^{+0.02}_{-0.01}$	$-51.8^{+197.4}_{-928.4}$	$34372.9^{+3808.7}_{-2625.2}$	OH
SDSS J094708.27+461010.0	$10.521^{+0.216}_{-0.189}$	$0.326^{+0.028}_{-0.024}$	$2.941^{+0.251}_{-0.22}$	$205.0^{+18.6}_{-16.3}$	$-264.7^{+20.6}_{-22.1}$	$197.6^{+22.6}_{-18.8}$	$30.0^{+11.4}_{-5.7}$	$8.2^{+0.8}_{-0.8}$	$0.58^{+0.07}_{-0.05}$	$-71.0^{+198.5}_{-213.8}$	$-21786.8^{+9921.8}_{-7717.0}$	OH
	NB	NB	NB	NB	NB	NB	NB	NB	NB	NB	NB	NB
HE 1012−1540	$8.074^{+0.002}_{-0.002}$	$-0.316^{+0.008}_{-0.008}$	$0.207^{+0.005}_{-0.005}$	$-222.5^{+4.3}_{-4.6}$	$-191.1^{+0.4}_{-0.4}$	$49.0^{+1.9}_{-1.8}$	$14.0^{+0.3}_{-0.3}$	$1.3^{+0.1}_{-0.0}$	$0.83^{+0.0}_{-0.01}$	$552.7^{+3.7}_{-3.7}$	$-55562.1^{+850.4}_{-850.4}$	P
SDSS J102915+172927	$8.537^{+0.038}_{-0.033}$	$-0.481^{+0.03}_{-0.034}$	$1.062^{+0.075}_{-0.066}$	$-31.1^{+3.4}_{-3.6}$	$-23.7^{+2.7}_{-3.3}$	$-68.7^{+3.9}_{-4.4}$	$10.9^{+0.3}_{-0.2}$	$8.6^{+0.0}_{-0.0}$	$0.12^{+0.01}_{-0.01}$	$1952.3^{+15.6}_{-19.6}$	$-49546.0^{+552.3}_{-552.3}$	P
SDSS J103402.70+070116.6	$8.917^{+0.075}_{-0.094}$	$-1.482^{+0.122}_{-0.153}$	$2.209^{+0.181}_{-0.227}$	$-97.0^{+1.2}_{-3.4}$	$-178.5^{+6.2}_{-8.9}$	$35.4^{+7.0}_{-11.0}$	$10.2^{+0.1}_{-0.2}$	$2.3^{+0.2}_{-0.3}$	$0.63^{+0.03}_{-0.04}$	$775.0^{+41.4}_{-55.4}$	$-65816.8^{+49.8}_{-102.9}$	P
	$10.714^{+0.263}_{-0.02}$	$-4.385^{+0.425}_{-0.033}$	$6.535^{+0.633}_{-0.241}$	$-188.8^{+36.2}_{-1.5}$	$-366.7^{+24.4}_{-0.1}$	$-126.1^{+38.5}_{-0.8}$	$24.3^{+17.8}_{-0.0}$	$9.3^{+2.1}_{-0.1}$	$0.46^{+0.12}_{-0.0}$	$-426.0^{+81.6}_{-27.7}$	$-27566.6^{+17448.6}_{-82.0}$	IH
SDSSJ103556.11+064143.9	$9.26^{+0.121}_{-0.035}$	$-2.106^{+0.202}_{-0.058}$	$3.131^{+0.3}_{-0.087}$	$87.9^{+12.0}_{-2.3}$	$2.2^{+4.7}_{-6.3}$	$-20.0^{+4.8}_{-0.2}$	$22.2^{+1.0}_{-1.0}$	$7.1^{+0.2}_{-0.1}$	$0.52^{+0.03}_{-0.01}$	$2137.3^{+60.4}_{-50.3}$	$-32395.0^{+1110.9}_{-1568.4}$	IH
	$12.915^{+0.102}_{-0.061}$	$-8.218^{+0.171}_{-0.102}$	$12.216^{+0.254}_{-0.346}$	$300.8^{+42.6}_{-25.2}$	$-60.8^{+43.7}_{-31.4}$	$25.1^{+11.4}_{-13.5}$	$147.8^{+25.5}_{-11.8}$	$11.9^{+0.4}_{-0.2}$	$0.86^{+0.02}_{-0.01}$	$-99.4^{+873.1}_{-641.6}$	$25522.1^{+5791.8}_{-2555.6}$	OH
SDSS J105519.28+232234.0	$9.313^{+0.197}_{-0.173}$	$-0.922^{+0.119}_{-0.136}$	$3.204^{+0.481}_{-0.421}$	$155.4^{+29.0}_{-25.8}$	$-150.7^{+19.3}_{-19.3}$	$90.2^{+8.6}_{-5.4}$	$15.2^{+2.7}_{-2.7}$	$4.9^{+0.4}_{-0.2}$	$0.52^{+0.04}_{-0.05}$	$790.4^{+169.0}_{-236.6}$	$-45745.3^{+4608.7}_{-4608.7}$	IH
SDSS J120441.38+120111.5	$8.213^{+0.021}_{-0.016}$	$-2.304^{+0.168}_{-0.228}$	$6.814^{+0.678}_{-0.499}$	$92.3^{+9.6}_{-9.1}$	$-149.9^{+10.1}_{-13.8}$	$6.2^{+4.3}_{-5.2}$	$12.8^{+0.7}_{-0.6}$	$3.7^{+0.3}_{-0.3}$	$0.55^{+0.04}_{-0.04}$	$597.9^{+110.1}_{-169.3}$	$-53841.3^{+1714.2}_{-1142.8}$	IH
SDSS J124719.46−034152.4	$6.874^{+0.081}_{-0.108}$	$-1.879^{+0.135}_{-0.18}$	$3.581^{+0.351}_{-0.263}$	$-141.4^{+15.7}_{-19.6}$	$-102.9^{+5.2}_{-10.4}$	$88.2^{+6.9}_{-5.6}$	$9.9^{+2.9}_{-0.0}$	$5.0^{+0.3}_{-0.2}$	$0.41^{+0.05}_{-0.05}$	$1263.5^{+31.8}_{-31.8}$	$-55819.2^{+2448.5}_{-2448.5}$	IH
	NB	NB	NB	NB	NB	NB	NB	NB	NB	NB	NB	NB
LAMOST J125346.09+075343.1	$7.856^{+0.006}_{-0.005}$	$-0.208^{+0.008}_{-0.008}$	$0.723^{+0.028}_{-0.027}$	$188.3^{+6.8}_{-6.8}$	$-148.3^{+4.7}_{-4.9}$	$2.6^{+2.6}_{-2.7}$	$13.4^{+0.4}_{-0.3}$	$1.9^{+0.1}_{-0.2}$	$0.75^{+0.03}_{-0.02}$	$766.8^{+40.7}_{-42.5}$	$-56611.4^{+914.8}_{-774.1}$	P
SDSS J131326.89−001941.4	$4.472^{+0.866}_{-1.126}$	$-3.561^{+0.874}_{-1.136}$	$9.327^{+3.014}_{-2.318}$	$92.1^{+7.3}_{-6.7}$	$-443.7^{+81.5}_{-124.4}$	$99.5^{+33.6}_{-43.7}$	$20.4^{+39.8}_{-8.5}$	$8.5^{+3.3}_{-1.6}$	$0.41^{+0.26}_{-0.13}$	$-1256.6^{+383.5}_{-264.5}$	$-34000.2^{+35769.3}_{-16692.3}$	IH
HE 1310−0536	$0.259^{+0.29}_{-0.29}$	$-8.32^{+0.311}_{-0.311}$	$17.184^{+0.644}_{-0.644}$	$-284.9^{+13.2}_{-12.5}$	$-448.9^{+16.8}_{-15.2}$	$47.0^{+3.4}_{-3.2}$	$99.7^{+38.3}_{-26.0}$	$19.0^{+0.7}_{-0.7}$	$0.68^{+0.06}_{-0.07}$	$2216.2^{+238.5}_{-238.5}$	$15227.9^{+8052.8}_{-8052.8}$	OH
HE 1327−2326	$7.332^{+0.028}_{-0.022}$	$-0.686^{+0.028}_{-0.023}$	$0.755^{+0.025}_{-0.031}$	$-279.3^{+12.7}_{-10.7}$	$-68.7^{+1.4}_{-1.3}$	$287.8^{+8.5}_{-10.6}$	$91.4^{+18.5}_{-17.0}$	$7.4^{+0.0}_{-0.0}$	$0.85^{+0.02}_{-0.03}$	$1522.3^{+4.9}_{-5.6}$	$11193.7^{+5154.1}_{-6091.2}$	OH
HE 1424−0241	$1.915^{+0.468}_{-0.54}$	$-1.738^{+0.134}_{-0.154}$	$8.108^{+0.723}_{-0.627}$	$-26.0^{+5.5}_{-7.0}$	$-233.7^{+16.1}_{-22.8}$	$44.9^{+2.2}_{-2.1}$	$8.8^{+0.7}_{-0.6}$	$0.9^{+0.5}_{-0.3}$	$0.81^{+0.06}_{-0.09}$	$58.6^{+38.9}_{-23.9}$	$-71087.9^{+2804.7}_{-1869.8}$	IH
SDSS J144256.37−001542.7	NB	NB	NB	NB	NB	NB	NB	NB	NB	NB	NB	NB
	$6.366^{+0.089}_{-0.221}$	$-0.233^{+0.013}_{-0.032}$	$2.033^{+0.283}_{-0.113}$	$93.2^{+6.6}_{-7.6}$	$42.0^{+8.0}_{-6.4}$	$217.1^{+9.0}_{-9.0}$	$39.1^{+5.2}_{-2.6}$	$6.7^{+0.1}_{-0.1}$	$0.71^{+0.03}_{-0.02}$	$1832.0^{+27.4}_{-18.2}$	$-14290.8^{+3324.2}_{-1662.1}$	OH
Pristine 221.8781+9.7844	$3.941^{+0.29}_{-0.38}$	$0.432^{+0.041}_{-0.031}$	$6.4^{+0.602}_{-0.46}$	$-249.6^{+12.4}_{-18.2}$	$-194.4^{+12.6}_{-19.9}$	$-6.7^{+12.7}_{-8.7}$	$14.1^{+2.3}_{-1.1}$	$4.9^{+0.7}_{-0.5}$	$0.49^{+0.01}_{-0.01}$	$123.6^{+83.8}_{-119.7}$	$-47818.2^{+5527.2}_{-3684.8}$	IH/S
SDSS J164234.48+443004.9	$7.283^{+0.048}_{-0.072}$	$1.869^{+0.196}_{-0.13}$	$1.742^{+0.182}_{-0.121}$	$-124.6^{+6.1}_{-9.1}$	$-143.0^{+4.5}_{-6.1}$	$-6.7^{+8.7}_{-5.8}$	$9.2^{+0.0}_{-0.0}$	$1.6^{+0.2}_{-0.2}$	$0.72^{+0.03}_{-0.04}$	$539.8^{+82.0}_{-41.0}$	$-70959.7^{+2586.2}_{-0.0}$	P
SDSS J173403.91+644633.0	$8.374^{+0.131}_{-0.058}$	$4.823^{+1.691}_{-0.752}$	$3.089^{+1.083}_{-0.481}$	$66.2^{+25.0}_{-16.7}$	$-174.4^{+20.0}_{-15.0}$	$-200.0^{+16.2}_{-23.1}$	$13.0^{+5.5}_{-2.7}$	$7.7^{+1.8}_{-1.3}$	$0.33^{+0.07}_{-0.06}$	$980.4^{+414.3}_{-207.1}$	$-43731.4^{+9796.3}_{-7347.2}$	IH
	NB	NB	NB	NB	NB	NB	NB	NB	NB	NB	NB	NB
SDSS J174259.67+253135.8	$5.293^{+0.294}_{-0.336}$	$3.185^{+0.399}_{-0.349}$	$2.0^{+0.25}_{-0.219}$	$74.6^{+26.6}_{-21.6}$	$-348.1^{+23.9}_{-27.3}$	$-58.7^{+8.8}_{-7.6}$	$8.0^{+1.3}_{-0.7}$	$1.0^{+0.2}_{-0.2}$	$0.77^{+0.06}_{-0.04}$	$-227.0^{+71.9}_{-61.6}$	$-78634.3^{+5992.5}_{-3424.3}$	IH/ω/P
	NB	NB	NB	NB	NB	NB	NB	NB	NB	NB	NB	NB
2MASS J18082002−5104378	$7.40^{+0.02}_{-0.03}$	$-0.189^{+0.007}_{-0.008}$	$-0.163^{+0.006}_{-0.007}$	$2.19^{+0.53}_{-0.53}$	$-45.4^{+1.6}_{-1.7}$	$-5.2^{+0.2}_{-0.2}$	$7.6^{+0.1}_{-0.1}$	$6.3^{+0.1}_{-0.1}$	$0.091^{+0.006}_{-0.005}$	$1520.0^{+17.0}_{-18.4}$	$-64227.3^{+509.0}_{-509.0}$	P
BPS CS 22891−0200	$-2.803^{+0.469}_{-0.469}$	$-5.036^{+0.219}_{-0.219}$	$-6.553^{+0.285}_{-0.285}$	$255.7^{+11.1}_{-11.1}$	$-93.4^{+4.6}_{-4.9}$	$222.1^{+14.0}_{-12.5}$	$64.0^{+18.9}_{-11.1}$	$7.4^{+0.6}_{-0.6}$	$0.8^{+0.03}_{-0.02}$	$-1788.2^{+160.3}_{-171.0}$	$1304.9^{+7251.3}_{-6445.6}$	OH
BPS CS 22885−0096	$2.413^{+0.302}_{-0.302}$	$0.123^{+0.007}_{-0.007}$	$-3.701^{+0.2}_{-0.2}$	$-145.0^{+8.6}_{-8.1}$	$-241.8^{+12.1}_{-12.9}$	$223.8^{+7.2}_{-7.2}$	$9.3^{+0.6}_{-1.3}$	$3.6^{+0.3}_{-0.3}$	$0.44^{+0.06}_{-0.06}$	$5.2^{+36.0}_{-29.7}$	$-63004.7^{+2672.9}_{-2672.9}$	IH/S
BPS CS 22950−0046	$-6.594^{+0.353}_{-0.243}$	$8.665^{+0.144}_{-0.21}$	$-8.233^{+0.199}_{-0.137}$	$59.4^{+8.2}_{-7.7}$	$-70.6^{+5.8}_{-5.5}$	$-222.9^{+6.8}_{-5.6}$	$41.7^{+3.6}_{-3.2}$	$2.5^{+0.4}_{-0.4}$	$0.89^{+0.02}_{-0.02}$	$-572.2^{+56.5}_{-56.5}$	$-14149.5^{+2904.8}_{-2582.0}$	OH
BPS CS 30336−0049	$-4.037^{+0.507}_{-0.475}$	$3.41^{+0.135}_{-0.144}$	$-9.176^{+0.386}_{-0.362}$	$-31.8^{+6.6}_{-6.6}$	$-643.6^{+25.2}_{-23.6}$	$119.8^{+1.9}_{-2.4}$	$122.7^{+51.1}_{-41.4}$	$8.1^{+0.8}_{-0.8}$	$0.88^{+0.03}_{-0.04}$	$1489.5^{+305.3}_{-305.3}$	$19080.8^{+11833.4}_{-11833.4}$	OH
HE 2139−5432	$0.746^{+0.54}_{-0.607}$	$-2.466^{+0.183}_{-0.206}$	$-8.023^{+0.597}_{-0.672}$	$-48.5^{+11.6}_{-12.3}$	$-264.7^{+18.4}_{-20.7}$	$-113.8^{+8.5}_{-8.5}$	$9.8^{+1.1}_{-0.9}$	$1.1^{+0.5}_{-0.3}$	$0.79^{+0.05}_{-0.06}$	$87.2^{+37.9}_{-27.1}$	$-66571.3^{+4078.3}_{-3625.1}$	IH

Table 4 – *continued*

Identifier	X (kpc)	Y (kpc)	Z (kpc)	U (km s^{-1})	V (km s^{-1})	W (km s^{-1})	Apo (kpc)	Peri (kpc)	ε	L_z (km s^{-1} kpc)	E (km^2 s^{-2})	Orbit
HE 2239−5019	$5.857^{+0.137}_{-0.142}$	$-0.731^{+0.047}_{-0.049}$	$-3.406^{+0.217}_{-0.226}$	$125.2^{+4.6}_{-4.6}$	$-540.5^{+29.3}_{-30.5}$	$-248.0^{+3.9}_{-3.7}$	$52.9^{+16.6}_{-10.4}$	$6.8^{+0.0}_{-0.0}$	$0.77^{+0.05}_{-0.05}$	$-1792.6^{+141.3}_{-141.3}$	$-4551.9^{+7794.6}_{-7145.0}$	OH
HE 2323−0256	$6.687^{+0.076}_{-0.053}$	$7.11^{+0.29}_{-0.411}$	$-11.698^{+0.674}_{-0.476}$	$-53.7^{+4.4}_{-5.3}$	$-199.4^{+8.4}_{-6.1}$	$20.4^{+5.7}_{-4.2}$	$15.4^{+0.5}_{-0.6}$	$2.8^{+0.2}_{-0.2}$	$0.68^{+0.03}_{-0.03}$	$44.7^{+94.9}_{-78.1}$	$-48598.2^{+1025.7}_{-1172.2}$	IH

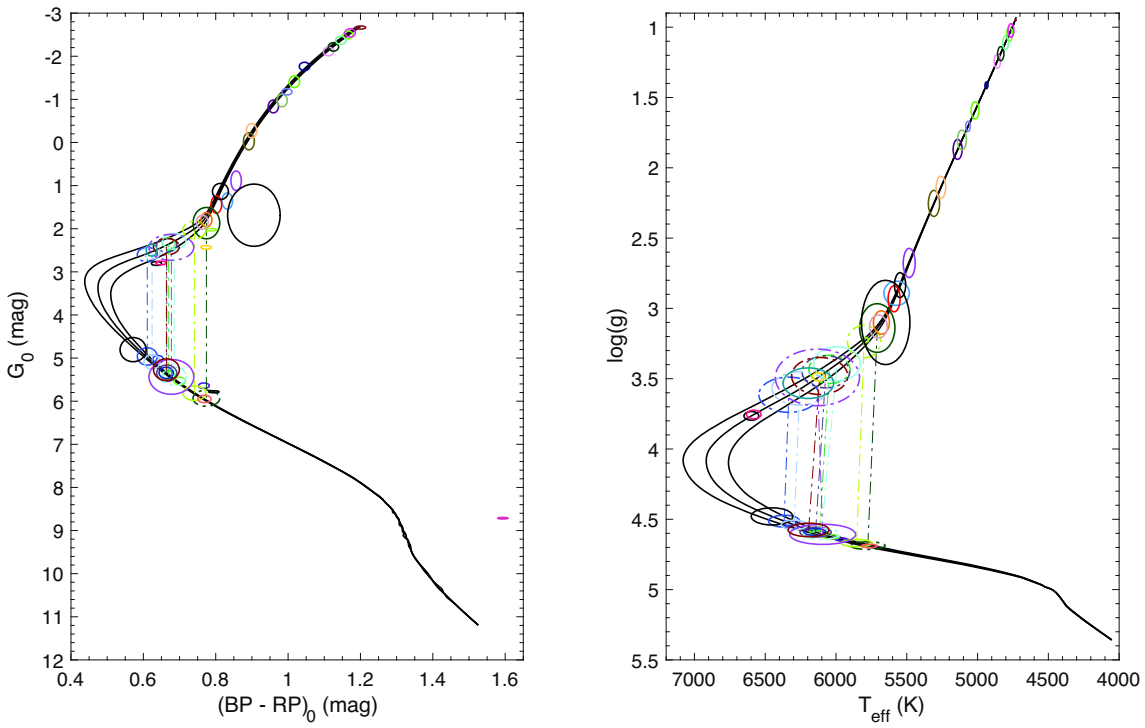

Figure 1. Position of the sample stars in the CMD (left) and the log (g) versus $T_{\rm eff}$ plane (right). The ellipses represent the position of the stars within 1σ and the black lines correspond to the three isochrones with log (A/yr) = 10.05, 10.10, 10.15 and metallicity [Fe/H] = −4 dex. If the dwarf-giant degeneracy is not broken, the two possible solutions are represented and connected by a dot–dashed line of the same colour code. Each colour represents a star and the colour-code is the same as the colour-code for the markers in Fig. 2 and the panel's titles in Figs A1–A42 (available Online). Solutions with integrated probability ($\int_{d-3\sigma}^{d+3\sigma} P(r)dr$) lower than 5 per cent are not shown and solutions with integrated probability in the range [5 per cent, 50 per cent] are shown with dot–dashed ellipses.

For all 42 stars in our sample, we show the results of our analysis in Figs A1–A42 (available Online). In all figures, the top-left panel shows the distance likelihood functions and posterior PDFs, the top-middle panel presents the log(g) PDF, while the top-right panel shows the effective temperature PDF. The orbit of the star in Galactic Cartesian coordinates is presented in the bottom panels of the figures.

In the subsections of Appendix A (available Online), we discuss in detail the results for every star in the sample sorted by right ascension. Specifically, we focus on the inferred distances, stellar parameters, and orbits using a MW halo prior and, when it yields different results, we also discuss the use of the disc+halo prior. A global comparison between the inferred stellar parameters form our work and the values from the literature is described in Appendix B (available Online) and shown in the two panels of Fig. B1.

We did a comparison between the distances inferred in this work and the ones inferred by Bailer-Jones et al. (2018). These authors use a posterior probability composed by the astrometric likelihood shown in equation (8) and a MW prior that is based on a Gaia-observed Galaxy distribution function accurately describing the overall distribution of all MW stars. This is naturally more biased to higher densities in the thin disc and thus results in closer distances for most of the stars.

Frebel et al. (2018) compiled a list of 29 UMP stars inferring orbital parameters starting from the MW prior described in Bailer-Jones et al. (2018), but fixing the length-scale parameter to $L = 0.5$. As both the initial assumptions and the focus of the analysis given in Frebel et al. (2018) significantly differ from the approach taken in this work, we refrain from a further qualitative comparison.

5 DISCUSSIONS

Our combined analysis of the *Gaia DR2* astrometry and photometry with stellar population models for low-metallicity stars allows us to infer the stellar parameters and orbital properties of the 42 known

UMP stars. We derive well constrained properties for most stars and, in particular, we are now in a position to unravel the possible origin of the heterogeneous sample of UMP stars found to date.

5.1 Insights on the orbits of UMP stars

Apart from two ambiguous cases, we can classify the orbits of the UMP stars within three loosely defined categories:

(i) 19 'inner halo' stars, arbitrarily defined as having apocentres smaller than 30 kpc.
(ii) 12 'outer halo' stars with apocentre larger than 30 kpc.
(iii) Strikingly, 11 stars that have 'MW plane' orbits, by which we mean that they stay confined close to the MW plane ($|Z| < 3.0$ kpc).

Fig. 2 attempts to show these different kind of orbits, displaying on the top panel the vertical component of the action-angle J_z versus the rotational component J_ϕ ($=L_z$) for all the UMP in our sample. In this space, the stars confined to the MW plane (denoted by a star marker) are constrained to the lower part of the diagram, while the halo stars have larger J_z. Stars that have a prograde motion have $J_\phi > 0$ and stars with retrograde orbits lie in the $J_\phi < 0$ part of the diagram. We note how the Caffau star (SDSS J102915+172927) and 2MASS J18082002−5104378 occupy a special place in this plane and they are the only stars on a quasi-circular orbit at large J_ϕ and low J_z.

It is appealing to assign a tentative origin to stars in these three categories. The 'inner halo' stars could well be stars accreted on to the MW during its youth, when its mass was smaller and therefore its potential well less deep than it is now. At that time, more energetic orbits would have been unbound and left the MW in formation. 'Outer halo' orbits tend to have very radial orbits in this sample (likely a consequence of the window function imparted by the various surveys that discovered these UMP stars; see below), which makes it easier to identify them. It is tempting to see those as being brought in through the accretion of faint dwarf galaxies on to the MW throughout the hierarchical formation of its halo. Although no UMP has been found in MW satellite dwarf galaxies yet, we know of many extremely metal-poor stars in these systems, down to [Fe/H] $= -4$ (e.g. Tafelmeyer et al. 2010) and UMP stars are expected to be present as well (Salvadori, Skúladóttir & Tolstoy 2015). We note that, among the two 'halo' categories, there is a distinct preference for prograde over retrograde orbits.

The 11 'MW plane' orbits are much more unexpected:

(i) 8 stars (SDSS J014036.21+234458.1, BD+44 493, HE 0233−0343, HE 0330+0148, HE 1012−1540, SDSS J103402.70+070116.6, LAMOST J125346.09+075343, SDSS J164234.48+443004.9) share similar rosette orbits within a wide range of angular momentum along the z axis ($83 \lesssim L_z \lesssim 885$ km s^{-1} kpc). These stars orbit close to the plane, but not on circular orbits.
(ii) SDSS J102915+172927 and 2MASS J18082002−5104378 (Figs A19 and A35 available Online), are on almost circular orbits close to the solar radius.
(iii) SDSS J174259.67+253135.8 (Fig. A34, available Online) is retrograde and more likely on an 'inner halo' orbit that remains close to the MW plane.

The first 10 of those stars, excluding SDSS J174259.67+253135.8, all have positive L_z and thus a prograde orbit, which is unlikely to be a random occurrence (< 1 per cent chance). It is worth noting that it is very unlikely the selection functions that led to the discovery of the UMP stars biased the sample for/against prograde orbit. The origin of those stars is puzzling but we can venture three different hypothesis for their presence in the sample, all of which must account for the fact that this significant fraction of UMP stars, which are expected to be very old, appears to know where the plane of the MW is located, even though the MW plane was unlikely to be in place when they formed.

Scenario 1: The first obvious scenario is that these stars formed in the MW disc itself after the HI disc settled. In this fashion, the stars were born with a quasi-circular orbit and then the presence of a dynamical heating mechanism is mandatory to increase the eccentricity and the height from the plane as a function of time. We find that all the prograde 'MW plane' stars and few catalogued as inner halo stars that are confined within $Z_{\rm max} < 15$ kpc and $d_{\rm apo} < 25$ kpc (see Fig. 2) overlap in the parameters space ($Z_{\rm max}$, $d_{\rm apo}$, L_z, E) with a population of known stars at higher metallicity that Haywood et al. (2018) hypothesize to be born in the thick disc and then dynamical heated by the interaction between the disc and a merging satellite. However, the question is whether in a relatively well-mixed HI disc it is possible to form stars so completely devoid of metals.

Scenario 2: The second scenario is that these stars were brought into the MW by the accretion of a massive satellite dwarf galaxy. Cosmological simulations have shown that merger events are expected to sometimes be aligned with the disc. As a result, significant stellar populations currently in the disc might actually be merger debris (Gómez et al. 2017). Alternatively, Scannapieco et al. (2011), show that 5–20 per cent of disc stars in their simulated MW-like disc galaxies were not formed *in situ* but, instead, accreted early from now disrupted satellites on co-planar orbits. Additionally, it is well known that the accretion of a massive system on to the MW will see its orbit align with the plane of the MW via dynamical friction, as shown by Peñarrubia, Kroupa & Boily (2002) or Abadi et al. (2003). From these authors' simulations, one would expect orbits to become such that they would end up with larger eccentricities than the satellite's orbit at the start of the merging process and also aligned with the disc by dynamical friction and tidal interactions, which is compatible with our orbital inference for the remarkable UMP stars. If such an accretion took place in the MW's past, it could have brought with it a significant fraction of the UMP stars discovered in the solar neighbourhood. The accretion of the so-called Gaia-Enceladus satellite in the Milky Way's past (Belokurov et al. 2018; Haywood et al. 2018; Helmi et al. 2018) could be an obvious culprit, however Gaia-Enceladus was discovered via the mainly halo-like and retrograde orbit of its stars whereas the vast majority of the stars we find here are on prograde orbits. In fact, there is no evidence of a particular overdensity of stars in the top-left region of the J_z versus J_ϕ of Fig. 2 where Gaia-Enceladus stars are expected to be found. It would therefore be necessary to summon the presence of another massive or several less massive accretion events on to the MW if this scenario is valid.

Scenario 3: Finally, the third scenario that could explain the presence of this significant fraction of UMP stars that remain confined to the plane of the MW would be one in which these stars originally belonged to one or more of the building blocks of the proto-MW, as it was assembling into the MW that we know today. Fully cosmological simulations confirm that stars that are at the present time deeply embedded in our Galaxy do not need to have their origin in the proto-Galaxy. El-Badry et al. (2018) find in their cosmological simulations that of all stars formed before $z = 5$ presently within 10 kpc of the Galactic centre less than half were already in the main progenitor at $z = 5$. Over half of these extremely

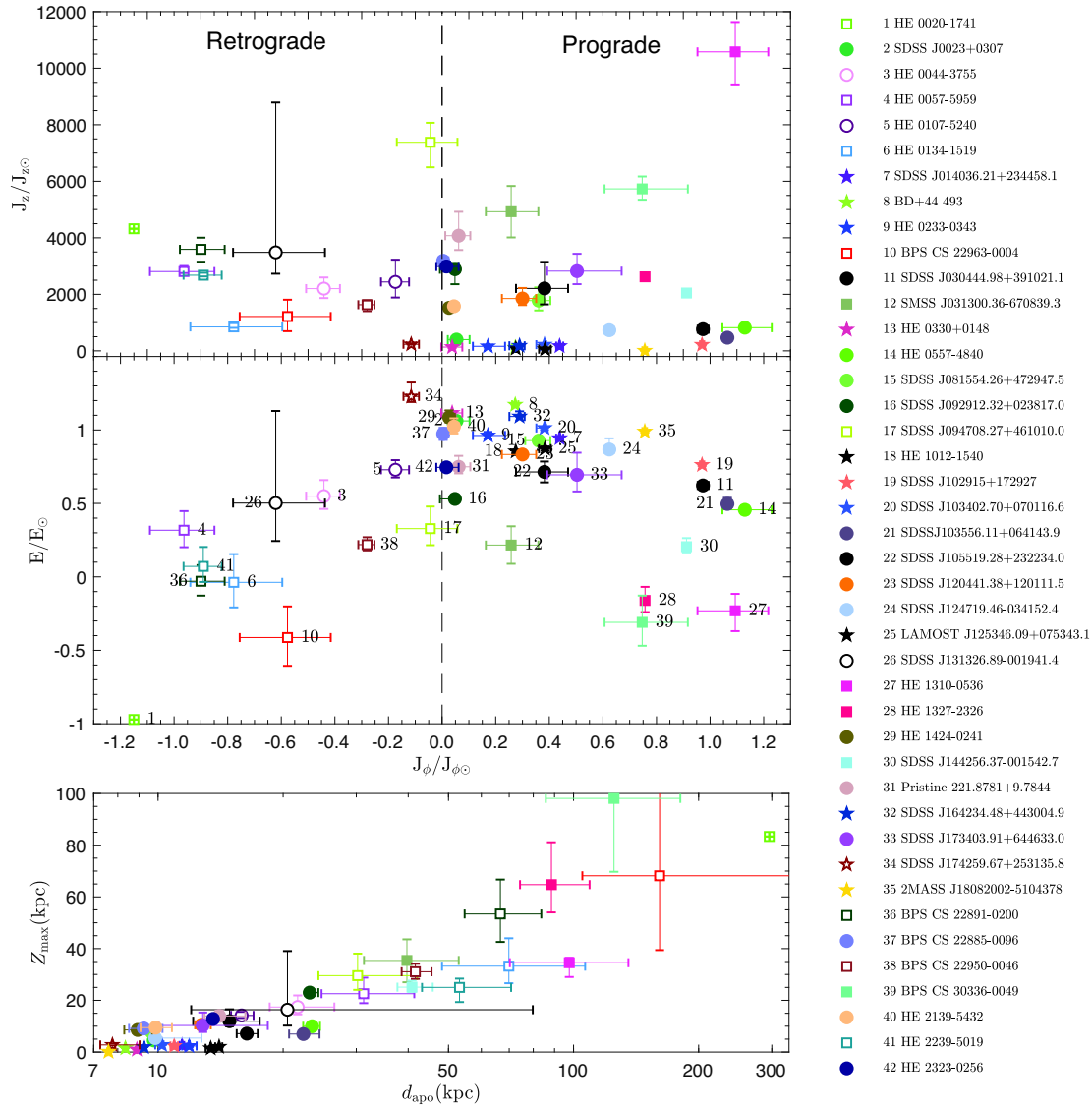

Figure 2. Position of the sample stars in the rotational action J_ϕ ($=L_z$) and vertical action J_z space (top panel), in the energy and rotational action space, and in the maximum height versus apocentre of the stars' orbits (bottom panel). The rotational and vertical action and the Energy are scaled by the Sun values respectively $J_{\phi\odot} = 2009.92\,\mathrm{km\,s^{-1}\,kpc}$, $J_{z\odot} = 0.35\,\mathrm{km\,s^{-1}\,kpc}$, and $E_\odot = -64943.61\,\mathrm{km^2\,s^{-2}}$. Stars within our 'MW planar' sample that are confined close to the MW plane are marked with a star symbols, while 'inner halo' and 'outer halo' stars are represented by circles and squares, respectively. Retrograde stars, which are located on the left side of the top and central panels ($J_\phi < 0\,\mathrm{km\,s^{-1}\,kpc}$) are denoted with empty marker, while prograde stars are shown with a filled marked. The colour-coding is the same as in Fig. 1 and as the title of Figs A1–A42 (available Online) and helps to differentiate the stars. The full legend is provided on the side of this figure. The number associated to each star also corresponds to the number of the subsection in the Appendix A (available Online) in which the individual results are discussed.

old stars would thus make their way into the main Galaxy in later merging events and find themselves at $z = 5$ inside different building blocks that are up to 300 kpc away from the main progenitor centre. In such a scenario, we can expect that whatever gas-rich blocks formed the backbone of the MW disc brought with it its own stars, including UMP stars. Yet, for such a significant number of UMP stars to align with the current MW plane, it is necessary to assume that the formation of the MW's disc involved a single massive event that imprinted the disc plane that is aligned with the orbit of its stars. The presence of many massive building blocks would have likely led to changes in the angular HI disc alignment. Similarly, the MW cannot have suffered many massive accretions since high redshift or the disc would have changed its orientation (Scannapieco et al. 2009). This would be in line with expectations that the MW has had an (unusually) quiet accretion history throughout its life (Wyse 2001; Stewart et al. 2008).

5.1.1 *The Caffau star and 2MASS J18082002−5104378*

SDSS J102915+172927 (see Fig. A19, available Online), also known as 'the Caffau star' (Caffau et al. 2011), and 2MASS J18082002−5104378 (see Fig. A35, available Online) both have a disc-like prograde orbit but while the Caffau Star reaches a height of 2.3 kpc from the MW plane, the latter star is

confined within 0.166 kpc, confirming the results from Schlaufman, Thompson & Casey (2018). Both stars represent outliers inside the surprising sample of 'MW planar' stars that typically have more eccentric orbits. For these stars, scenario 3, as outlined above, might be an interesting possibility. A merging between the building blocks of the proto-MW could have brought in these UMP stars and their orbit circularized by dynamical friction.

5.1.2 Coincidence with the Sagittarius stream

We note that four of the 'halo' stars (SDSS J092912.32+023817.0, SDSS J094708.27+461010.0, Pristine221.8781+9.7844 and BPS CS 22885−0096) have orbits that are almost perpendicular to the MW plane (see Figs A16, A17, A31, and A37 available Online), coinciding with the plane of the stellar stream left by the Sagittarius (Sgr) dwarf galaxy as it as being tidally disrupted by the MW. We therefore investigate if these stars belong to the stream by comparing their proper motions and distances with the values provided by the N-body simulation of Law & Majewski (2010) (hereafter LM10; Fig. 3). It is clear that SDSS J094708.27+461010.0 has a proper motion that is incompatible with the simulation's particles. On the other hand, we find that SDSS J092912.32+023817.0, Pristine221.8781+9.7844, and BPS CS 22885−0096 have proper motions that are in broad agreement with those of the simulation. These stars could be compatible with the oldest wraps of the Sgr galaxy but we are nevertheless cautious in this assignment since only the young wraps of the stream were constrained well with observations in the Law & Majewski (2010) model. Older wraps rely on the simulation's capability to trace the orbit back in the MW potential that is itself poorly constrained and has likely changed over these time-scales, and the true 6D phase-space location the older warps could therefore easily deviate significantly from the simulation's expectations.

5.1.3 A connection between SDSS J174259.67+253135.8 and ω Centauri?

SDSS J174259.67+253135.8 is the only star of the 'MW planar' sample that has a retrograde motion and its orbital properties are, in fact, similar enough to those of the ω Centauri (ωCen) stellar cluster to hint at a possible connection between the two. It should be noted, however, that the L_z of ωCen's orbit is about twice that of this star. Nevertheless, given the dynamically active life that ωCen must have had in the commonly-held scenario that it is the nucleus of a dwarf galaxy accreted by the Milky Way long ago (e.g. Zinnecker et al. 1988; Mizutani, Chiba & Sakamoto 2003), the similarity of the orbits is intriguing enough to warrant further inspection.

5.2 Limits of the analysis and completeness

The heterogeneous UMP sample comes from multiple surveys conducted over the years, with their own, different window functions for the selection of the targets and it can thus by no means be called a complete or homogeneous sample. To reconstruct the full selection function of this sample is nearly impossible since it includes so many inherited window functions from various surveys and follow-up programs. As far as we can deduce, however, none of the programs would have specifically selected stars on particular orbits. We therefore consider the clear preference of the UMP star population for orbits in the plane of the MW disc a strong result of this work but we caution the reader not to consider the ratio of 'inner halo,' 'outer halo,' and 'MW plane' orbits as necessarily representative of the true ratios, which will require a more systematic survey to confirm.

We note that due to the different abundance patterns of these stars, [Fe/H] is not always a good tracer of the total metallicity [M/H]. However, not all stars in this sample are equally well-studied and therefore constraints on [M/H] are inhomogeneous. This has led us to nevertheless choose a cut on [Fe/H] as this is the common quantity measured by all the cited authors.

Another limitation of this work comes from the isochrones we use, which are the most metal-poor isochrones available in the literature at this time and have [Fe/H] = −4 dex with solar-scaled α-abundances. Beyond the fact that some stars in our sample are significantly more metal-poor than this, not all stars follow this abundance pattern and as a result their total metal-content can change, in turn affecting the colour of the isochrones. We estimate, however, that this will be a small effect at these low metallicities, as low-metallicity isochrones are relatively insensitive to small variations in metallicity, and take this into account adding a systematic uncertainty of 0.01 mag in quadrature to the model (see Section 3.1.1). This is unlikely to affect the final results on the evolutionary phase and the typology of the orbits. A final potential limitation of this work stems from the possible binary of some of the studied stars. If, unbeknownst to us, a star is in fact a binary system whose component are in the same or a similar evolutionary phase, their photometry would not be representative of their true properties and our distance inference would be biased. Similarly a binary star would like have its velocity be affected, leading to flawed orbital parameters. For known binary stars, we nevertheless take these effects into account and our distance and orbital inference should not be severely affected by this binarity issue.

5.3 Future outlook

As described in 5.2, the current sample and analysis of their dynamics is quite limited by an unknown and complicated selection function. With proper motion, parallax, and the exquisite photometry from *Gaia DR2*, we plan to apply the same bayesian framework described in Section 3 to all the EMP stars within the Pristine survey (Starkenburg et al. 2017a) to investigate their stellar properties and orbits. As the completeness and purity of this sample is very well understood (Youakim et al. 2017) and this sample is much larger, this will open up more quantitative avenues to explore the role of extremely metal-poor stars in the big picture of the accretion history of the MW.

6 CONCLUSIONS

Combining the *Gaia DR2* photometric and astrometric information in a statistical framework, we determine the posterior probability distribution function for the distance, the stellar parameters (temperature and surface gravity), and the orbital parameters of 42 UMPs (see Tables 3 and 4). Given that 11 of those stars remain confined close to the MW plane, we use both a pure halo prior and a combined disc+halo prior. Folding together distance posterior and orbital analysis we find that 18 stars are on the main sequence and the other 24 stars are in a more evolved phase (subgiant or giant).

Through the orbital analysis, we find that 11 stars are orbiting close to the plane of the disc, with maximum height above the disc within 3 kpc. We hypothesize that they could have once belonged to a massive building block of the proto-MW that formed the backbone of the MW disc, or that they were brought into

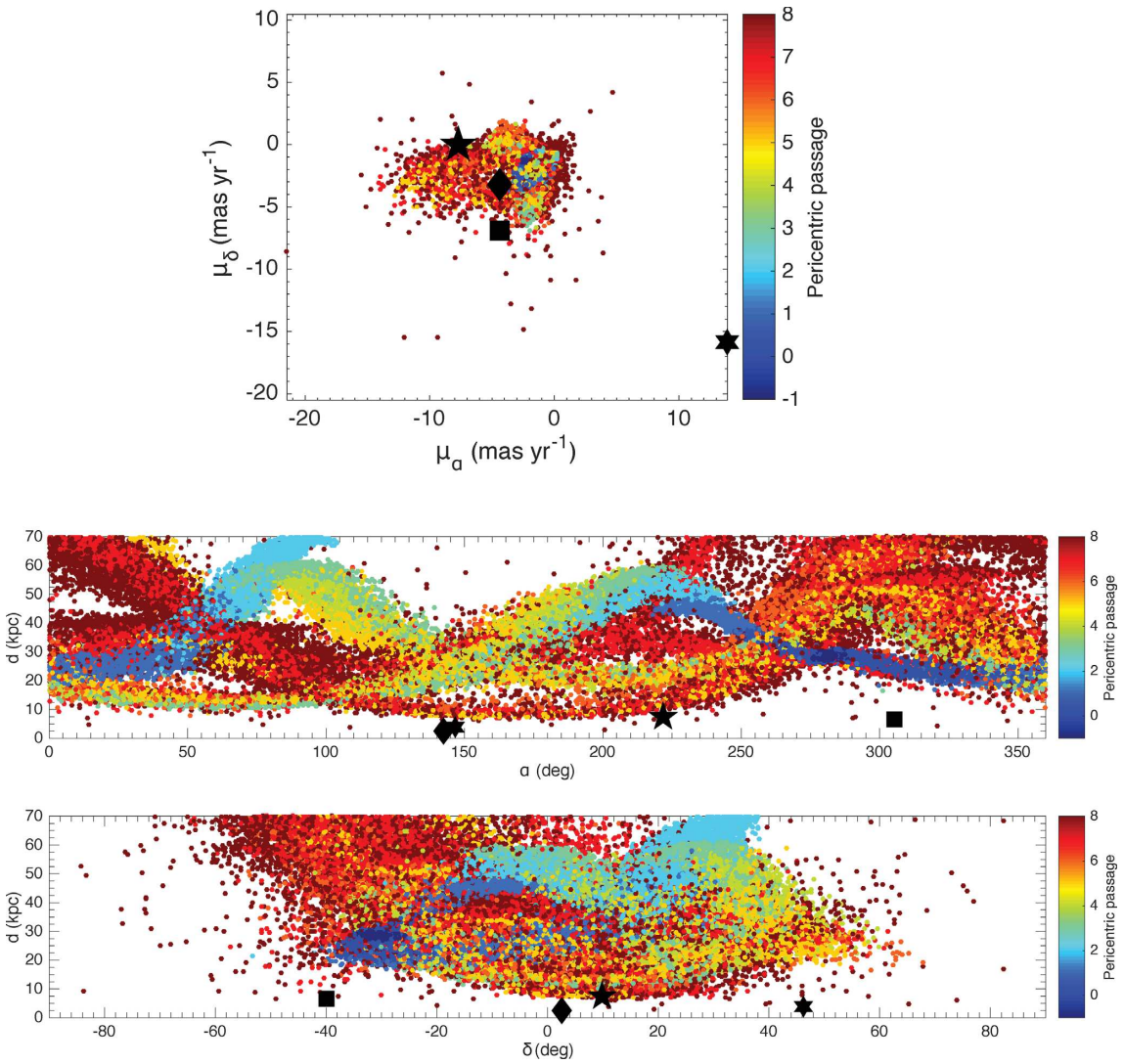

Figure 3. Top: proper motion space for the particles of the LM10 simulation (dots), and SDSS J092912.32+023817.0 (black diamond), SDSS J094708.27+461010.0 (black hexagram), Pristine221.8781+9.7844 (black pentagram), and BPS CS 22885−0096 (black square). The colour-code for the LM10 simulation indicates the pericentric passage on which the particle became unbound from Sgr. A pericentric passage value of −1 indicates debris which is still bound at the present day, while a value of 0 indicates debris stripped on the most recent pericentric passage of Sgr, and a value above 1 corresponds to successive pericentric passages. Centre: heliocentric distance d as a function of right ascension α for the LM10 simulation and the candidates. Bottom: heliocentric distance d as a function of declination δ for the LM10 simulation and the candidates. The LM10 simulation is shown within 70 kpc from the Sun for the centre and bottom panel.

the MW via a specific, massive hierarchical accretion event, or they might have formed in the early disc and have been dynamically heated. Another 31 stars are from both the 'inner halo' (arbitrarily defined as having $r_{\rm apo} < 30$ kpc) and were accreted early on in the history of the MW, or the 'outer halo' hinting that they were accreted on to the Galaxy from now-defunct dwarf galaxies. Of these halo stars, SDSS J092912.32+023817.0, Pristine221.8781+9.7844, and BPS CS 22885−0096, could possibly be associated with the Sagittarius stream, although they would need to have been stripped during old pericentric passages of the dwarf galaxy. SDSS J174259.67+253135.8 could also possibly be associated with ωCen as its progenitor.

The work presented here provides distances, stellar parameters, and orbits for all known UMP stars and, hence, some of the oldest stars known. To understand their position and kinematics within the Galaxy it is very important to reconstruct the early formation of the MW and/or the hierarchical formation of some of its components. We foresee a statistical improvement of this first study with the arrival of homogeneous and large data sets of EMP stars, such as observed within the Pristine or SkyMapper surveys (Starkenburg et al. 2017a; Wolf et al. 2018). With these surveys, the window function and the selection criteria of the objects for which distances and orbits are derived will be much better known.

ACKNOWLEDGEMENTS

We would like to thank Benoit Famaey, Misha Haywood, and Paola Di Matteo for the insightful discussions and comments.

FS, NFM, NL, and RI gratefully acknowledge funding from CNRS/INSU through the Programme National Galaxies et Cos-

mologie and through the CNRS grant PICS07708. FS thanks the Initiative dExcellence IdEx from the University of Strasbourg and the Programme Doctoral International PDI for funding his PhD. This work has been published under the framework of the IdEx Unistra and benefits from a funding from the state managed by the French National Research Agency as part of the investments for the future program. ES and AA gratefully acknowledge funding by the Emmy Noether program from the Deutsche Forschungsgemeinschaft (DFG). JIGH acknowledges financial support from the Spanish Ministry project MINECO AYA2017-86389-P, and from the Spanish MINECO under the 2013 Ramón y Cajal program MINECO RYC-2013-14875. KAV thanks NSERC for research funding through the Discovery Grants program.

This research has made use of use of the SIMBAD data base, operated at CDS, Strasbourg, France (Wenger et al. 2000). This work has made use of data from the European Space Agency (ESA) mission *Gaia* (https://www.cosmos.esa.int/gaia), processed by the *Gaia* Data Processing and Analysis Consortium (DPAC, https://www.cosmos.esa.int/web/gaia/dpac/consortium). Funding for the DPAC has been provided by national institutions, in particular the institutions participating in the *Gaia* Multilateral Agreement.

REFERENCES

Abadi M. G., Navarro J. F., Steinmetz M., Eke V. R., 2003, ApJ, 597, 21
Abohalima A., , Frebel A., 2018, ApJs, 238, 36
Aguado D. S., Allende Prieto C., González Hernández J. I., Carrera R., Rebolo R., Shetrone M., Lambert D. L., Fernández-Alvar E., 2016, A&A, 593, 13
Aguado D. S., Allende Prieto C., González Hernández J. I., Rebolo R., Caffau E., 2017a, A&A, 604, 7
Aguado D. S., González Hernández J. I., Allende Prieto C., Rebolo R., 2017b, A&A, 605, 10
Aguado D. S., González Hernández J. I., Allende Prieto C., Rebolo R., 2018b, ApJ, 852, 6
Aguado D. S., Allende Prieto C., González Hernández J. I., Rebolo R., 2018a, ApJ, 854, 4
Allende Prieto C. et al., 2015, A&A, 579, 6
Arentsen A., Starkenburg E., Shetrone M. D., Venn K. A., Depagne É., McConnachie A. W., 2019, A&A, 621, A108
Bailer-Jones C. A. L., Rybizki J., Fouesneau M., Mantelet G., Andrae R., 2018, AJ, 156, 58
Bailer-Jones C. A. L., 2015, PASP, 127, 994
Beers T. C., Christlieb N., 2005, ARA&A, 43, 531
Beers T. C., Preston G. W., Shectman S. A., 1985, AJ, 90, 2089
Belokurov V., Erkal D., Evans N. W., Koposov S. E., Deason A. J., 2018, MNRAS, 478, 611
Binney J., Tremaine S., 2008, Galactic Dynamics, 2nd edn. Princeton Univ. Press, Princeton
Bland-Hawthorn J., Gerhard O., 2016, ARA&A, 54, 529
Bonifacio P. et al., 2015, A&A, 579, 20
Bonifacio P. et al., 2018, A&A, 612, 10
Bovy J., 2015, ApJS, 216, 29
Caffau E. et al., 2011, Nature, 477, 67
Caffau E. et al., 2013a, A&A, 560, 7
Caffau E. et al., 2013b, A&A, 560, 9
Caffau E. et al., 2016, A&A, 595, 6
Cayrel R. et al., 2004, A&A, 416, 1117
Choi J., Dotter A., Conroy C., Cantiello M., Paxton B., Johnson B. D., 2016, ApJ, 823, 102
Christlieb N., Wisotzki L., Graßhoff G., 2002, A&A, 391, 397
Christlieb N., Gustafsson B., Korn A. J., Barklem P. S., Beers T. C., Bessell M. S., Karlsson T., Mizuno-Wiedner M., 2004, ApJ, 603, 708
Cohen J. G., Christlieb N., McWilliam A., Shectman S., Thompson I., Melendez J., Wisotzki L., Reimers D., 2008, ApJ, 672, 320
Cui X.-Q. et al., 2012, Res. Astron. Astrophys., 12, 1197
Dotter A., 2016, ApJS, 222, 8
Eisenstein D. J. et al., 2011, AJ, 142, 24
El-Badry K. et al., 2018, MNRAS, 480, 652
Evans D. W. et al., 2018, A&A, 616, 21
Frebel A., Norris J. E., 2015, ARA&A, 53, 631
Frebel A., Collet R., Eriksson K., Christlieb N., Aoki W., 2008, ApJ, 684, 588
Frebel A., Chiti A., Ji A. P., Jacobson H. R., Placco V. M., 2015, ApJ, 810, 7
Frebel A., Ji A. P., Ezzeddine R., Hansen T. T., Chiti A., Thompson I. B., Merle T., 2018, preprint (arXiv:1810.01228)
Freeman K., Bland-Hawthorn J., 2002, ARA&A, 40, 487
Gaia Collaboration, 2016, A&A, 595, 36
Gaia Collaboration, 2018, A&A, 616, A1
Gómez F. A. et al., 2017, MNRAS, 472, 3722
Greif T. H., 2015, Comput. Astrophys. Cosmol., 2, 36
Hansen T. et al., 2015, ApJ, 807, 17
Haywood M., Di Matteo P., Lehnert M. D., Snaith O., Khoperskov S., Gómez A., 2018, ApJ, 863, 113
Helmi A., , Babusiaux C., Koppelman H. H., Massari D., Veljanoski J., Brown A. G. A., 2018, Nature, 563, 85
Hernitschek N. et al., 2018, ApJ, 859, 32
Ito H., Aoki W., Beers T. C., Tominaga N., Honda S., Carollo D., 2013, ApJ, 773, 33
Karlsson T., Bromm V., Bland-Hawthorn J., 2013, Rev. Mod. Phys., 85, 809
Keller S. C. et al., 2014, Nature, 506, 463
Lai D. K., Bolte M., Johnson J. A., Lucatello S., Heger A., Woosley S. E., 2008, ApJ, 681, 1524
Law D. R., Majewski S. R., 2010, ApJ, 714, 229
Li H., Aoki W., Zhao G., Honda S., Christlieb N., Suda T., 2015, PASJ, 67, 84
Lindegren L. et al., 2018, A&A, 616, A2
Marigo P., Girardi L., Bressan A., Groenewegen M. A. T., Silva L., Granato G. L., 2008, A&A, 482, 883
Meléndez J., Placco V. M., Tucci-Maia M., Ramírez I., Li T. S., Perez G., 2016, A&A, 585, 5
Mizutani A., Chiba M., Sakamoto T., 2003, ApJ, 589, L89
Navarro J. F., Frenk C. S., White S. D. M., 1997, ApJ, 490, 493
Nordlander T., Amarsi A. M., Lind K., Asplund M., Barklem P. S., Casey A. R., Collet R., Leenaarts J., 2017, A&A, 597, 16
Norris J. E. et al., 2013, ApJ, 762, 16
Norris J. E., Christlieb N., Korn A. J., Eriksson K., Bessell M. S., Beers T. C., Wisotzki L., Reimers D., 2007, ApJ, 670, 774
Paxton B., Bildsten L., Dotter A., Herwig F., Lesaffre P., Timmes F., 2011, ApJS, 192, 3
Peñarrubia J., Kroupa P., Boily C. M., 2002, MNRAS, 333, 779
Placco V. M. et al., 2016, ApJ, 833, 13
Placco V. M., Frebel A., Lee Y. S., Jacobson H. R., Beers T. C., Pena J. M., Chan C., Heger A., 2015, ApJ, 809, 136
Plez B., Cohen J., Meléndez J., 2005, Hill V., Francois P., Primas F., Proceedings of The International Astronomical Union. p. 228
Roederer I. U., Preston G. W., Thompson I. B., Shectman S. A., Sneden C., Burley G. S., Kelson D. D., 2014, AJ, 147, 136
Salpeter E. E., 1955, ApJ, 121, 161
Salvadori S., Skúladóttir Á., Tolstoy E., 2015, MNRAS, 454, 1320
Scannapieco C., White S. D. M., Springel V., Tissera P. B., 2009, MNRAS, 396, 696
Scannapieco C., White S. D. M., Springel V., Tissera P. B., 2011, MNRAS, 417, 154
Schlaufman K. C., Thompson I. B., Casey A. R., 2018, ApJ, 867, 98
Schlegel D. J., Finkbeiner D. P., Davis M., 1998, ApJ, 500, 525
Schönrich R., Binney J., Dehnen W., 2010, MNRAS, 403, 1829
Sharma S., 2017, ARA&A, 55, 213
Starkenburg E. et al., 2017a, MNRAS, 471, 2587
Starkenburg E. et al., 2018, MNRAS, 481, 3838

Starkenburg E., Oman K. A., Navarro J. F., Crain R. A., Fattahi A., Frenk C. S., Sawala T., Schaye J., 2017b, MNRAS, 465, 2212
Stewart K. R., Bullock J. S., Wechsler R. H., Maller A. H., Zentner A. R., 2008, ApJ, 683, 597
Tafelmeyer M. et al., 2010, A&A, 524, 21
Wenger M. et al., 2000, A&AS, 143, 9
Wolf C. et al., 2018, PASA, 35, 29
Wyse R. F. G., 2001, in Funes J. G., Corsini E. M., eds, ASP Conf. Ser., Vol. 230, Galaxy Disks and Disk Galaxies. Astron. Soc. Pac., San Francisco, p. 71
Yanny B. et al., 2009, AJ, 137, 4377
Yong D. et al., 2013, ApJ, 762, 49
York D. G. et al., 2000, AJ, 120, 1579
Youakim K. et al., 2017, MNRAS, 472, 2963
Zinnecker H., Keable C. J., Dunlop J. S., Cannon R. D., Griffiths W. K., 1988, in Grindlay J. E., Philip A. G. D., eds, IAU Symposium, Vol. 126, The Harlow-Shapley Symposium on Globular Cluster Systems in Galaxies. Kluwer Academic Publishers, Dordrecht, p. 603

SUPPORTING INFORMATION

Supplementary data are available at *MNRAS* online.

Appendix A. Individual results.
Appendix B. Comparison with values from the literature.

Please note: Oxford University Press is not responsible for the content or functionality of any supporting materials supplied by the authors. Any queries (other than missing material) should be directed to the corresponding author for the article.

This paper has been typeset from a TEX/LATEX file prepared by the author.

APPENDIX A: INDIVIDUAL RESULTS

A1 HE 0020-1741

Figure A1 shows our results for HE 0020-1741, an ultra metal-poor star studied by Placco et al. (2016). Even if the parallax from Gaia DR2 has a large uncertainty ($\varpi = 0.1456 \pm 0.0384$ mas; red solid line for the MW halo prior and a red dot-dashed line for the disc+halo prior in the top-left pane), it is enough to break the dwarf/giant degeneracy obtained from the photometric solution (black line). The final PDFs are shown, using the MW halo prior and the disc+halo prior, respectively as the solid blue and the dot-dashed blue curves in that panel and, in both cases, the final scenario is a giant located at 10.3 ± 0.4 kpc. The stellar parameters we infer are in agreement with the values from the literature. In the lower panels of Figure A1, both the orbits calculated from the inferred distances from the PDF and Gaia astrometry only are shown, respectively marked by the blue and the red lines. The orbital parameters relative to the distance PDF represent an unbound orbit, while the Gaia astrometric distance leads to a more benign orbit that remains in the inner part of the MW halo.

A2 SDSS J0023+0307

Figure A2 summarises our results for SDSS J0023+0307, which is a mega metal-poor star found by Aguado et al. (2018a). The Gaia parallax is not very informative ($\varpi = 0.2697 \pm 0.1406$ mas; red solid line for the MW halo prior and a red dot-dashed line for the disc+halo prior in the top-left panel) and cannot break the dwarf/giant degeneracy inherent to the photometric solution (black line). It is nevertheless entirely compatible with that inference. The final PDFs are shown, using the MW halo prior and the disc+halo prior, respectively as the solid blue and the dot-dashed blue curves in that panel and, in both cases, yields a more likely dwarf solution at 2.71 ± 0.14 kpc along with a less likely sub-giant solution at 11.03 ± 0.73 kpc. The stellar parameters we infer for the most likely dwarf solution are entirely compatible with the literature values. Combined with the exquisite Gaia proper motions, the two distance solutions yield drastically different orbits. The sub-giant distance peak implies an unbound orbit that is shown in orange, while the (more likely) dwarf solution produces a more benign orbit that remains within the inner MW (shown in blue), supporting the distance of the latter solution as the valid one. While eccentric, this orbit surprisingly remains confined close to the MW plane ($|Z| < 5.0$ kpc)

A3 HE 0044-3755

HE 0044-3755 is an ultra metal-poor star studied by Cayrel et al. (2004) and our results for this star are shown in Figure A3. The distance PDF constrains the distance to 5.70 ± 0.25 kpc. This result leads to a giant solution that is compatible with the values in the literature. The orbit of this star is typical of a halo star.

A4 HE 0057-5959

Our results for HE 0057-5959 are shown in Figure A4, taking the literature values from Norris et al. (2013). From the distance PDF, we see a disagreement between the photometric and the astrometric likelihoods, which we cannot trace to any obvious source, but the astrophysical parameter inference is compatible with the literature values. For this giant, we show the orbit inferred both from our full astrometric and photometric analysis (blue orbit) and when using only the Gaia astrometry with the MW prior (red orbit). In both cases, HE 0057-5959 remains in the inner region of the MW halo (apocentre < 30 kpc).

A5 HE 0107-5240

HE 0107-5240 is likely a binary system (Arentsen et al. 2018) discovered by radial velocity variation. Its spectrum does not present double lines indicating that the light is not polluted by the secondary. It is a hyper metal-poor star analysed by Christlieb et al. (2004). Our results are shown in Figure A5 and we infer a distance of 14.3 ± 1.0 kpc, corresponding to the giant solution because the probability of the dwarf solution is entirely suppressed by the Gaia parallax information. Our values for surface gravity and effective temperature are in perfect agreement with the literature values. The orbit of this star is typical of an eccentric halo orbit and remains within $15.9^{+1.0}_{-0.9}$ kpc.

A6 HE 0134-1519

Our analysis of HE 0134-1519 (Hansen et al. 2015) is shown in Figure A6. This is another case for which the astrometric and photometric likelihoods disagree, yielding very different orbits, even though it is clear this star is a giant, in agreement with the literature. Both orbital solutions are indicative of a halo star, but the closer Gaia-only distance solution yields an orbit that remains much closer to the Galactic center (apocentre of $25.7^{+4.6}_{-1.7}$ kpc vs. $70.2^{+49.3}_{-20.7}$ kpc).

A7 SDSS J014036.21+234458.1

For the dwarf star SDSS J014036.21+234458.1 (Yong et al. 2013, Figure A7), the astrometric and photometric distances are technically in disagreement, but the distance inferences are so similar that it does not impact our results. We infer a distance of 0.76 ± 0.02 kpc and an orbit that brings SDSS J014036.21+234458.1 close to the MW plane ($|Z| < 2.5$ kpc).

A8 BD+44 493

Our results for BD+44 493 (Ito et al. 2013, Figure A8) are strongly constrained by the exquisite Gaia parallax, yielding a distance of 0.211 ± 0.003 kpc. Just like with SDSS J0023+0307, this star is eccentric and stays extremely close to the MW plane ($|Z| < 1.5$ kpc). It has an apocentre at the Solar circle.

A9 HE 0233-0343

The combined astrometric and photometric analysis of HE 0233-0343 (Hansen et al. 2015, Figure A9) yields an accurate distance of 1.09 ± 0.04 kpc. Despite this, our $\log(g)$ inference is incompatible with the literature value, but the very accurate Gaia parallax lends support to our inference. Like the previous star, HE 0233-0343 remains confined to the region of the MW disc, with $|Z| < 2.6$ kpc and an apocentre of $11.9^{+0.5}_{-0.4}$ kpc.

A10 BPS CS 22963-0004

For this UMP studied by Roederer et al. (2014), we infer a distance of 4.5 ± 0.4 kpc (Figure A10). Our astrophysical parameter inference disagrees with the literature values but the MESA isochrones strongly constrain our temperature inference. The difference could hint at systematics in these isochrones or the Roederer et al. (2014) analysis. Despite the currently proximity to this star, its orbit brings it very far into the MW halo, with $r_{\rm apo} = 155.8^{+183.4}_{-55.0}$ kpc.

A11 SDSS J030444.98+391021.1

The Gaia parallax of SDSS J030444.98+391021.1 (Aguado et al. 2017b, Figure A11) is very uncertain ($\varpi = 0.0752 \pm 0.1929$ mas) but, in case of the halo prior, strongly suppresses the dwarf solution (1% of the PDF). However, the orbital analysis shows that the favoured giant scenario implies that this star is not bound to the MW. According to this, we repeat the analysis with the disc+halo prior finding that the inferred distances are not significantly changed but the fractional probability of the peaks is. With this prior, the dwarf solution represents 21% of the PDF. Taking into account the orbital analysis, the dwarf solution appears to be the more realistic distance estimate (1.51 ± 0.07 kpc). This solution is also compatible with the $\log(g)$ of Aguado et al. (2017b), contrary to the result from the giant solution. We note that a slightly larger distance for the dwarf solution would be entirely compatible with the Gaia parallax and we think that the low likelihood of the dwarf solution could be driven further down than it should by a systematic in the models we use. With our favoured close-by distance, this star has the orbit of an inner halo object.

A12 SMSS J031300.36-670839.3

For this star with the lowest iron-abundance ([Fe/H] < -6.53, Nordlander et al. 2017, Figure A12), we infer a distance of 12.0 ± 0.8 kpc corresponding to the giant solution ($\log(g) = 1.8 \pm 0.1$). The literature $\log(g)$ is however in better agreement with the Gaia-only distance that is a little closer. The orbital analysis implies that this star has a fairly eccentric orbit and that, using the Gaia-only distance, it is compatible with an inner halo object. With the final posterior, we infer an outer halo orbit.

A13 HE 0330+0148

As we can see in Figure **??**, the analysis fails for this carbon-enhanced star (also known as G77-61) and its location in the colour-magnitude diagram does not coincide with the isochrone models. The strong carbon bands dominate in the spectrum (Dahn et al. 1977) , where the Gaia DR2 BP filter is sensitive, leading to an abnormal value of $(BP - RP)$ colour and, as a consequence, this star lays outside the isochrone range. This could also explain the strong disagreement between the photometric-only and astrometric-only distance likelihood functions (see Figure A13). We don't think that the binarity can affects the photometry because the companion is most likely an unseen white dwarf with a period of 250 days (Dearborn et al. 1986), which means that the Gaia DR2 magnitudes correspond to the magnitude of the star itself and not that of the binary system. In this case, we favour the Gaia-only inference with 78 ± 1 pc. HE 0330+0148 has a very radial orbit and its current position near the Sun is near its apocentre. Its orbit is close to the MW plane ($|Z| < 2.8$ kpc).

A14 HE 0557-4840

The inferred result on HE 0557-4840 (Norris et al. 2007, Figure A14) shows it is a giant halo star at a distance of 20.0 ± 1.3 kpc. Although the peaks of the astrometric and photometric solutions are shifted by ≈ 6 kpc, these are compatible due to the Gaia parallax that is poorly constrained ($\varpi = 0.0389 \pm 0.0207$ mas).

A15 SDSS J081554.26+472947.5

Our results on SDSS J081554.26+472947.5 (Aguado et al. 2018b, Figure A15) show that the star is a dwarf that is located at a distance of 1.59 ± 0.07 kpc and orbits within the inner halo. Our stellar parameter inference is in agreement with the literature values.

A16 SDSS J092912.32+023817.0

The distance PDF for this star (Bonifacio et al. 2015; Caffau et al. 2016, Figure A16) shows two solutions that are not strongly constrained due to the non-informative Gaia parallax ($\varpi = 0.1276 \pm 0.1872$ mas). Using a MW halo prior, the sub-giant scenario has a greater likelihood (68% vs. 32%), but it yields an orbit that is not bound to the MW. We therefore reanalyse this star using a disc+halo orbit, finding that the dwarf solution is now preferred (95% vs. 5%). Hence, this star is located at a distance of 2.4 ± 0.2 kpc (dwarf solution) and its orbit is perpendicular to the disc with $r_{\rm apo,dwarf} = 23.5^{+2.6}_{-1.4}$ kpc.

A17 SDSS J094708.27+461010.0

The distance to SDSS J094708.27+461010.0 is not constrained by the Gaia parallax ($\varpi = 0.1989 \pm 0.2299$ mas, Aguado et al. 2017a, Figure A17). However, for similar reasons to those mentioned above, we favour the dwarf scenario (distance of 3.8 ± 0.3 kpc) as a larger distance would mean that this star is not bound to the MW. The orbital analysis shows that its orbital plane is perpendicular to the MW plane.

A18 HE 1012-1540

For HE 1012-1540 (Roederer et al. 2014, Figure A18), the combination of photometric likelihood and the exquisite Gaia parallax leads to a distance of 0.384 ± 0.004 kpc and strongly implies that this is a dwarf star. It is worth noting that the inferred stellar parameters are not in agreement with the literature in which the giant solution is preferred, but the latter seems hardly compatible with the strongly constrained distance. The orbit of this star implies that it remains confined close to the MW plane but has a high eccentricity ($\epsilon = 0.83^{+0.00}_{-0.01}$).

A19 SDSS J102915+172927

SDSS J102915+172927, which is currently the most metal-poor star known (Caffau et al. 2011), is presented in Figure A19. The dwarf solution from the photometric likelihood is in agreement with the Gaia parallax and yields a well-constrained distance of 1.28 ± 0.05 kpc. We infer a higher surface gravity than in the literature, but our effective temperature inference is compatible. The orbital analysis shows that this star has the orbit of a disc star with an almost circular orbit around the galactic centre ($\epsilon = 0.12^{+0.01}_{-0.01}$) that remains close to the MW plane ($|Z| < 2.3$ kpc). These orbital properties differ from but supersede those of Caffau et al. (2012) that were based on PPMXL Catalogue for proper motions (Roeser, Demleitner & Schilbach 2010, $\mu_\alpha = -12.8 \pm 3.9$ mas/yr and $\mu_\delta = -6.7 \pm 3.9$ mas/yr).

A20 SDSS J103402.70+070116.6

Our results for SDSS J103402.70+070116.6 (Bonifacio et al. 2018) are shown in Figure A20 and, as we can see, the Gaia parallax does not allow us to break the dwarf/sub-giant degeneracy ($\varpi = 0.2874 \pm 0.1367$ mas). The dwarf solution ($P_{\rm dwarf} = 89\%$ vs. $P_{\rm giant} = 11\%$) at 2.79 ± 0.26 kpc implies an eccentric orbit ($\epsilon = 0.63^{+0.03}_{-0.04}$) that remains confined to the Galactic plane ($|Z| < 2.7$ kpc). On the other hand, the subgiant solution at 8.3 ± 0.6 kpc brings that star further out in the halo $r_{\rm apo} = 24.3^{+17.8}_{-0.0}$ kpc. Repeating the analysis with the disc+halo prior, the two new solutions are in agreement within the uncertainties with previous results, but now the sub-giant scenario is strongly suppressed (0.6%).

A21 SDSS J103556.11+064143.9

For this star (Bonifacio et al. 2015), the Gaia parallax is negative and does not help to constrain the distance ($\varpi = -0.3912 \pm 0.3163$ mas). Our analysis implies that the dwarf solution at 3.97 ± 0.34 kpc is more likely and this is confirmed by the orbital analysis that yields a large value for the apocentre in case of the giant solution ($r_{\rm apo} = 147.8^{+25.5}_{-11.8}$ kpc). Just like with SDSS J103402.70+070116.6 above, the literature $\log(g)$ falls in-between the two solutions we obtain and only the effective temperature inference is compatible with the literature.

A22 SDSS J105519.28+232234.0

The distance PDF for this star (Aguado et al. 2017b, Figure A22) indicates a strongly preferred distance of 3.49 ± 0.45 kpc corresponding to the dwarf solution, with the effective temperature in agreement with the literature. The inferred orbital parameters indicate an inner halo orbit.

A23 SDSS J120441.38+120111.5

The analysis on this star (Placco et al. 2015, Figure A23) leads to the conclusion that this star is a subgiant located at a distance of 7.03 ± 0.54 kpc from the Sun with an inner halo-like orbit.

A24 SDSS J124719.46-034152.4

The Gaia parallax on this star is poorly constraining ($\varpi = 0.3075 \pm 0.2098$ mas, Figure A24) and, combined with the photometric likelihood, we obtain a favoured distance of 4.17 ± 0.32 kpc corresponding to the dwarf solution that has an inner halo orbit. The far less likely sub-giant solution yields an orbit that is not bound to the MW. For the stellar parameters, the inferred effective temperature is compatible with the literature value (Caffau et al. 2013b).

A25 LAMOST J125346.09+075343.1

Figure A25 shows our results for LAMOST J125346.09+075343.1 (Li et al. 2015) and, as we can see, the Gaia likelihood is not in agreement with the photometric one. Our combined distance analysis favours the sub-giant scenario and a distance of 0.766 ± 0.016 kpc, which is close to the Gaia-only inference (0.698 ± 0.018 kpc). The surface gravity we infer is compatible with the value in the literature but our analysis implies a hotter star. Both the orbits from Gaia and the distance PDF show that LAMOST J125346.09+075343.1 remains confined to the MW plane, even though it has a high eccentricity ($\epsilon = 0.75^{+0.03}_{-0.02}$).

A26 SDSS J131326.89-001941.4

The Gaia parallax for this object is poorly constraining ($\varpi = 0.2976 \pm 0.0972$ mas, Figure A26) and we obtain using a pure halo prior that the preferred solution, a giant ($> 99\%$ chance), is located at the distance of 8.6 ± 2.9 kpc, with the inferred stellar parameters that are in agreement with the literature (Allende Prieto et al. 2015; Frebel et al. 2015; Aguado et al. 2017b). From the orbital analysis, this star is classifiable as inner halo.

A27 HE 1310-0536

The Gaia parallax ($\varpi = 0.0078 \pm 0.0342$ mas) rules out the dwarf solution for HE 1310-0536 (Figure A27; Hansen et al. 2015) and we infer a distance of 20.6 ± 0.9 kpc. The inferred stellar parameters are not in agreement with the literature, but this could stem from systematics in the red-giant-branch part of the isochrones we rely on. The orbit of this star clearly brings it in the outer parts of the halo, with $r_{\rm apo} = 99.7^{+38.3}_{-26.0}$ kpc.

A28 HE 1327-2326

The results for HE 1327-2326 are shown in Figure A28, and, despite the fact that the Gaia and the photometric likelihoods are not in good agreement, the sub-giant scenario is clearly favoured. The distance obtained for the combined analysis is 1.21 ± 0.02 kpc (or 1.09 ± 0.03 kpc for the Gaia only analysis) and the inferred effective temperature deviates somewhat from the literature value (Frebel et al. 2008). Even though the combined and Gaia-only distances yield significantly different orbits, they both imply halo orbits.

A29 HE 1424-0241

This giant star is located at a distance of 10.3 ± 1.0 kpc (Figure A29) and the inferred stellar parameters are in agreement with the literature (Cohen et al. 2008; Norris et al. 2013). The orbital analysis shows that HE 1424-0241 has an inner-halo orbit with high a eccentricity ($\epsilon = 0.81^{+0.06}_{-0.09}$).

A30 SDSS J144256.37-001542.7

The distance PDF for the combined analysis of SDSS J144256.37-001542.7 (Caffau et al. 2013a; Figure A30) still shows two peaks because of the poorly constraining Gaia parallax ($\varpi = -0.3910 \pm 0.2981$ mas). The giant solution and its distance of 11.3 ± 1.0 kpc is the preferred one with a halo prior ($P_{\rm giant} = 87\%$ vs. $P_{\rm dwarf} = 13\%$) but implies an unbound orbit whereas the dwarf solution at 2.68 ± 0.27 kpc yields a more benign halo orbit with $r_{\rm apo} = 39.1^{+5.2}_{-2.6}$ kpc. Similar distances are found with a disc+halo prior but with the dwarf solution as preferred scenario ($P_{\rm dwarf} = 84\%$ vs. $P_{\rm giant} = 16\%$).

A31 Pristine 221.8781+9.7844

The small Gaia parallax of Pristine 221.8781+9.7844 (Starkenburg et al. 2018; $\varpi = 0.1187 \pm 0.0940$ mas) rules out the dwarf solution. Hence the final picture of a sub-giant located at 7.36 ± 0.55 kpc from the Sun. As we can see from Figure A31, the inferred stellar parameters agree with the literature and the orbit we infer for Pristine 221.8781+9.7844 indicate that this star has a halo orbit almost perpendicular to the MW plane.

A32 SDSS J164234.48+443004.9

SDSS J164234.48+443004.9 (Figure A32) is a dwarf star located at a distance of 2.66 ± 0.16 kpc (Figure A32). The stellar parameters are compatible with the literature values (Aguado et al. 2016). The orbital analysis suggests that this star remains confined to the MW plane, but has a high eccentricity ($\epsilon = 0.72^{+0.03}_{-0.04}$).

A33 SDSS J173403.91+644633.0

SDSS J173403.91+644633.0 has a non-informative Gaia parallax ($\varpi = -0.1052 \pm 0.2702$ mas) that does not break the dwarf/giant degeneracy (Figure A33). The dwarf solution with a distance of 5.46 ± 1.02 kpc is nevertheless strongly preferred by the photometric analysis and yields a more realistic inner halo orbit that remains bound to the MW, contrary to the giant solution. The inferred stellar parameters are in agreement with those from the Aguado et al. (2017a) analysis.

A34 SDSS J174259.67+253135.8

Similarly to the previous star, the Gaia parallax of SDSS J174259.67+253135.8 ($\varpi = -0.1628 \pm 0.1870$ mas) does not allow us to discriminate between the dwarf and giant solutions but the giant solution implies an orbit with a very large apocentre beyond 700 kpc and we therefore favour the dwarf solution at 4.46 ± 0.52 kpc (Figure A34). With this distance, SDSS J174259.67+253135.8 (Bonifacio et al. 2015) is on an eccentric orbit that remains close to the MW plane ($|Z| < 2.7$ kpc).

A35 2MASS J18082002-5104378

Schlaufman, Thompson & Casey (2018) show that this star is in a binary system. The orbital parameters they derive show that this binary system has a very low eccentric orbit and is confined to the MW plane ($|Z| < 0.13$ kpc). From our distance analysis, the photometric likelihood is not in agreement with the exquisite Gaia parallax ($\varpi = 1.6775 \pm 0.0397$ mas), but we derive a similar overall solution at a distance of 0.647 ± 0.012 kpc and stellar parameters in agreement with the literature values (Meléndez et al. 2016, Figure A35). In agreement with the work from Schlaufman, Thompson & Casey (2018), we derive that the orbit is very close to the MW plane and even confined inside the thin disc ($|Z| < 0.166$ kpc) with a very low eccentricity of $\epsilon = 0.090^{+0.006}_{-0.005}$.

A36 BPS CS 22891-0200

The PDF of BPS CS 22891-0200 (Roederer et al. 2014; Figure A36) shows that is a giant star near the tip (see also Figure **??**), located at the distance of 14.7 ± 0.5 kpc. Our inferred stellar parameters do not match the values from the literature. The orbit of BPS CS 22891-0200 brings it far out into the halo of the MW ($r_{\rm apo} = 64.0^{+18.9}_{-11.1}$ kpc).

A37 BPS CS 22885-0096

Figure A37 presents our results for BPS CS 22885-0096 (Roederer et al. 2014), indicating that it is a giant at a distance of 6.65 ± 0.22 kpc, even though the stellar parameters we infer differ from the literature values. The orbit of this star is confined to a very narrow plane that is perpendicular to the MW plane.

A38 BPS CS 22950-0046

The Gaia parallax for this star ($\varpi = 0.0587 \pm 0.0270$ mas) clearly rules out the dwarf solution (Figure A38). As the plots show, this halo giant star is at a distance of 19.1 ± 0.3 kpc and the inferred stellar parameters are not in agreement with the literature (Roederer et al. 2014).

A39 BPS CS 30336-0049

Figure A39 shows that BPS CS 30336-0049 is located at 15.5 ± 0.7 kpc and follows an orbit that brings it far into the MW halo ($r_{\rm apo} = 122.7^{+51.1}_{-41.4}$ kpc). The inferred effective temperature matches the value from the literature (Lai et al. 2008), while our constraints on the gravity yields a slightly lower $\log(g)$.

A40 HE 2139-5432

Our results on HE 2139-5432 are summarised in Figure A40, and they lead to the conclusion that this star is a giant located at a distance of 11.0 ± 0.9 kpc from the Sun. The inferred surface gravity is in agreement with the literature (Norris et al. 2013) but the effective temperature is slightly cooler. The inferred orbit indicates that HE 2139-5432 is an inner halo star with a high eccentricity ($\epsilon = 0.79^{+0.05}_{-0.06}$).

A41 HE 2239-5019

For this star, the photometric and the astrometric likelihoods are in agreement, indicating the subgiant scenario at 4.19 ± 0.28 kpc is the valid solution (Figure A41). The orbit of HE 2239-5019 brings it at fairly large distances in the halo, with $r_{\rm apo} = 52.9^{+16.6}_{-10.4}$ kpc. The inferred surface gravity and effective temperature are compatible with the values from literature (Hansen et al. 2015).

A42 HE 2323-0256

Although the Gaia parallax is uncertain ($\varpi = 0.0038 \pm 0.0359$ mas), it helps break the dwarf/giant degeneracy. The final solution is that of a giant at a distance of 14.2 ± 0.6 kpc, belonging to the halo (Figure A42). We obtain higher values for the effective temperature and surface gravity than Roederer et al. (2014).

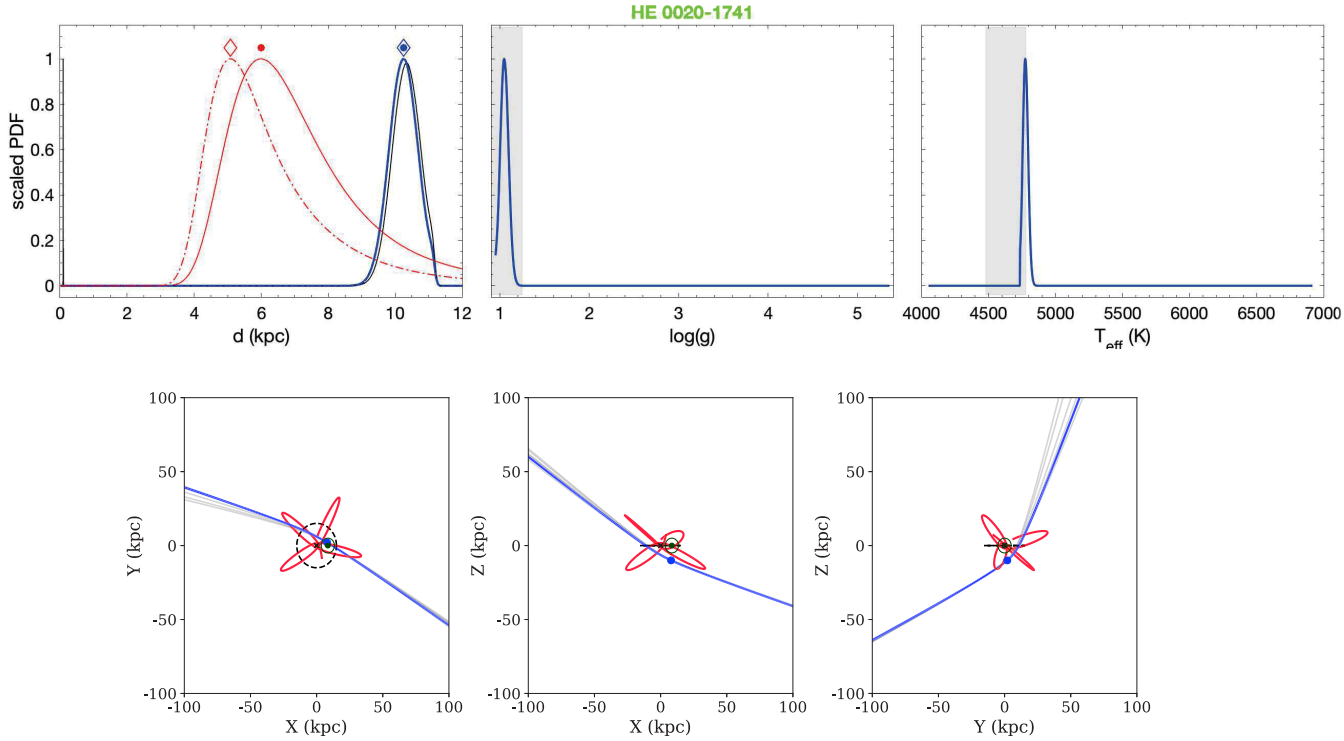

Figure A1. Left top: posterior probability (blue solid line and blue dot-dashed line respectively using a halo and a disc+halo prior), photometric likelihood (black line), and the product between the astrometric likelihood and MW prior (red solid line and red dot-dashed line respectively using a halo and a disc+halo prior) as a function of distance for HE 0020-1741. The coloured dots and the diamonds represent the position of the maxima of their same colour distribution respectively using a halo and a disc+halo prior. Center top: posterior probability as a function of log(g) (blue solid line for MW halo prior and blue dash-dot line for disc+halo prior). The gray box represents the surface gravity from literature within 1σ. Right top: posterior probability as a function of T_{eff} (blue solid line for MW halo prior and blue dot-dashed line for disc+halo prior). The gray box represents the effective temperature from literature within 1σ. The PDFs are rescaled to 1. Bottom panels: Blue and red lines are, respectively, the projected orbits of HE 0020-1741 for the most probable distance from PDF and for the distance from Gaia astrometric only inference in the plane YX (left), ZX (center) and ZY (right). The Galactic plane within 15 kpc (black line) and the Sun (green dot) are shown. Gray orbits represent randomisations around the values of position, distance, radial velocity and proper motions.

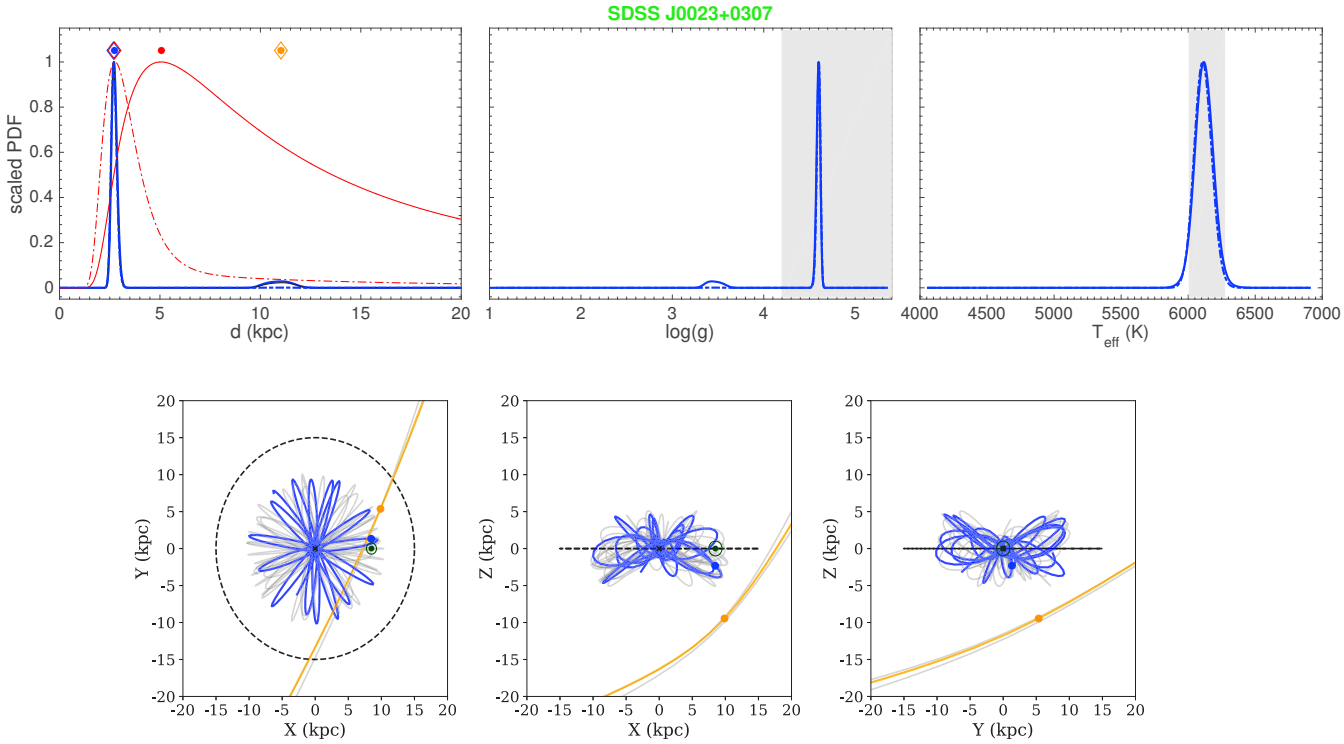

Figure A2. Left top: posterior probability (blue solid line and blue dot-dashed line respectively using a halo and a disc+halo prior), photometric likelihood (black line), and the product between the astrometric likelihood and MW prior (red solid line and red dot-dashed line respectively using a halo and a disc+halo prior) as a function of distance for SDSS J0023+0307. The coloured dots and the diamonds represent the position of the maxima of their same colour distribution respectively using a halo and a disc+halo prior. Center top: posterior probability as a function of log(g) (blue solid line for MW halo prior and blue dash-dot line for disc+halo prior). The gray box represents the surface gravity from literature within 1σ. Right top: posterior probability as a function of T_{eff} (blue solid line for MW halo prior and blue dot-dashed line for disc+halo prior). The gray box represents the temperature from literature within 1σ. The PDFs are rescaled to 1. Bottom panels: Blue and orange lines are, respectively, the projected orbits of SDSS J0023+0307 for the most probable distance and for the second peak in the distance posterior in the plane YX (left), ZX (center) and ZY (right). The Galactic plane within 15 kpc (black line) and the Sun (green dot) are shown. Gray orbits represent randomisations around the values of position, distance, radial velocity and proper motions.

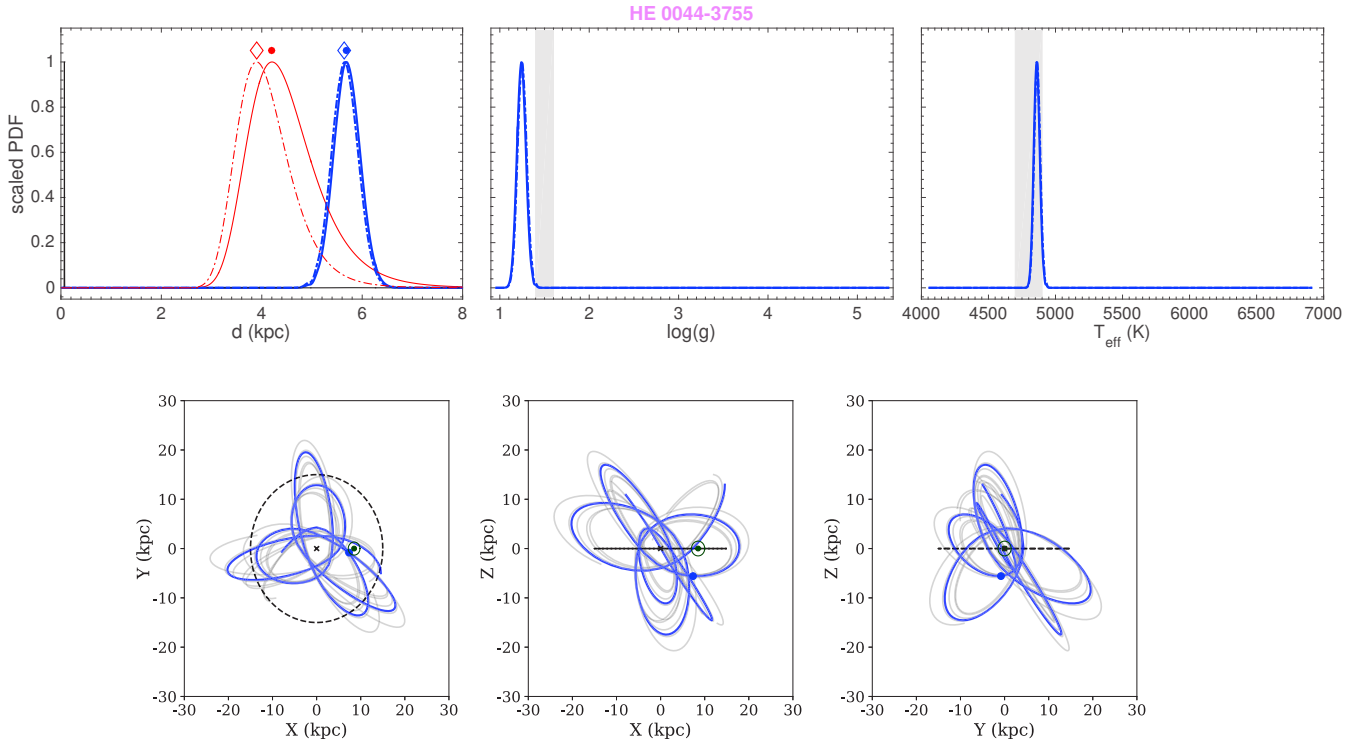

Figure A3. Same as Figure A2, but for HE 0044-3755.

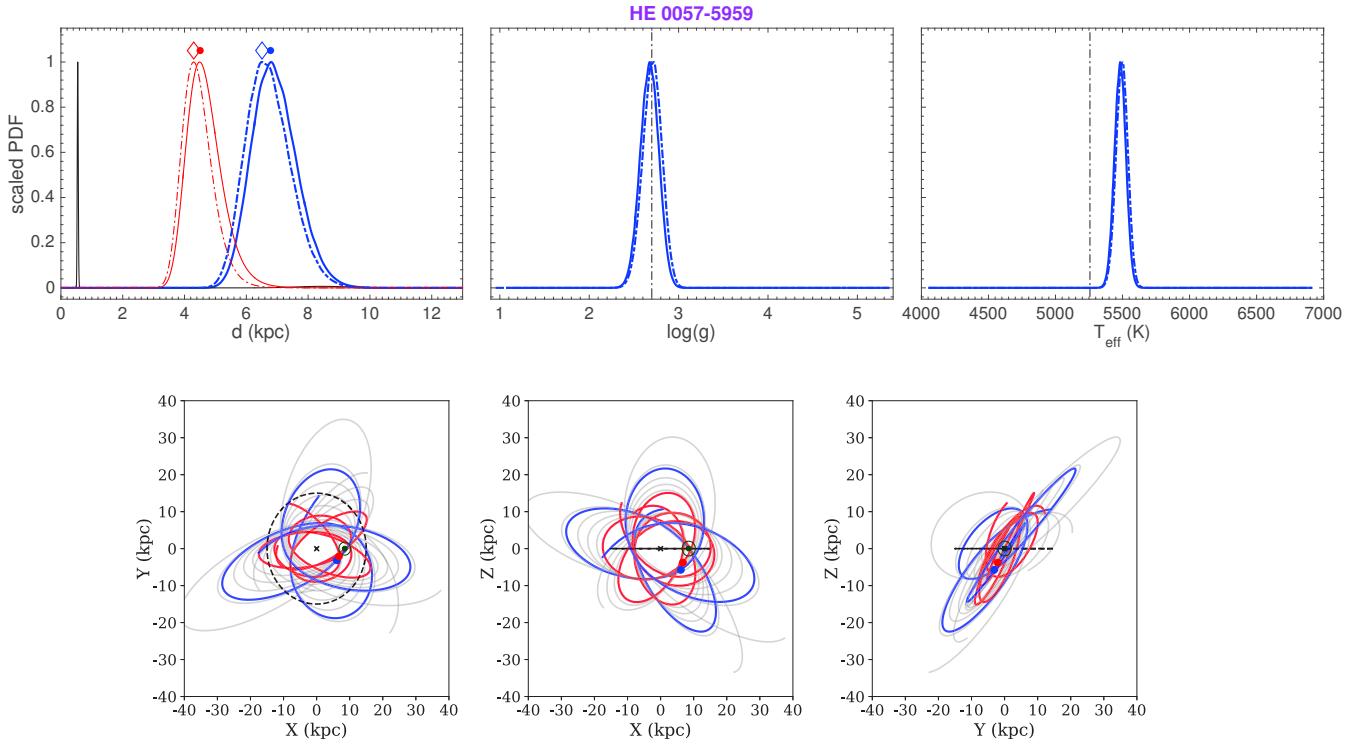

Figure A4. Same as Figure A2, but for HE 0057-5959. For this star, the orbit inferred from the product between the astrometric likelihood and MW halo prior is shown with the red line.

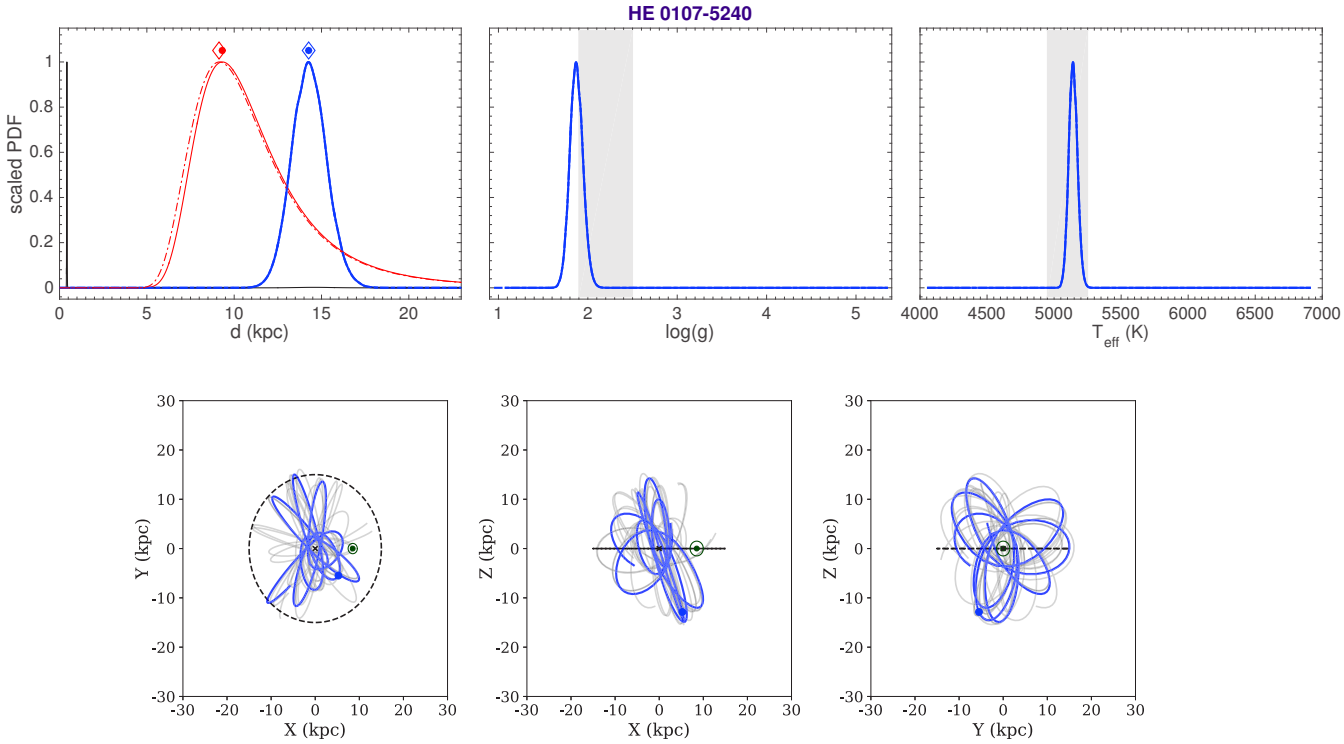

Figure A5. Same as Figure A2, but for HE 0107-5240.

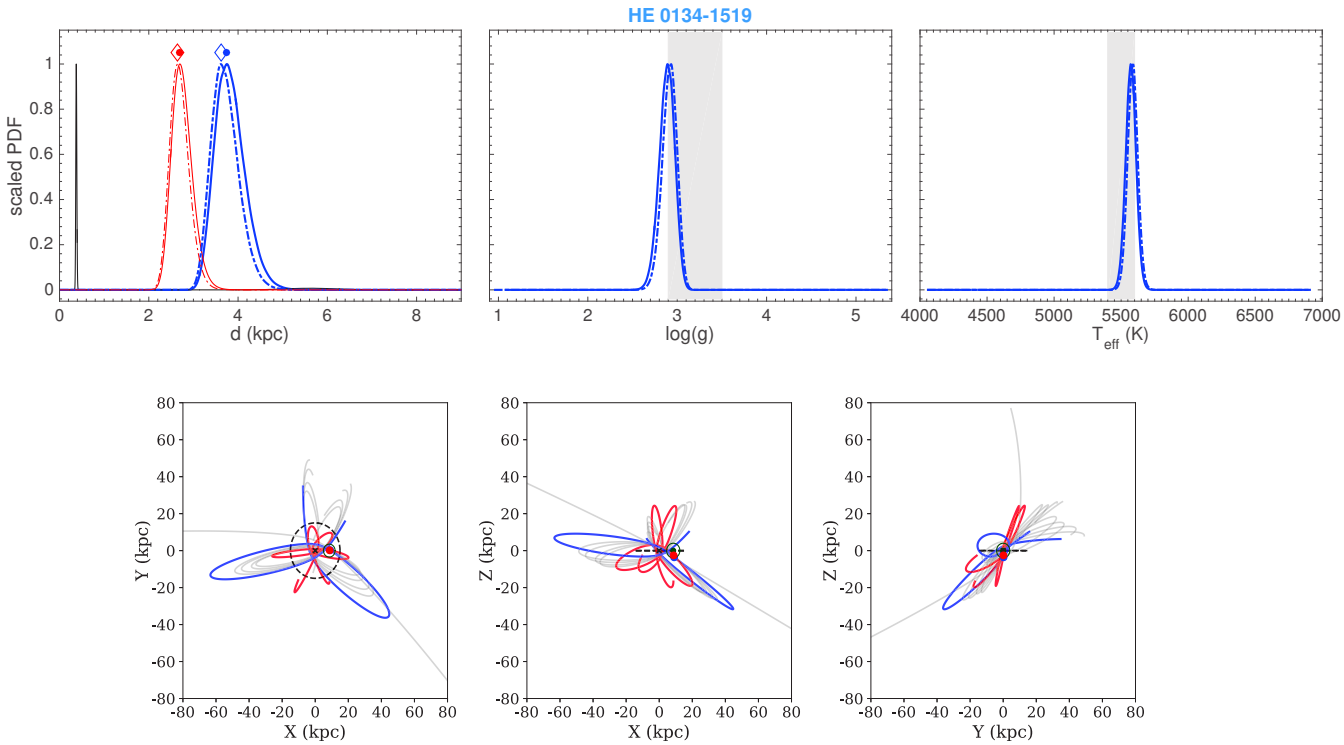

Figure A6. Same as Figure A2, but for HE 0134-1519. For this star, the orbit inferred from the product between the astrometric likelihood and MW halo prior is shown with the red line.

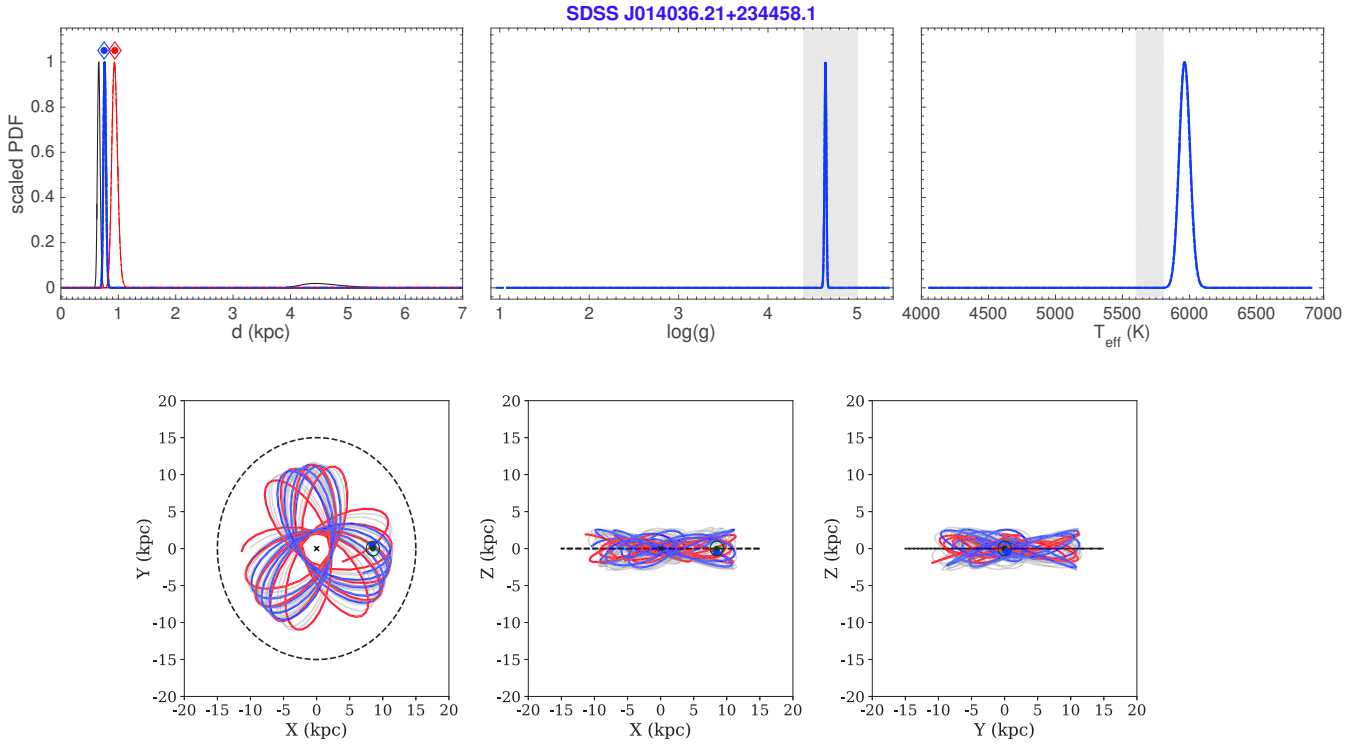

Figure A7. Same as Figure A2, but for SDSS J014036.21+234458.1. For this star, the orbit inferred from the product between the astrometric likelihood and MW halo prior is shown with the red line.

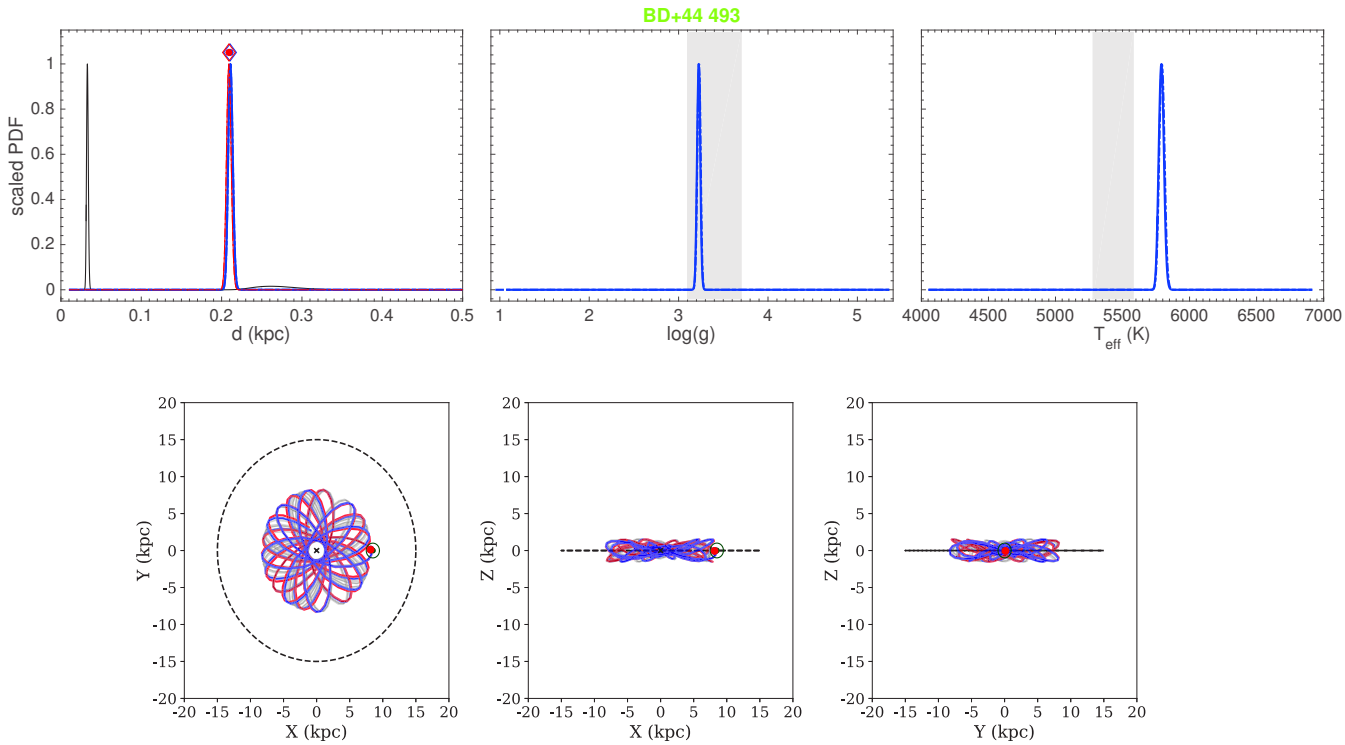

Figure A8. Same as Figure A2, but for BD+44 493. For this star, the orbit inferred from the product between the astrometric likelihood and MW halo prior is shown with the red line.

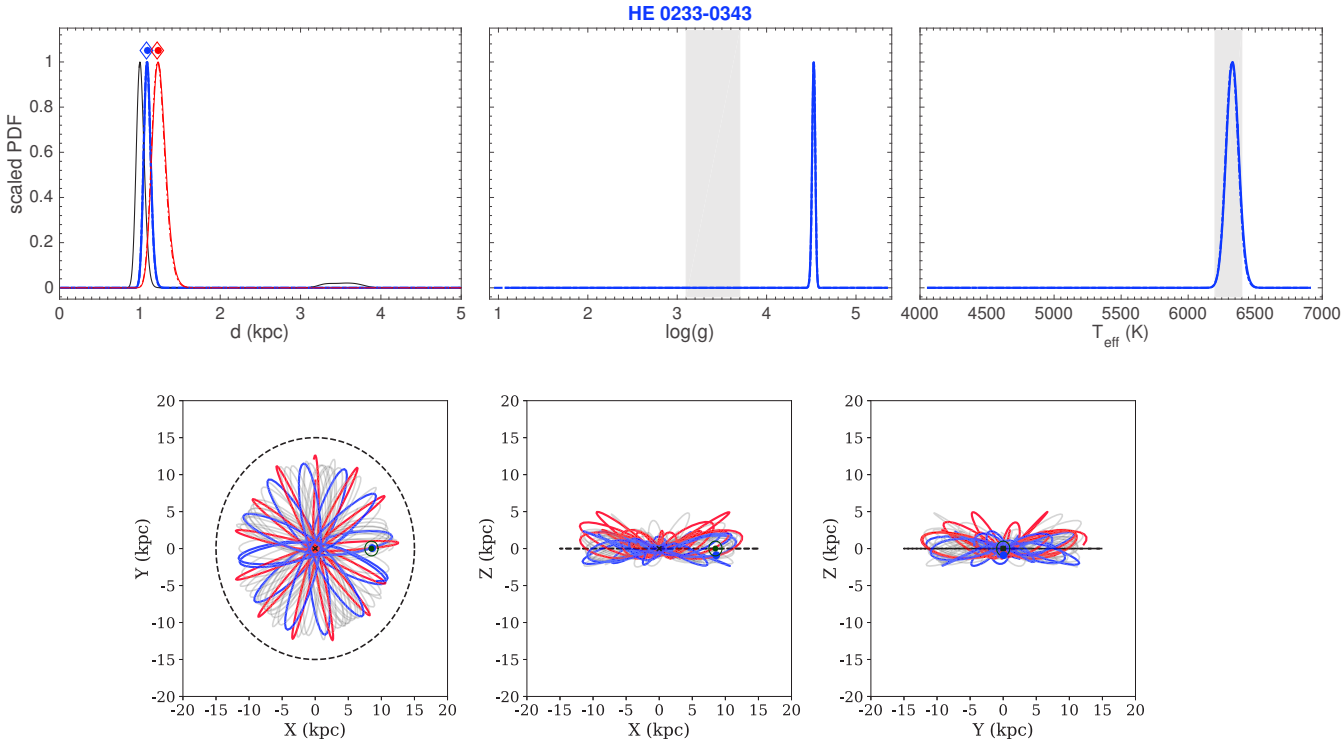

Figure A9. Same as Figure A2, but for HE 0233-0343. For this star, the orbit inferred from the product between the astrometric likelihood and MW halo prior is shown with the red line.

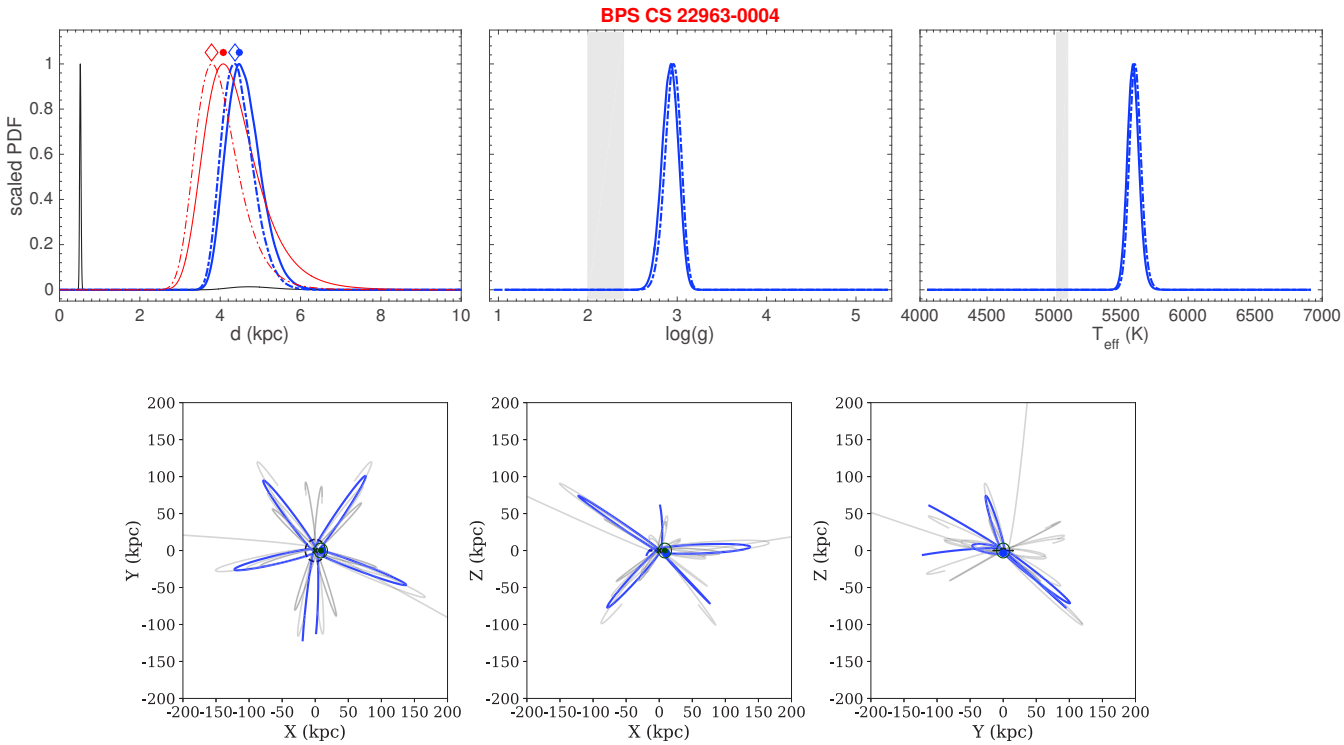

Figure A10. Same as Figure A2, but for BPS CS 22963-0004.

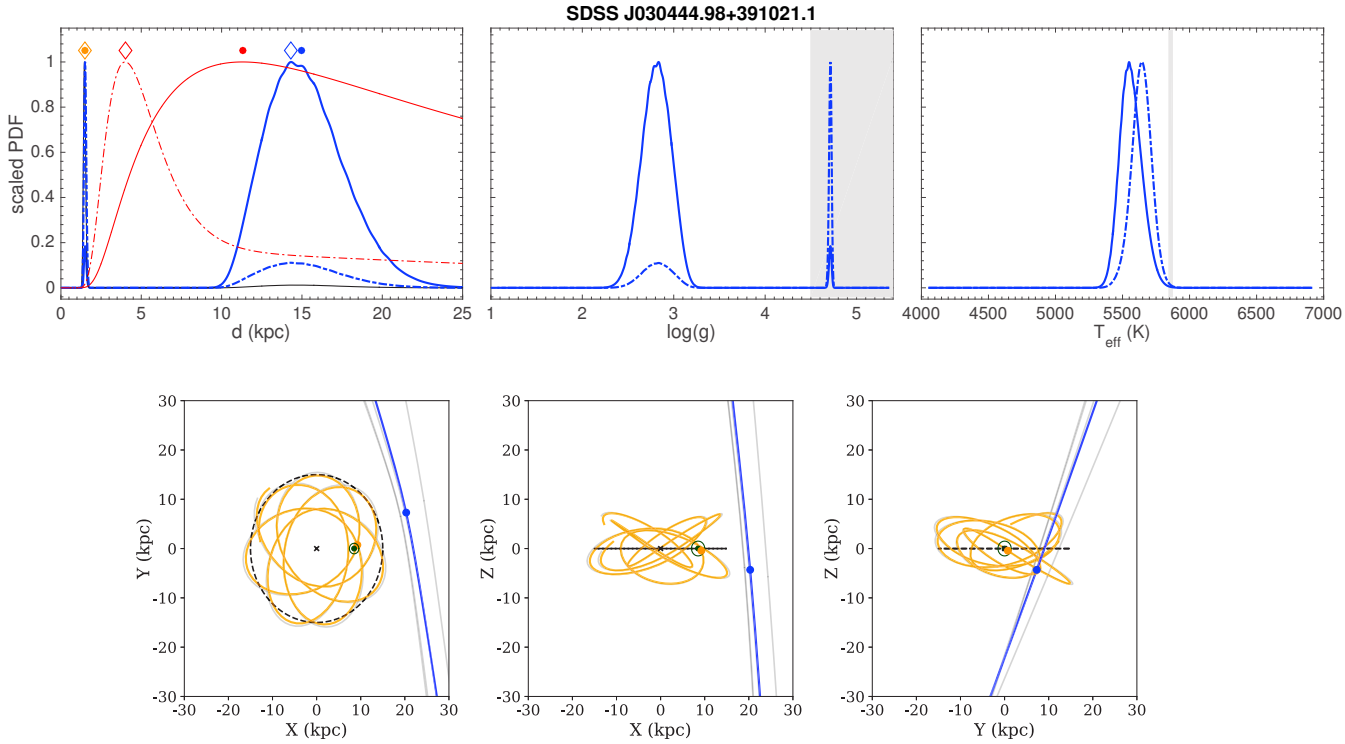

Figure A11. Same as Figure A2, but for SDSS J030444.98+391021.1.

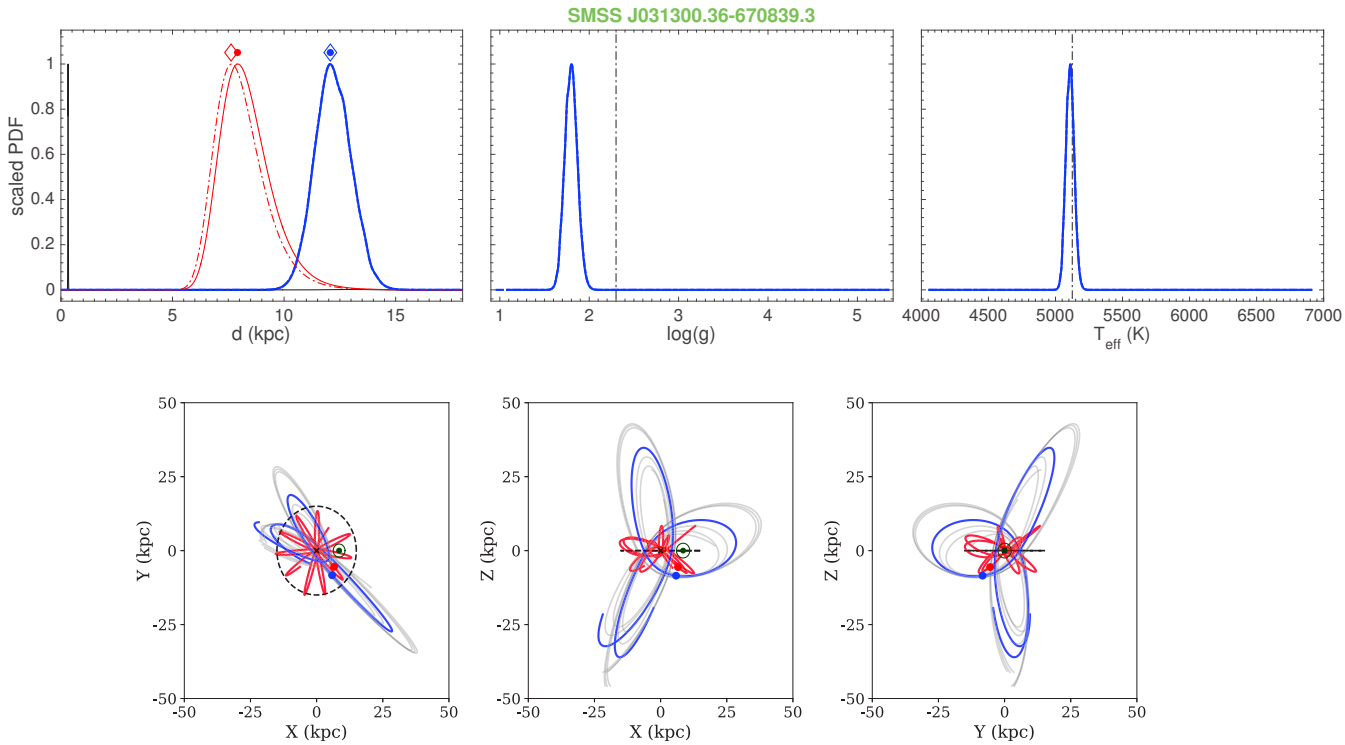

Figure A12. Same as Figure A2, but for SMSS J031300.36-670839.3. For this star, the orbit inferred from the product between the astrometric likelihood and MW halo prior is shown with the red line.

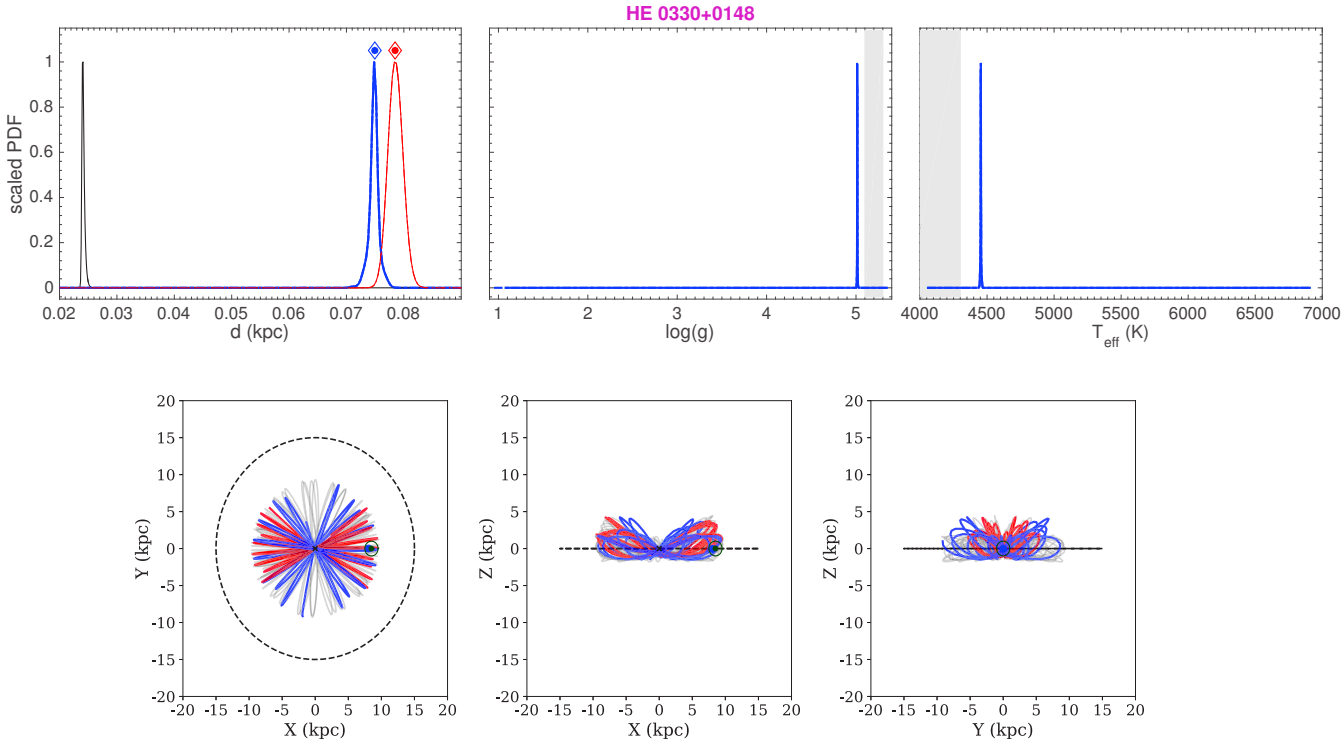

Figure A13. Same as Figure A2, but for HE 0330+0148. For this star, the orbit inferred from the product between the astrometric likelihood and MW halo prior is shown with the red line.

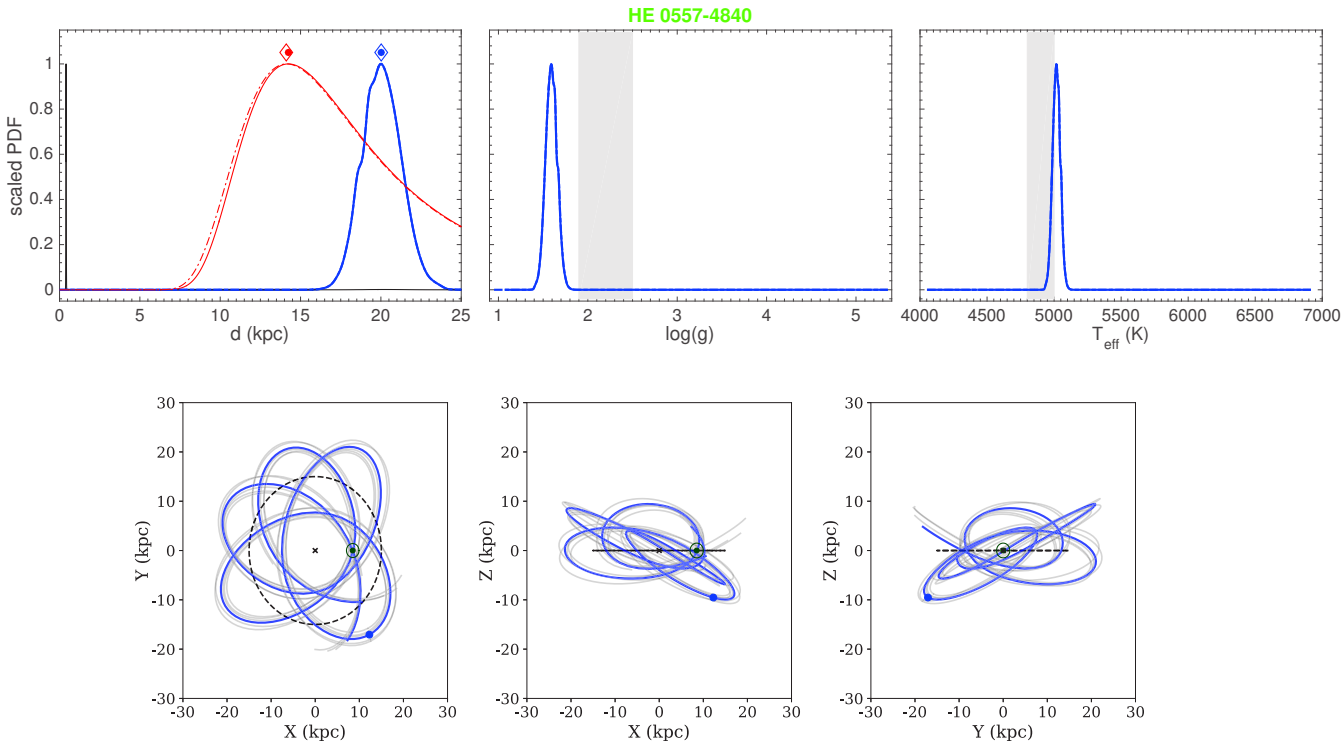

Figure A14. Same as Figure A2, but for HE 0557-4840.

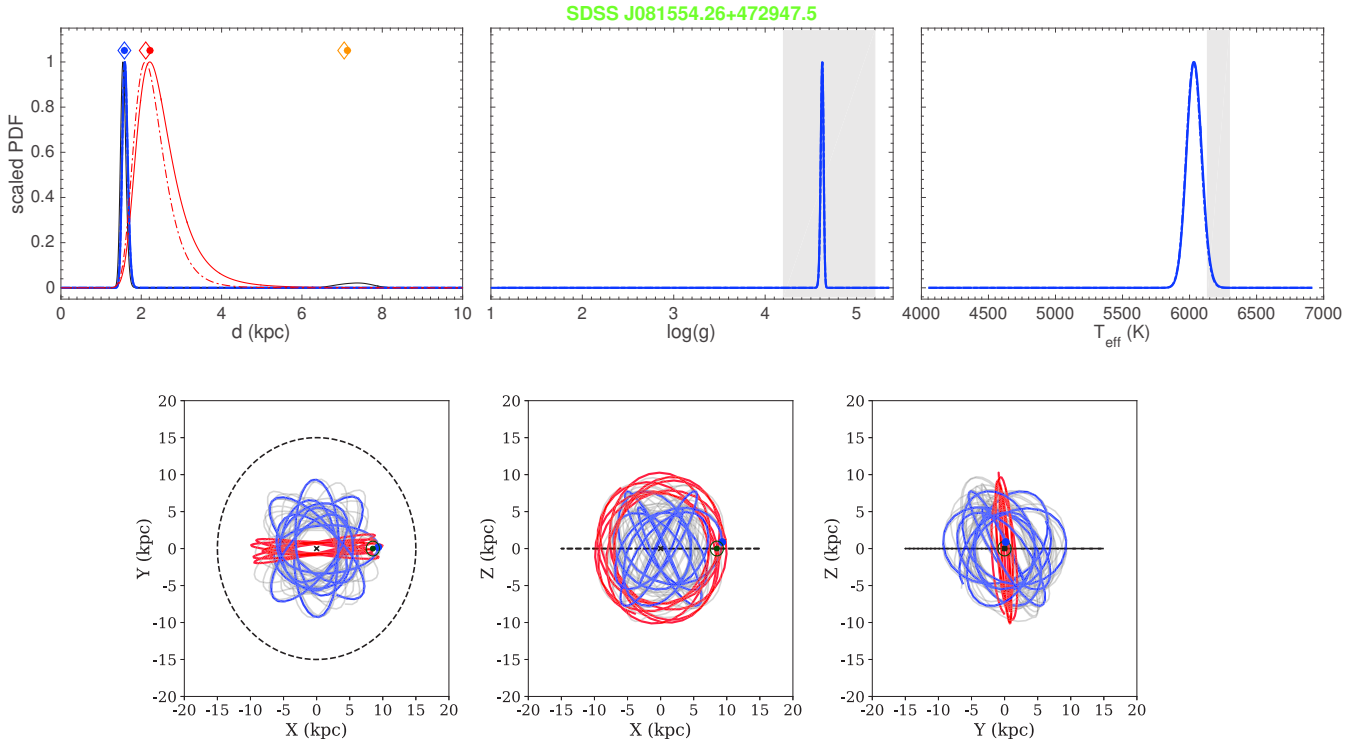

Figure A15. Same as Figure A2, but for SDSS J081554.26+472947.5. For this star, the orbit inferred from the product between the astrometric likelihood and MW halo prior is shown with the red line.

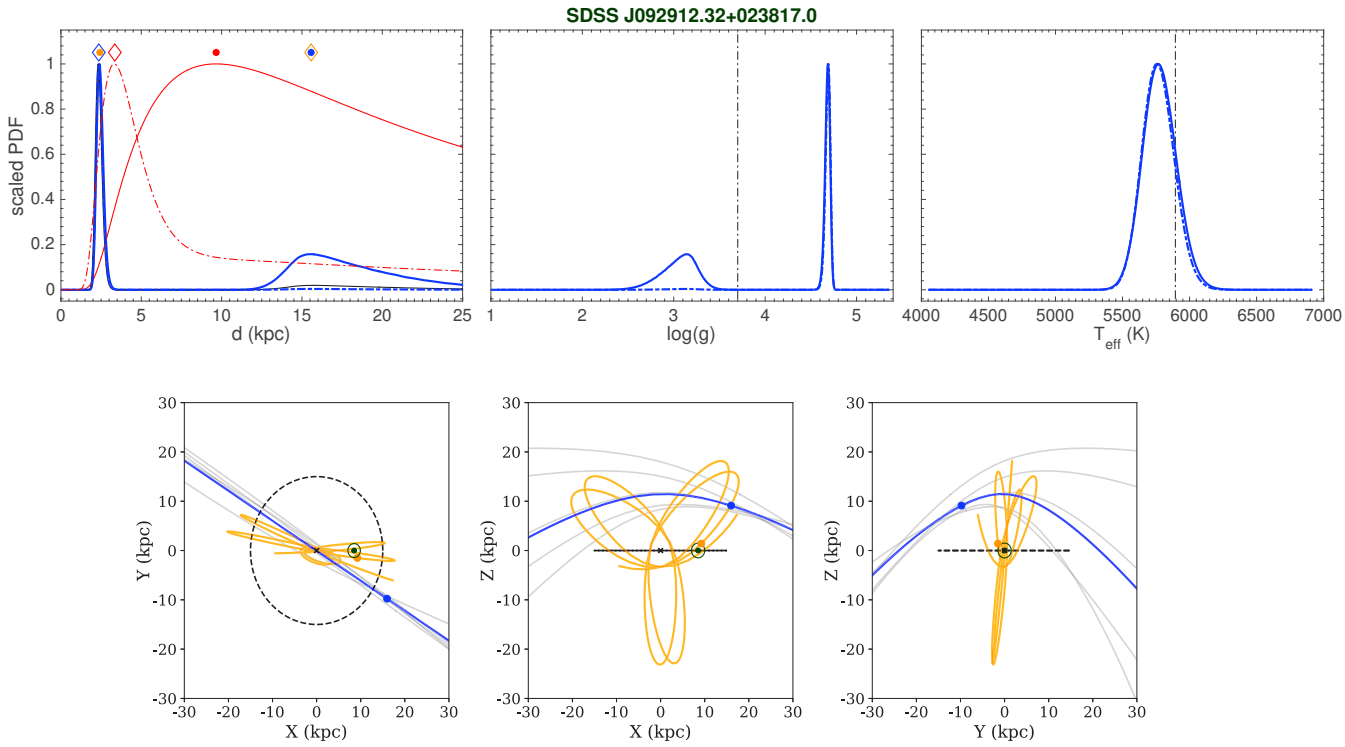

Figure A16. Same as Figure A2, but for SDSS J092912.32+023817.0.

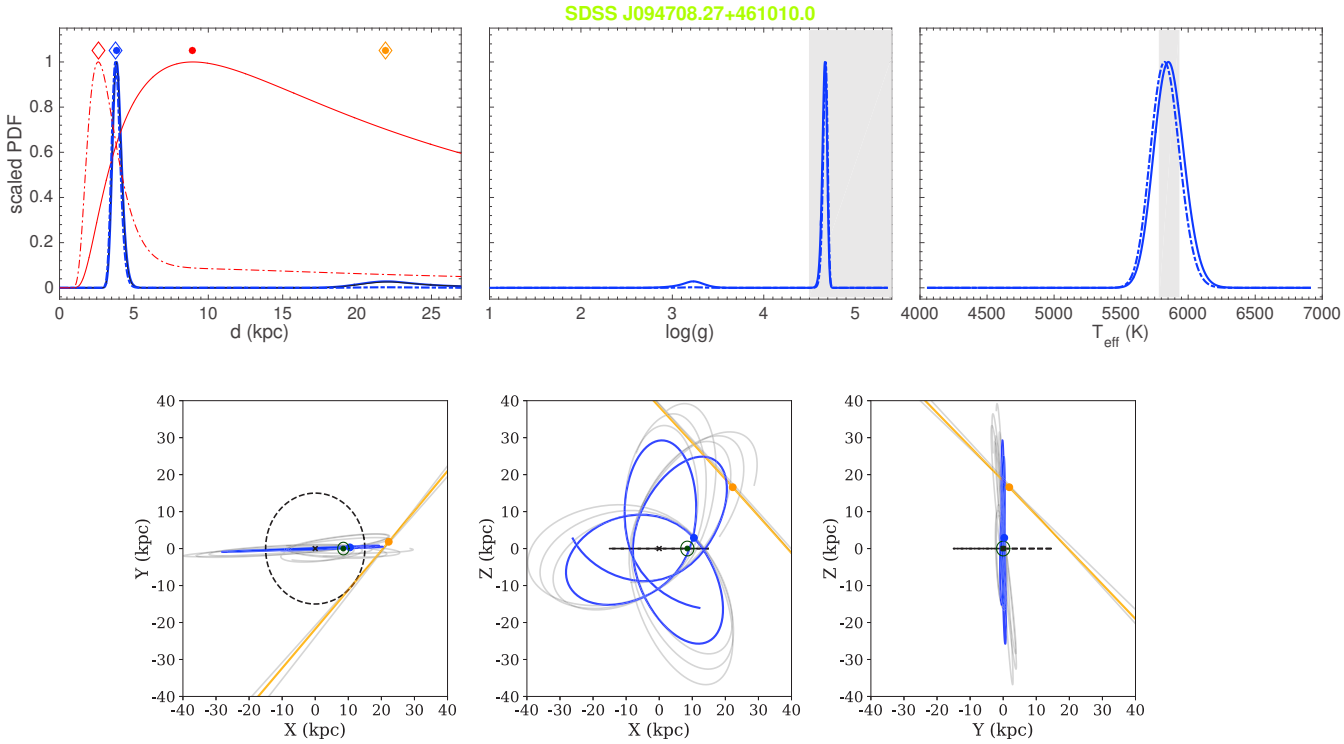

Figure A17. Same as Figure A2, but for SDSS J094708.27+461010.0.

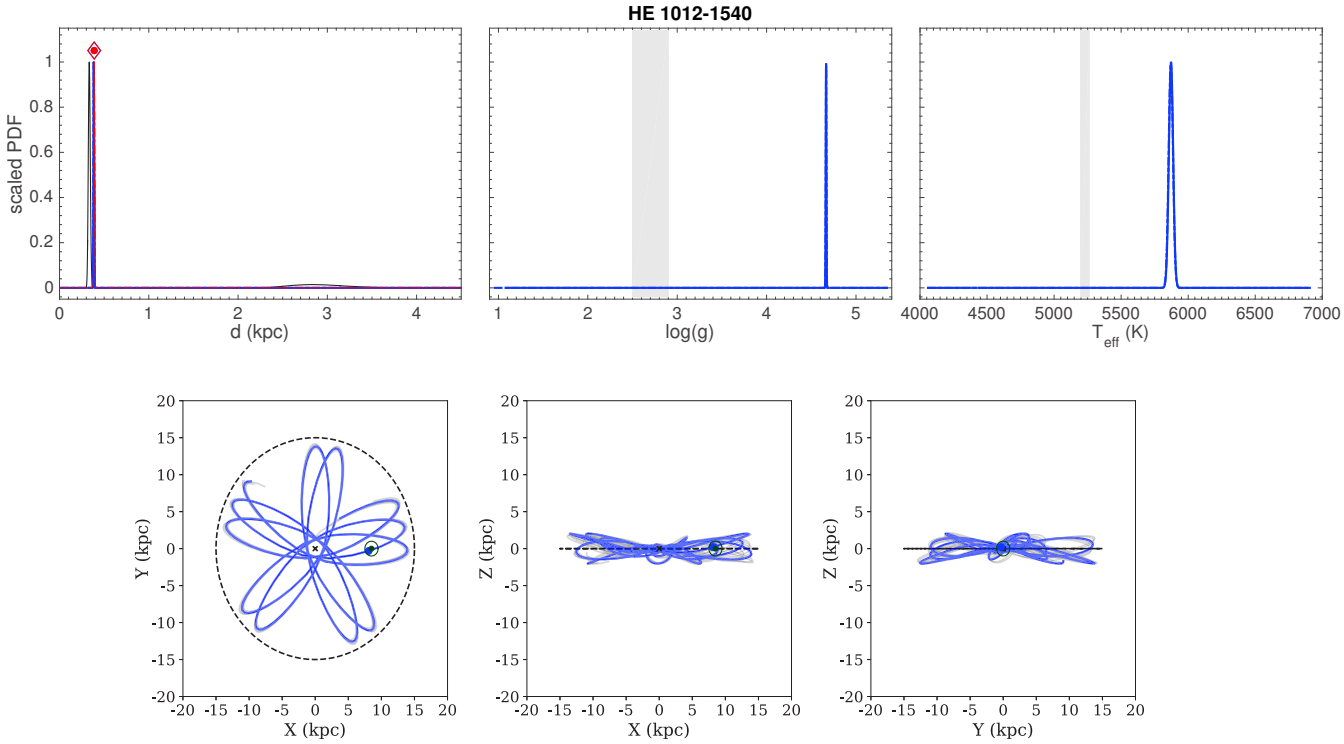

Figure A18. Same as Figure A2, but for HE 1012-1540.

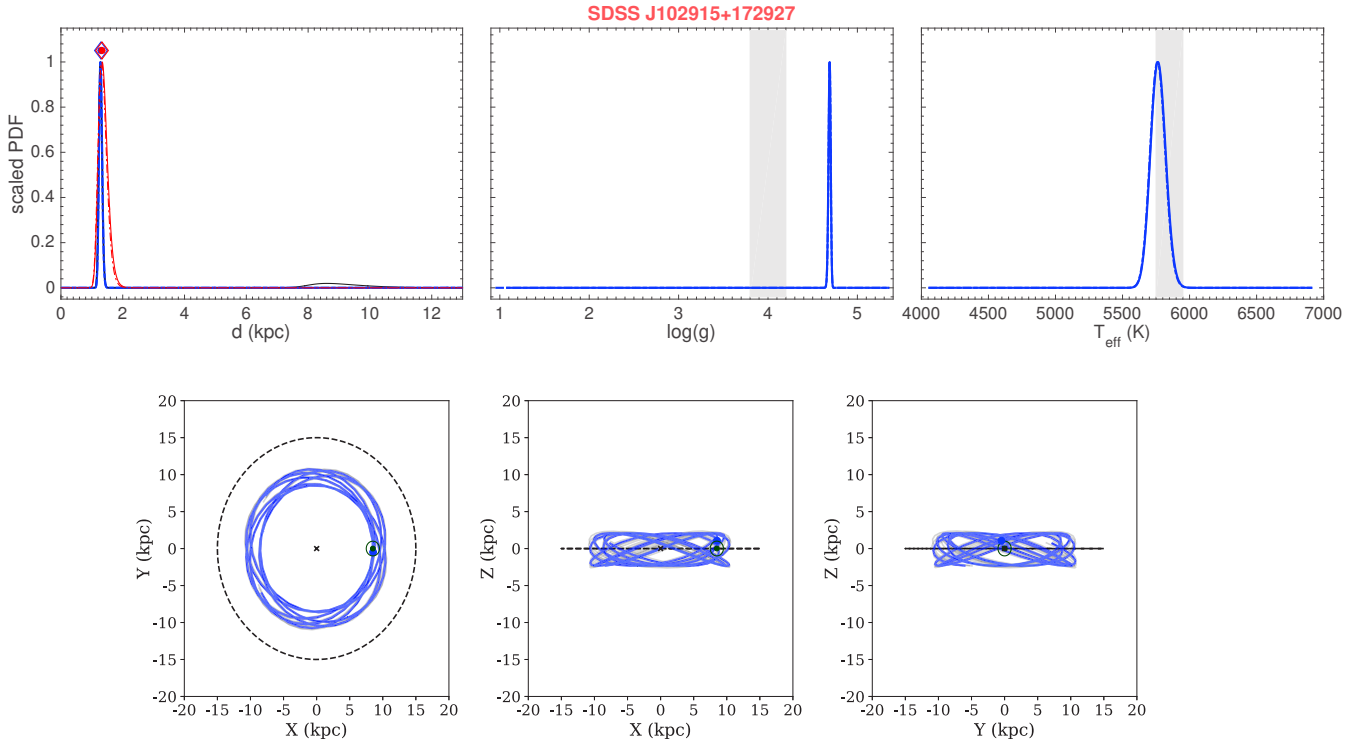

Figure A19. Same as Figure A2, but for SDSS J102915+172927.

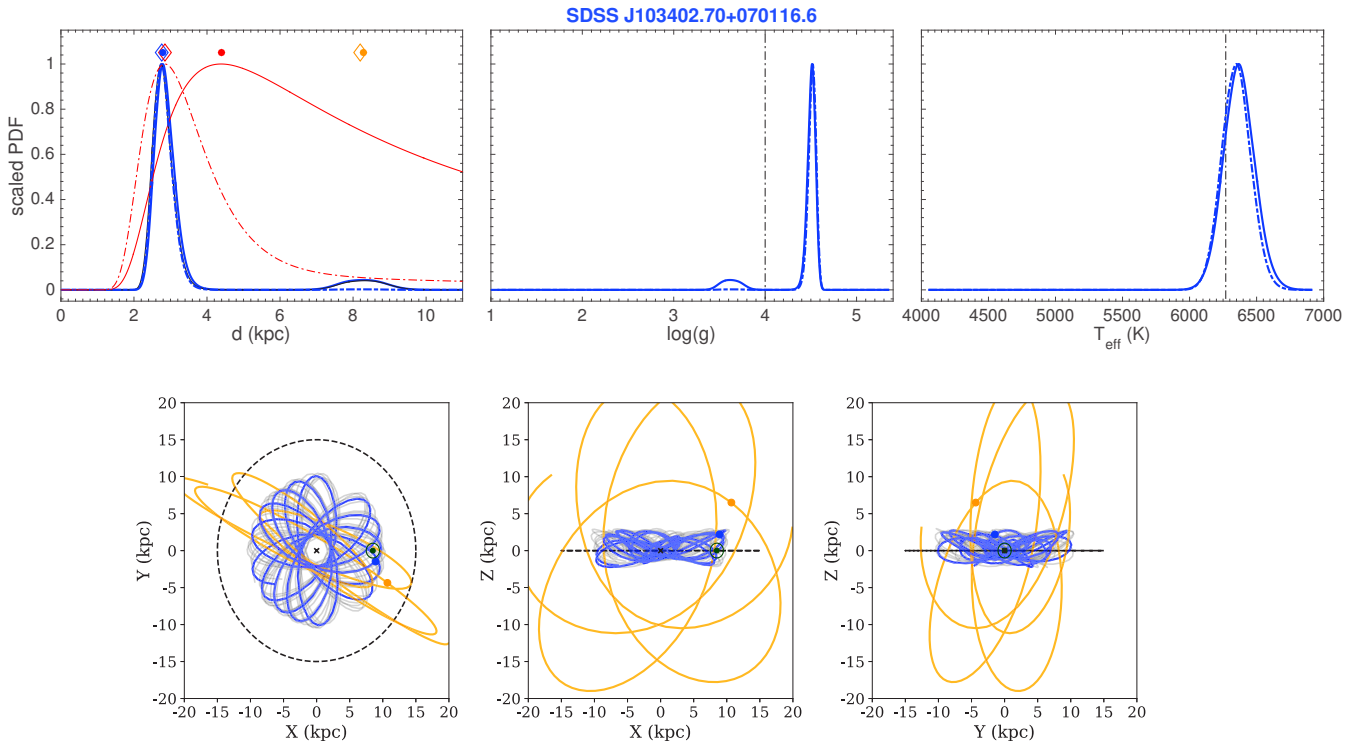

Figure A20. Same as Figure A2, but for SDSS J103402.70+070116.6.

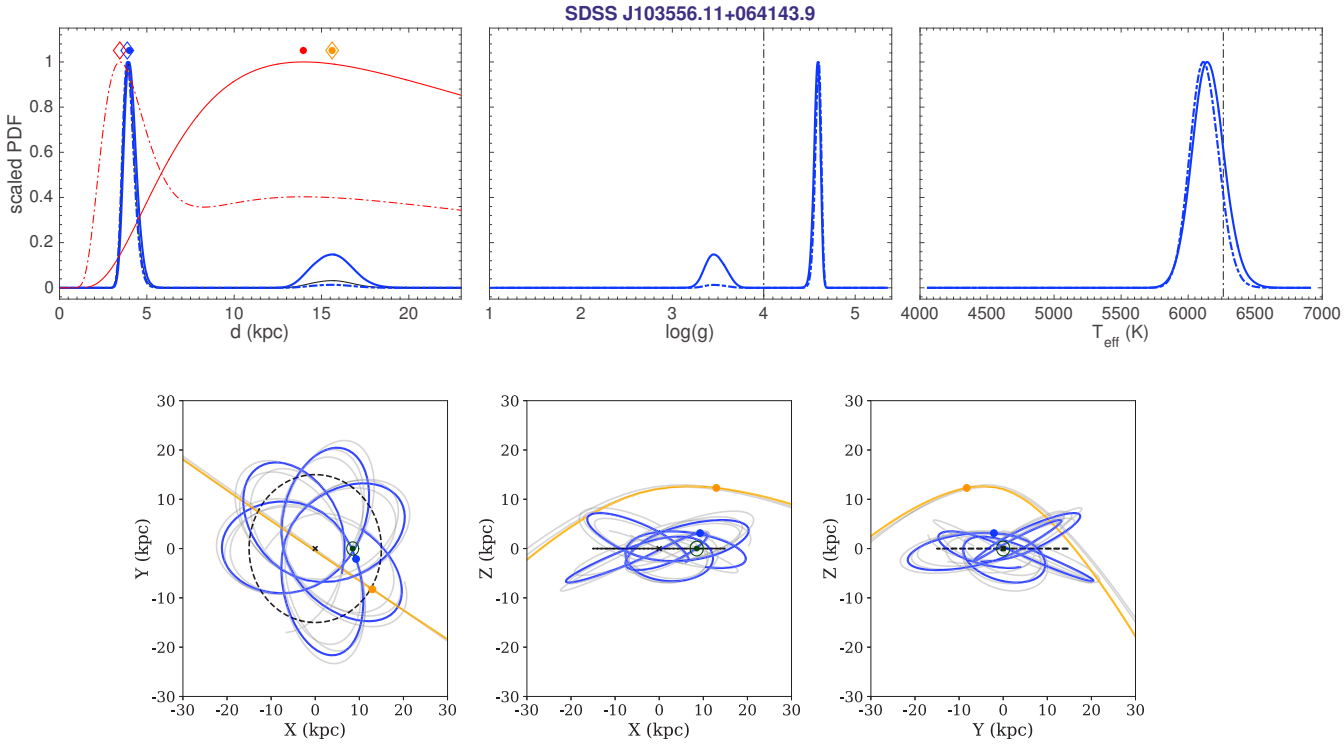

Figure A21. Same as Figure A2, but for SDSS J103556.11+064143.9.

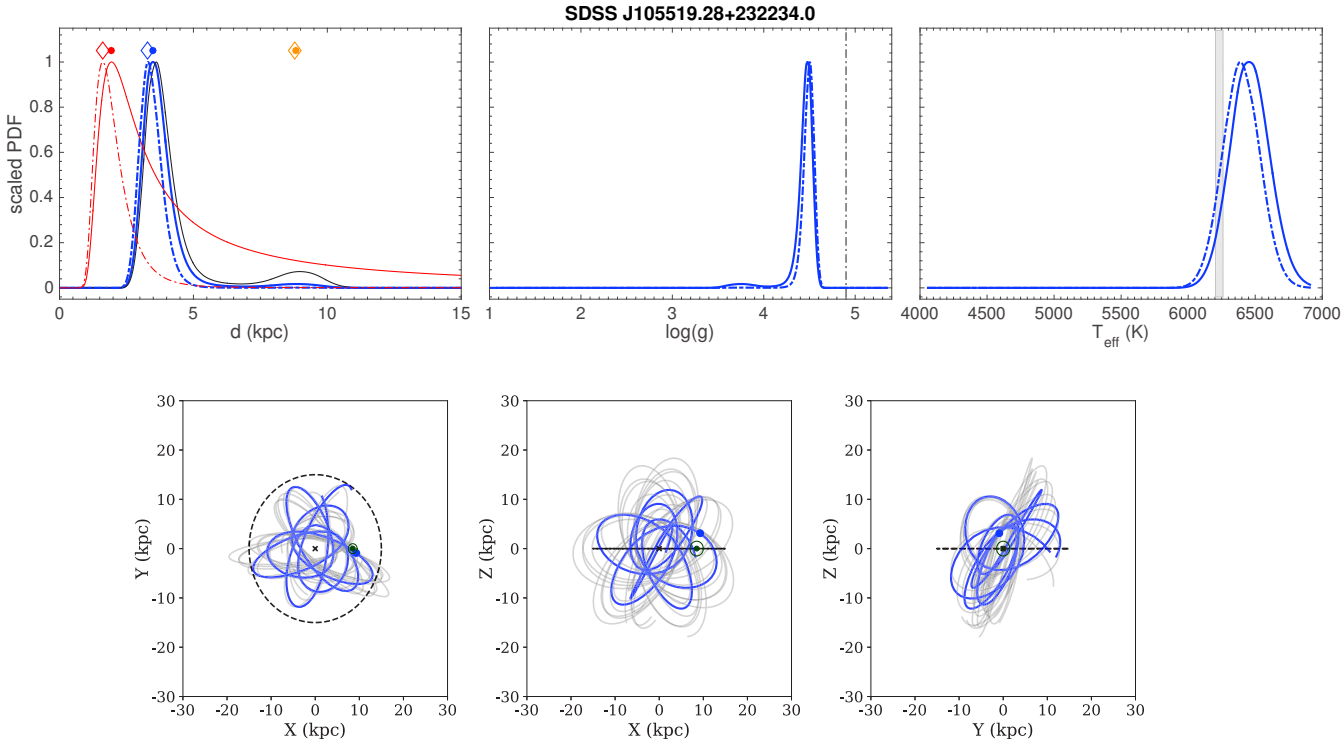

Figure A22. Same as Figure A2, but for SDSS J105519.28+232234.0.

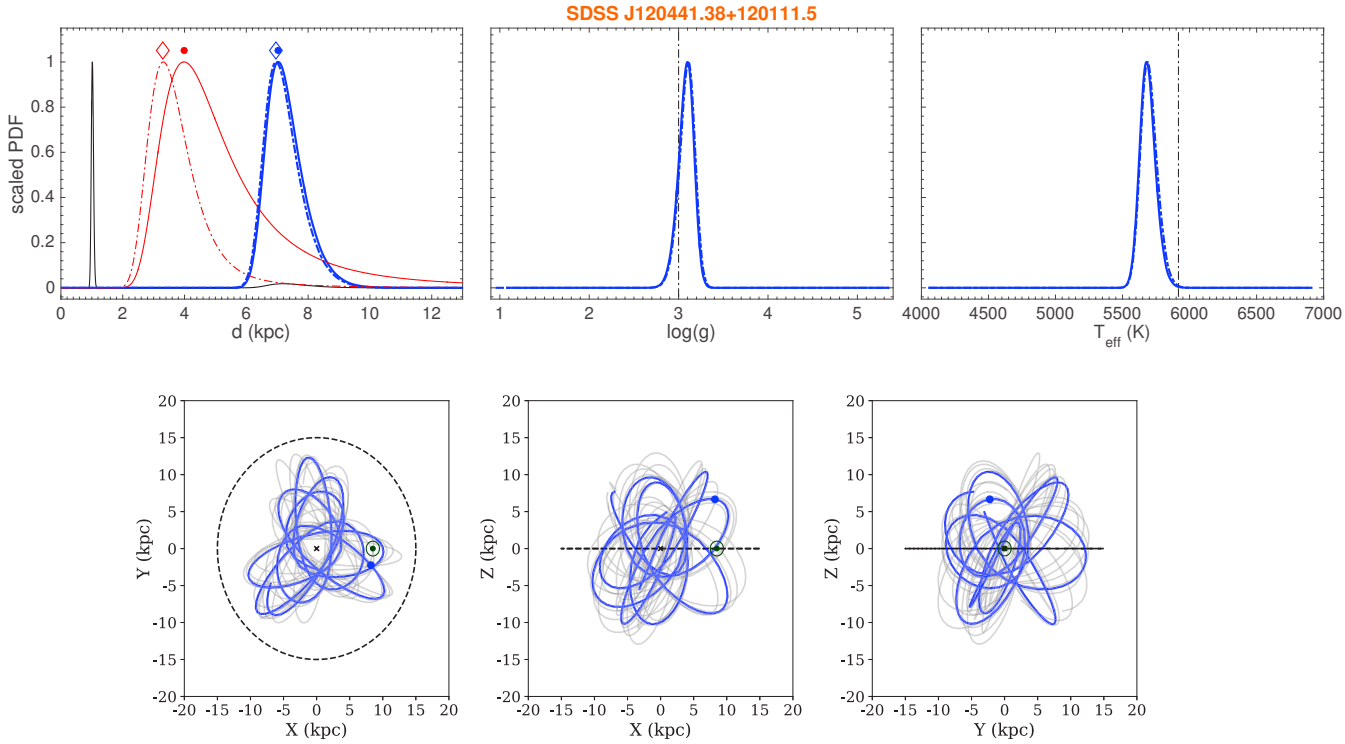

Figure A23. Same as Figure A2, but for SDSS J120441.38+120111.5.

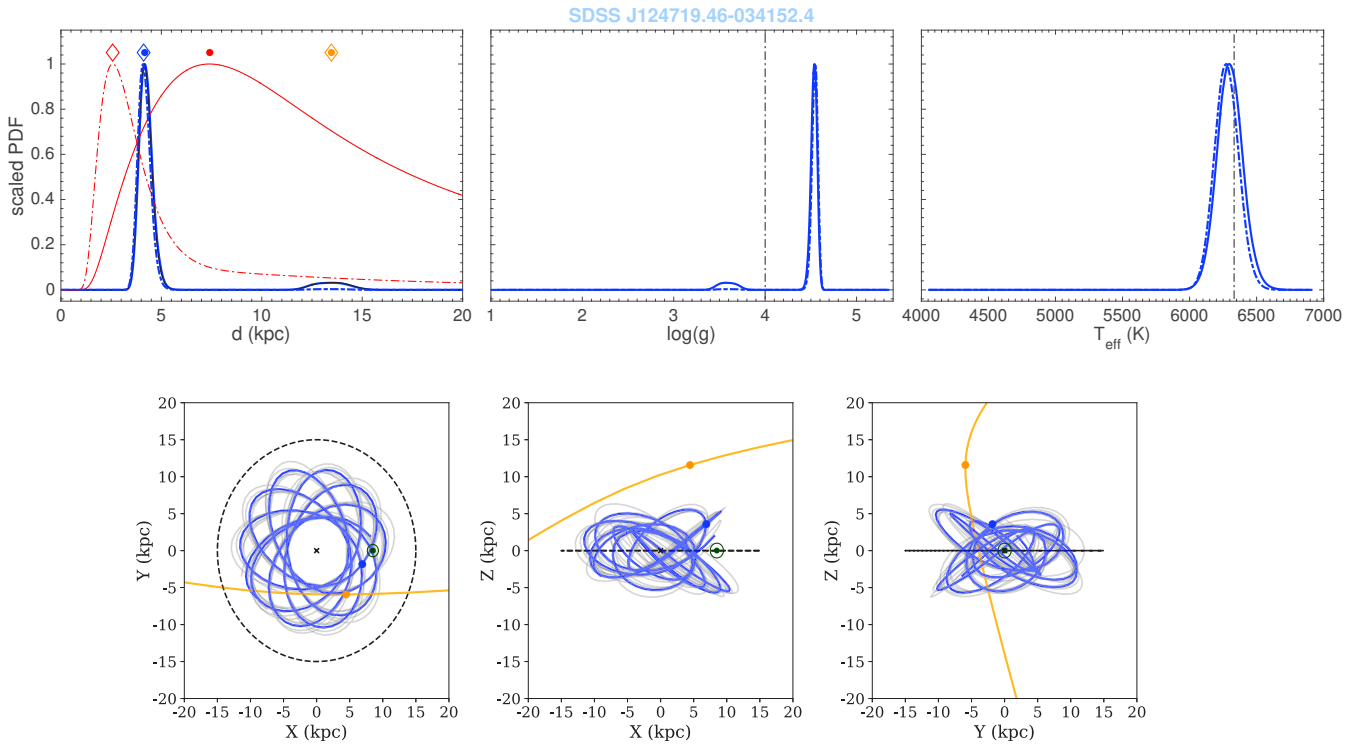

Figure A24. Same as Figure A2, but for SDSS J124719.46-034152.4.

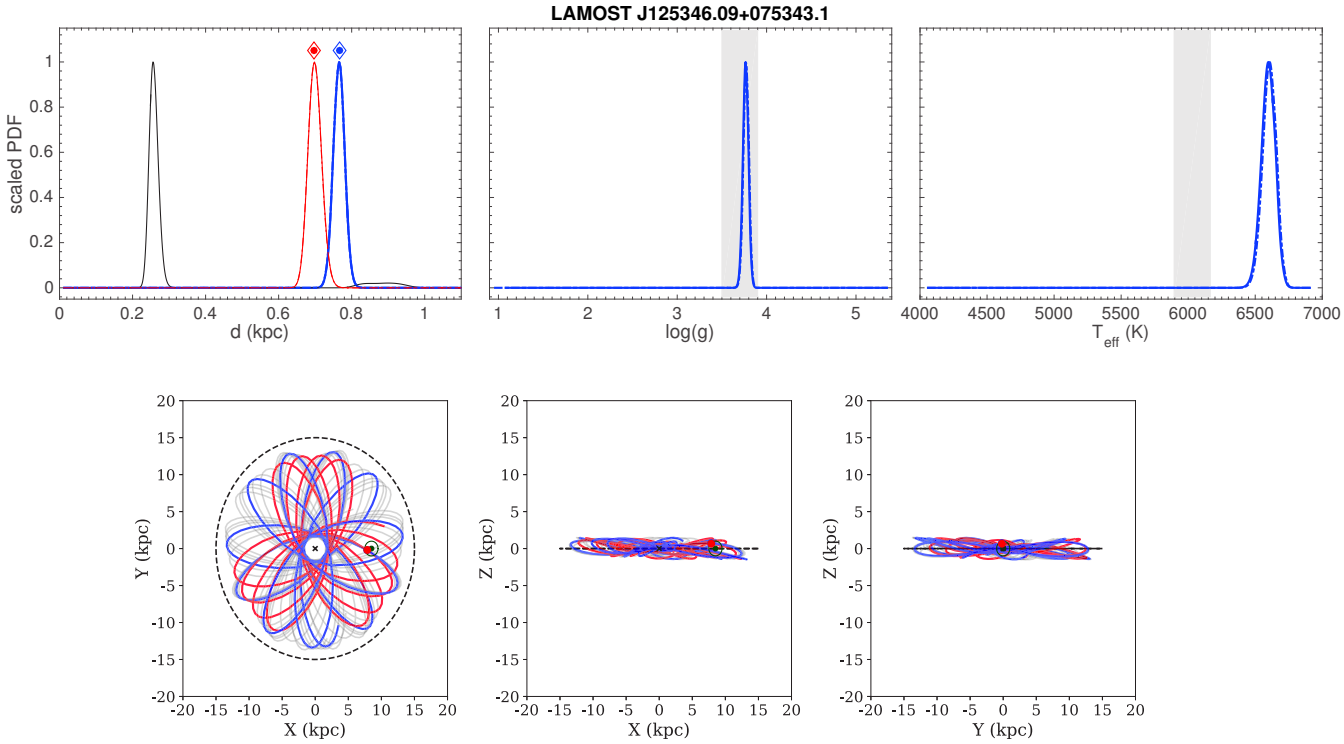

Figure A25. Same as Figure A2, but for LAMOST J125346.09+075343.1. For this star, the orbit inferred from the product between the astrometric likelihood and MW halo prior is shown with the red line.

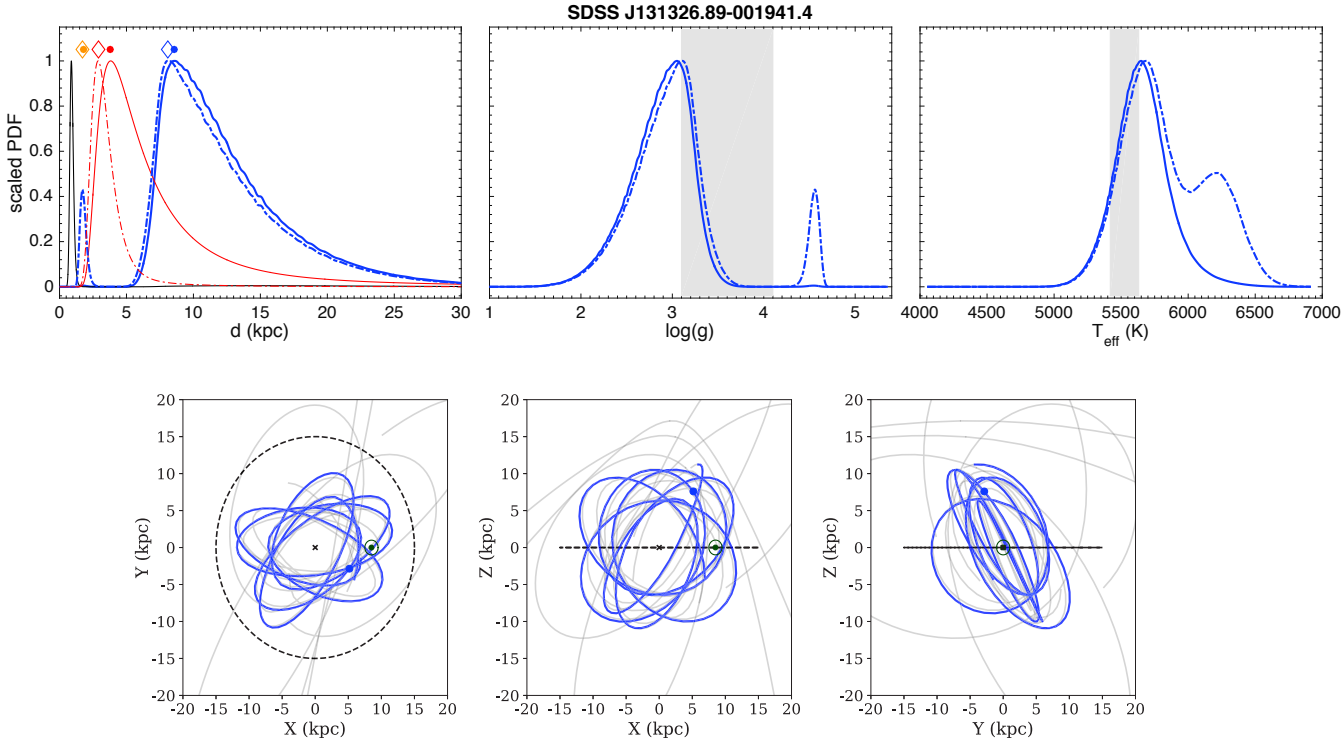

Figure A26. Same as Figure A2, but for SDSS J131326.89-001941.4.

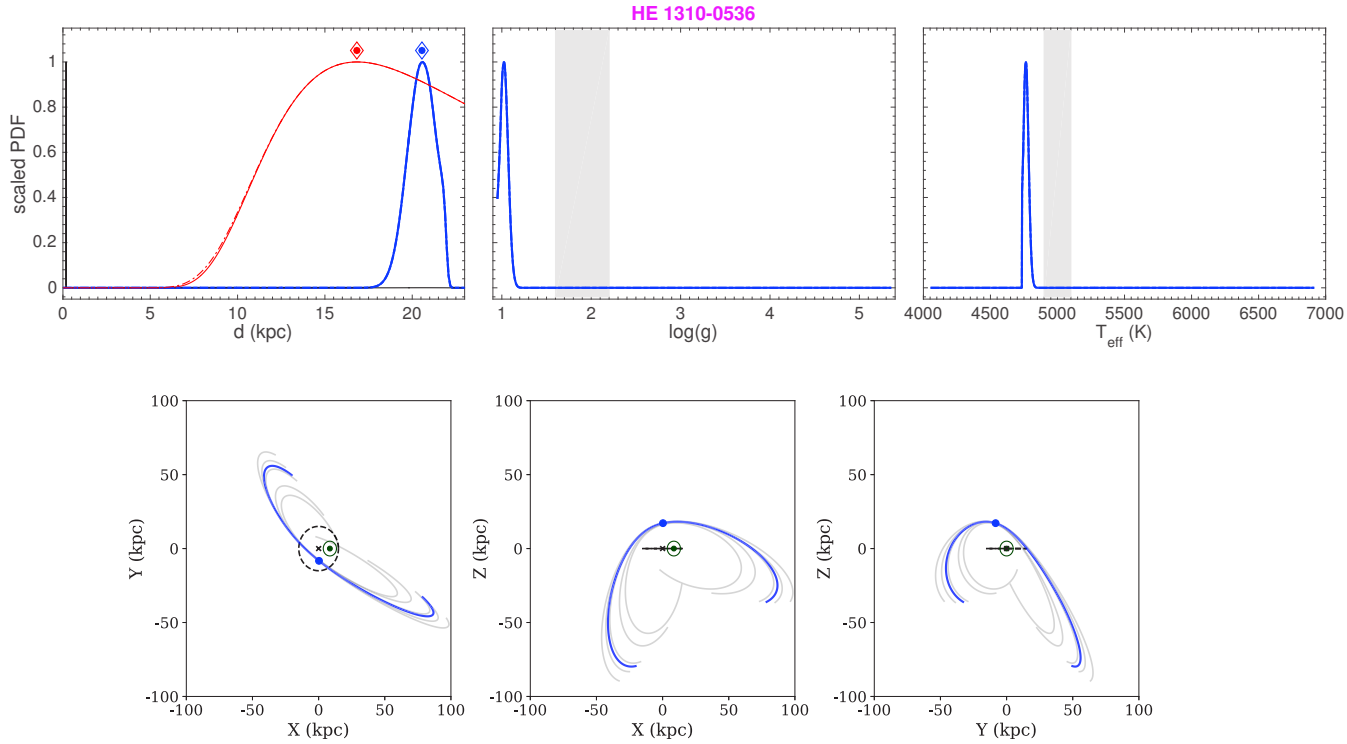

Figure A27. Same as Figure A2, but for HE 1310-0536.

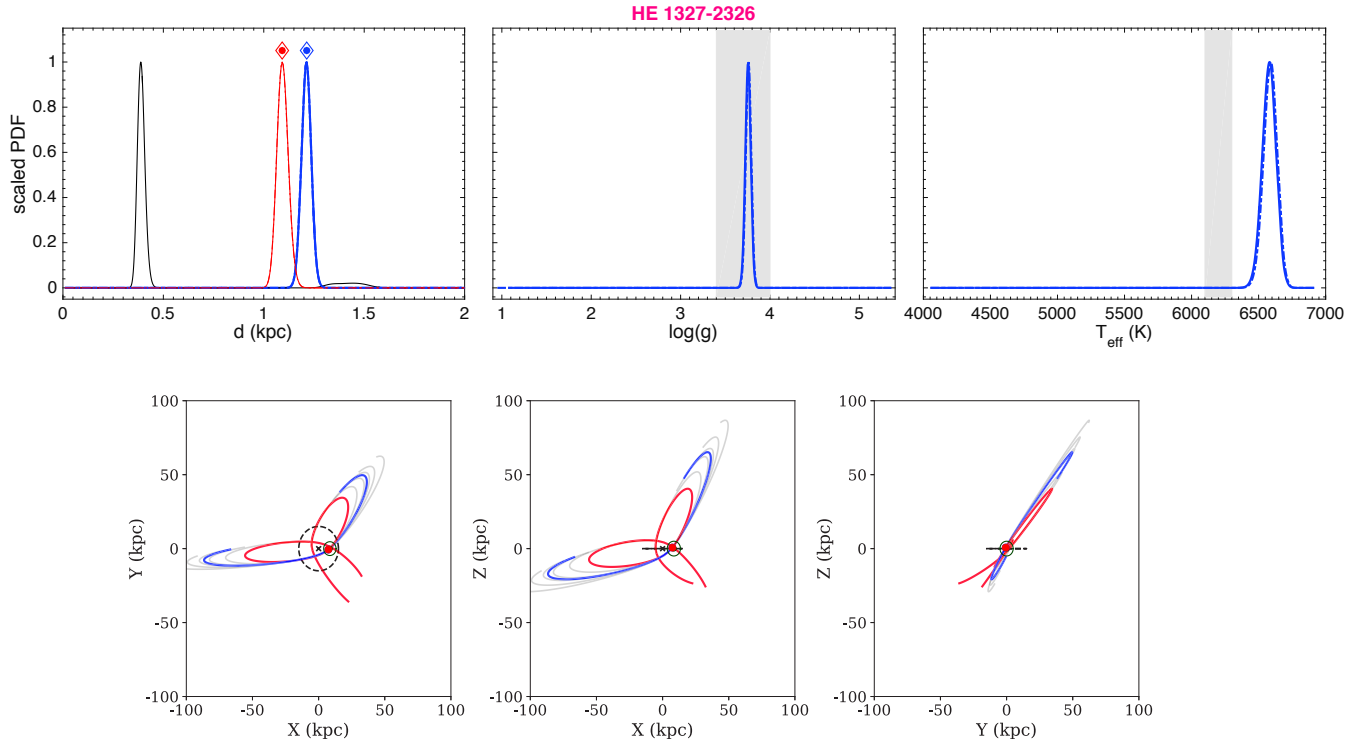

Figure A28. Same as Figure A2, but for HE 1327-2326. For this star, the orbit inferred from the product between the astrometric likelihood and MW halo prior is shown with the red line.

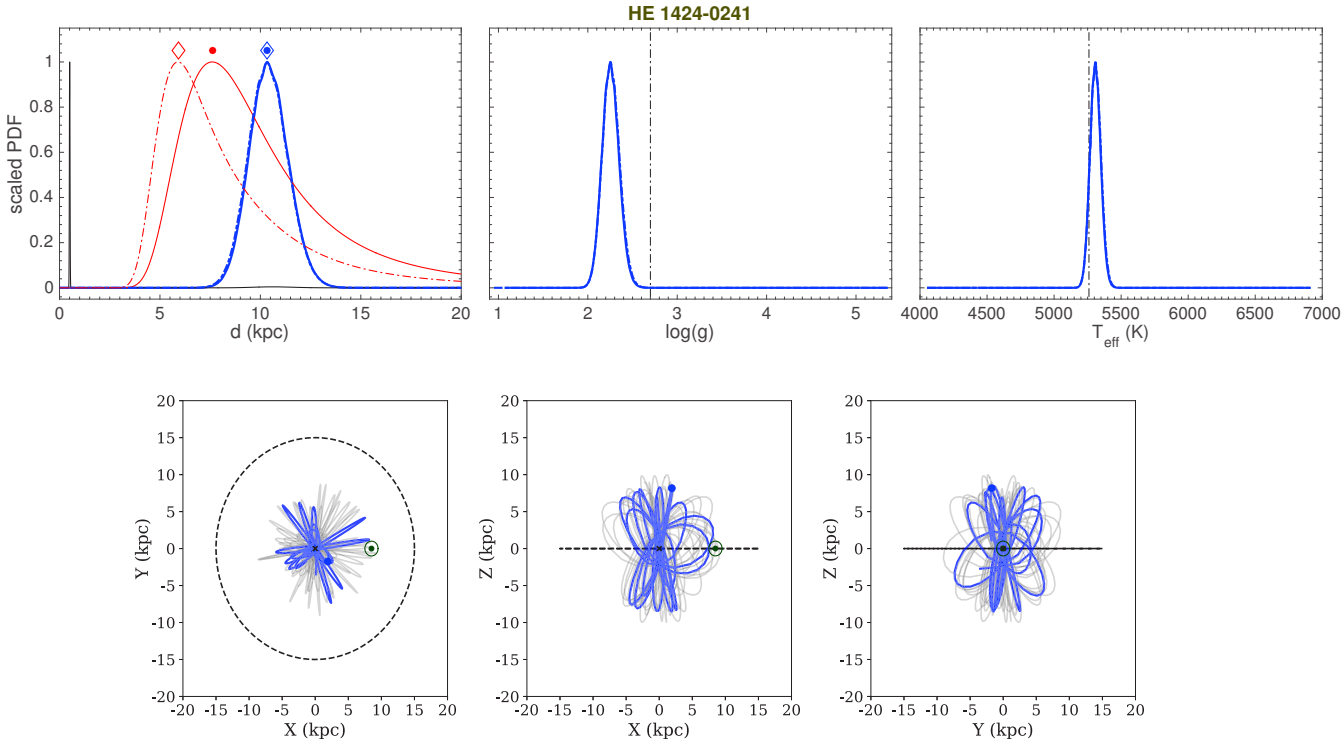

Figure A29. Same as Figure A2, but for HE 1424-0241.

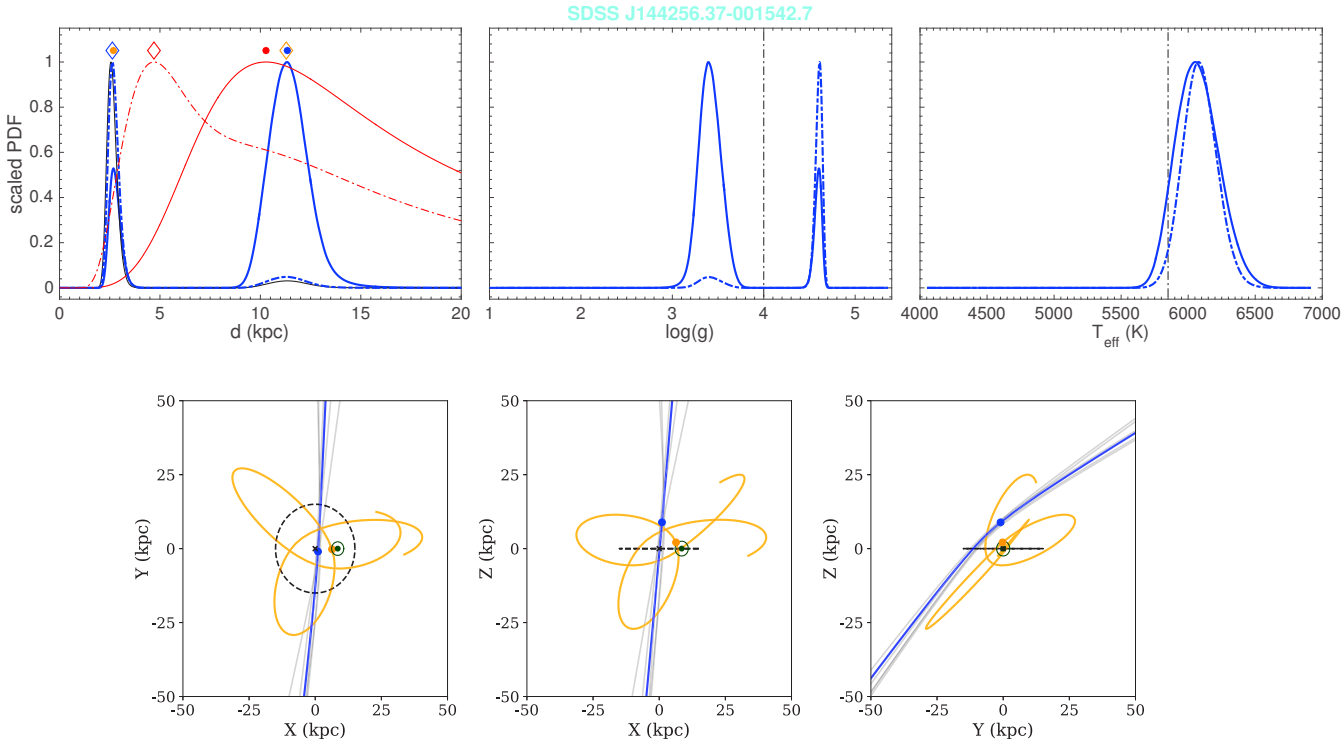

Figure A30. Same as Figure A2, but for SDSS J144256.37-001542.7.

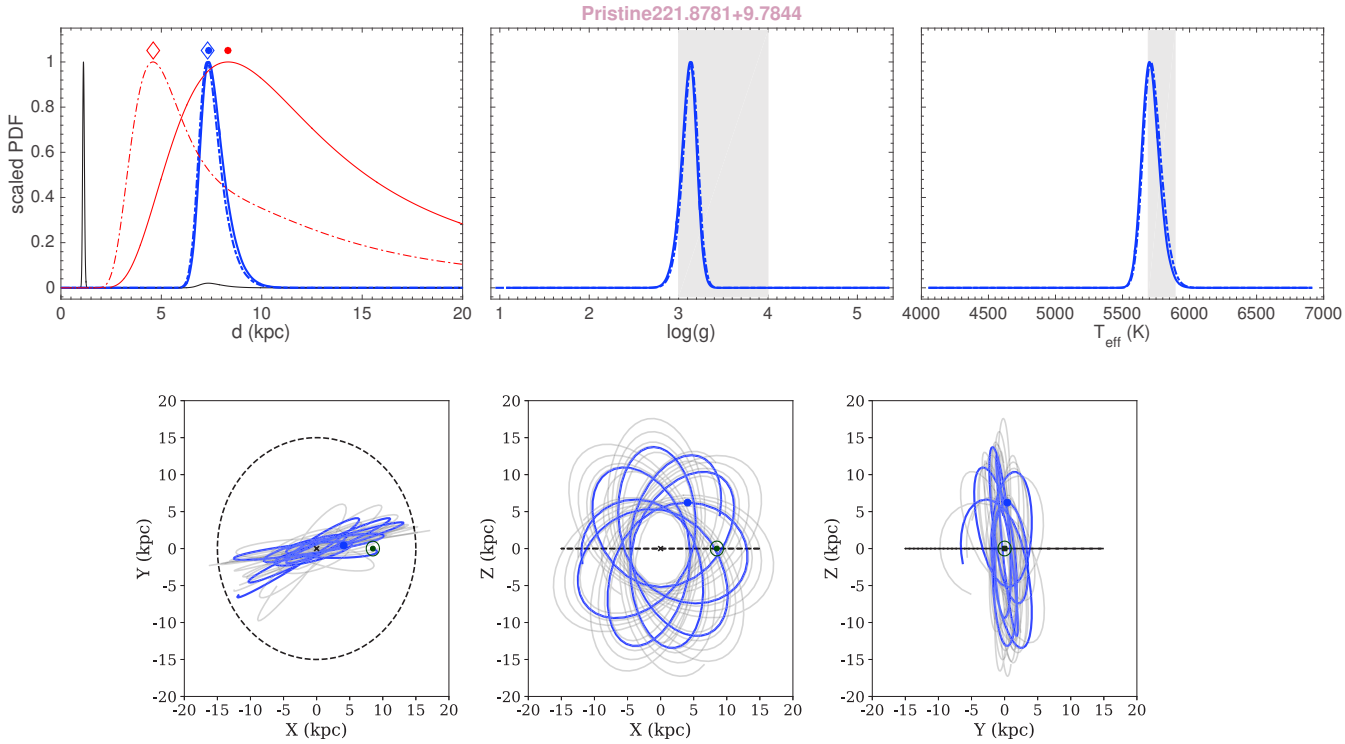

Figure A31. Same as Figure A2, but for Pristine221.8781+9.7844.

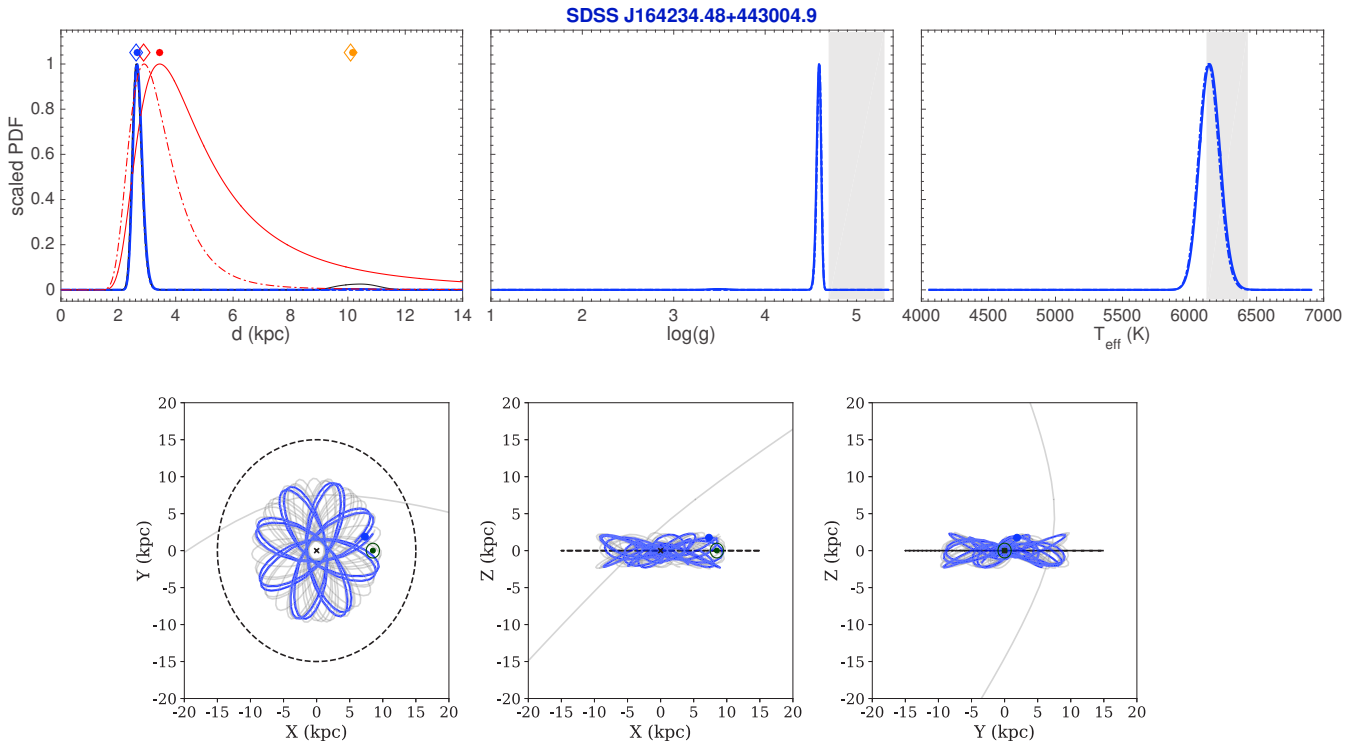

Figure A32. Same as Figure A2, but for SDSS J164234.48+443004.9.

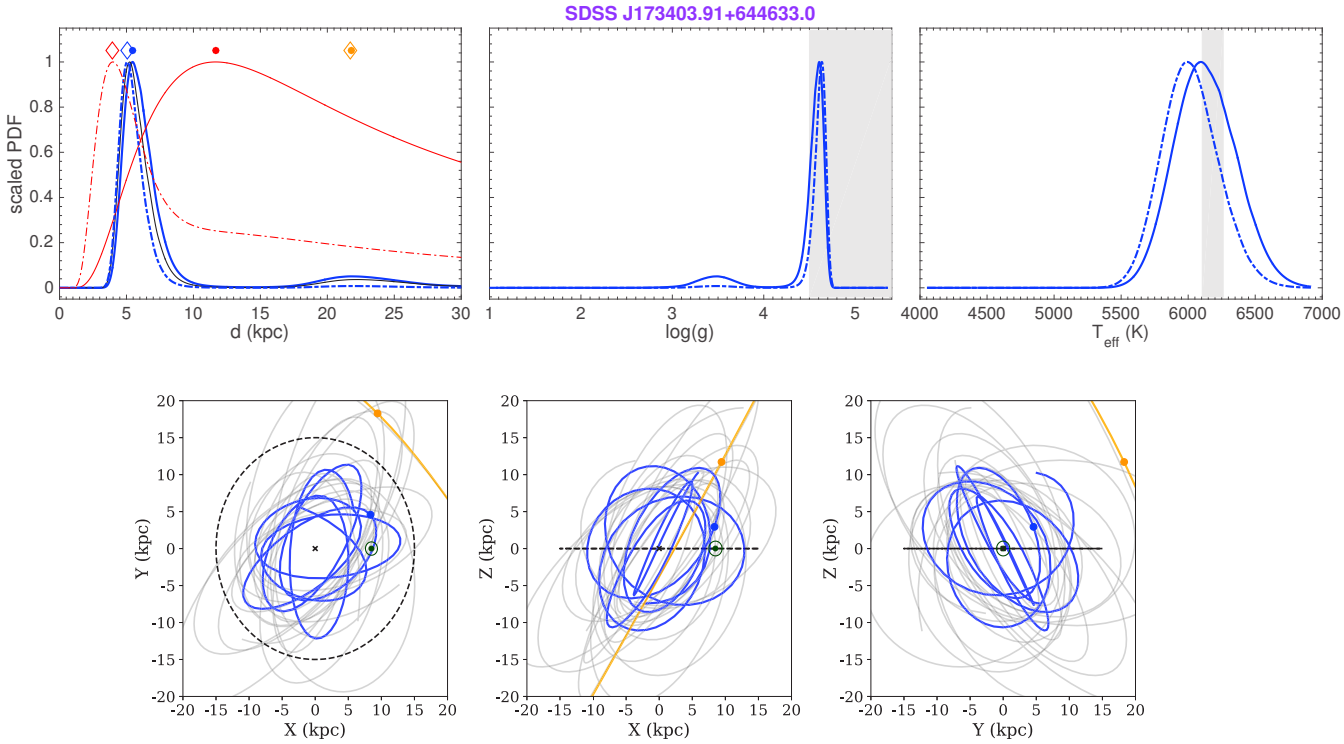

Figure A33. Same as Figure A2, but for SDSS J173403.91+644633.0.

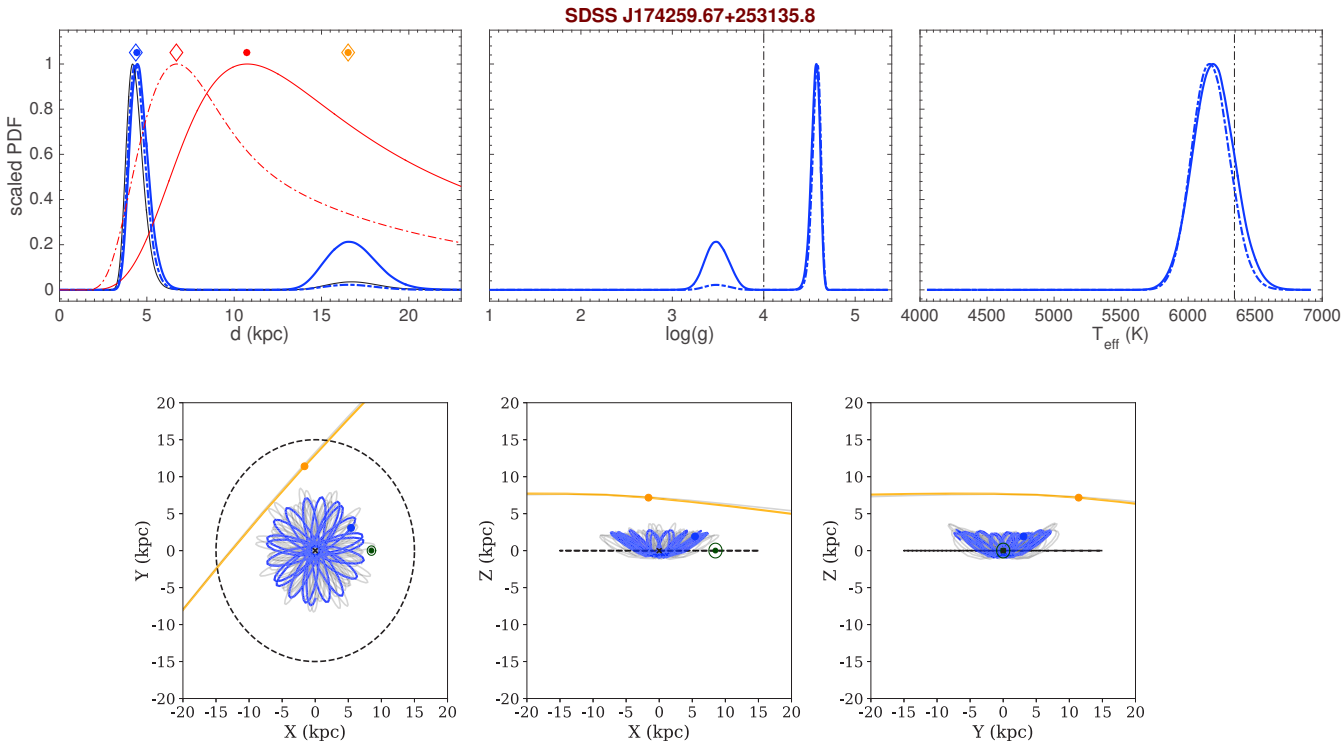

Figure A34. Same as Figure A2, but for SDSS J174259.67+253135.8.

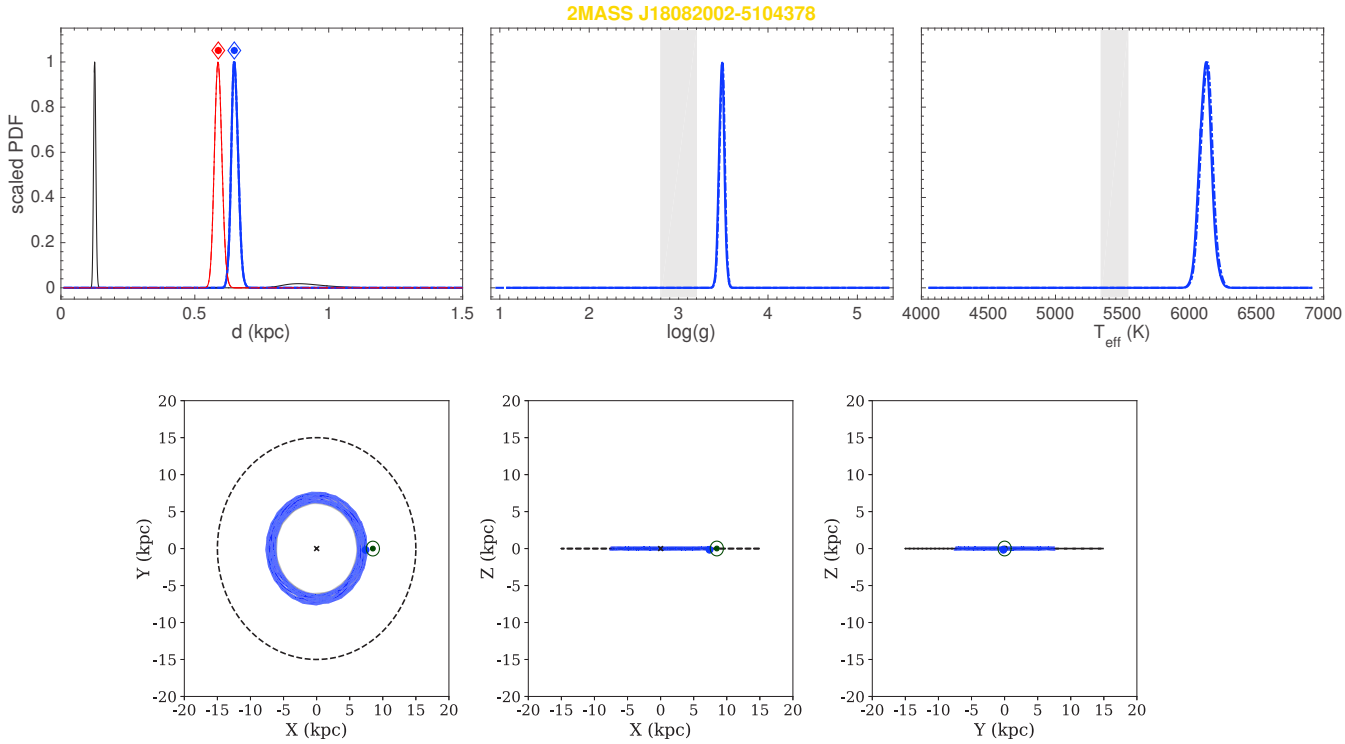

Figure A35. Same as Figure A2, but for 2MASS J18082002-5104378.

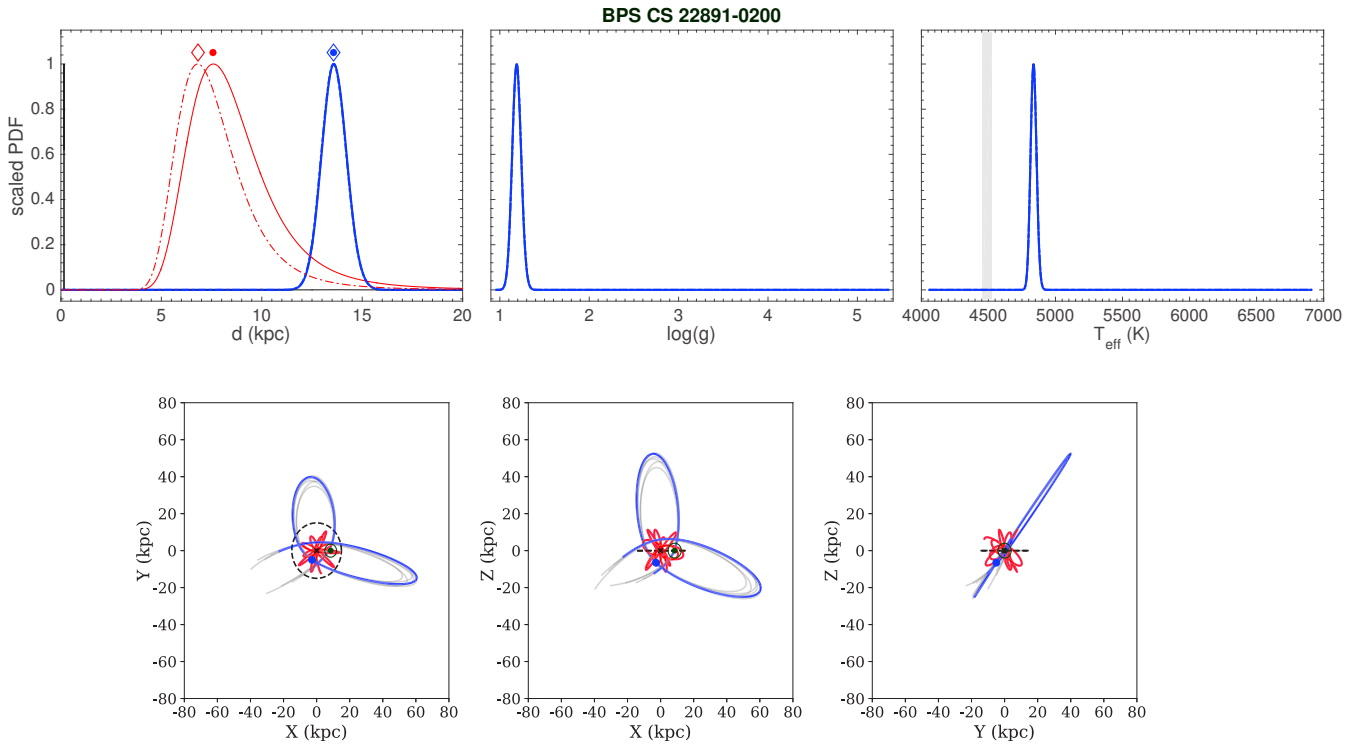

Figure A36. Same as Figure A2, but for BPS CS 22891-0200. The literature value for surface gravity is out of range in the plot. For this star, the orbit inferred from the product between the astrometric likelihood and MW halo prior is shown with the red line.

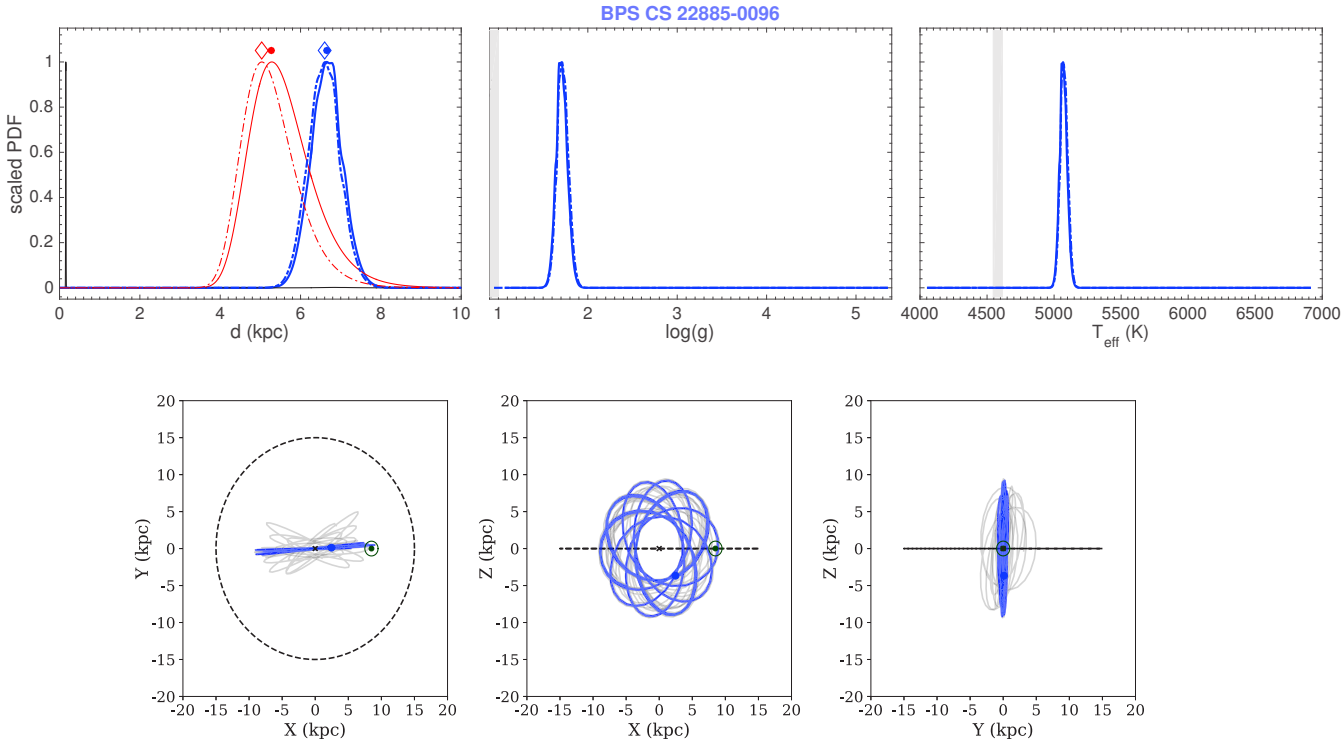

Figure A37. Same as Figure A2, but for BPS CS 22885-0096.

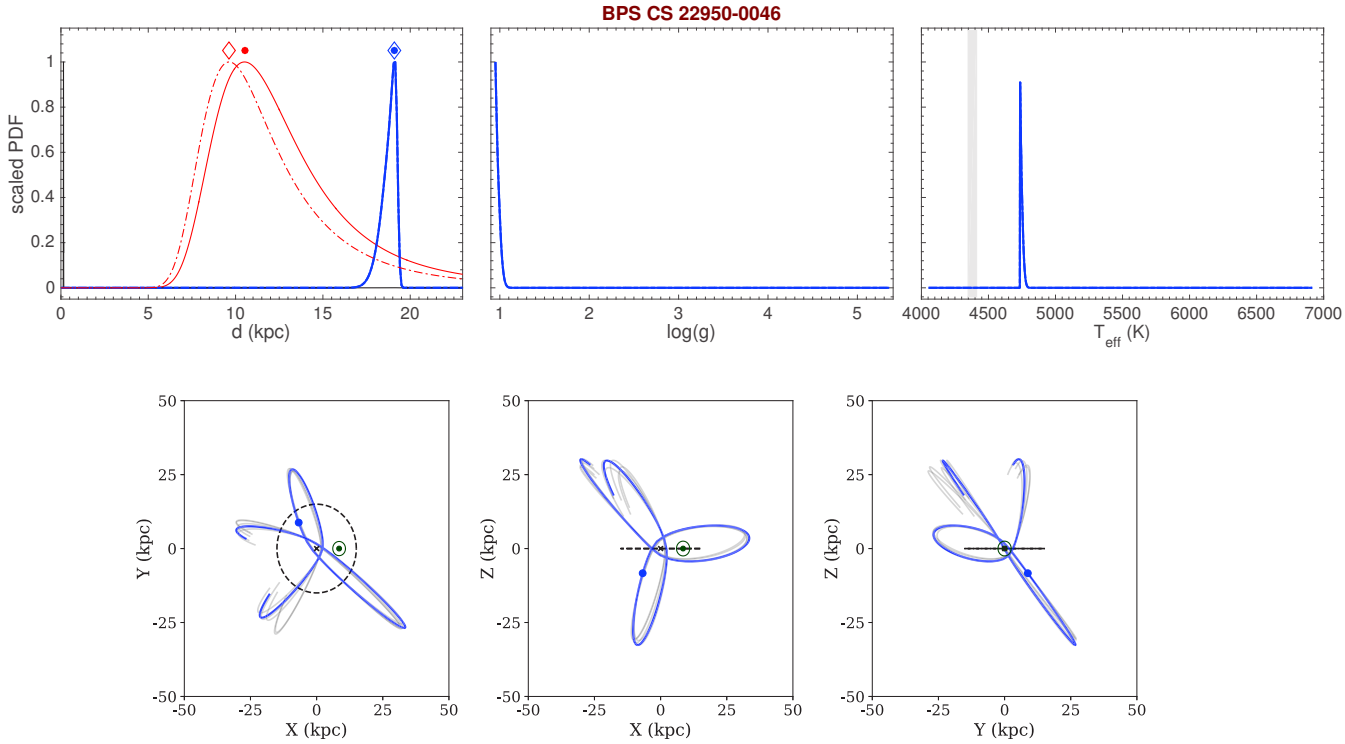

Figure A38. Same as Figure A2, but for BPS CS 22950-0046. The literature value for surface gravity is out of range in the plot.

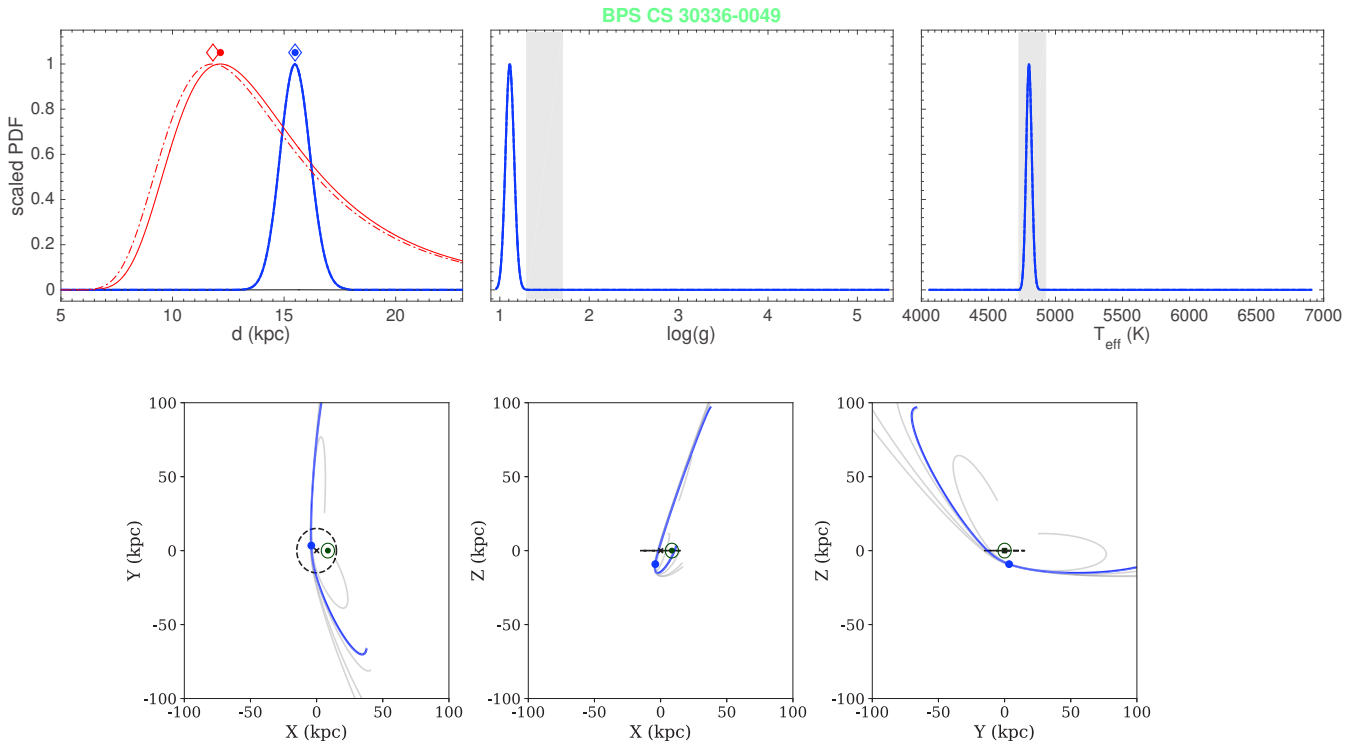

Figure A39. Same as Figure A2, but for BPS CS 30336-0049.

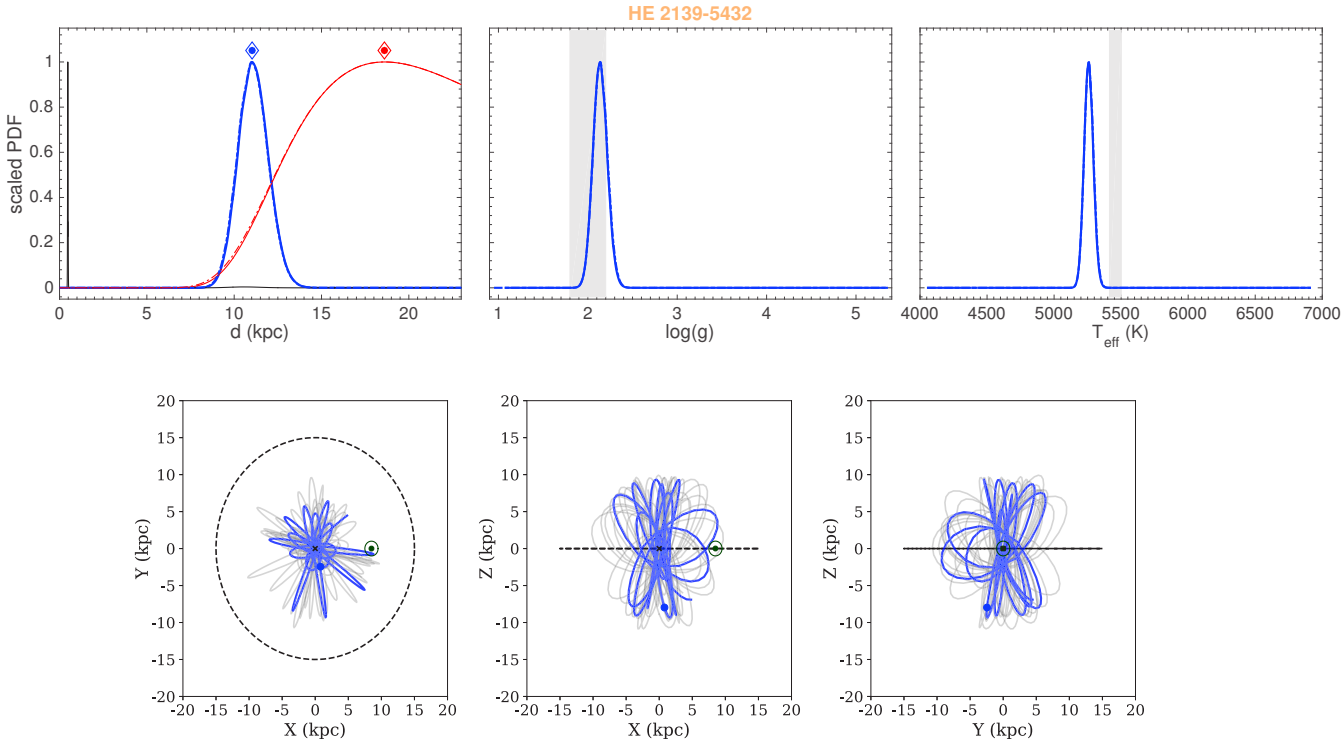

Figure A40. Same as Figure A2, but for HE 2139-5432.

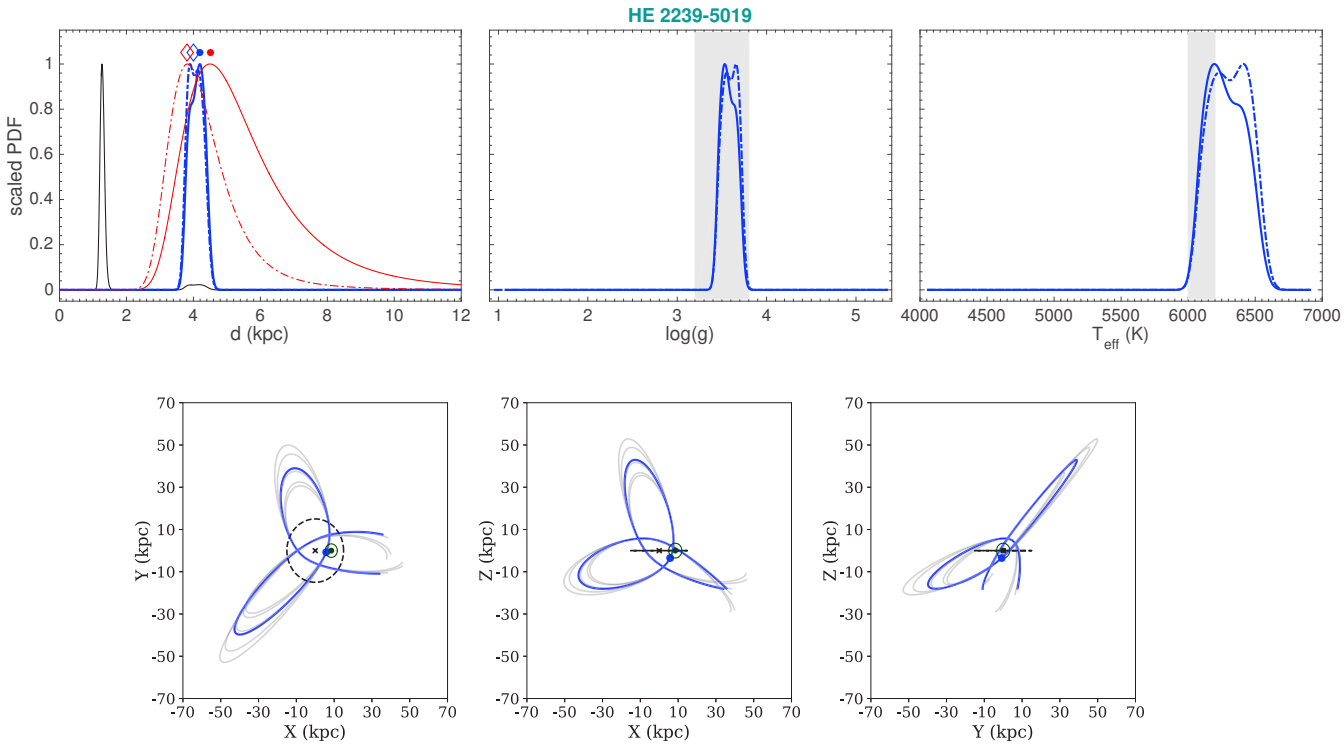

Figure A41. Same as Figure A2, but for HE 2239-5019.

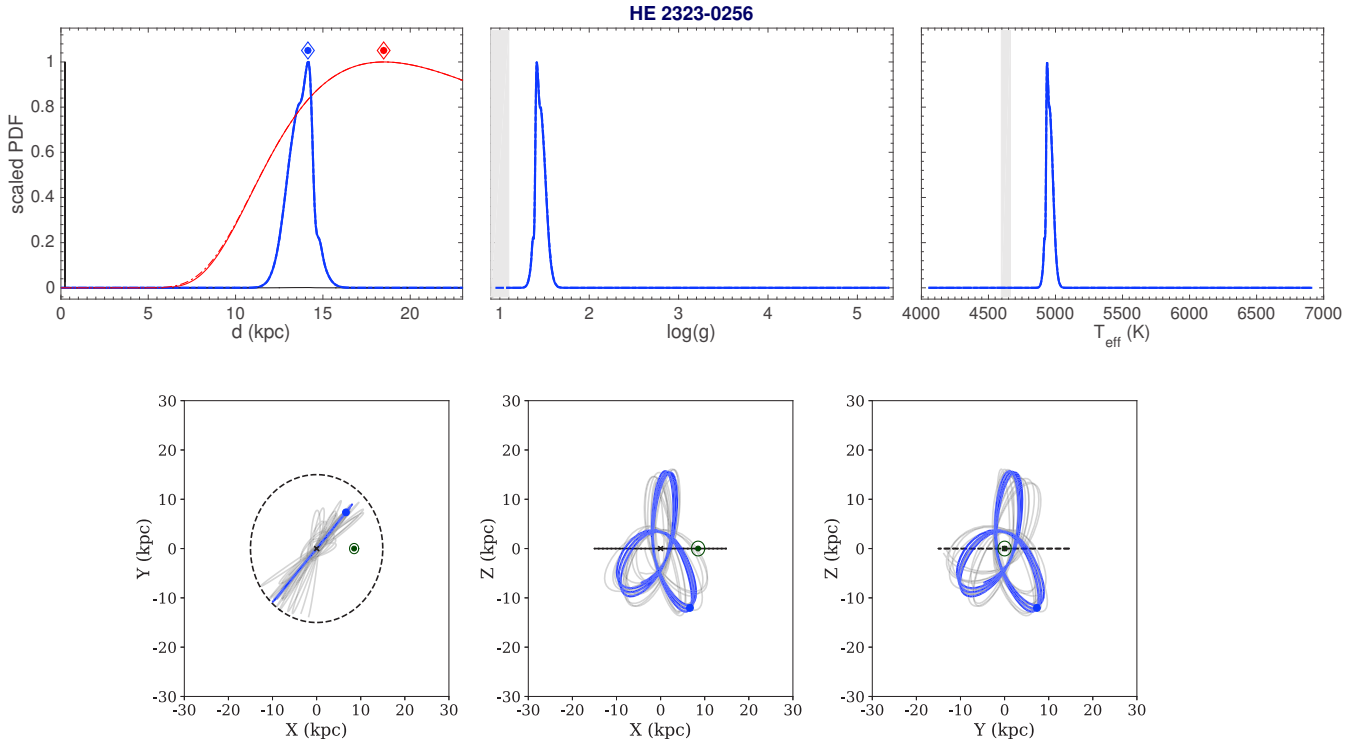

Figure A42. Same as Figure A2, but for HE 2323-0256.

APPENDIX B: COMPARISON WITH VALUES FROM LITERATURE

A global comparison between the stellar parameters inferred in this work and the values found in the literature is reported in the two panels of Figure B1. As we can see, we find a broad agreement for the effective temperature (left panel) and the surface gravity (right panel). Possible systematics are involved both in our method (e.g. $T_{\rm eff} - \log(g)$ relation in the MESA/MIST isochrones) and the multiple spectroscopic methods used by different authors (e.g. grid based models, synthetic spectra, data-driven analysis etc.).

REFERENCES

Aguado D. S., Allende Prieto C., González Hernández J. I., Carrera R., Rebolo R., Shetrone M., Lambert D. L., Fernández-Alvar E., 2016, A&A, 593, A10

Aguado D. S., Allende Prieto C., González Hernández J. I., Rebolo R., 2018a, ApJL, 854, L34

Aguado D. S., Allende Prieto C., González Hernández J. I., Rebolo R., Caffau E., 2017a, A&A, 604, A9

Aguado D. S., González Hernández J. I., Allende Prieto C., Rebolo R., 2017b, A&A, 605, A40

—, 2018b, ApJL, 852, L20

Allende Prieto C. et al., 2015, A&A, 579, A98

Arentsen A., Starkenburg E., Shetrone M. D., Venn K. A., Depagne É., McConnachie A. W., 2018, arXiv e-prints

Bonifacio P. et al., 2015, A&A, 579, A28

—, 2018, A&A, 612, A65

Caffau E. et al., 2012, A&A, 542, A51

—, 2013a, A&A, 560, A15

Caffau E. et al., 2011, Nature, 477, 67 EP

Caffau E. et al., 2013b, A&A, 560, A71

—, 2016, A&A, 595, L6

Cayrel R. et al., 2004, A&A, 416, 1117

Christlieb N., Gustafsson B., Korn A. J., Barklem P. S., Beers T. C., Bessell M. S., Karlsson T., Mizuno-Wiedner M., 2004, ApJ, 603, 708

Cohen J. G., Christlieb N., McWilliam A., Shectman S., Thompson I., Melendez J., Wisotzki L., Reimers D., 2008, ApJ, 672, 320

Dahn C. C., Liebert J., Kron R. G., Spinrad H., Hintzen P. M., 1977, ApJ, 216, 757

Dearborn D. S. P., Liebert J., Aaronson M., Dahn C. C., Harrington R., Mould J., Greenstein J. L., 1986, ApJ, 300, 314

Frebel A., Chiti A., Ji A. P., Jacobson H. R., Placco V. M., 2015, ApJL, 810, L27

Frebel A., Collet R., Eriksson K., Christlieb N., Aoki W., 2008, ApJ, 684, 588

Hansen T. et al., 2015, ApJ, 807, 173

Ito H., Aoki W., Beers T. C., Tominaga N., Honda S., Carollo D., 2013, ApJ, 773, 33

Lai D. K., Bolte M., Johnson J. A., Lucatello S., Heger A., Woosley S. E., 2008, ApJ, 681, 1524

Li H., Aoki W., Zhao G., Honda S., Christlieb N., Suda T., 2015, PASJ, 67, 84

Meléndez J., Placco V. M., Tucci-Maia M., Ramírez I., Li T. S., Perez G., 2016, A&A, 585, L5

Nordlander T., Amarsi A. M., Lind K., Asplund M., Barklem P. S., Casey A. R., Collet R., Leenaarts J., 2017, A&A, 597, A6

Norris J. E. et al., 2013, ApJ, 762, 25

Norris J. E., Christlieb N., Korn A. J., Eriksson K., Bessell M. S., Beers T. C., Wisotzki L., Reimers D., 2007, ApJ, 670, 774

Placco V. M. et al., 2016, ApJ, 833, 21

Placco V. M., Frebel A., Lee Y. S., Jacobson H. R., Beers T. C., Pena J. M., Chan C., Heger A., 2015, ApJ, 809, 136

Roederer I. U., Preston G. W., Thompson I. B., Shectman S. A., Sneden C., Burley G. S., Kelson D. D., 2014, The Astronomical Journal, 147, 136

Roeser S., Demleitner M., Schilbach E., 2010, AJ, 139, 2440

Schlaufman K. C., Thompson I. B., Casey A. R., 2018, ArXiv e-prints

Starkenburg E. et al., 2018, MNRAS, 481, 3838

Yong D. et al., 2013, ApJ, 762, 26

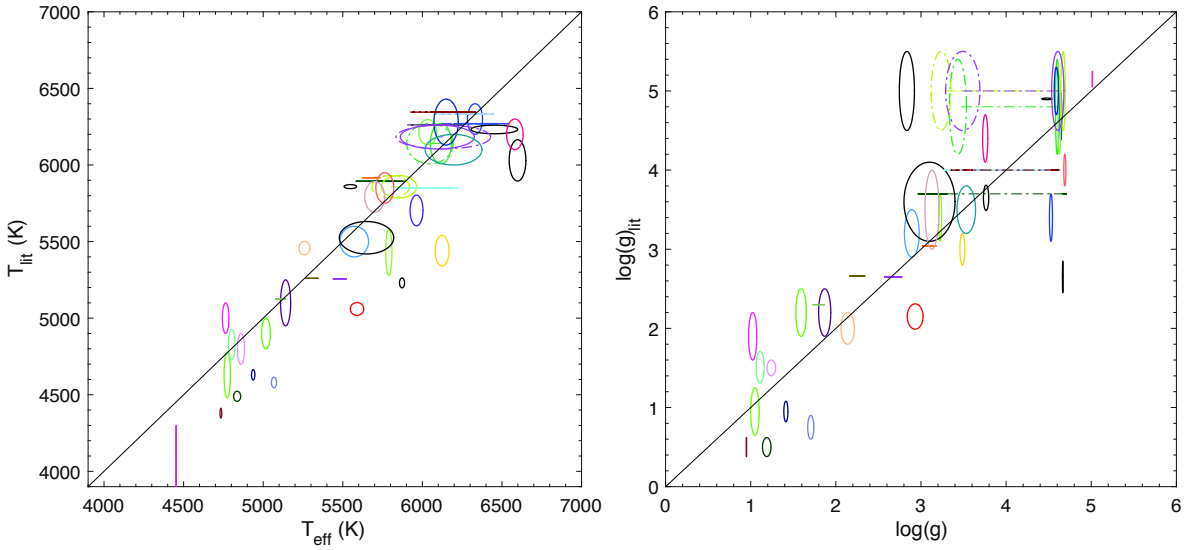

Figure B1. Comparison between inferred effective temperature $T_{\rm eff}$ (left panel), surface gravity $\log(g)$ (right panel) and the values from the literature. The ellipses represent the position of the stars within 1 sigma and the black line corresponds to the 1:1 relation. If the dwarf-giant degeneracy is not broken, the two possible solutions are represented and connected by a dot-dashed line of the same colour code. Each colour represents a star and the colour-code is the same as the colour-code for the markers in Figures 1 - 2 and the panel's titles in Figures A1 - A42. Solutions with integrated probability ($\int_{d-3\sigma}^{d+3\sigma} P(r)dr$) lower than 5% are not shown and solutions with integrated probability in the range $[5\%, 50\%]$ are shown with dot-dashed ellipses.

CHAPTER

3 The Pristine survey - X. A large population of low-metallicity stars permeates the Galactic disk.

This Chapter contains the work from Sestito et al. (2020a) that has been published on Monthly Notices of the Royal Astronomical Society as a form of letter. This work extends the kinematical analysis, started in the previous Chapter, on a very robust statistical firm. It bridges the gap from the ultra metal-poor regime analysed in Sestito et al. (2019) to the very metal-poor regime, metallicity at which the disk has been already explored in the past. For this analysis, I select VMPs from the Pristine survey (Starkenburg et al., 2017b; Aguado et al., 2019), especially the stars observed at the Isaac Newton Telescope, and from a catalogue of VMP from Li et al. (2018) observed by the LAMOST survey. As regards the sample from the Pristine survey, the radial velocities have been calculated using synthetic stellar spectra with the same resolution of INT spectrograph, while the systematics and offsets on the velocities have been inferred with an overlap of stars observed at high-resolution with the Gemini and CFHT facilities. A large fraction of the LAMOST sample is contaminated by metal-rich stars, therefore a selection of bona fide very metal-poor stars has been obtained cross-matching these data with the public LAMOST data release. So the distances and kinematical parameters have been inferred. This work shows that a population of stars confined to the disk exists at all metallicities and significantly prefer the prograde motion. This is in line with the results from the previous work (Sestito et al., 2019). Similar conclusions to the previous Chapter on the nature of this planar population have been discussed, pointing out that whatever their origin is, it will undoubtedly open a window on the early assembly of the Milky Way. And future metal-poor surveys and high-resolution simulations should investigate on this population of planar stars.

Monthly Notices
of the
ROYAL ASTRONOMICAL SOCIETY

MNRAS **497,** L7–L12 (2020)
Advance Access publication 2020 February 13

doi:10.1093/mnrasl/slaa022

The Pristine survey – X. A large population of low-metallicity stars permeates the Galactic disc

Federico Sestito,[1,2]★ Nicolas F. Martin,[1,3] Else Starkenburg,[2] Anke Arentsen,[2] Rodrigo A. Ibata,[1] Nicolas Longeard,[4] Collin Kielty,[5] Kristopher Youakim,[2] Kim A. Venn,[5] David S. Aguado,[6] Raymond G. Carlberg,[7] Jonay I. González Hernández,[8,9] Vanessa Hill,[10] Pascale Jablonka,[4,11] Georges Kordopatis,[10] Khyati Malhan,[12] Julio F. Navarro,[5] Rubén Sánchez-Janssen,[13] Guillame Thomas,[14] Eline Tolstoy,[15] Thomas G. Wilson,[16,17] Pedro A. Palicio,[8,9,10] Spencer Bialek,[5] Rafael Garcia-Dias,[8] Romain Lucchesi,[4] Pierre North,[4] Yeisson Osorio,[8] Lee R. Patrick[8] and Luis Peralta de Arriba[6,16]

Affiliations are listed at the end of the paper

Accepted 2020 February 5. Received 2020 February 5; in original form 2019 November 19

ABSTRACT

The orbits of the least chemically enriched stars open a window on the formation of our Galaxy when it was still in its infancy. The common picture is that these low-metallicity stars are distributed as an isotropic, pressure-supported component since these stars were either accreted from the early building blocks of the assembling Milky Way (MW), or were later brought by the accretion of faint dwarf galaxies. Combining the metallicities and radial velocities from the Pristine and LAMOST surveys and *Gaia* DR2 parallaxes and proper motions for an unprecedented large and unbiased sample of 1027 very metal poor stars at [Fe/H] ≤ -2.5 dex, we show that this picture is incomplete. We find that 31 per cent of the stars that currently reside spatially in the disc ($|Z| \leq 3$ kpc) do not venture outside of the disc plane throughout their orbit. Moreover, this sample shows strong statistical evidence (at the 5.0σ level) of asymmetry in their kinematics, favouring prograde motion. The discovery of this population implies that a significant fraction of stars with iron abundances [Fe/H] ≤ -2.5 dex merged into, formed within, or formed concurrently with the MW disc and that the history of the disc was quiet enough to allow them to retain their disc-like orbital properties, challenging theoretical and cosmological models.

Key words: Galaxy: abundances – Galaxy: disc – Galaxy: evolution – Galaxy: formation – Galaxy: halo – Galaxy: kinematics and dynamics.

1 INTRODUCTION

As successive generations of stars are formed from the gaseous material that is chemically enriched by earlier generations of stars, the most chemically pristine stars provide a unique window into the oldest components of the Milky Way (hereafter MW; Freeman & Bland-Hawthorn 2002; Karlsson, Bromm & Bland-Hawthorn 2013), dating back to times when our Galaxy was still assembling. It is expected that low-metallicity stars, whose iron abundance is lower than a few thousands of the Sun's ([Fe/H] ≤ -2.5 dex) were formed at most 2–3 Gyr after the big bang (El-Badry et al. 2018). Since the then proto-Milky Way was still in the process of chaotically accreting, it is commonly expected that the most metal-poor stars mainly trace the spheroid of the MW. These stars should either be present in the deepest parts of the Galactic potential well if they were accreted at the formation of the MW, or further out in the stellar halo if they formed in dwarf galaxies that were accreted on to the MW at later times (White & Springel 2000; Brook et al. 2007; Gao et al. 2010; Salvadori et al. 2010; Tumlinson 2010; Ishiyama et al. 2016; Starkenburg et al. 2017a; El-Badry et al. 2018; Griffen et al. 2018). The inescapable conclusion of this scenario is that low-metallicity stars should follow pressure-supported orbits and that they should be most prominent in

★ E-mail: federico.sestito@astro.unistra.fr

the central regions of the MW or in its diffuse stellar halo. Moreover, these stars should be absent from the MW disc because stars formed very early in the proto-disc were scattered into the halo during the dynamic assembly process. The disc's successive generation of stars are expected to have formed from already enriched gas.

Recent work by Sestito et al. (2019) has shown the orbital properties of the 42 most pristine stars known in the ultra metal-poor regime (UMP, [Fe/H] < -4.0 dex) using the photometric and kinematic data of the Data Release 2 (DR2) of the *Gaia* satellite (Gaia Collaboration 2016, 2018). Surprisingly, roughly a quarter of those stars orbit close or within the plane of the MW disc. Whilst tentative, the small size of the sample and inhomogeneous data collection methods in this literature sample prevent a firm conclusion on the orbital parameters of the most metal-poor stars.[1] In this work, we revisit these interesting findings with our more unbiased and very large sample of stars, putting the work on the orbital properties of very metal-poor stars (VMP) on a much firmer statistical footing.

In general, the rarity of low-metallicity stars among the bulk of the more metal-rich MW stars has long limited the mapping of their distribution. However, recent, systematic, and large spectroscopic surveys (Allende Prieto et al. 2014; Li, Tan & Zhao 2018) and specific photometric surveys (Starkenburg et al. 2017b; Wolf et al. 2018) yield increasingly large spectroscopic samples of such stars. In this work, we use two well-known samples of VMP stars ([Fe/H] ≤ -2.0 dex) in order to study the orbital properties of the most metal-poor stars focussing on the disc region. The Large sky Area Multi-Object fiber Spectroscopic Telescope (LAMOST; Cui et al. 2012) probes all Galactic latitudes and does not select stars to specifically focus on the regions of the MW halo at high Galactic latitudes. We complement this sample with VMPs from the spectroscopic follow-up campaign of the Pristine survey (Youakim et al. 2017; Aguado et al. 2019). The resulting combined sample of 1027 stars below [Fe/H] ≤ -2.5 dex from LAMOST (667 stars) and the Pristine survey (360 stars), with the synergy of the exquisite *Gaia* DR2 data, provides a unique data set to study the orbital properties of VMP stars, as it is both large and selected purely on metallicity without any pre-selection on kinematics.

We describe the data samples in Section 2, before turning to our results in Section 3 and implications for our understanding of the formation and (early) evolution of the MW galaxy in Section 4.

2 DATA

2.1 The Pristine sample

The Pristine survey is a photometric survey that aims at efficiently finding the most metal-poor stars (Starkenburg et al. 2017b). It is based on narrow-band Ca H&K photometry obtained with the MegaCam wide-field camera on the 3.6 m Canada–France–Hawaii Telescope (CFHT). In this work, we use the VMP stars ([Fe/H] < -2.0 dex) photometrically selected from the narrow-band photometry and then spectroscopically followed-up with the IDS spectrograph at the 2.54 m Isaac Newton Telescope (INT) at Observatorio del Roque de los Muchachos. This sample and its analysis are described in Aguado et al. (2019). The sample is composed of 576 genuine VMP stars, of which 360 with [Fe/H] ≤ -2.5 dex, 66 are EMP stars ([Fe/H] < -3.0 dex), and none are UMP. The sample spans a magnitude range of $11.5 \leq G \leq 16.5$ mag. We derive the radial velocities of these VMP stars using the `fxcor` task (a Fourier cross-correlation method) from IRAF (Tody 1986, 1993) with an appropriate synthetic template spectra for each star matching within 250 K in temperature, 0.5 dex in [Fe/H], and 1 dex in carbon abundance. A sub-sample of these stars ($\sim$20) was subsequently followed-up with high-resolution at CFHT with Echelle SpectroPolarimetric Device for the Observation of Stars (ESPaDOnS; Donati 2003; Donati et al. 2006; Venn et al. 2019) and at Gemini with GRACES (Gemini Remote Access to CFHT ESPaDOnS Spectrograph, Chene et al. 2014, Kielty et al. in preparation). From this overlapping sub-sample, we assessed the magnitude of any systematic errors on the radial velocities and found a systematic offset of $\mu_{\rm off} = 4.9 \pm 3.4\,{\rm km\,s^{-1}}$ in the mean and a standard deviation between both sets of measurements of $\sigma_{\rm sys} = 10.5 \pm 4.1\,{\rm km\,s^{-1}}$. Together with the individual measurement uncertainties on the radial velocity derivation, these uncertainties are propagated in the derivation of the orbital parameters and their uncertainties.

2.2 The LAMOST sample

Li et al. (2018) presented new metallicities for a set of 10 000 VMP star candidates from LAMOST DR3 (Cui et al. 2012; Zhao et al. 2012), spanning a magnitude range of $9.0 \leq G \leq 18.0$ mag. We note there is a spurious effect in this VMP sample, and $\sim$ 5 per cent of stars accumulate at the lower effective temperature limit of the employed model grid. Our own analysis shows these are spurious metal-rich stars that contaminate the sample. Therefore, we clean this sample accordingly, resulting a final selection of 4838 VMP stars, of which 667 have [Fe/H] ≤ -2.5 dex, 41 are EMP, and none are UMP. For a detailed description of the cleaning steps see Appendix A and Fig. A1–A2 therein (available online).

2.3 Determination of distances and orbital properties

We infer distances for stars from both surveys following the Bayesian method described in Sestito et al. (2019). In short, we derive a probability distribution function (PDF) of the heliocentric distance to a star by combining its photometric (*G*, *BP*, and *RP* magnitudes) and astrometric data (parallax ϖ) from *Gaia* DR2 with a sensible MW stellar density prior and MESA/MIST isochrone models (Choi et al. 2016; Dotter 2016) for stars of old age (>11 Gyr). This Bayesian method to infer distance does not require a reliable parallax measurement, but does take into account all parallax information available (even negative values). As discussed in Sestito et al. (2019), the choice of the MW density prior affects the results only when the distance PDF has two solutions (i.e. both a dwarf and a giant solution) changing the probabilities associated with the two solutions, but not the values of the distances. After finding that a significant fraction of UMP stars reside close to the MW plane (Sestito et al. 2019), we therefore chose an MW density prior composed by the sum of a halo component described by a power law, and a disc component described by an exponential distribution law. Subsequently, we derive the orbits using the `galpy` code[2] (Bovy 2015) providing it with the inferred distances, the radial velocities, and the exquisite *Gaia* DR2 proper motions, together with the uncertainties and systematics. For the gravitational

[1] Very similar kinematical signatures are found by Di Matteo et al. (2019) for a small sample of 54 stars peaked around [Fe/H] $= -3$ dex.

[2] The PYTHON package for Galactic dynamics Galpy by Bovy (2015) can be found at http://github.com/jobovy/galpy.

potential, we use a more massive halo (1.2×10^{12} M$_\odot$) compared to *MWPotential14* from GALPY (0.8×10^{12} M$_\odot$) in agreement with the value from Bland-Hawthorn & Gerhard (2016), an exponentially cut-off bulge, a Miyamoto Nagai Potential disc, and a Navarro, Frenk & White (1997) dark matter halo. The Local Standard of Rest circular velocity, Sun peculiar motion, and distance from the Galactic Centre are the same as assumed by Sestito et al. (2019; see also references therein). The table with the inferred orbital parameters is provided as online material.

The possible bias towards giants or dwarfs due to observational constraints in the Pristine and LAMOST survey is expected to not produce a bias in the prograde versus retrograde population, and therefore in our main result.

3 RESULTS

We derive the orbital properties of our sample, focussing on the following quantities: the azimuthal action J_ϕ, which is equivalent to the z-axis component of a star's angular momentum; the vertical action, J_z, which conveys information about how far a star's orbit brings it away from the Galactic plane; and the eccentricity of the orbit, ϵ. The top panel of Fig. 1 shows the distribution of stars in the J_z–J_ϕ plane, colour coded by the eccentricity of a given star's orbit, for our full sample with [Fe/H] ≤ -2.5 dex, complemented by the 42 UMP stars ([Fe/H] ≤ -4.0 dex) from Sestito et al. (2019). We see a clear population of stars that remain close to the MW plane (very small J_z), although not all of these stars are on perfectly circular orbits. More importantly, the sample exhibits a strong asymmetry between prograde ($J_\phi > 0$) and retrograde ($J_\phi < 0$) stars, where prograde stars dominate with an angular momentum up to the Sun's value.

The bottom panels of Fig. 1 show the same action plot divided into four metallicity bins, respectively the UMP stars populated only by the 42 stars from Sestito et al. (2019), the $-4.0 <$ [Fe/H] ≤ -3.0 dex bin, the $-3.0 <$ [Fe/H] ≤ -2.5 dex regime, and, to be complete, the bin with $-2.5 <$ [Fe/H] ≤ -2.0 dex, where the signature of a disc population is well studied (Beers et al. 2002; Reddy & Lambert 2008; Ruchti et al. 2011; Li & Zhao 2017). We note that Carollo et al. (2019) already report signatures of the disc population to a metallicity of [Fe/H] $\gtrsim -3.0$ dex. Separating the sample in these metallicity bins makes it evident that the prograde stars that remain close to the MW plane inhabit all [Fe/H] ranges. Focussing on the region of the diagram that is populated by disc-like stars, with $0.5 < J_\phi/J_{\phi\odot} < 1.2$ and $J_z/J_{z\odot} < 0.125 \times 10^4$, we assess the significance of the asymmetry through a direct comparison with the retrograde stars of similar properties ($-1.2 < J_\phi/J_{\phi\odot} < -0.5$ and same $J_z/J_{z\odot}$ range). Assuming Poisson statistics, we find that the prograde region is 5.0σ overdense compared to its retrograde counterpart for the [Fe/H] ≤ -2.5 dex regime, or 1.9σ overdense for the [Fe/H] < -3.0 dex. For these two regimes, the overdensity of disc-like stars in the prograde box remains similar and the lower significance in the lower metallicity bin is driven by the smaller numbers. When adopting a two-dimensional Kolmogorov–Smirnov test (Peacock 1983; Fasano & Franceschini 1987) we find that we can discard the hypothesis that these different samples, from the ultra metal-poor regime to the VMP regime (VMP, [Fe/H] < -2.0 dex), are drawn from a different parent distribution. There is no bias we can think of in the two surveys at the base of our sample that would preferentially overselect prograde over retrograde stars. In particular, no selection on the motion of stars was applied to either of the two surveys that were designed before the *Gaia* DR2 data were available. We have tested that our results are similar whether we restrict ourselves only to these stars with reliable parallax information (see Appendix B and B1 therein, available online).

In order to quantify the underlying fraction of disc-like stars in the low-metallicity regime, we look at the population of low-metallicity stars located within 3 kpc of the MW plane. From this selection, we can identify two samples, (i) the disc-like stars with the maximum excursion from the MW plane $|Z_{\rm max}| \leq 3$ kpc in a prograde motion ($J_\phi/J_{\phi\odot} > 0$) and (ii) the halo-like stars that are either passing through the disc or that are close to the plane in a retrograde motion. Of the population of stars with [Fe/H] ≤ -2.5 dex and with $|Z| <$ 3 kpc, ~ 31 per cent belongs to the disc-like sample (i). Although a disc-like component of the MW has been confirmed down to [Fe/H] $= -2.3$ dex (e.g. Li & Zhao 2017), and more recently, Carollo et al. (2019) reported a signature to [Fe/H] $\gtrsim -3.0$ dex, this is the first time we find strong and statistically significance evidence of such a population for the lowest metallicity stars ([Fe/H] ≤ -2.5 dex). We conclude that an important fraction of the 1069 low-metallicity stars from our sample plus the Sestito et al. (2019) UMP sample in fact reside in the MW disc.

4 DISCUSSION AND CONCLUSION

Understanding the origins of these stars has major implication for the assembly and evolution of the MW. Simulated disc galaxies for which maps are published of low-metallicity stars with [Fe/H] ≤ -2.5 dex in either density (Tumlinson 2010; Starkenburg et al. 2017a) or kinematical space (El-Badry et al. 2018) do not commonly bear this feature. This is either due to the MW having a unique formation path or to these simulations not including all the necessary physical ingredients to produce such a feature. We propose three different scenarios to explain this observational feature: minor mergers, the assembly of the proto-MW, and the *in situ* formation of this component of the disc at early times. We note that these scenarios are not mutually exclusive.

First, it is possible that the observed low-metallicity stars were brought into the MW plane through the minor merging of small satellites that deposited their stars in the environment of the disc, that was already in place, after their orbit decayed via dynamical friction (Scannapieco et al. 2011) and the eccentricity enhanced by tidal interaction (Peñarrubia, Kroupa & Boily 2002; Abadi et al. 2003). Results from cosmological simulations have shown that the disrupted merged satellite can be aligned with the disc (Gómez et al. 2017). Some simulations (Scannapieco et al. 2011; Karademir et al. 2019) show that up to 5–20 per cent of the disc stars have not formed *in situ* but were brought in from now-merged satellites.

Alternatively, or additionally, low-metallicity disc-like stars could have been born in and brought in from the building blocks that formed the disc of the proto-MW at early times. In such a scenario at high redshift, we can expect that whatever gas-rich blocks formed the backbone of the MW disc also brought its own stars, including low-metallicity ones.

Cosmological simulations (El-Badry et al. 2018) show that, of all stars currently within 10 kpc from the MW centre and formed before redshift $z = 5$, less than half were already in the main progenitor at $z = 5$. Over half of these extremely old stars would make their way into the main Galaxy in later merging events and find themselves at $z = 5$ inside different galaxies that are up to 250 kpc away from the main progenitor centre. These two mergers scenarios can naturally funnel stars in the inner regions of the main galaxy, to be observed on orbits close to the disc plane today.

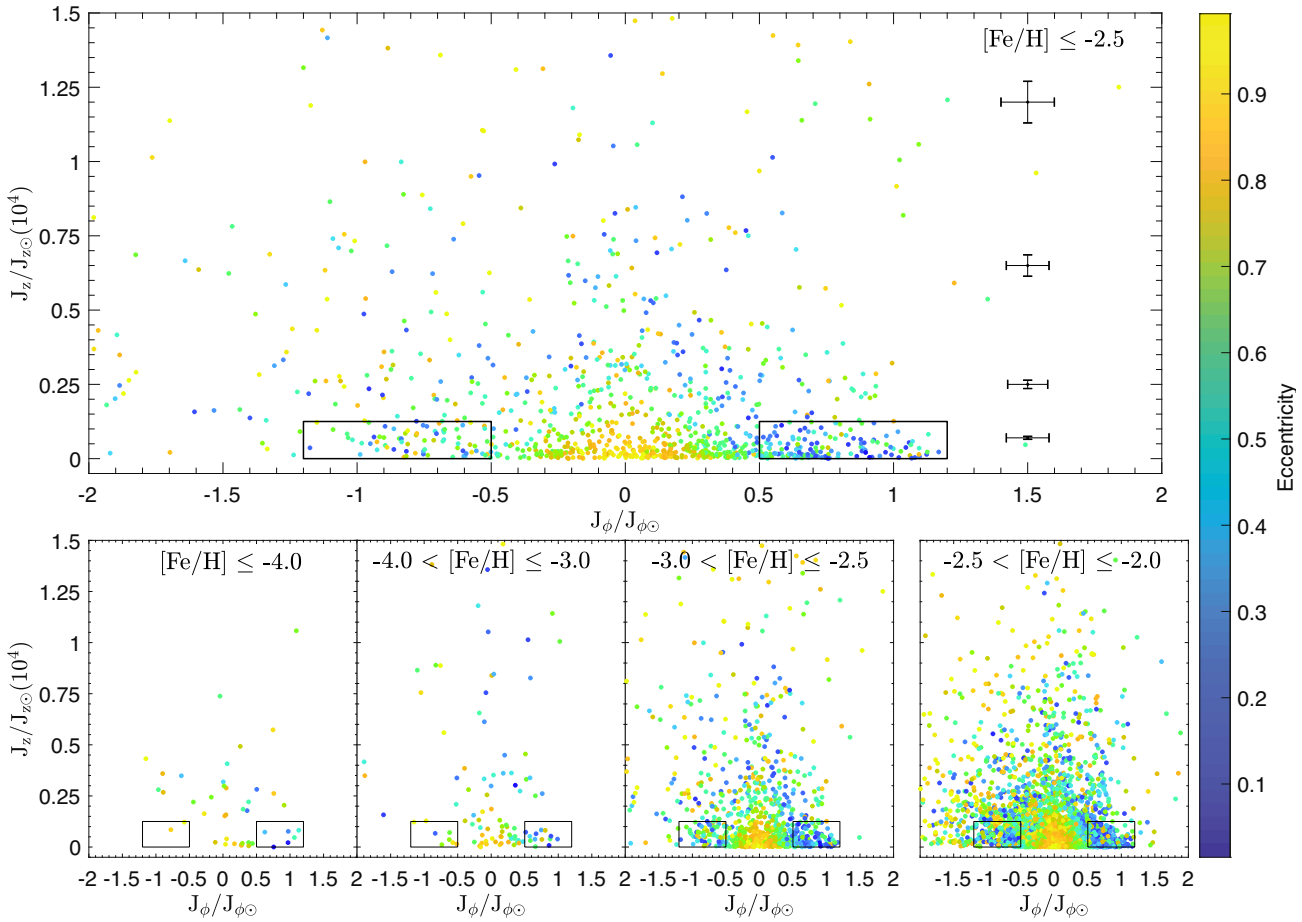

Figure 1. Vertical action versus azimuthal action component colour coded by eccentricity. Top panel: our sample + Sestito et al. (2019) stars with [Fe/H] ≤ -2.5 dex are shown. Typical uncertainties for four bins in $J_z/J_{z\odot}$ are shown on the right. Bottom panels from left to right: our sample + Sestito et al. (2019) stars with [Fe/H] ≤ -2.0 dex is divided into four metallicity ranges. The action quantities are scaled by the solar values (i.e. $J_{\phi\odot} = 2009.92\,\mathrm{km\,s^{-1}}$ kpc, $J_{z\odot} = 0.35\,\mathrm{km\,s^{-1}}$ kpc). We detect an asymmetry and the predominance for the prograde motion (right box in each panel) versus the retrograde planar stars (left box in each panel) with 5.0σ level for stars with [Fe/H] ≤ -2.5 dex.

For the third scenario, the *in situ* formation at early times, it is necessary to invoke the presence of pockets of pristine gas in the MW's gaseous disc during the first few Gyr of the Universe. This scenario implies that the MW plane was already defined within 2–3 Gyr and that this plane has not significantly changed over the last 10–11 Gyr. Consequently, the MW cannot have suffered dramatic merger and/or accretion events that would have likely tilted its disc and/or randomized the orbit of the EMP stars (Scannapieco et al. 2009). Such a scenario would be in line with the commonly accepted idea that the MW has undergone a very quiet accretion history (Wyse 2001; Stewart et al. 2008). However, two main questions arise from this scenario. The first question is whether it is possible to form stars so completely devoid of metals in a relatively well-mixed interstellar medium disc in this stage of evolution of the MW. The second question relates to the mechanisms that can push the stars from the small radius of their birth place to the solar neighbourhood and from the likely circular orbit of their birth to the range of observed eccentricities of the orbits we observe them on today. Radial migration is very efficient in pushing outwards the orbital radius whilst conserving their circularity (Sellwood & Binney 2002; Haywood 2008; Schönrich & Binney 2009). For stars with higher orbital eccentricity at birth (Brook et al. 2004; Bird et al. 2013; Minchev, Chiappini & Martig 2013), radial migration is less efficient (Martig, Minchev & Flynn 2014) but non-linear interactions between the MW bar and its spiral arms (Minchev & Famaey 2010) or perturbations from infalling minor mergers (Quillen et al. 2009) could redistribute their angular momentum.

One important implication of this work is that the disc region should not be avoided in the search and study for the most metal-poor stars, contrary to what has frequently been done in the past. Moreover, cosmological zoom-in simulations should be revisited to reproduce this population of low-metallicity stars with disc-like kinematics. Whatever the true origin of these prominent disc-like low-metallicity stars, they undoubtedly open a window on the assembly of the oldest parts of the MW and pose a challenge to our understanding of very early Galaxy formation in general.

ACKNOWLEDGEMENTS

We want to thank Ivan Minchev for the insightful comments and suggestions on radial migration. We are also grateful to the anonymous referee for their comments and support. This work has made use of data from the European Space Agency (ESA) mission

Gaia (https://www.cosmos.esa.int/gaia), processed by the *Gaia* Data Processing and Analysis Consortium (DPAC, https://www.cosmos.esa.int/web/gaia/dpac/consortium). Funding for the DPAC has been provided by national institutions, in particular the institutions participating in the *Gaia* Multilateral Agreement. We gratefully acknowledge the Isaac Newton Group (ING) staff, in particular the support astronomers and staff at the INT/WHT for their expertise and help with observations. We also thank the Canada-France-Hawaii Telescope staff for performing the observations in queue mode. Based on observations obtained with MegaPrime/MegaCam, a joint project of CFHT and CEA/DAPNIA, at the Canada-France-Hawaii Telescope (CFHT) which is operated by the National Research Council (NRC) of Canada, the Institut National des Science de l'Univers of the Centre National de la Recherche Scientifique (CNRS) of France, and the University of Hawaii. The observations at the Canada-France-Hawaii Telescope were performed with care and respect from the summit of Maunakea which is a significant cultural and historic site. Guoshoujing Telescope (the Large sky Area Multi-Object fiber Spectroscopic Telescope, LAMOST) is a National Major Scientific Project built by the Chinese Academy of Sciences. FS thanks the Initiative dExcellence IdEx from the University of Strasbourg and the Programme Doctoral International PDI for funding his Ph.D. This work has been published under the framework of the IdEx Unistra and benefits from a funding from the state managed by the French National Research Agency as part of the investments for the future program. FS, NFM, and RAI gratefully acknowledge support from the French National Research Agency (ANR) funded project 'Pristine' (ANR-18-CE31-0017) along with funding from CNRS/INSU through the Programme National Galaxies et Cosmologie and through the CNRS grant PICS07708. ES, AA, and KY gratefully acknowledge funding by the Emmy Noether program from the Deutsche Forschungsgemeinschaft (DFG). The authors acknowledge the support and funding of the International Space Science Institute (ISSI) for the international team 'Pristine'. FS acknowledges the support and funding of the Erasmus + programme of the European Union.

REFERENCES

Abadi M. G., Navarro J. F., Steinmetz M., Eke V. R., 2003, ApJ, 597, 21
Aguado D. S. et al., 2019, MNRAS, 490, 2241
Allende Prieto C. et al., 2014, A&A, 568, A7
Beers T. C., Drilling J. S., Rossi S., Chiba M., Rhee J., Führmeister B., Norris J. E., von Hippel T., 2002, AJ, 124, 931
Bird J. C., Kazantzidis S., Weinberg D. H., Guedes J., Callegari S., Mayer L., Madau P., 2013, ApJ, 773, 43
Bland-Hawthorn J., Gerhard O., 2016, ARA&A, 54, 529
Bovy J., 2015, ApJS, 216, 29
Brook C. B., Kawata D., Gibson B. K., Freeman K. C., 2004, ApJ, 612, 894
Brook C. B., Kawata D., Scannapieco E., Martel H., Gibson B. K., 2007, ApJ, 661, 10
Carollo D. et al., 2019, ApJ, 887, 22
Chene A.-N. et al., 2014, in Navarro R., Cunningham C. R., Barto A. A., eds, Proc. SPIE Conf. Ser., Vol. 9151, Advances in Optical and Mechanical Technologies for Telescopes and Instrumentation. SPIE, Bellingham, p. 915147
Choi J., Dotter A., Conroy C., Cantiello M., Paxton B., Johnson B. D., 2016, ApJ, 823, 102
Cui X.-Q. et al., 2012, Res. Astron. Astrophys., 12, 1197
Di Matteo P., Spite M., Haywood M., Bonifacio P., Gómez A., Spite F., Caffau E., 2019, preprint (arXiv:1910.13769)
Donati J. F., 2003, ASP Conf. Ser. Vol. 307, ESPaDOnS: An Echelle SpectroPolarimetric Device for the Observation of Stars at CFHT. Astron. Soc. Pac., San Francisco, p. 41
Donati J. F., Catala C., Landstreet J. D., Petit P., 2006, ASP Conf. Ser. Vol. 358, ESPaDOnS: The New Generation Stellar Spectro-Polarimeter. Performances and First Results, Astron. Soc. Pac., San Francisco, p. 362
Dotter A., 2016, ApJS, 222, 8
El-Badry K. et al., 2018, MNRAS, 480, 652
Fasano G., Franceschini A., 1987, MNRAS, 225, 155
Freeman K., Bland-Hawthorn J., 2002, ARA&A, 40, 487
Gaia Collaboration, 2016, A&A, 595, A1
Gaia Collaboration, 2018, A&A, 616, A1
Gao L., Theuns T., Frenk C. S., Jenkins A., Helly J. C., Navarro J., Springel V., White S. D. M., 2010, MNRAS, 403, 1283
Gómez F. A. et al., 2017, MNRAS, 472, 3722
Griffen B. F., Dooley G. A., Ji A. P., O'Shea B. W., Gómez F. A., Frebel A., 2018, MNRAS, 474, 443
Haywood M., 2008, MNRAS, 388, 1175
Ishiyama T., Sudo K., Yokoi S., Hasegawa K., Tominaga N., Susa H., 2016, ApJ, 826, 9
Karademir G. S., Remus R.-S., Burkert A., Dolag K., Hoffmann T. L., Moster B. P., Steinwandel U. P., Zhang J., 2019, MNRAS, 487, 318
Karlsson T., Bromm V., Bland-Hawthorn J., 2013, Rev. Mod. Phys., 85, 809
Li C., Zhao G., 2017, ApJ, 850, 25
Li H., Tan K., Zhao G., 2018, ApJS, 238, 16
Martig M., Minchev I., Flynn C., 2014, MNRAS, 443, 2452
Minchev I., Famaey B., 2010, ApJ, 722, 112
Minchev I., Chiappini C., Martig M., 2013, A&A, 558, A9
Navarro J. F., Frenk C. S., White S. D. M., 1997, ApJ, 490, 493
Peacock J. A., 1983, MNRAS, 202, 615
Peñarrubia J., Kroupa P., Boily C. M., 2002, MNRAS, 333, 779
Quillen A. C., Minchev I., Bland-Hawthorn J., Haywood M., 2009, MNRAS, 397, 1599
Reddy B. E., Lambert D. L., 2008, MNRAS, 391, 95
Ruchti G. R. et al., 2011, ApJ, 737, 9
Salvadori S., Ferrara A., Schneider R., Scannapieco E., Kawata D., 2010, MNRAS, 401, L5
Scannapieco C., White S. D. M., Springel V., Tissera P. B., 2009, MNRAS, 396, 696
Scannapieco C., White S. D. M., Springel V., Tissera P. B., 2011, MNRAS, 417, 154
Schönrich R., Binney J., 2009, MNRAS, 396, 203
Sellwood J. A., Binney J. J., 2002, MNRAS, 336, 785
Sestito F. et al., 2019, MNRAS, 484, 2166
Starkenburg E., Oman K. A., Navarro J. F., Crain R. A., Fattahi A., Frenk C. S., Sawala T., Schaye J., 2017a, MNRAS, 465, 2212
Starkenburg E. et al., 2017b, MNRAS, 471, 2587
Stewart K. R., Bullock J. S., Wechsler R. H., Maller A. H., Zentner A. R., 2008, ApJ, 683, 597
Tody D., 1986, in Crawford D. L., ed., Proc. SPIE Conf. Ser. Vol. 627, Instrumentation in Astronomy VI. SPIE, Bellingham, p. 733
Tody D., 1993, in Hanisch R. J., Brissenden R. J. V., Barnes J., eds, ASP Conf. Ser. Vol. 52, Astronomical Data Analysis Software and Systems II. Astron. Soc. Pac., San Francisco, p. 173
Tumlinson J., 2010, ApJ, 708, 1398
Venn K. et al., 2020, MNRAS, 492, 3241
White S. D. M., Springel V., 2000, in Weiss A., Abel T. G., Hill V., eds, The First Stars. p. 327, Springer-Verlag, Berlin Heidelberg
Wolf C. et al., 2018, PASA, 35, e010
Wyse R. F. G., 2001, in Funes J. G., Corsini E. M., eds, ASP Conf. Ser. Vol. 230, Galaxy Disks and Disk Galaxies. Astron. Soc. Pac., San Francisco, p. 71
Youakim K. et al., 2017, MNRAS, 472, 2963
Zhao G., Zhao Y.-H., Chu Y.-Q., Jing Y.-P., Deng L.-C., 2012, Res. Astron. Astrophys., 12, 723

SUPPORTING INFORMATION

Supplementary data are available at *MNRASL* online.

Appendix A. The cleaning of the Lamost sample.
Appendix B. Results with good parallax data.

Please note: Oxford University Press is not responsible for the content or functionality of any supporting materials supplied by the authors. Any queries (other than missing material) should be directed to the corresponding author for the article.

[1]*Université de Strasbourg, CNRS, Observatoire astronomique de Strasbourg, UMR 7550, F-67000 Strasbourg, France*
[2]*Leibniz Institute for Astrophysics Potsdam (AIP), An der Sternwarte 16, D-14482 Potsdam, Germany*
[3]*Max-Planck-Institut für Astronomie, Königstuhl 17, D-69117 Heidelberg, Germany*
[4]*Institute of Physics, Laboratoire d'astrophysique, École Polytechnique Fédérale de Lausanne (EPFL), Observatoire, CH-1290 Versoix, Switzerland*
[5]*Department of Physics and Astronomy, University of Victoria, PO Box 3055, STN CSC, Victoria, BC V8W 3P6, Canada*
[6]*Institute of Astronomy, University of Cambridge, Madingley Road, Cambridge CB3 0HA, UK*
[7]*Department of Astronomy and Astrophysics, University of Toronto, Toronto, ON M5S 3H4, Canada*
[8]*Instituto de Astrofísica de Canarias, Vía Láctea, E-38205 La Laguna, Tenerife, Spain*
[9]*Departamento de Astrofísica, Universidad de La Laguna, E-38206 La Laguna, Tenerife, Spain*
[10]*Laboratoire Lagrange, Université de Nice Sophia-Antipolis, Observatoire de la Côte d'Azur, CNRS, Bd de l'Observatoire, CS 34229, F-06304 Nice cedex 4, France*
[11]*GEPI, Observatoire de Paris, Université PSL, CNRS, Place Jules Janssen, F-92190 Meudon, France*
[12]*The Oskar Klein Centre for Cosmoparticle Physics, Department of Physics, Stockholm University, AlbaNova, SE-10691 Stockholm, Sweden*
[13]*UK Astronomy Technology Centre, Royal Observatory, Blackford Hill, Edinburgh EH9 3HJ, UK*
[14]*NRC Herzberg Astronomy and Astrophysics, 5071 West Saanich Road, Victoria, BC V9E 2E7, Canada*
[15]*Kapteyn Astronomical Institute, University of Groningen, Landleven 12, NL-9747AD Groningen, the Netherlands*
[16]*Isaac Newton Group of Telescopes, E-38700 Santa Cruz de La Palma, Spain*
[17]*SUPA, School of Physics and Astronomy, University of St. Andrews, North Haugh, Fife KY16 9SS, UK*

This paper has been typeset from a TEX/LATEX file prepared by the author.

APPENDIX A: THE CLEANING OF THE LAMOST SAMPLE

There is a spurious effect in the VMP sample by Li et al. (2018), where the $\sim$ 5% of stars accumulate at the lower effective temperature limit of the employed model grid. Most of these stars are located in the direction of the Galactic plane, a region with high extinction (see Figure A1). A cross-match with the public LAMOST DR3 (Zhao et al. 2012; Cui et al. 2012) catalogue shows that many of these stars actually have high metallicities ([Fe/H] > -1 dex), see Figure A2. An independent check of the metallicity of these stars with ULySS (University of Lyon Spectroscopic analysis Software, Koleva et al. 2009; Arentsen et al. 2019) confirms their metal-rich nature. We therefore clean the sample from contaminants ([Fe/H] > -2 dex) by selecting stars with $T_{\rm eff,Li} > 4500$ K and removing stars with $[{\rm Fe/H}]_{Public} > -1.5$ dex. We additionally require the signal-to-noise ratio in the blue part of the spectrum to be higher than 20 when $[{\rm Fe/H}]_{Li} < -3.0$ dex to ensure a robust determination of metallicity at these low metallicities. We note there is also an offset of $\sim$ 0.5 dex between the [Fe/H] from Li et al. (2018) and the [Fe/H] from public LAMOST DR3 (Zhao et al. 2012; Cui et al. 2012), but since the $[{\rm Fe/H}]_{Li}$ values have been checked to be on the same scale as high-resolution observations (Li et al. 2018), we have adopted these values. Our final selection results in a total of 4838 VMP stars, of which 667 with [Fe/H] ≤ -2.5 dex, 41 are EMP and none are UMP.

APPENDIX B: RESULTS WITH GOOD PARALLAX DATA

Here in Figure B1, we show the same action plot as Figure 1 but for the stars with $\sigma_{\varpi}/\varpi < 10\%$ and $\varpi > 0$ mas. It illustrates that our results are similar whether we restrict ourselves only to these stars with the most reliable parallax information.

REFERENCES

Arentsen A., et al., 2019, A&A, 627, A138
Cui X.-Q., et al., 2012, Research in Astronomy and Astrophysics, 12, 1197
Koleva M., Prugniel P., Bouchard A., Wu Y., 2009, A&A, 501, 1269
Li H., Tan K., Zhao G., 2018, ApJS, 238, 16
Sestito F., et al., 2019, MNRAS, 484, 2166
Zhao G., Zhao Y.-H., Chu Y.-Q., Jing Y.-P., Deng L.-C., 2012, Research in Astronomy and Astrophysics, 12, 723

This paper has been typeset from a TEX/LATEX file prepared by the author.

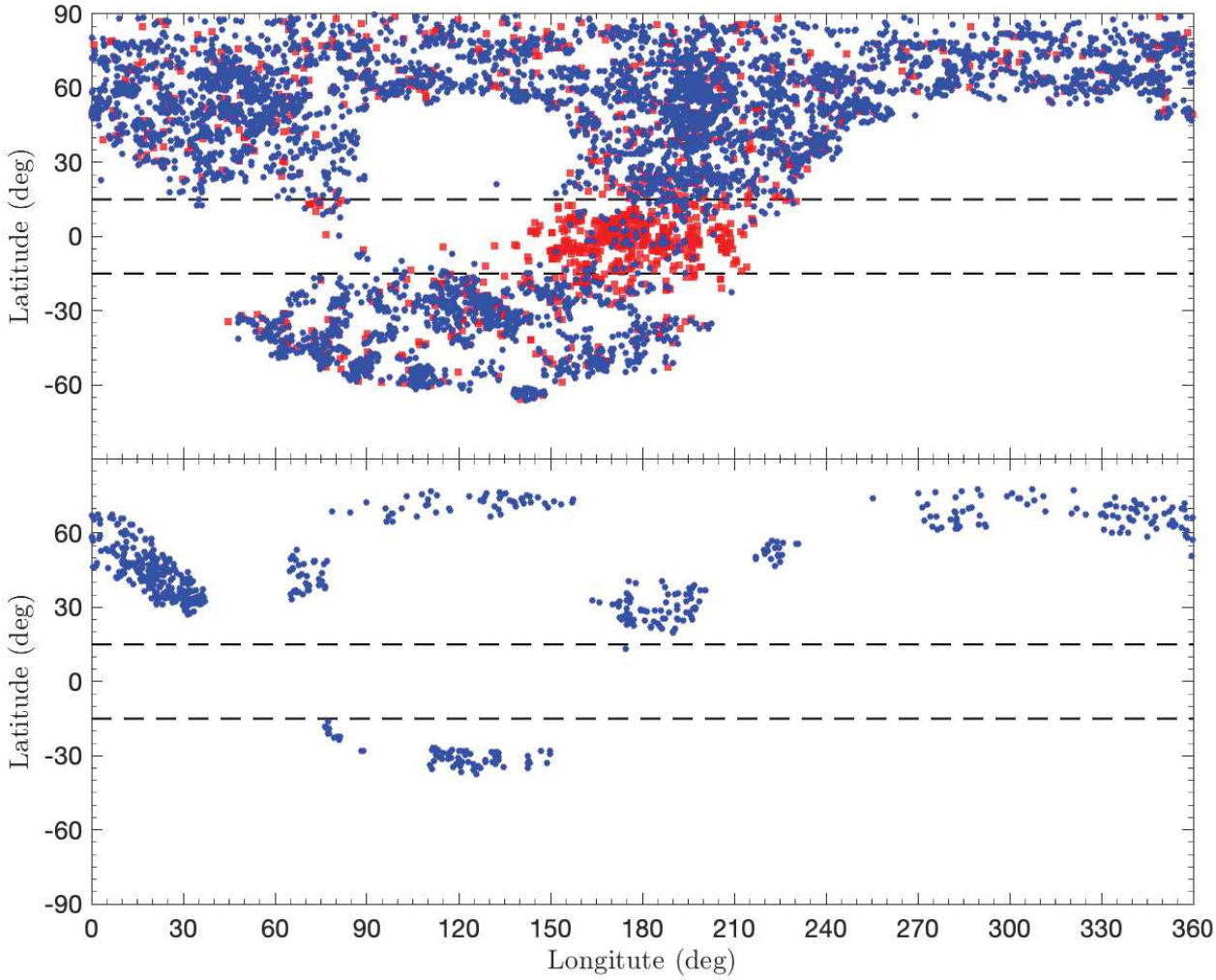

Figure A1. Galactic longitude and latitude distribution of the Very Metal-poor Stars from Pristine and LAMOST DR3 sample. Top panel: the cleaned LAMOST (blue circles) and the removed stars from Li et al. (2018) (red squares). The removed stars in this sample correspond to the stars with $T_{eff,Li} < 4500$ K, $[Fe/H]_{Public} > -1.5$ dex and signal to noise ratio in g band < 20 when $[Fe/H]_{Li} < -3.0$ dex. The cleaned sample consists of 4838 VMP stars (see Appendix A for the selection of the sample). Bottom panel: the 576 VMP stars from the Pristine sample observed at INT. The Galactic plane is shown by dashed lines within latitude ±15 deg.

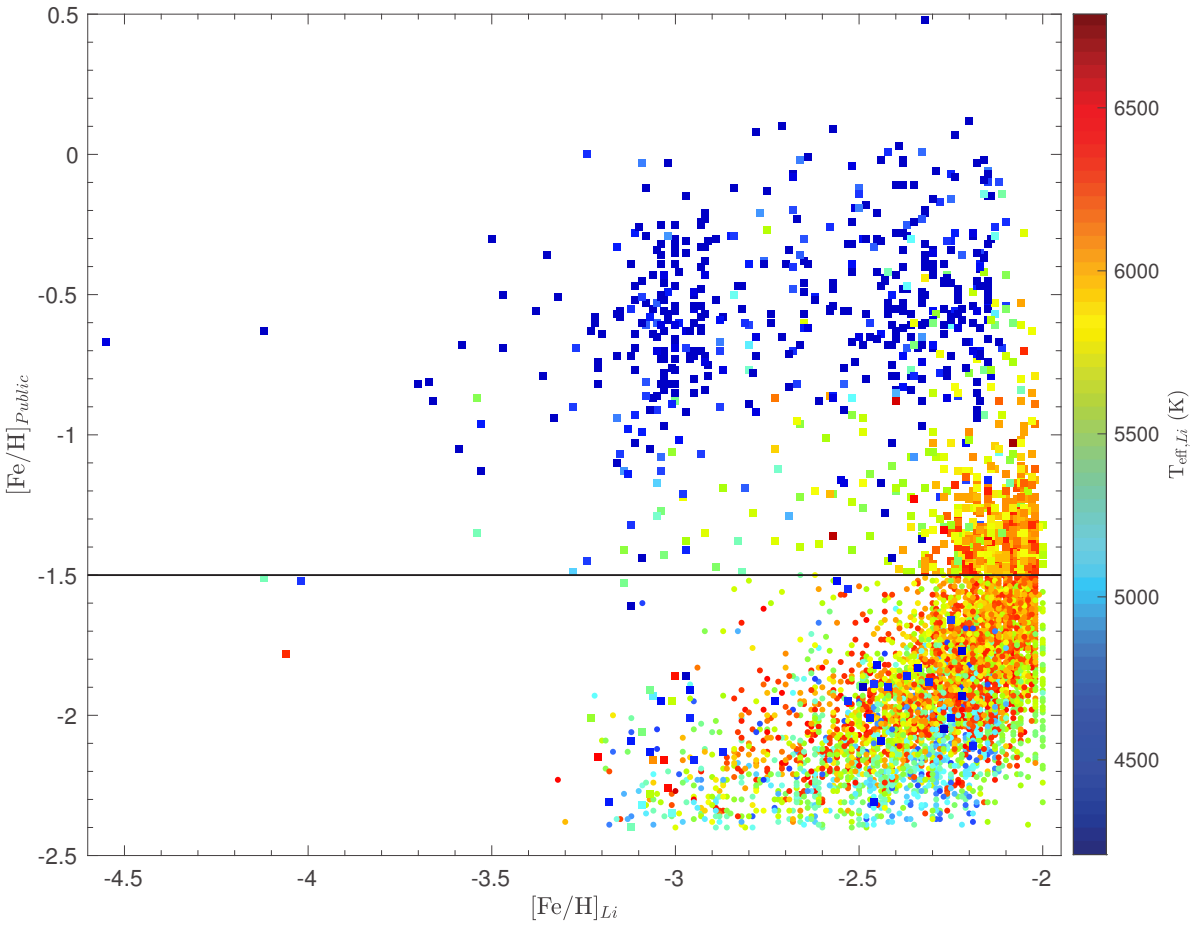

Figure A2. Estimates of [Fe/H] from Public LAMOST vs. Li et al. (2018) colour-coded by effective temperature from Li et al. (2018). The cleaned sample (circle) is obtained by selecting stars with $T_{\rm eff,Li} > 4500$ K, $[Fe/H]_{Public} < -1.5$ dex and signal to noise ratio in the g band above 20 when $[Fe/H]_{Li} < -3.0$ dex. The removed stars are marked with a square (see Appendix A for the selection of the sample). Note that the measurement of the $[Fe/H]_{Public}$ saturates at the lower limit of [Fe/H] = −2.4 dex (i.e., a star with a true [Fe/H] = −3.0 dex has a public LAMOST [Fe/H] = −2.4 dex).

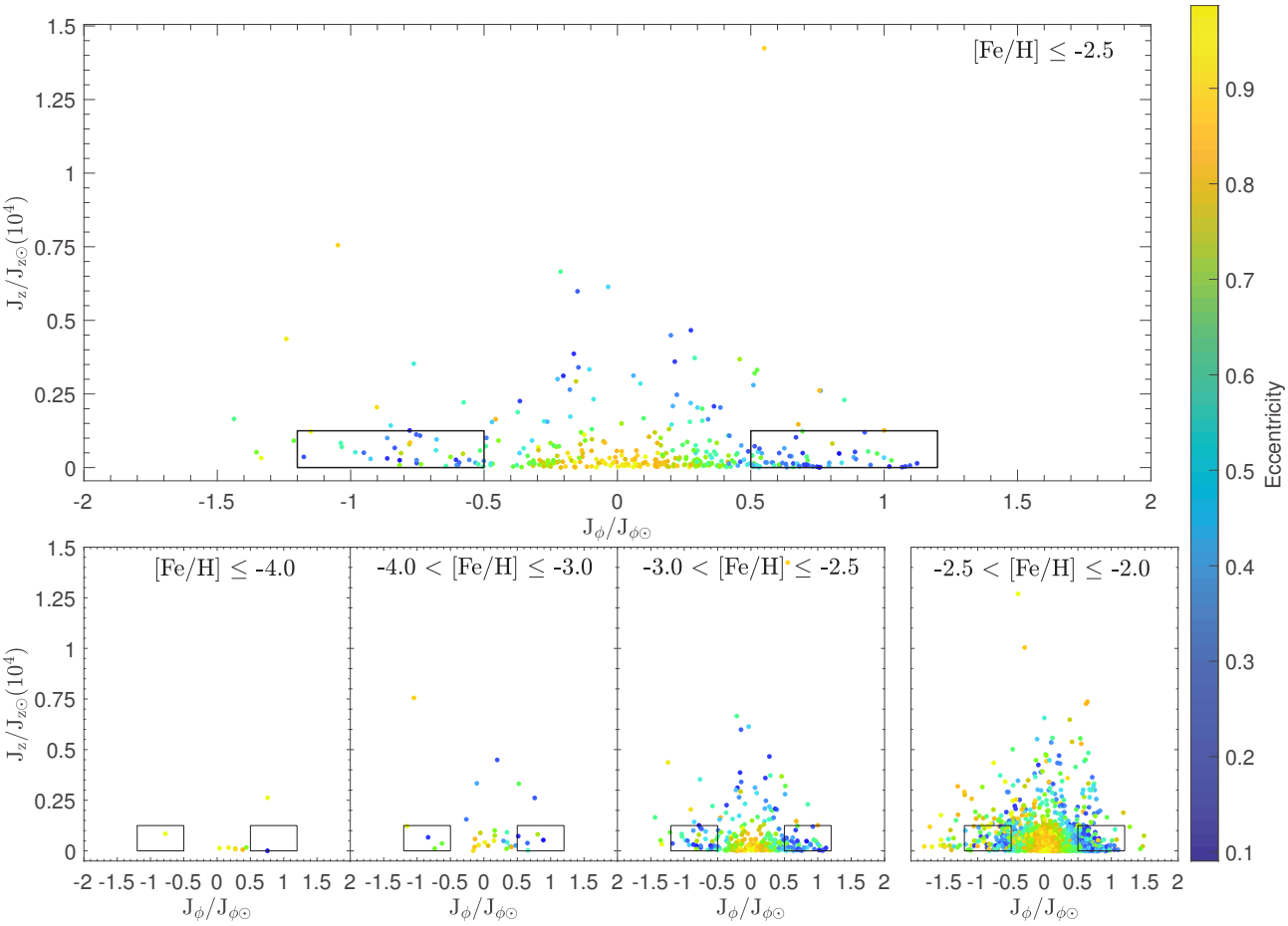

Figure B1. Vertical action vs. azimuthal action component colour-coded by eccentricity for the stars with $\sigma_{\varpi}/\varpi < 0.1$. Top panel: our sample+Sestito et al. (2019) stars with [Fe/H] ≤ -2.5 dex are shown. Bottom panels from left to right: our sample+Sestito et al. (2019) stars with [Fe/H] ≤ -2.0 dex is divided into 4 metallicity ranges. The sample of stars with $\sigma_{\varpi}/\varpi < 0.1$ is the $\sim$ 45% of the total.

CHAPTER

4 Exploring the origin of low-metallicity stars in Milky Way-like galaxies with the NIHAO-UHD simulations

Previous theoretical studies (e.g., Starkenburg et al., 2017b; El-Badry et al., 2018) pointed out that the oldest and most metal-poor stars should be distributed in a pressure-supported fashion. Therefore, the spheroid of the Milky Way, such as the inner and outer halo, together with dwarf satellites, are ideal places to hunt for these objects. These theoretical studies and, consequently, observational surveys did not focus on the distribution of the most metal-poor stars in the disk region, since this latter region is crowded by younger and metal-rich stars. However, if the most metal-poor stars are following a non-rotating spheroid, an equal number of prograde and retrograde stars should be expected to be found in the disk region, since it intersects the halo. Surprisingly, Sestito et al. (2019, 2020a) found that a non-negligible fraction of the most metal-poor stars does not venture far out from the plane of the Milky Way, and significantly prefer the prograde motion. Observations possess various limits that impede to discern the true nature and origin of this planar population. With simulations, it is possible to remove some of the limitations and to better investigate the origin of the most metal-poor stars, as I do in this Chapter.

Buck et al. (2020) proposed a new suite of high-resolution cosmological simulations, called NIHAO-UHD. The simulated galaxies, 6 in total, can resolve substructures with a resolution of ~ 200 pc, and therefore ideal to analyse the distribution of the most metal-poor stars in the disk. This Chapter 4 contains the work submitted to Monthly Notices of the Royal Astronomical Society, Sestito et al. (2020b). Figure 4.1 (Buck et al., 2020) displays the 6 simulated galaxies in the NIHAO-UHD suite, showing the dark matter, the gas, the stellar density distribution, and a rendering in RGB colours. These galaxies are spanning a wide range in mass, from 6.96×10^{11} $M_{\odot}$ to 2.79×10^{12} $M_{\odot}$ as regards the dark matter content, and different formation and accretion history. For this work, I select the 5 simulated galaxies with a spiral shape as the Milky Way.

In Sestito et al. (2020b), a test on the distribution of the most metal-poor star particles has been performed, showing that these simulations posses a slowly-rotating spheroid. The rotation of the spheroid, although slower than the disk, will induce some star particles to be confined to the plane and rotate with prograde motion. Although this effect, the prograde planar star particles are following the distribution of the more metal-rich thick disk, and exceeding the population of the slowly-rotating spheroid. As in the observations, the prograde planars are favored respect the retrograde counterpart. Then, since these data are coming

from simulation, it is possible to trace back the position of the star particles to investigate their origin and check when they have been accreted in the main galaxy. The majority of the retrograde planar very metal-poor star particles has been brought in during the early assembly of the galaxies. This is because, at that epoch, the proto-galaxy was still under formation, allowing to the mergers of size similar to the proto-galaxy to be deposited in the proto-disk with retrograde motion. Once the galaxy and the disk were well formed and shaped, later retrograde mergers, if they occur, can only be disrupted and dispersed in the halo, excluding the possibility to be deposited in the plane. Therefore, the retrograde planar stars can be used as an excellent tracer of the early assembly. On the other hand, the prograde planar population is sampling both the early and later accretion history, since later mergers can feel for a prolonged time the tidal forces of the disk and settle in the disk with co-planar motion. Also in this work, one of the simulated galaxy show a kinematical feature similar to the Milky Way, pointing out that our Galaxy might have experienced a chaotic early assembly.

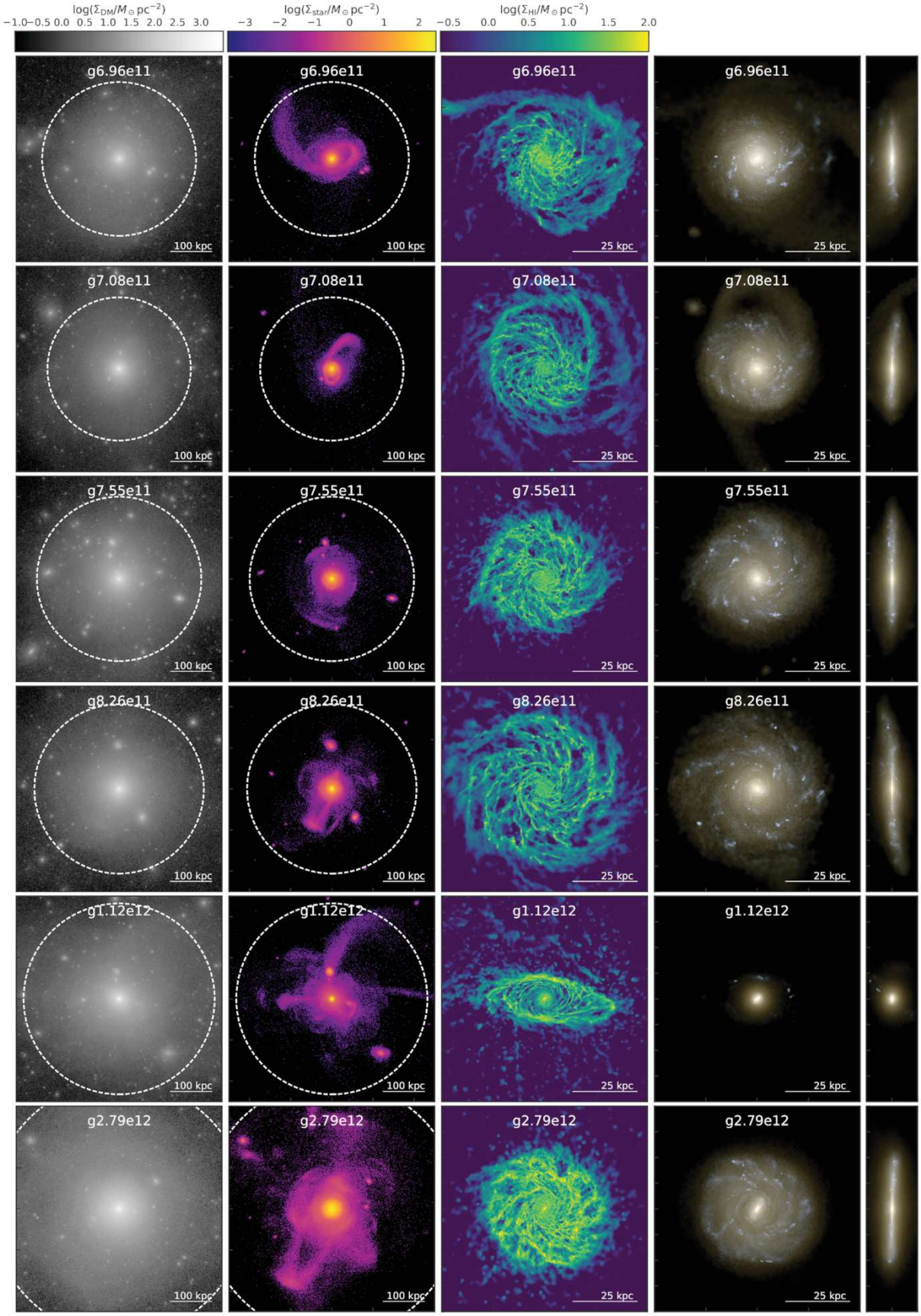

Figure 4.1: NIHAO-UHD simulations from Buck et al. (2020). The dark matter, the gas, the stellar density distribution, and a rendering in RGB colours is shown from left to right. For this work, only the simulated galaxies with spiral shape have been taken into account.

MNRAS **000**, 1–13 (2020) Preprint 28 September 2020 Compiled using MNRAS LATEX style file v3.0

Exploring the origin of low-metallicity stars in Milky Way-like galaxies with the NIHAO-UHD simulations

Federico Sestito,[1]★ Tobias Buck,[2] Else Starkenburg,[2,3] Nicolas F. Martin,[1,4] Julio F. Navarro,[5] Kim A. Venn,[5] Aura Obreja,[6] Pascale Jablonka,[7,8] & Andrea V. Macciò[9,10,4]

[1] *Université de Strasbourg, CNRS, Observatoire astronomique de Strasbourg, UMR 7550, F-67000, France*
[2] *Leibniz Institute for Astrophysics Potsdam (AIP), An der Sternwarte 16, D-14482 Potsdam, Germany*
[3] *Kapteyn Astronomical Institute, University of Groningen, Landleven 12, 9747 AD Groningen, The Netherlands*
[4] *Max-Planck-Institut für Astronomie, Königstuhl 17, D-69117, Heidelberg, Germany*
[5] *Department of Physics and Astronomy, University of Victoria, PO Box 3055, STN CSC, Victoria BC V8W 3P6, Canada*
[6] *Universitäts-Sternwarte München, Scheinerstraße 1, D-81679 München, Germany*
[7] *Institute of Physics, Laboratoire d'astrophysique, École Polytechnique Fédérale de Lausanne (EPFL), Observatoire, CH-1290 Versoix, Switzerland*
[8] *GEPI, Observatoire de Paris, Université PSL, CNRS, Place Jules Janssen, F-92190 Meudon, France*
[9] *New York University Abu Dhabi, PO Box 129188, Saadiyat Island, Abu Dhabi, United Arab Emirates*
[10] *Center for Astro, Particle and Planetary Physics (CAP^3), New York University Abu Dhabi*

Accepted XXX. Received YYY; in original form ZZZ

ABSTRACT

The kinematics of the most metal-poor stars provide a window into the early formation and accretion history of the Milky Way. Here, we use 5 high-resolution cosmological zoom-in simulations ($\sim 5\times10^6$ star particles) of Milky Way-like galaxies taken from the NIHAO-UHD project, to investigate the origin of low-metallicity stars ([Fe/H] ≤ -2.5). The simulations show a prominent population of low-metallicity stars confined to the disk plane, as recently discovered in the Milky Way. The ubiquity of this finding suggests that the Milky Way is not unique in this respect. Independently of the accretion history, we find that $\gtrsim$ 90 per cent of the retrograde stars in this population are brought in during the initial build-up of the galaxies during the first few Gyrs after the Big Bang. Our results therefore highlight the great potential of the retrograde population as a tracer of the early build-up of the Milky Way. The prograde planar population, on the other hand, is accreted during the later assembly phase and samples the full galactic accretion history. In case of a quiet accretion history, this prograde population is mainly brought in during the first half of cosmic evolution ($t \lesssim 7$ Gyr), while, in the case of an on-going active accretion history, later mergers on prograde orbits are also able to contribute to this population. Finally, we note that the Milky Way shows a rather large population of eccentric, very metal-poor planar stars. This is a feature not seen in most of our simulations, with the exception of one simulation with an exceptionally active early building phase.

Key words: Galaxy: formation – Galaxy: kinematics and dynamics – Galaxy: evolution – Galaxy: disc – Galaxy: halo – Galaxy: abundances

1 INTRODUCTION

The most chemically pristine stars, which likely include some of the oldest stars in the Milky Way, are relics of the early formation and assembly of our Galaxy (e.g., Freeman & Bland-Hawthorn 2002; Karlsson et al. 2013). For example, El-Badry et al. (2018) show that, in the cosmological FIRE simulations, stars with [Fe/H] ≤ -2.5 formed at most 3 Gyr after the Big Bang. During that time, the Milky Way (hereafter MW) was still assembling. The expectation is therefore that these stars are distributed in a pressure-supported fashion, i.e., the spheroid; either located in the deepest part of the MW potential well if accreted at early times, or spread out to the outer reaches of the stellar halo if born in accreted dwarf galaxies (White & Springel 2000; Brook et al. 2007; Gao et al. 2010; Salvadori et al. 2010; Tumlinson 2010; Ishiyama et al. 2016; Starkenburg et al. 2017a; El-Badry et al. 2018; Griffen et al. 2018). Some orbits from the pressure-supported distribution might be kinematically coincident with the disk, although for this distribution the

★ E-mail: federico.sestito@astro.unistra.fr

number of prograde and retrograde stars would be expected to be similar. Alternatively, some of the low-metallicity stars can cross the disk with halo kinematics.

However, thanks to the exquisite data from the Gaia mission (Gaia Collaboration et al. 2016, 2018, hereafter Gaia DR2), Sestito et al. (2019, hereafter S19) found that a surprisingly large fraction (11 stars, $\sim$ 26 per cent) of the 42 ultra metal-poor stars (UMP, [Fe/H] ≤ -4.0) known at the time do not venture far out from the MW plane ($|z_{\rm max}| \lesssim 3$ kpc) and have orbits that span a wide range of eccentricities, from quasi-circular to rosette-shaped orbits. Out of the 11 stars confined to the disk, 10 UMPs have prograde motion, sharing the same sense of rotation as the MW disk, while one UMP has a retrograde orbit. Sestito et al. (2020, hereafter S20) extended the kinematical analysis to the very metal-poor regime (VMP, [Fe/H] ≤ -2.0) using 583 VMP stars from the Pristine survey (Starkenburg et al. 2017b; Aguado et al. 2019) and 4838 VMPs from a cleaned sample of the LAMOST survey (Cui et al. 2012; Li et al. 2018). S20 found that a similarly large fraction of the sample kinematically inhabits the plane of the MW, from the VMP to the UMP regime. They also show that the prograde motion is largely favoured compared to retrograde orbits. S19 and S20 propose three non mutually-exclusive scenarios to explain the observations. The first scenario is that this population was brought in by accretion events where satellites deposited their stars into the disk by dynamical friction and tidal interactions. In the second scenario, these stars were born in the gas-rich building blocks that formed the backbone of the proto-MW disk. Finally, in the last scenario, these stars formed in situ after the interstellar medium (hereafter ISM) of the disk settled, presumably from still chemically pristine pockets of gas.

Di Matteo et al. (2020) analysed a sample of 54 VMP from the ESO Large Program "First Stars" finding very similar kinematical signatures to S19 and S20. They suggest that the MW thick disk extends to the UMP regime, down to [Fe/H] ~ -6.0 and that the population of this early disk shares the same kinematical properties because it experienced the same violent heating process, i.e., the accretion of the Gaia-Enceladus satellite (Belokurov et al. 2018; Helmi et al. 2018). Venn et al. (2020), analysing the high-resolution spectra of 28 bright low-metallicity stars ([Fe/H] ≤ -2.5), also found that a subsample is confined to the MW disk, sharing a wide range of eccentricities, with the majority in prograde motion.

Because it is clear that the retrograde stars cannot be easily explained in in-situ star formation scenarios, their presence — even if they represent a minority population — places important constraints on the early formation history of the galaxy. We note that, precisely for this reason, some of the important big merger events of the MW have been picked up from their retrograde signatures, such as, e.g., Gaia-Enceladus-Sausage (Belokurov et al. 2018; Helmi et al. 2018) and Sequoia (Myeong et al. 2019; Barbá et al. 2019) and Thamnos (Koppelman et al. 2019). Additional information on the kinematical components of the MW seems to be encoded in the chemical abundances of disk stars (e.g. Navarro et al. 2011). In fact, already prior to the Gaia mission such chemical peculiarities in combination with distinct kinematical features were used to identify debris stars associated with the merger event that brought ωCen into the MW, which is most likely coincident with Gaia-Enceladus-Sausage (Meza et al. 2005; Navarro et al. 2011). Helmi et al. (2018) and Koppelman et al. (2019) demonstrate a different [α/Fe] between some accreted halo populations and the presumed in-situ population at a metallicity between ~ -2.5 and ~ -0.5. Monty et al. (2020) find that the stars dynamically associated with Gaia-Enceladus-Sausage and Sequoia have a different [α/Fe] ratio than those of the Galactic halo. For the most metal-poor stars, which are the subject of this work, the measurement of [α/Fe] and other elements tracers of the star formation (i.e., neutron-capture elements) becomes challenging. Moreover, we know from previous works that differences between systems in [α/Fe] become less pronounced at very low metallicity (e.g., Venn et al. 2004; Jablonka et al. 2015; Frebel & Norris 2015), while the chemistry of neutron-capture elements, such as Yttrium and Europium, has shown to be a promising accretion diagnostic (Recio-Blanco et al. 2020).

In this paper, we use the MW-like simulated galaxies present in the NIHAO-UHD[1] cosmological zoom-in simulations (Buck et al. 2020) to investigate how the oldest and most metal-poor stars assemble into the main galaxy. In particular, we focus on those stars that are confined to the disk at the present day. This suite is composed of 5 high-resolution spiral galaxies with $\sim$ 200 pc resolution and are, therefore, ideal to disentangle the different structures of the galaxies (Buck et al. 2018, 2019c). The resolution allows us to analyse the spatial and kinematical distribution of the most metal-poor stars, focusing on the inner region of the galaxies.

Section 2 describes the main properties of the NIHAO-UHD simulations, while, in Section 3, the analysis and discussions on the origin of the most metal-poor stars are reported. In Section 3.1, we investigate the rotation of the VMP spheroids in the simulations. The comparison between the observations and the simulated galaxies is shown in Section 3.2. Section 3.3 describes the formation of the simulated galaxy and their accretion history. The age-metallicity relation is shown in Section 3.4, and the origin of the most metal-poor star particles is investigated in Section 3.5. The conclusions drawn from this analysis are presented in Section 4.

2 NIHAO-UHD COSMOLOGICAL ZOOM-IN SIMULATIONS

The NIHAO-UHD simulations (Buck et al. 2020) are a set of cosmological simulations with a higher mass resolution and the same initial conditions and feedback parameters as the Numerical Investigation of a Hundred Astronomical Objects simulation suite (Wang et al. 2015, NIHAO). All the NIHAO galaxies adopt cosmological parameters from the Planck Collaboration et al. (2014) cosmology. Therefore $\Omega_m = 0.3175$, $\Omega_\Lambda = 0.6825$, $\Omega_b = 0.0049$, $\mathrm{H}_0 = 67.1\,\mathrm{km\,s^{-1}\,Mpc^{-1}}$, and $\sigma_8 = 0.8344$. The corresponding age of the Universe is $t_{\rm Universe} = 13.83$ Gyr. Each simulation consists of 64 snapshots equally spaced in time with a separation of $\sim$ 215 Myr. The final snapshots of the NIHAO-UHD simulations at $z = 0$ are publicly available at `https://tinyurl.com/nihao-uhd` which redirects to `https://www2.mpia-hd.mpg.de/~buck/#sim_data`.

The NIHAO-UHD set is composed of six zoom-in simulations `g2.79e12`, `g1.12e12`, `g8.26e11`, `g7.55e11`, `g7.08e11` and `g6.96e11`, for which the name corresponds to the halo mass of the dark matter (hereafter DM) only run. The stellar mass of the galaxies varies between $1.5 \times 10^{10}\,\mathrm{M}_\odot$ to $15.9 \times 10^{10}\,\mathrm{M}_\odot$. Each galaxy is resolved with more than 10^7 particles (gas+star+DM) inside the virial radius while the stellar disks contain $\gtrsim 3 \times 10^6$ star particles. The mass of DM particles spans a range between 1–5$\times 10^5\,\mathrm{M}_\odot$, gas particles between 2–9$\times 10^4\,\mathrm{M}_\odot$, and star particles between 0.7–3.0$\times 10^4\,\mathrm{M}_\odot$. The simulations have been evolved with a modified version of the smoothed particle hydrodynamics (SPH)

[1] UHD stands for Ultra High Definition.

code GASOLINE2 (Wadsley et al. 2017) with star formation and feedback prescriptions as presented in Stinson et al. (2006) and Stinson et al. (2013). The adopted feedback prescriptions result in a spatial distribution of young stellar particles in good agreement with the spatial distribution of young stellar clusters in local galaxies (Buck et al. 2019b). Chemical enrichment from core-collapse supernova (SNII) and supernova Ia (SNIa) is implemented following Raiteri et al. (1996) using rescaled SNII yields from Woosley & Weaver (1995) and SNIa yields from Thielemann et al. (1986). No Population III pre-enrichment is assumed and iron and oxygen have been tracked individually.

The NIHAO-UHD galaxies are characterised by a thin disk of scale length ~ 5 kpc and a total scale height of $\lesssim 1$ kpc that matches key observational properties of the MW, such as the age-velocity dispersion relation of the stellar disk (Buck et al. 2020) or the chemical bimodality of disk stars (Buck 2020). Furthermore, one of the simulated galaxies, g2.79e12, has recently been used to study intrinsic variations in the length of the galactic stellar bar (Hilmi et al. 2020). The galaxy g1.12e12 has a spheroidal shape and is therefore not considered in this study. Table 1 reports the main properties of the NIHAO-UHD simulated galaxies used in our study. For a more detailed discussion of the galaxy properties we refer the reader to Buck et al. (2019a) and Buck et al. (2020).

For the simulated galaxy g8.26e11, several early snapshots have not been saved, complicating the tracking of the position of the star particles across time. Consequently, we exclude this galaxy when we are analysing snapshots at other times than the present day.

3 RESULTS AND DISCUSSIONS

The NIHAO-UHD simulations provide a set of physical quantities for each particle, such as their position at redshift 0, (x, y, z), their Galactocentric velocity, (v_x, v_y, v_z), their age, their metallicity, [Fe/H], and their birth position, $(x_{\rm birth}, y_{\rm birth}, z_{\rm birth})$. In all our analysis, we align the z-axis of the coordinate system with the total angular momentum of the disk stars such that the galactic disk lies within the $x-y$ plane. Using the AGAMA package (Vasiliev 2019) we further derive the orbital action momentum vector, (J_ϕ, J_r, J_z) for each star particle corresponding to its orbit in the fixed gravitational potential of the simulated galaxy at redshift $z = 0$.

In order to compare the population of planar stars in the simulations with that of the MW observations, as in Section 3.2, we need to mimic the window function of the photometric and spectroscopic surveys used to discover them. A deep analysis and reconstruction of the selection functions is not the aim of this work; however, we mimic the window function of the observed VMP stars in S20, which also contain the stars analysed in S19, by selecting metal-poor star particles that are close to the location of stars in the observed sample. As also discussed in S19 and S20, the multiple selection functions imparted by different metal-poor surveys do not insert a bias against or in favour of the prograde/retrograde population. Moreover, mimicking the spatial window function is not expected to result in mimicking the kinematical features of the MW. This is also not desired, as we want to study these properties and not set them a priori. Because of the arbitrary choice of the orientation of the Galactocentric cartesian axes in the simulations, for each observed VMP star at position $(x_{\rm obs}, y_{\rm obs}, z_{\rm obs})$, we first select all the VMP star particles that inhabit a torus with $R_{\rm torus} = (x^2_{\rm obs} + y^2_{\rm obs})^{1/2}$, we set the width of the torus to 0.75 kpc, at the height $z = z_{\rm obs}$. Usually, multiple star particles populate this volume, in which case the final choice of particle is done selecting the one inside the torus that minimises the difference in metallicity $|[{\rm Fe/H}]_{\rm obs} - [{\rm Fe/H}]_{\rm particle}|$. Since the observed samples in S19 and S20 exclude the bulge and the bar of the MW (see Appendix in S20), the orientation of the bar in the simulated galaxies does not influence this attempt in reproducing the window function. The mimicking of the window function only applies to Section 3.2, where we compare more directly with observations, while for Sections 3.3, 3.4, and 3.5 all VMP stars ($[{\rm Fe/H}] \leq -2.0$) that are taken into account have a distance from the centre of the galaxy $R \leq 40$ kpc and exclude the bulge region ($R \geq 4$ kpc) .

3.1 Do the low-metallicity stars confined to the disk follow a spheroidal distribution?

The most metal-poor stars mainly inhabit the spheroid of the MW. However, as recently pointed out by observations (e.g., Sestito et al. 2019, 2020; Di Matteo et al. 2020), a non-negligible fraction of these stars is kinematically confined to the disk, favouring the prograde motion. Naturally, even if all stars were to be distributed in a non-rotating or a slowly-rotating spheroid, one would expect a subset of them to overlap with the disk at any time, and an even smaller subset to be confined to the disk kinematically. Benefitting from the completeness of our simulations — in which, in contrast to observations, we can assess the complete metal-poor population — it is insightful to quantify if the number of metal-poor stars kinematically confined to the disk exceeds the expectations from a spheroidal (rotating or non-rotating) distribution.

To this end, we perform the following exercise: we select the low-metallicity star particles ($[{\rm Fe/H}] \leq -2.5$) of the NIHAO-UHD simulations that are spatially in the stellar disk $|z| \leq 3$ kpc (i.e., close to the $x-y$ plane of the coordinate system), excluding the bulge region ($R \geq 4$ kpc). Their distribution in the rotational velocity v_ϕ vs. the perpendicular velocity $v_\perp = |v_z|$ space is shown in the top-left panel of Figure 1 and indicates that the spheroid has a slow prograde rotation in this simulation (g8.26e11). This signal is consistently present in the 5 simulations studied in this analysis. In the top-middle and top-right panels of Figure 1, the coordinate system is rotated around the x-axis, such that the stellar disk moves out of the $x-y$ plane and onto an angle of 45° and 90° respectively. In this new frame of reference, we apply the same selection of star particles. As the rotational angle increase, the mean rotational velocity of the spheroid decreases, illustrating that the rotation is indeed strongest in the $x-y$ plane. This rotation will lead to star particles being dragged towards the disk and co-rotate with it, although with smaller rotational velocity than the disk (see Figure 7 from Buck et al. 2020, for the rotation curve of these simulated galaxies).

In the second row of panels in Figure 1, we correct the rotational velocity by the mean rotation of the population and we measure the number of prograde and retrograde star particles as a function of the perpendicular velocity. These two populations are selected on their corrected rotational velocity, in the range $50 \leq v_\phi \leq 250\,{\rm km\,s^{-1}}$ for the prograde star particles and in the same range with opposite signs for the retrograde star particles. In case of a spheroidal distribution around the mean rotation, the fraction of prograde and retrograde orbits should be equal and constant regardless of whether the chosen plane coincides with the galactic disk or is at an angle. We however see that at 0°, there is a predominance of prograde metal-poor stars confined to small perpendicular velocities (i.e., not venturing far from the disk plane). For planes rotated out of the disk (second and third panels in the middle row of Figure 1), the number of retrograde and prograde stars is similar and more weakly depends on the perpendicular velocity.

Table 1. Properties of the simulated galaxies in NIHAO-UHD (Buck et al. 2020). For each simulated galaxy, we report the masses of the single stellar, gas, and dark matter particles ($m_{\rm star}$, $m_{\rm gas}$, $m_{\rm DM}$), together with the total mass components (stellar $M_{\rm star}$, gas $M_{\rm gas}$, and dark matter $M_{\rm DM}$), the total mass at the virial radius $M_{\rm virial}$, the virial radius $R_{\rm virial}$, the galaxy's disk scale length R_d, its thick disk scale height $h_{z,\rm thick}$ at the solar circle as defined via double exponential fit to the vertical stellar density, the mass of the VMP star particles within 40 kpc from the galactic centre, and its percentage relative to the total stellar mass.

Galaxy	$m_{\rm star}$ (10^4 M$_\odot$)	$M_{\rm star}$ (10^{10} M$_\odot$)	$m_{\rm gas}$ (10^4 M$_\odot$)	$M_{\rm gas}$ (10^{10} M$_\odot$)	$m_{\rm DM}$ (10^5 M$_\odot$)	$M_{\rm DM}$ (10^{11} M$_\odot$)	$M_{\rm virial}$ (10^{12} M$_\odot$)	$R_{\rm virial}$ (kpc)	R_d (kpc)	$h_{z,\rm thick}$ (kpc)	$M_{\rm VMP}^{\rm 40\,kpc}$ (10^8 M$_\odot$)	P(VMP) (per cent)
g2.79e12	3.13	15.9	9.38	18.48	5.141	27.90	3.13	306	5.57	1.3	12.25	0.77
g8.26e11	1.32	3.40	3.96	6.09	2.168	8.26	0.91	206	5.12	1.4	1.39	0.41
g7.55e11	0.93	2.72	2.78	6.79	1.523	7.55	0.85	201	4.41	1.4	4.13	1.52
g7.08e11	0.68	2.00	2.03	3.74	1.110	7.08	0.55	174	3.90	1.0	4.19	2.10
g6.96e11	0.93	1.58	0.93	4.79	1.523	6.96	0.68	187	5.70	1.4	3.47	2.20

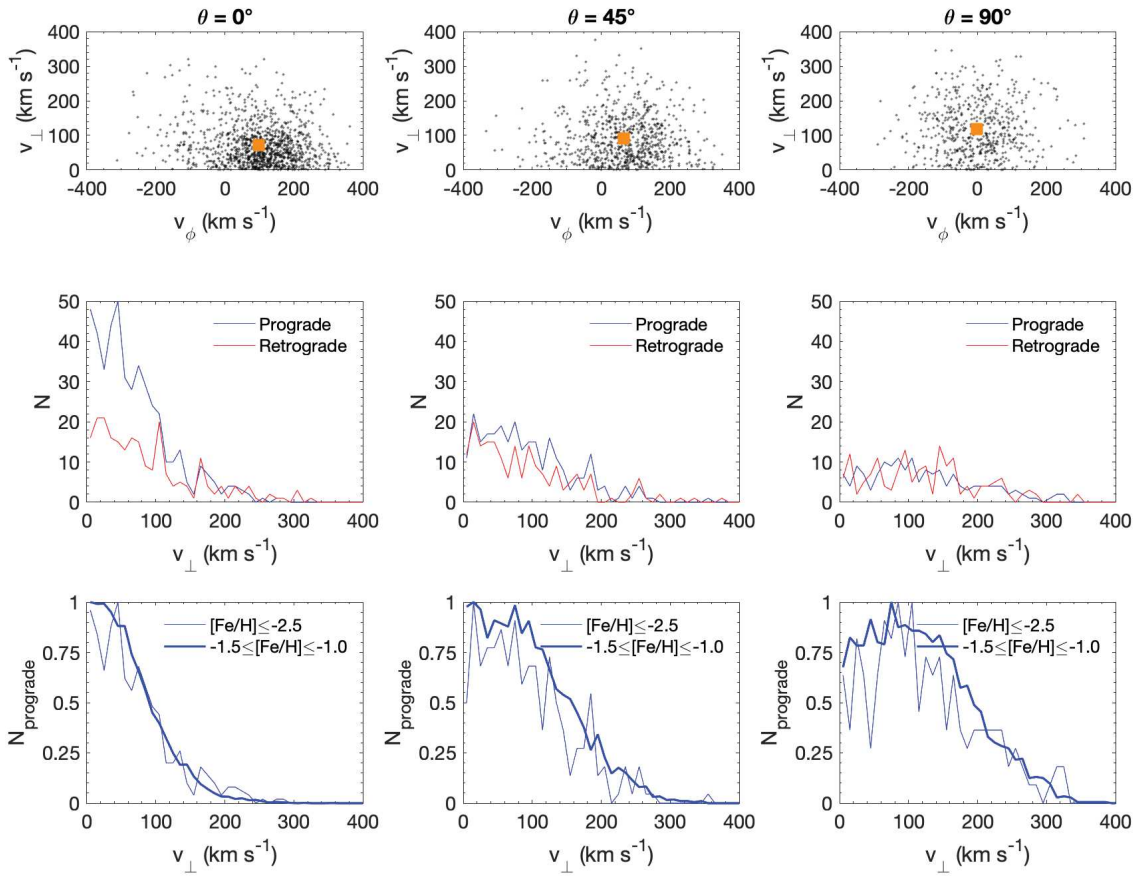

Figure 1. Test of a spheroidal distribution for simulation g8.26e11. Top panels: rotational velocity v_ϕ vs. perpendicular velocity $v_\perp = |v_z|$ for the star particles located in the disk ($|z| \leq 3$ kpc, $R \geq 4$ kpc) for three rotational angle (0, 45, 90°) and with [Fe/H] ≤ -2.5. The dark orange marker represents the centroid of the distribution in this space. Middle row panels: the number of prograde and retrograde stars as a function of the perpendicular velocity is shown in blue and red, respectively, and for the three rotational angles (0, 45, 90°). These distributions have been corrected by the mean rotation of the spheroid and selecting star particles with $50 \leq v_\phi \leq 250\,{\rm km\,s^{-1}}$ for the prograde and $-250 \leq v_\phi \leq -50\,{\rm km\,s^{-1}}$ for the retrograde. Bottom panels: the comparison between the number of the low-metallicity prograde ([Fe/H] ≤ -2.5, thinner line) and the more metal-rich prograde population ($-1.5 \leq$ [Fe/H] ≤ -1.0, thicker line) as a function of $v_\perp$.

The bottom panels in Figure 1 show a comparison between the low-metallicity prograde population and the more metal-rich prograde population that contains the thick disk ($-1.5 \leq$ [Fe/H] ≤ -1.0). These panels indicate that the low-metallicity population has a similar distribution to that of the more metal-rich star particles, especially for low perpendicular velocities and for small rotational angle. This means that the population of low-metallicity prograde planar star particles behaves similarly to the thick disk, and likely exceeds the expected number of star particles drawn from a simple, slowly-rotating spheroidal distribution.

The preference for prograde motion among the very metal-poor stars in the region of the simulated disk is qualitatively in agreement with the observations (e.g., Sestito et al. 2019, 2020). While the simulations host spheroids that are clearly rotating, the mean motion of the MW is still under debate. Recently, thanks to the LAMOST survey (Cui et al. 2012), Tian et al. (2019, 2020) found that the MW spheroid is slowly-rotating in a prograde motion ($v_\phi \sim 29\,\mathrm{km\,s^{-1}}$) and that the rotational velocity decreases at larger distances. Accreted structures in the MW halo, either retrograde and prograde, complicate the estimation of the rotational velocity of the spheroid and can lead to different results depending on the tracers used (Deason et al. 2011).

In conclusion we see that, despite the more significant rotation of the spheroid in these simulations compared to the MW, there is a clear signature on top of that of a very low-metallicity population that spatially and kinematically reside in a (thicker) disk, just as we see in the MW galaxy. Although none of these simulations exactly resemble the MW in its formation history, there is still a lot we can learn from studying the origin of this population that seems to be ubiquitous throughout the different simulated galaxies. In the next section, we will provide a more in-depth comparison between the types of orbits these star particles have in the simulations and the observations in the MW and we will pursue a deeper understanding of the origin of these populations with different orbital properties in Section 3.5.

3.2 NIHAO-UHD simulations vs. the observed low-metallicity MW disk

The action-angle variables (hereafter action vector, or action) are a useful tool to analyse dynamical populations. In particular, the action coordinates J_ϕ and J_z can reveal a population of the VMP stars in the disk of the MW, as highlighted by S19 and S20.

The simulated galaxies are not models of the MW. This means that the kinematic of star particles may differ systematically from the MW's because of differences in the mass and spatial distribution of the DM, stars, and gas. To minimise these effects, we scale the components of the actions by their norm. This is illustrated in Figure 2, where we compare the action space of `g2.79e12` (central panel) with that of the MW observations from S19 and S20 (right panel). The VMP star particles in the simulation are selected in the aforementioned way to mimic the observational window function. This plot shows the azimuthal action component $J_\phi/J_{\rm TOT}$ versus the difference between the vertical and the radial action component $(J_z - J_r)/J_{\rm TOT}$, where both axes are normalised by the norm of the action vector $J_{\rm TOT}$. In this action space, stars with planar orbits, prograde and retrograde, inhabit regions with high $|J_\phi/J_{\rm TOT}|$ and low $|(J_z - J_r)/J_{\rm TOT}|$, repsectively. Therefore, we define the star particles with prograde and planar orbits to be confined in the region with $J_\phi/J_{\rm TOT} \geq 0.75$ and the star particles with retrograde motion that are confined in the disk to have $J_\phi/J_{\rm TOT} \leq -0.75$. At the bottom of this space are found star particles that are confined to the disk but have very radial orbits (i.e., eccentric) orbits. Star particles with halo-like kinematics inhabit the remainder of the space.

Figure 3 shows the same action space as in Figure 2 but divided in metallicity bins for all the NIHAO-UHD simulated galaxies[2] as well as for the MW. From this plot, a population of planar stars is clearly recognisable in all simulations, from the VMP samples to the most metal-poor samples. The action space of Figures 2 and 3 show that this population of planar star particles in prograde motion spans a wide range of eccentricities (from low to high values of J_r, inhabiting the lower border of the action space). Moreover, as with the MW observations (Sestito et al. 2019, 2020), the simulated galaxies show some stars that are confined to the disk with retrograde orbits. Similarly to observations, the prograde sample is more populated than the retrograde one for all galaxies and at all metallicities. Table 2 reports the ratio between the prograde and retrograde planar populations, $N_{\rm pro}/N_{\rm retro}$, as a function of the metallicity and the simulated galaxy. In most simulated galaxies this ratio is > 5.50, except for `g7.55e11` which has a lower ratio of ~ 3.4. These numbers are significantly higher than what is observed for the MW (~ 1.7), as also reported in Table 2. This indicates that the simulations has an even larger population of prograde stars at low metallicity. As we already pointed out, each photometric and spectroscopic survey has its own selection function for hunting metal-poor stars; however, none of them should impart a bias for/against retrograde and prograde population. In Section 3.1, we report that the spheroids of the simulated galaxies are slowly rotating in a prograde motion while the MW spheroid is, at best, slowly rotating. This difference may impact the direct comparison of the $N_{\rm pro}/N_{\rm retro}$ ratios.

Careful comparison between the observed metal-poor MW and the NIHAO-UHD simulated galaxies in Figure 3 reveals another interesting feature in the lower hemicircle of the action space ($(J_z - J_r)/J_{\rm TOT} \lesssim 0$, $-1 \leq J_\phi/J_{\rm TOT} \leq 1$), outside of the black boxes. Looking at the MW panels, there is a pronounced overdensity of stars in this area, a feature that is not matched in most of the simulations except (qualitatively) in `g7.55e11`. In this locus of action space we find stars that have large motion in the radial component (large J_r), compared to a smaller motion on the vertical axis (J_z), therefore these are planar stars with high eccentricity, the majority of them on prograde orbits. A more in-depth discussion on the origin of this orbital structure is presented below.

3.3 Growth history of the galaxies

Tracking the haloes and their properties such as the mass (DM, gas, and stellar components) and position is helpful to better understand how the simulated galaxies grew. The total stellar mass within the virial radius of the main halo, the total stellar mass of accreted material (also measured within the virial radius of the dwarf galaxies prior to accretion), and the virial mass as a function of the cosmic time are shown in Figure 4. For each simulated galaxy, the time at which the simulation assembles 25 per cent (t_{25}), 50 per cent (t_{50}), and 90 per cent (t_{90}) of their present stellar mass is indicated by vertical lines. Simulations `g2.79e12`, `g7.55e11`, and `g7.08e11` reach t_{25} and t_{50} after ~ 4 Gyr and $5 - 6$ Gyr, respectively. On the other hand, for simulation `g6.96e11`, this happens at ~ 7 Gyr and ~ 9 Gyr. This can be explained by a more continuous accretion of mass in this latter simulation, for which the total accreted mass is

[2] For `g8.26e11`, the action-angle variables are safe to use as their calculation is independent of the snapshots at the early Universe.

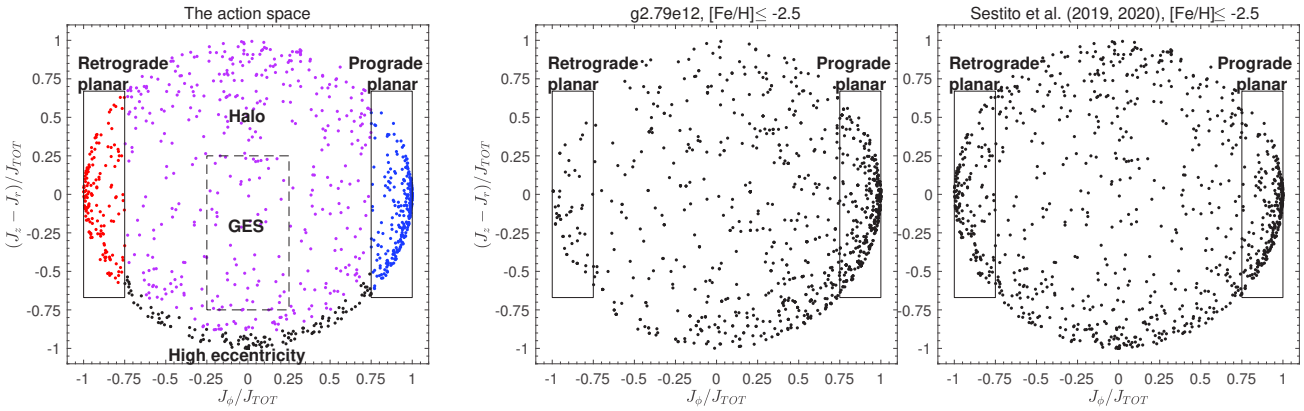

Figure 2. Action momentum space for star particles in the simulation and stars in the MW. Left panel: Sketch of the action space. The x-axis shows the azimuthal component of the action vector $J_\phi/J_{\rm TOT}$, a prompt for the rotational motion. Prograde orbits have $J_\phi/J_{\rm TOT} \geq 0$, while star particles with retrograde motion have $J_\phi/J_{\rm TOT} < 0$. The y-axis, $(J_z - J_r)/J_{\rm TOT}$, is the difference between the vertical component, which tracks the vertical motion of the particle/star, and the radial component of the action vector, which is an indication of its radial motion. Both axes are normalised by the norm of the action vector, $J_{\rm TOT}$. This is helpful for a comparison between galaxies with different physical properties. The black boxes represent the loci we define for prograde planar (right box, also shown with blue dots) and the retrograde planar stars (left box, also marked by red dots). The halo-like star particles are denoted by magenta dots, while the star particles with high eccentricity are marked by black dots. The dashed-line box represents the region where Gaia-Enceladus-Sausage (i.e., GES) has been discovered (Belokurov et al. 2018; Helmi et al. 2018). Central panel: the star particles with [Fe/H] ≤ -2.5 from simulation `g2.79e12` selected to mimic observations. Right panel: MW observations from S19 and S20. In the both the central and right panel, the star particles are marked with black dots.

Table 2. Prograde vs. retrograde planar asymmetry. The ratio $N_{\rm pro}/N_{\rm retro}$ between the number of star particles with prograde/retrograde planar orbits is reported as a function of the metallicity range for the simulated galaxies and the observed VMP stars in the MW (Sestito et al. 2020).

Galaxy	[Fe/H] ≤ -2.5	$-2.5 \leq$ [Fe/H] ≤ -2.0	$-3.0 \leq$ [Fe/H] ≤ -2.5	$-4.0 \leq$ [Fe/H] ≤ -3.0	[Fe/H] ≤ -4.0
Milky Way	1.72	1.89	1.67	1.82	11.11
`g2.79e12`	7.14	9.09	8.33	6.25	2.33
`g8.26e11`	9.09	12.50	8.33	–	2.33
`g7.55e11`	3.45	3.13	3.23	6.25	7.14
`g7.08e11`	6.25	7.69	6.67	5.00	–
`g6.96e11`	5.56	7.69	5.88	7.14	2.00

a large fraction of the final galaxy (see also Figure 3 of Buck et al. 2020).

Figure 5 shows the projection on the $x-y$ plane and the $r-z$ plane (where the coordinate system is chosen such that the z-axis aligns with the total angular momentum of the stellar disk) of the VMP particle's position at 4 different time-frames for the simulated galaxies `g2.79e12` and `g7.08e11`. Figures 4 and 5 show that, in the first few Gyr, the galactic building blocks (of which the most massive will be the main MW progenitor) of mass $10^5 - 10^9$ M$_\odot$ merge together and assemble the proto-galaxy. These building blocks, bring in the most metal-poor star particles, together with the gas and the DM. Once the proto-galaxy is assembled, other merger events are responsible for bringing in more of the VMP star particles in the main structure. The number of late mergers and the mass they contribute varies from simulation to simulation, from a quiet accretion history after $\sim$ 4 Gyr for `g2.79e12` and `g7.08e11` to a more turbulent and continued merging history for `g6.96e11` and `g7.55e11`.

As noted before, simulation `g7.55e11` matches best the MW orbital property observations. This is true both for the ratio of metal-poor prograde vs. retrograde star particles, as well as for the existence of a significant population of high eccentricity planar star particles of low metallicity (see Figure 3). Simulation `g7.55e11` stands out from the others in its very active and chaotic early merging phase in which more building blocks are coming together than in other simulations. Tracing the star particles belonging to this high eccentricity feature in `g7.55e11` back in time, we find that these belong to multiple merger events. Only $\sim$ 20 per cent of them are formed within 50 kpc of the center of the main halo, while the remaining particles were born in multiple satellites initially up to a distance of 300 kpc. These later merge with the main galaxy. In particular, Figure 4 shows that two massive satellites are merging at times $\sim$ 4 Gyr (also visible in Figure 5) and $\sim$ 7 Gyr. The stellar masses of the merging satellites are $M_{\rm stellar} = 3.0\times10^8$ M$_\odot$ ($M_{\rm TOT} = 6.7\times10^{10}$ M$_\odot$) and $M_{\rm stellar} = 1.3\times10^9$ M$_\odot$ ($M_{\rm TOT} = 6.7\times10^{10}$ M$_\odot$), respectively. In both cases, the total mass (DM+gas+stars) of the merging satellites is about $\sim$20–25 percent of the main halo's mass. Before the first merger, $\sim$ 24 ($\sim$ 55) percent of the prograde (retrograde) star particles present in the high eccentricity feature are already in place as the result of this early merging phase. The first merger, accreted at the end of the building blocks phase, is responsible for bringing in $\sim$ 22 ($\sim$ 40) percent of the progrades (retrogrades) into the high eccentricity component, while the second merger has brought in $\sim$ 46 per cent of the prograde and none of the retrograde star particles.

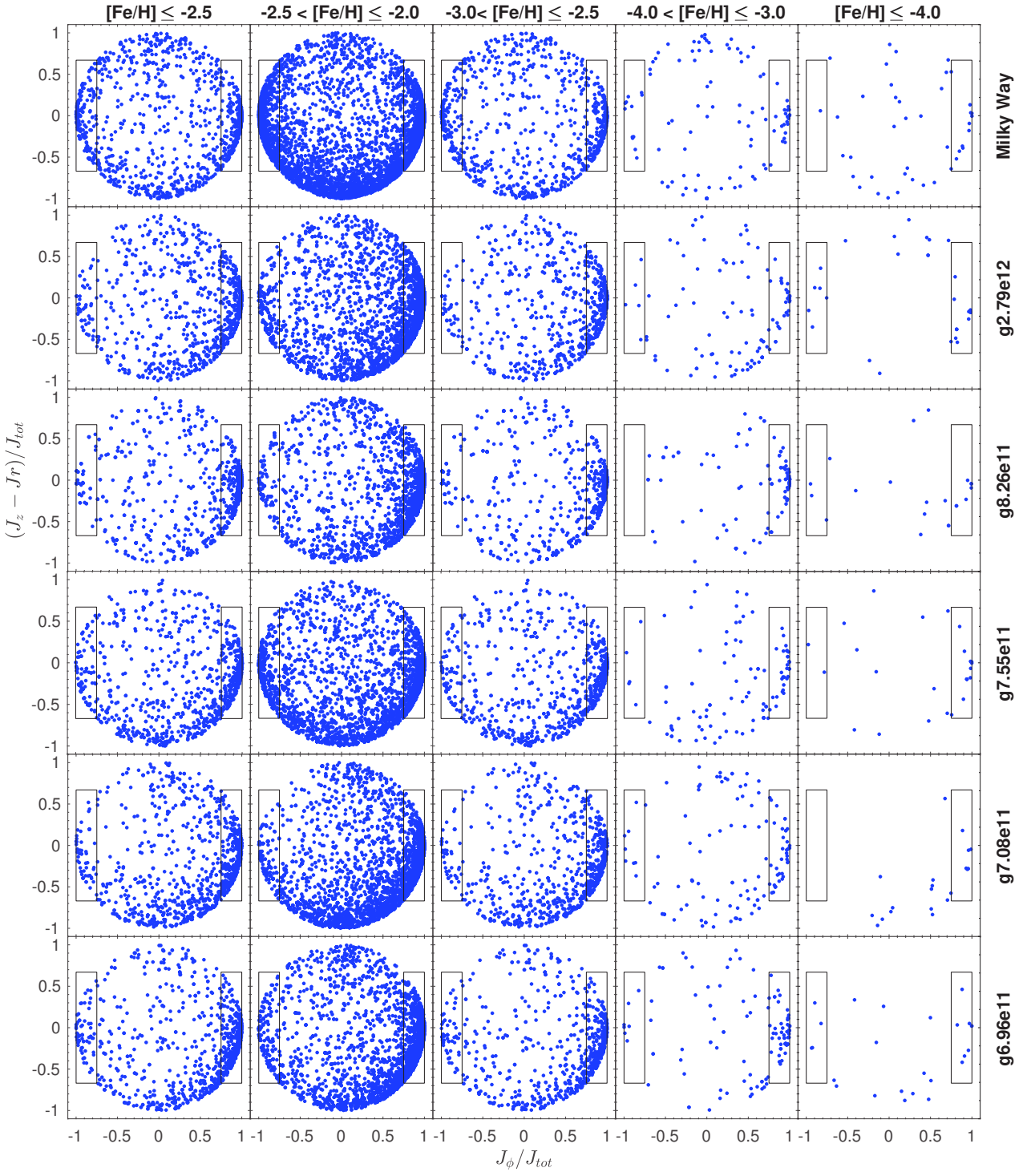

Figure 3. Metallicity decomposition of the simulated galaxies and MW observations in action space. The first row of panels displays the observations from S19 and S20, while the other rows show the simulated galaxies of the NIHAO-UHD suite, corrected for the observational window function as explained in the text. Each row is divided into metallicity bins. To better visualise the population of the most metal-poor star particles ([Fe/H] ≤ -2.5), the left column of panels shows all stars in the most metal-poor sample. From the second to the fourth column, the sample of the VMP stars has been separated according to their metallicity, from the VMP to the UMP regime. In each panels, the black boxes on the right and on the left represent the loci the populations of prograde planar and retrograde planar star particles.

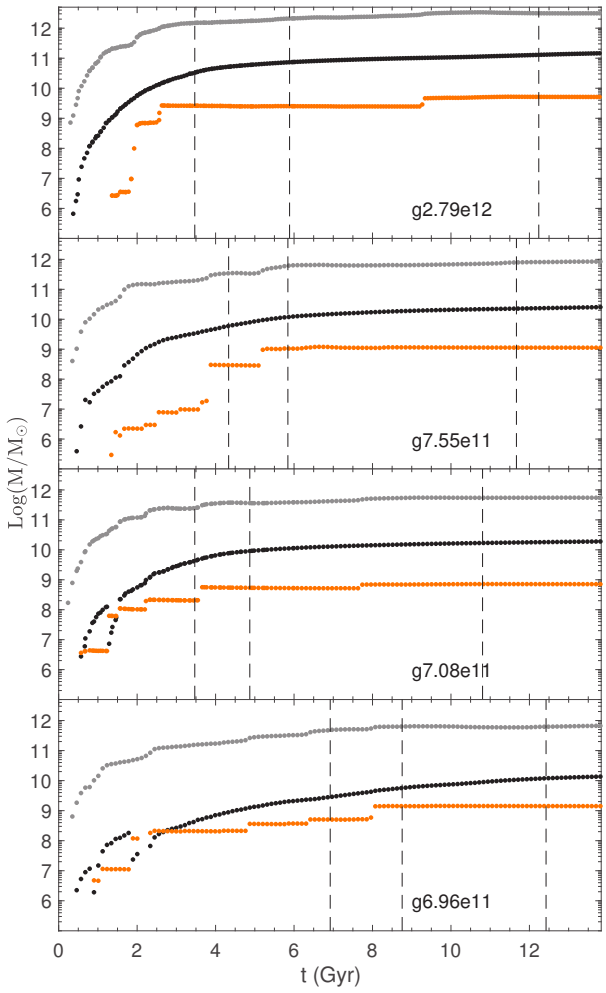

Figure 4. Virial mass (gray), main halo stellar mass (black), and accreted stellar mass (dark orange) as a function of time. The stellar mass in a sphere with a radius of $r = 75$ kpc centred in the main halo is denoted by black dots, the total accreted stellar mass from satellites within the same radius is marked with dark orange dots, and the total virial mass of the main halo is shown by gray dots. Vertical lines represent the time at which the stellar component of the main halo reached 25 per cent (left vertical line), 50 per cent (middle vertical line), and 90 per cent (right vertical line) of the total stellar mass. As previously mentioned, simulation `g8.26e11` is not shown as no reliable distinction between accreted and in-situ stars can be made. Note that the apparent reduction in main halo stellar mass for simulations `g7.08e11` and `g6.96e11` at very early cosmic times is due to the ongoing major mergers at those times.

Exploring the Auriga simulations, Gómez et al. (2017) found that later massive merging events ($M_{\rm TOT} \sim 10^{10}$–10^{11} M$_\odot$) are able to accrete stars with kinematics that resemble the disk population. This is in line with the two later massive merging events present in simulation `g7.55e11`.

It is clear that the MW experienced an active merging episode in its history, as evidenced by the recent discoveries of mainly the Gaia-Enceladus-Sausage structure and several other structures (e.g., Gaia-Sequoia and Thamnos) that might or might not be related (see, e.g., the review presented in Helmi 2020). Our finding that the significant population of high eccentricity planar star particles of low metallicity in the MW is not reproduced in all simulations, but rather might be the outcome of a more particular merger history, shows that this population in particular will be interesting to take into account when studying the merger picture of the MW in more detail. High-resolution spectroscopy of the low-metallicity planar stars, both prograde, retrograde, and highly eccentric, could provide further information on the precise formation history of the MW.

3.4 How old are the most metal-poor stars?

Since the abundance of metals in the ISM of the Galaxy increases gradually with successive generations of stars, the expectation is that VMP stars must have formed at early times, when the ISM was still relatively unpolluted. However, it is theoretically also possible that they form later from pockets of very isolated, unpolluted gas.

Figure 6 shows the distribution of the age of all the VMP star particles in the NIHAO-UHD simulations as a function of their metallicity. The metallicity-age plot is divided in a grid of 0.1 dex in metallicity and 0.1 Gyr in age and colour-coded by the number density of star particles in each pixel. Overall, the simulations indicate that indeed the most metal-poor stars are also the oldest ones. Only 0.7–12.0 percent of all VMP star particles are younger than 12 Gyr, while 35–77 percent are younger than 13 Gyr. Their minimum age is, across all simulations, $\gtrsim 9.1$ Gyr. In the extremely metal-poor regime (EMP, [Fe/H] ≤ -3.0), 19–42 per cent of stars are younger than $\sim$ 13 Gyr, while only a few star particles are younger than 12 Gyr ($\lesssim 0.7$ per cent). Similarly, in the UMP regime, only 11–36 per cent are younger than $\sim$ 13 Gyr, and ≤ 0.7 per cent are younger than 12 Gyr. This result is in agreement with findings from the APOSTLE (Starkenburg et al. 2017a) and FIRE simulations (El-Badry et al. 2018) of MW-like galaxies.

While most of the VMP stars are thus truly old, Figure 6 also shows a population of stars in simulation `g7.08e11` with [Fe/H] < -2.5 and an age $\leq$ 10.5 Gyr. Selecting this younger subsample of star particles, we find that they were born in the same dwarf galaxy ($M_{\rm tot} = 4.89 \cdot 10^{10}$ M$_\odot$, $M_{\rm star} = 1.95 \cdot 10^{8}$ M$_\odot$, and $M_{\rm gas} = 5.46 \cdot 10^{9}$ M$_\odot$) that entered the virial radius ($R_{\rm virial} = 174$ kpc for `g7.08e11`) at time $t \sim 5.84$ Gyr after the Big Bang. This younger population of low-metallicity star particles is not born during the first peak of star formation in this small galaxy (there are much older stars present in this system), but the older population has not been efficient in polluting the ISM to higher metallicity. Alternatively, an infall of new, chemically pristine gas has occurred between the star formation episodes.

3.5 Where do the most metal-poor stars come from?

An important goal of this paper is to answer the question of where the low-metallicity stars come from in order to distinguish between the three scenarios put forward in S19 and S20 (in short: later minor merging, came in with the early building block phase, or later in-situ formation in a quiescent disk). To do so, the NIHAO-UHD simulations provide the birth position ($x_{\rm birth}$, $y_{\rm birth}$, $z_{\rm birth}$) of the star particles, and, from each snapshot, we can track the position of the particles as a function of time ($x(t)$, $y(t)$, $z(t)$). With these quantities, it is possible to reconstruct the history of the most metal-poor stellar populations and connect the present kinematical properties to their counterparts at high-redshift.

From the previous analysis of the age-metallicity relation for the most metal-poor star particles (see Figure 6), it becomes clear that the population of star particles with [Fe/H] ≤ -2.5 is also the oldest ($\geq$ 12 Gyr), with almost no younger contaminants

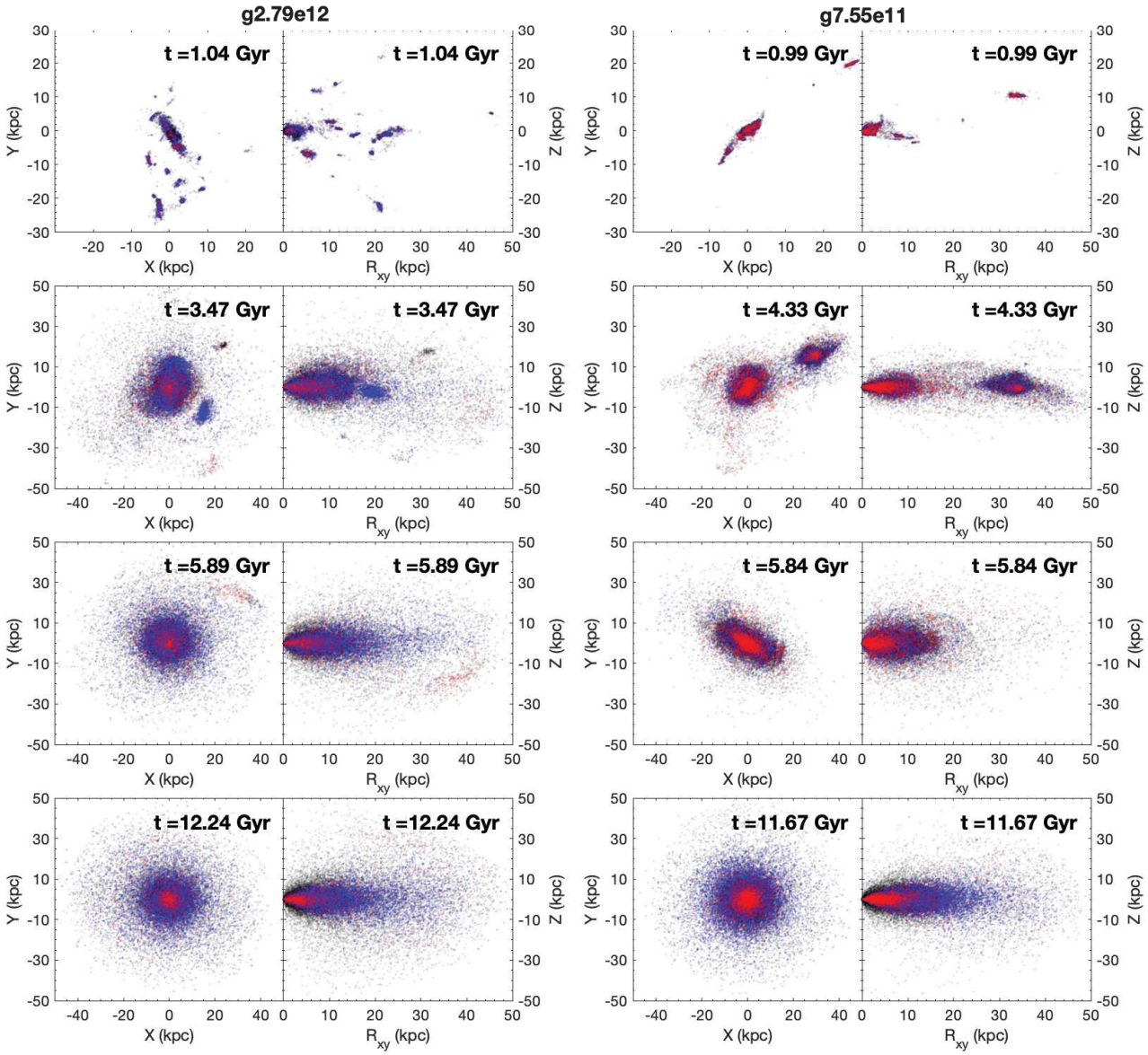

Figure 5. Snapshots of the VMP particle distribution. Projection of the spatial distribution of the VMP star particles along the $x - y$ and $R_{xy} - z$ planes for the simulations `g2.79e12` (on the left) and `g7.55e11` (on the right) at four different time ($t \sim 1$ Gyr, t_{25}, t_{50}, t_{90}). Star particles with prograde planar orbits, retrograde planar motion, and halo-like distribution are denoted by blue, red, and black dots, respectively. To better visualise the component with the smaller number of particles, the halo-like star particles (black) have been plotted first, then the prograde planar components (blue), and the retrograde planar stars (red) have been overplotted on top of the others. In the right hand panels for `g7.55e11` at time t_{25} ($t = 4.33$ Gyr), one of the two massive mergers responsible for depositing star particles in the bottom part of the action space (see discussion in Sections 3.2 and 3.3) is visible at $x \sim 30$ kpc, $y \sim 20$ kpc, $z \sim 0$ kpc, $R_{xy} \sim 35$ kpc.

(see Section 3.4 for the discussion on the youngest population in `g7.08e11`). For this reason, we select this low-metallicity population ([Fe/H] ≤ -2.5) to better investigate when they were formed and accreted onto the main galaxy. We pay particular attention to the star particles that end up in prograde and retrograde planar orbits.

Figure 7 shows the time at which the low-metallicity star particles first enter a sphere of radius 50 kpc centred on the main halo as a function of the age of the particle. In this figure, the over-densities of star particles with the same accretion time reflect the accretion of satellites. When these small galaxies merge with the MW-like galaxy, they often deposit stars with a range of stellar ages. Star particles accreted from less dense environments, such as from a filament or a stream from a disrupting satellite in the outskirts of the galaxy, appear as more sparse and uncorrelated events.

The percentages of low-metallicity star particles that enter the main halo (out to a radius of 50 kpc) at times t_{25}, t_{50}, and t_{90} are summarised in Figure 8 and the fraction is reported in Table 3. In all simulations, a majority (between 54 and 72 per cent) of all low-metallicity star particles are already brought in by t_{25}. This percentage is in line with the overall build-up of mass in their stellar haloes at these radii. The majority of these stars that are brought in by the early accretion events via the galactic building blocks (or

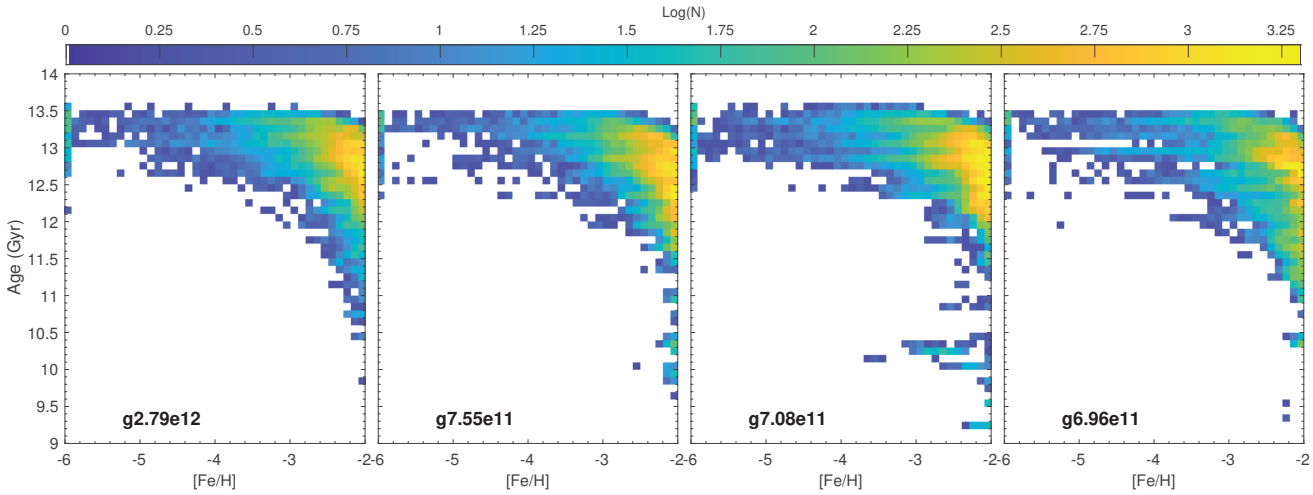

Figure 6. Age vs. [Fe/H] for the VMP star particles in the simulated galaxies. Each pixel of size 0.1 Gyr × 0.1dex is colour-coded by the logarithm of the particle counts. Star particles with [Fe/H] < −6 are reported in the pixels of [Fe/H] = −6 for a better representation. A younger population of low-metallicity stars is visible in the panel of simulation `g7.08e11`, as discussed in Section 3.4, these star particles are brought in by a dwarf satellite, in which the older population has not been efficient in polluting the ISM, or pockets of pristine gas were accreted at a later moment. Tracking problems in simulation `g8.26e11` might have affected the age, and to be cautious, `g8.26e11` has been removed.

are part of the main progenitor) of the proto-MW-like galaxy end up on halo orbits, consistent with the picture of a more metal-poor population that is distributed in a spheroid (e.g., El-Badry et al. 2018). However, as already demonstrated in Sections 3.1 and 3.2 and Figure 3, a non-negligible fraction of star particles are deposited with planar orbits and prograde motion.

Figures 7 and 8 and Table 3 provide a clear answer regarding the origin of this particular population. The majority of planar low-metallicity stars, both in prograde and retrograde orbits, are brought in at early times, with only a small role for the alternative scenario of later minor mergers. Some building blocks contribute star particles that end up in prograde motion as well as some that end up in retrograde orbits; this is especially true for merging events in the very chaotic early phases of the build-up of the proto-galaxies. In line with this scenario, Horta et al. (2020) detect an observational signature in the chemodynamical properties of the MW bulge, pointing out to an accretion event that happened during the building blocks phase. Because all VMP star particles in the simulations are born within ∼ 4 Gyr (see Figures 6 and 7), before the formation of the stable, thin and extended disk in these galaxies (see Figure 10 in Buck et al. 2020), we can rule out the hypothesis that this VMP population formed at later times in the disk itself.

However, there are also interesting differences between the galaxies in the populations of star particles that end up on retrograde and prograde planar orbits. For `g7.55e11` and `g6.96e11`, ∼ 37 per cent of the present day prograde planar stars are already in place at t_{25}, whereas, for `g7.08e11` and `g2.79e12`, this number is ∼ 62 and ∼ 90 per cent, respectively. This difference can be explained by a difference in the formation and accretion history. Simulated galaxies with a more extended merger/accretion history, such as `g7.55e11` and `g6.96e11`, will homogeneously gain star particles with prograde planar and halo-like orbits across cosmic time compared to simulations, like `g7.08e11` and `g2.79e12`, that have a very quiet accretion history after the first few Gyr. This is also in agreement with Gómez et al. (2017), where they show with the Auriga simulations that later merger events can bring a significant percentage of old and metal-poor star particles with prograde planar motion into the stellar disks. A very similar result has been found by Scannapieco et al. (2011) looking at ΛCDM simulations, showing that late accretions can deposit their stars in a nearly co-planar orbits.

The population of retrograde planar stars, on the other hand, shows a more consistent picture among the simulations with different accretion histories. The majority of this population (≳ 90 percent of this final population) has been assembled at t_{25} in simulations `g2.79e12`, `g7.55e11`, and `g7.08e11`. For galaxy `g6.96e11` this value is ∼ 74 percent.

The picture that emerges here is that whereas retrograde planar low-metallicity stars are almost exclusively tracing a phase of very early build-up, their prograde counterparts are sampling more the full accretion history of the galaxy. This can be explained by the fact that prograde mergers experience the tidal forces of the main galaxy's gravitational potential well for a prolonged period (see e.g., Abadi et al. 2003; Peñarrubia et al. 2002), meaning that later mergers have a much higher chance to sink deep into the potential well if they are prograde rather than retrograde. While retrograde mergers might still happen at later times as well, their higher relative impact speed results in a more violent tidal force, and their stars will typically be disrupted at much larger radii in the Galactic halo. Another reason for this might be given by a simple selection bias. The general suppression of late time retrograde mergers results from the fact that we are looking at disk galaxies to start with. For example, Martin et al. (2018) showed that late time retrograde mergers trigger stronger morphological changes compared to prograde mergers. Thus, by selecting galaxies with a strong stellar disk we might be biasing ourselves towards less retrograde late time mergers.

4 CONCLUSIONS

We use the NIHAO-UHD cosmological zoom-in simulations, a suite of high-resolution simulated spiral galaxies, with the aim to explore the properties of the oldest and most metal-poor stars, such as their accretion time, their age, and the relation between their kinematical

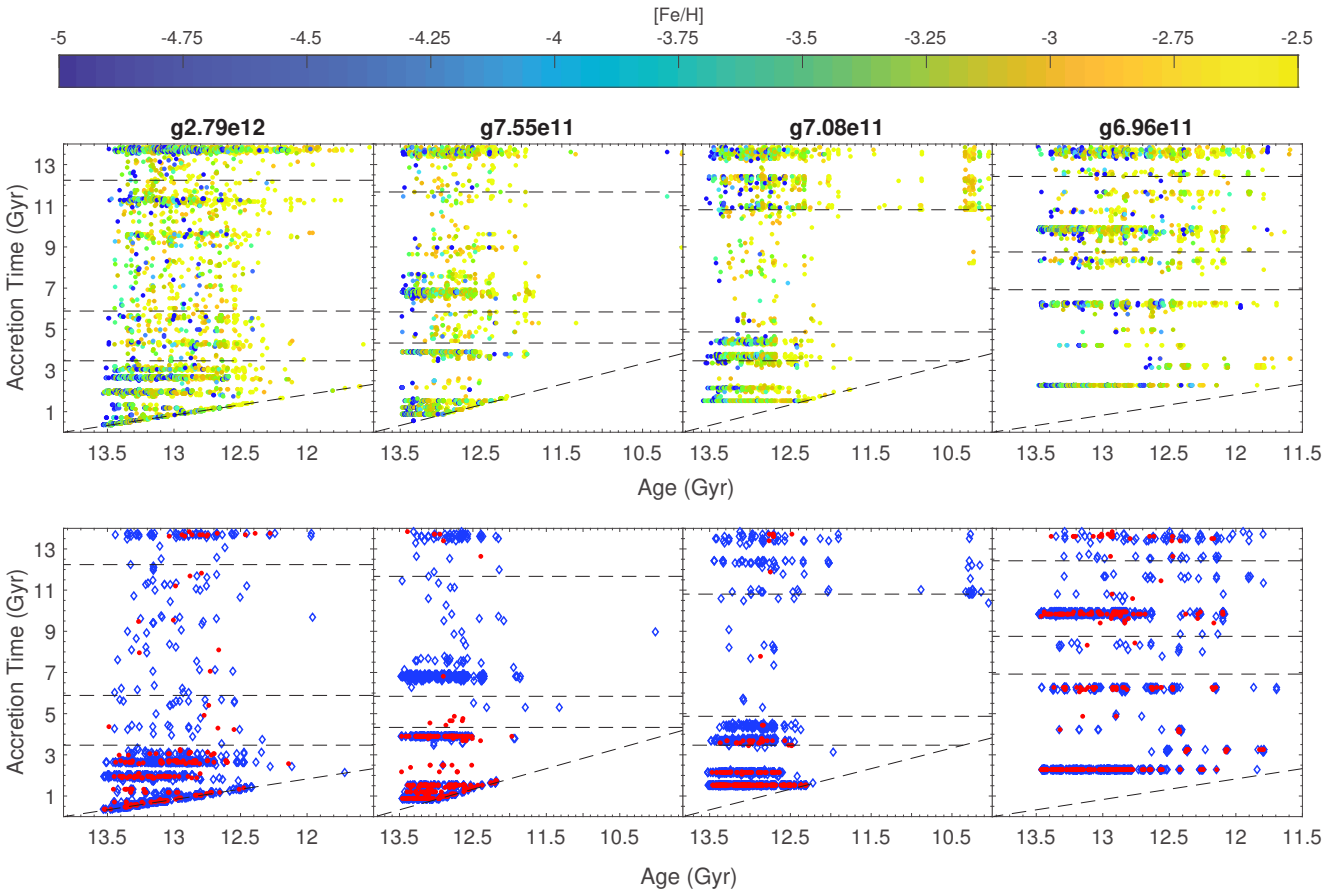

Figure 7. Accretion times of the low-metallicity star particles. Top panels: Accretion time vs. age for low-metallicity ([Fe/H] ≤ -2.5) star particles within a Galactocentric radius of 50 kpc colour-coded by [Fe/H]. Bottom panels: the accretion time vs. the age of the star particles as above, but now only for prograde planar star particles (displayed as blue rhombi) and retrograde planar particles (marked with a red dot). The horizontal dashed lines represent the time at which the main halo reached the 25 per cent (lower line), the 50 per cent (middle line), and the 90 per cent (upper line) of the total stellar mass. The region below the inclined dashed line is forbidden since star particles would have been accreted before their formation. Star particles that lie on the inclined line have a birth position below 50 kpc. Simulation `g8.26e11` has been removed due to tracking problems.

Table 3. Fraction of low-metallicity star particles ([Fe/H] ≤ -2.5) in the main halo as a function of time. The fractions are reported for all the sample, the halo low-metallicity population, the prograde planar, and the retrograde planar population brought in by the building blocks and merger events at the time t_{25}, t_{50}, and t_{90}. At each time, the ratio between the prograde and the retrograde planar population, N_{pro}/N_{retro} is also reported. t_{25}, t_{50}, and t_{90} are defined as the time when the main halo has assembled the 25 per cent, the 50 per cent, and the 90 per cent of the present stellar mass.

Simulation	Accreted at $t \leq t_{25}$ All | Halo | Pro | Retro | N_{pro}/N_{retro}	Accreted at $t \leq t_{50}$ All | Halo | Pro | Retro | N_{pro}/N_{retro}	Accreted at $t \leq t_{90}$ All | Halo | Pro | Retro | N_{pro}/N_{retro}
`g2.79e12`	0.72 | 0.66 | 0.90 | 0.90 | 6.25	0.76 | 0.70 | 0.92 | 0.92 | 6.25	0.84 | 0.81 | 0.96 | 0.95 | 6.25
`g7.55e11`	0.67 | 0.69 | 0.38 | 0.97 | 1.54	0.68 | 0.71 | 0.38 | 0.99 | 1.52	0.94 | 0.92 | 0.97 | 0.99 | 3.85
`g7.08e11`	0.71 | 0.68 | 0.62 | 0.91 | 3.57	0.89 | 0.86 | 0.94 | 0.98 | 5.00	0.90 | 0.87 | 0.95 | 0.98 | 5.00
`g6.96e11`	0.54 | 0.55 | 0.37 | 0.74 | 2.44	0.56 | 0.58 | 0.38 | 0.75 | 2.50	0.92 | 0.90 | 0.96 | 0.93 | 5.00

properties and the origin of the star particles. These properties are difficult to infer from observational data, and we use the cosmological simulations as a tool to interpret the observations. In particular, we detect in the NIHAO-UHD simulations the signature of a low-metallicity population that spatially and kinematically resides in the disk. Such ensemble is composed of prograde and retrograde star particles, as also observationally detected by Sestito et al. (2019, 2020) and Di Matteo et al. (2020). As in the observations, all the simulated galaxies agree on the prevalence for a prograde planar population. While the halos of the simulated galaxies are more significantly rotating that the observed halo stars of the MW, it is also clear that, independently, they also host a population of pro-

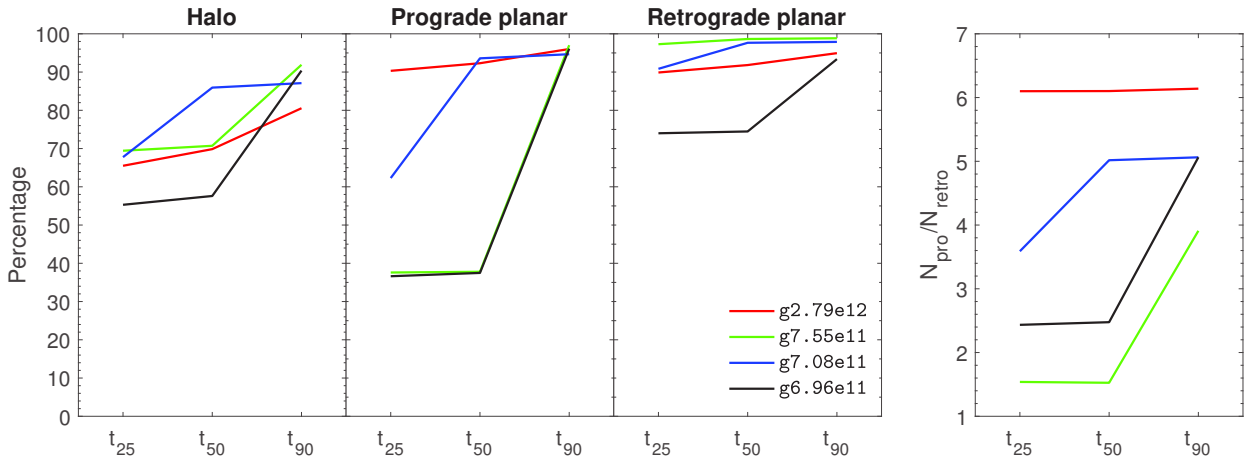

Figure 8. Fraction of the halo, prograde planar, and retrograde planar stellar population in the main halo out to a radius of 50 kpc as a function of time, relative to the distribution at the present time. From the first to the third panel: the percentage of the halo, the prograde planar, and the retrograde planar populations calculated at the time t_{25}, t_{50}, and t_{90}, respectively. Right panel: ratio $N_{\rm pro}/N_{\rm retro}$ between the number of the prograde and retrograde planar star particles calculated at the time t_{25}, t_{50}, and t_{90}. The legend is the same for all the panels.

grade planar stars that follow the velocity distribution of the more metal-rich thick disk.

We find that the presence of the low-metallicity star particles that kinematically inhabit the disk is explained by two scenarios. The first, dominating, scenario is that during the first few Gyr, the proto-galaxy is undergoing a violent process of assembling, during which the building blocks (and the main MW progenitor) of stellar mass of $10^5 - 10^9\,{\rm M}_\odot$ are merging together. During this phase the proto-galaxy and, therefore, the proto-disk are still assembling and the gravitational potential well is much shallower than at the present day. Therefore, the merging building blocks, often with a size comparable to the main MW progenitor (see e.g. Fig. 4), can deposit their star particles in the inner part of the main halo, either in prograde or retrograde planar orbits.

The second scenario is linked to later merger events. As the proto-galaxy grows in mass and the disk forms, later accretions bring in more prograde planar star particles, but fewer star particles on retrograde planar orbits. This may result from the fact that satellites on prograde orbits tend to sink onto the plane before disrupting, whereas retrograde orbits less so. When those galaxies finally disrupt they deposit their star particles on prograde planar orbits. Late time retrograde mergers, on the other hand, increase the relative impact speed of merging dwarf and main galaxy leading to more severe tidal forces which violently disrupt the dwarf and deposit star particles on more eccentric halo-like orbits.

A third possible scenario, the formation of the low-metallicity stars in the disk, has to be ruled out in these simulations. The VMP star particles formed within ~ 4 Gyr, when the proto-galaxy is still assembling. The formation of the disk and the settling of the ISM happens after these low-metallicity star particles were already born, either in the building blocks, or in the satellites that will later be accreted.

There is ample evidence for (massive) merger events in the early MW (e.g., Belokurov et al. 2018; Helmi et al. 2018; Koppelman et al. 2018, 2019; Barbá et al. 2019; Myeong et al. 2019; Bonaca et al. 2020). The properties of the very metal-poor stars cannot be viewed in isolation from these events as, for instance, evidenced by how well they trace the spatial and kinematical structure of the thick disk in all simulations, and they can help to constrain this picture further. Additionally, we find that, independently of the exact formation history of the galaxy, the vast majority of the star particles on retrograde planar orbits has been deposited there at very early times, therefore this population might provide a unique opportunity to investigate the very early merging phase of the MW.

In conclusion, the simulated MW-like galaxies in the NIHAO-UHD suite confirm that the low-metallicity stars are an ideal probe of the galaxy formation during the infant Universe, and therefore, Galactic Palaeontology (or Archaeology) surveys should hunt for the most metal-poor stars, not only in the spheroidal components of the MW, but also in its disk.

ACKNOWLEDGEMENTS

The authors would like to thank Amina Helmi for insightful discussions that helped to improve this manuscript. FS thanks the Initiative dExcellence IdEx from the University of Strasbourg and the Programme Doctoral International PDI for funding his Ph.D. This work has been published under the framework of the IdEx Unistra and benefits from a funding from the state managed by the French National Research Agency as part of the investments for the future program. FS acknowledges the support and funding of the Erasmus+ programme of the European Union. TB acknowledges support by the European Research Council under ERC-CoG grant CRAGSMAN-646955. TB gratefully acknowledges the Gauss Centre for Supercomputing e.V. (https://www.gauss-centre.eu) for funding this project by providing computing time on the GCS Supercomputer SuperMUC at Leibniz Supercomputing Centre (https://www.lrz.de). This research was carried out on the High Performance Computing resources at New York University Abu Dhabi; Simulations have been performed on the ISAAC cluster of the Max-Planck-Institut für Astronomie at the Rechenzentrum in Garching and the DRACO cluster at the Rechenzentrum in Garching. We greatly appreciate the contributions of all these computing allocations. FS and NFM gratefully acknowledge support from the French National Research Agency (ANR) funded project "Pristine" (ANR-18-CE31-0017) along with funding from

CNRS/INSU through the Programme National Galaxies et Cosmologie and through the CNRS grant PICS07708. ES gratefully acknowledge funding by the Emmy Noether program from the Deutsche Forschungsgemeinschaft (DFG). AO is funded by the Deutsche Forschungsgemeinschaft (DFG, German Research Foundation) - MO 2979/1-1. The authors acknowledge the support and funding of the International Space Science Institute (ISSI) for the international team "Pristine". This research made use of the following PYTHON packages: PYNBODY AND TANGOS (Pontzen et al. 2013; Pontzen & Tremmel 2018), MATPLOTLIB (Hunter 2007), SCIPY (Jones et al. 01), NUMPY (Walt et al. 2011), IPYTHON and JUPYTER (Pérez & Granger 2007; Kluyver et al. 2016)

DATA AVAILABILITY

The data underlying this article will be shared on reasonable request to the corresponding author.

REFERENCES

Abadi M. G., Navarro J. F., Steinmetz M., Eke V. R., 2003, ApJ, 597, 21
Aguado D. S., et al., 2019, MNRAS, 490, 2241
Barbá R. H., Minniti D., Geisler D., Alonso-García J., Hempel M., Monachesi A., Arias J. I., Gómez F. A., 2019, ApJ, 870, L24
Belokurov V., Erkal D., Evans N. W., Koposov S. E., Deason A. J., 2018, MNRAS, 478, 611
Bonaca A., et al., 2020, ApJ, 897, L18
Brook C. B., Kawata D., Scannapieco E., Martel H., Gibson B. K., 2007, ApJ, 661, 10
Buck T., 2020, MNRAS, 491, 5435
Buck T., Ness M. K., Macciò A. V., Obreja A., Dutton A. A., 2018, ApJ, 861, 88
Buck T., Macciò A. V., Dutton A. A., Obreja A., Frings J., 2019a, MNRAS, 483, 1314
Buck T., Dutton A. A., Macciò A. V., 2019b, MNRAS, 486, 1481
Buck T., Ness M., Obreja A., Macciò A. V., Dutton A. A., 2019c, ApJ, 874, 67
Buck T., Obreja A., Macciò A. V., Minchev I., Dutton A. A., Ostriker J. P., 2020, MNRAS, 491, 3461
Cui X.-Q., et al., 2012, Research in Astronomy and Astrophysics, 12, 1197
Deason A. J., Belokurov V., Evans N. W., 2011, MNRAS, 411, 1480
Di Matteo P., Spite M., Haywood M., Bonifacio P., Gómez A., Spite F., Caffau E., 2020, A&A, 636, A115
El-Badry K., et al., 2018, MNRAS, 480, 652
Frebel A., Norris J. E., 2015, ARA&A, 53, 631
Freeman K., Bland-Hawthorn J., 2002, ARA&A, 40, 487
Gaia Collaboration et al., 2016, A&A, 595, A1
Gaia Collaboration et al., 2018, A&A, 616, A1
Gao L., Theuns T., Frenk C. S., Jenkins A., Helly J. C., Navarro J., Springel V., White S. D. M., 2010, MNRAS, 403, 1283
Gómez F. A., et al., 2017, MNRAS, 472, 3722
Griffen B. F., Dooley G. A., Ji A. P., O'Shea B. W., Gómez F. A., Frebel A., 2018, MNRAS, 474, 443
Helmi A., 2020, arXiv e-prints, p. arXiv:2002.04340
Helmi A., Babusiaux C., Koppelman H. H., Massari D., Veljanoski J., Brown A. G. A., 2018, Nature, 563, 85
Hilmi T., et al., 2020, MNRAS,
Horta D., et al., 2020, arXiv e-prints, p. arXiv:2007.10374
Hunter J. D., 2007, Computing In Science & Engineering, 9, 90
Ishiyama T., Sudo K., Yokoi S., Hasegawa K., Tominaga N., Susa H., 2016, ApJ, 826, 9
Jablonka P., et al., 2015, A&A, 583, A67
Jones E., Oliphant T., Peterson P., et al., 2001–, SciPy: Open source scientific tools for Python, http://www.scipy.org/
Karlsson T., Bromm V., Bland-Hawthorn J., 2013, Reviews of Modern Physics, 85, 809
Kluyver T., et al., 2016, in Loizides F., Schmidt B., eds, Positioning and Power in Academic Publishing: Players, Agents and Agendas. pp 87 – 90
Koppelman H., Helmi A., Veljanoski J., 2018, ApJ, 860, L11
Koppelman H. H., Helmi A., Massari D., Price-Whelan A. M., Starkenburg T. K., 2019, A&A, 631, L9
Li H., Tan K., Zhao G., 2018, ApJS, 238, 16
Martin G., Kaviraj S., Devriendt J. E. G., Dubois Y., Pichon C., 2018, MNRAS, 480, 2266
Meza A., Navarro J. F., Abadi M. G., Steinmetz M., 2005, MNRAS, 359, 93
Monty S., Venn K. A., Lane J. M. M., Lokhorst D., Yong D., 2020, MNRAS, 497, 1236
Myeong G. C., Vasiliev E., Iorio G., Evans N. W., Belokurov V., 2019, MNRAS, 488, 1235
Navarro J. F., Abadi M. G., Venn K. A., Freeman K. C., Anguiano B., 2011, MNRAS, 412, 1203
Peñarrubia J., Kroupa P., Boily C. M., 2002, MNRAS, 333, 779
Pérez F., Granger B. E., 2007, Computing in Science and Engineering, 9, 21
Planck Collaboration et al., 2014, A&A, 571, A16
Pontzen A., Tremmel M., 2018, The Astrophysical Journal Supplement Series, 237, 23
Pontzen A., Roškar R., Stinson G. S., Woods R., Reed D. M., Coles J., Quinn T. R., 2013, pynbody: Astrophysics Simulation Analysis for Python
Raiteri C. M., Villata M., Navarro J. F., 1996, A&A, 315, 105
Recio-Blanco A., Fernández Alvar E., de Laverny P., Antoja T., Helmi A., Crida A., 2020, arXiv e-prints, p. arXiv:2007.08313
Salvadori S., Ferrara A., Schneider R., Scannapieco E., Kawata D., 2010, MNRAS, 401, L5
Scannapieco C., White S. D. M., Springel V., Tissera P. B., 2011, MNRAS, 417, 154
Sestito F., et al., 2019, MNRAS, 484, 2166
Sestito F., et al., 2020, MNRAS, 497, L7
Starkenburg E., Oman K. A., Navarro J. F., Crain R. A., Fattahi A., Frenk C. S., Sawala T., Schaye J., 2017a, MNRAS, 465, 2212
Starkenburg E., et al., 2017b, MNRAS, 471, 2587
Stinson G., Seth A., Katz N., Wadsley J., Governato F., Quinn T., 2006, MNRAS, 373, 1074
Stinson G. S., Brook C., Macciò A. V., Wadsley J., Quinn T. R., Couchman H. M. P., 2013, MNRAS, 428, 129
Thielemann F. K., Nomoto K., Yokoi K., 1986, A&A, 158, 17
Tian H., Liu C., Xu Y., Xue X., 2019, ApJ, 871, 184
Tian H., Liu C., Wang Y., Xu Y., Yang C., Zhang B., Xue X.-X., 2020, ApJ, 899, 110
Tumlinson J., 2010, The Astrophysical Journal, 708, 1398
Vasiliev E., 2019, MNRAS, 482, 1525
Venn K. A., Irwin M., Shetrone M. D., Tout C. A., Hill V., Tolstoy E., 2004, AJ, 128, 1177
Venn K. A., et al., 2020, MNRAS, 492, 3241
Wadsley J. W., Keller B. W., Quinn T. R., 2017, MNRAS, 471, 2357
Walt S. v. d., Colbert S. C., Varoquaux G., 2011, Computing in Science and Engg., 13, 22
Wang L., Dutton A. A., Stinson G. S., Macciò A. V., Penzo C., Kang X., Keller B. W., Wadsley J., 2015, MNRAS, 454, 83
White S. D. M., Springel V., 2000, in Weiss A., Abel T. G., Hill V., eds, The First Stars. p. 327 (arXiv:astro-ph/9911378), doi:10.1007/10719504_62
Woosley S. E., Weaver T. A., 1995, ApJS, 101, 181

This paper has been typeset from a TEX/LATEX file prepared by the author.

CHAPTER

5 Conclusions

This thesis presents new results for Galactic Archæology. For instance, the discovery of a population of the most metal-poor stars kinematically confined to the disk of the Milky Way was not explored by previous studies and deviates from the general expected spheroidal distribution. This population of *planar* stars is groupable into prograde and retrograde subgroups. Chapter 2 (Sestito et al., 2019) shows that in the ultra metal-poor regime, a quarter of the discovered UMPs do not venture far out from the disk. These planar UMPs show a wide range of eccentricities, with the most metal-poor star known orbiting with a quasi-circular prograde motion. Although the sample is very limited in number, there is a net preference for the prograde planar motion. This preference is not arising from the composite window functions imparted by the multiple surveys. In Chapter 3 (Sestito et al., 2020a), this kinematical analysis has been extended to the very metal-poor regime, in order to explore the metallicity regime from the UMP to the VMP tail of the Milky Way disk discovered so far. The larger sample provided by the Pristine (Starkenburg et al., 2017b) and LAMOST (Cui et al., 2012) surveys has put the results on a firmer statistical footing. It has been shown that the number of prograde planars stars is largely outrivaling the number of their retrograde counterpart. The presence of planar stars and the observed asymmetry in the direction of rotation have been detected at all metallicity regimes. The asymmetry suggests that the distribution of the planar stars is not in agreement with what is expected from a spheroidal and pressure-supported distribution. Three mutually non-exclusive scenarios have been proposed to explain the planar population described in Chapters 2 and 3. The first, i.e., the in-situ scenario, invokes the presence of metal-devoid pockets of interstellar medium (ISM) in the Milky Way after the disk settled. In the second scenario, the planar stars were formed and brought in, together with the ISM and the dark matter, by the building blocks that formed the proto-disk. While in the last scenario, this planar population was deposited by later accretion events that were dragged into the plane of the Milky Way.

From the observations, it was not possible to discriminate between the multiple scenarios that create this kinematical feature, i.e., the in-situ formation, the formation in the early assembly phase, and the later merging events. This is mainly due to the limits in the observations arising from the size and spatial distribution of the sample, the lack of chemical information that might trace the star formation of their sites of origin, and the multiple window functions imparted by the different surveys that discovered these metal-devoid stars. On the

other hand, high-resolution cosmological simulations can provide an excellent tool to check if this planar population is a common kinematic feature or if it does depend on a particular assembly and accretion history. Furthermore, it is possible to track the star particles back in time and study their origin. For this investigation, in Chapter 4 (Sestito et al., 2020b), I have utilised 5 simulated spiral galaxies from the NIHAO-UHD suite (Buck et al., 2020), with a resolution that is capable of spatially resolving sub-kpc structures. As a first result, the NIHAO-UHD galaxies show the presence of the planar population, with a preference for the prograde group as in the observed Milky Way. This set of simulated galaxies possess a slowly-rotating halo, meaning that the rotation can induce some star particles to be confined to the disk with prograde motion. However, I found that the velocity distribution of the prograde planar population is exceeding what would be expected from a slowly-rotating spheroidal distribution and much more closely resembles that of the more metal-rich thick disk. Keeping in mind though that non of these galaxies do resemble the Milky Way in full, I have explored the origin of the most metal-poor stars in NIHAO-UHD. The simulated galaxies indicate that both the retrograde and prograde planar stars are connected to the formation history of the galaxies. For instance, the majority (> 90 per cent) of the retrograde planar population has been brought in during the early galactic assembly, independently of the formation and accretion history of the simulated galaxies. On the other hand, the prograde population is tracing both the building blocks phase and later accretion events. This is because during the early assembly, the proto-galaxy was much smaller in size and merging satellites (sometimes with sizes comparable to the proto-galaxy) were allowed to deposit their stars in the inner region of the gravitational potential, and retain their retrograde or prograde motion. Once the galaxy is well shaped and formed, only prograde accreted satellites could deposit their stars in a co-planar fashion, since they can feel the tidal forces for a prolonged time. Later retrograde satellites, on the other hand, have less time to feel the disk's gravitational potential and they end up being disrupted and mainly dispersed in the halo. The chemistry and kinematics of the discovered prograde and retrograde planar stars help us understand the early assembly of the Galaxy and the later accretions. Therefore, these results can be important for our understanding of the Milky Way.

One avenue to study these interesting populations in more detail is high-resolution spectroscopy. For this reason, high-resolution spectroscopic follow-up are needed to measure neutron-capture, such as Europium, Barium, and Yttrium, and $\alpha-$ elements, such as Magnesium, Calcium, Carbon, and Oxygen. Their presence and their chemical abundances in the most metal-poor stars are strictly connected to the physical mechanisms that polluted the interstellar medium of their formation sites in the early Universe. Therefore, we can learn about the star formation efficiency and history of the building blocks that formed our Galaxy, and also disentangle the various populations inside the Milky Way. Lastly, all of these are important to learn more about the formation and accretion history of our Galaxy at early times. With these motivations, I am planning to use the observational facilities with the highest resolution, such as the Ultraviolet and Visual Échelle Spectrograph (UVES) at the Very Large Telescope (VLT), the Gemini High Resolution Optical Spectrograph (GHOST) at the Gemini telescopes, and the Échelle SpectroPolarimetric Device for the Observation of Stars (ESPaDOnS) at the Canada-France-Hawaii Telescope (CFHT). With these instruments, it will be possible to cover a wide range in magnitudes, and explore with high-resolution different regions of the Milky Way. These facilities are perfect to measure the weak lines of the neutron-capture elements with high accuracy, precision, and thereby keeping exposure

times reasonably short.

The near future will provide a wealth of data for Galactic Archæology, since new large ground-based multi-objects spectroscopic surveys will see the light. These are most importantly WEAVE (Dalton et al., 2012) and 4MOST (de Jong et al., 2019), that will scan both the Northern and the Southern Sky, respectively. Regarding WEAVE, and its synergy with the Pristine survey, it has been predicted that it will discover approximately ~ 8000 new extremely metal-poor stars (Aguado et al., 2019), largely surpassing the actual numbers for this old population. The chemical information from these surveys will be complemented by future data releases of Gaia satellites. The Gaia ESA satellite will enlarge the number of sources with photometric and astrometric solutions, reduce the uncertainties on the measurements, and also provide stellar parameters for the brightest sample. This powerful synergy will be crucial for chemo-dynamical studies of the Milky Way, and they will be essential to further investigate the present distribution of stars and their relation with the history of the Galaxy.

In a more distant future, other observational facilities will start to acquire data. For my field of science, the most exciting new developments in new instrumentation are the Large Synoptic Survey Telescope (LSST, also known as the Vera C. Rubin Observatory, Ivezic et al., 2008), the Sloan Digital Sky Survey-V (SDSS-V, Kollmeier et al., 2017), the Maunakea Spectroscopic Explorer (MSE, The MSE Science Team et al., 2019), the Extremely Large Telescope (ELT, Tamai et al., 2016), and the James Webb Space Telescope (JWST, Gardner et al., 2006). The LSST will scan the Southern hemisphere covering up to 18000 deg^2, and with its field of view of ~ 9.6 deg^2 and effective diameter of 6.7 m it will reach a depth of $25-28$ mag with its filters (u, g, r, i, z, y). This limit in magnitude will be essential to resolve several regions of the Milky Way, from the bulge to the outer halo and satellites up to ~ 450 kpc. Moreover, it will provide exquisite proper motions reaching $3-4$ magnitudes fainter than the Gaia satellite up to a distance of 100 kpc (Rich, 2018, and references therein). The MSE will probably replace the CFHT and it will be able to acquire up to 3000 spectra in the low-resolution configuration. The sensitivity and properties of this telescope and its equipments are ideal for several science cases, from exoplanet, to very metal-poor stars in the Milky Way, to high-redshift objects (The MSE Science Team et al., 2019), and it can complement the information from various other surveys. SDSS-V (Kollmeier et al., 2017), on the heels of the SDSS survey, will observe both the Northern and the Southern hemispheres using multiple observatories. It will map the Milky Way and Local Volume galaxies with multi-object and integral field spectroscopy covering the optical and the near infrared. It will target up to 5 million stars in the Galaxy, and up to 25 million spectra in the Milky Way and nearby galaxies. Moreover, it will point towards black holes with the aim of inferring their properties. ELT, with a diameter of 39 m and equipped with adaptive optics and multiple instruments on board, will be capable of reaching high-resolution with small noise both in the optical and in the near infrared. For instance, the High Resolution Spectrograph (HIRES) will have a resolution of R~ 100,000 ideal to measure very weak lines as in the most metal-poor stars, and its performance is also optimal for exoplanets and high-redshift science. With a lower resolution (up to R~ 15000), another interesting instrument at ELT is the Multi-Object Spectrograph (MOSAIC). Although the resolution is lower than the one from HIRES, MOSAIC will be ideal to simultaneously spectroscopically follow-up up to 200 targets. MOSAIC will map the stars in the inner region of our Galaxy and it will also turn its gaze towards galaxies at high-redshift. With this combination of instruments, ELT will be ideal for the investigation of objects in the Milky Way and at much higher redshift. From space, JWST (Gardner et al., 2006), composed by hexagonal

mirrors with a total diameter of 6.6 m, will acquire infrared data. It will be able to explore the distant and infant Universe, and directly probe the star formation regions and the assembly of the galaxies. The science case for JWST does not stop with high redshift physics, but it comprehends also exoplanets and solar objects, star forming regions in the Local Volume, hence JWST will try to answer questions from the origins of life to the end of the dark ages and the first lights.

With all of these facilities and surveys, together with the aforementioned WEAVE and 4MOST, the Sky will be scanned from the near ultraviolet to the near infrared covering both the Milky Way and the extragalactic sources. Future chemo-dynamical investigations will largely benefit from this wealth of data creating an unprecedented multi-dimensional map of the Galaxy. On the other hand, the huge dataset will also cover high-redshift studies and it will be possible to probe directly the early Universe. Both the investigations of the Milky Way with its satellites and of systems at high-redshift will help to answer the questions on the formation of the first stars, the formation and evolution of galaxies, the nature and properties of the Dark Matter and Dark Energy.

As the amount of data will drastically increase, new fast and efficient analysis techniques must be developed. For instance, methods based on machine learning and neural network can provide the desired improvement. In my next position postdoc, I plan to use a convolutional neural network, called *StarNet* (Fabbro et al., 2018; Bialek et al., 2019; Venn et al., 2019) and developed at the University of Victoria, to extract chemical information from both high-resolution spectra and WEAVE+Pristine data. This tool has been tested and trained on both observed and synthetic stellar spectra. I will use this tool, and improve on it by incorporating my Bayesian inference methods (Sestito et al., 2019) to additionally infer precise stellar parameters with the Gaia space mission (upcoming DR3) photometry and astrometry, and therefore independently from the spectra themselves. This data analysis suite of tools will not only be extremely fast but also reduce the error budget in my upcoming chemo-dynamical analyses. In this way, I will rapidly and efficiently infer the chemical abundances and kinematical properties from the observations, with the ultimate goal to reconstruct a high precision and multi-dimensional map of the Milky Way.

In conclusion, in the coming years, our knowledge on the early Universe and all the topics related to Galactic Archæology or Palæontology will be largely expanded on and it will benefit from an unprecedented onslaught of new high-quality data and new high-performing analysis methods.

APPENDIX

A The Pristine survey - V. A bright star sample observed with SOPHIE

This Appendix contains a work in which I am one of the main co-authors, and it is published in MNRAS (Bonifacio et al., 2019). This work presents the high-resolution spectroscopic follow-up of bright low-metallicity candidates selected within the Pristine survey. The sample of bright candidates ($V < 14.5$ mag), composed by 40 stars, was observed at the Observatoire de Haute Provence (OHP) with the 1.93 meter telescope and SOPHIE échelle spectrograph ($R \sim 39000$).

As discussed in the Introduction, usually the Pristine candidates are selected calibrating the photometric metallicities with SDSS filters. This bright sample is in a magnitude range in which the SDSS filters saturate, and they was observed before Gaia DR2. In order to explore this brighter magnitudes, the Pristine colour-colour space was recalibrated using the APASS broad-band photometry. In this work, I recalibrated the photometry of the APASS filters to be used with the Pristine narrow-band filter, contributed to the observational list of bright candidates, I carried out part of the observations at OHP, and I performed the kinematical analysis.

A result of this brighter exploration is that the selection of low-metallicity stars with APASS photometry is not efficient as with SDSS passbands. No stars have been found in the extremely metal-poor regime, although 9 stars have a photometric metallicity [Fe/H] ≤ -3.0. 8 stars have been confirmed to be very metal-poor. However, since the observational campaign started before Gaia DR2, APASS was the only way to select bright metal-poor candidates. In this work, it is also shown that the selection of the low-metallicity stars with Gaia DR2 will be very promising.

Monthly Notices
of the
ROYAL ASTRONOMICAL SOCIETY

MNRAS **487,** 3797–3814 (2019)
Advance Access publication 2019 May 17

doi:10.1093/mnras/stz1378

The Pristine survey – V. A bright star sample observed with SOPHIE

P. Bonifacio [1]★ E. Caffau,[1] F. Sestito,[2,3] C. Lardo [4] N. F. Martin,[2,5] E. Starkenburg,[3] L. Sbordone,[6] P. François,[1] P. Jablonka,[1,4] A. A. Henden,[7] S. Salvadori [1,8,9] J. I. González Hernández,[10] D. S. Aguado,[11] V. Hill,[12] K. Venn,[13] J. F. Navarro,[1] A. Arentsen,[3] R. Sanchez-Janssen [14] and R. Carlberg[15]

Affiliations are listed at the end of the paper

Accepted 2019 May 14. Received 2019 May 14; in original form 2019 April 24

ABSTRACT

With the aim of probing the properties of the bright end of the Pristine survey and its effectiveness in selecting metal-poor stars, we selected a sample of bright candidate metal-poor stars combining Pristine *CaHK* photometry with APASS *gi* photometry, before the *Gaia* second data release became available. These stars were observed with the SOPHIE spectrograph at the 1.93 m telescope of Observatoire de Haute Provence and we used photometry and parallaxes from *Gaia* DR2 to derive their atmospheric parameters. Chemical abundances were determined from the spectra for 40 stars of the sample. Eight stars were confirmed to be very metal-poor ([Fe/H] < -2.0), as expected from the photometric estimate. No star was found with [Fe/H] < -3.0, although for nine stars the photometric estimate was below this value. Three multiple systems are identified from their multipeaked cross-correlation functions. Two metal-poor stars with [Fe/H] ≈ -1.0 have an age estimate of about 4 Gyr. Accretion from a satellite galaxy is a possible explanation for these 'young metal-poor stars', but they could also be field blue stragglers. Galactic orbits for our sample of stars allowed us to divide them into three classes that we label 'Halo', 'Thick', and 'Thin' and tentatively identify as halo, thick disc, and thin disc. We present a new method for deriving photometric metallicities, effective temperatures, and surface gravities by combining *Gaia* parallaxes, photometry, and Pristine *CaHK* photometry. Comparison with spectroscopic metallicities shows a very good agreement and suggests that we can further improve the efficiency of Pristine *CaHK* in selecting metal-poor stars.

Key words: stars: abundances – stars: atmospheres – stars: kinematics and dynamics – stars: Population II – Galaxy: abundances – Galaxy: evolution.

1 INTRODUCTION

Very old stars are witnesses of the early phases of galaxy evolution, and for this reason it is useful to study in detail large samples of such stars. Ever since Baade (1944) introduced the concept of Pop I and Pop II stars, it was clear that Pop II stars were rare objects characterized by high radial velocities (Oort 1926a,b) and peculiar spectra, with strong CH bands and weak CN bands (Lindblad 1922; Keenan 1942; Popper 1947; Keenan, Morgan & Münch 1948). It was not until the work of Schwarzschild, Spitzer & Wildt (1951) that it was clear that the weakening of the CN bands and strengthening of the CH bands could be ascribed to a lower abundance of metals in these stars. The same year Chamberlain & Aller (1951) demonstrated that the 'A-type subdwarfs' HD 140283 and HD 119445 are deficient in Ca and Fe with respect to the Sun.

In the following years the main sources of metal-poor stars were objective prism surveys (Bidelman & MacConnell 1973; Bond 1980). Follow-up observations then relied on suitable intermediate-band photometric observations (see e.g. Norris, Bessell & Pickles 1985, for DDO photometry) and, when possible on high-resolution spectroscopy (e.g. Luck & Bond 1981). At the end of the 20th century, two large-scale objective-prism survey boosted considerably the number of known metal-poor stars: the HK Survey (Beers, Preston & Shectman 1985, 1992) and the Hamburg-ESO survey (Christlieb 2003). Some attempts were made for a follow-up to determine photometric metallicities for the HK survey (Anthony-Twarog et al. 2000) using the *uvbyCa* system (Anthony-Twarog et al. 1991; Twarog & Anthony-Twarog 1995; Anthony-Twarog &

★ E-mail: Piercarlo.Bonifacio@observatoiredeparis.psl.eu

Twarog 1998), and using the *uvby* − *β* system (Schuster et al. 1996, 1999, 2004). However, this proved as time-consuming as medium resolution spectroscopy (e.g. Allende Prieto et al. 2000) and was not continued. Only in the 21st century, with the advent of wide-field CCD imagers, two surveys attempted to select metal-poor stars directly from photometry: the SkyMapper Southern Sky Survey (Keller et al. 2007; Casagrande et al. 2019) and the Pristine survey (Starkenburg et al. 2017, hereafter Paper I). Some attempts to select metal-poor stars have also been made using existing data bases of spectral types (Meléndez et al. 2016) or wide-band surveys (Schlaufman & Casey 2014). For the latter catalogue the success rate is of the order of 3 per cent for stars with [Fe/H] ≤ -3.0 and 36 per cent for stars with [Fe/H] ≤ -2.0 (Schlaufman & Casey 2014; Placco et al. 2019). Two extremely metal-poor stars selected from mismatch of the spectral-type with the colours and follow-up medium resolution spectroscopy have been published so far (Meléndez et al. 2016; Cain et al. 2018).

The Pristine Survey has proven to be successful in selecting extremely metal-poor stars at faint magnitudes, but has, so far, not been as successful in selecting bright stars. This is in spite of the fact that the *CaHK* filter is so narrow that even stars with $V = 10$ are not saturated. In this paper we continue the investigation of bright candidate metal-poor stars in the Pristine Survey, which we began in Caffau et al. (2017, hereafter Paper II). In Paper II for the photometric selection we combined the Pristine *CaHK* photometry with the broad-band SDSS photometry (York et al. 2000). We concluded that at the bright end, the SDSS photometry is not reliable because of saturation and we advocated the use of APASS (Henden et al. 2018, 2015; Henden & Munari 2014; Henden et al. 2009, https://www.aavso.org/apass) photometry instead. This survey is all-sky and has been designed precisely to bridge the magnitude gap between the all-sky photometry provided by the Tycho experiment on board the ESA Hipparcos satellite (Hoeg et al. 1997), with a limiting magnitude of $V \sim 11.5$, and the large deep photometric surveys, like SDSS (York et al. 2000), that have a bright limit of $g \sim 14.5$. The sample presented in this paper has been in fact selected using Pristine *CaHK* photometry and APASS photometry. We selected a sample of 47 stars, brighter than $g = 14.5$, and with estimated photometric metallicity below −1.5. The mean of the metallicities estimated from photometry is −2.51, and nine stars were expected to have metallicity ≤ -3.0. We observed them at Observatoire de Haute Provence with the SOPHIE (Bouchy & Sophie Team 2006) spectrograph, fed by the 1.93 m telescope. To determine atmospheric parameters and orbits for our program stars, we made use of the second data release (Arenou et al. 2018, hereafter Gaia DR2; Gaia Collaboration 2018) of the *Gaia* mission (Gaia Collaboration 2016).

2 OBSERVATIONS AND DATA REDUCTION

The SOPHIE spectra were acquired during two runs, the first between 2018 February 16 and February 20 (observer P. Bonifacio) and the second between 2018 April 13 and April 17 (observer F. Sestito). We always used the High Efficiency mode, which provides a resolving power $R = 39\,000$, with one fibre on the object (fibre A) and one on the sky (fibre B). The spectra cover the wavelength range 387.2–694.3 nm. The typical integration time was 1 h for each star. During the observations we aimed at a signal-to-noise ratio, as estimated from the exposure-meter, in the range 15–20. For some stars we took several exposures or lengthened the exposure time in order to reach this.

The spectra were processed on the fly by the SOPHIE pipeline that makes use of the calibration frames taken at the beginning of the night (bias, flat-field, Th-Ar, and Fabry-Perot étalon). The pipeline also does a cross-correlation analysis to determine the star's radial velocity v_r. We used the G2 or the K5 mask, depending on the star's effective temperature, for this cross-correlation. In spite of the low S/N ratio of the spectra, the formal error on the radial velocity estimated by the pipeline was of the order of a few tens of $\mathrm{m\,s^{-1}}$ and always less than $0.1\,\mathrm{km\,s^{-1}}$. The masks used are optimized for solar metallicity stars and some of our stars are definitively of lower metallicity. We measured some of the stars with our own software, using more appropriate masks (see Section 3), and we concluded that the radial velocities measured by the SOPHIE pipeline are accurate, although a more appropriate estimate on the error in the radial velocity, including the template mismatch, is $0.5\,\mathrm{km\,s^{-1}}$. In order to make the spectra ready for analysis with MyGIsFOS (Sbordone et al. 2014), we subtracted the sky from the spectrum in fibre A and Doppler shifted the spectrum by $-v_r$. To perform the sky subtraction, we did not simply subtract the spectrum of fibre B from that of fibre A, since this would have severely degraded the signal-to-noise ratio. Instead we performed a median filtering of the sky spectrum prior to subtraction, and subtracted a mean sky continuum. The drawback is that sky lines (both emission and absorption) cannot be subtracted. We therefore made sure not to use the spectral intervals affected by sky lines. In some cases, when the spectra were particularly noisy, we approximated the sky continuum by a spline fitted to a few continuum points selected interactively.

3 MULTIPLE SYSTEMS

Three stars in our sample showed multiple peaks in the cross-correlation function. Only one was observed at different epochs and for this system we can confirm that it is indeed a binary. For the other two stars, we cannot exclude the presence of an alignment of unbound stars along the line of sight, although in no case suitable neighbouring stars were found in the Gaia DR2 data. Since the SOPHIE pipeline is not designed to extract radial velocities for stars with multiple peaks in the cross-corelation function, the radial velocities were determined for all three stars by cross-correlation over the range 420–680 nm. We used a synthetic spectrum, with parameters close to the photometric estimates of each star, and the velocities were then measured by fitting gaussians to the peaks. The derived velocity is sensitive to the limits selected to perform the fit, repeated measurements allowed us to estimate an error of $0.3\,\mathrm{km\,s^{-1}}$.[1] For these stars we do not provide atmospheric parameters or chemical abundances. To estimate the effect of the veiling, some hypothesis on the luminosity ratio of the two stars should be made. A reliable estimate can only be made if the orbital parameters of the binary are known.

3.1 Pristine_111.9501+44.1449

This system was observed only on the night of 2018 February 18, barycentric julian date BJD = 2458 168.291 8411. The

[1]The estimated error here is smaller than what we estimated for the radial velocities measured by the SOPHIE pipeline, because in that case we estimated the error due to the template mismatch. In the case of the SOPHIE pipeline we could use only two templates for all the stars. Here the template has been selected carefully from a large library of synthetic spectra, to match closely the estimated parameters of each star.

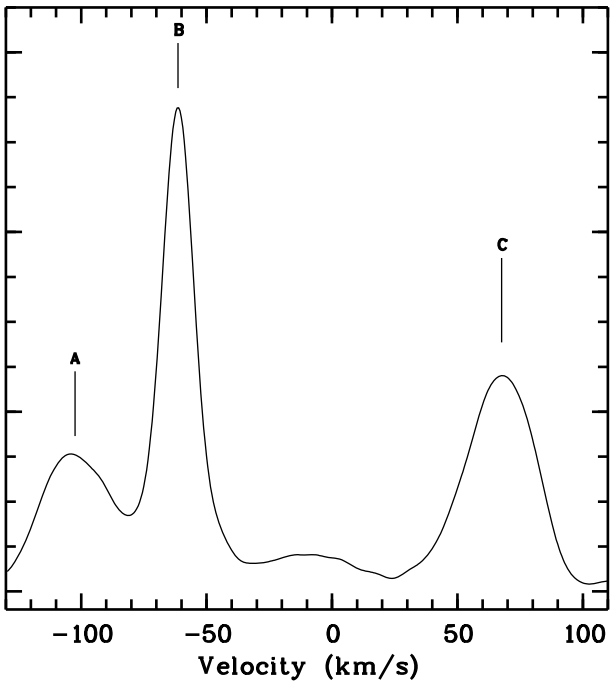

Figure 1. Cross-correlation functions for Pristine_111.9501+44.1449 for the observation of 2018 February 18. Three peaks are clearly visible, marked A, B, and C.

cross-correlation function shown in Fig. 1 shows three distinct peaks at $-102.4\,\mathrm{km\,s^{-1}}$, $-61.4\,\mathrm{km\,s^{-1}}$, and $+67.6\,\mathrm{km\,s^{-1}}$. In Gaia DR2 there is no nearby companion. Although we cannot exclude the possibility of a chance alignment, we consider this unlikely. In order to produce a composite spectrum with lines from each star, the stars must be of roughly the same luminosity. If the three stars were not at the same distance, this would only be possible if they were in different evolutionary stages, hence different intrinsic luminosity, in a way to exactly compensate the difference in distance. Although not impossible, this seems contrived and it is more likely that this is a triple system. If so, it must be hierarchical in order to be stable, thus there will be two stars of the triplet that are closer and a third one that orbits the couple. With a magnitude $G = 13.4$ this system will also have precise epoch radial velocities from the *Gaia* RVS. Nevertheless further observations of this system are strongly encouraged in order to allow to determine its orbit.

3.2 Pristine_113.6058+45.8841

This system was observed on three nights in 2018 February and on two nights in 2018 April. On the night of February 17, the cross-correlation function appears clearly double-peaked allowing for a clean determination of the radial velocities. The night after the cross-correlation function appeared again double peaked and the peaks moved closer by about $2\,\mathrm{km\,s^{-1}}$. At the other three epochs the cross-correlation function appears single peaked, although broad. At these epochs it is impossible to determine reliably the radial velocities of the two components, we estimated the mean velocity of the system by fitting a single gaussian to the peak. The distortion of the line profiles suggests that in April the two systems 'crossed', i.e. the system that appeared to the blue in February appears to the red in April. The measured radial velocities are summarized in Table 1. Given that this system is bright ($G = 12.4$), the *Gaia* mission will provide accurate epoch radial velocities that will provide a reliable spectroscopic orbit.

Table 1. Measured radial velocities of Pristine_113.6058+45.8841.

BJD	RV1 $\mathrm{km\,s^{-1}}$	RV2 $\mathrm{km\,s^{-1}}$	Mean $\mathrm{km\,s^{-1}}$	Comment
2458167.4587807	8.2	25.4	16.8	Double peak
2458168.3459378	9.2	24.4	16.8	Double peak
2458170.2661661			16.6	Single peak
2458224.3983226			16.6	Single peak
2458226.3199328			16.7	Single peak

3.3 Pristine_230.2650+00.9137

This system was observed only on 2018 April 16, barycentric julian date 2458 224.545 8990 and its cross-correlation function shows two clear peaks at $-110.4\,\mathrm{km\,s^{-1}}$ and $-68.4\,\mathrm{km\,s^{-1}}$. The Gaia DR2 reports a radial velocity for this star of $-85.1\,\mathrm{km\,s^{-1}}$ with an error of $5.9\,\mathrm{km\,s^{-1}}$ for an epoch of 2015.5 and with only five radial velocity measurements. This radial velocity is compatible, within errors, with the centre-of-mass velocity of the system derived from our measurements of $-89.4\,\mathrm{km\,s^{-1}}$. It should be noted that for a star of this magnitude ($G = 12.02$) the expected error on the radial velocity is less than $3\,\mathrm{km\,s^{-1}}$(Sartoretti et al. 2018). The fact that the error is larger than this supports the notion that the stars display radial velocity variations. At the end of the mission the accumulated data should allow us to determine a spectroscopic orbit. The system has a companion at 0.″01 in the Gaia DR2 data. Star Gaia DR2 4420599693613027456 has $G = 20.8$ and $G_{\mathrm{BP}} - G_{\mathrm{RP}} = 0.557$, it has no parallax or proper motion measurement. The star is too faint to be responsible for the secondary line system visible in our spectrum. If it were gravitationally bound to Pristine_230.2650+00.9137 at the distance of 308 pc, as derived from the *Gaia* parallax, its angular separation implies a linear separation of about 3 pc. Its colour is too blue to be an M dwarf, so if it were physically bound to Pristine_230.2650+00.9137 it could only be a white dwarf to explain the difference in luminosity. With the above considerations we believe that it is more likely that it is just a fortuitous alignment and Gaia DR2 4420599693613027456 and Pristine_230.2650+00.9137 are not gravitationally bound. However the *Gaia* end of mission data should be able to provide at least a proper motion for Gaia DR2 4420599693613027456 and that will allow to decide if the two are a common proper motion pair.

4 CHEMICAL ANALYSIS

4.1 Atmospheric parameters

To derive the stellar parameters, we used Gaia DR2. Reddennings were derived from the maps of Green et al. (2018). By using the parallax, we derived the absolute G magnitude.[2] This latter value combined with the *Gaia* ($G_{\mathrm{BP}} - G_{\mathrm{RP}}$) colour was compared to PARSEC (Bressan et al. 2012; Marigo et al. 2017) isochrones of metallicity close to the metallicity estimate, in order to derive the effective temperature (T_{eff}) and the surface gravity ($\log g$) of each star (see e.g. Fig. 2). This procedure can require few iterations: the metallicity of the isochrones first to compare to the star's photometry is initially taken from the photometric estimate

[2] $G_{\mathrm{abs}} = G + 5 + 5\log(\varpi)$

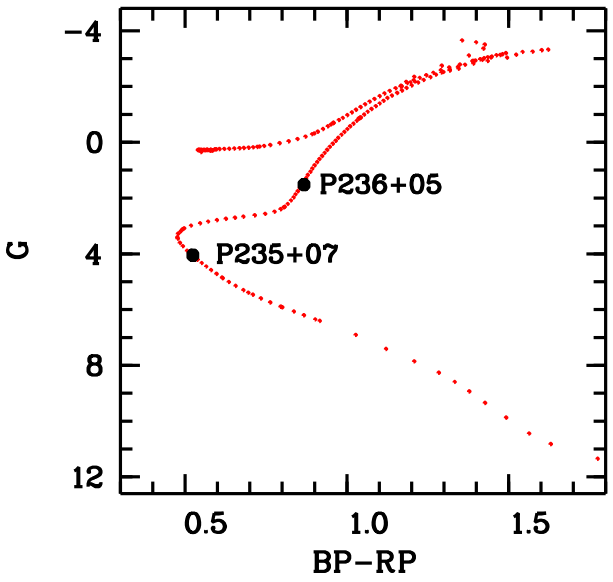

Figure 2. The comparison of the *Gaia* photometry to Parsec isochrones of [M/H] = −2 and an age of 9 Gyr for two metal-poor stars of the sample (Pristine_235.0537+07.5988 and Pristine_236.7635+05.4474).

(Starkenburg et al. 2017); with the derived $T_{\rm eff}$ and $\log g$ a new metallicity is obtained from the spectrum analysis; if this latter values is different from the initial guess, the comparison with isochrones of closer metallicities is repeated. The *Gaia* parallax is very good (relative error less than 10 per cent) for 85 per cent of our sample (40 stars). Only two stars have a relative error on the parallax larger than 30 per cent: Pristine_213.1910+14.7927 (relative error of 35 per cent) and Pristine_212.2541+11.4580 (relative error of 51 per cent). Unsurprisingly these two stars are the most distant since they are giants. The red giant branches of different metallicity are very closely packed in the colour magnitude diagram, implying that the surface gravity estimate obtained with our procedure is in this case robust against errors in the parallax. Changing the absolute magnitude of either star by what implied by a change of $\pm 1\sigma$ in the parallax would place the star far from any isochrone in the colour-magnitude diagram. Furthermore the metallicity is derived from the mean Fe I abundance, that is only very little affected by the adopted surface gravity. This fact also contributes to make our procedure robust against errors in the parallax.

We checked our derived $T_{\rm eff}$ against the temperatures derived using the Infrared Flux Method, as implemented by González Hernández & Bonifacio (2009), using 2MASS *JHK* photometry. We find that the two sets of temperature are very well correlated and compatible within errors. A linear fit provides $T_{\rm eff}$(adopted) = 1.0285 × $T_{\rm eff}$(IRFM) − 39.8 K, with an r.m.s around the fit of 105 K. We take this external comparison as representative of the systematic uncertainty in our effective temperatures. The uncertainties linked to the uncertainty in the *Gaia* photometry are negligible with respect to this.

For the majority of the stars, the age of the isochrone matching the photometry of the stars was larger than about 7 Gyr, and it was for all but four stars, larger than 5.5 Gyr. Pristine_195.1494+06.5655 is an evolved star, with [Fe/H] = −2.35. When we compare its *Gaia* photometry to an isocrone of −2.0 metallicity, we find that the star fit well for an age of 2.5 Gyr (see Fig. 3), this is strange for a metal-poor star. But at this stage in evolution, a slightly smaller reddening would reconcile the star with an older isochrone,

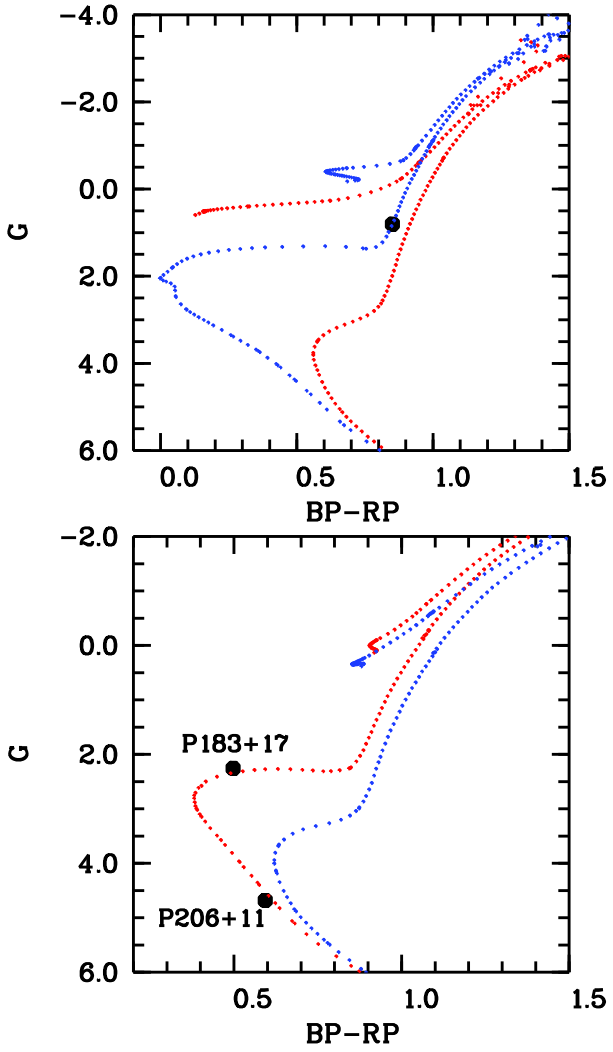

Figure 3. Upper panel: the comparison of *Gaia* photometry of Pristine_195.1494+06.5655 to Parsec isochrones of metallicity [M/H] = −2 for ages of 12.6 Gyr (red dots) and 2.5 Gyr (blue dots). Lower panel: the comparison of the *Gaia* photometry of Pristine_183.4550+17.0927 and Pristine_206.9304+11.8894 to Parsec isochrones at [M/H] = −1 for ages of 4 and 11 Gyr (red and blue, respectively).

we therefore do not consider its age estimate robust. The next youngest star is Pristine_113.7050+45.5860 (Age = 3.5 Gyr), with [Fe/H] = −0.57, that has an orbit consistent with the thin disc (see Section 5.1). Pristine_183.4550+17.0927 ([Fe/H] = −0.82) and Pristine_206.9304+11.8894 ([Fe/H] = −1.18) are consistent with an age of 4 Gyr. They both seem too young to be this metal-poor (see Fig. 3). In fact the Milky Way essentially shut down its vigourous star formation 9 Gyr ago, to start again forming stars at a lower rate at the time of the formation of the thin disc (Haywood et al. 2016), thus the young age of these stars suggests that they belong to the thin disc, while their kinematics and metallicity are consistent with the thick disc (see Section 5.1). They could be blue stragglers, like HR 3220 (Fuhrmann & Bernkopf 1999), but we note that stars that are young, metal-poor and α enhanced have also been pointed out by Haywood et al. (2013, see their fig. 17), Martig et al. (2015), and Chiappini et al. (2015). A young age and low metallicity may also be the sign of stars that have been formed in satellite galaxies or clusters and then accreted by the Milky Way. Among the ultra faint galaxies/clusters

Table 2. Stellar parameters.

Star	RA[a] h:m:s	Dec[a] d:m:s	V mag	RV km s^{-1}	$T_{\rm eff}$ 10^3 K	log g [cgs]	ξ km s^{-1}	[Fe/H]
Pristine_110.0459+43.0522	07:20:11.03	+43:03:08	13.47	− 84.9	5260	2.62	1.5	−2.42 ± 0.24
Pristine_110.4208+40.8947	07:21:41.01	+40:53:41	14.49	− 85.5	5643	3.60	1.5	−1.57 ± 0.40
Pristine_111.5919+44.0179	07:26:22.07	+44:01:05	13.09	− 51.4	6166	3.80	1.5	−0.70 ± 0.20
Pristine_112.0456+43.9914	07:28:10.90	+43:59:29	14.07	+15.3	6370	4.00	1.5	−0.53 ± 0.24
Pristine_112.3237+44.2279	07:29:17.70	+44:13:40	12.88	− 0.9	6319	4.29	1.5	−0.87 ± 0.22
Pristine_112.5667+45.9455	07:30:16.02	+45:56:44	13.20	− 67.3	6400	3.85	1.5	−0.76 ± 0.15
Pristine_112.6119+45.7784	07:30:26.88	+45:46:42	12.24	+22.1	6266	4.13	1.5	−0.77 ± 0.16
Pristine_113.0244+45.6965	07:32:05.86	+45:41:47	14.49	− 19.4	6165	4.00	1.5	−0.13 ± 0.26
Pristine_113.4132+41.9324	07:33:39.19	+41:55:57	14.08	+1.0	6183	4.00	1.5	−1.02 ± 0.24
Pristine_113.4275+45.6423	07:33:42.62	+45:38:32	14.35	− 13.9	6410	4.00	1.5	−0.49 ± 0.31
Pristine_113.6421+45.4681	07:34:34.12	+45:28:06	14.11	+8.6	6043	3.90	1.3	−0.58 ± 0.18
Pristine_180.8898+15.6500	12:03:33.55	+15:39:00	12.97	+15.7	6500	4.10	1.5	−1.71 ± 0.17
Pristine_180.8994+16.3260	12:03:35.88	+16:19:34	11.77	− 17.8	4970	2.36	2.0	−1.04 ± 0.13
Pristine_181.4437+13.4888	12:05:46.50	+13:29:20	13.15	− 45.7	6097	4.43	1.3	−0.88 ± 0.15
Pristine_182.2972+13.1228	12:09:11.35	+13:07:22	12.69	+92.0	6521	4.39	1.5	−1.46 ± 0.17
Pristine_183.1390+16.1839	12:12:33.34	+16:11:02	13.26	− 13.0	5130	3.54	1.0	−0.51 ± 0.15
Pristine_183.4550+17.0927	12:13:49.22	+17:05:34	13.38	+40.8	6725	3.83	1.5	−0.82 ± 0.12
Pristine_185.5596+15.5893	12:22:14.32	+15:35:21	13.85	+36.6	6463	4.28	1.5	−1.22 ± 0.15
Pristine_188.4543+15.1750	12:33:49.02	+15:10:30	12.60	+10.9	6072	4.10	1.3	−0.46 ± 0.15
Pristine_191.9208+16.0031	12:47:40.99	+16:00:11	12.79	+11.8	5433	2.35	1.5	−1.23 ± 0.14
Pristine_192.4508+12.7922	12:49:48.20	+12:47:54	13.44	− 8.3	6262	4.12	1.5	−1.38 ± 0.14
Pristine_193.5777+10.3945	12:54:18.66	+10:23:41	14.10	− 68.9	6300	4.55	1.5	−1.74 ± 0.21
Pristine_195.1494+06.5655	13:00:35.82	+06:33:56	12.37	+352.7	5370	2.80	1.5	−2.35 ± 0.24
Pristine_198.3167+14.9688	13:13:16.02	+14:58:08	13.12	10.8	6410	4.36	1.5	−0.59 ± 0.13
Pristine_206.8050+00.7423	13:47:13.20	+00:44:32	12.89	+59.4	5482	3.10	1.5	−1.92 ± 0.23
Pristine_206.9304+11.8894	13:47:43.29	+11:53:22	13.69	+72.5	6409	4.48	1.5	−1.18 ± 0.32
Pristine_212.2541+11.4580	14:09:00.98	+11:27:29	12.80	− 146.0	4514	1.05	2.0	−1.67 ± 0.35
Pristine_213.1910+14.7927	14:12:45.85	+14:47:34	13.94	− 61.2	5100	1.90	2.0	−2.81 ± 0.17
Pristine_216.1506+14.1298	14:24:36.14	+14:07:47	14.56	− 52.6	5754	2.50	1.5	−1.32 ± 0.33
Pristine_234.0338+12.6370	15:36:08.10	+12:38:13	13.01	− 170.8	6603	4.20	1.5	−2.49 ± 0.08
Pristine_235.0278+07.5059	15:40:06.65	+07:30:21	13.79	+65.7	6442	3.13	1.5	−1.12 ± 0.34
Pristine_235.0537+07.5988	15:40:12.89	+07:35:56	13.73	− 126.7	6680	4.32	1.5	−2.19 ± 0.13
Pristine_236.4719+15.3328	15:45:53.24	+15:19:58	14.25	− 142.5	6444	4.35	1.5	−1.75 ± 0.21
Pristine_236.7635+05.4474	15:47:03.25	+05:26:51	13.19	− 213.2	5370	2.94	1.5	−2.03 ± 0.17
Pristine_238.2716+07.5917	15:53:05.17	+07:35:30	14.42	− 86.1	5202	2.48	1.8	−2.32 ± 0.22
Pristine_240.2908+07.9401	16:01:09.79	+07:56:24	13.87	− 0.5	5023	1.78	2.0	−2.16 ± 0.24
Pristine_241.1299+06.3632	16:04:31.16	+06:21:48	14.12	− 159.9	6269	4.00	1.5	−1.57 ± 0.20
Pristine_246.4406+15.0900	16:25:45.74	+15:05:24	13.75	+107.5	6081	2.63	1.5	−1.59 ± 0.17
Multiple systems								
Pristine_111.9501+44.1449	07:27:48.06	+44:08:42	13.49					
Pristine_113.6058+45.8841	07:34:25.39	+45:53:03	12.52					
Pristine_230.2650+00.9137	15:21:03.59	+00:54:49	12.19					
F stars and stars with low S/N spectra								
Pristine_113.6744+45.8738	07:34:41.87	+45:52:26	14.29	+92.5				
Pristine_219.0145+11.6057	14:36:03.46	+11:36:20	14.02	− 4.0				
Pristine_232.8856+07.8678	15:31:32.54	+07:52:04	12.91	− 82.4				
Pristine_237.8581+07.1456	15:51:25.96	+07:08:44	13.73	− 50.0				

Note. [a] J2000, from Gaia DR2.
The number after the ± next to [Fe/H] is the line-to-line scatter.

that orbit the Milky Way, there are some that are metal-poor, yet considerably younger than the bulk of the metal-poor stars in the Milky Way. One good example is Crater (Belokurov et al. 2014; Bonifacio et al. 2015; Kirby, Simon & Cohen 2015; Voggel et al. 2016) with a metallicity of −1.7 and an age of only 7 Gyr. Presently the existence of a galaxy/cluster, not yet detected or disrupted, with metallicity −1.0 and an age of 4 Gyr cannot be excluded.

4.2 Chemical abundances from atomic lines

The chemical composition of the stars was derived by using the pipeline MyGIsFOS (Sbordone et al. 2014). MyGIsFOS can be used also to derive the stellar parameters through ionization equilibrium (to derive log g), and excitation equilibrium (for $T_{\rm eff}$), and can derive also the micro-turbulence from Fe I lines of different strength.

Table 3. Chemical abundances of iron, sodium, magnesium, aluminium, silicon, and sulphur.

Star	A(Fe I)	A(Fe II)	A(Na)	A(Mg)	A(Al)	A(Si I)	A(Si II)	A(S)
Pristine_110.0459+43.0522	5.10 ± 0.28	4.69 ± 0.08		5.36 ± 0.23				
Pristine_110.4208+40.8947	5.95 ± 0.40	5.54	4.54	6.43 ± 0.71				
Pristine_111.5919+44.0179	6.82 ± 0.20	6.79 ± 0.25	5.79	7.05 ± 0.05				
Pristine_112.0456+43.9914	6.99 ± 0.24	7.14 ± 0.42		7.15 ± 0.20				
Pristine_112.3237+44.2279	6.65 ± 0.15	6.59 ± 0.17	5.42	6.97 ± 0.16		6.96	7.05	
Pristine_112.5667+45.9455	6.76 ± 0.22	6.77 ± 0.12	5.88 ± 0.22	6.99 ± 0.13			7.21	
Pristine_112.6119+45.7784	6.75 ± 0.16	6.74 ± 0.18		7.11 ± 0.15		7.12		
Pristine_113.0244+45.6965	7.39 ± 0.26	7.43 ± 0.30		7.57 ± 0.05				
Pristine_113.4132+41.9324	6.50 ± 0.24	6.25 ± 0.26		6.91 ± 0.12				
Pristine_113.4275+45.6423	7.03 ± 0.31	7.10 ± 0.51	6.14	7.26 ± 0.20				
Pristine_113.6421+45.4681	6.94 ± 0.18	6.88 ± 0.16	5.57	7.05 ± 0.16				
Pristine_113.7050+45.5860	6.95 ± 0.25	6.92 ± 0.30		6.98 ± 0.15				
Pristine_180.0750+16.3239	7.48 ± 0.16	7.48 ± 0.16	6.60 ± 0.18	7.45 ± 0.15	6.81	7.68 ± 0.14	7.82 ± 0.01	7.70
Pristine_180.8898+15.6500	5.81 ± 0.17	5.61 ± 0.14		6.16 ± 0.13		6.98		
Pristine_180.8994+16.3260	6.48 ± 0.13	6.37 ± 0.18		6.91 ± 0.18				
Pristine_181.4437+13.4888	6.64 ± 0.15	6.44 ± 0.12	5.63 ± 0.15	7.12 ± 0.11		6.85 ± 0.01		
Pristine_182.2972+13.1228	6.06 ± 0.17	5.84 ± 0.15		6.40 ± 0.15				
Pristine_183.1390+16.1839	7.01 ± 0.15	6.66 ± 0.25	5.99 ± 0.09	7.33 ± 0.26		7.24 ± 0.15		
Pristine_183.4550+17.0927	6.70 ± 0.12	6.77 ± 0.10	5.73	7.21 ± 0.10		7.00	7.03	
Pristine_185.5596+15.5893	6.30 ± 0.15	6.07 ± 0.10		6.83 ± 0.20				
Pristine_188.4543+15.1750	7.09 ± 0.15	7.06 ± 0.21	5.95 ± 0.11	7.36 ± 0.25		7.23 ± 0.14	7.51	
Pristine_191.9208+16.0031	6.29 ± 0.14	6.17 ± 0.13	5.02	6.79 ± 0.13		6.57		
Pristine_192.4508+12.7922	6.14 ± 0.14	6.02 ± 0.13		6.67 ± 0.19				
Pristine_193.5777+10.3945	5.78 ± 0.21	5.52 ± 0.09	4.52	6.26 ± 0.28				
Pristine_195.1494+06.5655	5.17 ± 0.24	5.04 ± 0.14	3.77	5.60 ± 0.14		7.04		
Pristine_198.3167+14.9688	6.93 ± 0.13	6.81 ± 0.15	5.84 ± 0.06	7.20 ± 0.21			6.99	
Pristine_206.8050+00.7423	5.60 ± 0.23	5.74 ± 0.65		6.03 ± 0.21				
Pristine_206.9304+11.8894	6.34 ± 0.32	6.30		6.58 ± 0.08				
Pristine_212.2541+11.4580	5.85 ± 0.35	5.80 ± 0.49		6.83 ± 0.39				
Pristine_213.1910+14.7927	4.71 ± 0.17	5.00		5.03 ± 0.39				
Pristine_216.1506+14.1298	6.20 ± 0.33	6.09 ± 0.08		6.41 ± 0.35				
Pristine_234.0338+12.6370	5.03 ± 0.08	4.80 ± 0.13		5.45 ± 0.12				
Pristine_235.0278+07.5059	6.40 ± 0.34	6.59 ± 0.11		7.01 ± 0.32				
Pristine_235.0537+07.5988	5.33 ± 0.13	5.12 ± 0.04		5.74 ± 0.06				
Pristine_236.4719+15.3328	5.77 ± 0.21	5.60 ± 0.23	4.92	6.07 ± 0.11				
Pristine_236.7635+05.4474	5.49 ± 0.17	5.34 ± 0.25		5.98 ± 0.10				
Pristine_238.2716+07.5917	5.20 ± 0.22	4.93 ± 0.29	3.87	5.47 ± 0.24				
Pristine_240.2908+07.9401	5.36 ± 0.24	5.26 ± 0.34		5.95 ± 0.35				
Pristine_241.1299+06.3632	5.95 ± 0.20	5.91 ± 0.18		6.38 ± 0.12				
Pristine_246.4406+15.0900	5.93 ± 0.17	6.10 ± 0.31						

Note. The number after the ± next to an abundance is the line-to-line scatter, if there is none, the abundance has been derived from a single line.

With the quality of this sample of spectra, and also thanks to the availability of Gaia DR2, we prefered to use MyGIsFOS just to derive the chemical abundances. For the micro-turbulence, due to the general low signal-to-noise ratio, no weak line could be detected, so we fixed this value in the analysis, looking at stars with similar parameters (see e.g. Cayrel et al. 2004; Bonifacio et al. 2007). For stars with $T_{\rm eff}$ <5000 K or log g <2.0 we assumed $\xi = 2.0\,{\rm km\,s^{-1}}$. For stars with 5000 K≤ $T_{\rm eff}$we adopted $\xi = 1.5\,{\rm km\,s^{-1}}$. There are five exceptions to these criteria. For Pristine_246.4406+15.0900, that is an HB star, we assumed $\xi = 1.5$. For Pristine_238.2716+07.5917, that is a warm giant, we adopted $\xi = 1.8\,{\rm km\,s^{-1}}$, rather than $1.5\,{\rm km\,s^{-1}}$ because this provided a better balance of Fe I and Fe II. For the three high metallicity F-dwarfs Pristine_113.6421+45.4681, Pristine_180.0750+16.3239, and Pristine_188.4543+15.1750, with 6000 K ≤$T_{\rm eff}$≤6100 K, we adopted $\xi = 1.3\,{\rm km\,s^{-1}}$, intermediate between that of the Sun and Procyon (Steffen, Caffau & Ludwig 2013). In Table 2 we present the coordinates for all the data sample. Stellar parameters, including [Fe/H], are provided only for the stars for which we could perform a chemical analysis. In Tables 3, 4, and 5 we provide all the abundance measurements. For each element we provide the line-to-line scatter that can be used as an error estimate. In cases for which the line-to-line scatter is less than 0.1 dex, the error is dominated by the errors due to the uncertainties in the atmospheric parameters. When only one line is measured for a given element, there is no value provided. In these cases, an estimate of the statistical error could be derived from S/N in the spectrum, however one may also assume that also in these cases the error is dominated by the error on atmospheric parameters. To help estimating such errors, we provide in Table 6 the variation in abundances for star Pristine_183.1390+16.1839 for changes of ±100 K in $T_{\rm eff}$, ±0.3 dex in log g and $+0.2\,{\rm km\,s^{-1}}$ for ξ. In Fig. 4 the spectra, in the wavelength range of the Mg I b triplet, of the nine most metal-poor stars in the sample are shown. The quality of the spectra can be appreciated as well as the fact that even at very low signal-to-noise ratios the Mg I b triplet lines can be measured.

Table 4. Chemical abundances of calcium to manganese.

Star	A(Ca)	A(Sc)	A(Ti I)	A(Ti II)	A(V)	A(Cr I)	A(Cr II)	A(Mn)
Pristine_110.0459+43.0522	4.32			2.62 ± 0.31		2.66 ± 0.12		
Pristine_110.4208+40.8947	5.12 ± 0.49			4.64		4.38 ± 0.93		
Pristine_111.5919+44.0179	6.04 ± 0.17	2.79 ± 0.21	4.32 ± 0.12	4.73 ± 0.32		4.96 ± 0.18		4.91
Pristine_112.0456+43.9914	6.26 ± 0.30	3.16		5.09 ± 0.27		5.10 ± 0.14	5.89 ± 0.28	
Pristine_112.3237+44.2279	5.71 ± 0.16	2.44 ± 0.20	4.22 ± 0.10	4.39 ± 0.16		4.76 ± 0.11	4.97 ± 0.09	4.69 ± 0.19
Pristine_112.5667+45.9455	5.86 ± 0.16	2.73 ± 0.08	4.27 ± 0.30	4.47 ± 0.18		4.92 ± 0.10	4.88 ±	4.45 ± 0.02
Pristine_112.6119+45.7784	5.92 ± 0.16	2.64 ± 0.09	4.28 ± 0.21	4.51 ± 0.22		4.93 ± 0.24	4.84 ± 0.03	4.86 ± 0.07
Pristine_113.0244+45.6965	6.44 ± 0.22					4.78		
Pristine_113.4132+41.9324	5.64 ± 0.22	2.43 ± 0.06	4.41 ± 0.05	4.35 ± 0.21		4.64 ± 0.03		
Pristine_113.4275+45.6423	6.02 ± 0.31	2.82	4.62	4.90 ± 0.60		4.90 ± 0.13		
Pristine_113.6421+45.4681	6.06 ± 0.18	2.82 ± 0.20	4.62 ± 0.34	4.89 ± 0.36		5.25 ± 0.25	5.27 ± 0.01	4.98 ± 0.23
Pristine_113.7050+45.5860	6.01 ± 0.25	2.94		4.83 ± 0.14		5.06 ± 0.02		
Pristine_180.0750+16.3239	6.43 ± 0.15	3.62	5.00 ± 0.21	4.80 ± 0.14	4.10 ± 0.05	5.60 ± 0.15	5.53 ± 0.08	5.60 ± 0.15
Pristine_180.8898+15.6500	5.08 ± 0.11	1.57 ± 0.15	3.60 ± 0.22	3.67 ± 0.17		3.85 ± 0.15		
Pristine_180.8994+16.3260	5.66 ± 0.10		4.25 ± 0.10	4.10 ± 0.15				4.47
Pristine_181.4437+13.4888	5.80 ± 0.11	2.42 ± 0.29	4.41 ± 0.09	4.40 ± 0.11		4.80 ± 0.07	4.72	4.38 ± 0.11
Pristine_182.2972+13.1228	5.15 ± 0.15	1.86 ± 0.11	3.82 ± 0.11	3.83 ± 0.18		4.20 ± 0.19		
Pristine_183.1390+16.1839	6.26 ± 0.15	2.95 ± 0.16	4.87 ± 0.11	4.65 ± 0.25	3.88 ± 0.15	5.30 ± 0.13	4.95 ± 0.25	5.12 ± 0.16
Pristine_183.4550+17.0927	5.87 ± 0.12	2.76 ± 0.21	4.39 ± 0.22	4.58 ± 0.10		4.95 ± 0.21	4.82 ± 0.01	4.50
Pristine_185.5596+15.5893	5.50 ± 0.11	2.23 ± 0.11	4.07 ± 0.19	4.10 ± 0.09		4.32 ± 0.09		
Pristine_188.4543+15.1750	6.13 ± 0.12	2.84 ± 0.18	4.69 ± 0.22	4.75 ± 0.17		5.29 ± 0.09	5.24 ± 0.20	5.13 ± 0.07
Pristine_191.9208+16.0031	5.38 ± 0.15	2.08 ± 0.09	3.97 ± 0.10	4.05 ± 0.16		4.33 ± 0.12	4.20 ± 0.06	3.94 ± 0.13
Pristine_192.4508+12.7922	5.37 ± 0.16	2.03 ± 0.05	3.98 ± 0.18	4.08 ± 0.11		4.27 ± 0.17		
Pristine_193.5777+10.3945	5.02 ± 0.09	1.42		3.50 ± 0.20		3.79 ± 0.17		
Pristine_195.1494+06.5655	4.49 ± 0.24			2.90 ± 0.18		3.23 ± 0.43		
Pristine_198.3167+14.9688	5.97 ± 0.12	2.58 ± 0.13	4.53 ± 0.06	4.54 ± 0.14		5.07 ± 0.05	5.03 ± 0.08	4.96 ± 0.04
Pristine_206.8050+00.7423	4.73 ± 0.22			3.74 ± 0.19		3.48 ± 0.10		
Pristine_206.9304+11.8894	5.51							
Pristine_212.2541+11.4580	4.77 ± 0.25	1.67	3.74 ± 0.41	3.43 ± 0.41		4.29 ± 0.46		
Pristine_213.1910+14.7927	4.36							
Pristine_216.1506+14.1298	5.52 ± 0.35	2.36 ± 0.20		4.24 ± 0.38		4.15 ± 0.25		
Pristine_234.0338+12.6370	4.56	0.82		2.87 ± 0.08		3.08		
Pristine_235.0278+07.5059	5.37 ± 0.11	2.44 ± 0.46	3.93 ±	4.36 ± 0.35		4.93 ± 0.49	4.61	
Pristine_235.0537+07.5988	4.43 ± 0.09	1.01		3.07 ± 0.11			3.59	
Pristine_236.4719+15.3328	4.89 ± 0.22			3.72 ± 0.25		3.60 ± 0.03		
Pristine_236.7635+05.4474	4.69 ± 0.20	1.36 ± 0.19	3.20 ± 0.11	3.24 ± 0.12		3.43 ± 0.09		
Pristine_238.2716+07.5917	4.47			3.01 ± 0.09		3.39 ± 0.77		
Pristine_240.2908+07.9401	4.73 ± 0.37	1.61 ± 0.61	3.02 ± 0.20	3.10 ± 0.09		3.14 ± 0.09		
Pristine_241.1299+06.3632	5.30 ± 0.21	1.26		3.83 ± 0.18		3.77 ± 0.18		
Pristine_246.4406+15.0900	5.26 ± 0.41	1.65	3.56 ± 0.03	3.71 ± 0.17			4.28 ± 0.21	

Note. The number after the ± next to an abundance is the line-to-line scatter, if there is none, the abundance has been derived from a single line.

The agreement between the Fe abundances derived from Fe I and Fe II lines is generally good, and the mean difference A(Fe I) – A(Fe II) is 0.09 dex with a standard deviation of 0.15 dex. We note however that there is a tendency, especially at low metallicity for [Fe I/H] to be larger than [Fe II/H], this cannot be ascribed to NLTE or NLTE-3D effects, neglect of which produces the opposite effect (Amarsi et al. 2016). This is an example that shows how a non-spectroscopic gravity does not, in general, satisfy spectroscopic diagnostic criteria. This is likely due to inadequacies in our modelling.

In Figs 5–7 the [X/Fe] versus [Fe/H] are shown. The solar abundances are from Lodders, Palme & Gail (2009), except for S and Fe, whose solar values are from Caffau et al. (2011). The α-elements, as expected, are enhanced with respect to Fe in the metal-poor stars. The large scatter in Fig. 5 is due to the low S/N in the observed spectra. One star, Pristine_212.2541+11.8045, shows a quite large enhancement in Mg, [Mg/Fe] $\sim$ 1. The Mg abundance is derived from three Mg I lines (470, 517, and 552 nm) with a large line-to-line scatter of 0.39 dex in wavelength ranges where the S/N ratio is from 4 to 9. We think the star is in fact Mg rich, but probably less than 1 dex. The iron-peak elements, shown in Fig. 6, are within the uncertainties, compatible with Fe.

Sr and Ba (Fig. 7) show a large scatter. According to Korotin et al. (2015), for our sample of stars the NLTE corrections for Ba are generally not large, within −0.1 dex for the unevolved stars, only for few giants the correction can be up to −0.2 or −0.3 dex. These corrections do not change the general picture of the behaviour of the Ba abundance. Two stars (Pristine_234.0338+12.6370 and Pristine_235.0278+07.5059) show a large [Ba/Fe]>0.6. For the latter star the Ba abundance is based on one single line, the Ba II line at 649 nm with S/N = 24. The Ba abundance for Pristine_235.0278+07.5059 is derived from the Ba II line at 693 nm where S/N = 12.

Seven stars (Pristine_112.3237+44.2279, Pristine_180.0750+16.3239, Pristine_180.8898+15.6500, Pristine_188.4543+15.1750, Pristine_192.4508+12.7922, Pristine_234.0338+12.6370, and Pristine_236.4719+15.3328), all dwarfs, show the Li doublet at 670.7 nm. The abundance we derive is uncertain

Table 5. Chemical abundances of cobalt to barium.

Star	A(Co)	A(Ni)	A(Cu)	A(Zn)	A(Sr)	A(Y)	A(Zr)	A(Ba)
Pristine_110.0459+43.0522								
Pristine_110.4208+40.8947					2.34			1.00
Pristine_111.5919+44.0179		5.51			2.87 ± 0.09			1.78 ± 0.38
Pristine_112.0456+43.9914		5.82 ± 0.21			2.84			1.89 ± 0.20
Pristine_112.3237+44.2279		5.47 ± 0.17		3.77	2.54	1.04		
								1.59 ± 0.10
Pristine_112.5667+45.9455		5.45 ± 0.09		4.02	2.94	1.51 ± 0.09		1.84 ± 0.40
Pristine_112.6119+45.7784		5.53 ± 0.13		3.96	2.82 ± 0.33			1.83
Pristine_113.0244+45.6965								
Pristine_113.4132+41.9324		5.21			2.29			1.44 ± 0.01
Pristine_113.4275+45.6423		5.49			2.27 ± 0.41			1.97 ± 0.26
Pristine_113.6421+45.4681		5.65 ± 0.16			3.24			1.94 ± 0.09
Pristine_113.7050+45.5860					2.60			2.18
Pristine_180.0750+16.3239	5.28	6.32 ± 0.20		4.55	2.88	1.89 ± 0.04		2.08 ± 0.14
Pristine_180.8898+15.6500		4.59			1.23			0.84 ± 0.22
Pristine_180.8994+16.3260		5.31 ± 0.02			2.34			1.15 ± 0.20
Pristine_181.4437+13.4888		5.38 ± 0.21		3.82 ± 0.04				1.48 ± 0.13
Pristine_182.2972+13.1228		4.71			1.75 ± 0.18			0.82 ± 0.20
Pristine_183.1390+16.1839	5.29	5.80 ± 0.21	4.15 ± 0.49	4.06 ± 0.41	2.63	1.49 ± 0.27	2.44	1.82 ± 0.23
Pristine_183.4550+17.0927		5.50 ± 0.11		3.93	2.65	1.20		1.57 ± 0.19
Pristine_185.5596+15.5893		5.03 ± 0.03			1.73			1.05 ± 0.14
Pristine_188.4543+15.1750		5.84 ± 0.17	3.80	4.30	2.55	1.32 ± 0.14		1.88 ± 0.11
Pristine_191.9208+16.0031		5.03 ± 0.16	2.83	3.39 ± 0.03	2.14	0.62 ± 0.01		1.21 ± 0.05
Pristine_192.4508+12.7922		4.93 ± 0.02			2.11	1.05		
								1.15 ± 0.03
Pristine_193.5777+10.3945								0.50
Pristine_195.1494+06.5655		3.64			1.40 ± 0.42			−0.10 ± 0.26
Pristine_198.3167+14.9688		5.64 ± 0.14		3.89 ± 0.08	2.71	1.43		1.75 ± 0.18
Pristine_206.8050+00.7423		4.15						0.39 ± 0.29
Pristine_206.9304+11.8894								1.29
Pristine_212.2541+11.4580		4.70 ± 0.42						0.54
Pristine_213.1910+14.7927								
Pristine_216.1506+14.1298					1.97			1.15 ± 0.33
Pristine_234.0338+12.6370					0.28			1.04
Pristine_235.0278+07.5059		5.16						2.21
Pristine_235.0537+07.5988					1.05			
Pristine_236.4719+15.3328								0.67 ± 0.11
Pristine_236.7635+05.4474		4.18			1.15 ± 0.08			0.33 ± 0.20
Pristine_238.2716+07.5917		4.02			0.81			0.07 ± 0.21
Pristine_240.2908+07.9401		3.87						−0.29 ± 0.10
Pristine_241.1299+06.3632		4.79			1.86			0.84 ± 0.22
Pristine_246.4406+15.0900						0.49 ± 0.22		

Note. The number after the ± next to an abundance is the line-to-line scatter, if there is none, the abundance has been derived from a single line.

due to the low S/N ratio, but, for the metal-poor stars, it is compatible with the Spite plateau (Spite & Spite 1982). Star Pristine_180.0750+16.3239 is at solar metallicity and its spectrum shows a strong Li feature. This is not uncommon for metal-rich stars to have a high Li abundace (see e.g. Mott et al. 2017). Its A(Li)-LTE abundance is of 2.80 ± 0.10; the 3D-NLTE correction of 0.05 (Harutyunyan et al. 2018) is small when compared to the uncertainty related to the quality of this spectrum.

4.3 Carbon abundances from the *G* band

For all the stars with $T_{\rm eff}$ >5800 K the *G* band is too weak to be measurable on our spectra. For the 13 cooler stars we managed to derive the C abundance by applying an additional smoothing with a Gaussian of 10 km s^{-1} FWHM and fitting the band with synthetic spectra computed in 1D LTE. The line list adopted for the CH lines is that of Masseron et al. (2014). The derived C abundances are provided in Table 7. The uncertainty is dominated by the continuum placement and we estimated it to be 0.3 dex for all stars. All of the stars qualify as carbon normal, according to the scheme proposed by Bonifacio et al. (2018b).

4.4 F stars and low S/N stars

We could not derive [Fe/H] for four stars. Pristine_219.0145+11.6057 and Pristine_232.8856+07.8678 are F stars, with a sizeable $v \sin i$ in the range 15–30 km s^{-1}, of metallicity close to solar. Such stars are not adapted to the methods of analysis we use in this work, therefore we only provide radial velocities. Pristine_219.0145+11.6057 shows the core of Hα in emission. For Pristine_113.6744+45.8738 and Pristine_237.8581+07.14566, we have a spectrum with very poor signal-to-noise ratio and only the radial velocity is provided.

Table 6. Variations in abundances, in the sense 'adopted' – 'new value', for star Pristine_183.4550+17.0927 as a result of a change in one of the atmospheric parameters.

Abundance	$T_{\rm eff}$ +100 K	$T_{\rm eff}$ −100 K	log g +0.3 dex	log g -0.3 dex	ξ +0.2 km s^{-1}
A(Na I)	−0.06	+0.07	−0.02	+0.04	+0.03
A(Mg I)	−0.11	+0.12	−0.09	+0.14	+0.05
A(Si I)	+0.01	−0.01	+0.06	−0.06	+0.02
A(Ca I)	−0.09	+0.10	−0.03	+0.08	+0.07
A(Sc II)	−0.02	+0.05	+0.16	−0.15	+0.10
A(Ti I)	−0.12	+0.13	−0.02	+0.02	+0.08
A(Ti II)	−0.03	+0.03	+0.09	−0.10	+0.07
A(V I)	−0.12	+0.13	+0.00	+0.00	+0.01
A(Cr I)	−0.10	+0.14	−0.01	+0.06	+0.10
A(Cr II)	+0.06	−0.05	+0.15	−0.14	+0.09
A(Mn I)	−0.02	+0.09	+0.06	+0.06	+0.15
A(Fe I	−0.09	+0.10	−0.03	+0.04	+0.09
A(Fe II)	+0.02	−0.02	+0.12	−0.16	+0.10
A(Co I)	−0.05	+0.04	+0.05	−0.07	+0.15
A(Ni I)	−0.07	+0.06	+0.02	−0.02	+0.08
A(Cu I)	−0.05	+0.11	+0.05	+0.02	+0.10
A(Zn I)	−0.01	+0.02	+0.08	−0.08	+0.07
A(Sr II)	−0.02	+0.02	+0.10	−0.12	+0.03
A(Y II)	+0.00	+0.00	+0.18	−0.18	+0.15
A(Zr II)	−0.01	+0.06	+0.15	−0.17	+0.05
A(Ba II)	−0.04	+0.04	+0.10	−0.10	+0.19

5 GALACTIC ORBITS

It is useful to use the astrometric solution from Gaia DR2 to derive distances and orbital parameters for our sample of stars. From the parallax, we first calculate the distance probability distribution function multiplying the parallax likelihood as introduced by Bailer-Jones (2015) by a proper Milky Way density profile prior that takes into account the disc and the halo component of the Galaxy as described in Sestito et al. (2019). We assume as a zero offset for the parallax the value $\varpi_0 = -0.065$ mas, this is an average of the offsets found by Arenou et al. (2018) from comparison to external catalogues of open clusters. We underline that the final classification of the orbits would have been the same even if we had not applied this offset. With the inferred distances, the radial velocities measured from high-resolution spectroscopy and the exquisite proper motion from Gaia DR2, we computed the orbital parameters using `galpy`[3] package (Bovy 2015). We use their *MWPotential14*, which is a Milky Way gravitational potential composed of a power law, exponentially cut-off bulge, a Miyamoto Nagai Potential disc, and a Navarro, Frenk & White (1997) dark matter halo, but using a more massive halo with a mass of 1.2×10^{12}M$_\odot$ compatible with the value from Bland-Hawthorn & Gerhard (2016) (versus 0.8×10^{12}M$_\odot$ for the halo used in *MWPotential14*). We assume that the distance between the Sun and the Galactic centre is 8.0 kpc, that the Local Standard of Rest circular velocity is $V_c = 239$ km s^{-1}, and that the peculiar motion of the Sun is ($U_0 = -11.10$ km s^{-1}, $V_0 + V_c = 251.24$km s^{-1}, $W_0 = 7.25$km s^{-1}) as described in Schönrich, Binney & Dehnen (2010; note that we changed the sign of U_0 since in our adopted system U is positive towards the Galactic anticentre).

[3] http://github.com/jobovy/galpy

As a check of the robustness of our derived orbits, we computed Galactic orbits also using `gravpot16` (Fernández-Trincado 2019), which assumes a semi-steady gravitational potential based on the Besançon model[4] and assuming no offset in the parallaxes. The classification of the orbits we arrive at is the same for most stars, the only noticeable exception is Pristine_216.1506+14.1298, which in this case has an unbound orbit. Even with this potential, however, making the parallax larger by 1σ turns the orbit in bound although still with a very large apocentric distance. The space velocities and some of the quantities defining the Galactic orbits can be found Tables A1 and A2 in Appendix A, available online.

5.1 Orbit classification

In order to investigate the relationships (if any) between chemical and kinematical properties of the stars, we decided to classify the orbits by using a minimum of assumptions on the kinematical structure of the Milky Way. We therefore decided to use as main classification parameter $Z_{\rm max}$, the maximum excursion of the star from the Galactic plane and the rotational action $J_\phi/J_{\phi\odot}$, normalized to the solar value.[5] We classify as 'Halo' all stars with $Z_{\rm max} > 4$ kpc. We classify as 'Thin' all stars with $Z_{\rm max} \leq 1$ kpc and $J_\phi/J_{\phi\odot} > 0.2$. All the other stars have either 1 kpc $< Z_{\rm max} < 4$ or ($Z_{\rm max} \leq 1$ kpc and $J_\phi/J_{\phi\odot} \leq 0.2$) and these we call 'Thick'. Note that although the names we chose are clearly suggestive of the different components of the Galaxy, our classification is purely phenomenological and based on the stellar dynamics, without any assumption as to the origin or history of any component. This approach is different from what is often used in the literature (see e.g. Bensby & Lind 2018), where knowledge of the kinematical parameters of each population is assumed and a probability is derived for each star to belong to any of the assumed populations. In our case the only assumption is the underlying Galactic potential used to compute the orbits. As discussed above, the use of different plausible potentials and methods of integration leads to the same classification.

Let us now examine the chemical and kinematical properties of the different classes of stars. In Fig. 8 [α/Fe], defined as the average of [Mg/Fe] and [Ca/Fe] is shown as a function of [Fe/H] and different symbols identify the different classes of stars. It is obvious that there is a trend of decreasing [α/Fe] with increasing [Fe/H] both for the 'Thin' stars and for the 'Halo' stars. The visual perception is confirmed by the non-parametric Kendall's τ test that provides a probability of correlation of 99.87 per cent for the 'Thin' sample and 98.77 per cent for the 'Halo' sample. On the other hand the 'Thick' sample shows no hint of correlation and displays a constant [α/Fe] = 0.39 with a dispersion of 0.07 dex, that is far smaller than the errors on the single data points. If we ignore the presence of a trend with [Fe/H] for the 'Halo' sample, we find a mean [α/Fe] = 0.47 with a small dispersion of 0.08, again, much smaller than the errors on the single measurements. Considering these dispersions, we cannot make a strong claim that [α/Fe] is different in the two samples, yet there is an indication. If we couple this indication with the presence of a trend with [Fe/H] for the 'Halo' and none for the 'Thick', we can conclude that the two samples show a different behaviour of [α/Fe]. Another feature that stands out in Fig. 8 is that the 'Thin' sample extends to much lower

[4] https://fernandez-trincado.github.io/GravPot16/index.html

[5] A star with $J_\phi/J_{\phi\odot} = 1$ rotates like the Sun around, the Galactic center, a low value indicates a slow rotation, and a negative value a retrograde rotation.

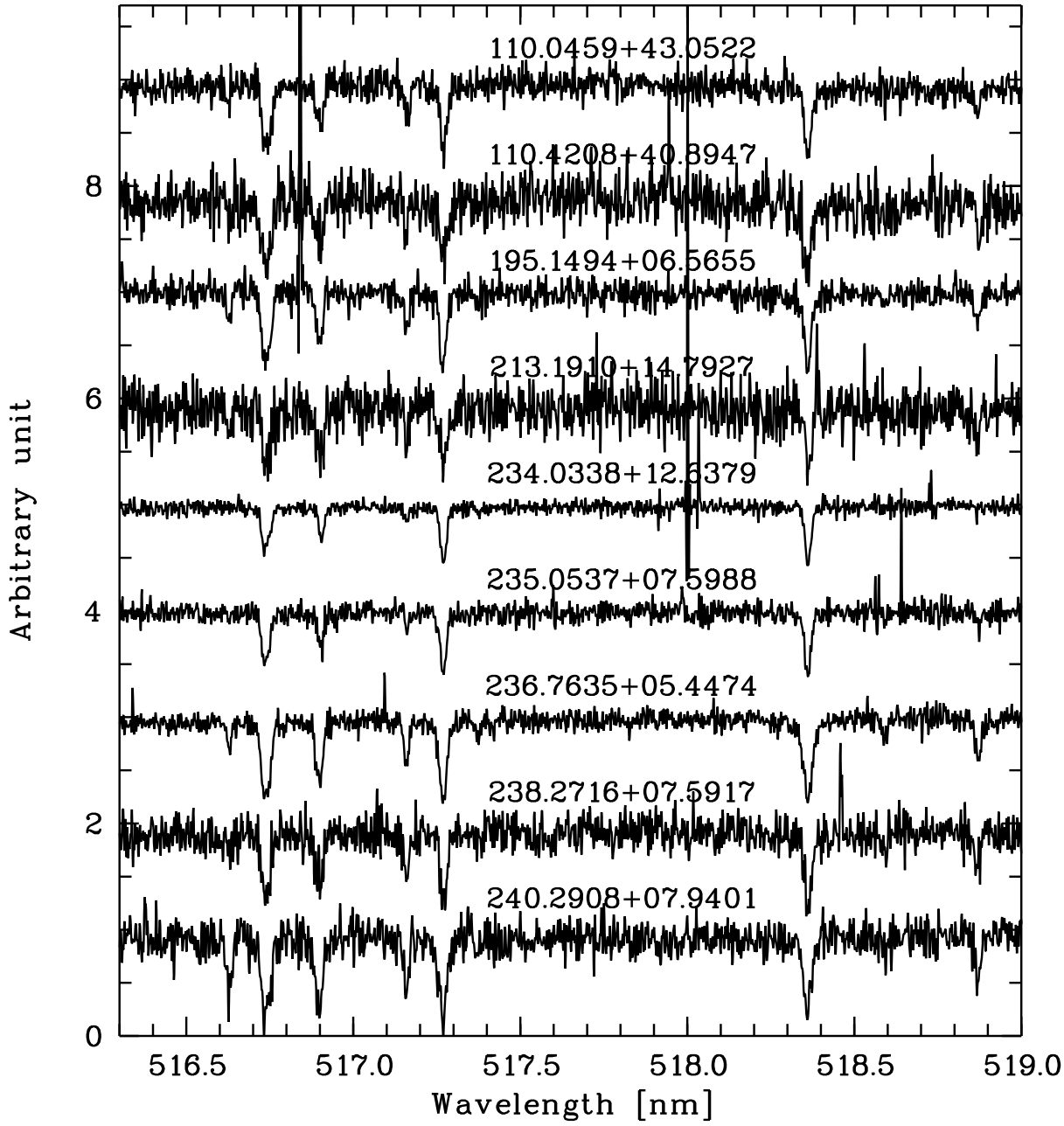

Figure 4. The Mg I b region of the observed spectra for the most metal-poor stars in the sample.

metallicities than what are normally associated with the Thin disc and the most metal-poor stars display an α enhancement similar to that of the 'Thick' sample. This, perhaps, should not come as a surprise since we know of extremely metal-poor stars such as 2MASS J1808–5104 with [Fe/H] $= -3.84$ (Spite et al. 2019) that is on a thin disc orbit (Schlaufman, Thompson & Casey 2018; Sestito et al. 2019).

In Fig. 9 we show [Fe/H] (upper panel) and [α/Fe] as a function of the apocentre distance. The 'Thin' sample has on average a higher metallicity than the other two samples. It has also a considerable extension in $r_{\rm apo}$, reaching out to 18 kpc. The 'Thick' sample, instead, has a much wider spread in metallicity, but is not as spatially extended, it reaches out to 14.3 kpc, and half of the sample has $r_{\rm apo} < 10$ kpc. The 'Halo' sample is the most spatialy extended.

In Fig. 10, [Fe/H] (upper panel) and [α/Fe] are shown as a function of age. Our age estimates are very crude and essentially a by-product of the parameter determination procedure, yet we believe that it is worth to have a look at them. The overall trend agrees with the expectations of cosmological chemical evolution models coupled with *N*-body simulation of the Milky Way formation (e.g. Salvadori et al. 2010). In the upper panel the 'Thin' and 'Thick' samples show a hint of an age–metallicity correlation, although, statistically, for both samples the probability of correlation is slightly less than 95 per cent and thus should not be considered significant. What is probably more interesting is that for the 'Thick' sample,

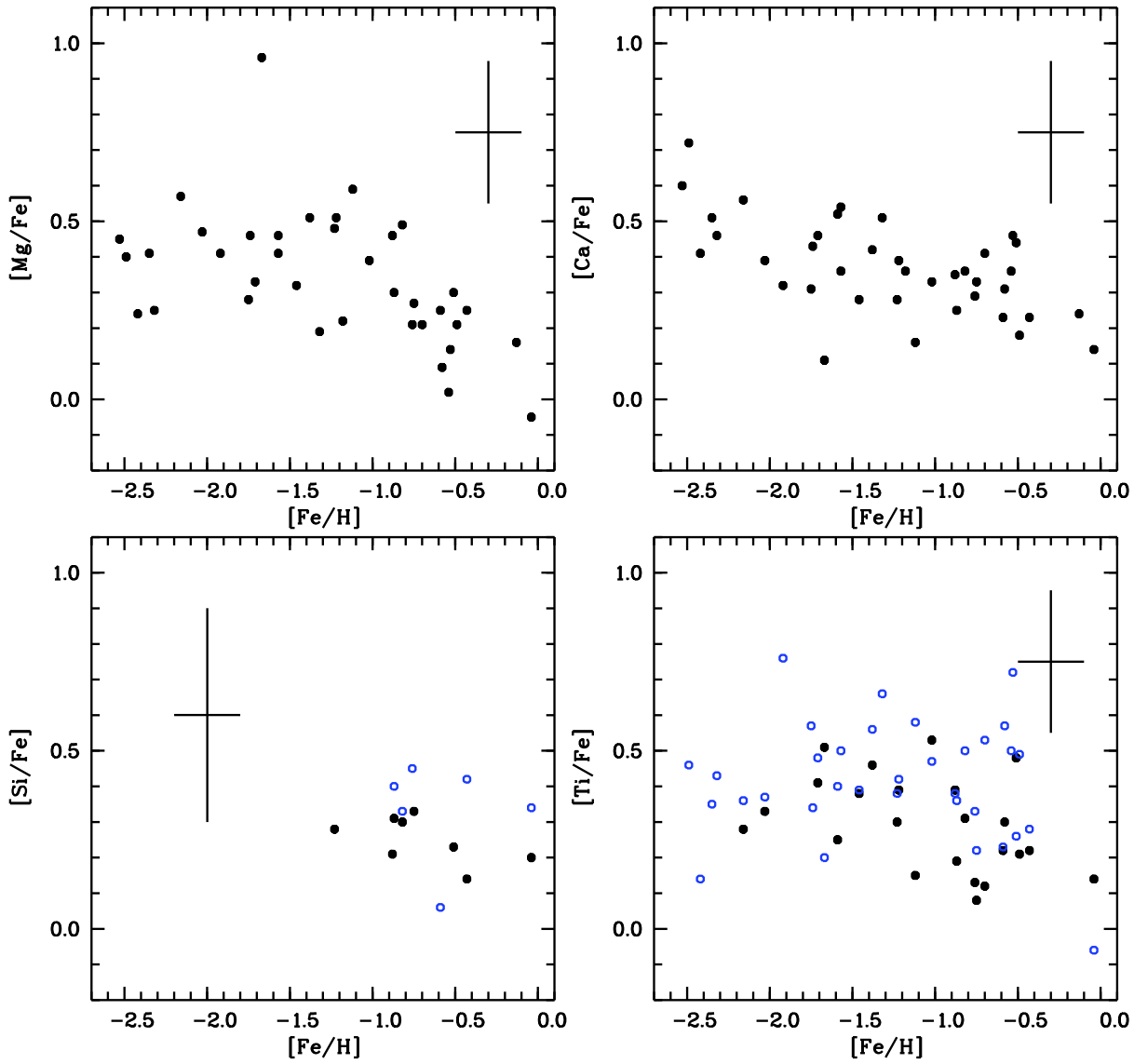

Figure 5. The α-elements: solid black are the neutral species, and open blue the ionized ones.

at old ages there is a large dispersion in [Fe/H], which is what cosmological chemical evolution models typically predict for the early evolutionary stages (e.g. Salvadori et al. 2010). The 'Halo' sample shows no hint of an age–metallicity correlation. Of the three samples, only the 'Thin' sample shows a clear correlation between age and [α/Fe] (99.71 per cent probability as estimated from Kendall's τ) and, as expected, the oldest stars have the higher [α/Fe].

5.2 Shooting stars

Two of the 'Halo' stars have large apocentric distances: Pristine_195.1494+06.5655 ($R_{\rm apo}$ = 40.7 kpc) and Pristine_216.1506+14.1298 ($R_{\rm apo}$ = 36.2 kpc). It is clear that with such large distances the influence of the nearby satellites of the Milky Way should be taken into account and that the stars may be in fact unbound to the Galaxy. For Pristine_216.1506+14.1298 the integration with the shallower potential used by the Besançon model and the use of the parallax at face value, without applying any offset, leads to an unbound orbit. From the chemical point of view, neither of these two stars seems different from the other 'Halo' stars. For Pristine_195.1494+06.5655, we already noted its possibly young age (4 Gyr), which could be easily understood if the star was formed recently in a satellite galaxy and then stripped and is currently just traversing the Milky Way (or has been accreted, if the orbit is, indeed bound).

5.3 Non-rotating old thin disc stars

Among our 'Thick' sample of stars there are three that have orbits that stay very close to the Galactic disc and could therefore be considered thin disc stars: Pristine_206.9304+11.8894 ($Z_{\rm max}$ = 1.0 kpc), Pristine_235.0537+07.5988 ($Z_{\rm max}$ = 0.5 kpc), and Pristine_236.4719+15.3328 ($Z_{\rm max}$ = 1.0 kpc). In spite of this all three stars have very elliptical orbits and low rotational velocities. Furthermore they are all metal-poor. Our condition on the rotational velocities places these stars in the 'Thick' sample and not in the 'Thin' sample. Pristine_235.0537+07.5988 and

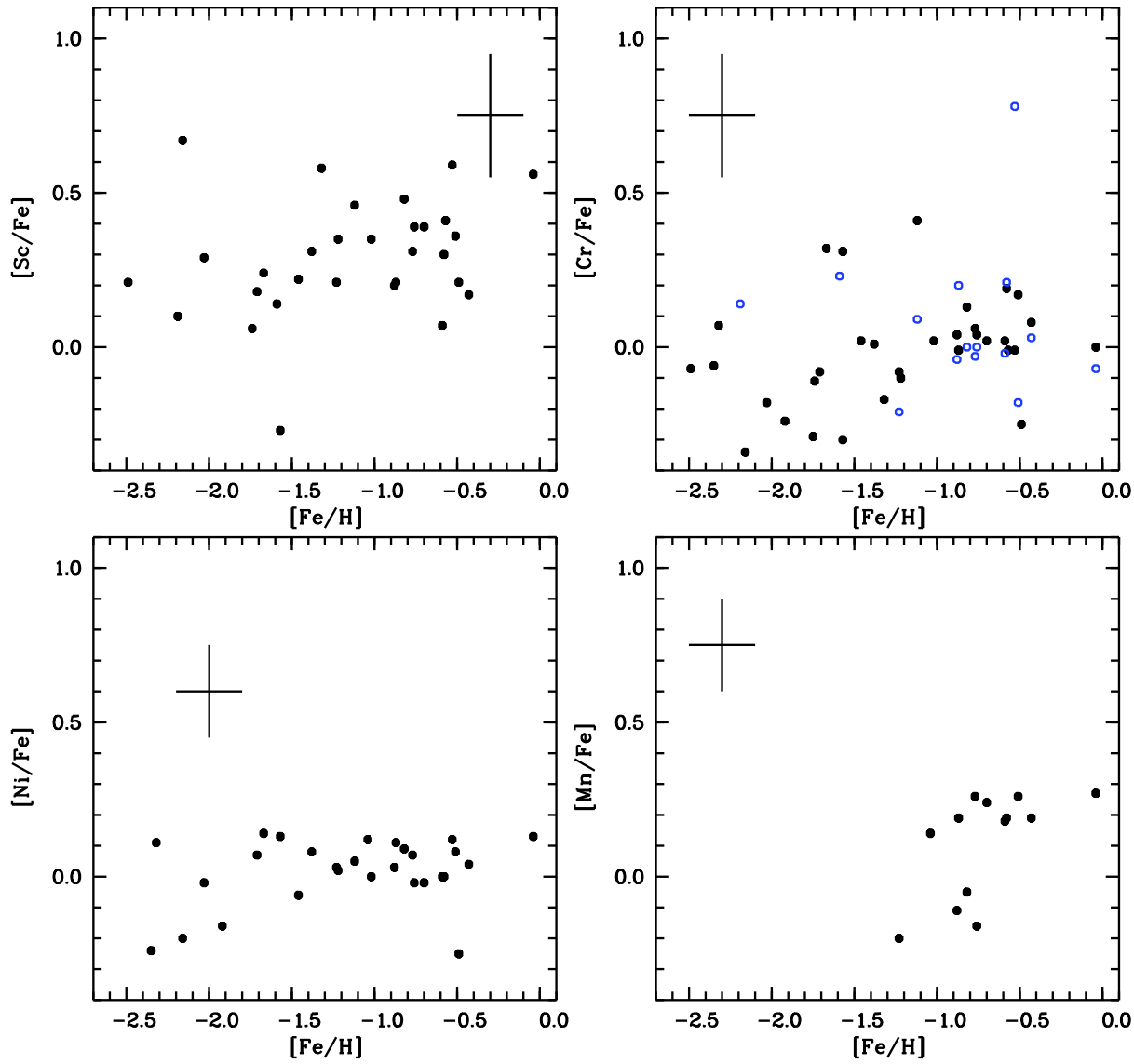

Figure 6. The elements of the Fe-peak: solid black are the neutral species, and open blue the ionized ones.

Pristine_236.4719+15.3328 are also old, while, as discussed before, Pristine_206.9304+11.8894 has an age estimate of 4 Gyr.

6 OUR NEW METHOD: COMBINING PRISTINE PHOTOMETRY WITH *GAIA*

The Gaia DR2 contains parallaxes (Luri et al. 2018), colours (Evans et al. 2018), and radial velocities (Sartoretti et al. 2018). The Pristine *CaHK* magnitudes are a very powerful addition to the *Gaia G*, $G_{BP,}$ and G_{RP} photometry, giving extra leverage on the star's metallicity. We computed synthetic *Gaia* photometry, as described in Bonifacio et al. (2018a), from the Castelli & Kurucz (2003) updated grid of ATLAS 9 fluxes.[6] There are only two differences with respect to the colours provided in Bonifacio et al. (2018a): we adopted the Gaia DR2 bandpasses (Evans et al. 2018) and for the flux of Vega we used, like done for the calibration of the *Gaia* photometry (Evans et al. 2018), the ATLAS 9 theoretical flux of Vega of Kurucz (1993). As was explained in Starkenburg et al. (2017), the *CaHK* magnitudes have been calibrated as AB magnitudes. In order to combine them with the *Gaia* magnitudes, we need to transform them to Vega magnitudes. To do so, we used the spectra of 582 spectrophotometric standard stars of the SDSS (York et al. 2000) that are in the Pristine footprint. We used the response function of the Ca H&K filter to compute the *CaHK* magnitude for each of the stars, with the same zero points adopted for the synthetic photometry, and compared these magnitudes to the observed *CaHK* magnitudes. There was no trend with colour or magnitude so the two magnitudes differ only by an offset: $CaHK_{\rm Vega} = CaHK_{\rm AB} + 0.18$, the error on the mean of this offset is 0.006 mag. In the following when we refer to *CaHK* we mean on the Vegamag system.

In a way similar to what we do when combining the *CaHK* photometry with the *gri* bands (Starkenburg et al. 2017; Youakim et al. 2017), we define a colour $(G - CaHK) - (G_{BP} - G_{RP})$. We decided to use this definition, rather than its inverse $(CaHK - G) - (G_{BP} - G_{RP})$ because for $T_{\rm eff} = 6000$ K the former combination

[6] http://wwwuser.oats.inaf.it/castelli/grids.html

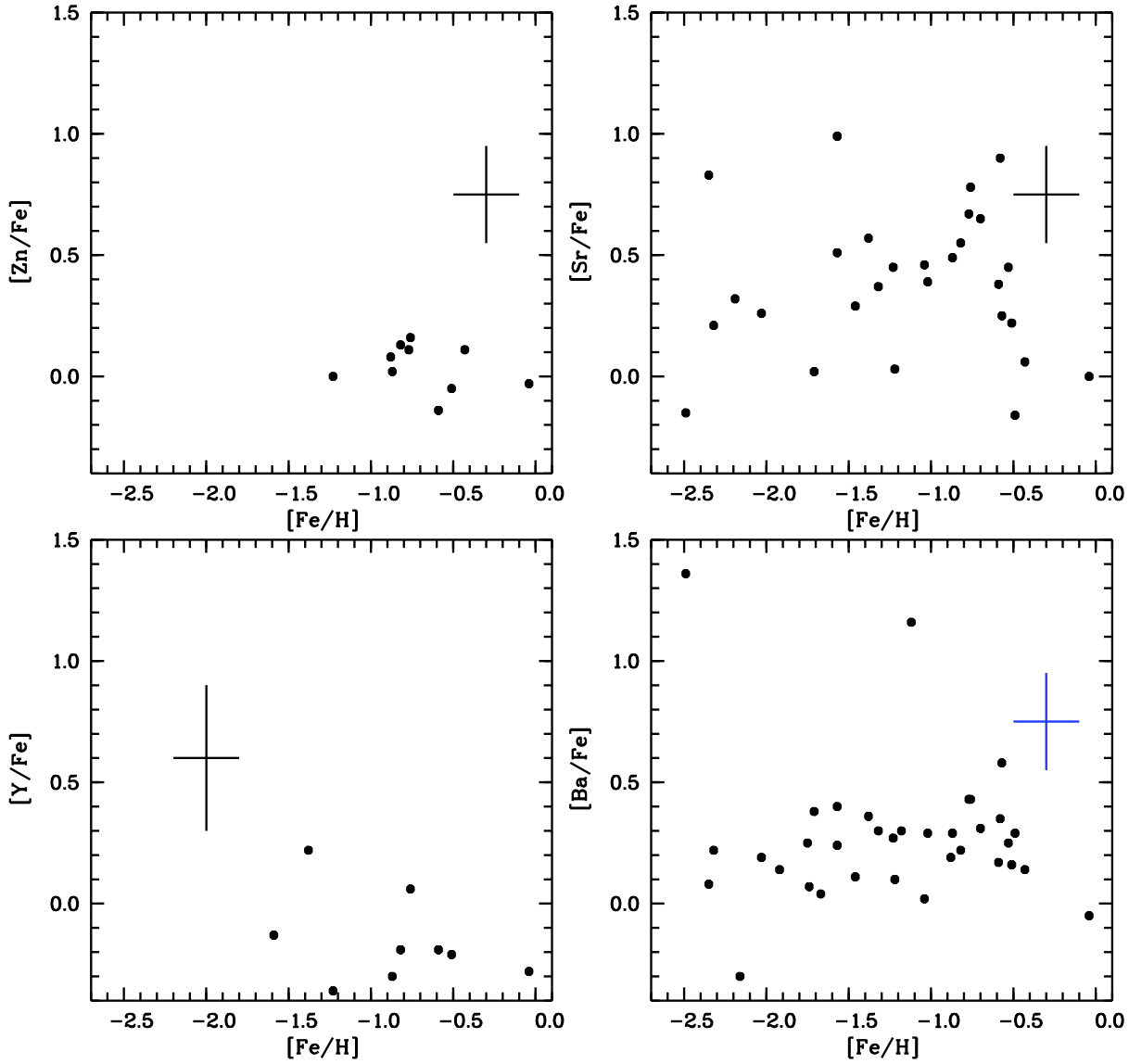

Figure 7. The heavy elements.

Table 7. Carbon abundances for the cool stars.

Star	A(C)
Pristine_110.0459+43.0522	6.26
Pristine_110.4208+40.8947	7.09
Pristine_180.8994+16.3260	7.57
Pristine_183.1390+16.1839	8.02
Pristine_191.9208+16.0031	7.42
Pristine_195.1494+06.5655	6.36
Pristine_206.8050+00.7423	6.85
Pristine_212.2541+11.4580	7.04
Pristine_213.1910+14.7927	6.41
Pristine_216.1506+14.1298	6.93
Pristine_236.7635+05.4474	6.74
Pristine_238.2716+07.5917	6.24
Pristine_240.2908+07.9401	6.63

spans about 5 magnitudes changing the metallicity from −4.0 to +0.5, but only 3 magnitudes in the latter case. The stretch in colour is illustrated in Fig. 11, where we show the synthetic colour–colour diagram, for surface gravity $\log g = 0.5$. The useful range of this colour–colour combination is for 4000 K $\leq T_{\rm eff} \leq$ 7000 K, at cooler and hotter temperatures the lines of constant metallicity cross. In this temperature range, for a given gravity, the position of the star in this diagram provides unambiguosly its effective temperature and metallicity. Of course, all the observed colours need to be corrected for the reddening, to do so we used the maps of Green et al. (2018) and the *Gaia* parallaxes to estimate the distances. The iterative procedure we used to estimate temperature, metallicity, and surface gravity from the observed colours is described in detail in Appendix C, available online. We treated in this way all the stars in Table 2 , seven of these land outside our grid when the appropriate gravity is assumed. In Fig. 12 we show the comparison between the spectroscopic [Fe/H] and the photometric metallicity estimates obtained from the above procedure, making use of *Gaia* parallaxes

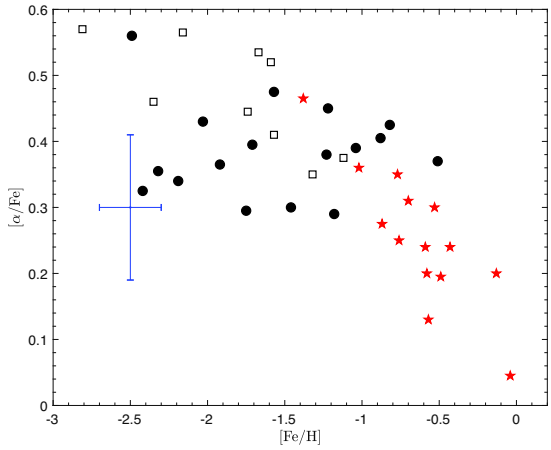

Figure 8. [α/Fe], as a function of [Fe/H]. The star symbols denote the stars classified as 'Thin', the round filled symbols denote the stars classified as 'Thick' and the open squares are the stars classified as 'Halo'.

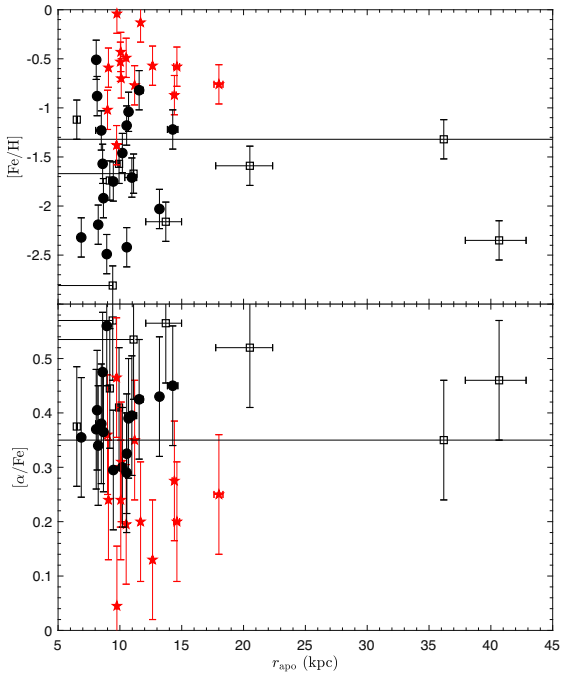

Figure 9. [Fe/H] (upper panel) and [α/Fe] (lower panel) as a function of the distance at the apogalacticon. The symbols are the same as in Fig. 8.

and photometry (filled symbols), and using only APASS photometry and no parallaxes (open symbols). It is clear that the use of the *Gaia* parallaxes improves considerably the photometric metallicity estimates because it allows to break the degeneracy between surface gravity and metallicity in the colours. If we select only the stars with the metallicity estimates that are closer to the spectroscopic ones ($|[Fe/H]_{spec} - [M/H]_{phot}| < 0.5$), we compute a linear rergession with an r.m.s. value of only 0.15 dex. The results of applying this 'calibration' to all the data points are shown in the upper panel of Fig. 12. While there remain some clear outliers, most stars have a photometric metallicity estimate that is fully compatible, within errors, with the spectroscopic estimates. This gives us confidence that these photometric metallicity estimates can be used to select metal-poor stars for follow-up spectroscopy, but also for statistical

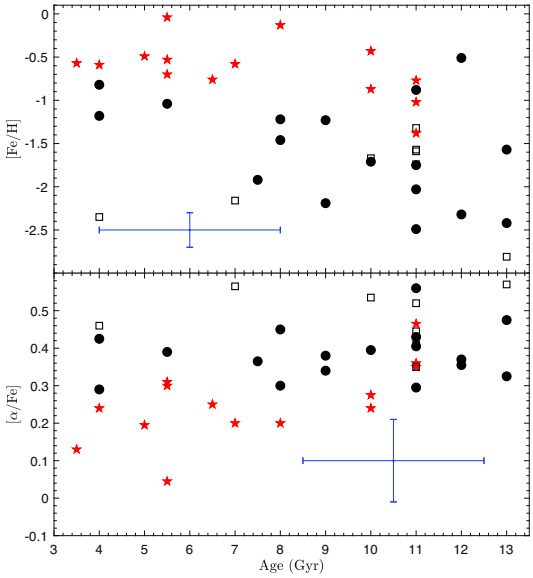

Figure 10. [Fe/H] (upper panel) and [α/Fe] (lower panel) as a function of the age. The symbols are the same as in Fig. 8.

studies (e.g. metallicity distribution functions) for large samples of stars.

It is reassuring to note that effective temperatures and surface gravities determined with this method are very close to what estimated making use of isochrones.

7 CONCLUSIONS

To probe the effectiveness of Pristine (Starkenburg et al. 2017) in selecting metal-poor stars at its bright end, we observed a sample of bright stars, selected as metal-poor, with SOPHIE at the OHP 1.93 m telescope. We derived chemical abundances for 40 stars, 25 of which are confirmed metal-poor ([Fe/H] < -1.0) and eight are found to be very metal-poor ([Fe/H] < -2.0). No star proved to be with [Fe/H] < -3.0 although for nine stars the photometric metallicity estimate was lower than this.

Our selection effectiveness appears to be lower than what was found by Youakim et al. (2017), although better than what was achieved in Caffau et al. (2017). The use of APASS photometry has clearly improved over SDSS photometry, for the bright end, yet it is still sub-optimal. The calibration we implemented using *Gaia* photometry, parallaxes, and Pristine photometry is very promising: the stellar parameters we derive are extremely close to the parameters derived from the isochrones and the metallicities are in good agreement with the [Fe/H] derived by the SOPHIE spectra. There are still exceptions of about 10 per cent of the stars that are expected to be extremely metal-poor from our photometric calibration and in fact happen to be either metal-rich or only slightly metal-poor.

In few cases the isochrones used to derive the stellar parameters are too young for the expected ages of metal-poor stars. These stars can be blue stragglers or stars evolved from blue stragglers, but in principle the Galaxy could host a young, relatively metal-poor population, probably accreted from a satellite galaxy. The latter hypothesis seems however unlikely if the stars are α-rich. Age and metallicity estimates of larger samples of stars should allow to decide if the fraction of these 'young metal-poor' stars is compatible with all of them being blue stragglers. Mass estimates,

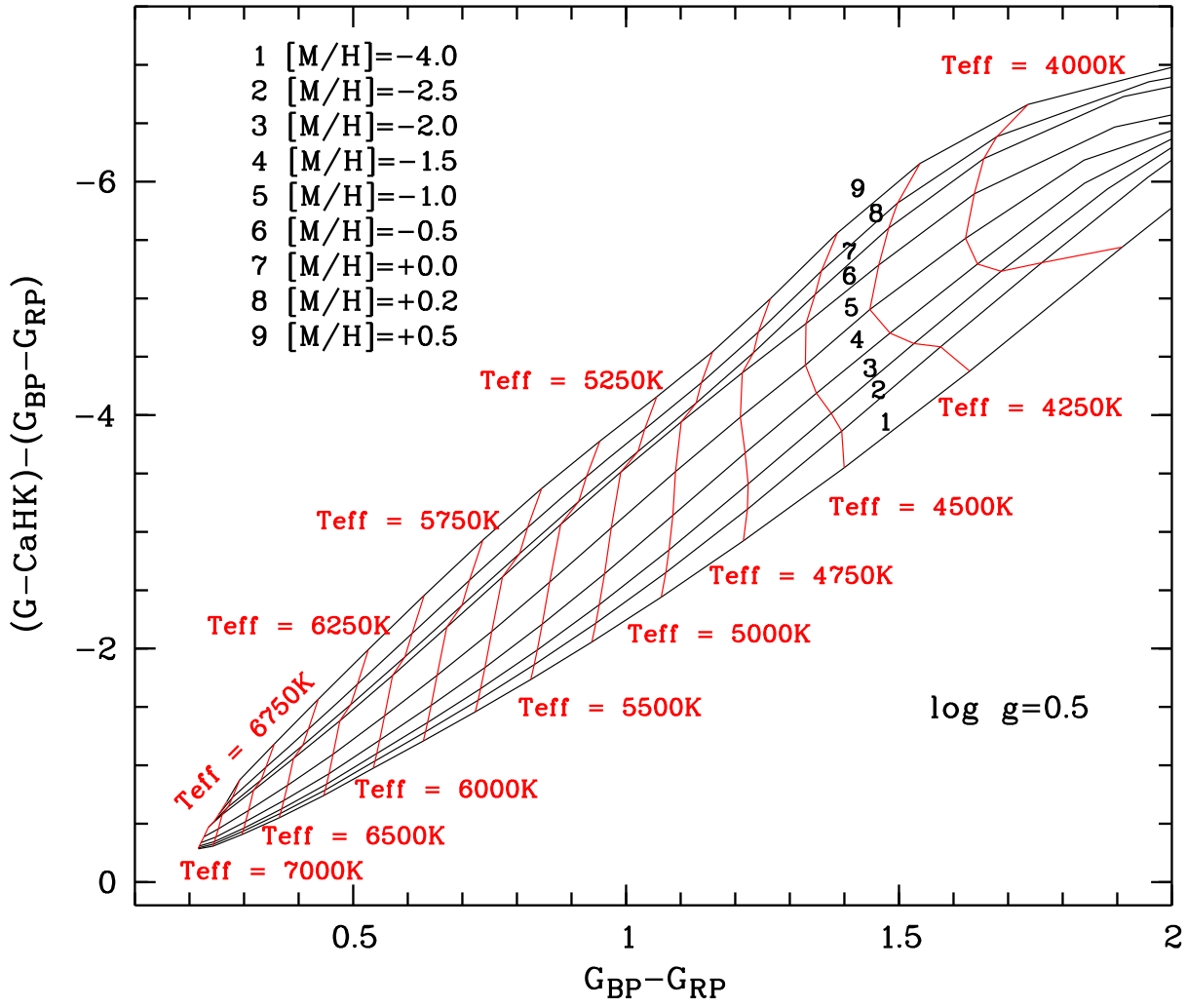

Figure 11. The theoretical colour–colour plane ($G_{BP} - G_{RP}$), [$(G - CaHK) - (G_{BP} - G_{RP})$] for a fixed surface gravity $\log g = 0.5$. Lines of constant metallicity are shown in black and those of constant T_{eff} in red.

for example for binary systems, should allow us to establish if the stars are indeed blue stragglers. Better quality spectra should be able to either measure or put a stringent upper limit on their Li abundance. Blue stragglers are not expected to have any Li (see e.g. Pritchet & Glaspey 1991; Glaspey, Pritchet & Stetson 1994; Carney, Latham & Laird 2005). Ryan et al. (2001, 2002) suggested a connection between Ultra-Li-depleted Halo Stars (stars for which no Li is measurable) and blue stragglers, suggesting that they are blue-stragglers-to-be. Recently, thanks to the Gaia DR2 parallaxes, Bonifacio et al. (2019) showed that three out of the four stars studied by Ryan et al. (2001) are indeed canonical blue stragglers, rather than blue-stragglers-to-be.

One of the stars (Pristine_180.0750+16.3239) has a very high Li abundance. Unfortunately, the relatively low signal-to-noise ratio does not allow us to make any assessment on the ^{6}Li contribution to the feature.

One star, Pristine_212.2541+11.8045, shows an enhancement in Mg, but not in Ca or Ti. The line-to-line scatter is large, surely due to a poor signal-to-noise ratio (<7 at 520 nm).

The astrometric data of *Gaia* allowed us to compute Galactic orbits for all the stars for which we could derive chemical abundances. In Section 5.1 we classified these orbits making a minimum of assumptions. It is suggestive that a classification that is only based on the orbital parameters translates into very clear abundance patterns.

We tentatively identify our 'Halo' sample with the classical 'outer halo' (Zinn 1985; Carollo et al. 2007, 2010). We are not in the position to discriminate whether these stars have been formed *in situ* or if they have been accreted. The *Gaia* data have permitted us to unveil a massive accretion event that, together with the thick disc, should dominate the metal-poor populations in the Solar vicinity (Belokurov et al. 2018; Haywood et al. 2018; Helmi et al. 2018). In particular Haywood et al. (2018) separated the stars into two sequences that they call 'Blue Sequence' and 'Red Sequence'. Gallart et al. (2019) argue that the 'Red sequence' is composed by halo stars formed *in situ*, while Haywood et al. (2018) interpret it as being dominated by the thick disc. In Appendix B, available online, we show in Fig. B1 that our sample belongs almost exclusively to the 'Blue Sequence', this is hardly surprising since the sample was selected to search for metal-poor stars. Our 'Halo' sample has very distinct chemical and kinematical properties; it may, nevertheless, be a mixture of stars formed *in situ* and stars accreted by one or several satellites. Haywood et al. (2018) argue that the stars that come from the single massive accretion event should be identified

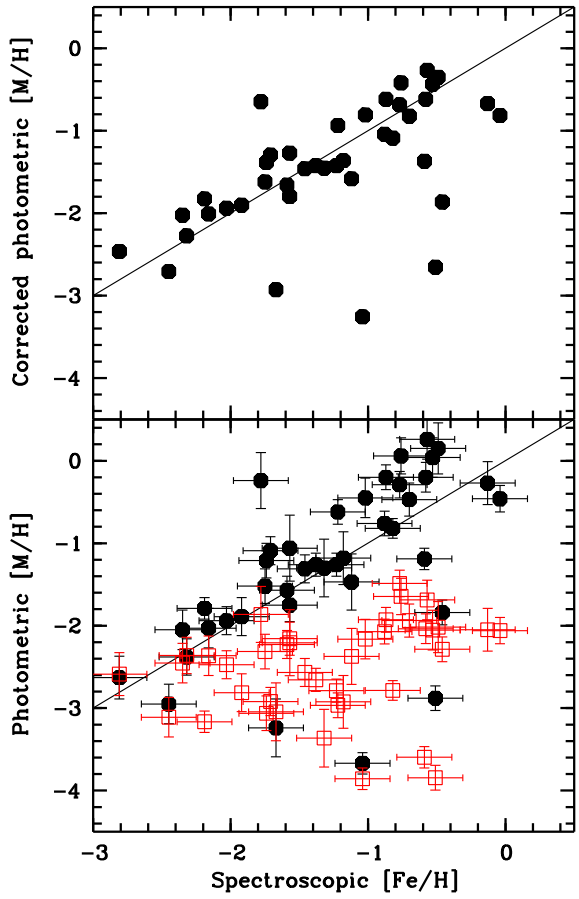

Figure 12. Comparison of the spectroscopic [Fe/H] with the photometric metallicity estimates. Lower panel: the estimate derived combining the *Gaia* data with the Pristine photometry, as described in the text as filled black hexagons, the estimate derived from APASS photometry and no estimate on gravities as open red squares. The line is the one-to-one relation, to guide the eye. Upper panel: the photometric metallicities as corrected with the linear fit described in the text.

with the 'low α' halo stars highlighted by Nissen & Schuster (2010), at [Fe/H] < -1.1, that form a unique sequence with the 'high α' stars at higher metallicity. Both our 'Halo' and our 'Thick' sample do not contain any of 'low α' stars like in Nissen & Schuster (2010).

We tentatively identify our 'Thin' sample as 'thin disc'. With respect to other samples of thin disc stars that have been presented in the literature, our sample spans a larger range in both metalliicty and apocentric distance. The metallicity distribution of our sample is however heavily biased towards lower metallicity and it should not be used to infer information on the metallicity distribution of the disc. However, we think that it is totally unbiased towards apocentric distances.

We tentatively identify the 'Thick' class as thick disc. With respect to other kinematical definitions of the thick disc our 'Thick' sample contains stars that are in very slow rotation or even in retrograde rotation, some stars have very small excursions from the Galactic plane. With respect to age, the 'Thick' class is predominantly old (age $\geq$ 8 Gyr), but not exclusively old. Besides the two suspect Blue Stragglers Pristine_183.4550+17.0927 and Pristine_206.9304+11.8894, we find Pristine_180.8994+16.3260 with an estimated age of 5.5 Gyr and Pristine_206.8050+00.7423 with an age estimate of 7.5 Gyr. As discussed above these may also be Blue Stragglers, or accreted from satellite galaxies. Probably the most surprising thing is that the 'Thick' class, which contains considerable diversity in terms of kinematics and age, and covers a wide range of metallicities, from nearly solar to -2.5, shows a uniform distribution of [α/Fe] $\approx$ 0.39. If the 'Thick' sample were just picked at random among diverse population, we would not expect such a chemical homogeneity. If a thick disc is formed by heating an old disc through satellite accretion events, we do expect a few retrograde or very slowly rotating orbits (see e.g. Jean-Baptiste et al. 2017). By looking at the kinematical diagrams Figs A1 and A2, we may conclude that the 'Thick' class may be interpreted either as a thick disc or as made dominantly by accreted stars from one or at most a few accretion events. If it were so, then the accreted galaxies should cover a wide range in metallicity, like the Sgr dSph (e.g. Bonifacio et al. 2004; Mucciarelli et al. 2017), and a sustained star formation rate that would produce high [α/Fe] ratios even at high metallicities. Both these facts suggest a rather massive galaxy, perhaps similar to Sgr dSph, with a mass of 10^8 $M_\odot$, or larger.

ACKNOWLEDGEMENTS

We acknowledge support from the Agence National de la Recherche (ANR), through contract N. 183787. We are grateful to the Programme National des Galaxies et Cosmologie of the Institut National des Sciences de l'Univers of CNRS, for allocating the SOPHIE time used to acquire the data and for financial support. The authors thank the International Space Science Institute, Berne, Switzerland, for providing financial support and meeting facilities to the international team 'Pristine'. FS and NFM gratefully acknowledge funding from CNRS/INSU through the Programme National Galaxies et Cosmologie and through the CNRS grant PICS07708. FS thanks the Initiative dExcellence IdEx from the University of Strasbourg and the Programme Doctoral International PDI for funding his PhD. This work has been published under the framework of the IdEx Unistra and benefits from a funding from the state managed by the French National Research Agency (ANR) as part of the investments for the future program. This research made use of the GravPot16 software, a community-developed core under the git version-control system on GitHub. This work has made use of data from the European Space Agency (ESA) mission *Gaia* (https://www.cosmos.esa.int/gaia), processed by the *Gaia* Data Processing and Analysis Consortium (DPAC, https://www.cosmos.esa.int/web/gaia/dpac/consortium). Funding for the DPAC has been provided by national institutions, in particular the institutions participating in the *Gaia* Multilateral Agreement. This study is based on observations acquired at the Observatoire de Haute Provence, programmes 17B.PNCG.BONI and 18A.PNCG.BONI.

REFERENCES

Allende Prieto C., Rebolo R., García López R. J., Serra-Ricart M., Beers T. C., Rossi S., Bonifacio P., Molaro P., 2000, AJ, 120, 1516
Amarsi A. M., Lind K., Asplund M., Barklem P. S., Collet R., 2016, MNRAS, 463, 1518
Anthony-Twarog B. J., Twarog B. A., 1998, AJ, 116, 1922
Anthony-Twarog B. J., Laird J. B., Payne D., Twarog B. A., 1991, AJ, 101, 1902
Anthony-Twarog B. J., Sarajedini A., Twarog B. A., Beers T. C., 2000, AJ, 119, 2882

Arenou F. et al., 2018, A&A, 616, A17 (Gaia DR2)
Baade W., 1944, ApJ, 100, 137
Bailer-Jones C. A. L., 2015, PASP, 127, 994
Beers T. C., Preston G. W., Shectman S. A., 1985, AJ, 90, 2089
Beers T. C., Preston G. W., Shectman S. A., 1992, AJ, 103, 1987
Belokurov V., Irwin M. J., Koposov S. E., Evans N. W., Gonzalez-Solares E., Metcalfe N., Shanks T., 2014, MNRAS, 441, 2124
Belokurov V., Erkal D., Evans N. W., Koposov S. E., Deason A. J., 2018, MNRAS, 478, 611
Bensby T., Lind K., 2018, A&A, 615, A151
Bidelman W. P., MacConnell D. J., 1973, AJ, 78, 687
Bland-Hawthorn J., Gerhard O., 2016, ARA&A, 54, 529
Bond H. E., 1980, ApJS, 44, 517
Bonifacio P. et al., 2007, A&A, 462, 851
Bonifacio P. et al., 2018a, A&A, 611, A68
Bonifacio P. et al., 2018b, A&A, 612, A65
Bonifacio P., Sbordone L., Marconi G., Pasquini L., Hill V., 2004, A&A, 414, 503
Bonifacio P., Caffau E., Zaggia S., François P., Sbordone L., Andrievsky S. M., Korotin S. A., 2015, A&A, 579, L6
Bonifacio P., Caffau E., Spite M., Spite F., 2019, Res. Notes Am. Astron. Soc., 3, 64
Bouchy F., Sophie Team, 2006, in Arnold L., Bouchy F., Moutou C., eds, Tenth Anniversary of 51 Peg-b: Status of and prospects for hot Jupiter studies. Frontier Group, Paris, France, p. 319
Bovy J., 2015, ApJS, 216, 29
Bressan A., Marigo P., Girardi L., Salasnich B., Dal Cero C., Rubele S., Nanni A., 2012, MNRAS, 427, 127
Caffau E. et al., 2017, Astron. Nachr., 338, 686 (Paper II)
Caffau E., Ludwig H.-G., Steffen M., Freytag B., Bonifacio P., 2011, Sol. Phys., 268, 255
Cain M. et al., 2018, ApJ, 864, 43
Carney B. W., Latham D. W., Laird J. B., 2005, AJ, 129, 466
Carollo D. et al., 2007, Nature, 450, 1020
Carollo D. et al., 2010, ApJ, 712, 692
Casagrande L., Wolf C., Mackey A. D., Nordlander T., Yong D., Bessell M., 2019, MNRAS, 482, 2770
Castelli F., Kurucz R. L., 2003, in Piskunov N., Weiss W. W., Gray D. F., eds, IAU Symp. Vol. 210, Modelling of Stellar Atmospheres. Kluwer, Dordrecht, p. A20, (arXiv:astro-ph/0405087)
Cayrel R. et al., 2004, A&A, 416, 1117
Chamberlain J. W., Aller L. H., 1951, ApJ, 114, 52
Chiappini C. et al., 2015, A&A, 576, L12
Christlieb N., 2003, in Schielicke R. E., ed., Reviews in Modern Astronomy Vol. 16, Reviews in Modern Astronomy. Wiley, New York. p. 191
Evans D. W. et al., 2018, A&A, 616, A4
Fernández-Trincado J. G., Ortigoza-Urdaneta M., Moreno E., Pérez-Villegas A., Soto M., 2019, MNRAS, preprint (arXiv:1904.05370)
Fuhrmann K., Bernkopf J., 1999, A&A, 347, 897
Gaia Collaboration, 2016, A&A, 595, A1
Gaia Collaboration, 2018, A&A, 616, A1
Gallart C., Bernard E. J., Brook C. B., Ruiz-Lara T., Cassisi S., Hill V., Monelli M., 2019, preprint (arXiv:1901.02900)
Glaspey J. W., Pritchet C. J., Stetson P. B., 1994, AJ, 108, 271
González Hernández J. I., Bonifacio P., 2009, A&A, 497, 497
Green G. M. et al., 2018, MNRAS, 478, 651
Harutyunyan G., Steffen M., Mott A., Caffau E., Israelian G., González Hernández J. I., Strassmeier K. G., 2018, AAP, 618, A16
Haywood M., Di Matteo P., Lehnert M. D., Katz D., Gómez A., 2013, A&A, 560, A109
Haywood M., Lehnert M. D., Di Matteo P., Snaith O., Schultheis M., Katz D., Gómez A., 2016, A&A, 589, A66
Haywood M., Di Matteo P., Lehnert M. D., Snaith O., Khoperskov S., Gómez A., 2018, ApJ, 863, 113
Helmi A., Babusiaux C., Koppelman H. H., Massari D., Veljanoski J., Brown A. G. A., 2018, Nature, 563, 85
Henden A., Munari U., 2014, Contrib. Astron. Obs. Skalnate Pleso, 43, 518
Henden A. A., Welch D. L., Terrell D., Levine S. E., 2009, American Astronomical Society Meeting Abstracts #214. p. 669
Henden A. A., Levine S., Terrell D., Welch D. L., 2015, American Astronomical Society Meeting Abstracts #225. p. 336.16
Henden A. A., Levine S., Terrell D., Welch D. L., Munari U., Kloppenborg B. K., 2018, American Astronomical Society Meeting Abstracts #232. p. 223.06
Hoeg E. et al., 1997, A&A, 323, L57
Jean-Baptiste I., Di Matteo P., Haywood M., Gómez A., Montuori M., Combes F., Semelin B., 2017, A&A, 604, A106
Keenan P. C., 1942, ApJ, 96, 101
Keenan P. O., Morgan W. W., Münch G., 1948, AJ, 53, 194
Keller S. C. et al., 2007, PASA, 24, 1
Kirby E. N., Simon J. D., Cohen J. G., 2015, ApJ, 810, 56
Korotin S. A., Andrievsky S. M., Hansen C. J., Caffau E., Bonifacio P., Spite M., Spite F., François P., 2015, A&A, 581, A70
Kurucz R., 1993, Solar Abundance Model Atmospheres for 0,1,2,4,8 km/s. Kurucz CD-ROM No. 19. Cambridge, MA: Smithsonian Astrophysical Observatory. p. 19
Lindblad B., 1922, ApJ, 55, 85
Lodders K., Palme H., Gail H.-P., 2009, Landolt Börnstein. Springer-Verlag, Berlin, Heidelberg, p. 712
Luck R. E., Bond H. E., 1981, ApJ, 244, 919
Luri X. et al., 2018, A&A, 616, A9
Marigo P. et al., 2017, ApJ, 835, 77
Martig M. et al., 2015, MNRAS, 451, 2230
Masseron T. et al., 2014, A&A, 571, A47
Meléndez J., Placco V. M., Tucci-Maia M., Ramírez I., Li T. S., Perez G., 2016, A&A, 585, L5
Mott A., Steffen M., Caffau E., Spada F., Strassmeier K. G., 2017, A&A, 604, A44
Mucciarelli A., Bellazzini M., Ibata R., Romano D., Chapman S. C., Monaco L., 2017, A&A, 605, A46
Navarro J. F., Frenk C. S., White S. D. M., 1997, ApJ, 490, 493
Nissen P. E., Schuster W. J., 2010, A&A, 511, L10
Norris J., Bessell M. S., Pickles A. J., 1985, ApJS, 58, 463
Oort J. H., 1926a, PhD thesis, Publications of the Kapteyn Astronomical Laboratory Groningen, vol. 40, p. 1
Oort J. H., 1926b, The Observatory, 49, 302
Placco V. M. et al., 2019, ApJ, 870, 122
Popper D. M., 1947, ApJ, 105, 204
Pritchet C. J., Glaspey J. W., 1991, ApJ, 373, 105
Ryan S. G., Beers T. C., Kajino T., Rosolankova K., 2001, ApJ, 547, 231
Ryan S. G., Gregory S. G., Kolb U., Beers T. C., Kajino T., 2002, ApJ, 571, 501
Salvadori S., Ferrara A., Schneider R., Scannapieco E., Kawata D., 2010, MNRAS, 401, L5
Sartoretti P. et al., 2018, A&A, 616, A6
Sbordone L., Caffau E., Bonifacio P., Duffau S., 2014, A&A, 564, A109
Schlaufman K. C., Casey A. R., 2014, ApJ, 797, 13
Schlaufman K. C., Thompson I. B., Casey A. R., 2018, ApJ, 867, 98
Schönrich R., Binney J., Dehnen W., 2010, MNRAS, 403, 1829
Schuster W. J., Nissen P. E., Parrao L., Beers T. C., Overgaard L. P., 1996, A&AS, 117, 317
Schuster W. J., Parrao L., Franco A., Beers T. C., Nissen P. E., 1999, Ap&SS, 265, 183
Schuster W. J., Beers T. C., Michel R., Nissen P. E., García G., 2004, A&A, 422, 527
Schwarzschild M., Spitzer Jr. L., Wildt R., 1951, ApJ, 114, 398
Sestito F. et al., 2019, MNRAS, 484, 2166
Spite M., Spite F., 1982, Nature, 297, 483
Spite M., Bonifacio P., Spite F., Caffau E., Sbordone L., Gallagher A J., 2019, AAP, 624, A44
Starkenburg E. et al., 2017, MNRAS, 471, 2587 (Paper I)

Steffen M., Caffau E., Ludwig H.-G., 2013, Mem. della Soc. Astron. Italiana Suppl., 24, 37
Twarog B. A., Anthony-Twarog B. J., 1995, AJ, 109, 2828
Voggel K., Hilker M., Baumgardt H., Collins M. L. M., Grebel E. K., Husemann B., Richtler T., Frank M. J., 2016, MNRAS, 460, 3384
York D. G. et al., 2000, AJ, 120, 1579
Youakim K. et al., 2017, MNRAS, 472, 2963
Zinn R., 1985, ApJ, 293, 424

SUPPORTING INFORMATION

Supplementary data are available at *MNRAS* online.

Appendix A. Kinematic properties
Appendix B. Evolutionary diagram
Appendix C. Triangulation and interpolation in the colour–colour plane

Please note: Oxford University Press is not responsible for the content or functionality of any supporting materials supplied by the authors. Any queries (other than missing material) should be directed to the corresponding author for the article.

[1]*GEPI, Observatoire de Paris, Université PSL, CNRS, Place Jules Janssen, F-92195 Meudon, France*
[2]*Université de Strasbourg, CNRS, Observatoire astronomique de Strasbourg, UMR 7550, F-67000, France*
[3]*Leibniz-Institut für Astrophysik Potsdam (AIP), An der Sternwarte 16, D-14482 Potsdam, Germany*
[4]*Laboratoire d'Astrophysique, Ecole Polytechnique Fédérale de Lausanne (EPFL), Observatoire de Sauverny, CH-1290 Versoix, Switzerland*
[5]*Max-Planck-Institut für Astronomie, Königstuhl 17, D-69117, Heidelberg, Germany*
[6] *European Southern Observatory, Alonso de Cordova 3109, Vitacura, Santiago, Chile*
[7] *AAVSO, Cambridge, MA 02138, USA*
[8] *Dipartimento di Fisica e Astronomia, Universitá degli Studi di Firenze, Via G. Sansone 1, I-50019 Sesto Fiorentino, Italy*
[9]*INAF/Osservatorio Astrofisico di Arcetri, Largo E. Fermi 5, I-50125 Firenze, Italy*
[10]*Instituto de Astrofísica de Canarias, Vía Láctea, 38205, La Laguna, Tenerife*
[11]*Institute of Astronomy, University of Cambridge, Madingley Road, CB3 0HA Cambridge, UK*
[12]*Université Côte d'Azur, Observatoire de la Côte d'Azur, CNRS, Laboratoire Lagrange, Bd de l'Observatoire, CS 34229, F-06304 Nice cedex 4, France*
[13]*Department of Physics and Astronomy, University of Victoria, PO Box 3055, STN CSC, Victoria, BC V8W 3P6, Canada*
[14]*STFC UK Astronomy Technology Centre, The Royal Observatory Edinburgh, Blackford Hill, Edinburgh, EH9 3HJ, UK*
[15]*Department of Astronomy & Astrophysics, University of Toronto, Toronto, ON M5S 3H4, Canada*

This paper has been typeset from a TEX/LATEX file prepared by the author.

APPENDIX A: KINEMATIC PROPERTIES

In this appendix we provide in Table,A1 and A2 the kinematic properties of the sample of stars we have analysed and some of the quantities derived from their Galactic orbits. The space velocities (U, V, W) are with respect to the Local Standard of Rest, U is positive towards the Galactic anti-centre, V in the direction of the Galactic rotation and W is perpendicular to the Galactic plane, positive in the northern Galactic hemisphere. We list also the mean specific angular momentum (angular momentum per unit mass) for the stars along their orbits, in units of $\mathrm{kpc}\times\mathrm{km\,s^{-1}}$. In Fig. A1 we provide the Toomre diagram for the sample of stars and in Fig. A2 the diagram of mean specific angular momentum versus the energy and J_z action for our sample.

APPENDIX B: EVOLUTIONARY DIAGRAM

In this appendix we show, in Fig, B1, the log ($T_{\rm eff}$) - log g diagram for our stars. This is morphologically equivalent to a colour-magnitude diagram. We recall that in our case the surface gravities have been derived from the G absolute magnitudes and the effective temperatures from the $G_{BP} - G_{RP}$ colours. As a reference we show on the diagram two PARSEC isochrones (Bressan et al. 2012; Marigo et al. 2017) of 11.5 Gyr and metalliciy -0.5 and -1.5. The isochrone of metallicity -0.5 is the one used by Haywood et al. (2016) to separate the "Blue Sequence", from the "Red Sequence" stars. The plot shows that all of our stars, except, perhaps two, belong to the "Blue Sequence".

APPENDIX C: TRIANGULATION AND INTERPOLATION IN THE COLOUR-COLOUR PLANE

In what follows, all colours are assumed to be corrected for reddening. We take advantage of the Gaia parallaxes also to estimate the surface gravity of the star via the Stefan-Boltzman equation (see e.g. equation (1) of Nissen et al. 1994). To do so, however, we need an estimate of the mass of the star, of its effective temperature and its bolometric magnitude. The mass is not very important, the old stars that are the main targets of the Pristine survey have masses in the range 0.7 to 0.9 $\mathrm{M}\odot$, this implies an uncertainty of only 0.1 dex in the surface gravity, therefore we can safely assume a mass of 0.8 $\mathrm{M}\odot$. The G band is very wide and the bolometric correction is very small, however we need to know the star's parameters in order to have the bolometric correction.

Once a first guess of the surface gravity is made we can interpolate in the theoretical colour-colour grid and determine the grid for this gravity. At this point, from the mathematical point of view, the problem is to determine the values of $T_{\rm eff}$ and metallicity for the observed values of $(G_{BP} - G_{RP})$ and $(G - CaHK) - (G_{BP} - G_{RP})$. $T_{\rm eff}$ and metallicity are assumed to be continuous functions of the two colours and their values are known only for a finite set of points in the colour-colour plane. These points are not on a regular grid in the colour-colour plane. Our approach is to divide the plane using a set of non-overlapping triangles and we decided to use the Delaunay triangulation (Delaunay 1934). This has the property that none of the points that define the triangulation is internal to the circumcircle of any triangle. To compute the triangulation we used the Fortran 90 code of Burkardt (2009), slightly modified to be used by our own code as a subroutine. To establish in which triangle lies our point we compute barycentric coordinates of the observed point for each triangle, when all three coordinates are ≥ 0 then the point is inside the triangle. At this point we could simply proceed to estimate the values of $T_{\rm eff}$ and metallicity at the observed point by barycentric interpolation[7]. This however could be sub-optimal if the three vertexes of the triangle lie on three different iso-metallicity line (see Fig. C1). The optimal interpolation is for a triangle, containing the observed point, that has a side along an iso-metallicity line. It is however trivial to find such a triangle, starting from the Delaunay triangle whose vertexes lie on three iso-metallicity lines. It is sufficient to consider the intersection of the median iso-metallicity line with the segment uniting the two other vertexes of the Delaunay triangle. Then consider the two triangles that have as one side the segment between this point and the original vertex at the median metallicity and as third vertex one of the two other vertexes of the Delaunay triangle. The observed point is necessarily internal to one of these two triangles and again we use barycentric coordinates to determine which of the two. Refer to Fig. C1 to picture the situation.

In summary we adopted the following iterative procedure:

(i) if $(G_{BP} - G_{RP}) \leq 0.8$ assume log g = 4.0, else assume log g = 2.5;
(ii) assume a metallicity –1.0;
(iii) interpolate in the theoretical colours to find the $T_{\rm eff}$ and bolometric correction that correspond to this $(G_{BP} - G_{RP})$;
(iv) compute the bolometric magnitude;
(v) use the Stefan-Boltzman equation, to estimate log g;
(vi) with the new log g go to point (iii) and iterate until the variation in log g is less than 0.1 dex;
(vii) with the current guess of log g interpolate in the theoretical colours to get the points in the colour-colour plane corresponding to this log g;
(viii) compute a Delaunay triangulation for this data set;
(ix) for each triangle compute the barycentric coordinates of the observed point;
(x) if the three barycentric coordinates are all positive (or zero) then the point is inside that triangle;
(xi) if the point is not in any of the triangles, set a warning condition exit the loop and process the next star;
(xii) check if the triangle lies between two iso-metallicity lines, if so proceed to point (xiv), else;
(xiii) refine the triangle identifying the non-Delaunay triangle that contains the point and lies between two subsequent iso-metallicity lines;
(xiv) use the barycentric coordinates to obtain the barycentric interpolated value of $T_{\rm eff}$ and metallicity;

[7] Once we know the three vertexes of the triangle, points P_1, P_2, P_3 we also now the value of $T_{\rm eff}(T_1, T_2, T_3)$ and metallicity at each point. If b_1, b_2, b_2 are the barycentric coordinates of a point inside the triangle, then the value of $T_{\rm eff}$ at that point can be estimated as $b_1T_1 + b_2T_2 + b_3T_3$ and likewise for metallicity.

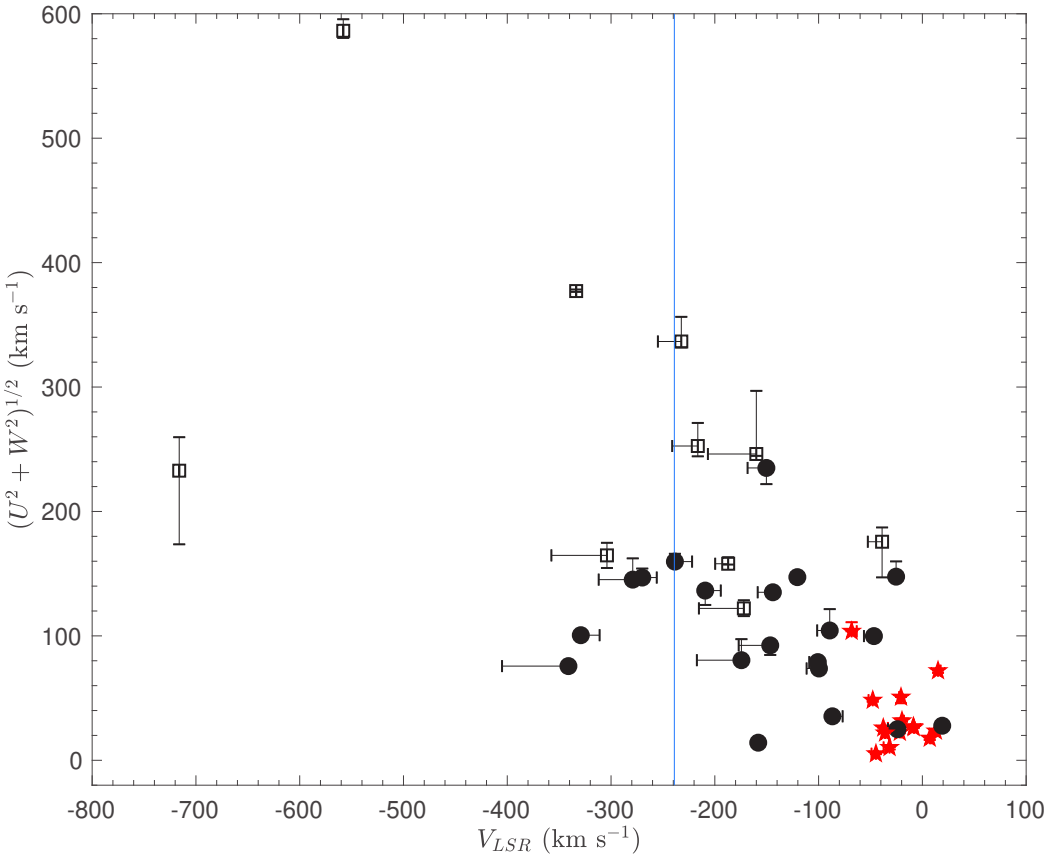

Figure A1. The Toomre diagram for our stars. Black dots are stars classified as "Thick", red stars are stars classified as "Thin" and open squares are stars classified as "Halo". 298.

(xv) with this new metallicity and the current gravity interpolate the theoretical colour $G_{BP} - G_{RP}$ for all effective temperatures;

(xvi) determine a new effective temperature by a spline interplation in this curve for the observed $G_{BP}-G_{RP}$ colour;

(xvii) with the new $T_{\rm eff}$compute a new bolometric correction and log g;

(xviii) chek the variation of $T_{\rm eff}$ and log g with respect to the previous estimates is "small enough" [8], if not go back to step (iii).

This paper has been typeset from a TEX/LATEX file prepared by the author.

[8] We used 50 K for $T_{\rm eff}$ and 0.1 dex for log g.

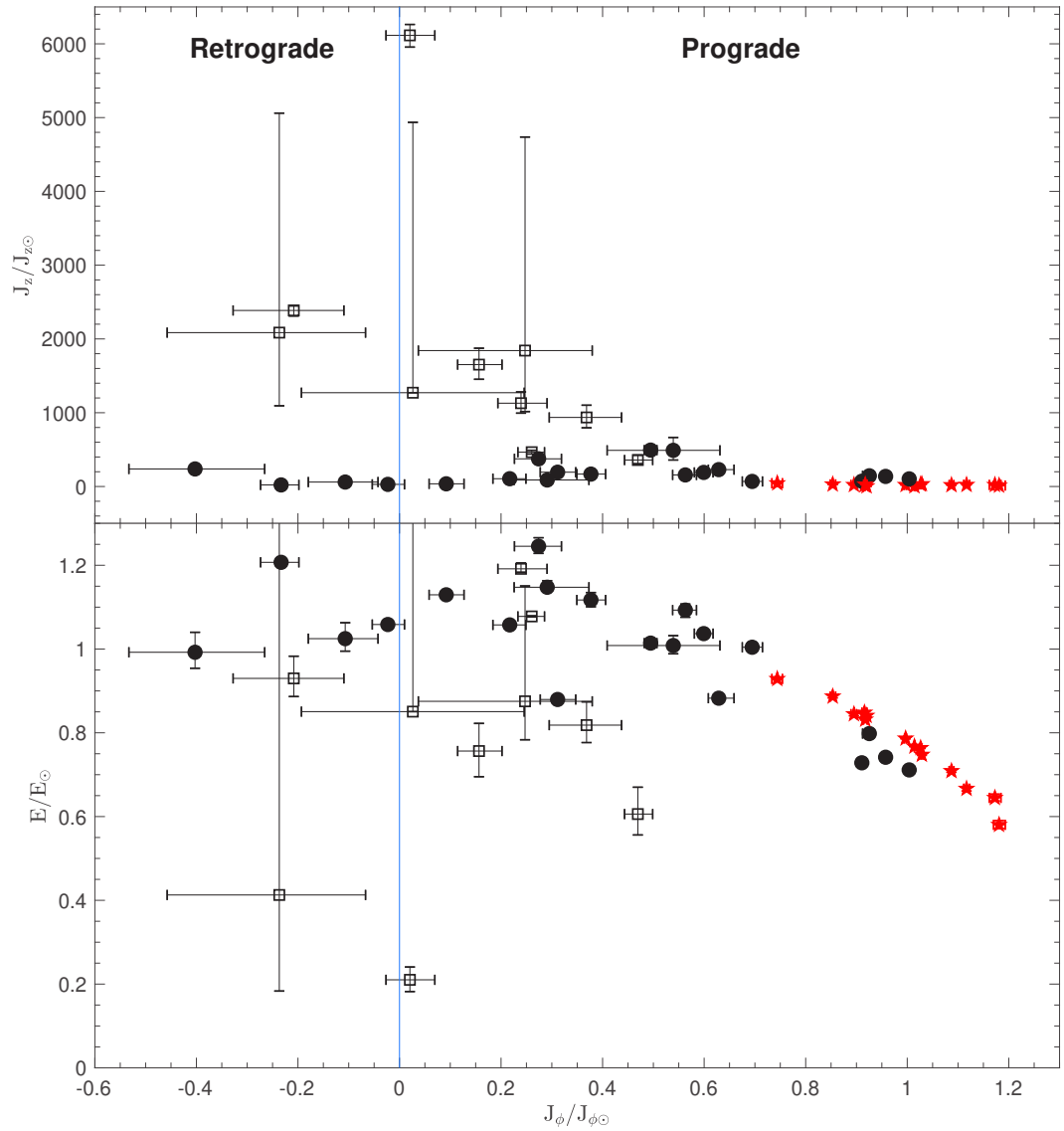

Figure A2. The specific energy versus rotational action J_ϕ (also knonw as specific angular momentum L_z) diagram for our stars (lower panel) and the J_z action (as defined in equation 6 of Binney 2012) versus rotational action (upper panel). All the quantites are normalized to the solar value. The symbols are the same as in Fig.A1.

Table A1. Inferred orbital parameters of the stars in the sample. The velocity (U,V,W) in the heliocentric frame, the apocentre and pericentre distances in the galactocentric frame are listed.

Target	U ($\mathrm{km\,s^{-1}}$)	V ($\mathrm{km\,s^{-1}}$)	W ($\mathrm{km\,s^{-1}}$)	Apo (kpc)	Peri (kpc)
Pristine_110.0459+43.0522	$33.9^{+1.0}_{-8.2}$	-341^{+1}_{-64}	$-67.7^{+2.6}_{-2.7}$	$10.6^{+0.2}_{-0.2}$	$2.4^{+0.9}_{-1.0}$
Pristine_110.4208+40.8947	8^{+1}_{-13}	-304^{+1}_{-54}	-164^{+10}_{-10}	$9.9^{+0.1}_{-0.1}$	$4.1^{+1.6}_{-1.1}$
Pristine_111.5919+44.0179	$38.8^{+1.0}_{-1.5}$	$-47.8^{+1.0}_{-4.1}$	$-28.8^{+0.4}_{-0.4}$	$10.1^{+0.1}_{-0.1}$	$7.1^{+0.1}_{-0.1}$
Pristine_112.0456+43.9914	$-24.4^{+1.0}_{-2.2}$	$-37.7^{+4.4}_{-1.0}$	$-9.0^{+0.9}_{-1.0}$	$10.0^{+0.1}_{-0.1}$	$8.9^{+0.1}_{-0.1}$
Pristine_112.3237+44.2279	$11.9^{+1.0}_{-1.7}$	$13.0^{+1.3}_{-1.0}$	$20.3^{+1.0}_{-1.0}$	$14.4^{+0.2}_{-0.2}$	$8.4^{+0.1}_{-0.1}$
Pristine_112.5667+45.9455	$70.6^{+1.0}_{-1.8}$	$15.1^{+2.5}_{-1.0}$	$-14.5^{+0.7}_{-0.8}$	$18.0^{+0.4}_{-0.3}$	$8.0^{+0.1}_{-0.1}$
Pristine_112.6119+45.7784	$-26.2^{+1.4}_{-1.0}$	$-8.4^{+0.9}_{-1.0}$	$1.6^{+0.4}_{-0.4}$	$11.2^{+0.1}_{-0.1}$	$8.3^{+0.1}_{-0.1}$
Pristine_113.0244+45.6965	$26.2^{+2.0}_{-1.0}$	$-19.6^{+1.8}_{-1.0}$	$18.0^{+1.4}_{-1.4}$	$11.7^{+0.1}_{-0.1}$	$8.4^{+0.1}_{-0.1}$
Pristine_113.4132+41.9324	$-2.8^{+1.4}_{-1.0}$	$-44.7^{+1.0}_{-4.3}$	$4.5^{+0.3}_{-0.4}$	$9.0^{+0.1}_{-0.1}$	$8.2^{+0.1}_{-0.1}$
Pristine_113.4275+45.6423	$8.6^{+1.0}_{-1.9}$	$-31.6^{+1.0}_{-5.7}$	$-5.6^{+0.4}_{-0.4}$	$10.5^{+0.1}_{-0.1}$	$9.1^{+0.1}_{-0.1}$
Pristine_113.6421+45.4681	$-14.1^{+1.0}_{-1.7}$	$7.1^{+1.2}_{-1.0}$	$-10.9^{+0.9}_{-1.0}$	$14.6^{+0.3}_{-0.2}$	$9.1^{+0.1}_{-0.1}$
Pristine_113.6744+45.8738	$-86.6^{+1.7}_{-1.0}$	$-46.7^{+1.0}_{-9.6}$	$49.6^{+0.7}_{-0.7}$	$12.9^{+0.1}_{-0.1}$	$7.2^{+0.1}_{-0.1}$
Pristine_113.7050+45.5860	$21.7^{+1.0}_{-1.5}$	$-8.6^{+1.0}_{-0.7}$	$-16.1^{+0.3}_{-0.3}$	$12.6^{+0.1}_{-0.1}$	$8.7^{+0.1}_{-0.1}$
Pristine_180.0750+16.3239	$17.1^{+1.0}_{-1.0}$	$-21.7^{+1.5}_{-1.0}$	$-14.7^{+0.5}_{-0.5}$	$9.8^{+0.1}_{-0.1}$	$7.6^{+0.1}_{-0.1}$
Pristine_180.8898+15.6500	$136.0^{+18.0}_{-1.0}$	$-279.0^{+1.0}_{-33.0}$	$-49.9^{+3.5}_{-4.3}$	$11.0^{+0.6}_{-0.4}$	$0.7^{+0.3}_{-0.3}$
Pristine_180.8994+16.3260	$9.2^{+4.2}_{-1.0}$	$-24.0^{+1.0}_{-9.1}$	$-23.2^{+0.9}_{-0.8}$	$10.7^{+0.1}_{-0.1}$	$7.8^{+0.1}_{-0.1}$
Pristine_181.4437+13.4888	$5.9^{+1.0}_{-0.6}$	$-100.7^{+1.0}_{-8.3}$	$-78.7^{+1.3}_{-1.6}$	$8.2^{+0.1}_{-0.1}$	$4.5^{+0.2}_{-0.2}$
Pristine_182.2972+13.1228	131^{+1}_{-12}	-209^{+15}_{-1}	$39.7^{+2.1}_{-2.4}$	$10.2^{+0.2}_{-0.2}$	$1.1^{+0.2}_{-0.2}$
Pristine_183.1390+16.1839	$-12.4^{+1.0}_{-1.8}$	$-86.7^{+9.9}_{-1.0}$	$-33.1^{+1.3}_{-1.5}$	$8.1^{+0.1}_{-0.1}$	$5.4^{+0.3}_{-0.2}$
Pristine_183.4550+17.0927	101^{+18}_{-1}	-89^{+1}_{-12}	$26.1^{+1.2}_{-1.1}$	$11.6^{+0.3}_{-0.3}$	$4.1^{+0.3}_{-0.1}$
Pristine_185.5596+15.5893	-144^{+13}_{-1}	$-25.3^{+1.0}_{-1.7}$	$32.2^{+0.5}_{-0.5}$	$14.3^{+0.4}_{-0.4}$	$6.0^{+0.1}_{-0.1}$
Pristine_188.4543+15.1750	$-49.9^{+1.0}_{-5.0}$	$-20.6^{+1.0}_{-1.8}$	$9.2^{+0.5}_{-0.5}$	$10.1^{+0.1}_{-0.1}$	$7.5^{+0.1}_{-0.1}$
Pristine_191.9208+16.0031	$-12.7^{+1.0}_{-1.0}$	$-158.2^{+1.0}_{-1.0}$	$-6.3^{+3.6}_{-5.3}$	$8.5^{+0.5}_{-0.2}$	$4.4^{+0.9}_{-1.2}$
Pristine_192.4508+12.7922	$-103.2^{+7.3}_{-1.0}$	$-68.2^{+4.9}_{-1.0}$	$-9.7^{+0.5}_{-0.5}$	$9.7^{+0.1}_{-0.1}$	$5.3^{+0.1}_{-0.1}$
Pristine_193.5777+10.3945	$-124.4^{+6.5}_{-1.0}$	-187^{+1}_{-13}	$-97.4^{+1.2}_{-1.0}$	$9.2^{+0.1}_{-0.1}$	$1.9^{+0.2}_{-0.4}$
Pristine_195.1494+06.5655	226^{+29}_{-1}	-232^{+1}_{-23}	$249.3^{+6.4}_{-6.4}$	$40.7^{+2.7}_{-2.2}$	$5.9^{+0.1}_{-0.1}$
Pristine_198.3167+14.9688	$21.8^{+1.7}_{-1.0}$	$-36.0^{+2.5}_{-1.0}$	$2.2^{+0.6}_{-0.6}$	$9.1^{+0.1}_{-0.1}$	$7.1^{+0.1}_{-0.1}$
Pristine_206.8050+00.7423	77^{+17}_{-1}	-174^{+1}_{-43}	$-22.4^{+9.8}_{-8.2}$	$8.7^{+0.1}_{-0.1}$	$1.6^{+0.6}_{-0.4}$
Pristine_206.9304+11.8894	$146.9^{+7.3}_{-1.0}$	-270^{+14}_{-1}	$0.2^{+2.4}_{-2.1}$	$10.5^{+0.2}_{-0.2}$	$0.4^{+0.2}_{-0.1}$
Pristine_212.2541+11.4580	$23.2^{+1.0}_{-1.0}$	$-716.1^{+1.0}_{-1.0}$	-232^{+27}_{-59}	$11.1^{+102.6}_{-0.1}$	$2.4^{+3.1}_{-1.3}$
Pristine_213.1910+14.7927	$-376.8^{+1.0}_{-1.0}$	$-333.6^{+1.0}_{-1.0}$	15^{+32}_{-16}	$9.4^{+6.4}_{-0.1}$	$3.4^{+1.6}_{-0.2}$
Pristine_216.1506+14.1298	$-575.5^{+1.0}_{-1.0}$	$-558.1^{+1.0}_{-1.0}$	112^{+48}_{-30}	$36.2^{+182.9}_{-22.9}$	$3.0^{+5.5}_{-2.0}$
Pristine_219.0145+11.6057	$-26.4^{+1.0}_{-3.8}$	$19.1^{+3.4}_{-1.0}$	$8.7^{+1.0}_{-1.0}$	$13.7^{+0.3}_{-0.2}$	$7.4^{+0.1}_{-0.1}$
Pristine_232.8856+07.8678	$-29.5^{+3.9}_{-1.0}$	-100^{+1}_{-12}	$-67.7^{+0.6}_{-0.7}$	$7.5^{+0.1}_{-0.1}$	$4.3^{+0.2}_{-0.3}$
Pristine_234.0338+12.6370	$-95.6^{+1.0}_{-1.3}$	$-120.5^{+1.0}_{-5.6}$	$-111.9^{+0.7}_{-0.6}$	$8.9^{+0.1}_{-0.1}$	$3.8^{+0.1}_{-0.1}$
Pristine_235.0278+07.5059	$11.2^{+1.0}_{-7.6}$	-172^{+1}_{-43}	$121.6^{+6.6}_{-6.2}$	$6.5^{+0.1}_{-0.1}$	$2.8^{+0.3}_{-0.3}$
Pristine_235.0537+07.5988	$-100.5^{+1.0}_{-1.5}$	-329^{+18}_{-1}	$-4.0^{+3.2}_{-2.9}$	$8.2^{+0.1}_{-0.1}$	$1.2^{+0.3}_{-0.2}$
Pristine_236.4719+15.3328	$-158.6^{+6.3}_{-1.0}$	-238^{+17}_{-1}	$18.9^{+6.0}_{-6.2}$	$9.5^{+0.1}_{-0.1}$	$0.6^{+0.6}_{-0.1}$
Pristine_236.7635+05.4474	-233^{+1}_{-13}	-150^{+1}_{-18}	$-32.4^{+8.1}_{-8.1}$	$13.2^{+0.1}_{-0.1}$	$1.7^{+0.2}_{-0.2}$
Pristine_237.8581+07.1456	158^{+27}_{-1}	-216^{+1}_{-25}	-197^{+10}_{-11}	$15.5^{+1.9}_{-1.6}$	$2.1^{+0.2}_{-0.2}$
Pristine_238.2716+07.5917	$-91.8^{+1.0}_{-7.7}$	-147^{+1}_{-30}	$10.5^{+6.4}_{-6.4}$	$6.9^{+0.1}_{-0.1}$	$1.9^{+0.3}_{-0.2}$
Pristine_240.2908+07.9401	-117^{+1}_{-40}	-39^{+1}_{-14}	131^{+15}_{-13}	$13.7^{+1.6}_{-1.3}$	$2.8^{+0.4}_{-0.5}$
Pristine_241.1299+06.3632	$-119.9^{+1.3}_{-1.0}$	-144^{+1}_{-15}	$-62.2^{+2.6}_{-2.7}$	$8.6^{+0.1}_{-0.1}$	$2.3^{+0.2}_{-0.2}$
Pristine_246.4406+15.0900	243^{+51}_{-1}	-160^{+1}_{-47}	$-38.7^{+8.0}_{-9.5}$	$20.5^{+2.8}_{-1.8}$	$2.6^{+0.2}_{-0.2}$

Table A2. Inferred orbital parameters of the stars in the sample. The eccentricity $\epsilon = (r_{apo} - r_{peri})/(r_{apo} + r_{peri})$ of the orbit, the energy and the rotational, the radial and the vertical components of the action (J_ϕ, J_r, J_z), the maximum height z_{max}, and the kind of orbit are listed.

Target	ϵ	E ($\mathrm{km\,s^{-1}km\,s^{-1}}$)	J_ϕ ($\mathrm{kpc\,km\,s^{-1}}$)	J_r ($\mathrm{kpc\,km\,s^{-1}}$)	J_z ($\mathrm{kpc\,km\,s^{-1}}$)	z_{max} (kpc)	Orbit
Pristine_110.0459+43.0522	$0.623^{+0.133}_{-0.098}$	$-64442.4^{+3098.1}_{-2478.5}$	$-809.3^{+275.6}_{-261.8}$	$392.9^{+135.8}_{-107.5}$	$83.8^{+8.2}_{-9.9}$	$2.53^{+0.16}_{-0.19}$	Thick
Pristine_110.4208+40.8947	$0.407^{+0.116}_{-0.140}$	$-60390.7^{+3438.7}_{-2813.4}$	$-418.5^{+198.4}_{-240.2}$	$207.8^{+154.9}_{-112.2}$	$840.3^{+21.7}_{-26.4}$	$9.18^{+0.38}_{-0.57}$	Halo
Pristine_111.5919+44.0179	$0.175^{+0.002}_{-0.002}$	$-54848.0^{+203.6}_{-254.4}$	$1799.0^{+10.7}_{-11.9}$	$38.2^{+0.8}_{-0.8}$	$7.7^{+0.6}_{-0.5}$	$0.61^{+0.03}_{-0.02}$	Thin
Pristine_112.0456+43.9914	$0.061^{+0.002}_{-0.002}$	$-51076.8^{+56.6}_{-63.7}$	$2003.5^{+3.6}_{-4.0}$	$5.0^{+0.4}_{-0.3}$	$7.7^{+0.8}_{-0.7}$	$0.60^{+0.03}_{-0.03}$	Thin
Pristine_112.3237+44.2279	$0.264^{+0.005}_{-0.005}$	$-43283.1^{+349.7}_{-349.7}$	$2244.8^{+12.1}_{-11.3}$	$112.4^{+5.0}_{-4.4}$	$8.0^{+0.7}_{-0.7}$	$0.83^{+0.05}_{-0.05}$	Thin
Pristine_112.5667+45.9455	$0.383^{+0.006}_{-0.006}$	$-37690.1^{+664.4}_{-569.5}$	$2373.4^{+24.4}_{-21.7}$	$270.0^{+13.1}_{-11.6}$	$4.6^{+0.4}_{-0.3}$	$0.73^{+0.04}_{-0.03}$	Thin
Pristine_112.6119+45.7784	$0.149^{+0.002}_{-0.002}$	$-49831.8^{+35.0}_{-31.8}$	$2038.4^{+0.9}_{-0.8}$	$30.8^{+0.7}_{-0.6}$	$1.6^{+1.0}_{-1.0}$	$0.27^{+0.00}_{-0.01}$	Thin
Pristine_113.0244+45.6965	$0.163^{+0.001}_{-0.001}$	$-48562.0^{+132.8}_{-110.7}$	$2067.8^{+3.8}_{-3.4}$	$38.0^{+0.5}_{-0.5}$	$11.7^{+1.5}_{-1.3}$	$0.87^{+0.07}_{-0.06}$	Thin
Pristine_113.4132+41.9324	$0.047^{+0.008}_{-0.008}$	$-55087.1^{+212.3}_{-179.7}$	$1840.7^{+10.0}_{-10.0}$	$2.7^{+1.0}_{-0.8}$	$6.3^{+0.4}_{-0.5}$	$0.49^{+0.02}_{-0.02}$	Thin
Pristine_113.4275+45.6423	$0.071^{+0.008}_{-0.008}$	$-49603.9^{+84.6}_{-76.2}$	$2062.9^{+3.5}_{-3.0}$	$7.1^{+1.8}_{-1.6}$	$10.1^{+1.4}_{-1.4}$	$0.73^{+0.05}_{-0.06}$	Thin
Pristine_113.6421+45.4681	$0.233^{+0.004}_{-0.004}$	$-41866.8^{+580.4}_{-491.1}$	$2356.9^{+24.0}_{-22.1}$	$90.6^{+4.6}_{-3.8}$	$7.7^{+0.9}_{-0.8}$	$0.82^{+0.06}_{-0.06}$	Thin
Pristine_113.6744+45.8738	$0.283^{+0.003}_{-0.003}$	$-48164.7^{+254.1}_{-231.0}$	$1924.3^{+19.0}_{-17.3}$	$114.7^{+2.3}_{-2.0}$	$48.1^{+2.6}_{-2.9}$	$2.18^{+0.08}_{-0.08}$	Thick
Pristine_113.7050+45.5860	$0.183^{+0.001}_{-0.001}$	$-46030.8^{+217.4}_{-201.9}$	$2185.0^{+9.7}_{-9.3}$	$50.7^{+0.5}_{-0.5}$	$7.0^{+0.6}_{-0.5}$	$0.68^{+0.03}_{-0.03}$	Thin
Pristine_180.0750+16.3239	$0.123^{+0.001}_{-0.001}$	$-54599.6^{+163.1}_{-175.7}$	$1849.1^{+7.1}_{-6.8}$	$19.1^{+0.3}_{-0.3}$	$1.4^{+0.1}_{-0.1}$	$0.23^{+0.01}_{-0.01}$	Thin
Pristine_180.8898+15.6500	$0.884^{+0.045}_{-0.045}$	$-66554.2^{+2470.1}_{-1940.8}$	$-214.9^{+129.9}_{-146.1}$	$781.1^{+37.0}_{-33.3}$	$21.2^{+3.6}_{-3.0}$	$1.33^{+0.16}_{-0.07}$	Thick
Pristine_180.8994+16.3260	$0.159^{+0.002}_{-0.002}$	$-51835.9^{+185.6}_{-212.1}$	$1859.9^{+18.3}_{-26.8}$	$33.8^{+1.2}_{-0.9}$	$51.1^{+11.0}_{-7.5}$	$1.96^{+0.18}_{-0.17}$	Thick
Pristine_181.4437+13.4888	$0.287^{+0.016}_{-0.019}$	$-67335.9^{+588.7}_{-504.6}$	$1204.3^{+37.1}_{-37.1}$	$79.9^{+9.9}_{-9.6}$	$67.2^{+4.5}_{-3.9}$	$1.95^{+0.10}_{-0.07}$	Thick
Pristine_182.2972+13.1228	$0.804^{+0.036}_{-0.038}$	$-68685.1^{+418.6}_{-307.0}$	$436.4^{+64.1}_{-66.6}$	$588.2^{+51.3}_{-45.8}$	$37.2^{+1.8}_{-1.8}$	$1.71^{+0.05}_{-0.13}$	Thick
Pristine_183.1390+16.1839	$0.199^{+0.022}_{-0.023}$	$-65222.0^{+752.9}_{-695.0}$	$1396.1^{+40.7}_{-39.1}$	$39.3^{+8.4}_{-8.1}$	$24.2^{+2.7}_{-2.5}$	$1.02^{+0.08}_{-0.07}$	Thick
Pristine_183.4550+17.0927	$0.476^{+0.022}_{-0.036}$	$-57319.9^{+383.1}_{-383.1}$	$1263.8^{+60.6}_{-41.1}$	$262.4^{+32.5}_{-41.8}$	$80.6^{+7.4}_{-9.6}$	$2.59^{+0.14}_{-0.25}$	Thick
Pristine_185.5596+15.5893	$0.405^{+0.020}_{-0.020}$	$-47302.1^{+716.9}_{-665.7}$	$1830.2^{+4.5}_{-4.7}$	$241.0^{+29.3}_{-26.2}$	$25.1^{+0.8}_{-0.7}$	$1.66^{+0.09}_{-0.07}$	Thick
Pristine_188.4543+15.1750	$0.146^{+0.005}_{-0.004}$	$-54018.1^{+90.2}_{-90.2}$	$1843.8^{+7.0}_{-6.7}$	$27.2^{+1.8}_{-1.6}$	$9.5^{+0.6}_{-0.6}$	$0.69^{+0.02}_{-0.02}$	Thin
Pristine_191.9208+16.0031	$0.305^{+0.160}_{-0.093}$	$-65487.5^{+1531.9}_{-1276.6}$	$1083.7^{+184.8}_{-261.7}$	$83.1^{+89.6}_{-44.8}$	$172.5^{+61.6}_{-46.2}$	$3.56^{+1.13}_{-0.71}$	Thick
Pristine_192.4508+12.7922	$0.297^{+0.016}_{-0.016}$	$-60309.6^{+161.1}_{-115.1}$	$1495.4^{+20.5}_{-21.2}$	$97.6^{+10.5}_{-9.4}$	$15.6^{+1.2}_{-1.2}$	$0.91^{+0.04}_{-0.04}$	Thin
Pristine_193.5777+10.3945	$0.649^{+0.058}_{-0.025}$	$-70002.9^{+92.0}_{-73.6}$	$523.3^{+50.8}_{-54.7}$	$392.5^{+27.5}_{-24.5}$	$163.8^{+8.8}_{-8.8}$	$4.28^{+0.25}_{-0.21}$	Halo
Pristine_195.1494+06.5655	$0.748^{+0.017}_{-0.018}$	$-13651.5^{+1986.9}_{-1821.3}$	$41.1^{+98.7}_{-94.6}$	$1864.6^{+203.6}_{-162.9}$	$2153.3^{+52.0}_{-55.9}$	$38.35^{+2.64}_{-2.15}$	Halo
Pristine_198.3167+14.9688	$0.123^{+0.002}_{-0.002}$	$-57589.0^{+242.5}_{-223.9}$	$1715.0^{+11.5}_{-9.8}$	$17.8^{+0.7}_{-0.6}$	$10.2^{+0.5}_{-0.6}$	$0.65^{+0.02}_{-0.02}$	Thin
Pristine_206.8050+00.7423	$0.688^{+0.066}_{-0.100}$	$-74524.1^{+1009.5}_{-415.7}$	$584.7^{+165.2}_{-130.8}$	$383.3^{+67.7}_{-74.5}$	$31.1^{+5.7}_{-5.5}$	$1.32^{+0.19}_{-0.16}$	Thick
Pristine_206.9304+11.8894	$0.932^{+0.020}_{-0.027}$	$-68746.9^{+735.4}_{-686.4}$	$-46.2^{+66.0}_{-61.6}$	$838.6^{+12.0}_{-14.8}$	$10.2^{+0.2}_{-0.2}$	$1.03^{+0.02}_{-0.01}$	Thick
Pristine_212.2541+11.4580	$0.871^{+0.059}_{-0.189}$	$-55237.6^{+62464.4}_{-1.0}$	$52.8^{+440.9}_{-440.9}$	$126.6^{+1.0}_{-1.0}$	$447.6^{+1290.5}_{-1.0}$	$14.19^{+101.54}_{-6.77}$	Halo
Pristine_213.1910+14.7927	$0.583^{+0.029}_{-0.086}$	$-56836.4^{+17888.5}_{-5962.8}$	$497.0^{+265.9}_{-422.4}$	$129.7^{+1.0}_{-1.0}$	$648.8^{+1019.1}_{-291.2}$	$9.07^{+7.84}_{-3.14}$	Halo
Pristine_216.1506+14.1298	$0.877^{+0.059}_{-0.029}$	$-26807.1^{+59580.8}_{-14895.2}$	$-475.8^{+341.4}_{-443.8}$	$796.4^{+1.0}_{-1.0}$	$734.5^{+1047.6}_{-349.2}$	$22.94^{+19.59}_{-11.76}$	Halo
Pristine_219.0145+11.6057	$0.298^{+0.011}_{-0.012}$	$-46200.0^{+476.3}_{-408.3}$	$2017.7^{+2.1}_{-2.1}$	$133.8^{+11.4}_{-11.0}$	$36.4^{+5.0}_{-5.0}$	$1.99^{+0.18}_{-0.19}$	Thick
Pristine_232.8856+07.8678	$0.274^{+0.030}_{-0.020}$	$-70980.0^{+939.9}_{-1110.8}$	$1131.5^{+44.1}_{-50.2}$	$67.4^{+11.2}_{-8.6}$	$55.2^{+2.9}_{-2.7}$	$1.62^{+0.06}_{-0.05}$	Thick
Pristine_234.0338+12.6370	$0.400^{+0.011}_{-0.009}$	$-65861.8^{+515.2}_{-554.8}$	$994.1^{+25.1}_{-25.1}$	$157.9^{+5.5}_{-4.7}$	$173.8^{+1.5}_{-1.3}$	$3.84^{+0.03}_{-0.03}$	Thick
Pristine_235.0278+07.5059	$0.388^{+0.047}_{-0.047}$	$-77380.5^{+909.0}_{-530.3}$	$481.1^{+103.1}_{-91.6}$	$74.6^{+13.1}_{-12.4}$	$397.7^{+53.8}_{-47.4}$	$4.74^{+0.63}_{-0.24}$	Halo
Pristine_235.0537+07.5988	$0.746^{+0.039}_{-0.053}$	$-78390.9^{+670.8}_{-545.0}$	$-468.7^{+70.4}_{-81.2}$	$434.6^{+35.8}_{-38.5}$	$7.5^{+0.5}_{-0.3}$	$0.55^{+0.02}_{-0.01}$	Thick
Pristine_236.4719+15.3328	$0.871^{+0.029}_{-0.097}$	$-73351.7^{+330.4}_{-220.3}$	$185.0^{+70.4}_{-67.7}$	$674.3^{+38.7}_{-38.7}$	$12.8^{+3.0}_{-2.3}$	$0.96^{+0.09}_{-0.02}$	Thin
Pristine_236.7635+05.4474	$0.773^{+0.026}_{-0.026}$	$-57119.4^{+117.0}_{-117.0}$	$625.8^{+71.8}_{-68.6}$	$699.9^{+45.7}_{-41.8}$	$68.3^{+2.8}_{-1.7}$	$3.09^{+0.12}_{-0.06}$	Thick
Pristine_237.8581+07.1456	$0.761^{+0.027}_{-0.035}$	$-49125.4^{+4286.9}_{-3980.7}$	$314.7^{+91.0}_{-84.5}$	$742.8^{+159.8}_{-125.6}$	$581.8^{+78.3}_{-69.9}$	$13.68^{+2.55}_{-2.38}$	Halo
Pristine_238.2716+07.5917	$0.560^{+0.041}_{-0.053}$	$-80881.5^{+1320.5}_{-1100.4}$	$550.6^{+90.5}_{-95.5}$	$194.5^{+22.9}_{-20.5}$	$132.1^{+19.5}_{-18.4}$	$2.84^{+0.30}_{-0.26}$	Thick
Pristine_240.2908+07.9401	$0.655^{+0.077}_{-0.073}$	$-53144.1^{+3606.9}_{-2705.2}$	$740.5^{+138.5}_{-147.7}$	$509.7^{+167.7}_{-115.3}$	$329.7^{+58.4}_{-49.4}$	$8.43^{+0.80}_{-1.59}$	Halo
Pristine_241.1299+06.3632	$0.579^{+0.021}_{-0.027}$	$-72550.9^{+1145.0}_{-1049.6}$	$757.8^{+58.1}_{-55.7}$	$285.4^{+17.6}_{-16.9}$	$59.2^{+1.4}_{-1.3}$	$1.94^{+0.08}_{-0.04}$	Thick
Pristine_246.4406+15.0900	$0.774^{+0.038}_{-0.031}$	$-39353.9^{+4164.6}_{-3239.1}$	$943.5^{+58.8}_{-52.6}$	$1062.0^{+210.5}_{-161.0}$	$126.4^{+22.9}_{-17.8}$	$6.68^{+1.71}_{-1.14}$	Halo

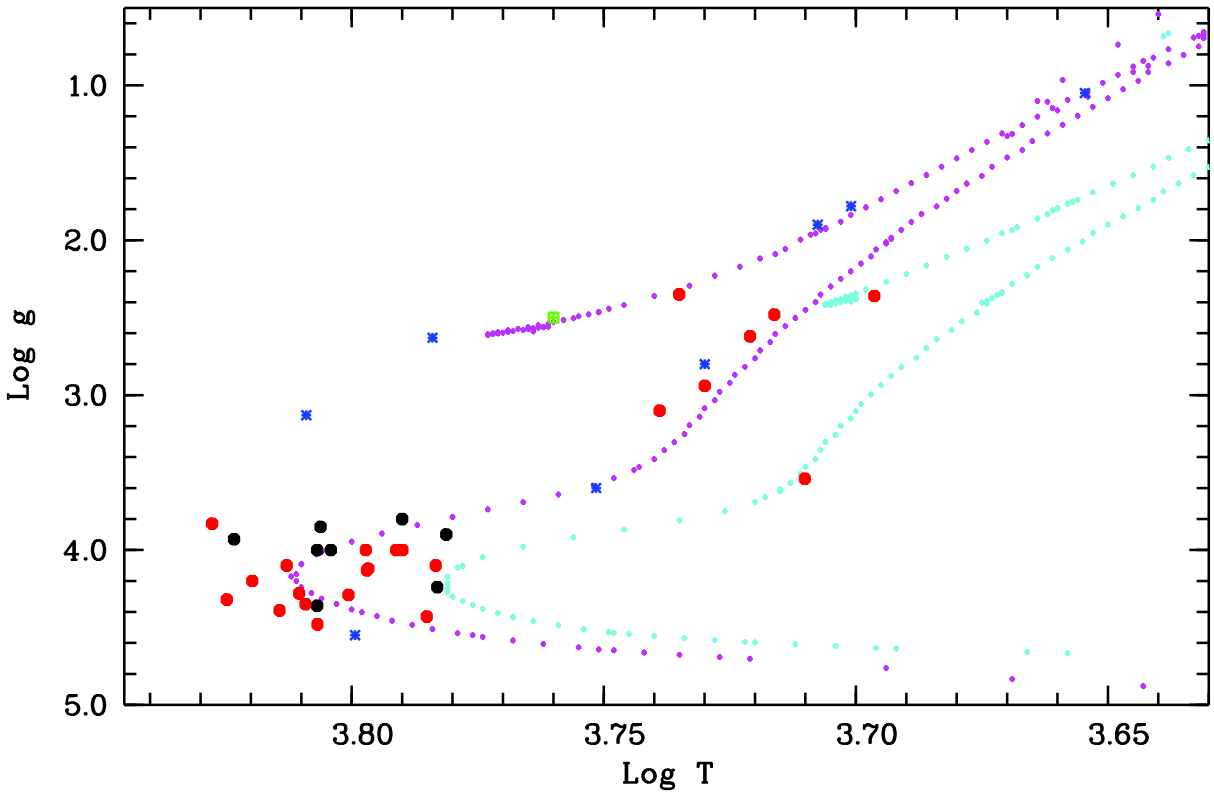

Figure B1. The log ($T_{\rm eff}$) - log g diagram for our stars. Black dots are stars classified as "Thin", red dots are stars classified as "Thick" and blue asterisks are stars classified as "Halo", the green crossed square is the star Pristine_216.1506+14.1298. The cyan dots are a PARSEC isochrone of 11.5 Gyr and metallicity −0.5 and the magenta dots one of metallicity −1.5.

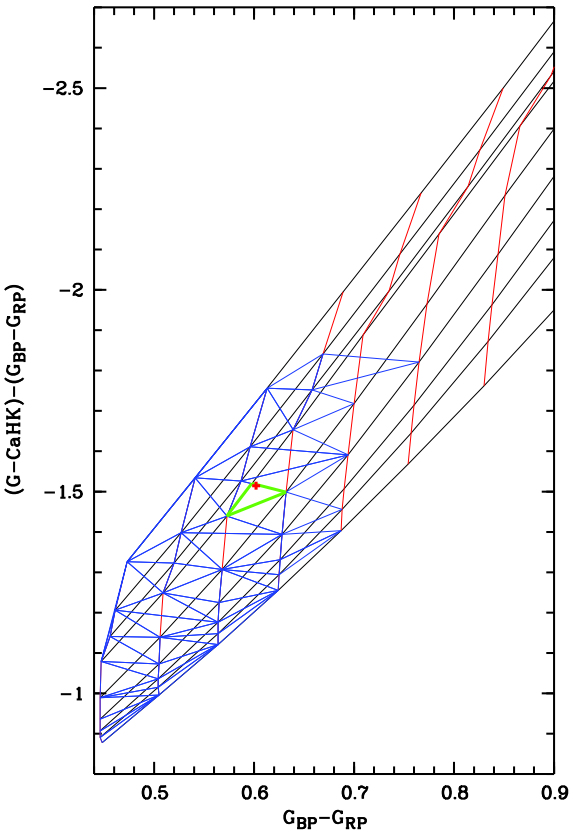

Figure C1. Illustration of how the triangle for interpolation is detemined. The underlying grid is the theoreticla colours interpolated for log g = 3.84 (black lines of constant metallicity, red of constant effective temperature), in blue a part of the Delaunay triangulation and in green the refined triangle (non-Delaunay) that is used to estimate the final metallicity. The red cross corresponds to the observed colours.

APPENDIX

B

The Pristine survey - IX. CFHT ESPaDOnS spectroscopic analysis of 115 bright metal-poor candidate stars

This Appendix contains the work led by Pristine collaborators at the University of Victoria and published on Monthly Notices of the Royal Astronomical Society (Venn et al., 2020), in which I am one of the main co-authors. This work is a high-resolution spectroscopic follow-up of 115 bright very metal-poor candidates selected by the Pristine survey. The sample has been observed at the Canada-France-Hawaii Telescope (CFHT) with the Échelle SpectroPolarimetric Device for the Observation of Stars (ESPaDOnS, $R \sim 68000$). The photometric metallicities were inferred with the SDSS broad-band filters coupled with the Pristine narrow-band filter, although the magnitude of the sample is at the very edge of the saturation of SDSS photometry. The spectroscopic metallicities were derived using the effective temperature and surface gravities inferred from my bayesian method (Sestito et al., 2019) as input for the analysis. In this sample, 28 out of 70 stars are confirmed to have a spectroscopic metallicity below [Fe/H] ≤ -2.5 and 5 out of 27 in the EMP regime, meaning a success rate of 40 and 19 per cent, respectively.

Thanks to the high-resolution of the instrument, it was possible to carry out detailed chemical abundances for α-, Iron-peak, and neutron-capture elements, i.e., Sodium, Magnesium, Calcium, Scandium, Titanium, Chromium, Iron, Nickel, Yttrium, and Barium. The majority of the stars show a similar chemical pattern to the normal metal-poor of the Galactic halo, however, one r-process rich star and a Mg-poor star was discovered. The kinematical analysis reveals the presence of stars with planar orbits as also shown in Sestito et al. (2019, 2020a), spanning a wide range of eccentricities, and few VMPs that are likely to be unbound. In this analysed sample, 8 stars display the typical low angular momentum signature of the accreted structure called Gaia-Enceladus-Sausage.

Monthly Notices
of the
ROYAL ASTRONOMICAL SOCIETY

MNRAS **492,** 3241–3262 (2020)
Advance Access publication 2019 December 23

doi:10.1093/mnras/stz3546

The Pristine survey – IX. CFHT ESPaDOnS spectroscopic analysis of 115 bright metal-poor candidate stars

Kim A. Venn [1★] Collin L. Kielty,[1] Federico Sestito,[2,3] Else Starkenburg,[3] Nicolas Martin,[2,4] David S. Aguado,[5] Anke Arentsen [3], Piercarlo Bonifacio [6], Elisabetta Caffau,[6] Vanessa Hill,[7] Pascale Jablonka,[6,8] Carmela Lardo [8], Lyudmilla Mashonkina,[9] Julio F. Navarro,[1] Chris Sneden,[10] Guillaume Thomas,[11] Kris Youakim [3], Jonay I. González-Hernández,[12,13] Rubén Sánchez Janssen,[14] Ray Carlberg[15] and Khyati Malhan[16]

Affiliations are listed at the end of the paper

Accepted 2019 December 10. Received 2019 December 10; in original form 2019 October 12

ABSTRACT

A chemo-dynamical analysis of 115 metal-poor candidate stars selected from the narrow-band *Pristine* photometric survey is presented based on CFHT high-resolution ESPaDOnS spectroscopy. We have discovered 28 new bright ($V < 15$) stars with [Fe/H] < -2.5 and 5 with [Fe/H] < -3.0 for success rates of 40 (28/70) and 19 per cent (5/27), respectively. A detailed model atmosphere analysis is carried out for the 28 new metal-poor stars. Stellar parameters were determined from SDSS photometric colours, *Gaia* DR2 parallaxes, MESA/MIST stellar isochrones, and the initial *Pristine* survey metallicities, following a Bayesian inference method. Chemical abundances are determined for 10 elements (Na, Mg, Ca, Sc, Ti, Cr, Fe, Ni, Y, and Ba). Most stars show chemical abundance patterns that are similar to the normal metal-poor stars in the Galactic halo; however, we also report the discoveries of a new r-process-rich star, a new CEMP-s candidate with [Y/Ba] > 0, and a metal-poor star with very low [Mg/Fe]. The kinematics and orbits for all of the highly probable metal-poor candidates are determined by combining our precision radial velocities with *Gaia* DR2 proper motions. Some stars show unusual kinematics for their chemistries, including planar orbits, unbound orbits, and highly elliptical orbits that plunge deeply into the Galactic bulge ($R_{\rm peri} < 0.5$ kpc); also, eight stars have orbital energies and actions consistent with the Gaia-Enceladus accretion event. This paper contributes to our understanding of the complex chemo-dynamics of the metal-poor Galaxy, and increases the number of known bright metal-poor stars available for detailed nucleosynthetic studies.

Key words: Galaxy: stellar content – Galaxy: kinematics and dynamics – Galaxy: abundances – stars: Population II – stars: abundances – stars: kinematics and dynamics.

1 INTRODUCTION

Very old stars are witness to the earliest epochs of galaxy formation and evolution. Most theoretical models of star formation at early times predict the formation of high-mass stars (e.g. Nakamura & Umemura 2001; Abel, Bryan & Norman 2002; Bromm 2013) that contributed to the reionization of the Universe. During their short lives, these massive stars initiate the formation of the chemical elements beyond hydrogen, helium, and lithium, and yet no star with such a primordial composition has yet been found. The fragmentation of the early star-forming regions has also been predicted (e.g. Schneider et al. 2003; Clark et al. 2011; Greif 2015; Hirano et al. 2015), providing an environment where lower mass ($\sim$1 $M_\odot$) stars could form, which would have much longer lifetimes. These old stars are expected to be metal poor, having formed from nearly pristine gas, and could be used to trace the chemical elements from the massive (first) stars and their subsequent supernovae (e.g. Frebel & Norris 2015; Hartwig et al. 2018; Salvadori et al. 2019).

In recent years, abundance patterns of metal-poor stars have been examined extensively (e.g. Keller et al. 2014; Ishigaki et al. 2018;

★ E-mail: kvenn@uvic.ca

Nordlander et al. 2019), pointing to the significance of low-energy (faint) supernovae, whose ejecta fall back on to their iron cores, thereby mainly expelling light elements. It is not clear if these low-energy supernovae were more common at ancient times, or if concurrent massive stars underwent direct collapse to black holes and ceased nearby star formation, erasing any direct evidence of their presence in the next generation of stars. Overall, metal-poor stars allow us to examine nucleosynthetic yields from one or a few supernova events to constrain the detailed physics of these events, such as neutron star masses, rotation rates, mixing efficiencies, explosion energies, etc. (Heger & Woosley 2010; Thielemann et al. 2018; Wanajo 2018; Jones et al. 2019; Müller et al. 2019). These yields are relevant for understanding the early chemical build-up and the initial conditions in the early Galaxy.

Chemical abundances also show variations between old metal-poor stars in different environments such as dwarf galaxies, suggesting that the first stages of enrichment were not uniform. Stars in the nearby dwarf galaxies typically have lower abundances of α- and odd-Z elements, attributed to their slower star formation histories and/or fewer number of high-mass stars overall (Venn et al. 2004; Tolstoy, Hill & Tosi 2009; Nissen & Schuster 2010; McWilliam, Wallerstein & Mottini 2013; Frebel & Norris 2015; Hayes et al. 2018), while significant variations in heavy r-process elements in some dwarf galaxies, and globular clusters, are discussed in terms of contributions from individual compact binary merger events, like GW170817 (e.g. Roederer 2011; Ji et al. 2016; Roederer, Hattori & Valluri 2018a; Ji, Drout & Hansen 2019). In addition, about a third of the [Fe/H] < -2.5 stars[1] in the Galactic halo show very high enhancements in carbon (the carbon-enhanced metal-poor stars, 'CEMP'; Yong et al. 2013; Aguado et al. 2019a; also see Kielty et al. 2017; Mardini et al. 2019), discussed as a signature of the earliest chemical enrichment in the Universe. However, at least one ultra-metal-poor star is not carbon enhanced (SDSS J102915+172927, Caffau et al. 2012), and the known metal-poor stars in the Galactic bulge do not show carbon enhancements (Howes et al. 2016; Lamb et al. 2017). Norris et al. (2013) suggest that there are likely multiple chemical enrichment pathways for old metal-poor stars dependent on the star formation environment, and also possibly binary mass-transfer effects (also see discussions by Starkenburg et al. 2014; Arentsen et al. 2019).

The majority of old, metal-poor stars in the Galactic halo are thought to have been accreted from dwarf galaxies at early epochs, based on cosmological hydrodynamical simulations of the Local Group (Ibata, Gilmore & Irwin 1994; Helmi et al. 1999; Ibata et al. 2004; Abadi et al. 2010; Starkenburg et al. 2017a; El-Badry et al. 2018). This is consistent with the high-velocity, eccentric, orbits determined from the exquisite *Gaia* DR2 data (Gaia Collaboration 2018) and spectroscopic radial velocities (RVs) for a majority of the ultra-metal-poor stars (Sestito et al. 2019) and the ultra-faint dwarf galaxies (Simon 2018). Interestingly, many of these orbits are also highly retrograde, similar to the diffuse halo merger remnants, Gaia-Enceladus (Belokurov et al. 2018; Haywood et al. 2018; Helmi et al. 2018; Myeong et al. 2018) and Gaia-Sequoia (Barbá et al. 2019; Myeong et al. 2019). However, some metal-poor stars have been found to have orbits that place them in the Galactic plane (Sestito et al. 2019), even with nearly circular orbits (e.g. SDSS J102915+172927, Caffau et al. 2012). These latter observations challenge the cosmological simulations since metal-poor stars are assumed to be old, and yet the Galactic plane is thought to have formed only ∼10 Gyr ago (e.g. Gianninas et al. 2015; Casagrande et al. 2016). Alternatively, Sestito et al. (2019) suggest that these stars may have be brought into the Galaxy from a merger that helped to form the disc.

Progress in this field will require large statistical samples of metal-poor stars in a variety of environments within the Local Group. Unfortunately, metal-poor stars are exceedingly rare and difficult to find, being overwhelmed by the more numerous metal-rich populations in the Galaxy. Examination of the Besançon model of the Galaxy (Robin et al. 2003), which is guided by a theoretical framework for the formation and evolution of the main stellar populations, suggests that a typical halo field has only one in ∼2000 stars with [Fe/H] < -3 between $14 < V < 18$ (Youakim et al. 2017). Enormous effort has gone into the discovery and study of extremely, ultra, and hyper metal-poor stars with [Fe/H] < -3.0, -4.0, and -5.0, respectively. Most of the known metal-poor stars have been found in dedicated surveys, such as objective prism surveys (the HK survey and Hamburg-ESO survey, Beers, Preston & Shectman 1992; Christlieb et al. 2002, 2008; Beers & Christlieb 2005; Frebel et al. 2006; Schörck et al. 2009), wide-band photometric surveys (Schlaufman & Casey 2014), and blind spectroscopic surveys, such as the Sloan Digital Sky Survey (SDSS) SEGUE and BOSS surveys (Yanny et al. 2009; Eisenstein et al. 2011; Dawson et al. 2013), and from the Large Sky Area Multi-Object Fibre Spectroscopic Telescope (LAMOST; Cui et al. 2012). According to the SAGA data base (see Suda et al. 2017, and references therein), there are ∼500 stars with [Fe/H] < -3.0, though fewer than half have detailed chemical abundances. Recently, narrow-band photometric surveys have shown higher success rates for finding metal-poor stars, particularly SkyMapper (Keller et al. 2007; DaCosta et al. 2019) and the *Pristine* survey (Starkenburg et al. 2017b; Youakim et al. 2017; Aguado et al. 2019a). *Pristine* photometry with follow-up Keck II/DEIMOS spectroscopy has also been used to increase sample sizes and improve the chemodynamical studies of faint satellites (Draco II and Sgr II, Longeard et al. 2018, 2019). At the same time, Simon (2018) has shown that *Gaia* DR2 proper motion cleaning may also be a promising way to find new metal-poor members of ultra-faint dwarf galaxies.

The *Pristine* survey uses a unique narrow-band filter centred on the Ca II H&K spectral lines ('CaHK') mounted on MegaPrime/MegaCam at the 3.6-m Canada France Hawaii Telescope (CFHT). When combined with broad-band SDSS *gri* photometry (York et al. 2000), this CaHK filter has been calibrated to find metal-poor candidates with $4200 < T < 6500$ K. The *Pristine* survey has proven successful at predicting metallicities for faint objects ($18 > V > 15$), based on results from medium-resolution spectroscopic follow-up (Youakim et al. 2017; Aguado et al. 2019a). For brighter objects, the success of the *Pristine* calibration is less certain. Caffau et al. (2017) observed 26 bright ($g < 15$) candidates with the FEROS spectrograph at the MPG/ESO 2.2-m telescope, but found only 5 stars with [Fe/H] < -2.0. It was thought that the selection may be affected by previously unrecognized saturation effects in the SDSS photometry. Thus, Bonifacio et al. (2019) selected bright candidates using a new *Pristine* calibration with the APASS photometry (cf. APASS DR10; Henden 2019); the observations of 40 targets with the SOPHIE spectrograph at Observatoire de Haute Provence found only eight stars with [Fe/H] < -2.0, and none with [Fe/H] < -3.0. Until now, the confirmation of the *Pristine* metallicity predictions below [Fe/H] $= -3.0$ has only been carried out for one star from high-resolution spectroscopy, Pristine_221.8781+09.7844 at [Fe/H] $= -4.7$ (1D, LTE) and $V = 16.4$ (Starkenburg et al. 2018).

[1]We adopt standard notation, such that $[X/H] = \log(X/H)_* - \log(X/H)_\odot$.

Table 1. Metal-poor targets (115) from the original *Pristine* survey footprint. Herein, 59 stars were selected with a *Pristine* metallicity [Fe/H]$_P$ < −2.5 and SDSS *(g−i)* and *(g−r)* calibrations with probabilities for both [Fe/H]$_P$gi and [Fe/H]$_P$gr < −2.25 greater than 80 per cent (dFe$_P$ = 1σ). For 10 stars, only the SDSS *(g−r)* calibration was available, as noted. Targets no longer in the *Pristine* catalogue, or with [Fe/H]$_P$ > −2.5, are also noted. The CaHK and SDSS *ugri* magnitudes are dereddened using the *E(B−V)* values from the (Schlegel, Finkbeiner & Davis 1998) maps; however, *V* and *I* are not dereddened (i.e. observer units). The SDSS colour temperature (T_{SDSS}) averages the dwarf and giant solutions (where dT =1σ), and the CFHT program labels are in the comments. Only a sample of the targets is shown here, and the full table is available online.

RA$_{SDSS}$ (deg)	DEC$_{SDSS}$ (deg)	V	I	$E(B-V)$	CaHK$_0$	u_0	g_0	r_0	i_0	T_{SDSS} (K)	dT (K)	[Fe]$_P$	dFe$_P$	COMM
High probability for [Fe/H]$_P$ ≤ −2.5 in the *Pristine* catalogue:														
180.2206	09.5683	14.92	13.99	0.021	15.822	16.439	15.172	14.625	14.392	5202.6	17.6	−2.82	0.02	16BC,17AC
181.2243	07.4160	14.95	14.33	0.015	15.361	15.949	15.044	14.804	14.707	6261.5	5.8	−2.78	0.01	17AC002
181.3464	11.6698	14.18	13.42	0.033	14.782	15.293	14.392	13.841	13.757	5504.8	15.6	−3.82	0.09	16AC031
181.4395	01.6294	14.67	13.66	0.020	15.562	16.345	14.961	14.357	14.078	5011.6	18.5	−3.82	0.09	16BC008

In this paper, we present the analysis of 115 bright (V < 15) metal-poor candidates from the *Pristine* survey, calibrated using the original SDSS *gri* photometry and observed at the CFHT with the high-resolution ESPaDOnS spectrograph. Such high-resolution spectra are necessary for detailed chemical abundances, as well as precision RVs for determining the kinematic properties. The power of combining chemical abundances with kinematic properties of stars is the backbone of the field of Galactic Archaeology (e.g. Freeman & Bland-Hawthorn 2002; Venn et al. 2004; Tolstoy et al. 2009; Frebel & Norris 2015). We confirm the success of the *Pristine* survey to find metal-poor stars even at bright magnitudes, determine the chemical abundances for 10 elements, calculate the kinematics of the stars in our sample, and interpret in the context of variations in nucleosynthetic sites, locations, and time-scales. The study of metal-poor old stars is unique to our Local Group, since only here can we resolve individual stars and study these rare targets that guide our understanding of the physics of star formation, supernovae, the early build-up of galaxies, and the epoch of reionization.

2 TARGET SELECTION

Targets were selected from the *Pristine* survey catalogue,[2] which includes 28 557 bright (V < 15) stars in the original ∼1000 sq. deg^2 footprint between 180 < RA < 256° and +00 < Dec < +16° (Starkenburg et al. 2017b; Youakim et al. 2017).

Pristine survey targets were cross-matched with the SDSS photometry to obtain *ugri* broad-band magnitudes used for colour temperature determinations and point-source identification. Additional selection criteria were adopted, as described by Youakim et al. (2017), including the removal of non-star contaminants (based on SDSS and CaHK flags), white dwarf contaminants (removing SDSS $u - g$ > 0.6, Lokhorst et al. 2016), variability flags from the Pan-STARRS1 photometry (Hernitschek et al. 2016), and the quality of the SDSS *gri*-band photometry. The SDSS *gri*-band photometry was further used for a colour selection, where 0.25 < $(g - i)_o$ < 1.5 and 0.15 < $(g - r)_o$ < 1.2 correspond to the temperature range 4200 K < $T_{\rm eff}$ < 6500 K, covering the tip of the red giant branch and the cooler main sequence to the main-sequence turn-off.

The 115 stars observed at CFHT with the high-resolution (R∼68 000) ESPaDOnS spectrograph (Donati et al. 2006) are listed in Table 1 including RA and DEC (from SDSS, in degrees), the dereddened SDSS $(ugri)_0$ and *Pristine*-CaHK$_0$ magnitudes, the V and I magnitudes [converted from the SDSS photometry using Jordi, Grebel & Ammon (2006) and not dereddened, thus in observer units], and the reddening $E(B - V)$ value. Extinction values are small for most stars, and we assume that all the extinction is in the foreground, therefore using the Schlegel et al. (1998) extinction maps. A summary of the CFHT ESPaDOnS observing runs that comprise this program is 16AC031 (23 targets), 16AC096 (17 targets), 16BC008 (25 targets), 17AC002 (30 targets), and 18BC018 (25 targets), which is 120 targets, with 5 repeat targets, thus 115 independent objects.

We note that this programme began immediately after the initial *Pristine* survey MegaCam observing runs, and the metallicity calibrations have improved over the course of these spectroscopic follow-up observations (2016A to 2018B). Of the 115 observed stars, 88 remain in the *Pristine* survey catalogue. In Table 1, we have 59 stars with a >80 per cent probability to have [Fe/H] < −2.25 using both the SDSS $g - r$ and $g - i$ colour calibrations, and with individual metallicity estimates of [Fe/H] < −2.5. Another 10 stars follow these selections using the SDSS $g - r$ colour alone. Youakim et al. (2017) showed that the SDSS i filter has saturation effects in some fields for stars in our magnitude range that can affect the SDSS $g - i$ selection criterion. An additional 46 stars were observed with ESPaDOnS; however, we now recognize 19 of those to have low probabilities to be metal poor, and 27 are no longer in the *Pristine* survey catalogue (e.g. due to the saturation effects in the SDSS photometry recognized later). Ironically, of those latter 27 stars, one star (Pristine_213.7879+08.4232) does appear to be metal poor, e.g. its Ca II triplet lines are weak and narrow. Possibly the *Pristine* survey selection function is now slightly overly strict; we retained this one metal-poor candidate. Thus, we have observed a total of 70 (59 + 10 + 1) metal-poor candidates selected from the original ∼1000 sq. deg^2 footprint of the *Pristine* survey. In total, there are 223 bright stars that meet all of the selection criteria described in this section, thus we have observed 31 per cent (70/223) of these candidates. Both of these distributions are shown in Fig. 1.

The selection criteria used here differ slightly from Youakim et al. (2017) and Aguado et al. (2019a), where stars with probability over 25 per cent in both $g - r$ and $g - i$ were selected for their medium-resolution spectroscopic programme. These lower limits were also adopted by Caffau et al. (2017) and Bonifacio et al. (2019) in their target selections, though using the APASS photometry in the latter paper. We emphasize that our target selections were made without a priori knowledge of the spectroscopic metallicities, other than for a small subset of five stars[3] in our final 2018B observing run.

[2]Internal-Catalogue-1802.dat.

[3]Five stars had interesting results from our concurrent medium-resolution spectral campaign, and were selected for observations with ESPaDOnS during our final 2018B run. Three were confirmed to be metal poor ([Fe/H] < −2.5), but two were not ([Fe/H] > −2.0). If we recalculate our success

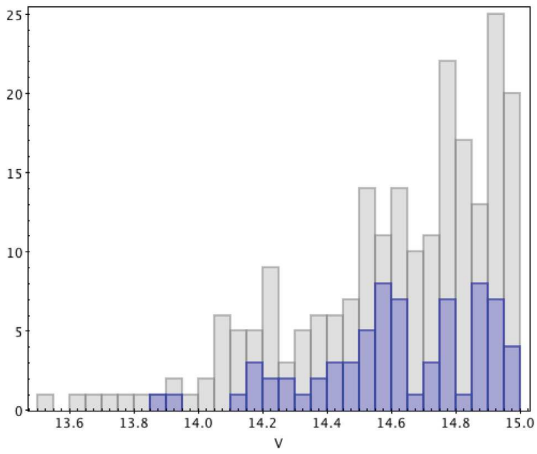

Figure 1. Histogram of the V magnitudes of 223 stars with high probabilities to be metal poor ([Fe/H] < -2.50) from the $(g-i)$ or $(g-r)$ calibrations in the *Pristine* survey original ∼1000 sq. deg^2 footprint (grey bars). The 70 stars observed with CFHT ESPaDOnS that also meet these criteria are overplotted (blue bars).

3 ESPADONS OBSERVATIONS

The CFHT high-resolution spectrograph ESPaDOnS was used between 2016A and 2018B to observe 115 new bright, metal-poor candidates found in the original CFHT-MegaCam survey footprint as part of the *Pristine* survey. ESPaDOnS was used in the 'star+sky' mode, providing a high-resolution (R=68 000) spectrum from 400 to 1000 nm, making it possible to determine precision RVs, stellar parameters, and chemical abundances.

Each observation was fully reduced using the Libre-Esprit pipeline.[4] This included subtraction of a bias and dark frames, flat-fielding for pixel-to-pixel variations, and masking bad pixels. ESPaDOnS records 40 orders, each one of them curved, such that Libre-ESpRIT performs a geometric analysis from the calibration exposures before it performs an optimal extraction. It also corrects for the tilt of the slit, determines the wavelength calibration from a thorium lamp exposure, and applies the heliocentric correction. The 'star+sky' mode enables good sky subtraction during the pipeline reductions. The final (combined) spectra were renormalized using an asymmetric k-sigma clipping routine.

As this is an exploratory programme, spectra were collected until signal-to-noise SNR>30 near 520 nm was reached per target; multiple exposures were coadded for fainter targets to reach this SNR. A full sample spectrum for one metal-poor target is shown in Fig. 2, where it can be seen the SNR worsens at shorter wavelengths. In addition, the red side of the CCD detector in this cross-dispersed Echelle spectrograph is less illuminated than the centre of each order, causing lower SNR in the interorder regions. Overall, this impacts the smoothness of the spectra. Spectral lines in the low-SNR regions were rejected from this analysis. In total, this observing campaign used over 150 h of CFHT ESPaDOnS time.

RVs (see Table 2) were determined by fitting several strong lines per star, and averaging the results from the individual lines together. This method was selected rather than a more rigorous use of a cross-correlation technique (e.g. IRAF/*fxcorr*) because of slight wavelength solution variations for lines in common between orders and the significant noise in the interorder regions. The typical uncertainty in RV is σRV $\leq$ 0.5 km s^{-1} for lines below 6000 Å. Variations between the RV solutions were noticed between the CaT lines (∼8500 Å) versus lines in the blue (below 6000 Å), ranging from 0 to 3 km s^{-1}. A similar offset was seen in CFHT ESPaDOnS spectra for CEMP stars by Arentsen et al. (2019), who showed that the RVs derived from lines below 6000 Å provide better agreement with RV standards. Therefore, we did not use any lines above 6000 Å for the RV measurements. The variations for common lines in overlapping orders were small (1–2 pixels, or ≤0.8 Å per line); when averaged over several lines (>10), this intrinsic variation corresponds to ≤0.5 km s^{-1}, the RV uncertainty that we adopt for all of our spectra. Multiple observations were spaced over a narrow range in time, so that no RV variability information is available for identifying potential binary systems.

rates without these five stars, then 38 per cent (25/65) are found with [Fe/H] < -2.5 and 16 per cent (4/25) with [Fe/H] < -3.0.

[4]Libre-ESpRIT is a self-contained data reduction package developed specifically for reducing the ESPaDOnS Echelle spectropolarimetric data developed by Donati et al. (1997).

4 SPECTROSCOPIC ANALYSIS

The analysis of stellar spectra requires a comparison with synthetic spectral calculations of the radiative transfer through a model atmosphere. In this paper, we adopt the ATLAS12 (Kurucz 2005) and MARCS (Gustafsson et al. 2008, further expanded by B. Plez) 1D, hydrostatic, plane-parallel models, in local thermodynamic equilibrium. These models are represented by an effective temperature ($T_{\rm eff}$), surface gravity (log g), and mean metallicity (represented as the iron abundance, [Fe/H]). The model atmospheres are generated with scaled solar abundances, but increased α element abundances to represent the majority of metal-poor stars in the Galaxy ([α/Fe]=0.0 to +0.4). Microturbulence (ξ) is assumed to scale with gravity, using the scaling relations by Sitnova et al. (2015) and Mashonkina et al. (2017a) for Galactic metal-poor dwarfs and giants, respectively.

Initial stellar parameters (temperature and metallicity) were determined from photometry. A colour temperature was determined from the SDSS *gri* colours and the semi-empirical calibrations from González Hernández & Bonifacio (2009), and metallicity was determined from the SDSS *gri* photometry with the *Pristine* Ca H&K filter, with calibrations described by Starkenburg et al. (2017b). Our targets range in colour temperature ($=T_{\rm SDSS}$) from 4700 to 6700 K, and have *Pristine* metallicities [Fe/H]$_{\rm Pristine} \lesssim -2.5$; see Table 1.

Sample spectra are shown for six targets: three hot (T∼6500 K), main-sequence turn-off stars and three cool (T∼4900 K) red giants in Fig. 4. These spectra are labelled with their target name, temperature (from the Bayesian inference method; see Section 4.1), and metallicity ([Fe/H]$_{\rm Q6}$ from this 'Quick Six' analysis; see Section 4.2).

4.1 Stellar parameters using SDSS and *Gaia* DR2 data, and MIST isochrones ('Bayesian inference' method)

Improved stellar temperatures and the gravity estimates were determined using a 'Bayesian inference' method developed by Sestito et al. (2019). A probability distribution function of the heliocentric distance to each star was inferred by combining the SDSS photometric colours and *Gaia* DR2 parallax data, with stellar isochrones, and a Milky Way stellar density prior. We apply the zero-point offset on the parallax of −0.029 mas recommended by Lindegren et al. (2018), but note that the *Gaia* team have discussed the possibility of spatially correlated parallax errors ranging from

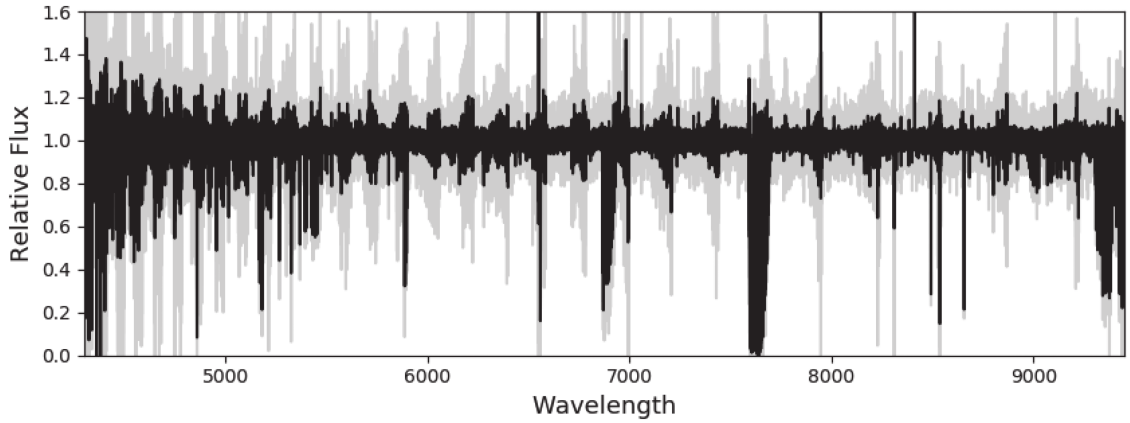

Figure 2. Full CFHT ESPaDOnS spectrum for Pristine-235.1449+08.7464 (grey), and smoothed by a 3-pixel boxcar (black). A signal-to-noise ratio (SNR) =30 near 520 nm was adopted for this exploratory survey, leaving very low SNR and non-smooth continuum on the red side of the detector and therefore in the interorder regions.

Table 2. *Gaia* DR2 parallaxes, and the derived distances (D), temperatures (T), and surface gravities (log g) from the Bayesian inference method (see Section 4.1, assuming $[Fe/H]_P$). Corresponding uncertainties are listed as dpar, dD, dT, and dlg, respectively. Metallicities are from our 'Quick Six' analysis (see Section 4.2) as the individual ion abundances, the weighted average $[Fe/H]_{Q6}$, the standard deviation σFe_{Q6}, and the total number of lines used are noted. For four targets, a second distance (D2 in Com) satisfies the Bayesian inference analysis but does not significantly affect the stellar parameters. For four other targets, a dwarf or giant solution has equal probability, and we examine both solutions independently. Stars no longer in the *Pristine* catalogue have been excluded since they are not metal-poor targets, with only one exception (RA=213.7879, DEC=+08.4232, noted as **). The full table is available online.

RA_{SDSS} (deg)	DEC_{SDSS} (deg)	par (mas)	dpar (mas)	D (kpc)	dD (kpc)	T (K)	dT (K)	log g	dlg	RV (km s^{-1})	Fe I Q6	Fe II Q6	[Fe/H] Q6	σFe Q6	N,Com
High probability for $[Fe/H]_P \leq -2.5$:															
180.2206	+09.5683	0.09	0.05	12.08	0.47	5070.6	20.9	1.86	0.05	23.0	4.54	4.31	−3.04	0.18	6
181.2243	+07.4160	0.47	0.05	2.28	0.07	6454.9	99.9	3.81	0.06	−147.0	4.46	4.18	−3.16	0.16	5
181.3464	+11.6698	1.23	0.03	0.60	0.01	6208.3	17.1	4.57	0.01	12.0	7.55	6.86	−0.22	0.15	5
181.4395	+01.6294	0.08	0.05	16.76	0.29	4934.9	8.2	1.41	0.02	206.0	4.83	4.57	−2.76	0.17	6

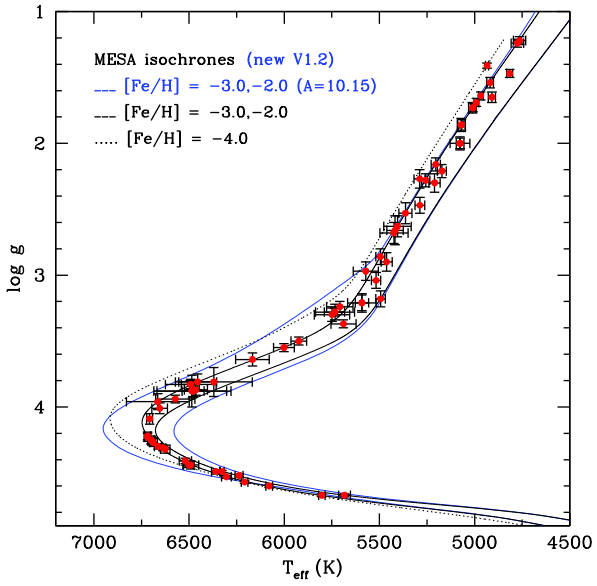

Figure 3. T_{eff} versus log g for 70 high-probability metal-poor stars selected from the *Pristine* survey. For illustration purposes, the isochrones for a single age of 14.1 Gyr are shown [or log(A/yr) =10.15]. The isochrones used for the stellar parameter estimates are from a previous version of MESA/MIST (shown in black), compared with isochrones from the newer version of MIST (V1.2, shown in blue).

0.1 to 0.01 mas; see discussion by Zinn et al. 2019. Isochrones are from the MESA/MIST library (Paxton et al. 2011; Choi et al. 2016; Dotter 2016), which reach the lowest metallicities ([Fe/H] ≤ -4); see Fig. 3. A flat age prior was assumed between 11 and 14 Gyr [or log(A/yr)=10.05–10.15], and we adopted the *Pristine* metallicities a priori.

Unique solutions for the stellar parameters were found for 85 of our targets (out of 89 stars; the 88 stars that remain in the *Pristine* survey catalogue after photometric quality cuts, and one star that we have retained; see Section 2). Another four stars have sufficiently large parallax errors that we could not distinguish between the dwarf or giant solutions; both are given in Table 2. It is recognized that determining the distance to a star simply by inverting the parallax measurement can lead to substantial errors, especially when the parallax is small (or even negative), and when there is a relatively large measurement uncertainty (e.g. $\Delta\pi/\pi > 0.1$); see Bailer-Jones et al. (2018). One advantage of this Bayesian inference method is that stars with negative parallax results and stars with very large parallax errors can be placed on to the isochrones and assumed to be distant. In Fig. 5, the Bayesian inferred distances are compared to the *Gaia* DR2 parallax measurements.

For two stars (Pristine_200.5298+08.9768 and Pristine_187.9785+08.7294), the Bayesian inferred distance method seemed to fail, placing these stars in the outer Galactic halo, even though they have relatively large parallax measurements with small uncertainties (0.46 ± 0.04 and 0.74 ± 0.04 mas in the *Gaia* DR2 catalogue), and they are metal rich (e.g. visibly strong Ca II triplet

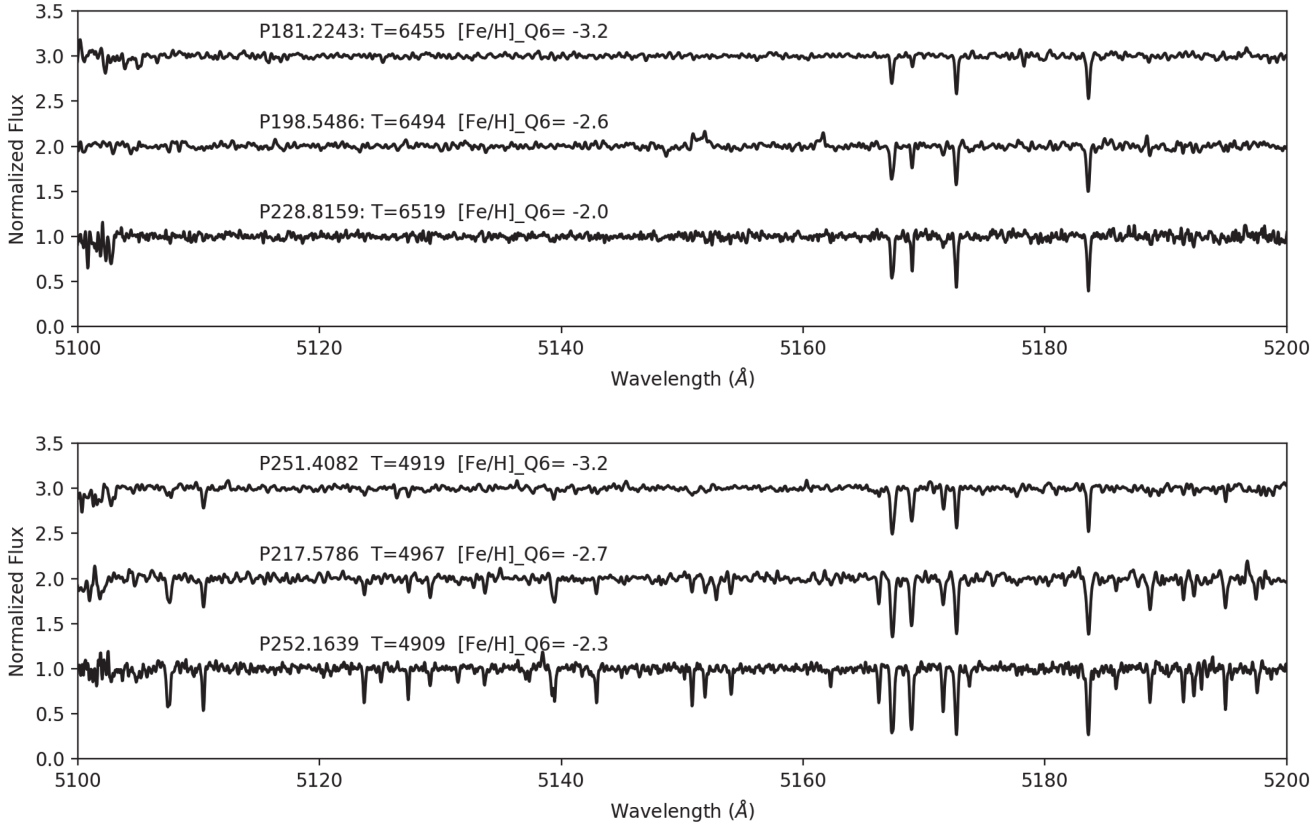

Figure 4. Sample CFHT ESPaDOnS spectra for three hot (T∼6500 K) main-sequence turn-off stars and three cool (T∼4900 K) red giants. Each spectrum is labelled with the target name, temperature from the Bayesian inference method, and spectroscopic metallicity from our 'Quick Six' analysis.

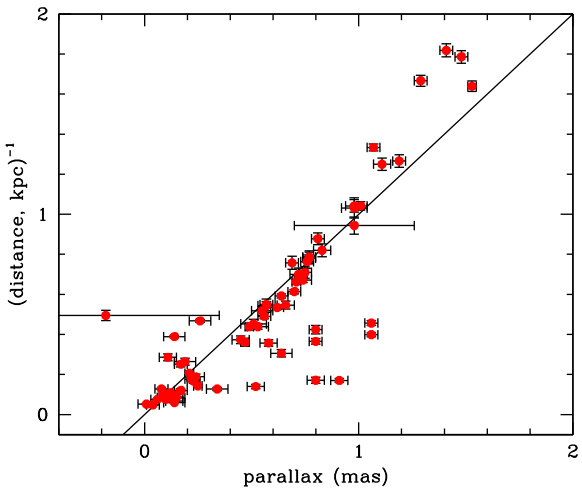

Figure 5. A comparison of the *Gaia* DR2 parallax measurements (with zero-point correction; see the text) and 1/(distance, in kpc) from the Bayesian inference method developed by Sestito et al. (2019) for our 70 metal-poor candidates.

lines). Since we had assumed that these stars are metal poor (from their *Pristine* metallicities), then the metal-poor isochrone used to compute their distances was incorrect, and resulted in a poor distance estimate. By adjusting their distances to simply 1/parallax (i.e. not using the metal-poor stellar isochrones), then both of these stars are located closer to the Sun, consistent with the majority of metal-rich stars in the Galaxy. For our main targets, stars that the *Pristine* survey identifies as metal poor and that are truly metal poor, then this will not be a problem, and we expect that this Bayesian inference method will provide very precise stellar parameters.

4.2 Initial ('Quick Six') spectroscopic metallicities

Adopting the stellar parameters from the Bayesian inference method described above (Section 4.1), then a model atmosphere was generated from both the MARCS and ATLAS grids. Elemental abundances were computed using a recent version of the 1D LTE spectrum analysis code MOOG (Sneden 1973; Sobeck et al. 2011).

As an initial spectroscopic metallicity estimate, a subset of six iron lines was selected that are observable in the good SNR regions of the ESPaDOnS spectra: 4× Fe I (λ4957, λ5269, λ5372, and λ5397) and 2× Fe II (λ4924 and λ5018). These are well known and fairly isolated spectral lines, with good atomic data[5] and line strengths across the parameter range. The equivalent widths of these six lines were measured using IRAF/*splot*,[6] measuring both the area

[5]Atomic data for the Fe I lines are from Blackwell, Petford & Shallis (1979) with high precision, or from the laboratory measurements from O'Brian et al. (1991). The Fe II lines have less certain atomic data from Raassen & Uylings (1998); however, a NLTE investigation by Sitnova et al. (2015) showed that these lines have tiny NLTE corrections and yield iron abundances in metal-poor stars within 0.1 dex of all the other Fe I and Fe II lines that they studied. We also note Roederer et al. (2018b) used 3 Fe I and 1 Fe II of these lines in their detailed iron analysis of six warm metal-poor stars.

[6]IRAF is distributed by the National Optical Astronomy Observatories, which is operated by the Association of Universities for Research in

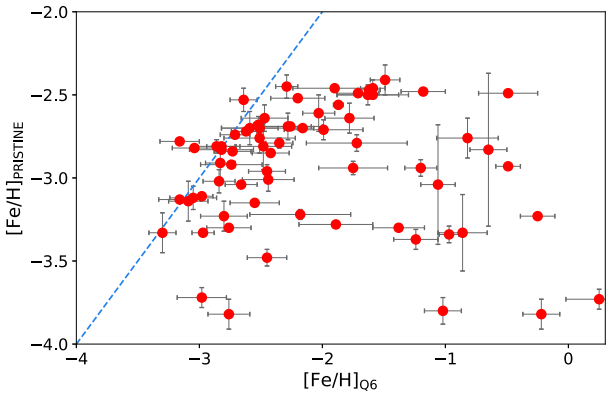

Figure 6. Comparisons of the 'Quick Six' $[Fe/H]_{Q6}$ spectral abundances compared with the *Pristine* $[Fe/H]_{Pristine}$ photometric predictions. Clearly, some of the *Pristine* metal-poor candidates are not metal-poor stars.

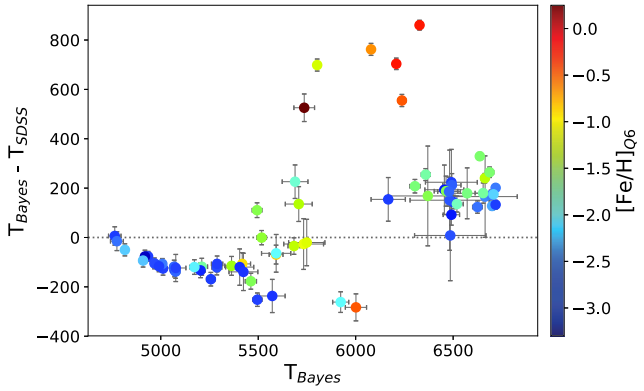

Figure 7. Comparisons of the *Pristine* survey colour temperature (T_{SDSS}) and the effective temperature determined from Bayesian inference method (T_{Bayes}) for our 70 metal-poor candidates. The data points are coloured by their metallicities from our spectroscopic $[Fe/H]_{Q6}$ analysis. As both temperature estimates adopted the *Pristine* photometric metallicity estimates $[Fe/H]_{Pristine}$ a priori, then clearly the metal-rich stars are not well calibrated.

under the continuum and by fitting a Gaussian profile, comparing the results. We call the average of these six LTE line abundances our 'Quick Six' spectroscopic metallicities ($[Fe/H]_{Q6}$), and these are used as an initial test of the *Pristine* metallicity estimates.

Departures from LTE are known to overionize the Fe I atoms due to the impact of the stellar radiation field, particularly in hotter stars and metal-poor giants. These non-LTE (NLTE) effects can be significant in our stellar parameter range, such that NLTE corrections typically reduce the line scatter and improve the Fe I=Fe II ionization balance (Sitnova et al. 2015; Amarsi et al. 2016; Mashonkina et al. 2019). NLTE effects are explored in this 'Quick Six' analysis, by comparing the results from Mashonkina et al. (2017a), Mashonkina et al. (2019), and the INSPECT table[7] (Lind, Bergemann & Asplund 2012; Amarsi et al. 2016). INSPECT provides data for one of the selected lines, Fe I λ5269, where the NLTE correction is $\Delta(\text{Fe I}) \leq 0.15$, over our parameter space, where Fe I(NLTE) = Fe I(LTE) + Δ(Fe I). Based on a similar treatment for inelastic collisions (of Fe I with H I), Mashonkina et al. (2017a) predict similar NLTE corrections for the other three Fe I lines (λ4957, λ5372, and λ5397). The largest NLTE corrections [Δ(Fe I) ∼ 0.3] are for stars on the subgiant branch, while main-sequence stars have ∼zero corrections. Recently, Mashonkina et al. (2019) have examined the impact of quantum mechanical rate coefficients for the inelastic collisions, and they find that the latter could be even larger (more positive) in the atmospheres of warm metal-poor stars, but smaller (even negative) in cool metal-poor stars and with a wide variation depending on the specific spectral line. This suggests that the NLTE calculations for Fe I need further study; however, given that these corrections in the literature are smaller than or equal to our measurement errors, then we do not apply the NLTE corrections in this 'Quick Six' analysis.

The Fe I and Fe II individual line abundances are averaged together to find $[Fe/H]_{Q6}$ and the standard deviation $\sigma[Fe/H]_{Q6}$. Each of these results and the total number of lines used ($\leq$6) are shown in Table 2. From this analysis, we find that several of the *Pristine* metal-poor candidates are not metal poor. A comparison of the $[Fe/H]_{Q6}$ iron abundances to the $[Fe/H]_{Pristine}$ predictions is shown in Fig. 6. These results are similar to the medium-resolution spectral analyses (Youakim et al. 2017; Aguado et al. 2019a), and discussed further in Section 4.5.

4.3 Comparing stellar temperatures

A comparison of stellar temperatures from the Bayesian inference method (Section 4.1) to the SDSS colour temperature (T_{SDSS}) is shown in Fig. 7. T_{SDSS} were the initial temperature estimates calculated using the InfraRed Flux Method,[8] assuming [Fe/H] = −2.5, and based on the SDSS ($g - i$) photometry. An average of the dwarf and giant solutions was used. For 10 stars, their ($g - i$) colours are unreliable because of saturation flags, and we adopt the relation based on the ($g - r$) colours from Ivezić et al. (2008). With this relation, a 200 K offset was applied to move from [Fe/H] = −0.5 to −2. Thus, we expect these values of T_{SDSS} to be an oversimplification, and are not surprised by the comparisons in Fig. 7, which are colour coded by the 'Quick Six' metallicities $[Fe/H]_{Q6}$.

Ignoring the metal-rich stars, then there is still a systematic offset between these methods for the metal-poor stars: the T_{SDSS} colour temperatures are too hot by ∼150 K for stars between $T = 4700$ and 5700 K, but they are too cool by ∼200 K for stars with $T > 6000$ K. This offset is similar to the uncertainties in the Bayesian inference method temperatures (T_{Bayes}) for most stars, where σT_{Bayes} ranges from ∼10 to 200 K (Table 2). The very small colour temperature errors $dT_{SDSS} \lesssim 10$ K in Table 1 are based on the difference between the dwarf/giant solutions, and are not realistic uncertainties.

4.4 Comparing gravity and Fe I=Fe II

Ionization balance has traditionally been used as an indicator of surface gravity in a classical model atmosphere analysis. Therefore, we compare the log g values from the Bayesian inference method (Section 4.1) to the difference in the [Fe I] and [Fe II] abundances, in Fig. 8. This figure is colour coded by the 'Quick Six' spectroscopic metallicities ($[Fe/H]_{Q6}$). For the metal-poor stars, the majority of our stars show Fe I=Fe II to within 2σ of the measurement errors,

Astronomy, Inc. (AURA) under cooperative agreement with the National Science Foundation.

[7]Non-LTE data obtained from the INSPECTdata base (version 1.0), available at http://inspect-stars.com.

[8]IRFM; see https://www.sdss.org/dr12/spectro/sspp_irfm/.

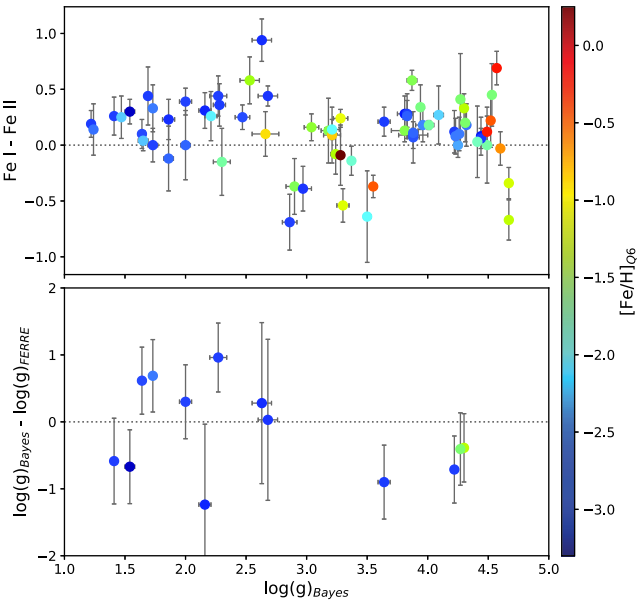

Figure 8. Comparisons of the surface gravities and iron ionization balance estimates for our 70 metal-poor candidates from the *Pristine* survey (top panel), and comparisons of our surface gravities versus those from the FERRE analysis of medium-resolution spectra (Aguado et al. 2019a) for 13 stars in common. The uncertainties in the gravities from FERRE can be quite large for the metal-poor stars due to a lack of suitable spectral signatures. The data points are coloured by their metallicities from our spectroscopic [Fe/H]$_{Q6}$ analysis.

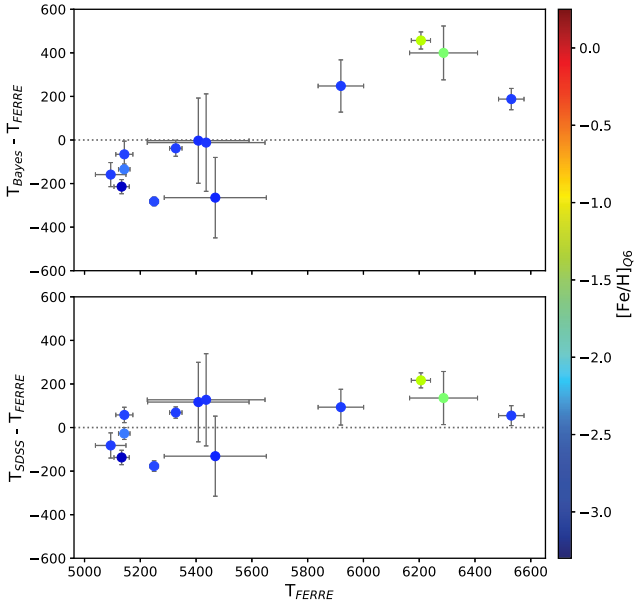

Figure 9. Temperature comparisons for 13 stars in common between the Bayesian inference analysis of our CFHT ESPaDOnS spectra and the FERRE analysis of medium-resolution spectra (top panel, Aguado et al. 2019a). The temperature offsets are slightly smaller when compared with the *Pristine* colour temperatures ($T_{\rm SDSS}$, bottom panel).

with a mean offset of [Fe I] − [Fe II] =+0.2. The measurement errors are calculated as the line-weighted average of Fe I and Fe II.

For stars with poor agreement between iron ionization states, the cause cannot be due to neglected NLTE effects, which appear to increase the Fe I abundance even further (see in Section 4.2). The offset is primarily seen in the cooler stars in our sample that are on the red giant branch (with lower gravities). For these stars, the NLTE corrections are expected to be small [Δ(Fe I)$\lesssim$0.15]. For stars closer to the main-sequence turn-off, the NLTE corrections can be larger; however, the offset between the Fe I and Fe II abundances seems smaller for those stars in our results. Therefore, the source of ionization equilibrium offsets is not yet clear.

For the metal-rich stars, we expect the surface gravities to be unreliable since the photometric *Pristine* metallicities [Fe/H]$_{\rm Pristine}$ were assumed a priori in the Bayesian inference method. We do not investigate the metal-rich stars beyond our 'Quick Six' analysis.

4.5 Comparisons with medium-resolution spectroscopic analyses (FERRE)

A simultaneous *Pristine* survey programme has been carried out for fainter stars ($15 < V < 17$) with medium-resolution ($R \sim 1800$) spectroscopy at the 2.4-m Isaac Newton Telescope (INT), 4.2-m William Herschel Telescope, and 3.6-m New Technology Telescope (Aguado et al. 2019a). These spectra have been observed with uniform spectral wavelength coverage, 360–550 nm, and analysed using the ASSET synthetic spectral grid (Koesterke, Allende Prieto & Lambert 2008). Both the observed and the synthetic spectra have been continuum normalized with the same functions, and the χ^2 minimization algorithm FERRE (Allende Prieto et al. 2006) is applied to derive the stellar parameters (temperature, gravity, metallicity, and carbonacity).

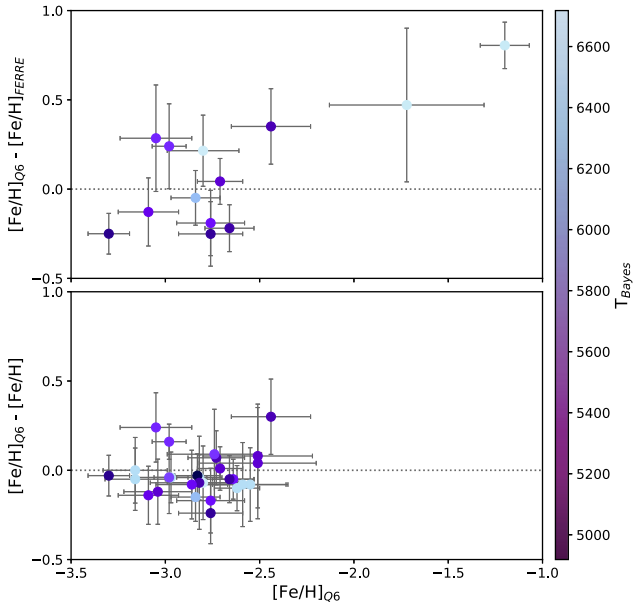

Figure 10. Metallicity comparisons for 13 stars in common between the [Fe/H]$_{Q6}$ analysis of our CFHT ESPaDOnS spectra and the FERRE analysis of medium-resolution spectra (top panel, Aguado et al. 2019a). [Fe/H]$_{Q6}$ values are also compared to the improved [Fe/H] values for our 28 very metal poor stars, which include more lines of both Fe I and Fe II. The errors in the bottom panel are dominated by the 'Quick Six' σ[Fe/H]$_{Q6}$ analysis.

The most recent analysis of the medium-resolution spectroscopic data includes 946 stars (Aguado et al. 2019a), where 13 of those stars are also in our sample of 70 high-probability metal-poor stars (recall that only 5 were observed at the INT first, and did not affect our target selections). In Figs 8, 9, and 10, the surface gravities, temperatures, and metallicities are compared between the two analyses for

the 13 stars in common. The large differences in gravity are from the *systematic* errors in the medium-resolution FERRE analysis. While the FERRE analysis struggles with precision gravities, both methods are still able to break the dwarf-giant degeneracies sufficiently.

There is a clear relationship between the temperatures such that those determined from isochrones in the Bayesian inference method are cooler by ∼200 K near 5000 K and hotter by ∼500 K near 6700 K compared to the FERRE temperatures. These offsets are slightly smaller when compared with the SDSS colour temperatures $T_{\rm SDSS}$. These temperature differences correlate with small-to-moderate metallicity offsets (Δ[Fe/H] $\leq$ 0.3) for stars cooler than 6000 K, whereas two of the hotter stars show larger metallicity offsets, Δ[Fe/H] ∼ 0.5. In summary, this analysis adopts the stellar parameters from the Bayesian inference method, and finds that the hot stars are hotter and less metal poor than the results from the medium-resolution FERRE analysis.

5 NEW STARS WITH [FE/H] ≤ −2.5

We have identified 28 new metal-poor stars, with a spectroscopic metallicity $[{\rm Fe/H}]_{\rm Q6} \leq -2.5$, and where both [Fe I/H] and [Fe II/H] are below −2.5 dex (with the exception of Pristine_198.5486+11.4123, with [Fe I/H]=−2.42, which we retain because of its interesting orbit, discussed below). In this section, a more complete LTE, 1D model atmosphere analysis is carried out for a larger set of spectral lines and chemical elements (see Table 3).

As a comparison star, a spectrum of HD 122563 from the CFHT archive was analysed using the same methods as for the *Pristine* survey targets. Its metallicity is adopted from the literature, i.e. [Fe/H] = −2.7 ± 0.1 (see Collet et al. 2018, and references therein), and our methods using its SDSS colours and *Gaia* DR2 parallax measurements yield stellar parameters that are in good agreement with the literature: $T_{\rm eff}$ = 4625 ± 50 K and $\log g$ = 1.6 ± 0.1. Microturbulence (ξ) was set to 2.0 km s^{-1} using the relationship with gravity from Mashonkina et al. (2017a).

For all 28 *Pristine* survey stars and HD122563, we identify and measure as many clean spectral lines as possible for a detailed abundance analysis, including more lines of Fe I and Fe II for higher precision iron abundances (than from the $[{\rm Fe/H}]_{\rm Q6}$ analysis). Starting with the spectral line list from Norris et al. (2017), spectral features were identified and measured using DAOSpec (Stetson & Pancino 2008), and frequently checked by measuring the area under the continuum using IRAF/*splot*. Atomic data were updated when appropriate by comparing to the *linemake* atomic and molecular line data base.[9] Abundance results from the model atmosphere analysis are compared to the solar (photospheric) abundances from Asplund et al. (2009).

5.1 Iron-group elements

The 28 new very metal poor stars were initially identified from their $[{\rm Fe/H}]_{\rm Q6}$ abundances in Table 2.

The iron abundances have been recalculated from 2–86 lines of Fe I and 2–6 lines of Fe II; see Table 4. A 3σ minimum equivalent width was used to calculate an upper limit for Fe II for one star. The line-to-line scatter in the Fe I abundances ranges from σ(Fe I) = 0.12 to 0.24, even when only a small number of lines were measured. This is noteworthy because when other elements have <4 lines, we adopt the larger of σ(X) or $\sigma({\rm Fe\ I})/\sqrt{(N_X)}$ as a better representation of their line scatter.

These extended iron-line measurements and abundances are not used to redetermine the spectroscopic stellar parameters for three reasons: (1) low sensitivity to the precise metallicity in the Bayesian inference method for the confirmed metal-poor stars, (2) insufficient number of lines of Fe II (and often Fe I) for a fully independent analysis, and (3) the SNR of our CFHT ESPaDOnS spectra (≤30) is such that individual measurements of weak lines remain somewhat uncertain. The total iron abundance [Fe/H] is calculated as a weighted mean of Fe I and Fe II, and the total error δ[Fe/H] as $\sigma([{\rm Fe/H}])/({\rm NFe\ I}+{\rm NFe\ II})^{1/2}$. These iron abundances are shown in Fig. 11 (top panel), where the errorbars include the systematic errors from the stellar parameter uncertainties added in quadrature (see Section 5.5, though the systematic errors tend to be much smaller).

There is good to fair agreement between Fe I and Fe II, such that [Fe I] − [Fe II] ranges from ∼−0.2 to +0.2. There is a median offset ∼+0.2 for the sample, which is *not* due to ignoring NLTE corrections (see the discussion in Section 4.2). This may be due to the lack of the Fe II lines in our metal-poor-stars spectra for robust measurements, but another possibility is a systematic gravity uncertainty $\Delta\log g$∼0.5. High-resolution spectra at bluer wavelengths (4000 Å) would provide more lines of Fe II to test this in the future. We also examine the slopes in the Fe I line abundances versus excitation potential (χ, in eV) to test our temperature estimates. A meaningful slope could be measured when N(Fe I)>15 and $\Delta\chi$ > 3 eV, and all slopes were found to be relatively flat, <0.1 dex eV^{-1}. This gives us more confidence in the fidelity of the temperatures $T_{\rm Bayes}$, and thereby the Bayesian inference method for calculating stellar parameters and uncertainties.

The other iron-group elements (Cr and Ni, listed in Table 4) are in good agreement with [Fe/H], and/or other Galactic halo stars at similar metallicities; see Fig. 11. Cr is determined from 1–3 lines of Cr I (5206.0, 5208.4, and 5409.8 Å); only the spectrum of Pristine_245.8356+13.8777 had sufficient SNR at blue wavelengths in that the lines at 4254.3, 4274.8, and 4289.7 Å could also be observed. [Cr/Fe] is subsolar in metal-poor stars, suggested as a NLTE effect (Bergemann & Cescutti 2010). Ni is determined from 1–2 lines of Ni I (5035.4 and 5476.9 Å). Three additional lines were available in the high-SNR spectrum of HD 122563 (5080.5, 6643.6, and 6767.8 Å). The [Ni/Fe] results are within 1σ of the solar ratio, similar to other Galactic halo stars.

5.2 α-elements

The α-element abundances (Mg and Ca) in the 28 new very metal poor stars are listed in Table 5. Upper limits are determined for some stars by computing 3σ minimum equivalent widths. The α-elements form through hydrostatic H- and He-core burning stages, though some Ca can also form later during SN Ia events. Because of these different nucleosynthetic sites, the [Mg/Ca] ratio need not scale together at all metallicities, as seen in some dwarf galaxies such as the Carina and Sextans dwarf galaxies (e.g. Venn et al. 2012; Jablonka et al. 2015; Norris et al. 2017), also the unusual star cluster NGC 2419 (Cohen & Kirby 2012). We also include our discussion of Ti in this section even though it does not form with the α-elements. The dominant isotope ^{48}Ti forms primarily through Si-burning in massive stars (e.g. Woosley, Heger & Weaver 2002),

[9] *linemake* contains laboratory atomic data (transition probabilities, hyperfine and isotopic substructures) published by the Wisconsin Atomic Physics and the Old Dominion Molecular Physics groups. These lists and accompanying line list assembly software have been developed by C. Sneden and are curated by V. Placco at https://github.com/vmplacco/linemake.

Table 3. Line list from Norris et al. (2017) with atomic data updates from *linemake* (see the text). Equivalent width measurements are provided per star (labelled by RA_{SDSS} only). The full table is available online.

Elem	Wavel (Å)	χ (eV)	log(*gf*)	180.2206 (mÅ)	181.2243 (mÅ)	181.4395 (mÅ)	181.6849 (mÅ)	189.9449 (mÅ)	193.8390 (mÅ)	196.3755 (mÅ)	198.3755 (mÅ)	201.8711 (mÅ)
Mg I	5172.684	2.710	− 0.40	165.2	105.0	181.3	56.0	94.2	185.7	160.4	109.5	72.3
Mg I	5183.604	2.715	− 0.18	161.6	124.9	214.4	86.0	112.2	201.7	186.5	139.0	90.7
Fe II	4923.922	2.891	− 1.21	65.7	25.3	92.9	–	28.3	101.0	108.1	39.6	–
Fe II	5018.435	2.891	− 1.35	79.7	–	104.4	–	35.9	94.0	88.6	53.5	–

Table 4. Iron-group and heavy element abundances in the new 28 metal-poor stars (labelled by RA_{SDSS}), and our analysis of HD122563. [Fe/H] is the weighted mean of Fe I and Fe II, and $\delta([Fe/H]) = \sigma([Fe/H])/\sqrt{(N\text{Fe I} + N\text{Fe II})}$.

RA_{SDSS}	[Fe/H] ± δ	log(Fe I) ±σ (*N*)	log(Fe II) ±σ (*N*)	[Cr/Fe] ±σ (*N*)	[Ni/Fe] ±σ (*N*)	[Y/Fe] ±σ (*N*)	[Ba/Fe] ±σ (*N*)
180.2206	− 2.92 ± 0.03	4.60 ± 0.18 (49)	4.45 ± 0.27 (4)	− 0.21 ± 0.13 (2)	− 0.05 ± 0.18 (1)	<+0.49	− 1.02 ± 0.18 (1)
181.2243	− 3.11 ± 0.07	4.50 ± 0.17 (4)	4.17 ± 0.14 (2)	–	–	<+1.85	<+1.37
181.4395	− 2.52 ± 0.02	4.99 ± 0.18 (86)	4.80 ± 0.26 (5)	− 0.37 ± 0.11 (3)	+0.03 ± 0.13 (2)	< − 0.12	− 1.13 ± 0.24 (2)
183.6849	− 3.16 ± 0.07	4.38 ± 0.24 (2)	4.30 ± 0.01 (2)	–	–	<+2.33	<+1.88
189.9449	− 2.78 ± 0.04	4.77 ± 0.12 (8)	4.50 ± 0.21 (2)	–	–	<+1.70	<+0.93
193.8390	− 2.80 ± 0.02	4.71 ± 0.21 (81)	4.49 ± 0.13 (5)	− 0.49 ± 0.12 (3)	− 0.24 ± 0.21 (1)	<+0.02	− 1.58 ± 0.21 (1)
196.3755	− 2.80 ± 0.02	4.70 ± 0.19 (61)	4.72 ± 0.16 (3)	− 0.17 ± 0.14 (2)	− 0.21 ± 0.19 (1)	<+0.3	<−0.56
198.5486	− 2.47 ± 0.05	5.08 ± 0.16 (9)	4.80 ± 0.29 (2)	+0.04 ± 0.11 (2)	<+0.45	<+1.23	<+0.39
201.8711	− 2.93 ± 0.11	4.57 ± 0.15 (2)	<4.71	–	–	<+2.10	<+1.65
203.2831	− 2.74 ± 0.02	4.77 ± 0.19 (59)	4.55 ± 0.15 (4)	− 0.27 ± 0.11 (3)	− 0.19 ± 0.19 (1)	<+0.01	− 0.76 ± 0.23 (3)
204.9008	− 2.73 ± 0.08	4.84 ± 0.18 (3)	4.66 ± 0.26 (2)	–	–	<+1.89	<+1.40
208.0798	− 2.94 ± 0.03	4.53 ± 0.14 (20)	4.83 ± 0.26 (2)	− 0.35 ± 0.10 (2)	<+0.16	<+1.15	<+0.57
210.0166	− 2.59 ± 0.02	4.92 ± 0.18 (64)	4.75 ± 0.13 (4)	− 0.20 ± 0.13 (2)	− 0.17 ± 0.18 (1)	<+0.51	+0.74 ± 0.20 (4)
213.7879	− 2.59 ± 0.02	4.93 ± 0.18 (61)	4.55 ± 0.17 (3)	− 0.09 ± 0.11 (3)	+0.11 ± 0.18 (1)	<+0.43	− 0.36 ± 0.14 (2)
214.5556	− 2.51 ± 0.05	5.01 ± 0.15 (10)	4.88 ± 0.35 (2)	<+0.07	<+0.69	+1.48 ± 0.11 (2)	+1.77 ± 0.22 (4)
217.5786	− 2.61 ± 0.02	4.88 ± 0.18 (79)	4.94 ± 0.18 (6)	− 0.11 ± 0.16 (4)	− 0.04 ± 0.18 (1)	+0.16 ± 0.13 (2)	+0.02 ± 0.18 (3)
229.1219	− 2.52 ± 0.04	5.02 ± 0.12 (8)	4.84 ± 0.17 (2)	+0.16 ± 0.12 (1)	–	<+1.59	<+0.44
233.5730	− 2.75 ± 0.02	4.77 ± 0.20 (75)	4.42 ± 0.28 (3)	− 0.25 ± 0.12 (3)	–	<+0.23	− 0.15 ± 0.32 (3)
235.1449	− 2.69 ± 0.04	4.85 ± 0.15 (16)	4.52 ± 0.13 (2)	<−0.16	–	<+1.41	+0.13 ± 0.15 (1)
237.8246	− 3.29 ± 0.04	4.28 ± 0.15 (13)	3.73 ± 0.04 (2)	<−0.32	<+0.50	<+1.29	+0.61 ± 0.34 (2)
240.4216	− 2.95 ± 0.03	4.56 ± 0.20 (41)	4.20 ± 0.22 (2)	− 0.35 ± 0.14 (2)	− 0.19 ± 0.20 (1)	<+0.64	+0.53 ± 0.29 (4)
245.5747	− 3.14 ± 0.04	4.37 ± 0.20 (18)	4.25 ± 0.09 (2)	<−0.30	<+0.38	<+1.14	<+0.52
245.8356	− 2.78 ± 0.03	4.73 ± 0.21 (52)	4.60 ± 0.25 (4)	− 0.41 ± 0.16 (5)	+0.18 ± 0.21 (1)	+0.73 ± 0.21 (1)	− 0.51 ± 0.12 (3)
248.4959	− 2.59 ± 0.02	4.91 ± 0.17 (74)	4.90 ± 0.31 (5)	− 0.26 ± 0.10 (3)	− 0.04 ± 0.12 (2)	<+0.16	− 0.18 ± 0.10 (3)
250.6963	− 2.55 ± 0.03	4.95 ± 0.20 (62)	4.95 ± 0.28 (4)	− 0.43 ± 0.12 (3)	+0.07 ± 0.14 (2)	<+0.18	− 0.03 ± 0.16 (3)
251.4082	− 3.27 ± 0.03	4.23 ± 0.18 (31)	4.19 ± 0.33 (3)	<−0.17	–	<+0.65	− 0.73 ± 0.18 (1)
253.8582	− 2.72 ± 0.02	4.80 ± 0.21 (65)	4.54 ± 0.07 (4)	− 0.15 ± 0.14 (2)	− 0.13 ± 0.21 (1)	<+0.35	− 0.51 ± 0.20 (3)
255.5555	− 2.83 ± 0.03	4.64 ± 0.18 (22)	4.99 ± 0.10 (2)	<−0.08	<−0.08	<+0.97	+0.35 ± 0.10 (3)
HD122563	− 2.76 ± 0.01	4.73 ± 0.15 (98)	4.86 ± 0.16 (5)	− 0.39 ± 0.08 (3)	+0.05 ± 0.10 (5)	−0.15 ± 0.11 (2)	− 0.77 ± 0.08 (3)

and yet it seems to scale with other α-elements in metal-poor stars in the Galaxy.

Mg is determined from 2–3 lines (5172.7, 5183.6, and 5528.4 Å), and a fourth line (4703.0 Å) was measurable in one star (Pristine_245.8356+13.8777). In Fig. 12, a larger scatter can be seen in the [Mg/Fe] results, though this is similar to the Galactic comparison stars. One star shows subsolar [Mg/Fe] by more than 1σ (Pristine_251.4082+12.3657). Another star has high [Mg/Fe]$\sim$+0.6, validated from all the three Mg I lines (Pristine_181.2243+07.4160), also shown in Fig. 13.

The calcium abundances are determined from 1–9 lines of Ca I. The [Ca/Fe] abundances are in good agreement with each other, and with the Galactic comparison stars, as seen in Fig. 12. The same star with low [Mg/Fe] (Pristine_251.4082+12.3657) also has a very low [Ca/Fe] upper limit. This star is discussed further in Section 6.2.

Titanium has been determined from 1–9 lines of Ti I and 2–11 lines of Ti II. When both are unavailable, upper limits are determined from the two Ti II lines (which provide stronger constraints than the Ti I features). In Fig. 12, the unweighted average results of [Ti I/Fe] and [Ti II/Fe] are shown.

NLTE corrections have not been incorporated for Mg, Ca, or Ti because they tend to be small to negligible ($\Delta \leq 0.1$ dex) according to the INSPECT data base (for Mg I) and Mashonkina, Sitnova & Belyaev (2017b, for Ca I). For Ti I, three lines (4981.7, 4991.1, and 4999.5 Å) are available in the INSPECT data base, which suggests large corrections $\Delta \sim$+0.5 dex. However, NLTE corrections for the same lines from Sitnova, Mashonkina & Ryabchikova (2016), using a model atom that includes important high excitation levels of Ti I, are significantly smaller, $\Delta \sim$+0.2 dex. NLTE corrections should be included, but most of our stars have Ti I $\sim$ Ti II to within 1σ (our measurement errors) in LTE. Therefore, for this analysis, where the maximum SNR per star is $\leq$30, we do not include the small NLTE corrections, and note that the good agreement with the Galactic comparison stars and Ti ionization balance furthers our confidence in the stellar parameters from the Bayesian inference method.

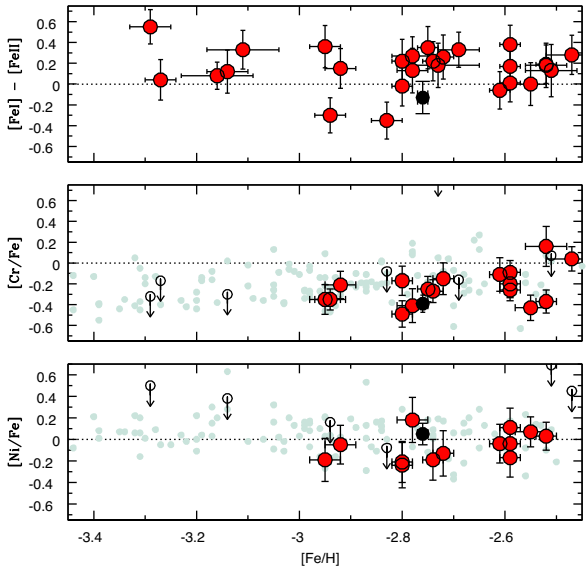

Figure 11. Iron-group (Fe, Cr, and Ni) abundances and upper limits in our 28 new very metal poor stars ([Fe/H] < -2.5, red points). Analysis results of the CFHT ESPaDOnS spectrum for the standard star HD 122563 are included (black point). Errorbars are the measurement errors and systematic errors combined in quadrature. Galactic comparison stars are included from the homogeneous analysis by Yong et al. (2013, small grey points).

No oxygen abundances or upper limits were determined since the [O I] 6300 and 6363 Å lines are weak and in a region that is poorly cleaned of telluric contaminants.

5.3 Odd elements

Odd elements, Na and Sc, are listed in Table 5. These have different nucleosynthetic sources and are not related to one another. We also include a comment on Li upper limits at the end of this section.

In metal-poor stars, sodium typically forms with the α-elements during core-collapse SN. On the other hand, scandium forms in the iron core of a massive star with a yield that strongly depends on the proton-to-neutron ratio (Y_e), and it is very sensitive to neutrino processes (e.g. Woosley et al. 2002; Curtis et al. 2019).

Sodium abundances are initially from the LTE analysis of the Na I D lines (5889.9 and 5895.9 Å), which unfortunately can be strong, therefore sensitive to microturbulence in a 1D LTE analysis, and also contaminated by interstellar Na. Furthermore, since they originate from the Na I ground state, they are subject to NLTE effects. NLTE corrections are similar between the INSPECT data base and Mashonkina et al. (2017c); $[\mathrm{Na/H}]_{\mathrm{NLTE}} = [\mathrm{Na/H}]_{\mathrm{LTE}} + \Delta\mathrm{Na}$, where $\Delta\mathrm{Na} = (-0.1)$–$(-0.6)$ dex. The Na I subordinate line (5688.2 Å) could only be used for upper limit estimates at the SNR of our spectra.

Despite the large NLTE corrections, four stars were found with initially very high Na I abundances (Pristine_251.4082+12.3657, Pristine_193.8390+11.4150, Pristine_217.5786+14.0379, and Pristine_250.6963+08.3743, in order of decreasing metallicity). These four stars also have the lowest RVs in our sample (-5, $+4$, -16, and -4 km s^{-1}, in order of decreasing metallicity), and we suggest they are contaminated by the interstellar Na lines. To test this, their Na I D line shapes were compared with other spectral lines in the same stars and found to be slightly broader (occasionally, the line core is even split); their Na I D line shapes are also broader than similar stars with higher RVs (where the interstellar lines are often seen offset from the stellar lines). Thus, in Fig. 14, the highest Na abundances are noted as upper limits only since they are most likely blended, and for the other stars the NLTE-corrected Na abundances are shown.

Sc II has been measured from 1–3 lines (5031.0, 5526.8, and 5657.9 Å) in five metal-poor *Pristine* stars, and the comparison star HD 122563, and upper limits were determined in the others. With an odd number of nucleons, this species undergoes strong hyperfine splitting, which affects line formation through de-saturation. The HFS corrections were found to be small (<0.1). Upper limits have also been determined for Sc II in most of the other new metal-poor stars. Upper limits were examined for Mn I as well, but did not provide interesting constraints.

Lastly, we mention Li in this section. Estimates from the Li I 6707 Å line provide upper limits that do not provide meaningful constraints, i.e. the upper limits are above the standard big bang nucleosynthesis value of $A(\mathrm{Li}) = 2.7$ (e.g. from WMAP, Spergel et al. 2003). Only two stars (Pristine_229.1219+00.9089 and Pristine_237.8246+10.1426) have 3σ equivalent width (35 mÅ) upper limits of $A(\mathrm{Li}) \leq 2.2$, which is similar to most metal-poor stars that lie on (or below) the Spite Plateau (e.g. see Bonifacio et al. 2018; Aguado et al. 2019b).

5.4 Heavy elements

Abundances for the neutron-capture elements Y and Ba in the 28 new very metal poor stars are listed in Table 4. Up to four lines of Ba II (4554.0, 5853.7, 6141.7, and 6496.9 Å) and two lines of Y II (4883.7 and 4990.1 Å) could be measured. Unfortunately, no lines or useful upper limits for Eu are available in our CFHT spectra. When no lines were observable, we determined upper limits from 3σ minimum equivalent width estimates. Hyperfine splitting and the isotopic splitting have been included in the Ba analysis. Most stars have [Ba/Fe] in good agreement with the Galactic comparison stars.

All the six lines were measured in only one star near [Fe/H] $= -2.5$ (Pristine_214.5555+07.4670). This star is enriched in both Y and Ba, and we identify it as an r-process-rich star. Without Eu, it cannot be further classified as r-I or r-II (Christlieb et al. 2004; Sakari et al. 2018b). Studies of r-process-rich stars have found a nearly identical main r-process pattern (from barium, A=56, to hafnium, A=72) in all types of stars, in all environments, and with variations only between the lightest and heaviest elements (see Roederer et al. 2010; Hill et al. 2017; Sakari et al. 2018a, and references therein). No other elements stand out in this star; however, as one of the hotter turn-off stars in our sample, there are not many other features or elements to analyse at the SNR of our spectra.

Two more stars show [Ba/Fe]$\gtrsim$+0.5 (Pristine_237.8246+10.1426 and Pristine_210.0166+14.6289). These lie above the typical [Ba/Fe] values found in the Galactic halo metal-poor stars by Roederer et al. (2014), and their results are securely derived from 2–4 Ba II line measurements. However, no Y II lines were observed in either (and the Y II upper limits do not provide useful constraints). The two may be moderately r-process-enriched stars.

Possibly of greater interest are the two most Ba-poor stars (Pristine_181.4395+01.6294 and Pristine_193.8390+11.4150). Low Ba is very unusual at their metallicities when compared with the other Galactic halo stars, as seen in Fig. 15. This composition is similar to stars in the Segue 1 and Hercules ultra-faint dwarf (UFD) galaxies (Koch et al. 2013; Frebel, Simon & Kirby 2014). In Segue 1, the Ba-poor stars were discussed as representative of inhomogeneous enrichment by a single (or few) supernova event, and therefore

Table 5. Light element abundances in the new 28 metal-poor stars (labelled by RA_{SDSS}), and our analysis of HD122563. When the number of lines $N_X < 4$ for species X, then $\sigma(X) = \sigma(\text{Fe I})/\sqrt{N_X}$.

RA_{SDSS}	[Na/Fe] $\pm\sigma$ (N)	[Mg/Fe] $\pm\sigma$ (N)	[Ca/Fe] $\pm\sigma$ (N)	[Sc/Fe] $\pm\sigma$ (N)	[TiI/Fe] $\pm\sigma$ (N)	[TiII/Fe] $\pm\sigma$ (N)
180.2206	+0.39 ± 0.13 (2)	+0.30 ± 0.11 (3)	+0.35 ± 0.10 (4)	–	+0.22 ± 0.13 (2)	+0.28 ± 0.11 (3)
181.2243	−0.23 ± 0.17 (1)	+0.67 ± 0.13 (2)	<+0.94	–	–	<+1.23
181.4395	+0.07 ± 0.13 (2)	+0.26 ± 0.11 (3)	+0.42 ± 0.19 (9)	−0.15 ± 0.11 (3)	+0.16 ± 0.19 (9)	+0.19 ± 0.16 (8)
183.6849	−0.18 ± 0.17 (2)	+0.13 ± 0.14 (3)	<+1.01	–	–	<+1.88
189.9449	+0.01 ± 0.08 (2)	+0.17 ± 0.08 (2)	<+0.65	–	–	<+0.92
193.8390	<+1.17	+0.37 ± 0.12 (3)	+0.33 ± 0.14 (8)	+0.08 ± 0.12 (3)	+0.09 ± 0.12 (8)	+0.17 ± 0.18 (8)
196.3755	+0.22 ± 0.13 (2)	+0.29 ± 0.11 (3)	+0.45 ± 0.24 (7)	–	+0.43 ± 0.25 (4)	+0.28 ± 0.19 (4)
198.5486	+0.24 ± 0.11 (2)	+0.25 ± 0.09 (3)	+0.53 ± 0.16 (1)	<+0.97	–	<+0.71
201.8711	−0.12 ± 0.11 (2)	−0.05 ± 0.11 (2)	<+1.16	–	–	<+1.59
203.2831	+0.66 ± 0.13 (2)	+0.02 ± 0.13 (2)	+0.21 ± 0.11 (3)	–	+0.43 ± 0.06 (6)	+0.50 ± 0.10 (5)
204.9008	−0.15 ± 0.18 (1)	−0.12 ± 0.13 (2)	<+0.96	–	–	<+1.36
208.0798	+0.26 ± 0.10 (2)	+0.09 ± 0.08 (3)	+0.45 ± 0.14 (1)	–	–	<+0.78
210.0166	+0.06 ± 0.13 (2)	+0.18 ± 0.11 (3)	+0.36 ± 0.28 (4)	<+0.44	+0.37 ± 0.11 (3)	+0.12 ± 0.13 (2)
213.7879	−0.12 ± 0.13 (2)	+0.33 ± 0.11 (3)	+0.44 ± 0.09 (4)	<+0.26	+0.45 ± 0.24 (7)	+0.45 ± 0.13 (2)
214.5556	+0.02 ± 0.12 (2)	+0.36 ± 0.09 (3)	<+0.82	<+1.11	–	<+0.96
217.5786	<+1.14	+0.22 ± 0.11 (3)	+0.55 ± 0.24 (6)	+0.09 ± 0.13 (2)	+0.23 ± 0.12 (5)	+0.55 ± 0.16 (10)
229.1219	−0.13 ± 0.09 (2)	+0.22 ± 0.09 (2)	–	–	+1.26 ± 0.12 (1)	+1.44 ± 0.12 (1)
233.5730	+0.65 ± 0.14 (2)	+0.24 ± 0.12 (3)	+0.39 ± 0.32 (5)	<+0.10	+0.24 ± 0.15 (4)	+0.28 ± 0.12 (3)
235.1449	−0.26 ± 0.11 (2)	+0.09 ± 0.11 (2)	<+0.67	<+1.16	–	<+0.94
237.8246	+0.00 ± 0.11 (2)	+0.04 ± 0.11 (2)	<+0.88	<+1.12	–	<+0.89
240.4216	+0.14 ± 0.14 (2)	+0.14 ± 0.12 (3)	+0.31 ± 0.12 (3)	<+0.54	+0.44 ± 0.14 (2)	+0.52 ± 0.14 (2)
245.5747	−0.17 ± 0.14 (2)	+0.14 ± 0.14 (2)	<+0.96	<+0.99	...	<+0.75
245.8356	+0.67 ± 0.15 (2)	+0.29 ± 0.11 (4)	+0.66 ± 0.22 (6)	+0.30 ± 0.15 (2)	+0.64 ± 0.15 (2)	+0.46 ± 0.25 (11)
248.4959	+0.39 ± 0.13 (2)	+0.14 ± 0.10 (3)	+0.35 ± 0.17 (7)	<+0.07	+0.48 ± 0.28 (4)	+0.36 ± 0.18 (5)
250.6963	<+1.71	+0.11 ± 0.12 (3)	+0.57 ± 0.38 (8)	+0.03 ± 0.20 (1)	+0.40 ± 0.24 (6)	+0.39 ± 0.12 (8)
251.4082	<+1.61	−0.20 ± 0.13 (2)	<+0.11	<+0.52	–	<+0.28
253.8582	+0.12 ± 0.15 (2)	+0.23 ± 0.12 (3)	+0.27 ± 0.20 (4)	<+0.20	+0.39 ± 0.24 (4)	+0.37 ± 0.18 (5)
255.5555	+0.76 ± 0.13 (2)	+0.29 ± 0.11 (3)	+0.46 ± 0.10 (3)	<+0.78	–	<+0.88
HD122563	+0.21 ± 0.11 (2)	+0.18 ± 0.09 (3)	+0.32 ± 0.14 (8)	+0.19 ± 0.11 (2)	+0.07 ± 0.05 (9)	+0.46 ± 0.08 (9)

possibly related to first stars. Higher SNR data for these two stars are warranted in order to test this hypothesis.

Finally, one star (Pristine_245.8356+13.8777) shows a high Y II abundance, but a normal Ba II abundance. A similar star was recently studied by Caffau et al. (2019, J0222−0313), where the authors show it is a CEMP-s star, having undergone mass transfer in a binary system with an Asymptotic Giant Branch (AGB) star. However, they also suggest that the AGB star in this system may have undergone a proton ingestion event just before the mass transfer that produced an enhancement in only the first s-process peak elements.

5.5 Abundance uncertainties

Total uncertainties in the chemical abundances are a combination of the measurement uncertainties and systematic errors in the stellar parameters, added in quadrature. For the measurement errors, when fewer than four lines are available for an element X, then we adopt the larger of $\sigma(X)$ or $\sigma(\text{Fe I})/\text{sqrt}(N_X)$. Since the Fe I lines are measured across the entire spectrum and over a range of equivalent widths and excitation potentials, then this assumes that $\sigma(\text{Fe I})$ captures the minimum measurement quality of our spectra. For the systematic errors, due to uncertainties in the stellar parameters, we determine the impact of the 1σ changes in temperature, gravity, and metallicity listed in Table 2.

A sample of the systematic uncertainties for three stars that cover the parameter space of this sample is shown in Table 7. It can be seen that temperature tends to be the dominant systematic error in the analysis of most elements. While we could further investigate the impact of the final metallicities [Fe/H] and uncertainties σ([Fe/H]) through iterations in the Bayesian inference method on the model atmospheres parameters, we did not; the only stars that we follow up in detail are those that did prove to be very metal poor, therefore the impact of adjusting for the final metallicities on the other stellar parameters is very small.

6 DISCUSSION

A total of 70 (out of 115) bright, metal-poor candidates have been observed with the CFHT ESPaDOnS spectrograph from the original footprint (∼1000 sq. deg) of the *Pristine* survey. These targets were selected to have a high probability for $[\text{Fe/H}]_{\text{Pristine}} < -2.5$, when the *Pristine* CaHK filter was calibrated with the SDSS $g-i$ and $g-r$ colours (60 stars), or only the SDSS $g-r$ colour alone (10 stars). We carry out a model atmosphere analysis by adopting stellar parameters determined from a Bayesian inference method that uses the SDSS colours, *Gaia* DR2 parallaxes, and MESA/MIST isochrones, assuming the initial *Pristine* survey metallicities. Out of these 70 selected stars, we have found 28 to indeed have low metallicities, [Fe/H] ≤ −2.5 (40 per cent). The *Pristine* survey had also predicted that 27 stars would have [Fe/H] ≤ −3.0, and 5 were found (19 per cent). Of the 42 remaining stars ($-2.5 < [\text{Fe/H}]_{Q6} < +0.25$), there are no obvious relationships with any other stellar parameters (e.g. see Fig. 16), although we notice that all of the candidates on the upper red giant branch were successfully selected and confirmed to be metal-poor stars.

The selections made in this paper differ from those used by Youakim et al. (2017) and Aguado et al. (2019a) (see Section 2)

Table 6. Total systematic errors (dX) per element species (X) due to the stellar parameters (T, $\log g$, [Fe/H]), added in quadrature, where dT and dlg are from Table 2 and δ[Fe/H] is from Table 4. Stars are labelled by RA_{SDSS}.

RA_{SDSS}	dFe I	dFe II	dNa	dMg	dCa	dSc	dTi I	dTi II	dCr I	dNi I	dY II	dBa II
180.2206	0.03	0.02	0.03	0.02	0.01	–	0.02	0.02	0.02	0.02	–	0.02
181.2243	0.09	0.03	0.07	0.08	–	–	–	–	–	–	–	–
181.4395	0.01	0.01	0.01	0.01	0.01	0.01	0.01	0.01	0.01	0.01	–	–
183.6849	0.04	0.01	0.03	0.03	–	–	–	–	–	–	–	–
189.9449	0.12	0.02	0.09	0.09	–	–	–	–	–	–	–	–
193.8390	0.04	0.01	0.05	0.04	0.03	0.01	0.05	0.01	0.04	0.04	–	–
196.3755	0.02	0.01	0.02	0.02	0.01	–	0.03	0.01	0.02	0.02	–	–
198.5486	0.04	0.01	0.03	0.03	0.03	–	–	–	0.04	–	–	–
201.8711	0.03	–	0.02	0.02	–	–	–	–	–	–	–	–
203.2831	0.01	0.01	0.02	0.02	0.01	–	0.02	0.01	0.01	0.01	–	0.01
204.9008	0.01	0.01	0.01	0.01	–	–	–	–	–	–	–	–
208.0798	0.07	0.03	0.07	0.06	0.05	–	–	–	0.06	–	–	–
210.0166	0.03	0.02	0.03	0.03	0.02	–	0.03	0.02	0.03	0.03	–	0.03
213.7879	0.03	0.03	0.03	0.04	0.02	–	0.03	0.03	0.03	0.03	–	0.03
214.5556	0.17	0.03	0.13	0.14	–	–	–	–	–	–	0.09	0.15
217.5786	0.01	0.01	0.02	0.02	0.01	0.01	0.02	0.01	0.01	0.01	–	–
229.1219	0.16	0.05	0.12	0.15	–	–	0.15	0.06	0.15	–	0.08	–
233.5730	0.02	0.01	0.02	0.02	0.01	–	0.02	0.01	0.02	–	–	0.01
235.1449	0.08	0.02	0.06	0.08	–	–	–	–	–	–	–	0.06
237.8246	0.09	0.03	0.07	0.07	–	–	–	–	–	–	–	0.06
240.4216	0.03	0.02	0.02	0.02	0.02	–	0.03	0.02	0.03	0.03	–	0.02
245.5747	0.08	0.03	0.07	0.08	–	–	–	–	–	–	–	–
245.8356	0.02	0.02	0.03	0.02	0.02	0.02	0.03	0.02	0.03	0.02	–	–
248.4959	0.02	0.01	0.03	0.02	0.01	–	0.02	0.02	0.02	0.02	–	0.02
250.6963	0.02	0.01	0.04	0.02	0.02	0.02	0.02	0.02	0.02	0.02	–	–
251.4082	0.02	0.01	0.03	0.02	–	–	–	–	–	–	–	0.02
253.8582	0.06	0.02	0.06	0.06	0.04	–	0.06	0.03	0.06	0.06	–	0.04
255.5555	0.03	0.02	0.03	0.03	0.02	–	–	–	–	–	–	0.02
HD122563	0.03	0.02	0.04	0.03	0.02	0.01	0.04	0.01	0.03	0.03	–	–

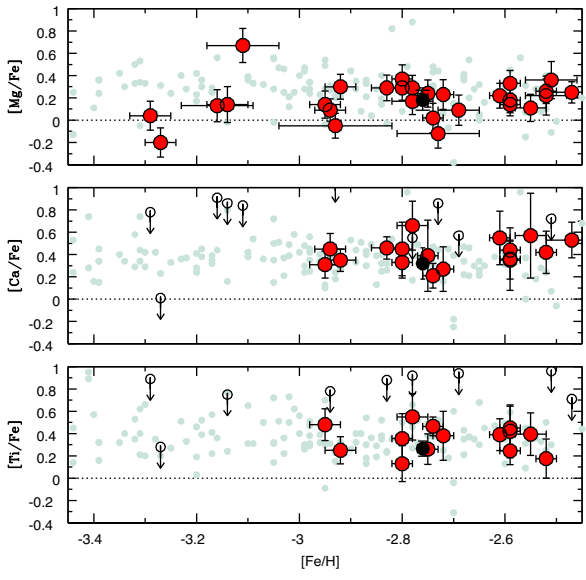

Figure 12. Mg, Ca, and Ti abundances and upper limits in the 28 new metal-poor stars ([Fe/H] < -2.5); the symbols are the same as in Fig. 11.

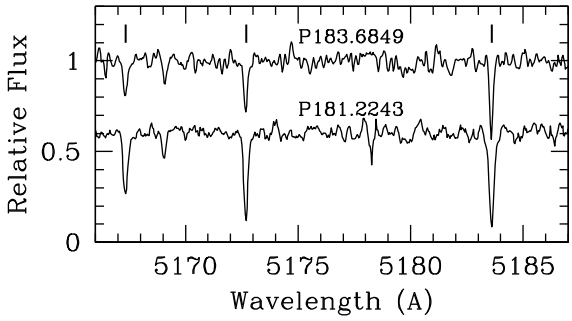

Figure 13. The spectrum of the Mg I*b* lines in the Mg strong star, P181.2243. This star is compared to Pristine_183.6849+04.8619, which has very similar stellar parameters [T∼6450, log(g)∼4, and [Fe/H] ∼−3.2], but is Mg normal.

being far more strict in the metal-poor probability cuts. Furthermore, about 1/3 of the targets in this programme were observed before the selection criteria were finalized. Nevertheless, our success rates are very similar to the results from the medium-resolution surveys. We do not reproduce the (lower) success rates for bright stars seen in earlier *Pristine* survey papers (Caffau et al. 2017; Bonifacio et al. 2019), partially due to our improved (more strict) selection criteria, partially due to differences between the SDSS and APASS photometry, and possibly due to the larger number of stars in this sample.

In the remainder of this discussion, we examine the kinematic and orbital properties of the 70 metal-poor candidates in this paper, and correlate those with their chemical abundances. We caution that these calculations and our interpretations are highly dependent on the accuracy of the adopted Milky Way potential (described in the next section). For example, our orbit integrations do not account for effects like the Galactic bar, which can significantly influence halo star orbits (e.g. Hattori, Erkal & Sanders 2016; Price-Whelan et al. 2016; Pearson, Price-Whelan & Johnston 2017).

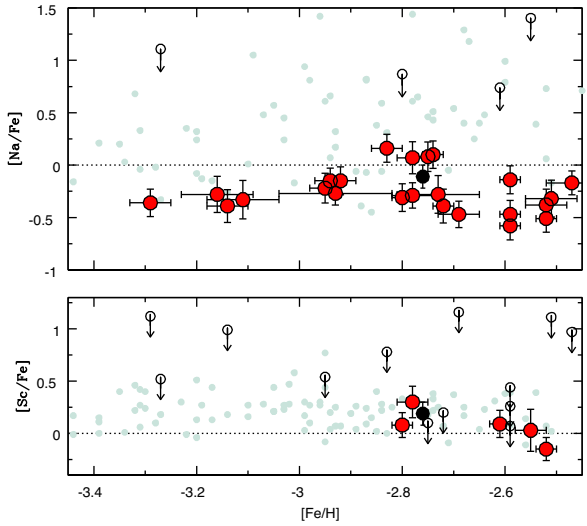

Figure 14. Na and Sc abundances and upper limits in the 28 new metal-poor stars ([Fe/H] < -2.5); the symbols are the same as in Fig. 11. NLTE corrections for Na have been applied from INSPECT (Amarsi et al. 2016).

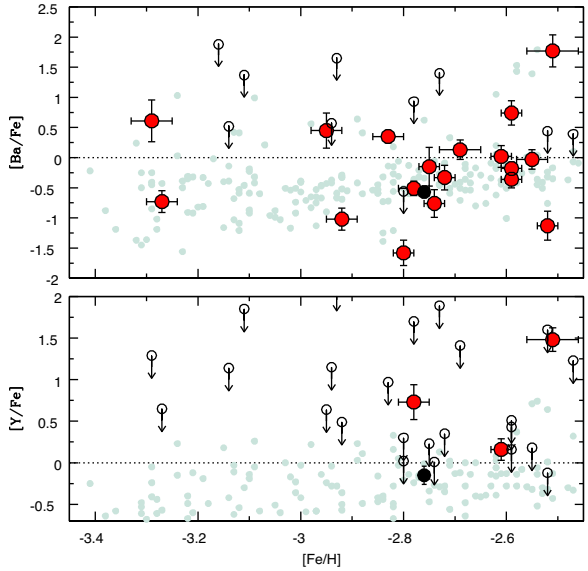

Figure 15. Ba and Y abundances and upper limits in the 28 new metal-poor stars ([Fe/H] < -2.5); the symbols are the same as in Fig. 11 with the exception of the Galactic comparison stars from Roederer et al. (2014, small grey points). We identify one star near [Fe/H] $= -2.5$ (Pristine_214.5556+07.4669) as an r-process-rich star, significantly enriched in both Y and Ba.

6.1 Kinematics and orbits

Galactocentric velocities (U, V, and W) are calculated for each star from their Galactic Cartesian coordinates (X, Y, Z) following the methods of Bird et al. (2019). The distance between the Sun and the Galactic centre is taken to be 8.0 kpc, the Local Standard of Rest circular velocity is $V_{\rm circ} = 239$ km s^{-1}, and the peculiar motion of the Sun is ($U_0 = 11.10$ km s^{-1}; $V_0 + V_{\rm circ} = 251.24$ km s^{-1}; $W_0 = 7.25$ km s^{-1}), as described in Schönrich, Binney & Dehnen (2010). The sign of U_0 is changed so that U is positive towards the Galactic anticentre. Errors in these velocities are propagated from the uncertainties in proper motion, RVs, and distance by calculating the mean dispersions from 1000 Monte Carlo realizations, and selecting from a Gaussian distribution in each of the original quantities.

With the distances from the Bayesian inference analysis,[10] precision RVs from our high-resolution spectra, and proper motions from the *Gaia* DR2 data base, then the orbital parameters for the sample are calculated using the Galpy package (Bovy 2015). The *MWPotential14* is adopted, a Milky Way gravitational potential composed of a power law, exponentially cut-off bulge, Miyamoto Nagai Potential disc, and Navarro, Frenk & White (1997) dark matter halo. A more massive halo is chosen following Sestito et al. (2019), with a mass of 1.2×10^{12} M$_\odot$, which is more compatible with the value from Bland-Hawthorn & Gerhard (2016).

The *UVW* velocities for the 70 highly probable metal-poor stars in this sample are given in Table A1 (see Appendix A). The Toomre diagram for these objects is shown in Fig. 17, colour coded by the [Fe/H]$_{\rm Q6}$ metallicities. Most of the metal-poor stars in our sample have halo-like velocities, as expected for their metallicities. One very metal poor star (Pristine_183.6849+04.8619, discussed below) appears to have disc-like dynamics.

6.2 Orbit analyses

To investigate the relationships between the chemical and kinematic properties of the stars in our sample, we examine their maximum excursions. This includes the apocentric and pericentric distances ($R_{\rm apo}$ and $R_{\rm peri}$), perpendicular distance from the Galactic plane ($Z_{\rm max}$), and eccentricity (e) of the derived orbits; see Table A1.

In Fig. 18, stars with $R_{\rm apo} < 15$ kpc and $Z_{\rm max} < 3$ kpc are considered to be confined to the Galactic plane (16 stars), while stars with $R_{\rm apo} > 30$ kpc are considered to be members of the outer halo (10 stars). The outer halo star Pristine_251.4082+12.3657 has the largest $R_{\rm apo}$ distance in our sample, with a highly eccentric orbit, and it is one of the most metal-poor stars ([Fe/H]=−3.3), with low abundances of [Mg/Fe] and [Ca/Fe] (see Fig. 12), and also low [Ba/Fe]. This chemical signature is typical of stars in or accreted from the nearby dwarf galaxies. Alternatively, it may have been accreted from an *ultra*-faint dwarf galaxy, since its chemistry is also similar to the unique stars CS 29498−043 and CS 29249−037 (Aoki et al. 2002; Depagne et al. 2002), both near [Fe/H] $= -4$. These stars have been proposed to be second-generation stars, which formed from gas enriched by a massive Population III first star, exploding as a fall-back supernova (see also Frebel et al. 2019), and as such they would have formed in a now accreted *ultra*-faint dwarf galaxy.

In Fig. 19, only stars with $R_{\rm apo} < 30$ kpc are shown. Clearly, most of the stars confined to the Galactic plane ($Z_{\rm max} < 3$ kpc) are the relatively metal-rich (interloping) stars in our sample. However, one of the most metal-poor stars (Pristine_183.6849+04.8619, [Fe/H] $= -3.1$) is also confined to the Galactic plane with a nearly circular orbit (e=0.3). This was also seen in the Toomre diagram (Fig. 17). A detailed view of the orbit of this star is shown in Fig. 20. Most of the spectral lines in this star are weak and so we were unable to determine many elemental abundances, only [Mg/Fe]=+0.13 (±0.14) and [Na/Fe]=−0.18 (±0.17), which are both quite low for a typical halo metal-poor star. Ultra-metal-poor stars ([Fe/H] $<$ −4) have been found on similar quasi-circular and planar orbits by

[10]For three stars, we reverted back to distances from their 1/parallax values based on unrealistical outer halo distances and other orbital properties. Two of these stars were discussed at the end of Section 4.1, and a third star is discussed in Appendix A.

Table 7. Samples of systematic errors per star (labelled by RA_{SDSS}) per elemental species, which were added in quadrature per star in Table 6. We note that if σFe I is used instead of σ[Fe/H], then the errors due to metallicity remain negligible.

RA_{SDSS}	Parameter	X ±dX	dFe I	dFe II	dNa I	dMg I	dCa I	dSc II	dTi I	dTi II	dCr I	dNi I	dY II	dBa II
193.8390	Temperature	4764 ± 32 K	0.04	−0.01	0.05	0.03	0.03	0.01	0.05	0.01	0.04	0.04	–	–
193.8390	Log g	1.22 ± 0.03	0.00	0.01	−0.01	−0.01	0.00	0.01	0.00	0.01	0.00	0.00	–	–
193.8390	[Fe/H]	−2.80 ± 0.02	0.00	0.00	0.00	0.00	0.00	0.00	0.00	0.00	0.00	0.00	–	–
213.7879	Temperature	5289 ± 29 K	0.03	0.00	0.03	0.03	0.02	–	0.03	0.01	0.03	0.03	–	0.02
213.7879	Log g	2.27 ± 0.07	0.00	0.03	0.00	−0.02	0.00	–	0.00	0.02	0.00	0.00	–	0.02
213.7879	[Fe/H]	−2.59 ± 0.02	0.00	0.00	0.00	0.00	0.00	–	0.00	0.00	0.00	0.00	–	0.00
214.5556	Temperature	6482 ± 203 K	0.17	0.02	0.13	0.14	–	–	–	–	–	–	0.09	0.15
214.5556	Log g	3.88 ± 0.05	0.00	0.02	0.00	−0.01	–	–	–	–	–	–	0.02	0.01
214.5556	[Fe/H]	−2.50 ± 0.05	0.00	0.00	0.00	0.00	–	–	–	–	–	–	0.00	0.00

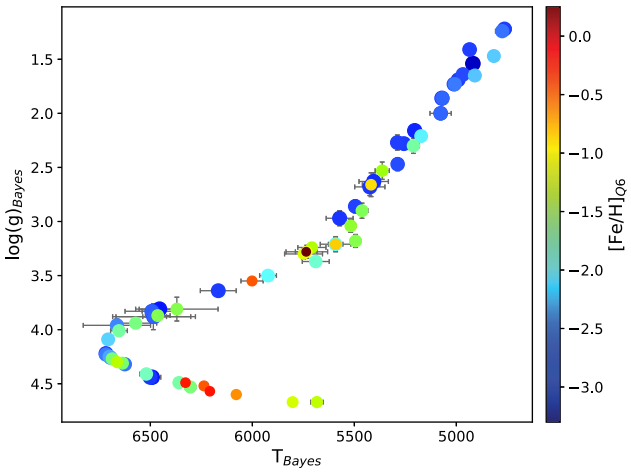

Figure 16. The HRD for the 70 metal-poor candidates in the *Pristine* survey, colour coded by their ('Quick Six') metallicities $[Fe/H]_{Q6}$ as determined from our high-resolution CFHT ESPaDOnS spectrum and Bayesian inference analysis. Stars that are not very metal poor, with [Fe/H] > -2.0, are located over all stellar parameters.

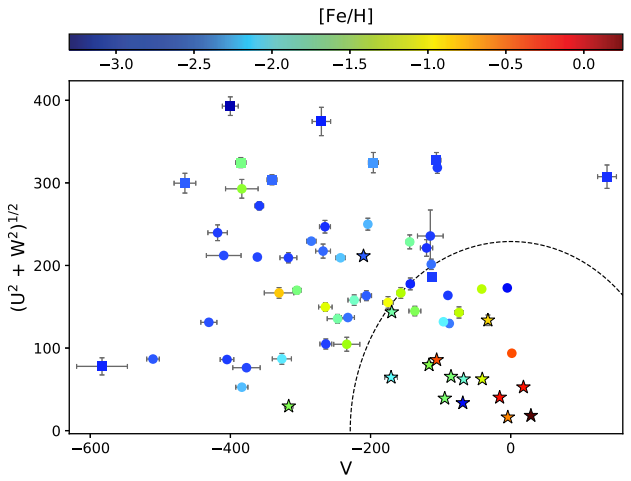

Figure 17. Toomre diagram for the 70 highly probable metal-poor stars in our *Pristine* survey sample. The dashed line represents stars potentially with disc dynamics ($V_{circ} = 239$ km s^{-1}). The symbols are the same as in Fig. 18.

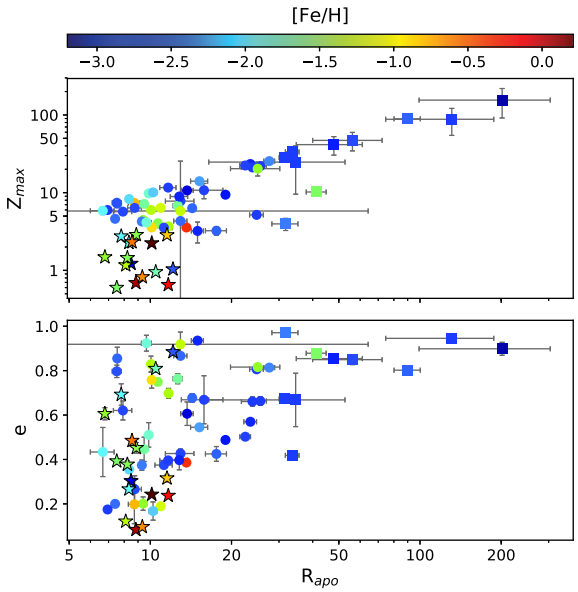

Figure 18. Perpendicular distance from the Galactic plane (Z_{max}) and eccentricity (e) of the orbits versus apocentric distance (R_{apo}) for the 70 high-probability metal-poor stars in this paper. For targets with $R_{apo} < 15$ and $Z_{max} < 3$ kpc, we adopt 'star' symbols, for $R_{apo} < 30$ kpc we adopt circle symbols, and when $R_{apo} > 30$ kpc we adopt square symbols. All targets are colour coded by their $[Fe/H]_{Q6}$ metallicities.

Sestito et al. (2019), and interpreted as stars that may have been brought in during the early merger phase of the building blocks of the proto-MW that eventually formed the disc.

Several (8) stars in our sample have orbits that take them deep into the Galactic bulge ($R_{peri} < 1$ kpc). All of these stars are on highly radial orbits ($e > 0.8$), and two are very metal poor; Pristine_250.6963+08.3743 at [Fe/H] $= -2.55 \pm 0.03$, and Pristine_201.8710+07.1810 at [Fe/H] $= -2.93 \pm 0.11$. While the former star shows typical halo abundances in [(Mg, Ca, Ti)/Fe] $= +0.4$ (± 0.4), the latter is clearly challenged in α-elements, [(Na, Mg)/Fe] $= -0.1$ (± 0.2). It is difficult to discern whether these stars formed in the bulge and have been flung out or if they have been accreted from the halo (or a dwarf galaxy) and moved inwards. As metal-poor stars in the bulge are thought to be older in absolute age (Tumlinson 2010; Howes et al. 2016; Starkenburg et al. 2017a; El-Badry et al. 2018; Frebel et al. 2019), then these could be extremely valuable objects for studies of the earliest stages of star formation in the Galaxy.

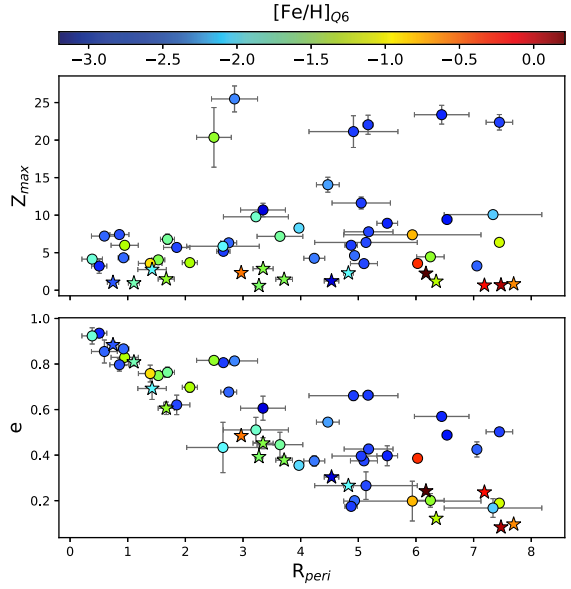

Figure 19. $Z_{\rm max}$ and eccentricity of the orbits versus pericentric distance $R_{\rm peri}$ for the stars within $R_{\rm apo}$ < 30 kpc. The symbols are the same as in Fig. 18. The very metal poor star confined within $Z_{\rm max}$ = 1 kpc (Pristine_183.6849+04.8619) near $R_{\rm peri}$ =4.5 kpc can be seen more clearly in this plot than Fig. 18.

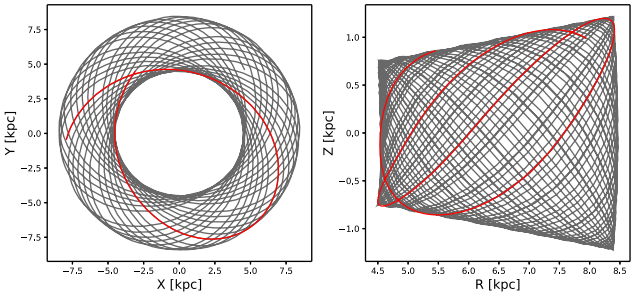

Figure 20. The orbit for the very metal poor star Pristine_183.6849+04.8619, from our adopted Galactic potential. The orbital properties are $R_{\rm apo}$ = 8.5 kpc, $Z_{\rm max}$ = 1.2 kpc, and eccentricity e=0.3. A sample single orbit is shown in red.

6.3 Action parameters

The orbital energy (E) and action parameters (vertical J_z, azimuthal J_ϕ) were determined during the Galpy orbit calculations (discussed above); these are shown in Fig. 21 and provided in Table A1. Values are scaled by the solar values, where $J_{\phi\odot}$ = 2009.92 km s^{-1} kpc, $J_{z\odot}$ = 0.35 km s^{-1} kpc, and $E_\odot$ = −64 943.61 (km s^{-1})^2. It is worth noting that stars with $J_\phi/J_{\phi\odot}$ = 1 rotate like the Sun around the Galactic Centre.

Among the very metal poor stars, we note that they are roughly evenly distributed between retrograde and prograde orbits, i.e. between $-1 < J_\phi/J_{\phi\odot} < 1$. The most retrograde metal-poor star with a bound orbit (near $J_\phi/J_{\phi\odot} = -1$) is Pristine_198.5486+11.4123. This star has $Z_{\rm max}$ = 3.2 kpc, placing it very close to the Galactic plane. Therefore, this star is travelling at nearly the speed of the Sun but in the opposite direction, close to the Galactic plane. This orbit is certainly unusual and suggests that it may have been accreted from a dwarf galaxy; however, its chemistry is like that of a normal metal-poor star, [Fe/H] = −2.5, [Mg/Fe]=+0.3, and [Ba/Fe]<+0.4.

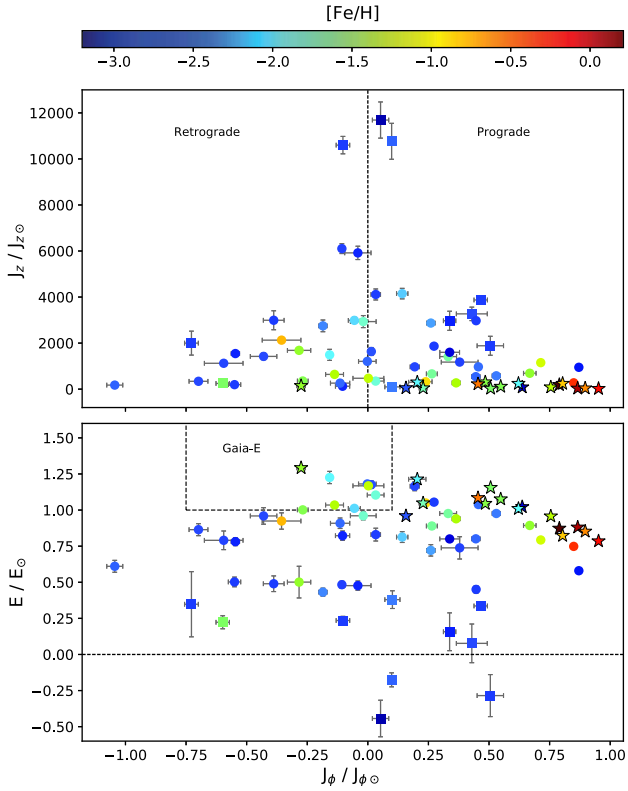

Figure 21. The orbit energies and rotational actions for the 70 high-probability metal-poor stars in this paper. The rotational action J_ϕ (= L_z) is compared with the vertical action J_z space (top panel) and the orbit energy (bottom panel), all normalized by the solar values. Prograde and retrograde regions are identified in the top panel. The symbols are as in Fig. 18. The region associated with Gaia-Enceladus is marked, above $E/E_\odot$ > 1 and −0.75 <$J_\phi/J_{\phi\odot}$ <0.1 (Belokurov et al. 2018; Haywood et al. 2018; Helmi et al. 2018; Myeong et al. 2018, 2019).

The very metal poor star Pristine_251.4082+12.3657, identified as having the largest $R_{\rm apo}$ value in this sample, is also found to have a large $Jz/Jz_\odot$ value and an unbound orbit ($E/E_\odot$ < 0). In total, the three stars in Fig. 21 appear to have unbound orbits, although we caution that our uncertainties in their orbits are quite small when based on the very small distance errors from the Bayesian inference method. Examination of their parallax errors shows that their orbits could be bound, consistent with $E/E_\odot \sim 0$. In Appendix A, we examine five more stars that appear to be dynamically unbound when their Bayesian inferred distances are used to determine their orbits. Two of those stars were discussed in Section 4.1, and it was shown that the orbital properties for these two metal-rich stars were significantly improved when 1/parallax was adopted for their distances. The same was found for a third star Pristine_213.7879+08.4232, even though this star has been confirmed to be metal poor. The parallax errors for these three stars are all very small, and therefore we have adopted the 1/parallax distance for the orbital analysis of these three stars. Finally, we removed two stars from this kinematic analysis, Pristine_181.4395+01.6294 and Pristine_182.5364+00.9431. Both stars have $R_{\rm apo}$ > 500 kpc and e ∼1, resulting in extreme and unbound orbits for any distance that we adopt.

One of the most exciting discoveries from the *Gaia* DR2 data set has been the identification of the Gaia-Enceladus dwarf galaxy (or galaxies) dissolved into the Milky Way halo. The region where stars may be associated with Gaia-Enceladus is shown in

Fig. 21, i.e. $E/E_{\odot} > 1$ and $-0.75 < J_{\phi}/J_{\phi\odot} < 0.1$ (Belokurov et al. 2018; Haywood et al. 2018; Helmi et al. 2018; Myeong et al. 2018, 2019). This includes eight stars in our sample that range from $-2.5 <$ [Fe/H]$_{Q6} < -1.0$, with a mean metallicity of $<$[Fe/H] $>=-2.0 \pm 0.5$; see Table A1. Only one of these stars is sufficiently metal poor to have made it into our detailed analysis sample, Pristine_250.6963+08.3743 ([Fe/H]$=-2.55 \pm 0.03$). This star has high α-element abundances [(Ca, Ti)/Fe]$\sim+0.4$, but lower magnesium such that [Mg/(Ca, Ti)]$=-0.3$, which is has been seen in some dwarf galaxies (e.g. Tri II, Venn et al. 2017). However, unlike most stars in dwarf galaxies, this star appears to have solar-like [Ba/Fe]$\sim$0 and [Sc/Fe]$\sim$0. It is unclear if this star is a true member of the original Gaia-Enceladus accretion event, but if so it would be among the most metal-poor stars yet found in that system (though also see Monty et al. 2019). As a final test, we examine the action–energy space of the newly discovered Gaia-Sequoia accretion event (Myeong et al. 2018, 2019), i.e. $E/E_{\odot} > 1$ and $J_{\phi}/J_{\phi\odot} < -1.5$, but find no targets in that parameter space.

7 CONCLUSIONS AND FUTURE WORK

The results from our follow-up spectroscopy of 115 bright metal-poor candidates selected from the *Pristine* survey have been presented based on the CFHT ESPaDOnS spectra. We have discovered 28 new very metal poor stars with [Fe/H] < -2.5 and five stars with [Fe/H] < -3.0, which imply success rates of 40 (28/70) and 19 per cent (5/27), respectively. These rates are higher than previous surveys, though in line with the *Pristine* medium-resolution programmes. A detailed model atmosphere analysis for the 28 new very metal poor stars has provided stellar parameters and chemical abundances for 10 elements (Na, Mg, Ca, Sc, Ti, Cr, Fe, Ni, Y, and Ba) and Li upper limits. Most stars show chemical abundance patterns that are similar to the normal metal-poor stars in the Galactic halo; however, we also report the discoveries of a new r-process-rich star (Pristine_214.5556+07.4670), a new CEMP-s candidate with [Y/Ba]$>$0 (Pristine_245.8356+13.8777), and an [Mg/Fe]-challenged star (Pristine_251.4082+12.3657), which has an abundance pattern typical of stars in dwarf galaxies or, alternatively, gas enriched by a massive Population III first star exploding as a fall-back supernova. Two stars are also interesting because they are quite Ba poor (Pristine_181.4395+01.6294 and Pristine_193.8390+11.4150), and resemble stars in the Segue 1 and Hercules UFDs, which have been interpreted as evidence for inhomogeneous enrichment by a single (or few) supernova event, and therefore possibly related to first stars.

The kinematics and orbits for all 70 of the metal-poor candidates have been determined using the *Gaia* DR2 data, our RVs, and adopting the *MWPotential14* in the Galpy package (with a slightly more massive halo). The majority of the confirmed metal-poor stars are members of the Galactic halo, although some stars show unusual kinematics for their chemistry. We report the discovery of a very metal poor ([Fe/H] $= -3.2 \pm 0.1$) star (Pristine_183.6849+04.8619) with a slightly eccentric ($e = 0.3$) prograde orbit confined to the Galactic plane ($Z_{\rm max} < 1.2$ kpc). We also find a metal-poor ([Fe/H] $= -2.5 \pm 0.1$) star (Pristine_198.5486+11.4123) on a highly retrograde orbit ($V = -510$ km s^{-1}, $J_{\phi}/J_{\phi\odot} = -1.0$) that remains close to the Galactic plane ($Z_{\rm max} < 3.2$ kpc). These two stars do not fit standard models for the formation of the Galactic plane, pointing towards more complex origins. An additional eight stars were found to have orbital energy and actions consistent with the Gaia-Enceladus accretion event, including one very metal poor star (Pristine_ 250.6963+08.3743) with [Fe/H]$=-2.5$ and chemical abundances that are common for stars in dwarf galaxies. Finally, eight stars have highly radial orbits that take them deep into the Galactic bulge ($R_{\rm peri} < 1$ kpc), including two very metal poor stars (Pristine_250.6963+08.3743 at [Fe/H] $= -2.55 \pm 0.03$, and Pristine_201.8710+07.1810 at [Fe/H] $= -2.93 \pm 0.11$, the latter star is also low in α-elements). If these stars formed in the bulge, they could be extremely valuable for studies of the earliest conditions for star formation in the Galaxy.

Currently, we are running a Gemini/GRACES Large and Long Program to follow up with high-SNR ($>$100) spectra for our best metal-poor candidates ([Fe/H] < -3.5) and with $V < 17$ selected from medium-resolution spectroscopy. We also plan to observe a selection of these stars with the upcoming Gemini GHOST spectrograph (Chene et al. 2014; Sheinis et al. 2017), which is anticipated to have excellent throughput at blue-UV wavelengths, providing far more iron-group lines for stellar parameter assessments and many more spectral lines of heavy neutron-capture (and light) elements.

In the near future, massively multiplexed high-resolution spectroscopic surveys ($R > 20\,000$) will be initiated, including the European WEAVE survey at the INTs (Dalton et al. 2012), the 4MOST survey at ESO (De Jong et al. 2019), and the SDSS-V survey comprising fields in both the Northern and Southern hemispheres (Kollmeier et al. 2017). These will provide the truly large statistical samples needed for the studies of the metal-poor Galaxy.

ACKNOWLEDGEMENTS

This work is based on observations obtained at the CFHT that is operated by the National Research Council of Canada, the Institut National des Sciences de l'Univers of the Centre National de la Recherche Scientique of France, and the University of Hawaii. This work has made use of data from the European Space Agency (ESA) mission *Gaia* (https://www.cosmos.esa.int/gaia), processed by the *Gaia* Data Processing and Analysis Consortium (DPAC; https://www.cosmos.esa.int/web/gaia/dpac/consortium). Funding for the DPAC has been provided by national institutions, in particular the institutions participating in the *Gaia* Multilateral Agreement. This research has made use of the SIMBAD data base, operated at CDS, Strasbourg, France (Wenger et al. 2000).

The authors wish to thank David Yong and Ian Roederer for helpful discussions on the detailed abundances of the new metal-poor stars. We are also grateful to the anonymous referee for their comments and support.

This work was funded in part through the National Science and Engineering Research Council Discovery Grants programme and the CREATE training programme on New Technologies for Canadian Observatories. The authors thank the International Space Science Institute (ISSI) in Berne, Switzerland, for providing financial support and meeting facilities to the international team *Pristine*. FS and NFM gratefully acknowledge funding from CNRS/INSU through the Programme National Galaxies et Cosmologie and through the CNRS grant PICS07708. FS thanks the Initiative dExcellence IdEx from the University of Strasbourg and the Programme Doctoral International PDI for funding his PhD. This work has been published under the framework of the IdEx Unistra and benefits from funding from the state managed by the French National Research Agency (ANR) as part of the investments for the future program. JIGH acknowledges financial support from the Spanish Ministry of Science, Innovation and Universities (MICIU) under

the 2013 Ramón y Cajal program MICIU RYC-2013-14875, and also from the Spanish ministry project MICIU AYA2017-86389-P.

The authors wish to recognize and acknowledge the very significant cultural role and reverence that the summit of Maunakea has always had within the indigenous Hawaiian community. We are most fortunate to have had the opportunity to conduct observations from this mountain.

REFERENCES

Abadi M. G., Navarro J. F., Fardal M., Babul A., Steinmetz M., 2010, MNRAS, 407, 435
Abel T., Bryan G. L., Norman M. L., 2002, Science, 295, 93
Aguado D. et al., 2019a, MNRAS, 490, 2241
Aguado D. S., González Hernández J. I., Allende Prieto C., Rebolo R., 2019b, ApJ, 874, L21
Allende Prieto C., Beers T. C., Wilhelm R., Newberg H. J., Rockosi C. M., Yanny B., Lee Y. S., 2006, ApJ, 636, 804
Amarsi A. M., Lind K., Asplund M., Barklem P. S., Collet R., 2016, MNRAS, 463, 1518
Aoki W., Norris J. E., Ryan S. G., Beers T. C., Ando H., 2002, ApJ, 576, L141
Arentsen A., Starkenburg E., Shetrone M. D., Venn K. A., Depagne É., McConnachie A. W., 2019, A&A, 621, A108
Asplund M., Grevesse N., Sauval A. J., Scott P., 2009, ARA&A, 47, 481
Bailer-Jones C. A. L., Rybizki J., Fouesneau M., Mantelet G., Andrae R., 2018, AJ, 156, 58
Barbá R. H., Minniti D., Geisler D., Alonso-García J., Hempel M., Monachesi A., Arias J. I., Gómez F. A., 2019, ApJ, 870, L24
Beers T. C., Christlieb N., 2005, ARA&A, 43, 531
Beers T. C., Preston G. W., Shectman S. A., 1992, AJ, 103, 1987
Belokurov V., Erkal D., Evans N. W., Koposov S. E., Deason A. J., 2018, MNRAS, 478, 611
Bergemann M., Cescutti G., 2010, A&A, 522, A9
Bird S. A., Xue X.-X., Liu C., Shen J., Flynn C., Yang C., 2019, AJ, 157, 104
Blackwell D. E., Petford A. D., Shallis M. J., 1979, MNRAS, 186, 657
Bland-Hawthorn J., Gerhard O., 2016, ARA&A, 54, 529
Bonifacio P. et al., 2018, A&A, 612, A65
Bonifacio P. et al., 2019, MNRAS, 487, 3797
Bovy J., 2015, ApJS, 216, 29
Bromm V., 2013, Rep. Prog. Phys., 76, 112901
Caffau E. et al., 2012, A&A, 542, A51
Caffau E. et al., 2017, Astron. Nachr., 338, 686
Caffau E. et al., 2019, A&A, 628, A46
Casagrande L. et al., 2016, MNRAS, 455, 987
Chene A.-N. et al., 2014, in Ramón N., Colin R. C., Allison A. B., eds, Proc. SPIE Conf. Ser. Vol. 9151, Advances in Optical and Mechanical Technologies for Telescopes and Instrumentation. SPIE, Bellingham, p. 915147
Choi J., Dotter A., Conroy C., Cantiello M., Paxton B., Johnson B. D., 2016, ApJ, 823, 102
Christlieb N. et al., 2002, Nature, 419, 904
Christlieb N. et al., 2004, A&A, 428, 1027
Christlieb N., Schörck T., Frebel A., Beers T. C., Wisotzki L., Reimers D., 2008, A&A, 484, 721
Clark P. C., Glover S. C. O., Smith R. J., Greif T. H., Klessen R. S., Bromm V., 2011, Science, 331, 1040
Cohen J. G., Kirby E. N., 2012, ApJ, 760, 86
Collet R., Nordlund Å., Asplund M., Hayek W., Trampedach R., 2018, MNRAS, 475, 3369
Cui X.-Q. et al., 2012, Res. Astron. Astrophys., 12, 1197
Curtis S., Ebinger K., Fröhlich C., Hempel M., Perego A., Liebendörfer M., Thielemann F.-K., 2019, ApJ, 870, 2
DaCosta G. S. et al., 2019, MNRAS, 489, 5900
Dalton G. et al., 2012, in Ian S. M., Suzanne K. R., Hideki T., eds, Proc. SPIE Conf. Ser. Vol. 8446, Ground-based and Airborne Instrumentation for Astronomy IV. SPIE, Bellingham, p. 84460P
Dawson K. S. et al., 2013, AJ, 145, 10
De Jong R. S., Others A., Others B., 4MOST team, 2019, The Messenger, 175, 3
Depagne E. et al., 2002, A&A, 390, 187
Donati J. F., Semel M., Carter B. D., Rees D. E., Collier Cameron A., 1997, MNRAS, 291, 658
Donati J. F., Catala C., Landstreet J. D., Petit P., 2006, in Casini R., Lites B. W., eds, ASP Conf. Ser. Vol. 358, Solar Polarization 4. Astron. Soc. Pac., San Francisco, p. 362
Dotter A., 2016, ApJS, 222, 8
Eisenstein D. J. et al., 2011, AJ, 142, 72
El-Badry K. et al., 2018, MNRAS, 480, 652
Frebel A., Norris J. E., 2015, ARA&A, 53, 631
Frebel A. et al., 2006, ApJ, 652, 1585
Frebel A., Simon J. D., Kirby E. N., 2014, ApJ, 786, 74
Frebel A., Ji A. P., Ezzeddine R., Hansen T. T., Chiti A., Thompson I. B., Merle T., 2019, ApJ, 871, 146
Freeman K., Bland-Hawthorn J., 2002, ARA&A, 40, 487
Gaia Collaboration, Brown A. G. A., Vallenari A., Prusti T., de Bruijne J. H. J., Babusiaux C., Bailer-Jones C. A. L., 2018, A&A, 616, A1
Gianninas A., Curd B., Thorstensen J. R., Kilic M., Bergeron P., Andrews J. J., Canton P., Agüeros M. A., 2015, MNRAS, 449, 3966
González Hernández J. I., Bonifacio P., 2009, A&A, 497, 497
Greif T. H., 2015, Comput. Astrophys. Cosmol., 2, 3
Gustafsson B., Edvardsson B., Eriksson K., Jørgensen U. G., Nordlund, Å., Plez B., 2008, A&A, 486, 951
Hartwig T. et al., 2018, MNRAS, 478, 1795
Hattori K., Erkal D., Sanders J. L., 2016, MNRAS, 460, 497
Hayes C. R. et al., 2018, ApJ, 852, 49
Haywood M., Di Matteo P., Lehnert M. D., Snaith O., Khoperskov S., Gómez A., 2018, ApJ, 863, 113
Heger A., Woosley S. E., 2010, ApJ, 724, 341
Helmi A., White S. D. M., de Zeeuw P. T., Zhao H., 1999, Nature, 402, 53
Helmi A., Babusiaux C., Koppelman H. H., Massari D., Veljanoski J., Brown A. G. A., 2018, Nature, 563, 85
Henden A. A., 2019, J. Am. Assoc. Var. Star Obs. (JAAVSO), 47, 130
Hernitschek N. et al., 2016, ApJ, 817, 73
Hill V., Christlieb N., Beers T. C., Barklem P. S., Kratz K.-L., Nordström B., Pfeiffer B., Farouqi K., 2017, A&A, 607, A91
Hirano S., Hosokawa T., Yoshida N., Omukai K., Yorke H. W., 2015, MNRAS, 448, 568
Howes L. M. et al., 2016, MNRAS, 460, 884
Ibata R. A., Gilmore G., Irwin M. J., 1994, Nature, 370, 194
Ibata R., Chapman S., Ferguson A. M. N., Irwin M., Lewis G., McConnachie A., 2004, MNRAS, 351, 117
Ishigaki M. N., Tominaga N., Kobayashi C., Nomoto K., 2018, ApJ, 857, 46
Ivezić Ž. et al., 2008, ApJ, 684, 287
Jablonka P. et al., 2015, A&A, 583, A67
Ji A. P., Frebel A., Simon J. D., Chiti A., 2016, ApJ, 830, 93
Ji A. P., Drout M. R., Hansen T. T., 2019, ApJ, 882, 170
Jones S., Côté B., Roepke F. K., Wanajo S., 2019, ApJ, 882, 170
Jordi K., Grebel E. K., Ammon K., 2006, A&A, 460, 339
Keller S. C. et al., 2007, PASA, 24, 1
Keller S. C. et al., 2014, Nature, 506, 463
Kielty C. L., Venn K. A., Loewen N. B., Shetrone M. D., Placco V. M., Jahandar F., Mészáros S., Martell S. L., 2017, MNRAS, 471, 404
Koch A., Feltzing S., Adén D., Matteucci F., 2013, A&A, 554, A5
Koesterke L., Allende Prieto C., Lambert D. L., 2008, ApJ, 680, 764
Kollmeier J. A. et al., 2017, preprint (arXiv:1711.03234)
Kurucz R. L., 2005, Mem. Soc. Astron. Ital. Suppl., 8, 14
Lamb M. et al., 2017, MNRAS, 465, 3536
Lind K., Bergemann M., Asplund M., 2012, MNRAS, 427, 50
Lindegren L. et al., 2018, A&A, 616, A2
Lokhorst D. et al., 2016, ApJ, 819, 124

Longeard N. et al., 2018, MNRAS, 480, 2609
Longeard N. et al., 2019, MNRAS, 491, 356
McWilliam A., Wallerstein G., Mottini M., 2013, ApJ, 778, 149
Mardini M. K. et al., 2019, ApJ, 875, 89
Mashonkina L., Jablonka P., Pakhomov Y., Sitnova T., North P., 2017a, A&A, 604, A129
Mashonkina L., Sitnova T., Belyaev A. K., 2017b, A&A, 605, A53
Mashonkina L., Jablonka P., Sitnova T., Pakhomov Y., North P., 2017c, A&A, 608, A89
Mashonkina L., Sitnova T., Yakovleva S. A., Belyaev A. K., 2019, A&A, 631, 43
Monty S., Venn K. A., Lane J. M. M., Lokhorst D., Yong D., 2019, preprint (arXiv:1909.11969)
Müller B. et al., 2019, MNRAS, 484, 3307
Myeong G. C., Evans N. W., Belokurov V., Sanders J. L., Koposov S. E., 2018, ApJ, 863, L28
Myeong G. C., Vasiliev E., Iorio G., Evans N. W., Belokurov V., 2019, MNRAS, 488, 1235
Nakamura F., Umemura M., 2001, ApJ, 548, 19
Navarro J. F., Frenk C. S., White S. D. M., 1997, ApJ, 490, 493
Nissen P. E., Schuster W. J., 2010, A&A, 511, L10
Nordlander T. et al., 2019, MNRAS, 488, L109
Norris J. E. et al., 2013, ApJ, 762, 28
Norris J. E., Yong D., Venn K. A., Gilmore G., Casagrande L., Dotter A., 2017, ApJS, 230, 28
O'Brian T. R., Wickliffe M. E., Lawler J. E., Whaling W., Brault J. W., 1991, J. Opt. Soc. Am. B Opt. Phys., 8, 1185
Paxton B., Bildsten L., Dotter A., Herwig F., Lesaffre P., Timmes F., 2011, ApJS, 192, 3
Pearson S., Price-Whelan A. M., Johnston K. V., 2017, Nat. Astron., 1, 633
Price-Whelan A. M., Sesar B., Johnston K. V., Rix H.-W., 2016, ApJ, 824, 104
Raassen A. J. J., Uylings P. H. M., 1998, A&A, 340, 300
Robin A. C., Reylé C., Derrière S., Picaud S., 2003, A&A, 409, 523
Roederer I. U., 2011, ApJ, 732, L17
Roederer I. U., Cowan J. J., Karakas A. I., Kratz K.-L., Lugaro M., Simmerer J., Farouqi K., Sneden C., 2010, ApJ, 724, 975
Roederer I. U., Preston G. W., Thompson I. B., Shectman S. A., Sneden C., Burley G. S., Kelson D. D., 2014, AJ, 147, 136
Roederer I. U., Hattori K., Valluri M., 2018a, AJ, 156, 179
Roederer I. U., Sneden C., Lawler J. E., Sobeck J. S., Cowan J. J., Boesgaard A. M., 2018b, ApJ, 860, 125
Sakari C. M. et al., 2018a, ApJ, 854, L20
Sakari C. M. et al., 2018b, ApJ, 868, 110
Salvadori S., Bonifacio P., Caffau E., Korotin S., Andreevsky S., Spite M., Skúladóttir Á., 2019, MNRAS, 487, 4261
Schlaufman K. C., Casey A. R., 2014, ApJ, 797, 13
Schlegel D. J., Finkbeiner D. P., Davis M., 1998, ApJ, 500, 525
Schneider R., Ferrara A., Salvaterra R., Omukai K., Bromm V., 2003, Nature, 422, 869
Schönrich R., Binney J., Dehnen W., 2010, MNRAS, 403, 1829
Schörck T. et al., 2009, A&A, 507, 817
Sestito F. et al., 2019, MNRAS, 484, 2166
Sheinis A. I. et al., 2017, in Christopher J. E., Luc S., Hideki T., eds, Proc. SPIE Conf. Ser. Vol. 9908, Ground-based and Airborne Instrumentation for Astronomy VI. SPIE, Bellingham, p. 990817
Simon J. D., 2018, ApJ, 863, 89
Sitnova T. et al., 2015, ApJ, 808, 148
Sitnova T. M., Mashonkina L. I., Ryabchikova T. A., 2016, MNRAS, 461, 1000
Sneden C. A., 1973, PhD thesis, Univ. Texas at Austin
Sobeck J. S. et al., 2011, AJ, 141, 175
Spergel D. N. et al., 2003, ApJS, 148, 175
Starkenburg E., Shetrone M. D., McConnachie A. W., Venn K. A., 2014, MNRAS, 441, 1217
Starkenburg E., Oman K. A., Navarro J. F., Crain R. A., Fattahi A., Frenk C. S., Sawala T., Schaye J., 2017a, MNRAS, 465, 2212
Starkenburg E. et al., 2017b, MNRAS, 471, 2587
Starkenburg E. et al., 2018, MNRAS, 481, 3838
Stetson P. B., Pancino E., 2008, PASP, 120, 1332
Suda T. et al., 2017, PASJ, 69, 76
Thielemann F.-K., Isern J., Perego A., von Ballmoos P., 2018, Space Sci. Rev., 214, 62
Tolstoy E., Hill V., Tosi M., 2009, ARA&A, 47, 371
Tumlinson J., 2010, ApJ, 708, 1398
Venn K. A., Irwin M., Shetrone M. D., Tout C. A., Hill V., Tolstoy E., 2004, AJ, 128, 1177
Venn K. A. et al., 2012, ApJ, 751, 102
Venn K. A., Starkenburg E., Malo L., Martin N., Laevens B. P. M., 2017, MNRAS, 466, 3741
Wanajo S., 2018, ApJ, 868, 65
Wenger M. et al., 2000, A&AS, 143, 9
Woosley S. E., Heger A., Weaver T. A., 2002, Rev. Mod. Phys., 74, 1015
Yanny B. et al., 2009, AJ, 137, 4377
Yong D. et al., 2013, ApJ, 762, 26
York D. G. et al., 2000, AJ, 120, 1579
Youakim K. et al., 2017, MNRAS, 472, 2963
Zinn J. C., Pinsonneault M. H., Huber D., Stello D., 2019, ApJ, 878, 136

SUPPORTING INFORMATION

Supplementary data are available at *MNRAS* online.

Table 1. Metal-poor targets (115) from the original *Pristine* survey footprint.
Table 2. *Gaia* DR2 parallaxes, and the derived distances (D), temperatures (T), and surface gravities (log g) from the Bayesian inference method (see Section 4.1, assuming $[Fe/H]_P$).
Table 3. Line list from Norris et al. (2017) with atomic data updates from *linemake* (see the text).
Please note: Oxford University Press is not responsible for the content or functionality of any supporting materials supplied by the authors. Any queries (other than missing material) should be directed to the corresponding author for the article.

APPENDIX A

The *UVW* velocities for the 70 highly probable metal-poor stars in this sample are given in Table A1.

Five stars were identified for a more careful dynamical analysis in Section 6.1. When their distances were determined from the Bayesian inference method, these stars had highly energetic and unbound orbits ($E/E_\odot < -0.5$), with $R_{apo} > 500$ kpc. These five stars are shown in Fig. A1.

As two of these stars (Pristine_200.5298+08.9768 and Pristine_187.9785+08.7294) were found to have higher metallicities than had been adopted for the MIST stellar isochrone in the Bayesian inference method, then we assumed that their Bayesian inferred distances were unreliable. Adopting their distances as 1/parallax from the *Gaia* DR2 data base, then we found sensible orbits and dynamical parameters for both the stars. Furthermore, the parallax errors were small for both the stars.

We found that the orbit solution for a third star (Pristine_213.7879+08.4232) was also significantly improved by rejecting the Bayesian inferred distance in favour of the 1/parallax value. Again, the parallax error is small, and the resulting orbital properties are less peculiar. It is not clear why the Bayesian method did not work for this star; however, we note that this was a target that we observed very early on and it is no longer in the *Pristine* survey catalogue. Investigating this star a bit further, we notice that the 1/parallax distance is closer than the Bayesian inferred distance, suggesting that the surface gravity for this star may be slightly

Table A1. Orbit and Action parameters for the 70 metal-poor candidates from the *Pristine* survey.

RA (deg)	DEC (deg)	pmra (μas yr^{-1})	pmdec (μas yr^{-1})	U (km s^{-1})	V (km s^{-1})	W (km s^{-1})	R_{apo} (kpc)	R_{peri} (kpc)	Eccentricity	Z_{max} (kpc)	$J_\phi/J_{\phi\odot}$	$J_z/J_{z\odot}$	$E/E_\odot$
180.2206	09.5683	1.47 ± 0.08	−3.68 ± 0.06	175.69 ± 6.90	−143.29 ± 5.31	−26.54 ± 1.96	23.5 ± 1.3	6.6 ± 0.5	0.57 ± 0.01	23.4 ± 1.3	−0.04 ± 0.05	5918.45 ± 289.73	0.477 ± −0.032
180.3789	00.9470	−14.76 ± 0.92	−5.28 ± 0.49	−101.97 ± 6.13	−73.77 ± 5.78	−100.36 ± 2.89	9.4 ± 0.3	6.3 ± 0.2	0.20 ± 0.03	4.5 ± 0.4	0.67 ± 0.03	689.95 ± 82.44	0.893 ± −0.011
181.2243	07.4160	1.98 ± 0.08	−8.19 ± 0.05	60.40 ± 1.88	−4.87 ± 1.86	−161.93 ± 0.92	19.0 ± 0.1	6.5 ± 0.1	0.49 ± 0.01	9.4 ± 0.1	0.87 ± 0.01	948.17 ± 13.67	0.58 ± −0.003
181.3464	11.6698	−14.31 ± 0.06	2.84 ± 0.03	−39.73 ± 0.65	−15.73 ± 0.26	6.31 ± 0.48	8.8 ± 0.0	7.5 ± 0.1	0.08 ± 0.00	0.7 ± 0.1	0.87 ± 0.0	32.49 ± 0.77	0.881 ± −0.001
181.3699	11.7636	−9.20 ± 0.06	−4.69 ± 0.03	−66.05 ± 3.11	−116.49 ± 4.39	44.36 ± 1.64	8.9 ± 0.1	3.4 ± 0.2	0.45 ± 0.02	2.9 ± 0.1	0.48 ± 0.02	303.79 ± 5.57	1.045 ± −0.002
181.4395	01.6294	−3.34 ± 0.08	−9.14 ± 0.04	134.17 ± 3.39	−768.5 ± 11.62	−177.4 ± 6.21	2345.5 ± 124.2	18.1 ± 0.3	0.98 ± 0.00	1049.8 ± 44.4	−2.4 ± 0.05	16291.42 ± 799.81	−1.919 ± −0.125
181.6953	13.8075	−16.18 ± 0.06	−3.44 ± 0.03	−164.22 ± 6.23	−156.8 ± 5.18	28.91 ± 1.87	11.7 ± 0.3	2.1 ± 0.1	0.70 ± 0.02	3.7 ± 0.2	0.36 ± 0.02	271.81 ± 17.54	0.94 ± −0.012
182.5364	00.9431	−43.19 ± 0.08	−49.25 ± 0.06	−124.30 ± 7.39	−702.83 ± 30.92	−103.95 ± 15.46	541.2 ± 437.2	7.9 ± 0.3	0.94 ± 0.04	164.9 ± 134.9	−1.77 ± 0.12	766.27 ± 167.98	−0.66 ± −0.285
183.6849	04.8619	−0.70 ± 0.11	−12.87 ± 0.12	31.50 ± 1.67	−68.32 ± 2.46	11.5 ± 1.24	8.5 ± 0.1	4.5 ± 0.1	0.30 ± 0.01	1.2 ± 0.1	0.64 ± 0.01	84.71 ± 4.01	1.022 ± −0.005
185.4110	07.4777	−70.21 ± 0.07	−37.42 ± 0.04	−146.72 ± 3.89	−305.15 ± 5.95	85.86 ± 1.97	10.7 ± 0.2	1.5 ± 0.1	0.75 ± 0.01	4.0 ± 0.2	−0.27 ± 0.02	352.7 ± 24.77	1.002 ± −0.012
187.9785	08.7294	−20.24 ± 0.10	2.84 ± 0.05	121.345 ± 6.39	−32.49 ± 2.74	−55.94 ± 0.52	11.5 ± 0.2	6.0 ± 0.1	0.32 ± 0.02	2.9 ± 0.2	0.80 ± 0.01	240.41 ± 19.72	0.823 ± 0.004
188.1264	08.7740	−6.31 ± 0.08	−7.70 ± 0.05	−47.33 ± 2.51	−247.10 ± 14.74	−126.96 ± 4.56	9.9 ± 0.2	3.2 ± 0.6	0.51 ± 0.06	9.8 ± 0.2	−0.02 ± 0.05	2933.74 ± 261.61	0.96 ± −0.028
189.9449	11.5534	3.40 ± 0.06	−55.97 ± 0.05	257.42 ± 4.44	−358.77 ± 6.12	−88.47 ± 2.14	24.8 ± 1.4	2.7 ± 0.1	0.81 ± 0.00	5.2 ± 0.4	−0.55 ± 0.03	194.46 ± 6.74	0.502 ± −0.034
190.6313	08.5137	−13.53 ± 0.10	−19.24 ± 0.05	−34.76 ± 1.66	−330.56 ± 21.07	−163.11 ± 6.21	8.7 ± 0.4	5.9 ± 1.2	0.20 ± 0.09	7.4 ± 0.3	−0.36 ± 0.08	2128.14 ± 48.96	0.924 ± −0.057
193.1159	08.0557	6.70 ± 0.06	−57.85 ± 0.04	140.26 ± 3.27	−169.78 ± 3.91	−30.26 ± 1.81	10.5 ± 0.1	1.1 ± 0.1	0.81 ± 0.02	1.0 ± 0.1	0.23 ± 0.02	44.76 ± 2.42	1.048 ± −0.005
193.5533	11.5037	1.37 ± 0.05	−1.21 ± 0.03	7.22 ± 0.13	−4.11 ± 0.12	14.51 ± 0.48	9.3 ± 0.0	7.7 ± 0.0	0.10 ± 0.00	0.8 ± 0.1	0.9 ± 0.0	40.68 ± 1.03	0.852 ± −0.0
193.8390	11.4150	0.98 ± 0.07	−2.19 ± 0.04	178.73 ± 4.59	−112.05 ± 3.29	−51.18 ± 1.35	33.6 ± 2.0	13.8 ± 0.5	0.42 ± 0.01	33.5 ± 1.9	−0.1 ± 0.03	10599.81 ± 378.3	0.235 ± −0.029
196.3755	08.5138	−1.46 ± 0.08	−6.48 ± 0.06	106.90 ± 4.63	−317.24 ± 12.03	−179.96 ± 4.05	23.9 ± 2.2	4.9 ± 0.8	0.66 ± 0.02	21.1 ± 2.1	−0.39 ± 0.04	2991.74 ± 412.01	0.49 ± −0.054
196.4117	14.3176	−18.78 ± 0.06	−9.71 ± 0.04	−35.04 ± 0.48	−40.59 ± 0.87	−51.6 ± 0.49	8.1 ± 0.1	6.4 ± 0.2	0.12 ± 0.00	1.2 ± 0.1	0.75 ± 0.0	86.87 ± 1.97	0.958 ± −0.002
196.5453	12.1211	25.63 ± 0.07	−56.26 ± 0.04	321.48 ± 11.69	−196.02 ± 6.99	−44.4 ± 3.69	31.8 ± 3.5	0.5 ± 0.1	0.97 ± 0.01	4.0 ± 0.7	0.1 ± 0.03	96.63 ± 5.86	0.38 ± −0.061
198.5486	11.4123	−47.39 ± 0.06	−46.31 ± 0.04	−86.24 ± 1.88	−510.48 ± 8.99	8.85 ± 1.27	17.6 ± 1.6	7.1 ± 0.1	0.42 ± 0.03	3.2 ± 0.4	−1.04 ± 0.03	174.96 ± 8.22	0.61 ± −0.041
200.0999	13.7228	−4.09 ± 0.06	−1.02 ± 0.04	−223.20 ± 6.01	−340.64 ± 7.01	206.07 ± 0.83	90.2 ± 10.1	9.9 ± 0.7	0.80 ± 0.01	89.2 ± 9.5	0.10 ± 0.01	10765.9 ± 780.77	−0.176 ± −0.048
200.5298	08.9768	−20.91 ± 0.08	−12.61 ± 0.04	−69.46 ± 8.35	−233.94 ± 18.62	78.19 ± 1.31	12.9 ± 51.3	0.4 ± 0.2	0.92 ± 0.06	5.8 ± 19.7	0.00 ± 0.06	472.31 ± 14.80	1.17 ± 0.01
200.7620	09.4375	8.03 ± 0.06	−4.98 ± 0.03	93.28 ± 1.30	1.62 ± 0.24	8.97 ± 0.59	13.6 ± 0.1	6.0 ± 0.1	0.39 ± 0.00	3.6 ± 0.1	0.85 ± 0.0	273.96 ± 7.04	0.748 ± −0.003
201.1158	15.4381	−8.64 ± 0.06	−1.74 ± 0.05	−62.21 ± 1.65	−67.21 ± 1.82	2.9 ± 0.53	8.3 ± 0.0	4.8 ± 0.1	0.27 ± 0.01	2.3 ± 0.1	0.62 ± 0.01	240.53 ± 10.05	1.01 ± −0.002
201.3732	08.4513	−17.04 ± 0.07	−3.15 ± 0.04	−144.52 ± 6.99	−175.08 ± 7.42	56.68 ± 0.87	10.1 ± 0.3	1.4 ± 0.2	0.76 ± 0.04	3.6 ± 0.2	0.24 ± 0.03	321.08 ± 11.49	1.049 ± −0.012
201.8711	07.1810	−78.20 ± 0.08	−13.09 ± 0.05	−239.77 ± 7.57	−265.05 ± 7.84	58.94 ± 1.00	15.0 ± 0.8	0.5 ± 0.1	0.94 ± 0.01	3.2 ± 1.0	−0.1 ± 0.03	124.81 ± 1.95	0.822 ± −0.032
202.3435	13.2291	−4.59 ± 0.05	−26.08 ± 0.02	145.13 ± 4.50	−264.49 ± 9.62	36.58 ± 2.37	10.1 ± 0.2	1.0 ± 0.2	0.83 ± 0.04	6.0 ± 0.2	−0.14 ± 0.04	640.0 ± 15.69	1.035 ± −0.016
203.2831	13.6326	−0.91 ± 0.05	−5.35 ± 0.03	105.34 ± 3.35	−284.55 ± 6.72	−203.82 ± 1.65	27.6 ± 1.3	2.9 ± 0.4	0.81 ± 0.02	25.5 ± 1.7	−0.19 ± 0.02	2748.57 ± 254.75	0.432 ± −0.028
204.9008	10.5513	10.65 ± 0.06	−33.88 ± 0.05	103.14 ± 8.51	−106.04 ± 6.33	−310.79 ± 3.75	31.5 ± 1.5	6.2 ± 0.2	0.67 ± 0.02	28.3 ± 1.6	0.47 ± 0.03	3873.18 ± 104.35	0.336 ± −0.022
205.1342	13.8234	−8.1 ± 0.07	−2.72 ± 0.06	−46.57 ± 5.60	−136.76 ± 8.5	137.12 ± 1.18	9.5 ± 0.3	3.6 ± 0.4	0.45 ± 0.05	7.2 ± 0.4	0.33 ± 0.03	1413.11 ± 31.15	0.976 ± −0.003
205.8131	15.3832	10.45 ± 0.06	−30.98 ± 0.04	190.87 ± 5.92	−113.35 ± 4.09	64.18 ± 2.01	14.3 ± 0.3	2.8 ± 0.1	0.68 ± 0.02	6.3 ± 0.3	0.45 ± 0.02	541.15 ± 12.38	0.801 ± −0.01
206.3487	09.3099	1.22 ± 0.06	−67.65 ± 0.04	324.56 ± 5.30	−385.14 ± 7.22	−2.39 ± 3.00	41.4 ± 3.5	2.7 ± 0.1	0.88 ± 0.01	10.2 ± 0.8	−0.6 ± 0.03	246.21 ± 2.21	0.223 ± −0.045
208.0798	04.4266	2.02 ± 0.07	−12.87 ± 0.07	81.27 ± 8.37	−120.10 ± 8.76	−205.75 ± 5.62	13.8 ± 0.7	3.4 ± 0.4	0.61 ± 0.05	10.7 ± 0.9	0.34 ± 0.04	1600.13 ± 53.45	0.8 ± −0.02
209.9364	15.9251	1.78 ± 0.08	−13.73 ± 0.07	56.47 ± 3.89	−87.63 ± 3.89	−116.8 ± 1.42	9.3 ± 0.1	4.2 ± 0.2	0.37 ± 0.02	4.3 ± 0.1	0.53 ± 0.02	578.82 ± 17.2	0.976 ± −0.002
210.0166	14.6289	−9.65 ± 0.05	−10.23 ± 0.05	−0.72 ± 1.52	−377.07 ± 19.55	76.2 ± 0.60	8.8 ± 0.5	5.1 ± 0.9	0.27 ± 0.06	6.4 ± 0.4	−0.43 ± 0.05	1421.89 ± 143.6	0.959 ± −0.057
210.8632	08.1797	−5.11 ± 0.06	−13.39 ± 0.05	41.58 ± 2.50	−170.72 ± 9.11	−49.28 ± 2.09	7.8 ± 0.1	1.4 ± 0.3	0.69 ± 0.05	2.8 ± 0.1	0.20 ± 0.04	300.71 ± 22.72	1.214 ± −0.004
213.2814	14.8983	−0.27 ± 0.08	−13.33 ± 0.07	74.25 ± 1.18	−105.65 ± 1.51	−42.69 ± 0.64	8.6 ± 0.1	3.0 ± 0.1	0.48 ± 0.01	2.3 ± 0.1	0.45 ± 0.01	220.76 ± 4.28	1.084 ± −0.002
213.7879	08.4232	5.67 ± 0.07	−15.94 ± 0.07	132.56 ± 27.58	−114.70 ± 18.31	−194.86 ± 15.19	15.8 ± 2.8	3.0 ± 0.7	0.67 ± 0.11	10.8 ± 2.4	0.38 ± 0.08	1174.7 ± 64.97	0.738 ± 0.077
214.5556	07.4670	−43.60 ± 0.05	−28.18 ± 0.05	−102.93 ± 3.36	−430.78 ± 11.45	81.29 ± 1.16	11.2 ± 0.8	5.1 ± 0.2	0.37 ± 0.01	3.5 ± 0.2	−0.70 ± 0.04	340.16 ± 6.67	0.864 ± −0.042
217.3861	15.1650	6.02 ± 0.06	−12.35 ± 0.06	−5.72 ± 2.14	−41.35 ± 1.0	−171.37 ± 1.03	10.9 ± 0.1	7.5 ± 0.1	0.19 ± 0.00	6.4 ± 0.1	0.71 ± 0.01	1150.58 ± 17.37	0.793 ± −0.002
217.5786	14.0379	−1.42 ± 0.05	−7.46 ± 0.04	191.61 ± 2.64	−361.55 ± 4.47	−86.38 ± 1.13	22.5 ± 1.0	7.5 ± 0.2	0.50 ± 0.01	22.4 ± 1.0	−0.11 ± 0.0	6103.43 ± 214.15	0.483 ± −0.024
217.6443	15.9633	−1.04 ± 0.06	−16.84 ± 0.06	53.01 ± 2.68	−85.20 ± 3.63	−38.39 ± 1.00	8.2 ± 0.0	3.7 ± 0.1	0.38 ± 0.02	1.5 ± 0.1	0.55 ± 0.02	112.75 ± 7.09	1.076 ± −0.006

Table A1 – *continued*

RA (deg)	DEC (deg)	pmra (μas yr^{-1})	pmdec (μas yr^{-1})	U (km s^{-1})	V (km s^{-1})	W (km s^{-1})	R_{apo} (kpc)	R_{peri} (kpc)	Eccentricity	Z_{max} (kpc)	$J_\phi/J_{\phi\odot}$	$J_z/J_{z\odot}$	$E/E_\odot$
218.4622	10.3683	− 2.14 ± 0.07	− 8.22 ± 0.07	− 20.40 ± 0.78	− 95.99 ± 1.48	− 130.24 ± 0.58	7.4 ± 0.0	4.9 ± 0.1	0.20 ± 0.01	4.6 ± 0.1	0.46 ± 0.01	968.5 ± 12.36	1.038 ± −0.003
228.4607	08.3553	− 3.84 ± 0.07	− 59.49 ± 0.09	192.77 ± 7.38	− 267.75 ± 10.58	− 100.5 ± 4.25	12.9 ± 0.7	0.9 ± 0.1	0.87 ± 0.01	4.3 ± 0.2	− 0.11 ± 0.04	261.09 ± 20.8	0.909 ± −0.036
228.6557	09.0914	− 15.11 ± 0.05	− 33.13 ± 0.06	− 18.70 ± 3.11	− 232.36 ± 9.37	− 135.68 ± 0.98	7.5 ± 0.0	0.6 ± 0.2	0.86 ± 0.05	7.2 ± 0.3	− 0.0 ± 0.04	1206.47 ± 29.75	1.181 ± −0.002
228.8159	00.2222	− 6.67 ± 0.09	− 59.12 ± 0.11	120.03 ± 4.60	− 223.37 ± 8.85	− 102.83 ± 4.26	9.7 ± 0.4	0.4 ± 0.2	0.92 ± 0.04	4.1 ± 0.3	0.03 ± 0.03	349.16 ± 37.54	1.104 ± −0.014
229.1219	00.9089	− 31.52 ± 0.06	− 33.97 ± 0.05	− 151.99 ± 0.39	− 409.54 ± 24.74	− 147.89 ± 0.89	12.9 ± 1.6	5.2 ± 0.4	0.43 ± 0.02	7.8 ± 0.5	− 0.59 ± 0.08	1122.98 ± 59.34	0.79 ± −0.064
233.5730	06.4702	− 3.73 ± 0.04	− 6.44 ± 0.05	47.28 ± 2.63	− 404.88 ± 9.71	− 71.97 ± 0.93	11.6 ± 0.8	5.1 ± 0.5	0.40 ± 0.02	11.6 ± 0.8	0.03 ± 0.02	4111.92 ± 239.13	0.83 ± −0.044
235.1449	08.7463	16.68 ± 0.05	− 25.74 ± 0.05	116.75 ± 5.29	− 104.67 ± 1.79	− 296.21 ± 4.42	25.6 ± 1.3	5.2 ± 0.1	0.66 ± 0.02	22.0 ± 1.3	0.45 ± 0.01	2973.52 ± 51.91	0.45 ± −0.026
235.7578	09.0000	− 29.80 ± 0.06	6.08 ± 0.06	− 185.50 ± 5.42	− 144.08 ± 4.88	133.52 ± 6.46	12.6 ± 0.5	1.7 ± 0.1	0.76 ± 0.02	6.8 ± 0.7	0.26 ± 0.02	663.13 ± 65.3	0.89 ± −0.022
236.1068	10.5311	− 3.87 ± 0.04	− 4.77 ± 0.04	49.11 ± 2.00	− 383.69 ± 8.65	18.86 ± 1.48	10.2 ± 0.3	7.3 ± 0.9	0.17 ± 0.04	10.1 ± 0.3	0.14 ± 0.02	4149.48 ± 228.01	0.813 ± −0.038
237.8246	10.1426	− 15.19 ± 0.05	− 12.74 ± 0.04	− 70.00 ± 2.78	− 583.25 ± 36.27	34.02 ± 10.0	34.6 ± 18.1	5.8 ± 0.1	0.67 ± 0.12	24.7 ± 15.2	− 0.73 ± 0.03	1998.84 ± 520.0	0.348 ± −0.226
237.9600	15.4022	− 11.75 ± 0.04	− 23.56 ± 0.03	− 91.49 ± 2.99	− 242.87 ± 6.53	− 188.22 ± 0.46	8.3 ± 0.1	4.0 ± 0.1	0.36 ± 0.01	8.3 ± 0.2	− 0.06 ± 0.02	2986.96 ± 133.31	1.012 ± −0.006
240.4216	09.6761	1.71 ± 0.03	− 11.53 ± 0.02	329.53 ± 14.23	− 270.18 ± 13.16	− 177.61 ± 9.54	47.9 ± 13.2	3.6 ± 0.4	0.85 ± 0.02	41.5 ± 11.1	0.34 ± 0.03	2968.97 ± 414.55	0.157 ± −0.131
245.4387	08.9954	− 25.09 ± 0.04	− 23.90 ± 0.03	− 2.07 ± 1.29	− 316.79 ± 6.09	29.47 ± 1.70	6.8 ± 0.1	1.7 ± 0.1	0.61 ± 0.03	1.5 ± 0.1	− 0.28 ± 0.02	143.66 ± 8.72	1.292 ± −0.007
245.5747	06.8844	− 0.49 ± 0.04	11.07 ± 0.03	− 307.45 ± 11.56	137.48 ± 13.46	5.32 ± 8.20	131.2 ± 56.6	3.2 ± 0.3	0.95 ± 0.02	88.0 ± 33.4	0.51 ± 0.05	1883.49 ± 411.94	− 0.285 ± −0.146
245.8356	13.8777	0.98 ± 0.03	− 2.39 ± 0.02	− 76.79 ± 2.01	− 89.61 ± 1.09	− 144.63 ± 1.55	6.9 ± 0.1	4.9 ± 0.1	0.17 ± 0.02	6.0 ± 0.1	0.27 ± 0.01	1865.8 ± 97.43	1.055 ± −0.002
246.5144	05.9826	2.42 ± 0.03	1.45 ± 0.02	− 5.81 ± 0.40	28.86 ± 0.75	− 17.21 ± 0.46	10.1 ± 0.1	6.2 ± 0.0	0.24 ± 0.01	2.2 ± 0.1	0.79 ± 0.0	189.37 ± 9.41	0.873 ± −0.002
246.8588	12.3193	− 8.20 ± 0.03	− 5.43 ± 0.02	− 23.27 ± 1.77	− 326.57 ± 13.64	83.74 ± 6.31	6.7 ± 0.7	2.7 ± 0.6	0.43 ± 0.11	5.9 ± 0.6	− 0.16 ± 0.01	1489.34 ± 239.52	1.226 ± −0.042
248.4394	07.9229	− 7.82 ± 0.05	− 20.68 ± 0.04	34.18 ± 1.02	− 94.12 ± 1.82	− 18.85 ± 0.35	7.5 ± 0.1	3.3 ± 0.1	0.39 ± 0.01	0.6 ± 0.1	0.51 ± 0.01	29.83 ± 1.04	1.155 ± −0.004
248.4959	15.0776	− 2.87 ± 0.03	− 11.51 ± 0.03	277.89 ± 11.70	− 464.93 ± 15.46	− 112.07 ± 2.48	56.2 ± 16.2	4.4 ± 0.5	0.85 ± 0.02	47.1 ± 12.6	0.43 ± 0.06	3269.42 ± 292.39	0.077 ± −0.134
250.6963	08.3743	− 6.84 ± 0.04	− 1.89 ± 0.04	− 21.03 ± 0.87	− 205.95 ± 7.35	162.04 ± 5.92	7.5 ± 0.3	0.9 ± 0.2	0.80 ± 0.03	7.4 ± 0.4	0.01 ± 0.01	1634.18 ± 172.91	1.176 ± −0.026
251.4082	12.3657	− 7.86 ± 0.06	− 1.27 ± 0.05	− 70.42 ± 2.20	− 400.15 ± 11.31	386.54 ± 11.06	201.6 ± 102.4	9.5 ± 0.7	0.90 ± 0.03	155.3 ± 63.8	0.05 ± 0.03	11 689.1 ± 785.88	− 0.444 ± −0.127
252.1639	15.0648	1.49 ± 0.03	− 5.48 ± 0.03	94.04 ± 5.86	− 203.86 ± 3.85	− 231.61 ± 4.19	15.2 ± 1.1	4.5 ± 0.2	0.54 ± 0.01	14.1 ± 1.0	0.26 ± 0.02	2869.78 ± 110.49	0.721 ± −0.04
253.8582	15.7240	− 2.22 ± 0.03	− 5.72 ± 0.03	88.00 ± 6.04	− 263.85 ± 8.44	− 57.11 ± 0.63	7.9 ± 0.6	1.9 ± 0.2	0.62 ± 0.04	5.7 ± 0.5	0.19 ± 0.02	968.04 ± 56.69	1.165 ± −0.031
254.5207	15.4969	14.12 ± 0.02	− 9.85 ± 0.03	44.56 ± 0.56	18.18 ± 0.26	− 28.06 ± 0.72	11.7 ± 0.1	7.2 ± 0.1	0.24 ± 0.00	0.7 ± 0.1	0.95 ± 0.0	20.13 ± 0.98	0.785 ± −0.001
254.5469	10.9129	− 21.80 ± 0.04	− 28.68 ± 0.04	260.45 ± 10.30	− 383.71 ± 23.23	133.82 ± 4.69	25.0 ± 5.2	2.5 ± 0.3	0.82 ± 0.01	20.4 ± 4.0	− 0.28 ± 0.05	1683.88 ± 96.41	0.501 ± −0.11
255.2671	14.9711	− 8.81 ± 0.04	− 40.50 ± 0.04	208.89 ± 3.70	− 210.05 ± 4.37	− 32.63 ± 0.96	12.1 ± 0.2	0.7 ± 0.1	0.88 ± 0.02	1.0 ± 0.1	0.16 ± 0.01	51.85 ± 1.75	0.96 ± −0.01
255.5555	10.8612	− 5.06 ± 0.04	− 15.51 ± 0.04	− 108.68 ± 9.34	− 418.27 ± 13.88	− 213.57 ± 1.85	12.8 ± 1.0	5.5 ± 0.2	0.40 ± 0.04	8.9 ± 0.4	− 0.55 ± 0.02	1544.81 ± 66.8	0.781 ± −0.028

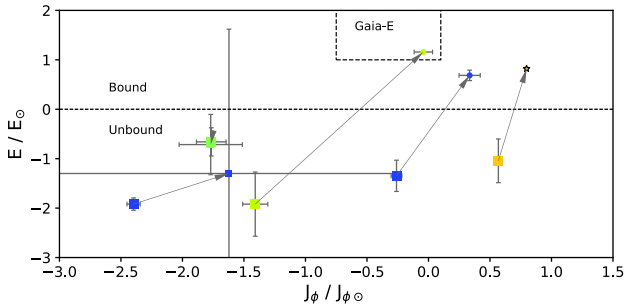

Figure A1. Comparison of the orbital parameters for five stars with unbound orbits from the dynamical analysis in Section 6.1. Large symbols are the parameters using the distances from the Bayesian inference method, and small symbols are those from adopting 1/parallax from the *Gaia* DR2 data base. Points coloured by $[Fe/H]_{Q6}$ using the same scheme same as in Fig. 16.

higher ($\log g = 2.3$, may be closer to $\log g \sim 3$). In that case, we find small corrections to the abundances, such that $\Delta\log(\text{Fe II}) \sim +0.3$, bringing Fe II into much better agreement with Fe I. The impact on [Fe/H] for this star is negligible though since the iron abundance is dominated by the more numerous spectral lines of Fe I. Minor adjustments to the other elements would have no significant effect on the chemical analysis and interpretation of this star.

Finally, when examining the impact of the distances for the two stars Pristine_182.5364 ([Fe/H]=−1.6) and Pristine_181.4395 ([Fe/H]=−2.8), we find that they always result in highly retrograde and unbound orbits. The orbit for the more metal poor of these two stars is highly uncertain when determined from its parallax ($\Delta\pi/\pi = 0.45$). Interestingly though, this star is also one of the [Ba/Fe]-poor stars discussed in Section 5.4 as possibly accreted from an ultra-faint dwarf galaxy. As a sanity check, we also calculated the orbits for all of the other metal-poor candidates in this analysis, but found only small offsets in their orbit and action parameters.

[1]*Department of Physics and Astronomy, University of Victoria, Victoria, BC V8W 3P2, Canada*
[2]*Université de Strasbourg, CNRS, Observatoire astronomique de Strasbourg, UMR 7550, F-67000 Strasbourg, France*
[3]*Leibniz-Institut für Astrophysik Potsdam (AIP), An der Sternwarte 16, D-14482 Potsdam, Germany*
[4]*Max-Planck-Institut für Astronomie, Königstuhl 17, D-69117 Heidelberg, Germany*
[5]*Institute of Astronomy, University of Cambridge, Madingley Road, Cambridge CB3 0HA, UK*
[6]*GEPI, Observatoire de Paris, Université PSL, CNRS, Place Jules Janssen, F-92195 Meudon, France*
[7]*Université Cote d'Azur, Observatoire de la Cote d'Azur, CNRS, Laboratoire Lagrange, Bd de l'Observatoire, CS 34229, F-06304 Nice Cedex 4, France Observatoire de la Cote d'Azur, BP 4229, F-06304 Nice, France*
[8]*Institute of Physics, Laboratoire d'astrophysique, Ecole Polytechnique Fédérale de Lausanne (EPFL), Observatoire, CH-1290 Versoix, Switzerland*
[9]*Institute of Astronomy, Russian Academy of Sciences, Pyatnitskaya st 48, 119017 Moscow, Russia*
[10]*Department of Astronomy, University of Texas at Austin, Austin, TX 78712, USA*
[11]*National Research Council Herzberg Astronomy and Astrophysics, 4071 West Saanich Road, Victoria, BC, V9E 2E7, Canada*
[12]*Instituto de Astrofísica de Canarias, Via Láctea E-38205, La Laguna, Tenerife, Spain*
[13]*Departamento de Astrofísica, Universidad de La Laguna, E-38206, La Laguna, Tenerife, Spain*
[14]*UK Astronomy Technology Centre, Royal Observatory Edinburgh, Blackford Hill, Edinburgh EH9 3HJ, UK*
[15]*Department of Astronomy and Astrophysics, University of Toronto, Toronto, ON M5S 3H4, Canada*
[16]*The Oskar Klein Centre, Department of Physics, Stockholm University, AlbaNova, SE-10691 Stockholm, Sweden*

This paper has been typeset from a TEX/LATEX file prepared by the author.

APPENDIX

C The analysis of the kinematical parameters

As shown in the Introduction and in the previous Chapters, thanks to the exquisite astrometric dataset of Gaia DR2 in synergy with ground-based spectroscopic information, it is possible to infer the distances and the orbital parameters of the stars. Chapters 2 and 3 discuss the kinematical analysis of the most pristine stars from the ultra metal-poor ([Fe/H] ≤ -4.0) to the very metal-poor regime ([Fe/H] ≤ -2.0), here, in this Appendix, a more detailed description of the orbital inference is presented.

For the inference of the orbital properties of the stars, the `galpy`[1] package developed by Bovy (2015) has been used in the previous Chapters. `galpy` is a `python` package for Galactic dynamics and it allows the user to select or customise the gravitational potential of the Galaxy. After setting the position (coordinates and heliocentric distance) and the motion (radial velocity and proper motions) of the objects, `galpy` performs the numerical integration of the orbit in `python` and in `C` for accelerated computations.

The standard gravitational potential in `galpy` is called `MWPotential14` (Bovy, 2015), and it is composed by a power-law cut-off bulge (exponent -1.8 and cut-off radius of 1.9 kpc), a Miyamoto-Nagai Potential disc (scale-length of 3.0 kpc and scale-height of 0.28 kpc, Miyamoto & Nagai, 1975), and a Navarro-Frenk-White dark matter halo (local dark matter density $\rho_{DM} = 0.008 \mathrm{M}_{\odot}\, pc^{-3}$, virial radius $r_{vir} = 245$ kpc, and virial mass $M_{vir} = 0.8 \times 10^{12}\, \mathrm{M}_{\odot}$, Navarro et al., 1997). The contribution of these three components (bulge, disc, and halo) to the radial force at the Sun distance is respectively $f_b = 0.05$, $f_d = 0.60$, and $f_h = 0.35$. In the works presented in Chapters 2 and 3, a higher virial mass of $M_{vir} = 1.2 \times 10^{12}\, \mathrm{M}_{\odot}$ is used, in accordance with the more recent value inferred by Bland-Hawthorn & Gerhard (2016). Moreover, the presence of the supermassive black hole at the centre of the Milky Way ($M_{SMBH} \sim 4 \times 10^6\, \mathrm{M}_{\odot}$ Ghez et al., 2005; Gravity Collaboration et al., 2019), Sagittarius A*, is taken into account and described with a keplerian potential for a more realistic and up-to-date potential. Another customisable feature in `galpy`, is the possibility to set the position and the motion of the Sun. In these works, the distance between the Sun and the Galactic centre is assumed to be 8.0 kpc, the Local Standard of Rest circular velocity is $V_c = 239\, \mathrm{km\, s^{-1}}$, and the peculiar motion of the Sun is ($U_0 = 11.10\, \mathrm{km\, s^{-1}}$, $V_0 + V_c = 251.24\, \mathrm{km\, s^{-1}}$, $W_0 = 7.25\, \mathrm{km\, s^{-1}}$) as described in Schönrich et al. (2010).

[1] http://github.com/jobovy/galpy

`galpy` does not take into account uncertainties on the input and on the output physical quantities, therefore a Monte Carlo approach has been developed to fully treat the uncertainties on all the input and output quantities as follow. All the input quantities, such as the radial velocity v_r, the proper motion on right ascension and declination μ_α and μ_δ, and the coordinates α and δ, have been considered with their uncertainties and described by a gaussian distribution. In the case of the two components of the proper motion, their correlation given by the coefficients in Gaia DR2 has been considered as a multivariate gaussian function. The possible correlation between coordinates and proper motions is not taken into account because it does not affect the results. The heliocentric distance has been described by the probability distribution function introduced in Chapter 2. From the probability distribution of these quantities, I take 1000 random drawings and calculate the orbit for each of them. For each of these calculations, the starting phase-space position has been integrated backwards and forwards in time for 2 Gyr and the orbital information has been extracted. The final values of the orbital parameters are calculated with a median of the Monte Carlo values, while the uncertainties are inferred taking the values relative to 68 per cent of the area of the distribution around the median of each quantity. Note that, there is no prior on the gaussianity of the output distributions. The set of orbital parameters used in Chapters 2 and 3 are the apocentre, the pericentre, the eccentricity, the maximum excursion from the plane, the velocity vector, the energy, the angular momentum vector (in this frame of reference, $L_z > 0$ means a prograde orbit), the Galactocentric cartesian position, and the action momentum vector (J_r, J_ϕ, J_z).

Bibliography

Abolfathi B., et al., 2018, ApJSupp, 235, 42

Aguado D. S., González Hernández J. I., Allende Prieto C., Rebolo R., 2018a, ApJ, 852, L20

Aguado D. S., Allende Prieto C., González Hernández J. I., Rebolo R., 2018b, ApJ, 854, L34

Aguado D. S., et al., 2019, MNRAS, 490, 2241

Allende Prieto C., Beers T. C., Wilhelm R., Newberg H. J., Rockosi C. M., Yanny B., Lee Y. S., 2006, ApJ, 636, 804

Arentsen A., Starkenburg E., Shetrone M. D., Venn K. A., Depagne É., McConnachie A. W., 2019, A&A, 621, A108

Arentsen A., et al., 2020, MNRAS, 491, L11

Baade W., 1946, PASP, 58, 249

Baade W., 1951, Publications of Michigan Observatory, 10, 7

Bailer-Jones C. A. L., 2015, Publications of the Astronomical Society of the Pacific, 127, 994

Bailer-Jones C. A. L., Rybizki J., Fouesneau M., Mantelet G., Andrae R., 2018, AJ, 156, 58

Barbá R. H., Minniti D., Geisler D., Alonso-García J., Hempel M., Monachesi A., Arias J. I., Gómez F. A., 2019, ApJ, 870, L24

Beers T. C., Christlieb N., 2005, ARAA, 43, 531

Beers T. C., Preston G. W., Shectman S. A., 1985, AJ, 90, 2089

Beers T. C., Preston G. W., Shectman S. A., 1992, AJ, 103, 1987

Beers T. C., Rossi S., Norris J. E., Ryan S. G., Shefler T., 1999, AJ, 117, 981

Beers T. C., et al., 2017, ApJ, 835, 81

Belokurov V., Erkal D., Evans N. W., Koposov S. E., Deason A. J., 2018, MNRAS, 478, 611

Bialek S., Fabbro S., Venn K. A., Kumar N., O'Briain T., Moo Yi K., 2019, arXiv e-prints, p. arXiv:1911.02602

Binney J., Tremaine S., 2008, Galactic Dynamics: Second Edition

Bland-Hawthorn J., Gerhard O., 2016, ARAA, 54, 529

Bonifacio P., et al., 2019, MNRAS, 487, 3797

Bovy J., 2015, ApJSupp, 216, 29

Bromm V., Coppi P. S., Larson R. B., 2002, ApJ, 564, 23

Brook C. B., Kawata D., Scannapieco E., Martel H., Gibson B. K., 2007, ApJ, 661, 10

Buck T., Obreja A., Macciò A. V., Minchev I., Dutton A. A., Ostriker J. P., 2020, MNRAS, 491, 3461

Bullock J. S., Boylan-Kolchin M., 2017, ARAA, 55, 343

Caffau E., et al., 2011, Nature, 477, 67

Caffau E., et al., 2017, Astronomische Nachrichten, 338, 686

Caffau E., et al., 2020, MNRAS, 493, 4677

Chambers K. C., et al., 2016, The Pan-STARRS1 Surveys (arXiv:1612.05560)

Choi J., Dotter A., Conroy C., Cantiello M., Paxton B., Johnson B. D., 2016, ApJ, 823, 102

Christlieb N., Wisotzki L., Graßhoff G., 2002, A&A, 391, 397

Christlieb N., Schörck T., Frebel A., Beers T. C., Wisotzki L., Reimers D., 2008, A&A, 484, 721

Cui X.-Q., et al., 2012, Research in Astronomy and Astrophysics, 12, 1197

Da Costa G. S., et al., 2019, MNRAS, 489, 5900

Dalton G., et al., 2012, WEAVE: the next generation wide-field spectroscopy facility for the William Herschel Telescope. p. 84460P, doi:10.1117/12.925950

Dinescu D. I., 2002, in van Leeuwen F., Hughes J. D., Piotto G., eds, Astronomical Society of the Pacific Conference Series Vol. 265, Omega Centauri, A Unique Window into Astrophysics. p. 365 (arXiv:astro-ph/0112364)

Dotter A., 2016, ApJSupp, 222, 8

Dotter A., Chaboyer B., Jevremović D., Kostov V., Baron E., Ferguson J. W., 2008, ApJSupp, 178, 89

Eggen O. J., Lynden-Bell D., Sandage A. R., 1962, ApJ, 136, 748

Eisenstein D. J., et al., 2011, AJ, 142, 72

El-Badry K., et al., 2018, MNRAS, 480, 652

Evans D. W., et al., 2018, A&A, 616, A4

Fabbro S., Venn K. A., O'Briain T., Bialek S., Kielty C. L., Jahandar F., Monty S., 2018, MNRAS, 475, 2978

Fattahi A., et al., 2016, MNRAS, 457, 844

Frebel A., Norris J. E., 2015, ARAA, 53, 631

Gardner J. P., et al., 2006, Space Science Reviews, 123, 485

Ghez A. M., Salim S., Hornstein S. D., Tanner A., Lu J. R., Morris M., Becklin E. E., Duchêne G., 2005, ApJ, 620, 744

Goldstein H., 1950, Classical mechanics

Gravity Collaboration et al., 2019, A&A, 625, L10

Greif T. H., Springel V., White S. D. M., Glover S. C. O., Clark P. C., Smith R. J., Klessen R. S., Bromm V., 2011, ApJ, 737, 75

Gustafsson B., Edvardsson B., Eriksson K., Jørgensen U. G., Nordlund Å., Plez B., 2008, A&A, 486, 951

Hamilton W. R., 1834, Philosophical Transactions of the Royal Society, pp 247–308

Hamilton W. R., 1835, Philosophical Transactions of the Royal Society, pp 95–144

Haywood M., Di Matteo P., Lehnert M. D., Snaith O., Khoperskov S., Gómez A., 2018, ApJ, 863, 113

Helmi A., White S. D. M., de Zeeuw P. T., Zhao H., 1999, Nature, 402, 53

Helmi A., Babusiaux C., Koppelman H. H., Massari D., Veljanoski J., Brown A. G. A., 2018, Nature, 563, 85

Henden A. A., Levine S., Terrell D., Welch D. L., Munari U., Kloppenborg B. K., 2018, in American Astronomical Society Meeting Abstracts #232. p. 223.06

Hill V., Christlieb N., Beers T. C., Barklem P. S., Kratz K. L., Nordström B., Pfeiffer B., Farouqi K., 2017, A&A, 607, A91

Hirano S., Bromm V., 2017, MNRAS, 470, 898

Hopkins P. F., Kereš D., Oñorbe J., Faucher-Giguère C.-A., Quataert E., Murray N., Bullock J. S., 2014, MNRAS, 445, 581

Irwin M., Lewis J., 2001, , 45, 105

Ivezic Z., et al., 2008, Serbian Astronomical Journal, 176, 1

Jenkins A., 2013, MNRAS, 434, 2094

Ji A. P., Frebel A., 2018, ApJ, 856, 138

Kajino T., Aoki W., Balantekin A. B., Diehl R., Famiano M. A., Mathews G. J., 2019, Progress in Particle and Nuclear Physics, 107, 109

Keller S. C., et al., 2007, PASA, 24, 1

Keller S. C., et al., 2014, Nature, 506, 463 EP

Kollmeier J. A., et al., 2017, arXiv e-prints, p. arXiv:1711.03234

Koposov S. E., Yoo J., Rix H.-W., Weinberg D. H., Macciò A. V., Escudé J. M., 2009, ApJ, 696, 2179

Landau L. D., Lifshitz E. M., 1969, Mechanics

Lee Y. S., et al., 2013, AJ, 146, 132

Li H., Tan K., Zhao G., 2018, ApJSupp, 238, 16

Lindegren L., et al., 2018, preprint, (arXiv:1804.09366)

Loeb A., 2010, How Did the First Stars and Galaxies Form?. Princeton University Press

Longeard N., et al., 2018, MNRAS, 480, 2609

Longeard N., et al., 2020, MNRAS, 491, 356

Malhan K., Ibata R. A., 2018, MNRAS, 477, 4063

Malhan K., Ibata R. A., 2019, MNRAS, 486, 2995

Meynet G., Ekström S., Maeder A., 2006, A&A, 447, 623

Meynet G., Hirschi R., Ekstrom S., Maeder A., Georgy C., Eggenberger P., Chiappini C., 2010, A&A, 521, A30

Meza A., Navarro J. F., Abadi M. G., Steinmetz M., 2005, MNRAS, 359, 93

Minniti D., et al., 2018, A&A, 616, A26

Miyamoto M., Nagai R., 1975, , 27, 533

Monty S., Venn K. A., Lane J. M. M., Lokhorst D., Yong D., 2020, MNRAS, 497, 1236

Myeong G. C., Vasiliev E., Iorio G., Evans N. W., Belokurov V., 2019, MNRAS, 488, 1235

Navarro J. F., Frenk C. S., White S. D. M., 1997, ApJ, 490, 493

Navarro J. F., Abadi M. G., Venn K. A., Freeman K. C., Anguiano B., 2011, MNRAS, 412, 1203

Nordlander T., Amarsi A. M., Lind K., Asplund M., Barklem P. S., Casey A. R., Collet R., Leenaarts J., 2017, A&A, 597, A6

Omukai K., Palla F., 2001, ApJ, 561, L55

Placco V. M., Frebel A., Beers T. C., Stancliffe R. J., 2014, ApJ, 797, 21

Plez B., 2012, Turbospectrum: Code for spectral synthesis (ascl:1205.004)

Rich R. M., 2018, in Chiappini C., Minchev I., Starkenburg E., Valentini M., eds, Vol. 334, Rediscovering Our Galaxy. pp 233–241 (arXiv:1712.02885), doi:10.1017/S1743921317009413

Salvadori S., Ferrara A., Schneider R., Scannapieco E., Kawata D., 2010, MNRAS, 401, L5

Sawala T., et al., 2016, MNRAS, 457, 1931

Sbordone L., Caffau E., Bonifacio P., Duffau S., 2014, A&A, 564, A109

Schlafly E. F., et al., 2018, ApJSupp, 234, 39

Schönrich R., Binney J., Dehnen W., 2010, MNRAS, 403, 1829

Sestito F., et al., 2019, MNRAS, 484, 2166

Sestito F., et al., 2020a, MNRAS,

Sestito F., et al., 2020b, arXiv e-prints, p. arXiv:2009.14207

Stacy A., Greif T. H., Bromm V., 2010, MNRAS, 403, 45

Stacy A., Bromm V., Lee A. T., 2016, MNRAS, 462, 1307

Starkenburg E., Shetrone M. D., McConnachie A. W., Venn K. A., 2014, MNRAS, 441, 1217

Starkenburg E., Oman K. A., Navarro J. F., Crain R. A., Fattahi A., Frenk C. S., Sawala T., Schaye J., 2017a, MNRAS, 465, 2212

Starkenburg E., et al., 2017b, MNRAS, 471, 2587

Starkenburg E., et al., 2018, MNRAS, 481, 3838

Starkenburg E., et al., 2019, MNRAS, 490, 5757

Stetson P. B., Pancino E., 2008, PASP, 120, 1332

Tamai R., Cirasuolo M., González J. C., Koehler B., Tuti M., 2016, in Ground-based and Airborne Telescopes VI. p. 99060W, doi:10.1117/12.2232690

The MSE Science Team et al., 2019, arXiv e-prints, p. arXiv:1904.04907

Tody D., 1986, in Crawford D. L., ed., Society of Photo-Optical Instrumentation Engineers (SPIE) Conference Series Vol. 627, Society of Photo-Optical Instrumentation Engineers (SPIE). p. 733, doi:10.1117/12.968154

Tody D., 1993, in Hanisch R. J., Brissenden R. J. V., Barnes J., eds, Astronomical Society of the Pacific Conference Series Vol. 52, Astronomical Data Analysis Software and Systems II. p. 173

Tominaga N., Iwamoto N., Nomoto K., 2014, ApJ, 785, 98

Tumlinson J., 2010, The Astrophysical Journal, 708, 1398

Venn K., et al., 2019, in Canadian Long Range Plan for Astronony and Astrophysics White Papers. p. 5 (arXiv:1910.00774), doi:10.5281/zenodo.3755910

Venn K. A., et al., 2020, MNRAS, 492, 3241

Vorobyov E. I., Akimkin V., Stoyanovskaya O., Pavlyuchenkov Y., Liu H. B., 2018, A&A, 614, A98

Wetzel A. R., Hopkins P. F., Kim J.-h., Faucher-Giguère C.-A., Kereš D., Quataert E., 2016, ApJ, 827, L23

White S. D. M., Springel V., 2000, in Weiss A., Abel T. G., Hill V., eds, The First Stars. p. 327 (arXiv:astro-ph/9911378), doi:10.1007/10719504_62

Willman B., Strader J., 2012, AJ, 144, 76

Yanny B., et al., 2009, AJ, 137, 4377

Yong D., et al., 2013, ApJ, 762, 26

York D. G., et al., 2000, AJ, 120, 1579

Youakim K., et al., 2017, MNRAS, 472, 2963

Youakim K., et al., 2020, MNRAS, 492, 4986

de Jong R. S., et al., 2019, The Messenger, 175, 3

van Haarlem M. P., et al., 2013, A&A, 556, A2

CHAPTER

6 Introduction and conclusions in French

Introduction : où en est l'archéologie (ou la paléontologie) galactique ?

L'un des objectifs de l'astronomie et de l'astrophysique est de comprendre la formation des premières structures dans l'Univers primitif et leurs propriétés physiques, et cela englobe plusieurs questions ouvertes. Par exemple, sur la formation des premières étoiles : comment former des étoiles à partir d'une composition chimiquement vierge du gaz, leur distribution de masse, comment les premières étoiles ont pollué et ionisé le milieu interstellaire et ont déclenché la formation de la prochaine génération d'étoiles, la physique des supernovae et la formation ultérieure d'éléments lourds. Ensuite, la formation de structures plus grandes : comment se forment les galaxies, la répartition en taille et en masse des premières galaxies, la quantité de leur contenu en étoiles, en gaz et en matière noire, la dichotomie entre les galaxies naines et les amas globulaires et leur relation avec le contenu chimique du gaz et la répartition de la matière noire. Il y a deux façons de répondre à ces questions. L'une consiste à observer à fort redshift et, par conséquent, à remonter le temps, lorsque l'Univers avait quelques milliards d'années. L'autre façon est d'examiner la chimie et la cinématique des étoiles formées dans l'Univers primitif qui sont encore vivantes et observables de nos jours dans la Voie lactée et ses satellites. Ce dernier domaine est ce qu'on appelle l'Archeologie ou Palaeontologie Galactique. Comme ces étoiles se sont formées dans l'Univers primitif et non pollué, elles doivent être de faible masse, et parmi les plus anciennes et les plus pauvres en métaux. À partir de leurs abondances chimiques, il est possible de reconstituer les archives fossiles de la première génération d'étoiles et de leurs sites de formation, tandis que la dynamique des étoiles les plus pauvres en métaux pourrait porter les empreintes de l'histoire de l'assemblage et de l'accrétion de la Voie lactée. L'introduction qui suit se concentre sur les propriétés générales des étoiles les plus pauvres en métaux, sur l'étude de Pristine comme chef de file de l'investigation de cette population d'étoiles, sur la révolution commencée avec le satellite Gaia et sur la synergie avec les études au sol. Les chapitres suivants sont une collection de travaux développés au cours de mon doctorat, et ils se concentrent sur l'étude dynamique des étoiles les plus pauvres en métaux en utilisant à la fois des observations (Chapitres 2 et 3) et des simulations cosmologiques à haute résolution (Chapitre 4).

0.1 Les étoiles les plus anciennes et les plus pauvres en métaux comme témoins du début de l'Univers

Cette section décrira les principales propriétés des étoiles les plus pauvres en métaux, en particulier leur importance, les attentes quant à l'endroit où les trouver, et un résumé des enquêtes les plus importantes sur les étoiles pauvres en métaux, qui sera suivi d'une section décrivant l'une des enquêtes photométriques les plus efficaces pour la recherche des étoiles les plus pauvres en métaux, l'enquête Pristine.

Tout d'abord, résumons la taxonomie des étoiles pauvres en métaux introduite par Beers & Christlieb (2005) et basée sur la teneur en métaux dans l'atmosphère stellaire.

Que signifie être très/extrêmement/ultra (...) pauvre en métaux ?

Beers & Christlieb (2005) a proposé une nouvelle nomenclature pour mieux distinguer combien une étoile manque de métaux. Tout d'abord, en définissant la métallicité comme :

$$[\mathrm{Fe/H}] = \log_{10}\left(\frac{N_{\mathrm{F}e}}{N_{\mathrm{H}}}\right)_{\star} - \log_{10}\left(\frac{N_{\mathrm{F}e}}{N_{\mathrm{H}}}\right)_{\odot}, \tag{1}$$

où N_{X} est le nombre d'atomes d'une espèce donnée, l'équation 1 fournit le rapport entre le nombre d'atomes de métal et les atomes d'hydrogène pour une étoile par rapport au Soleil. Comme l'abondance du fer est fortement liée à la teneur totale en métaux, en premier ordre, [Fe/H] = [M/H]. Avec cette définition, Beers & Christlieb (2005) a proposé la nomenclature figurant dans le tableau 0.1.

Table 0.1: Nomenclature des étoiles basée sur la métallicité telle que proposée dans Beers & Christlieb (2005).

[Fe/H]	Term	Acronym
$> +0.5$	Super metal-rich	SMR
~ 0.0	Solar	–
< -1.0	Metal-poor	MP
< -2.0	Very metal-poor	VMP
< -3.0	Extremely metal-poor	EMP
< -4.0	Ultra metal-poor	UMP
< -5.0	Hyper metal-poor	HMP
< -6.0	Mega metal-poor	MMP

Beers & Christlieb (2005) a également fourni une sous-classification des étoiles pauvres en métaux en groupes basés sur l'abondance du carbone et des éléments de capture des neutrons, tels que l'europium et le baryum. Les éléments de capture des neutrons peuvent être divisés en deux groupes principaux selon l'échelle de temps des réactions nucléaires dans lesquelles ils ont été produits. Si cette échelle de temps est beaucoup plus courte que le temps nécessaire à la désintégration du β^--decay[1], comme dans le cas de la phase

[1] β^--decay est le processus nucléaire à partir duquel un neutron se désintègre en un proton, un électron, et un électron antineutrino, i.e., $\rightarrow + +$

d'effondrement du noyau des supernovae et de la nucléosynthèse qui s'ensuit, puis des éléments à processus rapide (ci-après r-process) sont formés. D'autres environnements et phénomènes dont les énergies et les densités sont capables de produire des éléments de processus r sont les vents induits par les neutrinos dans les supernovae, les effondrements, les fusions d'étoiles à neutrons binaires et même les régions riches en neutrons dans l'Univers primitif selon des modèles cosmologiques inhomogènes (Kajino et al., 2019, et les références qui y sont faites). Au contraire, si l'échelle de temps pour leur synthèse est beaucoup plus grande que la désintégration β^-, comme dans l'atmosphère stellaire des étoiles à branches géantes asymptotiques (AGB), alors ces éléments sont appelés éléments à processus lent (ci-après s-processus). L'europium et le baryum sont tous deux formés par des réactions nucléaires de processus r et s, le premier étant principalement formé par des processus r. Un rapport entre les abondances de ces deux éléments, [Ba/Eu], peut aider à mieux distinguer quel était le principal canal qui a formé les éléments de capture des neutrons dans une étoile donnée pauvre en métaux. En particulier, les étoiles les plus pauvres en métaux avec des éléments à processus r amélioré et à processus s faible sont considérées comme faisant partie des objets les plus anciens, et se sont formées dans les $\lesssim 300$ Myr après la formation des premières étoiles (e.g., Frebel & Norris, 2015; Hill et al., 2017; Ji & Frebel, 2018).

Il a été observé qu'une grande partie des étoiles les plus pauvres en métaux sont enrichies en carbone, e.g., $15 - 20$ pour cent dans le régime VMP et 40 pour cent dans le régime EMP (Yong et al., 2013; Lee et al., 2013; Placco et al., 2014). Cette grande fraction d'étoiles enrichies en carbone pourrait être liée à des processus stellaires dans l'Univers primitif (qui se déroulent différemment de nos jours en raison d'un manque de métaux dans leur atmosphère), ou à la binarité. Si la carbonicité est associée à une abondance d'éléments de capture des neutrons, elle peut constituer un excellent outil pour dévoiler l'origine du progéniteur de cette étoile particulière pauvre en métaux et pour avoir une vue d'ensemble des processus physiques dans un environnement dépourvu de métaux. De nombreux scénarios ont été proposés pour expliquer l'amélioration du carbone. Par exemple, l'échange de masse dans un système binaire : si le compagnon atteignait la branche géante asymptotique, il polluerait l'atmosphère de l'étoile CEMP avec du carbone et des éléments du processus s. D'autre part, les étoiles CEMP non renforcées en éléments du processus s sont susceptibles d'être des étoiles simples (Starkenburg et al., 2014) dans lesquelles le carbone a été produit dans l'ancêtre. Les étoiles UMP massives et à rotation rapide du début de l'Univers (Meynet et al., 2006, 2010), ou les faibles supernovae (Tominaga et al., 2014), peuvent produire une grande quantité de carbone. Arentsen et al. (2019) a montré qu'une fraction des étoiles CEMP sans amélioration dans le processus s se trouvent dans un système binaire et ouvrent la possibilité que de multiples scénarios puissent produire une telle caractéristique. Par conséquent, une sous-classification basée sur la carbonicité couplée à des éléments de capture de neutrons pourrait aider à distinguer le progéniteur de ces étoiles pauvres en métaux. Le tableau 0.2 présente la sous-classification des étoiles pauvres en métaux basée sur l'europium, le baryum et le carbone, telle qu'elle a été introduite par Beers & Christlieb (2005).

Table 0.2: La définition des sous-classes de métaux pauvres telle que proposée dans Beers & Christlieb (2005).

Term	Properties
Neutron-capture-rich stars	
r-I	$0.3 \leq$ [Eu/Fe] ≤ 1.0 and [Ba/Eu] < 0.0
r-II	$0.3 \leq$ [Eu/Fe] > 1.0 and [Ba/Eu] < 0.0
s	[Ba/Fe] > 1.0 and [Ba/Eu] > 0.5
r/s	$0.0 <$ [Ba/Eu] < 0.5
Carbon Enhanced metal-poor stars	
CEMP	[C/Fe] > 1.0
CEMP-r	[C/Fe] > 1.0 and [Eu/Fe] > 1.0
CEMP-s	[C/Fe] > 1.0, [Ba/Fe] > 1.0, and [Ba/Eu] > 0.5
CEMP-no	[C/Fe] > 1.0 and $0.0 <$ [Ba/Fe] < 0.0

Pourquoi les étoiles pauvres en métal sont-elles importantes ?

Les étoiles peu abondantes en métaux peuvent fournir des informations précieuses et ouvrir une fenêtre sur les débuts de l'Univers. Au fur et à mesure de l'expansion de l'Univers primitif, et du découplage entre le rayonnement et la matière qui a produit le fond micro-onde cosmique (CMB), la température des baryons a diminué jusqu'à ce que la première recombinaison se produise, produisant les éléments les plus légers, tels que l'hydrogène, l'hélium et une petite quantité de lithium. La mesure du Lithium dans les étoiles les plus pauvres en métaux peut fournir une estimation de son abondance primordiale, et nous pouvons donc mieux déduire le contenu des baryons et le rapport baryon/photon dans l'Univers primitif.

La composition de ces étoiles chimiquement vierges est également utile pour déduire les propriétés des premières étoiles et la façon dont elles ont pollué le milieu interstellaire (ISM). Les premières étoiles, également appelées étoiles de population III, sont les canaux nécessaires pour former pour la première fois les éléments plus lourds que le lithium, et contribuent à polluer le MIS avec leurs éjecta et leurs supernovae. Les limites supérieures et inférieures de la masse et la distribution des premières étoiles, c'est-à-dire la fonction de masse initiale de ces objets, sont des questions encore ouvertes en physique et en astronomie. Plusieurs auteurs soulignent que les premières étoiles devraient être plus massives que les étoiles les plus massives que nous pouvons trouver de nos jours, couvrant une gamme allant de quelques dizaines à quelques milliers de masses solaires (e.g., Omukai & Palla, 2001; Bromm et al., 2002; Stacy et al., 2010; Loeb, 2010). La raison principale de ces étoiles massives est l'absence d'un réfrigérant efficace dans l'ISM. Les régions de formation des étoiles dans l'Univers primitif étaient composées d'hydrogène, d'hélium, de lithium et d'hydrogène moléculaire, ce dernier composant jouant le rôle de réfrigérant principal. En l'absence de métaux, tous les éléments chimiques sont plus lourds que l'hélium. La température et la densité dans les régions de formation des étoiles de l'Univers primitif sont plus élevées que celles auxquelles nous pouvons nous attendre aujourd'hui. Cela permet de former des objets protostellaires aussi massifs avec un équilibre entre le rayonnement et la force gravitationnelle [citep[e.g.,][et les références qui s'y trouvent]Loeb10. Des études plus récentes (e.g., Greif et al., 2011; Stacy et al., 2016; Hirano & Bromm, 2017; Vorobyov et al., 2018) montrent qu'il est possible de former des premières étoiles

d'une masse inférieure d'environ $\sim 0.1\,M_\odot$ grâce à la turbulence et à la fragmentation. Une première étoile massive en formation peut induire des instabilités dans son disque circumstellaire, et la fragmentation ultérieure produira les conditions idéales en termes de température et de densité pour former des étoiles de faible masse, comme le montre la figure **??**. Par conséquent, ces auteurs ouvrent le scénario selon lequel les premières étoiles de faible masse, et donc non polluées, sont encore présentes et peut-être observables dans l'Univers actuel. Les générations suivantes contiennent également beaucoup d'informations sur les premières étoiles et il est possible de retracer les éléments produits lors des explosions des premières supernovae, car on peut raisonnablement penser que l'ISM a été pollué par quelques explosions de supernovae.

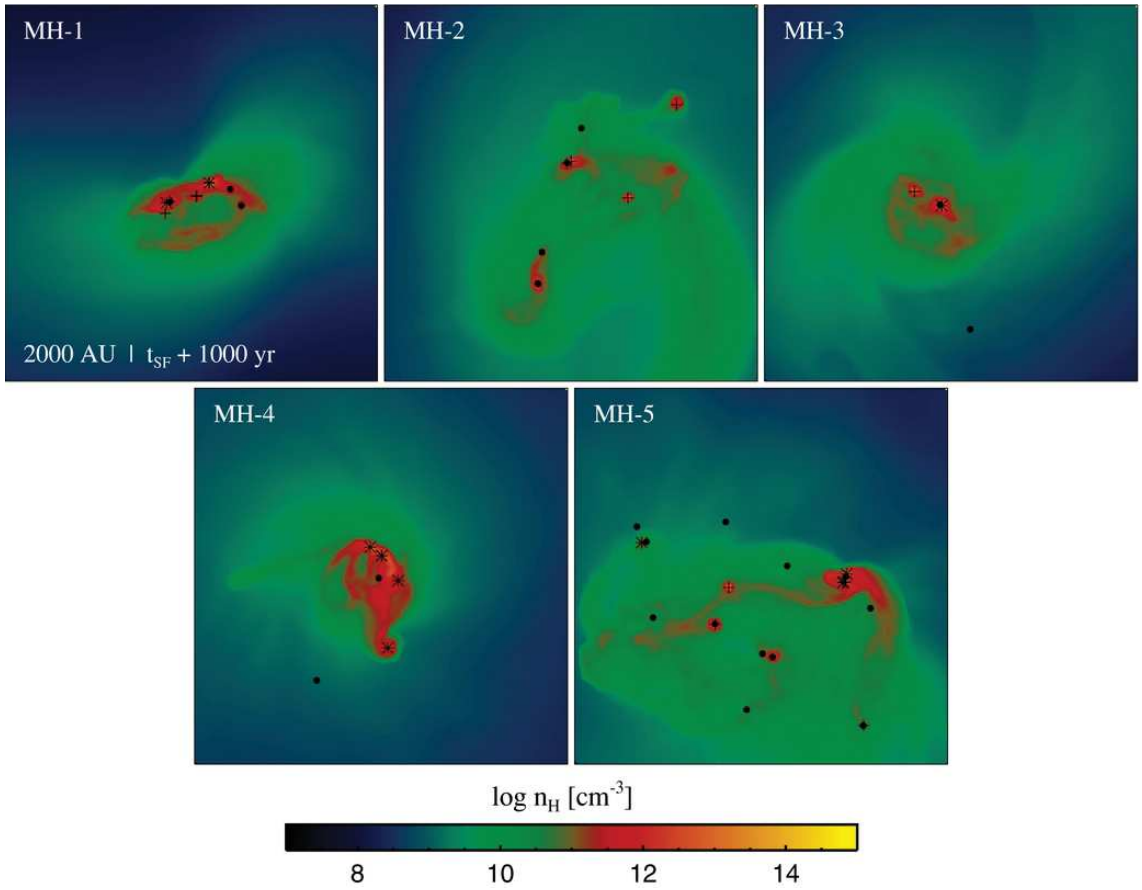

Figure 0.1: Formation des premières étoiles à partir de Greif et al. (2011). Les régions de formation des étoiles sont fragmentées et la formation de premières étoiles de faible masse est autorisée. Les protoétoiles de masse inférieure à $1\,M_\odot$, comprise entre $1\,M_\odot$ et $3\,M_\odot$, et supérieure à $3\,M_\odot$ sont désignées par des points noirs, des croix et des astérisques, respectivement. Chaque panneau a une taille de 2000 fois 2000 et représente une simulation de halo différente, codée par la couleur de la densité de l'hydrogène neutre. Les mécanismes de fragmentation et de refroidissement jouent un rôle crucial dans la formation des étoiles de faible masse de la population III.

Les distributions spatiales et cinématiques des étoiles les plus pauvres en métaux sont également instructives sur la formation et l'évolution des galaxies, soit des grandes galaxies, comme la Voie lactée et Andromède, soit aussi des galaxies naines. L'étude des étoiles les plus pauvres en métaux, ainsi que leur chimie, permet de mieux caractériser les propriétés de leurs sites de formation.

Historiquement, les étoiles pauvres en métaux ont été observées pour faire la lumière sur la formation et la structure de la Voie lactée. Par exemple, Baade (1946, 1951) a étudié les étoiles RR Lyrae pauvres en métaux pour mieux caractériser la forme et la distribution stellaire de la région intérieure de la Galaxie, puisque l'étude de la morphologie de la Voie lactée était encore dans sa phase pionnière. Les RR Lyrae sont une classe de variables périodiques sur la branche horizontale et, grâce à la relation précise entre la période de pulsation et leur luminosité, elles peuvent être utilisées comme bougies standard pour la détermination des distances à travers la Galaxie. Un autre exemple historique sur les étoiles pauvres en métal comme traceurs des premiers assemblages de la Voie lactée a été étudié par Eggen et al. (1962). Ils ont calculé les excentricités et les momenta angulaires à partir des vecteurs de vitesse de 221 étoiles naines. L'échantillon était composé d'étoiles à diverses métallicités. Eggen et al. (1962) a trouvé que la population pauvre en métaux a un grand excès d'ultraviolets qui s'explique par leur manque de métaux dans l'atmosphère, d'où la corrélation entre ces deux quantités. De plus, en couplant ces propriétés atmosphériques stellaires avec la cinématique, Eggen et al. (1962) a trouvé que l'excès d'ultraviolets, donc la métallicité, est bien corrélé avec l'excentricité. En particulier, les auteurs ont souligné que les étoiles pauvres en métaux (plus grand excès d'UV) ont de plus grandes excentricités et de petits moments angulaires, tandis que la population riche en métaux a de petites excentricités et de grands moments angulaires, en raison de leurs orbites circulaires. Eggen et al. (1962) a conclu que la différence des propriétés cinématiques des deux populations est strictement liée à la formation de la Voie lactée. Par exemple, l'effondrement de la matière qui a formé la proto-galaxie se déplaçait radialement vers l'intérieur, amenant les premières étoiles (les plus pauvres en métaux) et le gaz avec les mêmes orbites à haute excentricité. Au fil du temps cosmique, en 0.1 Gyr, les orbites stellaires et gazeuses se sont découplées, cette dernière composante formant un disque et circularisant son mouvement. Au fur et à mesure que le gaz se dépose et se réchauffe, la population riche en métaux se forme avec des orbites faiblement excentriques.

Comme nous le verrons dans les sections suivantes, nous pouvons aujourd'hui bénéficier d'un échantillon beaucoup plus important d'étoiles pauvres en métaux et la combinaison des informations chimiques et cinématiques nous éclairera sur l'assemblage et l'évolution de notre Voie lactée. Ces informations peuvent être complétées par une simulation cosmologique de pointe afin de mieux interpréter les résultats des observations.

Où trouver les étoiles les plus pauvres en métal ?

Au cours des deux dernières décennies, plusieurs études théoriques se sont penchées sur les endroits où l'on s'attend à observer les étoiles les plus pauvres en métaux (e.g., White & Springel, 2000; Brook et al., 2007; Salvadori et al., 2010; Tumlinson, 2010; Starkenburg et al., 2017a; El-Badry et al., 2018) pour mieux comprendre l'histoire de l'assemblage de la Voie lactée, et des galaxies en général. White & Springel (2000) avec des simulations numériques à haute résolution avec zoom avant a prédit que la population la plus âgée est concentrée au centre, trouvant que les ∼60 per cent de sont distribués dans les 10 kpc du centre de la galaxie simulée. White & Springel (2000) a également souligné que l'âge n'est pas nécessairement corrélé à la métallicité, montrant que les étoiles à faible métallicité peuvent être trouvées dans des galaxies naines plus jeunes et isolées. Avec cette image, ils ont rapporté que seulement 16 per cent des étoiles à faible métallicité peuplent les 10 kpc intérieurs de la galaxie simulée, et la majorité est distribuée dans le halo extérieur

et les satellites. Brook et al. (2007) a utilisé des simulations SPH chimiodynamiques cosmologiques de galaxies analogues à la Voie lactée pour étudier la distribution spatiale des étoiles de la population III à la fois à haut décalage horaire et de nos jours. Comme pour White & Springel (2000), ils ont découvert que la distribution de la population sans métal diffère de celle de la population la plus ancienne. Par exemple, cette dernière est plus concentrée dans la région du renflement, alors que la première est distribuée à travers le halo des analogues de MW simulés. De plus, les étoiles sans métal continuent à se former jusqu'au redshift $z \sim 4$, i.e., $\sim 2\,\mathrm{Gyr}$ après le Big Bang, dans le cas de satellites chimiquement isolés.

Starkenburg et al. (2017a) a utilisé les simulations du groupe local APOSTLE afin de prédire où les étoiles les plus pauvres en métaux et les plus anciennes peuvent être observées. L'ensemble des simulations APOSTLE (Sawala et al., 2016; Fattahi et al., 2016) est composé de 12 paires de halos sélectionnés dans le volume cosmologique DOVE (Jenkins, 2013). Ces simulations reproduisent les principales galaxies du Groupe Local dans leur distance, leur vitesse relative, à la fois radiale et tangentielle, leur masse totale, et elles sont suffisamment isolées par des halos plus petits. Starkenburg et al. (2017a) a défini les étoiles les plus anciennes comme les objets formés $< 0.8\,\mathrm{Gyr}$ après le Big Bang (redshift $z > 6.9$), et les étoiles les plus pauvres en métal avec $[\mathrm{Fe/H}] < -2.5$. Les auteurs ont décomposé les galaxies simulées en une région intérieure avec $R \leq 15\,\mathrm{kpc}$ du centre galactique et la région extérieure avec $15\,\mathrm{kpc} < R \leq 100\,\mathrm{kpc}$. Ils ont trouvé de façon intéressante que la majorité des étoiles les plus anciennes ont une métallicité $[\mathrm{Fe/H}] \leq -2.0$, et donc sont VMP, avec une petite queue atteignant $[\mathrm{Fe/H}] < -1.0$. En examinant la répartition par âge des étoiles les plus pauvres en métal, ils ont constaté que 50 per cent d'entre elles se sont formées dans les 1.1 Gyr après le Big Bang et 90 per cent d'entre elles se sont formées dans les 2.4 Gyr. Ces résultats, présentés sur la figure 0.2, sont en accord dans les régions intérieures et extérieures des galaxies simulées. Starkenburg et al. (2017a) a également souligné que les étoiles les plus anciennes sont concentrées dans la région intérieure des galaxies, bien que dans la périphérie la population soit encore âgée. La région extérieure des galaxies, ainsi que les satellites et la région intérieure, sont également des endroits idéaux pour rechercher les étoiles les plus pauvres en métal. El-Badry et al. (2018) a analysé les simulations cosmologiques de FIRE (Hopkins et al., 2014; Wetzel et al., 2016). Outre la distribution de l'âge et de la métallicité des étoiles les plus anciennes et les plus pauvres en métaux, en accord avec Starkenburg et al. (2017a), El-Badry et al. (2018) a également analysé leur distribution spatiale et cinématique. Ils ont constaté que la majorité des étoiles les plus anciennes s'accréditent lors de l'assemblage hiérarchique, c'est-à-dire ex-situ, et se répartissent de manière soutenue par la pression, c'est-à-dire un sphéroïde non rotatif. La contrepartie in situ, formée dans la partie intérieure de la galaxie, a été poussée vers l'extérieur soit par la formation d'étoiles éclatées, soit par la variation du potentiel gravitationnel à travers le temps cosmique. La distribution cinématique des étoiles de El-Badry et al. (2018) est illustrée par la figure 0.2, tandis que l'illustration schématique de l'assemblage des galaxies simulées est présentée par la figure 0.3.

Les travaux précités s'accordent à dire qu'il est probable de trouver les étoiles les plus pauvres en métal, et aussi les plus anciennes, réparties dans un sphéroïde soutenu par la pression, i.e., le halo, dans la région intérieure de la Galaxie, i.e., le renflement, et dans les satellites nains. Comme le halo recoupe le disque, la distribution sphéroïdale permettra également à certaines de ces étoiles les plus anciennes de transiter par la région du disque, ou même de ressembler à la cinématique de la population plus jeune et plus riche en métaux. Dans le cas de ce dernier type de mouvement, on devrait s'attendre à

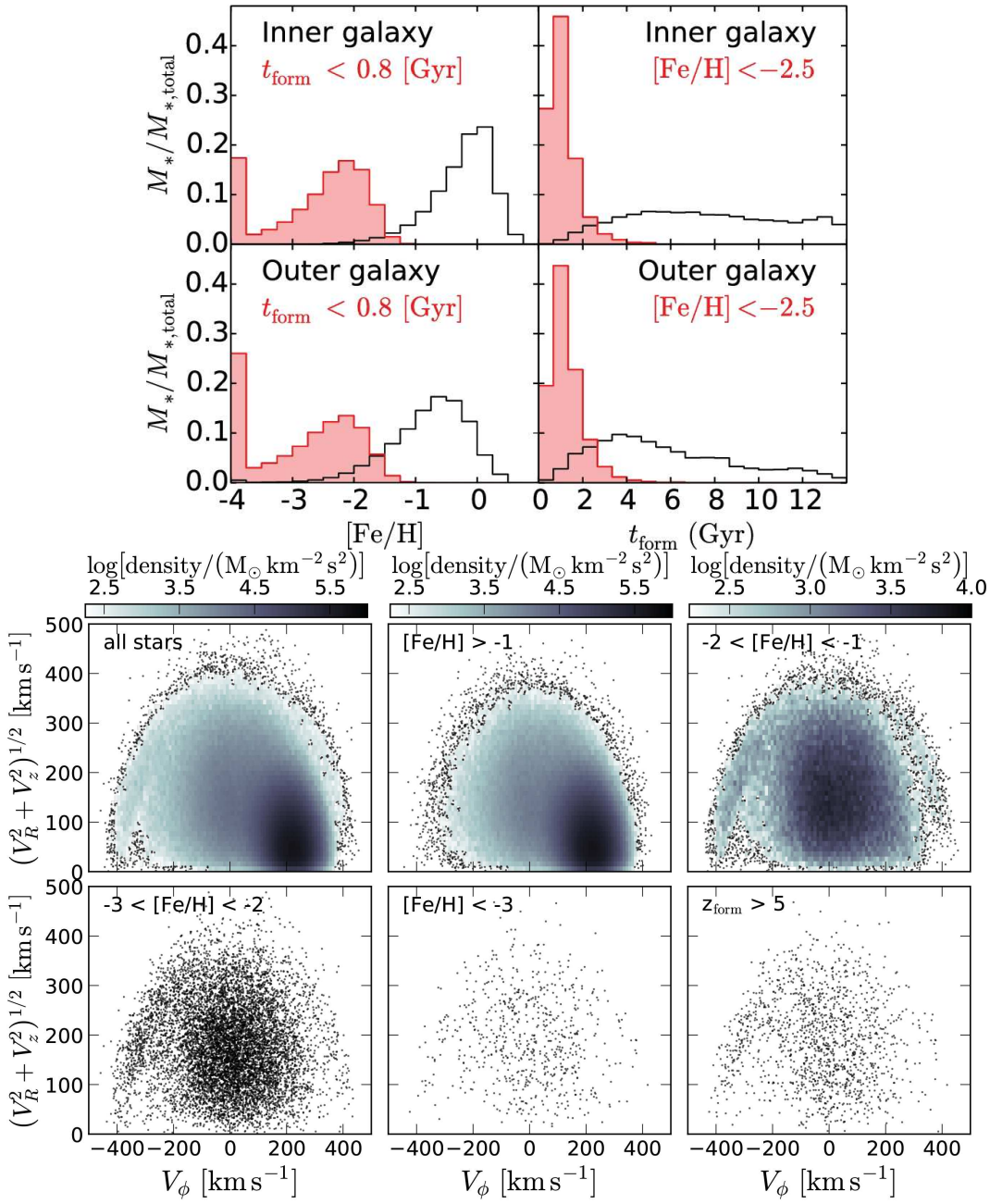

Figure 0.2: Répartition en âge, métallicité et vitesse des étoiles les plus pauvres en métaux et les plus anciennes. Panneaux supérieurs de Starkenburg et al. (2017a) : à gauche, la distribution de la métallicité des étoiles les plus anciennes ($t_{form} < 0.8\,$Gyr) dans les régions intérieures et extérieures des galaxies simulées dans les simulations APOSTLE. A droite, la distribution dans le temps de formation pour les étoiles les plus pauvres en métaux ([Fe/H] < -2.5). Ces panneaux montrent clairement comment la majorité des étoiles les plus anciennes sont distribuées dans le régime VMP, et la majorité des étoiles les plus pauvres en métaux se sont formées dans un délai de 3 Gyr. Panneaux inférieurs de El-Badry et al. (2018) : distribution cinématique dans la composante rotationnelle de la vitesse v_ϕ par rapport à la somme des composantes radiales et verticales $(v_R^2 + v_z^2)^{1/2}$. Les étoiles ont été divisées en bacs de métallicité, tandis que le panneau inférieur droit montre les étoiles formées au décalage vers le rouge $z > 5$. Les étoiles les plus pauvres en métal et les plus anciennes sont réparties dans un sphéroïde non rotatif, tandis qu'à une métallicité plus élevée, il y a un pic de haute densité coïncidant avec le disque ($v_\phi \sim 200\,$km s^{-1}, $(v_R^2 + v_z^2)^{1/2} < 100\,$km s^{-1}).

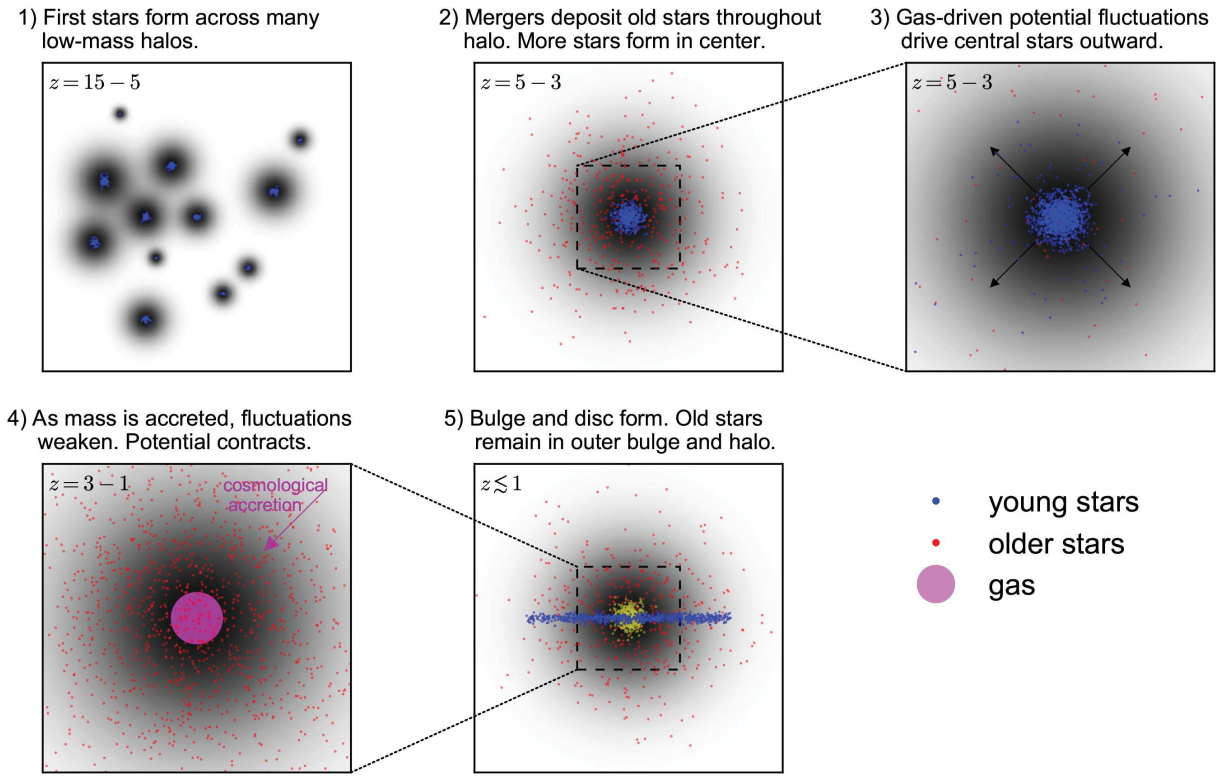

Figure 0.3: Croquis de l'assemblage des galaxies et de la distribution stellaire qui s'ensuit, tel que discuté dans El-Badry et al. (2018). À très fort redshift ($z > 5$, panneau 1), les premières étoiles se forment dans les halos de faible masse, puis fusionnent pour former la proto-galaxie ($3 < z < 5$, panneau 2) et déposent les étoiles dans la région intérieure. Des processus énergétiques, alimentés par des gaz, déplacent les étoiles vers l'extérieur, tandis que des étoiles plus jeunes se forment ($3 < z < 5$, panel 3). Après le dépôt du potentiel ($1 < z < 3$, panneau 4), le bulbe et le disque se sont formés ($z < 1$, panneau 5), tandis que les étoiles les plus anciennes et les plus pauvres en métaux sont réparties dans le bulbe et le halo.

trouver, approximativement, le même nombre de programmes et de rétrogrades. Jusqu'à présent, les simulations cosmologiques et les études d'observation se sont concentrées sur leur distribution globale et prédominante, tandis que dans les chapitres suivants []Sestito19,Sestito20,Sestito20b, j'étudierai la détection d'une population d'étoiles de faible métallicité confinées au disque de la Voie lactée. En particulier, cette population est largement favorable au mouvement prograde, difficile à concilier avec une distribution sphéroïdale non rotative.

Comment trouver les étoiles les plus pauvres en métal ?

Par définition, les étoiles pauvres en métaux ont une faible teneur en métaux dans leur composition atmosphérique, et donc plus la métallicité est faible, plus les raies du fer sont faibles dans les spectres. Cependant, il est possible de déduire la métallicité à partir des raies Ca II H et K (3968 − 3933). Il a été démontré que ce doublet est un excellent indicateur de la teneur en fer et qu'il est suffisamment fort pour être bien mesuré dans les étoiles les plus pauvres en métaux. Dans cette sous-section, je vais rendre compte des méthodes et des résultats de certaines des enquêtes les plus importantes utilisées pour la découverte des étoiles les plus pauvres en métaux tandis que, dans la section suivante, je décrirai en profondeur l'enquête Pristine (Starkenburg et al., 2017b), dont je suis membre.

L'un des premiers relevés à la recherche de ces objets rares et dépourvus de métaux a été le relevé HK (Beers et al., 1985), basé sur une combinaison de plaques à prismes-objectifs et d'un filtre étroit centré sur le doublet Ca H&K, capable d'atteindre des magnitudes de $B \sim 15.5$. L'étude HK a commencé à couvrir une zone de ~ 1940 deg^2 dans l'hémisphère sud en utilisant un total de 80 plaques photographiques. L'enquête de HK a trouvé un ensemble hétérogène d'objets célestes, la majorité d'entre eux étant des étoiles chaudes (types A et B) et des étoiles semblables au soleil avec de fortes raies Ca H&K (types G et K). La minorité de cet ensemble (objets de ~ 1800), qui sont des objets avec des lignes Ca faibles, ont été sélectionnés pour être des candidats pauvres en métal. Une campagne de suivi spectroscopique ultérieure a révélé que ce sous-échantillon est composé d'une grande variété d'objets, et pas seulement d'étoiles pauvres en métaux (Beers et al., 1985). Par exemple, des étoiles symbiotiques, des variables cataclysmiques, des étoiles du sous-marin O, des naines blanches, des étoiles des raies d'émission K et M Ca II, et même des objets extragalactiques comme les galaxies de Seyfert. Le nombre final d'étoiles confirmées très pauvres en métaux ([Fe/H] ≤ -2.0) était de 134, sur un échantillon de départ de 1800 objets. Pour souligner la rareté des étoiles à mesure que la métallicité diminue, ils n'ont trouvé que 5 étoiles avec [Fe/H] ≤ -3.5, dont une seule est ultra pauvre en métaux ([Fe/H] ≤ -4.0). La poursuite de cette enquête (e.g., Beers et al., 1992, 1999) a étendu l'échantillon à quelques milliers d'étoiles dans le régime VMP, tandis que dans le régime UMP, le nombre est resté inférieur à 10.

Une deuxième enquête importante qui a permis de découvrir des étoiles déficientes en métaux est l'enquête Hambourg/ESO (HES) couvrant ~ 6700 deg^2 dans le ciel de la haute latitude galactique sud (Christlieb et al., 2002, 2008). HES combine les intensités de lignes du doublet de calcium déduites des couleurs du prisme objectif et de la large bande, comme $(B - V)$, pour fournir une sélection plus efficace des candidats pauvres en métaux. De plus, HES atteint 2 magnitudes plus faibles que HK et, ensemble, le volume total recherché pour les étoiles les plus pauvres en métaux est multiplié par un facteur de 10 (Christlieb et al., 2008). Un résultat intéressant, également résumé dans Beers & Christlieb (2005) et confirmé par des études ultérieures (Arentsen et al., 2019, et les références qui y figurent), est que lorsque la métallicité diminue, la carbonicité augmente rapidement. L'étude HES a été utile pour cartographier diverses régions de notre Galaxie, puisque le nombre d'étoiles pauvres en métaux a fortement augmenté. Grâce à leur étude chimiodynamique (Beers et al., 2017), ils ont découvert la présence d'une population d'étoiles déficientes en métaux ([Fe/H] > 2.5) dans le voisinage du Soleil, avec une cinématique similaire à celle de la population plus riche en métaux du disque. Une population d'étoiles confinée au disque de la Voie lactée, bien que présentant des métallicités plus faibles, sera analysée en profondeur dans les chapitres suivants (voir aussi Sestito et al., 2019, 2020a). Beers et al. (2017) a également proposé de nouveaux

candidats membres pour le courant Helmi (Helmi et al., 1999) et les débris de marée de l'amas globulaire de ωCen (voir aussi Dinescu, 2002; Meza et al., 2005; Navarro et al., 2011).

Le SkyMapper Southern Survey, parmi divers objectifs scientifiques galactiques et extragalactiques, recherche avec une grande efficacité les étoiles les plus pauvres en métal de l'hémisphère sud (Keller et al., 2007; Da Costa et al., 2019). Grâce à une combinaison de filtres à bande moyenne, SkyMapper peut fournir une meilleure sélection de candidats pauvres en métaux parmi la population la plus riche en métaux, et fournit une estimation des métallicités photométriques. Cette combinaison, illustrée sur la figure 0.4, est composée d'une couleur sensible à la température $(g - i)$ et d'une quantité sensible à l'absorption de la métallicité, à savoir $m = v - g - 1.5(g - i)$, dans laquelle le filtre v couvre la région du doublet Ca du spectre stellaire. Comme le montre la figure 0.4, les étoiles les plus pauvres en métaux sont bien séparées de la population plus riche en métaux. La plage spectrale couverte par le filtre v est présentée par rapport au filtre H&K à bande étroite de Ca vierge sur la figure 0.6. Le suivi spectroscopique a permis de confirmer la grande efficacité du SkyMapper Southern Survey dans la sélection des étoiles les plus pauvres en métaux (Da Costa et al., 2019). En chiffres, ~ 19 pour cent des étoiles ayant une métallicité photométrique [Fe/H] ≤ -2.0 ont une métallicité spectroscopique confirmée de [Fe/H] ≤ -3.0, alors que seulement ~ 7 pour cent ne sont pas VMP, c'est-à-dire [Fe/H] > -2.0. A titre d'exemple, cette enquête a permis de découvrir l'étoile la plus pauvre en fer connue SMSS J031300.36 − 670839.3 (Keller et al., 2014; Nordlander et al., 2017) avec [Fe/H] < -6.5 et une grande abondance de carbone $A(C) \sim 6$.

Pour souligner à quel point les étoiles les plus pauvres en métaux sont rares, après 35 ans de la première enquête de HK, seules des étoiles à 42 du régime ultra pauvre en métaux ont été découvertes en tenant compte de toutes les enquêtes (Sestito et al., 2019). De plus, Youakim et al. (2017) estime que, si nous observons 800 étoiles à halo aléatoire dans la gamme de magnitude de $14 < V < 18$ mag, une seule est susceptible d'être extrêmement pauvre en métaux. En fait, l'une des plus grandes études spectroscopiques, le Sloan Digital Sky Survey (SDSS, York et al., 2000), n'a découvert par hasard que quelques UMPs (e.g., Caffau et al., 2011; Aguado et al., 2018a,b), bien qu'elle scanne le ciel entier. Par exemple, grâce au SDSS, l'étoile la plus pauvre en métal connue a été découverte (Caffau et al., 2011). Par conséquent, si nous voulons construire un large échantillon statistique des étoiles les plus pauvres en métaux, une sélection extrêmement efficace des candidats est cruciale. Dans la section suivante, l'enquête Pristine, l'une des enquêtes les plus efficaces dans la recherche des étoiles les plus pauvres en métaux, sera décrite en détail.

0.2 La chasse aux étoiles les plus pauvres en métal avec l'enquête Pristine

Le relevé Pristine (Starkenburg et al., 2017b) est à la recherche des étoiles les plus pauvres en métal dans la Voie lactée. Il s'agit d'un relevé photométrique basé sur un filtre à bande étroite centré sur le doublet Ca H&K, un indicateur de la métallicité. Le filtre Pristine est monté sur l'instrument MegaCam du télescope Canada-France-Hawaii (CFHT), et regarde donc vers le ciel du Nord. Le relevé Pristine a observé le ciel et a couvert jusqu'à ~ 5000 deg^2. La projection de l'empreinte primitive ainsi que la carte de la Voie lactée observée sont présentées sur la figure 0.5.

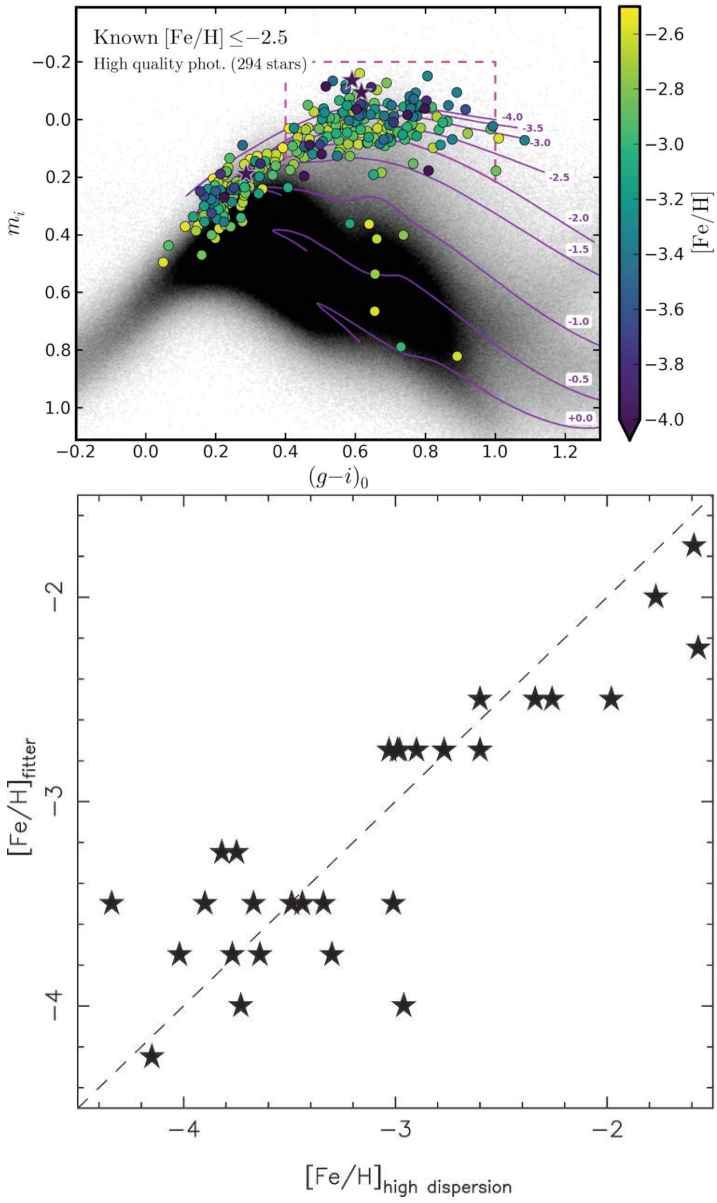

La découverte d'étoiles très pauvres en métaux grâce à la photométrie à bande étroite est très efficace pour diverses raisons. Il n'est pas nécessaire de présélectionner les cibles, tous les objets d'un champ de vision sont observés (modulo quelques trous de puce). De plus, le temps d'intégration est beaucoup plus court que celui des méthodes spectroscopiques, et de bonnes conditions météorologiques ne sont pas nécessaires.

La dépendance de la largeur équivalente de Ca H&K à la gravité de surface est beaucoup plus faible dans le régime très pauvre en métaux que pour les étoiles riches en métaux. Par conséquent, le doublet de Ca peut être utilisé comme un bon estimateur de la métallicité pour ces étoiles vierges. La figure 0.6 montre le comportement des raies Ca H&K des spectres synthétiques en fonction de la température effective, de la gravité superficielle et de la température. Plus la métallicité est élevée, plus les raies d'absorption du Ca H&K sont larges.

Comme le montre le panneau inférieur de la figure 0.6, dans la région spectrale autour des raies Ca H&K, les bandes C et N peuvent être présentes et responsables d'affecter la mesure de la métallicité. Cependant, il a été démontré (Starkenburg et al., 2017b), que le filtre Pristine est si étroit que les métallicités photométriques inférées sont beaucoup

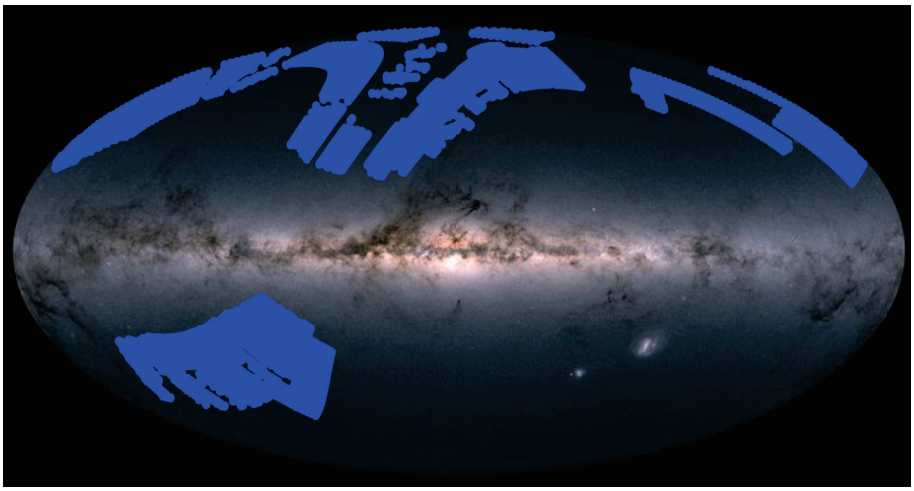

Figure 0.5: L'empreinte de pas vierge. L'empreinte de l'enquête Pristine (points bleus) est superposée à la carte Galaxy fournie par le Gaia Data Processing and Analysis Consortium (DPAC). Le relevé Pristine vise les étoiles les plus pauvres en métal dans la direction du halo de la Voie lactée. Pour le DPAC Gaia, le crédit est à : A. Moitinho / A. F. Silva / M. Barros / C. Barata, University of Lisbon, Portugal; H. Savietto, Fork Research, Portugal.

moins biaisées par les bandes de carbone et d'azote que d'autres filtres à bande plus large (e.g., le filtre v du SkyMapper Southern Survey Da Costa et al., 2019). Toutefois, une analyse plus quantitative de la dépendance et du biais du filtre Carbon in Pristine est en cours d'élaboration.

L'étalonnage de la métallicité photométrique

Afin de mesurer les métallicités photométriques, le filtre Pristine est couplé à la photométrie à large bande (e.g., SDSS, APASS, Gaia DR2 etc.). Une première étude de la faisabilité de la dérivation de la métallicité photométrique a été réalisée en utilisant des spectres synthétiques générés avec les Atmosphères Modèles en schéma radiatif et convectif (MARCS, Gustafsson et al., 2008) et TURBOSPECTRUM (Plez, 2012) et en essayant de trouver un espace colorimétrique capable de démêler les étoiles en fonction de leur métallicité. Ce diagramme est présenté dans la figure 0.7. L'axe horizontal, la couleur $(g - i)$ du SDSS (York et al., 2000), est sensible à la température, tandis que l'axe vertical, sensible aux raies d'absorption, est composé d'une combinaison du filtre Ca H&K, du filtre SDSS g, et d'un multiple de $(g - i)$. Comme le montre le panneau gauche de la figure 0.7, les étoiles synthétiques très pauvres en métal sont bien séparées de leur homologue riche en métal. De plus, l'étalonnage de la métallicité dans le régime très pauvre en métaux à température effective fixe dépend faiblement de la gravité de la surface par rapport aux étoiles synthétiques plus riches en métaux.

Ensuite, une calibration avec des objets réels observés au TCFH avec la MegaCam a été effectuée en sélectionnant des étoiles chevauchant l'empreinte du SDSS. Pour cette étape, les étoiles sélectionnées comprennent l'échantillon avec la photométrie *ugriz* et les métallicités spectroscopiques mesurées de l'étude SDSS/SEGUE (Yanny et al., 2009; Eisenstein et al., 2011) (voir le panneau droit de la Figure 0.7). Ce dernier est un relevé spectroscopique fournissant des métallicités et des paramètres stellaires issus de la spectroscopie, atteignant un chevauchement d'étoiles d'environ 18000. Pour mieux calibrer

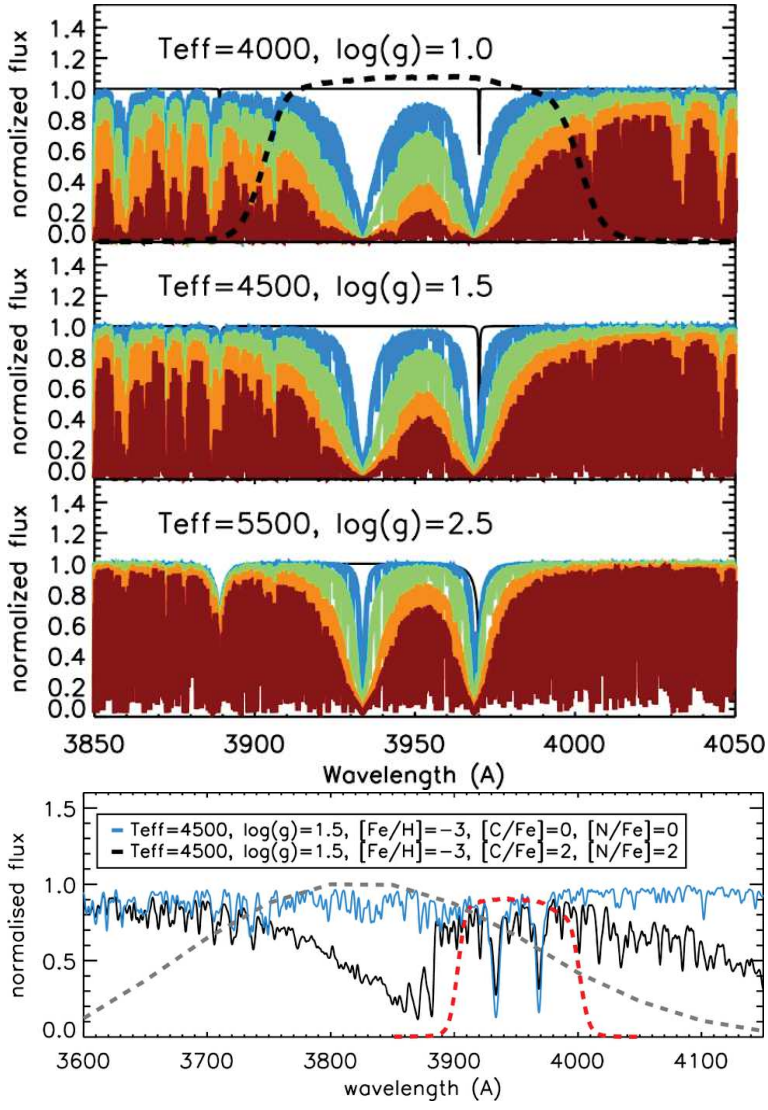

Figure 0.6: Le filtre Pristine Ca H&K. Les trois premiers panneaux : Spectres stellaires synthétiques avec métallicité [Fe/H] = 0.0 (rouge), [Fe/H] = −1.0 (orange), [Fe/H] = −2.0 (vert), [Fe/H] = −3.0 (bleu), et sans métaux (noir) pour les étoiles ayant une température effective et une gravité de surface différentes. Dans le panneau supérieur, le filtre Pristine est marqué d'une ligne pointillée. Panneau inférieur : Comparaison du filtre Pristine (rouge) et du filtre SkyMapper v (gris). Deux spectres synthétiques d'étoiles extrêmement pauvres en métal, à la même température effective et à la même gravité de surface, mais avec un renforcement différent du carbone et de l'azote, ont été surreprésentés. L'enrichissement du carbone et de l'azote produit deux bandes d'absorption visibles dans le spectre noir. Le filtre Pristine, avec sa conception étroite, est beaucoup moins biaisé par ces caractéristiques d'absorption qu'un filtre v plus large. Figure tirée de Starkenburg et al. (2017b).

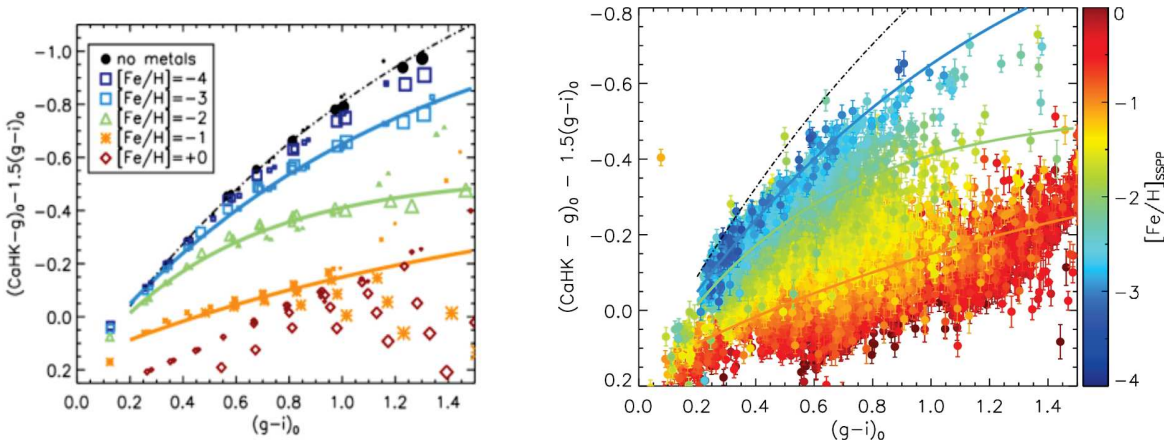

Figure 0.7: Le diagramme de couleur Pristine. Panneau de gauche : Photométrie extraite de spectres synthétiques stellaires à différentes métallicités, températures effectives et gravités de surface dans le diagramme couleur-propre. Panneau de droite : Chevauchement des étoiles dans l'empreinte primitive et SDSS/SEGUE dans le diagramme couleur primitive. Dans les deux panneaux, les lignes pleines représentent l'ajustement de la courbe de la métallicité photométrique codée en couleur comme marqueurs. La couleur $(g-i)$ est une approximation de la température effective, tandis que l'axe vertical est un indicateur de la métallicité. Figure tirée de Starkenburg et al. (2017b).

les métallités photométriques Pristine, plusieurs étapes de nettoyage sont appliquées à l'échantillon SDSS/SEGUE comme décrit dans Starkenburg et al. (2017b). La première étape consiste à éliminer les étoiles présentant de grandes incertitudes sur la métallicité, δ[Fe/H] $\geq$ 0.2, et sur la vitesse radiale, $\delta v_r \geq 10\,\mathrm{km\,s^{-1}}$. Une deuxième coupe a été appliquée aux étoiles dont le rapport signal/bruit est inférieur à 25 dans la gamme spectrale $[4000, 8000]$. Ensuite, les sources non ponctuelles identifiées par le SDSS et par le pipeline de la Cambridge Astronomical Survey Unit (CASU, Irwin & Lewis, 2001) ont été retirées de l'échantillon du SDSS/SEGUE afin d'améliorer l'étalonnage de la métallicité des couleurs vierges. Une suppression des objets variables présents dans le Pan-STARRS1 (Chambers et al., 2016) est nécessaire pour un meilleur calibrage. Les naines blanches contaminent également l'échantillon, c'est pourquoi une coupe photométrique a été appliquée pour éliminer ces objets dégénérés, en sélectionnant des étoiles avec un mag $(u-g)_0 \geq 0.6$. À l'ère des grandes enquêtes sur le ciel, il est possible de croiser les données entre les différentes enquêtes et de récupérer facilement des informations sur la nature des cibles, et, par conséquent, le retrait des contaminants de la liste des candidats pauvres en métaux est beaucoup plus efficace que par le passé. À titre de comparaison, dans les années de l'enquête HK, la majorité des candidats pauvres en métaux observés étaient des contaminants, tels que des étoiles chaudes, des variables et des objets cataclysmiques, des naines blanches, des étoiles de lignes d'émission, etc.

Maintenant que l'échantillon est filtré, l'espace colorimétrique de la figure 0.7 est pixélisé avec une largeur de 0,025 mag. Comme décrit dans Starkenburg et al. (2017b), pour chaque case ou pixel, une moyenne de la métallicité avec un écrêtage de 2σ est effectuée. Cette dernière procédure est nécessaire pour mieux éliminer les éventuels contaminants encore présents après les étapes de nettoyage précédentes. Comme les étoiles extrêmement pauvres en métal sont des objets rares, certaines régions du diagramme de couleur Pristine ne sont pas peuplées. Par conséquent, la métallicité photométrique des

pixels vides a été mise à égalité avec les bacs les plus proches. Selon Starkenburg et al. (2017b), les métallicités photométriques produites par la calibration SDSS peuvent atteindre une précision de ~ 0.2 dex jusqu'au régime extrêmement pauvre en métal, alors que la calibration commence à saturer dans le régime ultra pauvre en métal. Ce dernier point n'implique pas l'échec de l'étude Pristine dans la découverte d'étoiles extrêmement pauvres en métaux (voir Section 0.1), alors qu'il suggère un étalonnage sous-optimal à ce régime de métallicité. Une fois l'espace Pristine calibré et les métallicités photométriques calculées sur une empreinte de ~ 5000 deg^2 (voir la figure 0.5), alors les candidats les plus prometteurs ont été suivis par spectroscopie.

Le suivi spectroscopique

Une fois que les étoiles de l'empreinte primitive sont observées avec le filtre Ca H&K et qu'une métallicité photométrique leur a été attribuée, les étoiles les plus pauvres en métal sont suivies par spectroscopie avec des spectrographes à basse, moyenne ou haute résolution, selon leur magnitude. Les objets plus fins sont suivis spectroscopiquement avec des spectrographes à basse et moyenne résolution. Alors que les spectres des cibles brillantes sont acquis avec des installations à haute résolution. Par exemple, ces dernières cibles ont été observées au CFHT avec ESPaDOnS, au VLT avec UVES, au OHP avec SOPHIE, et au CAHA avec CAFÉ puis analysées par Caffau et al. (2017), Bonifacio et al. (2019) (voir annexe **??**), Venn et al. (2020) (voir annexe **??**), et Caffau et al. (2020).

Aguado et al. (2019) montrent les résultats d'une campagne spectroscopique à moyenne résolution de 3 ans avec un échantillon de 1007 candidats très pauvres en métaux. Les étoiles ont été observées, au moins avec un rapport signal/bruit d'environ 25, avec IDS ($R \sim 3300$) au télescope Isaac Newton, avec ISIS ($R \sim 2400$) au télescope William Herschel, et avec EFOSC2 ($R \sim 900$) au télescope New Technology. Les spectres ont été analysés à l'aide de `FERRE` (Allende Prieto et al., 2006), fournissant la métallicité et l'abondance du carbone.

En définissant le taux de réussite comme le rapport entre le nombre d'étoiles avec des [Fe/H] spectroscopiques en dessous d'une certaine valeur, $N([\mathrm{Fe/H}]_{spec} < X)$, et le nombre d'étoiles avec des [Fe/H] photométriques en dessous de la même valeur, Youakim et al. (2017) et Aguado et al. (2019) montrent que le taux de réussite de l'étude Pristine est de 23 per cent pour [Fe/H] ≤ -3.0, et 56 pour cent pour [Fe/H] ≤ -2.5. La comparaison entre la métallicité photométrique et spectroscopique des étoiles présentées dans Aguado et al. (2019) est illustrée sur la figure 0.8.

Ensuite, à partir d'une première investigation spectroscopique, les étoiles pauvres en métaux les plus prometteuses sont observées à l'aide de spectrographes à haute résolution, comme dans le cas de Pristine_221.8781 + 9.7844 (Starkenburg et al., 2018) décrit dans la sous-section suivante.

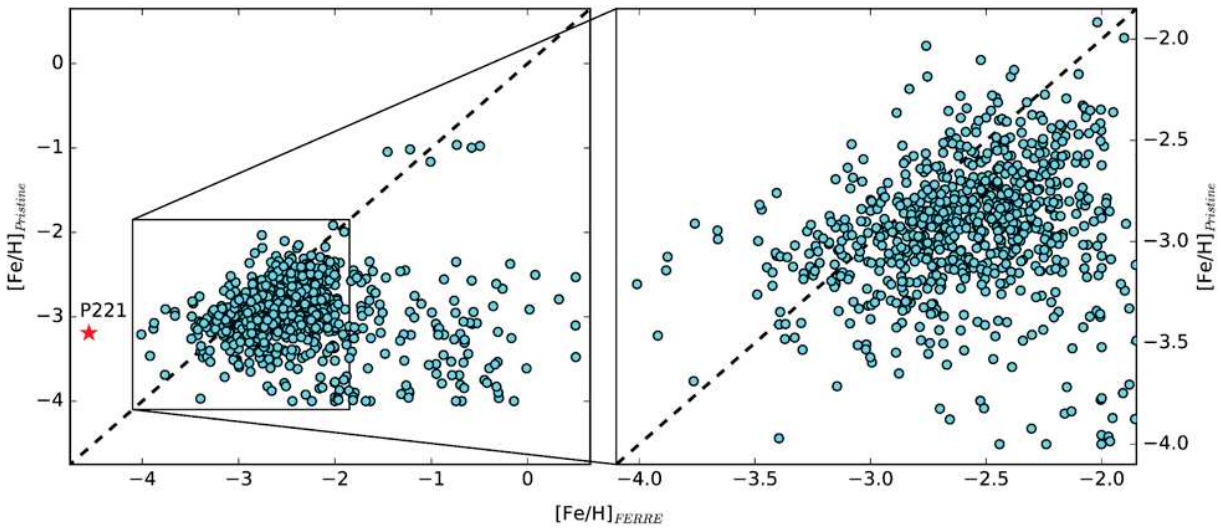

Figure 0.8: Métallicité photométrique vs. spectroscopique de Aguado et al. (2019). Les métallicités spectroscopiques déduites avec FERRE sur l'axe horizontal sont comparées à la métallicité photométrique de Pristine pour l'échantillon de 1007 candidats très pauvres en métaux. Le panneau de droite est un zoom sur la région la plus fréquentée du panneau de gauche. Pristine_221.8781 + 9.7844, une étoile ultra pauvre en métal découverte par la collaboration Pristine (voir Section 0.1), est marquée d'une étoile. Cette comparaison montre la grande efficacité de l'étude Pristine dans la sélection d'étoiles très pauvres en métaux par photométrie.

One of the most metal-poor star: Pristine_221.8781 + 9.7844

Comme décrit précédemment, l'enquête Pristine est à la recherche des étoiles les plus pauvres en métal de la Voie lactée. La découverte des étoiles les plus pauvres en métaux peut également être instructive pour mieux comprendre les mécanismes qui ont produit la quantité observable d'éléments dans les étoiles, à partir d'un mélange d'hydrogène, d'hélium et de lithium au début de l'Univers. L'étude de Pristine a permis de découvrir jusqu'à présent une étoile dans le régime ultra pauvre en métaux ([Fe/H] ≤ -4.0), appelée Pristine_221.8781 + 9.7844 (Starkenburg et al., 2018). L'étoile a été suivie par spectroscopie à moyenne résolution avec le WHT en utilisant ISIS (R$\sim$ 2400) et à haute résolution à l'ESO/Very Large Telescope avec UVES (R$\sim$ 30000). L'analyse des spectres à haute résolution a été réalisée à l'aide de quatre techniques différentes et indépendantes afin de mieux quantifier les différentes sources d'incertitudes et de systématique, et de fournir des mesures robustes des abondances chimiques, cruciales dans ce régime de métallicité. Très brièvement, les méthodes consistent en l'utilisation de FERRE (Allende Prieto et al., 2006), of MyGIsFOS (Sbordone et al., 2014), deux codes qui s'ajustent aux lignes spectrales données par une grille stellaire de spectres synthétiques. Le troisième et le quatrième sont DAOSPEC (Stetson & Pancino, 2008) et IRAF (Tody, 1986, 1993), qui utilisent l'approche classique de largeur équivalente. Alors que l'analyse des spectres à moyenne résolution a été faite en utilisant uniquement FERRE.

Dans le régime ultra pauvre en métaux, l'estimation des paramètres et des abondances stellaires est un problème difficile et, même avec des spectres à haute résolution, il n'est pas banal de briser la dégénérescence naine/géante. En anticipant sur la section 0.2, grâce à la parallaxe fournie par Gaia DR2, il a été possible de briser la dégénérescence susmentionnée pour Pristine_221.8781 + 9.7844. L'inférence de la dis-

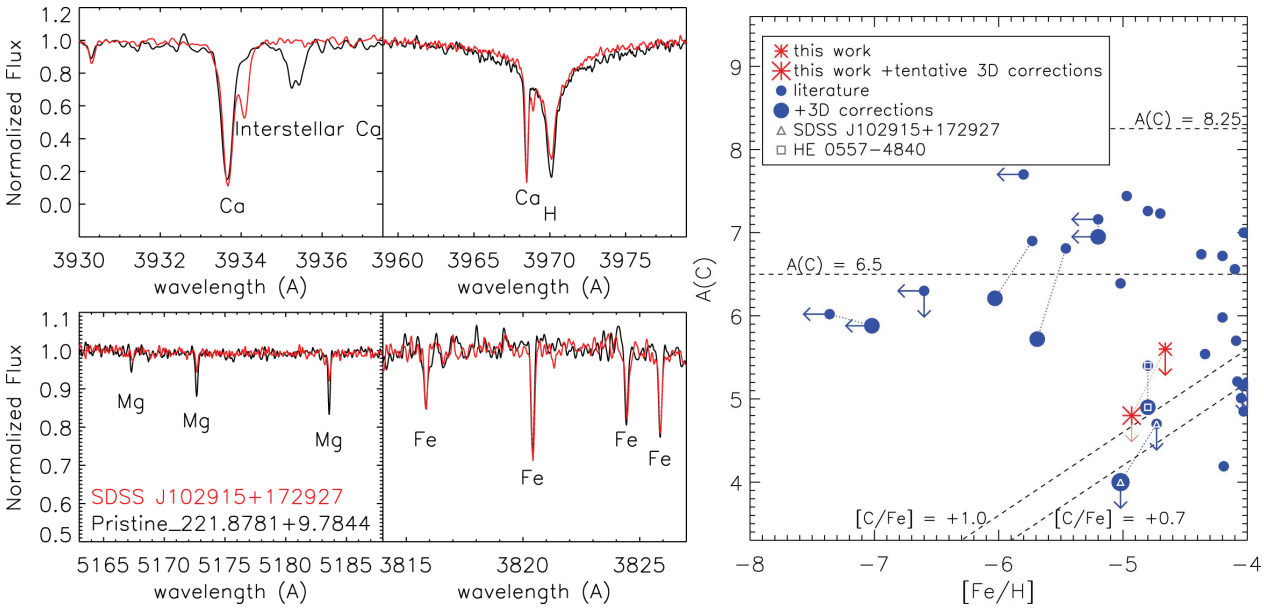

Figure 0.9: Pristine_221.8781+9.7844 contre d'autres étoiles UMP. Panneaux de gauche : comparaison entre les spectres de Pristine_221.8781+9.7844 (ligne noire) et de l'étoile de Caffau (SDSS J102915+172927, ligne rouge). Des exemples de lignes de fer, de magnésium et de calcium sont présentés. Ces panneaux montrent clairement la similarité entre les deux étoiles, et la nature ultra pauvre en métal de Pristine_221.8781 + 9.7844. Panneau de droite : Abondance de carbone vs. [Fe/H] pour les UMPs. Des corrections 3D provisoires de l'analyse spectroscopique ont été fournies pour un sous-échantillon de l'UMP (Starkenburg et al., 2018). La faible abondance de carbone de Pristine_221.8781+9.7844, ainsi que son faible [Fe/H], place cette étoile parmi les plus pauvres en métaux connus. Tous les panneaux sont de Starkenburg et al. (2018).

tance de la parallaxe suggère que l'étoile ne peut pas être une naine, comme le montre également Sestito et al. (2019). Avec cette information, l'analyse spectroscopique a trouvé que Pristine_221.8781 + 9.7844 a [Fe/H] $= -4.66 \pm 0.13$, avec une limite supérieure pour l'abondance de carbone de $A(C) = 5.6$, une faible abondance de carbone très inhabituelle pour ce régime de métallicité (Starkenburg et al., 2018). La combinaison de ces valeurs place cette étoile comme l'une des plus pauvres en métal connues, tout comme l'étoile de Caffau (SDSS J102915+172927, Caffau et al., 2011). La comparaison entre les spectres des deux étoiles est présentée sur les panneaux de gauche de la figure 0.9. Le panneau de droite de la figure 0.9 indique l'abondance du carbone en fonction de la métallicité pour les étoiles ultra pauvres en métaux, comme le montrent les travaux de Starkenburg et al. (2018). A noter que dans ce régime particulier pauvre en métaux, la métallicité totale peut différer de l'abondance du Fer ([Fe/H]), et donc d'une étoile, telle que Pristine_221.8781 + 9.7844 ([Fe/H] $= -4.66$), peut être plus pauvre en métaux qu'une étoile à [Fe/H] $\leq -6,5$, i.e., SMSS $J031300.36-670839.3$ (Nordlander et al., 2017). Dans le régime UMP, la majorité des étoiles est riche en carbone, et de nouvelles découvertes telles que Pristine_221.8781+9.7844 peuvent mettre plus de contraintes sur les multiples canaux de formation des éléments et des mécanismes de refroidissement dans l'Univers primitif.

Autres projets dans le cadre de l'enquête Pristine

L'enquête Pristine est très efficace pour trouver de nouvelles étoiles très pauvres en métaux, et elle permet d'étudier différentes régions de la Galaxie. Les résultats scientifiques de l'étude Pristine sont donc très larges. Comme le montre Longeard et al. (2018, 2020), l'étude Pristine est très efficace pour trouver des membres possibles de galaxies naines, puisqu'il est possible de sélectionner efficacement les membres candidats en utilisant les métallicités photométriques fiables. Les galaxies naines sont intéressantes pour diverses raisons, nous pouvons en apprendre davantage sur la partie de faible masse de la formation des galaxies (e.g., Koposov et al., 2009), elles sont des endroits idéaux pour tester le modèle cosmologique standard ΛCDM puisqu'on pense qu'elles sont dominées par la matière noire (e.g., Bullock & Boylan-Kolchin, 2017), et la compréhension de leur formation pourrait également éclairer la formation d'autres structures, par exemple les amas globulaires (e.g., Willman & Strader, 2012).

En outre, Arentsen et al. (2020) a montré que l'étude Pristine permettra de mieux voir la queue très pauvre en métal du renflement de la Voie lactée, qu'il est important de mieux démêler les multiples structures, telles que le halo intérieur, la barre et le disque, qui se chevauchent dans les très rares kpc au centre de la Voie lactée et de les relier à la formation et à l'histoire de l'évolution de la Galaxie.

Starkenburg et al. (2019) a souligné que le couplage du filtre CaH&K vierge et des filtres ugr du SDSS peut également être utilisé comme un outil puissant pour cartographier le halo extérieur de la Voie lactée en trouvant les étoiles de la branche horizontale bleue (BHBs). Les BHB sont d'excellentes bougies standard, et avec leurs distances fiables, elles sont idéales pour limiter la taille de la galaxie et son potentiel gravitationnel, qui est strictement lié à la teneur en matière noire, et aussi pour mieux identifier les sous-structures, telles que les cours d'eau. D'après Starkenburg et al. (2019), il s'avère que le filtre Pristine CaH&K couplé à la photométrie à large bande, en particulier avec le filtre u, est un diagnostic idéal pour discerner les BHB des étoiles bleues traînantes (BS), des objets plus faibles et plus compacts qui peuvent contaminer l'échantillon de candidats BHB.

Youakim et al. (2020) a étudié la fonction de distribution de la métallicité (MDF) du halo jusqu'au régime EMP, ce qui est très utile pour disséquer les structures galactiques à différents rayons, et aussi pour avoir une estimation du nombre d'amas globulaires par rapport à la population du champ. Ce dernier résultat montre que l'absence d'amas globulaires dans le régime extrêmement pauvre en métaux n'est pas due à un sous-échantillonnage statistique, mais indique plutôt un mécanisme physique probable qui empêche les GC extrêmement pauvres en métaux de se former ou de survivre.

0.3 La révolution de Gaia DR2

Le satellite Gaia est une mission de l'Agence spatiale européenne (ESA) dont l'objectif est de créer, pour la toute première fois, une carte multidimensionnelle précise de la Voie lactée constituée de plus d'un milliard de sources. Grâce aux données astrométriques et photométriques de ce satellite, il est possible de mieux cerner les propriétés physiques de la Galaxie, notamment grâce à la synergie des grands relevés spectroscopiques qui fournissent les abondances chimiques des étoiles. Les études chimiodynamiques peuvent fournir de précieuses indications non seulement sur la composition actuelle de la Voie lactée, mais elles permettraient de dévoiler la formation et l'évolution de la Galaxie.

Le télescope Gaia, placé au deuxième point lagrangien de l'orbite Soleil-Terre, balaye tout le ciel en mesurant la photométrie, l'astrométrie et en déduisant les paramètres stellaires des objets célestes, tels que les astéroïdes du système solaire, les étoiles de la Voie lactée, et il est capable d'atteindre des sources extragalactiques, les quasars e.g., Dans ce travail, la deuxième publication de données de Gaia (ci-après Gaia DR2) a été utilisée pour déduire la distance et les paramètres orbitaux d'étoiles très pauvres en métal, en utilisant à la fois les informations photométriques et astrométriques du catalogue Gaia.

Contenu de Gaia DR2

Le catalogue Gaia DR2 a été construit à partir des données collectées entre le 25 juillet 2014 et le 23 mai 2016, couvrant une période de 22 mois d'observations et il a été publié le 25 avril 2018. Les principaux paramètres utilisés dans le cadre de cette thèse sont la position sur le ciel, l'ascension droite (α) et la déclinaison (δ), la parallaxe astrométrique (ϖ), les mouvements propres en ascension droite et en déclinaison (μ_α, μ_δ), la photométrie (G, BP, et RP), et toutes les incertitudes sur ces quantités. Le tableau 0.3 contient le nombre de sources pour lesquelles Gaia DR2 fournit les paramètres, et il montre également une comparaison utile avec la première publication de données (Gaia DR1) afin de comprendre l'amélioration entre les deux publications. Par exemple, dans Gaia DR2, le nombre de sources avec des coordonnées mesurées, des mouvements propres et une parallaxe (sources à 5 paramètres) a augmenté d'un facteur 650 par rapport à Gaia DR1. Et pour seulement 21.3 pour cent des sources, la parallaxe et le mouvement propre ne sont pas fournis, contre 99.8 pour cent pour Gaia DR1. Comme nouveaux produits dans Gaia DR2, qui sont absents dans Gaia DR1, il y a la photométrie dans les bandes BP et RP, la température effective ($T_{\rm eff}$), l'extinction et le rougissement (A_G et E(BP−RP)), la vitesse radiale entre autres, comme indiqué dans le tableau 0.3. Toutes les quantités et informations extractibles de Gaia DR2, en particulier lorsqu'elles sont combinées avec des données provenant d'enquêtes au sol, contribuent à améliorer notre connaissance de la Voie lactée. Il est maintenant possible de disséquer les différentes structures qui composent la Galaxie, c'est-à-dire le disque mince et épais, le halo et le renflement, de découvrir des structures accrétées, de construire une carte 3D de l'extinction, de mieux comprendre le potentiel gravitationnel de la Voie lactée et le contenu en matière noire, de mieux comprendre l'évolution stellaire et la physique qui lui est liée, de recenser plus largement les petits objets du système solaire, etc. De plus, les grandes études peuvent bénéficier de Gaia en améliorant leur sélection grâce à des informations photométriques et astrométriques précises.

Gaia DR2 photométrie

Gaia DR2 (Evans et al., 2018) fournit la bande photométrique G pour toutes les sources, tandis que pour $\sim$ 80 pour cent d'entre elles, la photométrie est également répertoriée dans les bandes BP et RP. Le panneau supérieur gauche de la figure 0.10 montre la transmissivité des trois bandes de Gaia en fonction de la longueur d'onde. Comme indiqué, la bande G est un large filtre couvrant le domaine spectral entre $[330, 1050]$ nm, tandis que les bandes BP et RP couvrent respectivement $[330, 680]$ nm et $[630, 1050]$ nm. Une combinaison de ces bandes peut être utilisée comme indicateur de température (c'est-à-dire BP − RP). Les autres panneaux de la figure 0.10 montrent l'incertitude typique dans les trois bandes Gaia en fonction de l'amplitude. Dans la bande G, les incertitudes typiques

Table 0.3: Résultat de Gaia DR2 contre DR1.

Parameters	Gaia DR2	Gaia DR1
Total number of sources	1,692,919,135	1,142,679,769
Number of 5-parameters sources $(\alpha, \delta, \mu_\alpha, \mu_\delta, \varpi)$	1,331,909,727	2,057,050
Number of 2-parameters only sources (α, δ)	361,009,408	1,140,622,719
Sources with mean G magnitude	1,692,919,135	1,142,679,769
Sources with mean BP-band photometry	1,381,964,755	0
Sources with mean RP-band photometry	1,383,551,713	0
Sources with radial velocities	7,224,631	0
Variable sources	550,737	3,194
Known asteroids with epoch data	14,099	0
Gaia-CRF sources	556,869	2,191
Effective temperatures (T_{eff})	161,497,595	0
Extinction (A_G) and reddening (E(BP−RP))	87,733,672	0
Sources with radius and luminosity	76,956,778	0

dans la région lumineuse $G \sim 13$ mag est d'environ 1 millimag, alors qu'elle atteint quelques dizaines de millimag à $G \sim 20$ mag. Dans les bandes BP et RP, les incertitudes typiques dans la région lumineuse $G \sim 13$ mag est d'environ quelques millimètres, alors qu'elle atteint ~ 200 millimètre à $G \sim 20$ mag.

Gaia DR2 solutions astrométriques

Gaia DR2 fournit cinq paramètres astrométriques tels que la position dans le ciel (α, δ), le mouvement propre (μ_α, μ_δ), et la parallaxe (ϖ) pour ~ 79 pour cent des sources comme indiqué par Lindegren et al. (2018). Tous ces paramètres astrométriques sont les ingrédients clés pour déduire les distances et les orbites des étoiles.

Grâce à la précision de Gaia DR2, nous vivons aujourd'hui une époque où l'incertitude des données est dominée par la systématique et les décalages, en particulier pour les cibles brillantes. Par conséquent, lors de la dérivation d'autres grandeurs physiques, telles que la distance et les paramètres orbitaux, la systématique et les décalages des solutions astrométriques doivent être pris en compte. Un bon banc d'essai pour le décalage de la parallaxe consiste à mesurer cette quantité pour un échantillon de quasars. Les quasars sont des objets extragalactiques et éloignés, ce qui signifie que la parallaxe doit être cohérente avec zéro. Dans le cas de la systématique et des décalages, nous devons nous attendre à ce que la parallaxe, par exemple, soit distribuée autour de la valeur du décalage, en incluant également les valeurs négatives. Lindegren et al. (2018) a déduit que le décalage des quasars était de $\varpi_0 = -0.029\,\mathrm{mas}$.

Une autre question à prendre en compte est celle des éventuelles valeurs négatives de la parallaxe, c'est pourquoi on ne se contente pas d'inverser la parallaxe pour calculer la distance. Comme le montre Bailer-Jones (2015); Bailer-Jones et al. (2018), même si la mesure de la parallaxe a une distribution gaussienne (voir le panneau gauche de la figure 0.11), lorsque nous la représentons en fonction de la distance, la distribution obtenue n'est plus symétrique (voir le panneau droit de la figure 0.11), cela est clairement visible lorsque l'incertitude relative est supérieure à 20 pour cent, $\sigma_\varpi/\varpi > 0.2$. Pour cette raison, il n'est pas conseillé d'inverser la parallaxe, mais une approche bayésienne

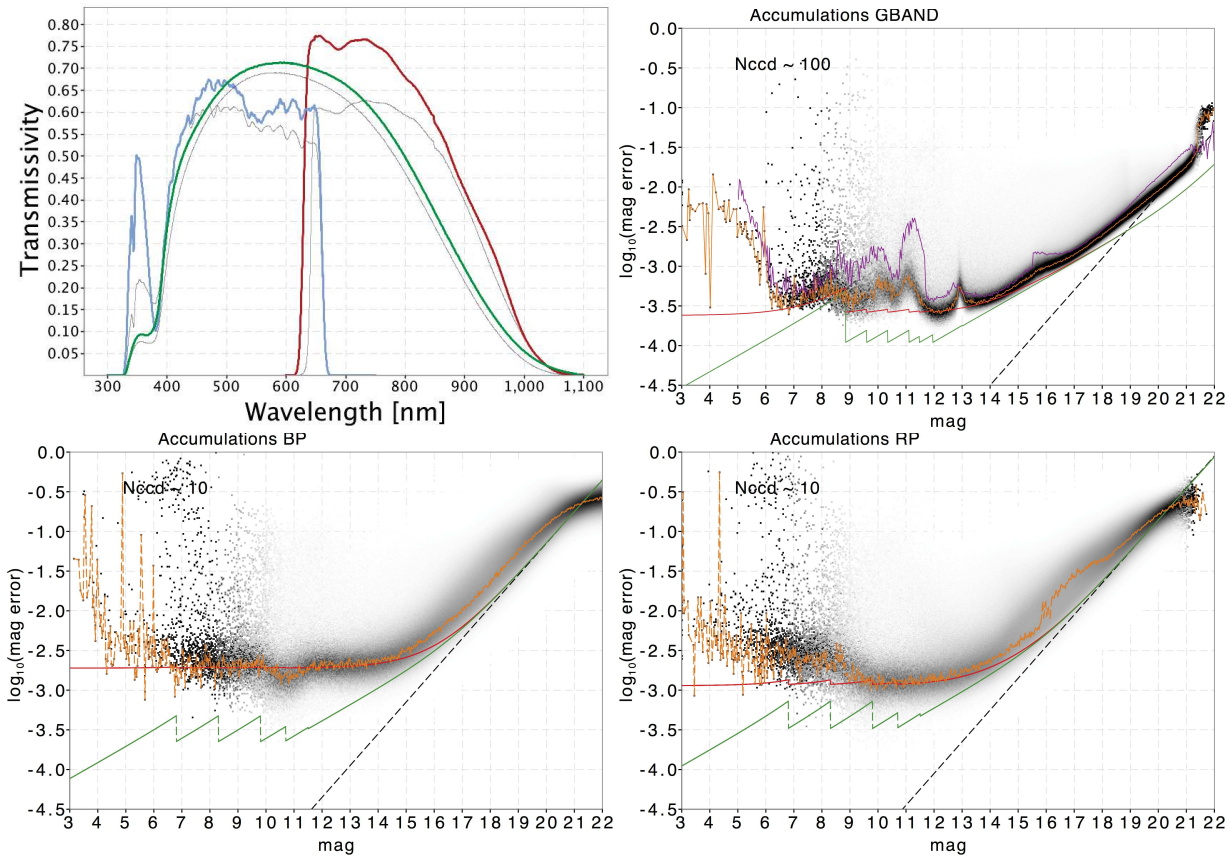

Figure 0.10: Propriétés des passeports Gaia. Panneau supérieur gauche : la courbe de transmissivité observée pour les filtres G (orange), BP (bleu) et RP (rouge) est représentée en fonction de la longueur d'onde. Les lignes grises indiquent l'espérance théorique de la courbe de transmissivité. Panneaux supérieur droit et inférieur : l'erreur sur les filtres Gaia en fonction de la magnitude. Les erreurs sont indiquées en échelle logarithmique. Figure tirée de Evans et al. (2018).

est obligatoire.

Une telle approche bayésienne est décrite en détail dans Bailer-Jones (2015), et considère que la fonction de distribution de probabilité PDF, ou le $P(r)$ postérieur, a une étoile à une certaine distance étant donné la parallaxe. La postérieure est le produit entre la probabilité, c'est-à-dire la probabilité d'avoir cette parallaxe étant donné un modèle et une incertitude sur la parallaxe $L(\varpi|\sigma_\varpi, M)$, et la antérieure, c'est-à-dire la probabilité d'avoir un certain modèle $P(M)$. Le précédent sur le modèle, par exemple, pourrait prendre en compte la distribution attendue des étoiles dans la Voie lactée, et il reflète nos connaissances et notre ignorance sur un processus physique. Une approche bayésienne pour déduire les distances a été utilisée dans ce travail (voir les chapitres 2 et 3), pour nos besoins, le postérieur prend également en compte les données photométriques et de parallaxe de Gaia DR2 selon toute vraisemblance, tandis que les connaissances sur la répartition par âge des étoiles très pauvres en métal ainsi que la répartition de la densité des étoiles dans la Voie lactée ont été insérées dans le précédent. L'utilisation de ces données photométriques et astrométriques dans un contexte bayésien permet de mieux contraindre la distance, en particulier dans les cas où la parallaxe a une valeur négative ou que son incertitude relative est importante. Inférer la distance avec une méthode précise

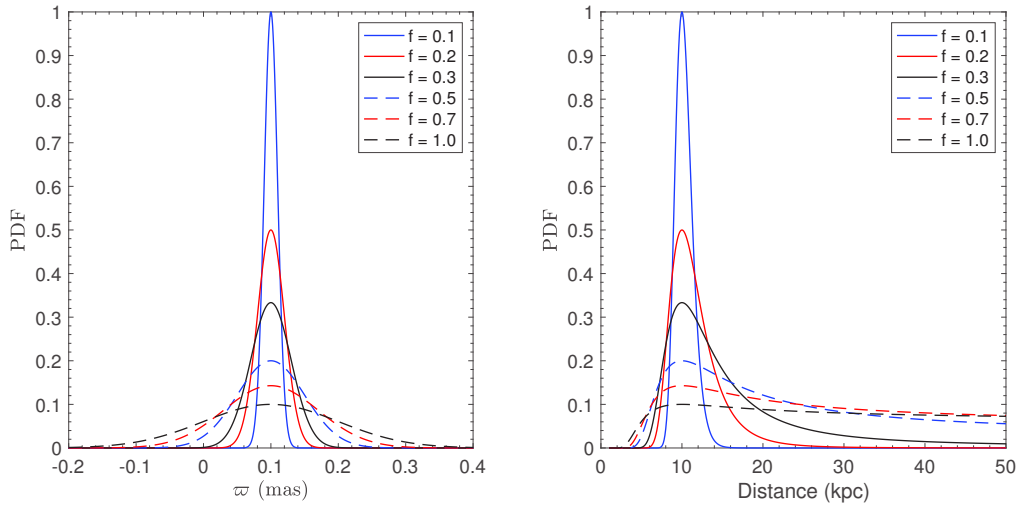

Figure 0.11: Panneau de gauche : Fonction de distribution gaussienne de la parallaxe pour une valeur fixe de $\varpi = 0.1\,\mathrm{mas}$ et différentes valeurs de l'incertitude relative $f = 0.1, 0.2, 0.3, 0.5, 0.7, 1.0$. Panneau de droite : Fonction de distribution de la mesure de la parallaxe en fonction de la distance. Les valeurs de la parallaxe et des incertitudes relatives sont les mêmes que dans le panneau de gauche. Une grande incertitude relative ($f > 0.1$) produit une distribution asymétrique en fonction de la distance. Pour des incertitudes relatives plus élevées, la distribution affiche un comportement plat à l'égard des grandes distances. Figure similaire à Bailer-Jones (2015).

et exacte est essentiel pour mieux comprendre la nature des objets observés, mesurer la température effective et la gravité de surface, et obtenir des paramètres orbitaux fiables.

Les résultats de la révolution

La synergie entre les relevés spectroscopiques au sol et le satellite Gaia produit une décomposition chimico-dynamique sans précédent de la Voie lactée. Par exemple, il est possible d'identifier de nouvelles structures dans la Voie lactée et des satellites accrétés dans notre Galaxie. Après la galaxie naine du Sagittaire, l'événement d'accrétion le plus célèbre est probablement celui appelé Gaia-Enceladus-Sausage (GES), un satellite accrété comparable en taille et en masse au Petit Nuage de Magellan ($M \sim 6 \times 10^8\,\mathrm{M}_\odot$ Belokurov et al., 2018; Haywood et al., 2018; Helmi et al., 2018). La découverte de cette structure accrétée a commencé avec Gaia DR1, dont Belokurov et al. (2018) a trouvé une structure légèrement rétrograde dans l'espace de vitesse. Helmi et al. (2018), afin de sonder les propriétés cinématiques et chimiques de Gaia-Enceladus-Sausage, a sélectionné des étoiles en commun entre Gaia DR2 (pour la cinématique) et APOGEE (pour la chimie et les vitesses de radail, Abolfathi et al., 2018). L'échantillon d'étoiles analysé habite la sphère d'un rayon de 5 kpc centrée sur le Soleil. Du côté cinématique de l'analyse, Helmi et al. (2018) a trouvé la présence dans le halo intérieur d'une structure avec un mouvement de rotation moyen légèrement rétrograde (voir les panneaux supérieurs de la figure 0.12). Alors que, grâce à l'APOGEE, Helmi et al. (2018) a trouvé une grande dispersion de la métallicité, ce qui signifie que le GES a formé des étoiles en de multiples rafales, et que le $[\alpha/\mathrm{H}]$ de sa queue plus riche en métal est inférieur à celui du disque épais de MW (voir les panneaux inférieurs de la Figure 0.12), impliquant un taux de formation d'étoiles inférieur à celui

du disque épais galactique. D'après le taux de formation des étoiles et la cinématique, Helmi et al. (2018) a trouvé que le progéniteur de GES a une masse de $M \sim 6 \times 10^8\,\mathrm{M}_\odot$ et qu'il a été accrété il y a $8 - 11\,\mathrm{Gyr}$. Avant Gaia, le travail d'identification de nouvelles structures dans la Voie lactée était une tâche difficile, bien que l'indice d'une nouvelle structure, et très probablement liée au GES, ait été détecté par Meza et al. (2005) puis confirmé par Navarro et al. (2011) en utilisant un échantillon hétérogène d'étoiles dans le voisinage solaire. Meza et al. (2005); Navarro et al. (2011) a également proposé que ωCen est un débris de la structure accrétée découverte.

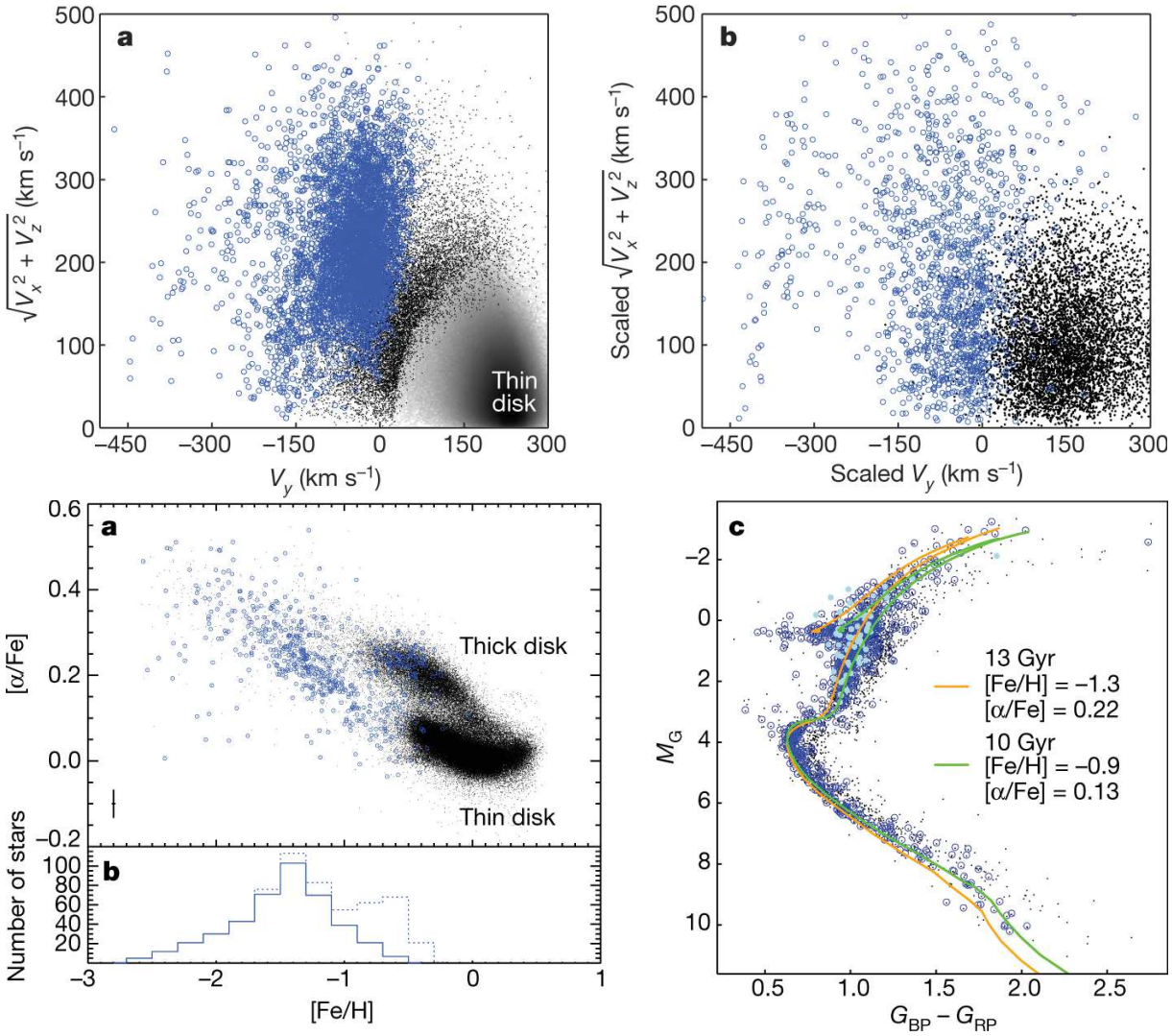

Figure 0.12: Les propriétés chimiodynamiques du Gaia-Enceladus-Sausage (GES) de Helmi et al. (2018). Panneaux supérieurs : espace de vitesse du voisinage solaire, les marqueurs gris indiquent le disque, les étoiles halo sont représentées par des points noirs, tandis que les cercles bleus indiquent la structure GES comme dans Helmi et al. (2018). Le panneau supérieur droit est le même mais en utilisant une simulation qui est capable de reproduire le disque épais et la structure GES accrétée. Panneaux du bas : a) abondance chimique des éléments α en fonction de la métallicité pour le GES (cercles bleus) et le disque+halo (points noirs). A noter, la séparation entre le GES et le disque. Les marqueurs GES dans la région du disque épais sont des contaminants provenant de ce dernier qui ont une cinématique similaire à celle du GES. b) la distribution de la métallicité du GES sans (avec) les contaminants est indiquée par la ligne pleine (pointillés). c) comparaison dans le HRD entre le GES (cercles bleus) et le halo dans le voisinage du Soleil (points noirs), les isochrones pauvres en métaux superposés sont indiqués par des lignes pleines.

Comme second exemple de cette révolution déjà commencée dans l'archéologie galactique, il y a la découverte d'une autre structure accrétée, le soi-disant Gaia-Sequoia (Barbá et al., 2019). Grâce à la synergie entre Gaia DR2, le DECam Plane Survey (DECaPS, Schlafly et al., 2018), et les variables VISTA dans le VLáctea Extended Survey (VVVX, Minniti et al., 2018), Barbá et al. (2019) a analysé les propriétés du Gaia-Sequoia, une grande structure découverte vers le renflement avec un $[\mathrm{Fe/H}] = -1.5 \pm 0.3$. Ils proposent deux scénarios pour la nature de cette structure, le premier est que Gaia-Séquoia est l'un des plus grands amas globulaires de la Voie lactée, avec une taille comparable ou supérieure à ωCen, alternativement la structure observée est le noyau d'une nouvelle galaxie naine plus étendue. Monty et al. (2020) en réanalysant les propriétés chimiodynamiques d'un échantillon de candidats Gaia-Sequoia a trouvé que cette structure peut être cinématiquement divisée en deux sous-groupes, un avec des orbites de faible énergie et un avec une énergie orbitale plus élevée, ce qui signifie que le premier sous-groupe est plus confiné dans la partie intérieure de la galaxie, tandis que le second est plus dispersé dans le halo proche. Gaia-Enceladus-Sausage et Gaia-Sequoia sont tous deux bien résumés et discutés dans Myeong et al. (2019). La figure 0.13 de Monty et al. (2020) montre que les deux structures accrétées habitent deux régions différentes de l'espace d'action (pour une introduction sur l'espace d'action et le vecteur de moment d'action, voir la figure 0.15 et la section 0.2).

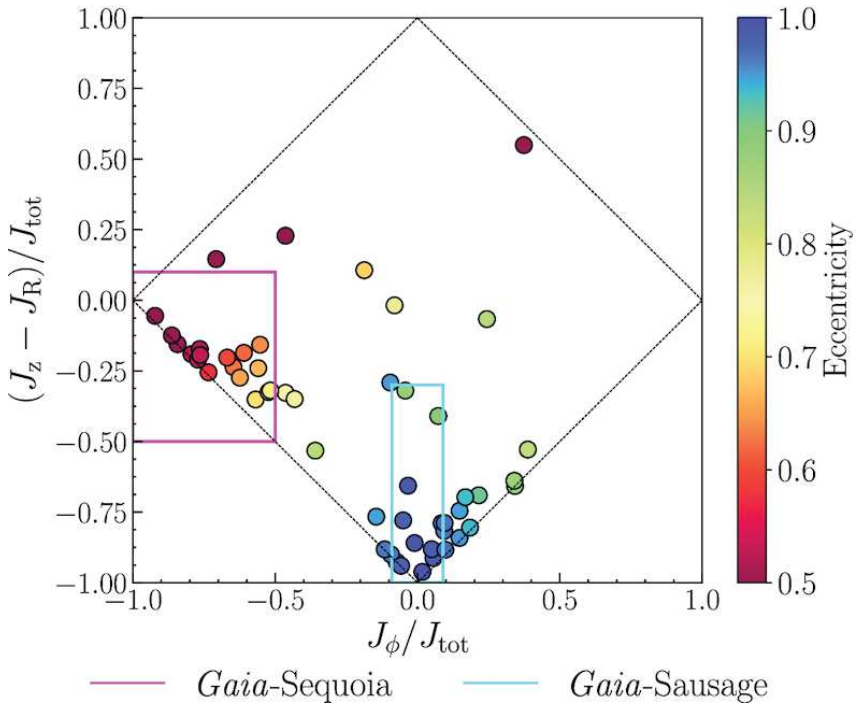

Figure 0.13: Les propriétés dynamiques de Gaia-Enceladus-Sausage et Gaia-Sequoia dans l'espace d'action de Monty et al. (2020). Anticipant la section 0.2, l'espace d'action est utile pour démêler la structure dans la Voie lactée avec une cinématique différente. L'abscisse est une approximation du mouvement de rotation, tandis que l'axe vertical est une approximation du mouvement vertical et radial. Dans l'espace d'action, les deux structures accrétées, Gaia-Enceladus-Sausage (GES, dans la boîte cyan) et Séquoia (dans la boîte magenta), habitent deux régions différentes, ce qui signifie un mouvement différent. GES tourne lentement avec une forte excentricité (> 0.7), tandis que les étoiles du Séquoia ont des orbites de rotation rétrogrades plus élevées et des excentricités plus faibles (< 0.7).

L'astrométrie et la photométrie précises de Gaia DR2 ont également été cruciales dans le développement de nouveaux algorithmes pour trouver efficacement de nouvelles structures. Par exemple, Malhan & Ibata (2018) a développé `STREAMFINDER`, un outil puissant pour détecter dynamiquement les structures de flux stellaires minces et froides cachées dans l'empreinte de Gaia DR2. La découverte de nouvelles structures et la caractérisation de la distribution stellaire du halo peuvent mieux limiter le potentiel de la Voie lactée (Malhan & Ibata, 2019).

L'enquête Pristine rencontre Gaia DR2

Avant Gaia DR2, les candidats pauvres en métaux de l'étude Pristine ont été sélectionnés pour estimer la métallicité photométrique en couplant le filtre Ca HK à bande étroite Pristine sensible à la métallicité avec la photométrie à large bande SDSS. En principe, il est possible de recalibrer la sélection de l'enquête Pristine en utilisant la photométrie Gaia DR2 G, BP et RP, et de créer un nouvel échantillon important de candidats pauvres en métaux. Cet étalonnage est en cours et deux options principales sont sur la table, l'une consiste à utiliser les précieuses informations que la parallaxe de Gaia DR2 peut fournir comme dans Bonifacio et al. (2019) et la seconde consiste à appliquer la même procédure

décrite dans la section 0.1. Le panneau gauche de la figure 0.14 montre la première tentative de calibrage de l'espace Pristine en utilisant les bandes Gaia. L'axe horizontal, $(BP-RP)_0$ est une approximation de la température, tandis que l'axe vertical est sensible à la métallicité. Comme le montre la figure 0.14, la première tentative de calibrage de l'espace Pristine avec Gaia DR2 est prometteuse car les étoiles les plus pauvres en métal sont bien séparées des étoiles plus riches en métal.

Le SDSS a fourni une photométrie exquise se reflétant dans une sélection efficace de candidats très pauvres en métaux, mais limitée à des magnitudes plus faibles que $V \sim 14.5$ mag. Alors qu'avec Gaia DR2, il est maintenant possible d'étendre l'étalonnage de l'espace Pristine vers une magnitude de 10 dans la bande V, où le filtre Ca HK à bande étroite Pristine commence à saturer. Un étalonnage provisoire de l'espace Pristine pour l'exploration des magnitudes lumineuses avant Gaia DR2 a été mis en place en utilisant la photométrie APASS *gri* (Henden et al., 2018). L'utilisation des filtres APASS a abouti à une sélection sous-optimale des étoiles les plus pauvres en métal, clairement améliorée par l'exquise photométrie de Gaia DR2, comme discuté dans Bonifacio et al. (2019) et présenté dans les panneaux de droite de la Figure 0.14.

Les étoiles brillantes sont particulièrement utiles lorsqu'il s'agit de lignes spectrales plus faibles, car nous pouvons les étudier avec une résolution spectroscopique et une précision plus élevées que les objets plus faibles. Ceci est bien décrit dans les documents Bonifacio et al. (2019) et Venn et al. (2020). Avec l'échantillon plus faible d'étoiles pauvres en métaux de l'étude Pristine, nous visons à couvrir tous les environnements de la Galaxie, y compris le halo (e.g., Youakim et al., 2020), le disque (e.g., Sestito et al., 2020a) et le renflement (e.g., Arentsen et al., 2020). Un suivi spectroscopique à haute résolution de ces nouveaux candidats brillants et extrêmement pauvres en métaux, sélectionnés avec Pristine+Gaia DR2, est en cours avec les spectrographes échelle au télescope CAHA (CAFÉ), au CFHT (ESPaDONS), et à GEMINI (GHOST).

Les améliorations apportées par Gaia DR2 ne s'arrêtent pas à la recalibration de la métallicité photométrique primitive vers des magnitudes plus brillantes, mais, grâce aux solutions astrométriques, il est possible d'inférer les paramètres cinématiques de ces objets rares, comme le montrent Sestito et al. (2019, 2020a, voir aussi Chapitres 2 et 3).

Compléter Gaia avec la spectroscopie multi-objets : une fenêtre unique sur les débuts de la galaxie

Les informations exquises fournies par le satellite Gaia peuvent être complétées par de grandes études au sol pour une étude chimiodynamique plus profonde et sans précédent de notre Galaxie. Par exemple, des quantités telles que les abondances chimiques, les paramètres stellaires et la vitesse radiale des objets trop faibles pour le spectromètre RVS de Gaia, peuvent être facilement accessibles par des études au sol. L'un des grands relevés au sol qui jouera un rôle crucial dans l'ologie de l'arche galactique est le WEAVE (WHT Enhanced Area Velocity Explorer, Dalton et al., 2012). WEAVE est basé sur un nouveau spectrographe à fibre multi-objets au télescope WHT et il verra le jour début 2021. WEAVE est divisé en plusieurs sous-enquêtes couvrant différents sujets et observant la Voie lactée et les objets extragalactiques. En ce qui concerne la Voie lactée, WEAVE disséquera le disque stellaire, le halo stellaire, d'autres structures telles que les courants stellaires et les amas. WEAVE étudiera également la queue très pauvre en métal de la Galaxie et les phases mal comprises de l'évolution stellaire, e.g., aux étoiles massives, aux étoiles variables, aux éjecta stellaires, etc. Il effectuera la spectroscopie en champ intégral

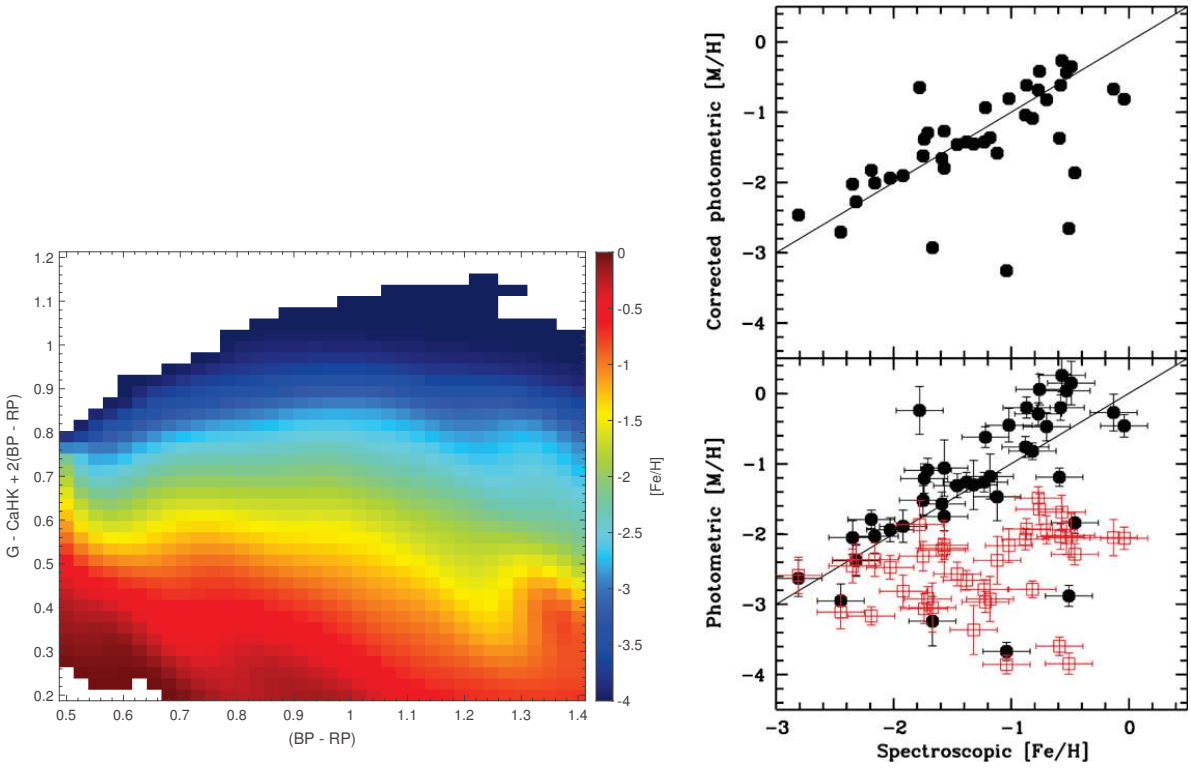

Figure 0.14: Panneau de gauche : L'étalonnage de l'espace primitif avec les bandes Gaia DR2. L'axe horizontal, $(BP - RP)$, est une approximation de la température effective. Plus la couleur est basse, plus la température effective est élevée. L'axe vertical est sensible à la métallicité. L'espace a été pixellisé et dans chaque case, la métallicité médiane a été calculée. La sélection des candidats pauvres en métaux est prometteuse avec la photométrie Gaia, les étoiles les plus pauvres en métaux sont bien séparées de la population plus riche en métaux. Panneaux de droite : Comparaison de la métallicité spectroscopique et de l'inférence photométrique pour les candidats brillants très pauvres en métaux (Bonifacio et al., 2019). Dans le panneau du bas, une comparaison entre l'étalonnage de la métallicité APASS+Pristine en rouge et la métallicité estimée de Gaia DR2+Pristine en noir (Bonifacio et al., 2019). Grâce à Gaia, la détermination de la métallicité photométrique dans la partie brillante de l'enquête Pristine a été largement améliorée par rapport à l'APASS, comme le montre le panneau du bas.

des galaxies proches et des galaxies naines, et il suivra spectroscopiquement les cibles extragalactiques étudiées dans la longueur d'onde radio, comme celles du Low-Frequency Array (LOFAR, van Haarlem et al., 2013).

La synergie entre la sous-enquête de l'Arche Galactique et celle de Pristine est particulièrement intéressante, car elle apporte une multitude de données sur la queue très pauvre en métal de la Voie lactée. Le protocole d'accord entre les deux enquêtes permettra à l'enquête Pristine de sélectionner les cibles les plus pauvres en métaux à observer en utilisant $\sim$ 2 pour cent des fibres de WEAVE. Compte tenu des taux de réussite de l'enquête Pristine dans sa sélection de candidats pauvres en métaux, et de la fonction de fenêtre de WEAVE, Pristine+WEAVE s'attend à découvrir environ $\sim$ 8000 de nouvelles étoiles extrêmement pauvres en métaux dont $\sim$ 100 devraient être ultra pauvres en métaux (Aguado et al., 2019), améliorant le nombre actuel (42 UMPs) de ce dernier et plus rare échantillon. Comme mentionné dans la section 0.1, l'analyse spectroscopique des

étoiles les plus pauvres en métaux est une tâche difficile, c'est pourquoi l'équipe Pristine développe un pipeline ad hoc, bien adapté aux étoiles très pauvres en métaux, pour optimiser l'extraction des informations des spectres WEAVE. L'analyse chimique des spectres Pristine+WEAVE sera complétée par les informations cinématiques extractibles de Gaia afin de caractériser efficacement les différentes régions de la Voie lactée.

De même que WEAVE qui couvrira l'hémisphère Nord, le télescope spectroscopique multi-objets de 4 m (4MOST, de Jong et al., 2019) sera opérationnel dans un avenir très proche, et il sera capable d'observer simultanément des objets de ~ 2400. 4MOST couvrira l'hémisphère sud, en complément de WEAVE. 4MOST jouera également un rôle crucial dans l'étude de la Voie lactée et des Nuages de Magellan. Toutes ces études fourniront des contraintes importantes sur la structure de la Voie lactée, sur les événements de fusion et d'accrétion survenus au cours de l'histoire de la Galaxie, et elles permettront d'explorer la queue très pauvre en métal des événements de fusion déjà découverts, comme Gaia-Enceladus-Sausage (e.g., Belokurov et al., 2018; Haywood et al., 2018; Helmi et al., 2018, voir Section 0.2) et Gaia-Sequoia (e.g., Barbá et al., 2019, voir Section 0.2), mais aussi de nouvelles découvertes.

Une introduction conviviale aux variables de l'angle d'action

Grâce à l'exquis ensemble de données astrométriques de Gaia DR2 en synergie avec les informations spectroscopiques au sol, il est possible de déduire les distances et les paramètres orbitaux des étoiles. Les chapitres 2 et 3 traitent de l'analyse cinématique des étoiles les plus primitives, du régime ultra pauvre en métaux ([Fe/H] ≤ -4.0) au régime très pauvre en métaux ([Fe/H] ≤ -2.0), tandis qu'une description plus approfondie du choix des paramètres pour l'inférence des paramètres cinématiques est présentée en annexe **??**.

Plusieurs grandeurs physiques sont utiles dans l'analyse cinématique des étoiles, à savoir la distance maximale et minimale du centre galactique appelé apocentre et péricentre, respectivement, la hauteur maximale du plan, l'excentricité de l'orbite, les vecteurs de vitesse et de position, l'énergie et le moment angulaire, et les variables de l'angle d'action. Ces dernières quantités physiques sont très utiles pour décrire le mouvement et démêler les structures ayant des orbites différentes, car elles sont constantes du mouvement. Ces quantités seront utilisées dans les chapitres suivants comme noyau de l'analyse cinématique et, comme elles ne peuvent être utilisées que par une niche de chercheurs, une introduction amicale suit.

Lorsqu'il s'agit d'un système physique, pas nécessairement en astronomie, il est possible de le décrire en utilisant le formalisme Hamiltonien (Hamilton, 1834, 1835; Goldstein, 1950; Landau & Lifshitz, 1969). Avec ce formalisme, l'évolution temporelle du système peut être définie à l'aide de l'équation hamiltonienne :

$$\frac{d\mathbf{p}}{dt} = -\frac{\partial \mathcal{H}}{\partial \mathbf{q}}, \quad \frac{d\mathbf{q}}{dt} = +\frac{\partial \mathcal{H}}{\partial \mathbf{p}} \tag{2}$$

où $(\mathbf{q}, \mathbf{p})$ sont des variables canoniques (telles que la position et son élan) et $\mathcal{H} = \mathcal{H}(\mathbf{q}, \mathbf{p}, t)$ est la fonction hamiltonienne qui décrit l'énergie du système. Par construction, elle dépend des variables canoniques et du temps. Il peut être plus pratique de remplacer la position et le moment par un nouvel ensemble de variables canoniques, l'angle et son moment $(\mathbf{\Theta}, \mathbf{J})$, également appelé l'action, afin de décrire facilement le mouvement. Parfois, le couple formé par l'angle et l'action (le moment) est appelé variable d'angle d'action. La relation entre les variables canoniques précédentes $(\mathbf{q}, \mathbf{p})$ et le moment des variables de

l'angle d'action est la suivante :

$$J_k \equiv \oint p_k dq_k. \tag{3}$$

Puisque $(\mathbf{\Theta}, \mathbf{J})$ sont des coordonnées canoniques, leurs crochets de Poisson[2] doivent satisfaire :

$$\{\Theta_i, J_j\} = \delta_{ij} \tag{4}$$

with δ_{ij} as the Kronecker delta.

Une des caractéristiques du vecteur de moment d'action est que l'intégration dans l'équation 3 ne dépend pas du choix de la trajectoire, et donc l'action est une constante du mouvement. Cela signifie que la nouvelle fonction hamiltonienne $\mathcal{W}$, écrite avec le nouvel ensemble de variables canoniques, ne dépend que du moment de l'action $\mathcal{W} = \mathcal{W}(\mathbf{J})$ et elle doit satisfaire :

$$\frac{d\mathbf{J}}{dt} = -\frac{\partial \mathcal{W}}{\partial \mathbf{\Theta}} = 0, \quad \frac{d\mathbf{\Theta}}{dt} = +\frac{\partial \mathcal{W}}{\partial \mathbf{J}}. \tag{5}$$

Cela implique que le vecteur de moment d'action peut être utilisé pour décrire l'orbite d'une particule et pour distinguer différents types de mouvement, tandis que les angles, c'est-à-dire les coordonnées, renseignent sur la position de la particule dans l'orbite donnée. En astronomie, le vecteur de moment d'action peut être utilisé pour identifier les orbites des étoiles et pour voir clairement si une étoile donnée est confinée au disque ou s'aventure loin dans le halo. Avec un grand échantillon d'étoiles, et en couplant éventuellement leur cinématique avec leur chimie, il est possible d'identifier des structures accrétées (Binney & Tremaine, 2008). Une première utilisation des variables d'angle d'action a déjà été signalée dans la section 0.2 en ce qui concerne la découverte de Gaia-Enceladus-Sausage. Dans les chapitres suivants, les actions sont largement utilisées pour mieux analyser la cinématique des étoiles les plus pauvres en métaux.

Habituellement, les variables d'angle d'action sont présentées en coordonnées cylindriques, (J_r, J_ϕ, J_z), car elles peuvent mieux décrire le mouvement en présence de rotation et d'un disque. $\mathbf{J}$ est exprimé en unités de $\mathrm{kpc} \cdot \mathrm{km\,s^{-1}}$, où la composante azimutale du moment d'action est généralement équivalente à la composante verticale du moment angulaire ($J_\phi \equiv L_z$). De manière générale, J_ϕ, J_r et J_z sont des approximations du mouvement dans les composantes rotationnelle, radiale et verticale, respectivement. Ainsi, les étoiles confinées au plan galactique, et donc ayant un petit mouvement dans la direction verticale, ont de petits J_z, les étoiles ayant une orbite prograde (rétrograde) ont des valeurs positives (négatives) de J_ϕ, tandis que plus l'excentricité est grande, plus la composante radiale du moment d'action J_r est importante.

Un schéma récapitulatif des espaces d'action, convivial et digeste, est esquissé dans la figure 0.15. Le panneau de gauche aide à l'interprétation des résultats décrits dans les chapitres **??** (Sestito et al., 2019) et **??** (Sestito et al., 2020a), dans lequel l'espace d'action utilisé est généré à partir de J_z et J_ϕ. Dans cet espace, les axes sont normalisés par les valeurs correspondantes pour le Soleil (voir Annexe **??**), supposé avoir une orbite circulaire programmée dans le disque. Par conséquent, les étoiles qui ne s'aventurent pas

[2] ont deux fonctions $f(\mathbf{q}, \mathbf{p}, t)$ et $g(\mathbf{q}, \mathbf{p}, t)$ les crochets de Poisson sont :

$$\{f, g\} \equiv \sum_{i=1}^{N} \left(\frac{\partial f}{\partial q_i} \frac{g}{p_i} - \frac{f}{p_i} \frac{g}{q_i} \right)$$

loin du plan de la Voie lactée ont des valeurs faibles de J_z, et celles-ci sont marquées par des points bleus, rouges et noirs. Les marqueurs bleus et rouges sont respectivement des étoiles prograde et rétrograde avec des orbites excentriques basses, tandis que les points noirs représentent des étoiles avec des excentricités élevées et susceptibles d'être confinées au disque avec un mouvement à la fois prograde ($J_\phi/J_{\phi,\odot} > 0$) et rétrograde ($J_\phi/J_{\phi,\odot} < 0$). Les marqueurs magenta représentent les étoiles ayant une orbite en forme de halo, d'où le grand J_z. Le panneau de droite illustre l'utilisation du moment d'action **J** comme dans le chapitre **??** (Sestito et al., 2020b). Un espace d'action différent a été utilisé pour une comparaison entre les galaxies simulées et la Voie lactée observée. Comme les galaxies simulées ont des tailles et des masses, et donc des potentiels gravitationnels, différents de ceux de la Voie lactée, la comparaison doit être faite en normalisant les axes par rapport à la norme du vecteur de moment d'action J_{TOT}. Toujours dans le chapitre **??**, j'ai exploré l'espace d'action en utilisant toutes les composantes de l'action. Ainsi, l'abscisse est la composante azimutale normalisée du moment d'action, i.e., J_ϕ/J_{TOT}, tandis que l'ordonnée prend en compte la différence entre la composante verticale et la composante radiale du vecteur d'action, i.e., $(J_z - J_r)/J_{TOT}$. Le même code couleur a été appliqué que dans le panneau de gauche, ce qui fait que les étoiles planes prograde (points bleus) et rétrogrades (points rouges) se trouvent respectivement à l'extrême droite et à l'extrême gauche de cet espace. Cela signifie que la majorité du mouvement est concentrée dans la composante azimutale, d'où les petits J_z et J_r, et donc leur différence. Les étoiles à forte excentricité probablement confinées dans le plan, d'où le grand J_r et le petit J_z, sont situées dans la région inférieure de cet espace (points noirs). Les étoiles de type halo peuplent la partie restante de l'espace (points magenta).

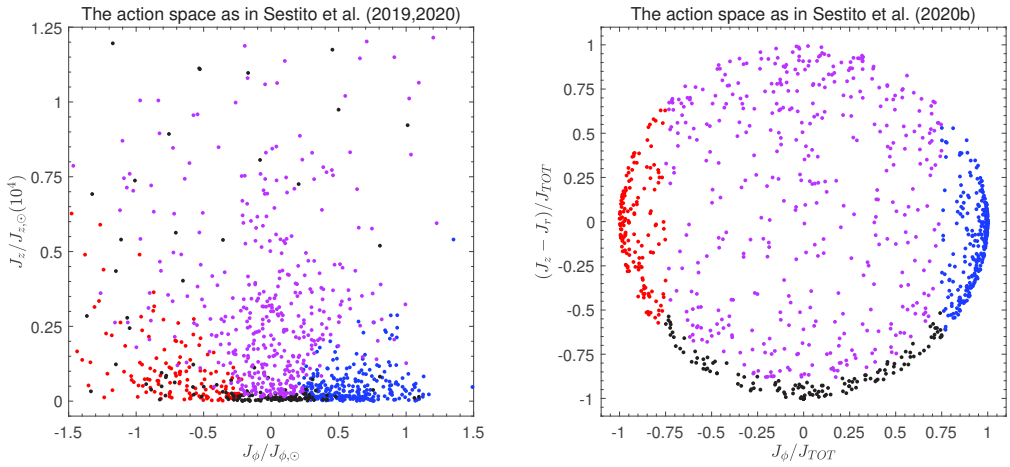

Figure 0.15: Croquis de l'espace d'action pour les étoiles/particules d'étoiles de faible métallicité ([Fe/H] $\leq -2,5$). Panneau de gauche : la composante azimutale vs. la composante verticale de l'action, J_ϕ vs. J_z comme dans Sestito et al. (2019, 2020a). Les étoiles qui restent confinées au disque possèdent de faibles valeurs de J_z. Parmi cet échantillon d'étoiles planaires, celles dont l'excentricité et le mouvement prograde (J_ϕ positif) sont plus faibles sont désignées par des points bleus, tandis que leurs homologues rétrogrades (J_ϕ négatif) sont désignés par des points rouges. Les étoiles planes à forte excentricité sont indiquées par des points noirs, tant prograde que rétrograde. Les étoiles dont l'orbite est en forme de halo sont affichées en magenta. Les axes sont tous deux normalisés par les composantes de l'action du Soleil, supposées avoir une orbite prograde circulaire dans le plan MW. Panneau de droite : espace d'action comme dans (Sestito et al. 2020b, en préparation) en utilisant toutes les composantes d'action. L'axe horizontal est la composante azimutale J_ϕ, tandis que l'axe vertical montre la différence entre la composante verticale et la composante radiale de l'action. Les deux axes sont normalisés par la norme de l'action J_{TOT}. Les particules d'étoile sont codées par couleur comme dans le panneau de gauche.

Dans les chapitres suivants

Les chapitres suivants étudieront la cinématique des étoiles les plus pauvres en métal de la Voie lactée. Je commencerai au chapitre 2 par la description des informations orbitales de toutes les étoiles ultra pauvres en métal, que l'on pense être parmi les plus anciens objets de notre Galaxie, et donc des traceurs de l'Univers naissant et de l'assemblage des galaxies. Je me concentrerai en particulier sur une population particulière confinée dans le plan de la Voie lactée. Dans le chapitre 3, j'étendrai l'analyse aux étoiles très pauvres en métaux découvertes par les études de la Pristine (Starkenburg et al., 2017b; Aguado et al., 2019) et de la LAMOST (Cui et al., 2012; Li et al., 2018). Cet échantillon sera essentiel pour combler le fossé entre la région de métallicité dans laquelle le disque a déjà été découvert et le régime ultra pauvre en métaux de Sestito et al. (2019). De plus, la taille de l'échantillon est nécessaire pour obtenir des résultats statistiquement robustes. Les deux travaux du chapitre 2 et 3 utilisent la précieuse synergie entre les enquêtes au sol et le satellite Gaia. En particulier, les données astrométriques et photométriques exquises de Gaia DR2 sont couplées à la métallicité et à la vitesse radiale des autres relevés pour déduire les distances, les paramètres stellaires et les précieuses informations cinématiques. Le chapitre 4 étudie l'origine des étoiles les plus pauvres en métaux, en

se concentrant également sur la présence de ces étoiles dans la région du disque, grâce à l'utilisation de l'une des simulations cosmologiques les plus performantes, la suite NIHAO-UHD (Buck et al., 2020). Tous les chapitres posent de nouvelles questions intéressantes sur la formation et l'évolution de la Galaxie.

Conclusions

Cette thèse présente de nouveaux résultats pour l'archéologie galactique. Par exemple, la découverte d'une population d'étoiles les plus pauvres en métaux, confinées cinématiquement au disque de la Voie lactée, n'a pas été explorée par les études précédentes et s'écarte de la distribution sphéroïdale générale attendue. Cette population d'étoiles *planaires* peut être regroupée en sous-groupes progrades et rétrogrades. Chapitre 2 (Sestito et al., 2019) montre que dans le régime ultra pauvre en métaux, un quart des UMP découverts ne s'aventurent pas loin du disque. Ces UMP planaires présentent un large éventail d'excentricités, l'étoile la plus pauvre en métaux connue étant en orbite avec un mouvement de prograde quasi-circulaire. Bien que l'échantillon soit très limité en nombre, il y a une nette préférence pour le mouvement planaire de prograde. Cette préférence n'est pas due aux fonctions de fenêtre composite que les enquêtes multiples ont permis d'obtenir. Dans le chapitre 3 (Sestito et al., 2020a), cette analyse cinématique a été étendue au régime très pauvre en métaux, afin d'explorer le régime de métallicité de l'UMP à la queue VMP du disque de la Voie lactée découvert jusqu'à présent. L'échantillon plus important fourni par les enquêtes Pristine (Starkenburg et al., 2017) et LAMOST (Cui et al., 2012) a permis de consolider les résultats sur une base statistique plus solide. Il a été démontré que le nombre d'étoiles planaires progrades est largement supérieur à celui de leur homologue rétrograde. La présence d'étoiles planaires et l'asymétrie observée dans le sens de la rotation ont été détectées à tous les régimes de métallicité. L'asymétrie suggère que la distribution des étoiles planaires n'est pas en accord avec ce qui est attendu d'une distribution sphéroïdale et soutenue par la pression. Trois scénarios mutuellement non exclusifs ont été proposés pour expliquer la population planaire décrite dans les chapitres 2 et 3. Le premier, le scénario in-situ, invoque la présence de poches de milieu interstellaire (ISM) dépourvues de métal dans la Voie lactée après l'installation du disque. Dans le second scénario, les étoiles planaires ont été formées et amenées, avec l'ISM et la matière noire, par les blocs de construction qui ont formé le proto-disque. Alors que dans le dernier scénario, cette population planaire a été déposée par des événements d'accrétion ultérieurs qui ont été entraînés dans le plan de la Voie lactée.

D'après les observations, il n'a pas été possible de distinguer les multiples scénarios qui créent cette caractéristique cinématique, à savoir la formation in situ, la formation dans la phase initiale d'assemblage et les événements de fusion ultérieurs. Cela est principalement dû aux limites des observations découlant de la taille et de la distribution spatiale de l'échantillon, au manque d'informations chimiques qui pourraient retracer la formation des étoiles sur leurs sites d'origine, et aux multiples fonctions de fenêtres données par les différentes études qui ont découvert ces étoiles dépourvues de métal. D'autre part, les simulations cosmologiques à haute résolution peuvent fournir un excellent outil pour vérifier si cette population planaire est une caractéristique cinématique commune ou si elle dépend d'un assemblage particulier et d'une histoire d'accrétion. De plus, il est possible de suivre les particules d'étoiles dans le temps et d'étudier leur origine. Pour cette enquête,

dans le chapitre 4 (Sestito et al., 2020b), j'ai utilisé 5 galaxies spirales simulées de la suite NIHAO-UHD (Buck et al., 2020), avec une résolution capable de résoudre spatialement des structures sous-puces. Comme premier résultat, les galaxies de la NIHAO-UHD montrent la présence de la population planaire, avec une préférence pour le groupe prograde comme dans la Voie lactée observée. Cet ensemble de galaxies simulées possède un halo à rotation lente, ce qui signifie que la rotation peut induire le confinement de certaines particules d'étoiles dans le disque avec un mouvement de prograde. Cependant, j'ai découvert que la distribution des vitesses de la population planaire de prograde dépasse ce que l'on pourrait attendre d'une distribution sphéroïdale à rotation lente et ressemble beaucoup plus à celle du disque épais plus riche en métaux. Tout en gardant à l'esprit qu'aucune de ces galaxies ne ressemble entièrement à la Voie lactée, j'ai exploré l'origine des étoiles les plus pauvres en métaux dans la NIHAO-UHD. Les galaxies simulées indiquent que les étoiles planaires rétrogrades et progrades sont toutes deux liées à l'histoire de la formation des galaxies. Par exemple, la majorité ($>$ 90 pour cent) de la population planaire rétrograde a été amenée au cours de l'assemblage galactique précoce, indépendamment de l'histoire de la formation et de l'accrétion des galaxies simulées. D'autre part, la population prograde retrace à la fois la phase de construction et les événements d'accrétion ultérieurs. En effet, lors de l'assemblage initial, la proto-galaxie était beaucoup plus petite et les satellites en fusion (parfois de taille comparable à la proto-galaxie) pouvaient déposer leurs étoiles dans la région intérieure du potentiel gravitationnel et conserver leur mouvement rétrograde ou prograde. Une fois la galaxie bien formée, seuls les satellites à accrétion prograde pouvaient déposer leurs étoiles de manière coplanaire, car ils pouvaient sentir les forces de marée pendant une période prolongée. En revanche, les satellites rétrogrades ultérieurs ont moins de temps pour ressentir le potentiel gravitationnel du disque et ils finissent par être perturbés et principalement dispersés dans le halo. La chimie et la cinématique des étoiles planaires progrades et rétrogrades découvertes nous aident à comprendre l'assemblage précoce de la Galaxie et les accrétions ultérieures. Par conséquent, ces résultats peuvent être importants pour notre compréhension de la Voie lactée.

La spectroscopie à haute résolution permet d'étudier plus en détail ces populations intéressantes. C'est pourquoi un suivi spectroscopique à haute résolution est nécessaire pour mesurer la capture de neutrons, tels que l'europium, le baryum et l'yttrium, et d'éléments $\alpha-$, tels que le magnésium, le calcium, le carbone et l'oxygène. Leur présence et leur abondance chimique dans les étoiles les plus pauvres en métaux sont strictement liées aux mécanismes physiques qui ont pollué le milieu interstellaire de leurs sites de formation dans l'Univers primitif. Par conséquent, nous pouvons en apprendre davantage sur l'efficacité de la formation des étoiles et sur l'histoire des éléments constitutifs qui ont formé notre Galaxie, et aussi démêler les différentes populations à l'intérieur de la Voie lactée. Enfin, tous ces éléments sont importants pour en savoir plus sur l'histoire de la formation et de l'accrétion de notre Galaxie au début des temps. Avec ces motivations, je prévois d'utiliser les installations d'observation ayant la plus haute résolution, telles que le spectrographe ultraviolet et visuel d'Echelle (UVES) du Very Large Telescope (VLT), le spectrographe optique à haute résolution Gemini (GHOST) des télescopes Gemini, et le dispositif spectro-polarimétrique d'Echelle pour l'observation des étoiles (ESPaDOnS) du télescope Canada-France-Hawaii (CFHT). Grâce à ces instruments, il sera possible de couvrir une large gamme de magnitudes, et d'explorer avec une haute résolution différentes régions de la Voie lactée. Ces installations sont parfaites pour mesurer les lignes de faiblesse des éléments de capture des neutrons avec une grande précision, et ainsi maintenir des temps d'exposition raisonnablement courts.

L'avenir proche fournira une mine de données pour l'archéologie galactique, puisque de nouveaux grands relevés spectroscopiques multi-objets au sol verront le jour. Il s'agit surtout des satellites WEAVE (Dalton et al., 2012) et 4MOST (de Jong et al., 2019), qui scanneront respectivement le ciel septentrional et le ciel austral. En ce qui concerne WEAVE, et sa synergie avec l'étude de Pristine, il a été prédit qu'il découvrira environ 8000 de nouvelles étoiles extrêmement pauvres en métal (Aguado et al., 2019), dépassant largement les chiffres réels pour cette ancienne population. Les informations chimiques issues de ces enquêtes seront complétées par les futures données des satellites Gaia. Le satellite Gaia de l'ESA élargira le nombre de sources avec des solutions photométriques et astrométriques, réduira les incertitudes sur les mesures et fournira également des paramètres stellaires pour l'échantillon le plus brillant. Cette puissante synergie sera cruciale pour les études chimio-dynamiques de la Voie lactée, et elles seront essentielles pour étudier plus avant la répartition actuelle des étoiles et leur relation avec l'histoire de la Galaxie.

Dans un avenir plus lointain, d'autres installations d'observation commenceront à acquérir des données. Pour mon domaine scientifique, les nouveaux développements les plus passionnants en matière de nouveaux instruments sont le grand télescope d'étude synoptique (LSST, également connu sous le nom de Vera C. Rubin Observatory, Ivezic et al., 2008), le Sloan Digital Sky Survey-V (SDSS-V, Kollmeier et al., 2017), le Maunakea Spectroscopic Explorer (MSE, The MSE Science Team et al., 2019), le télescope extrêmement grand (ELT, Tamai et al., 2016), et le télescope spatial James Webb (JWST, Gardner et al., 2006). Le LSST balayera l'hémisphère sud jusqu'à 18000 deg^2, et avec son champ de vision de ~ 9.6 deg^2 et son diamètre effectif de 6.7 m il atteindra une profondeur de $25-28$ mag avec ses filtres (u, g, r, i, z, y). Cette limite de magnitude sera essentielle pour résoudre plusieurs régions de la Voie lactée, du renflement au halo extérieur et aux satellites jusqu'à $\sim 450\,kpc$. De plus, elle fournira des mouvements propres exquis atteignant $3-4$; des magnitudes plus faibles que le satellite Gaia jusqu'à une distance de $100\,kpc$ (Rich, 2018, et les références qui s'y trouvent). Le MSE remplacera probablement le TCFH et pourra acquérir jusqu'à 3000 spectres dans la configuration à basse résolution. La sensibilité et les propriétés de ce télescope et de ses équipements sont idéales pour plusieurs cas scientifiques, de l'exoplanète, aux étoiles très pauvres en métal dans la Voie lactée, aux objets à fort décalage vers le rouge (The MSE Science Team et al., 2019), et il peut compléter les informations provenant de divers autres relevés. Le SDSS-V (Kollmeier et al., 2017), dans la foulée de l'enquête du SDSS, observera les hémisphères nord et sud en utilisant plusieurs observatoires. Il cartographiera la Voie lactée et le Volume local des galaxies grâce à la spectroscopie multi-objets et à la spectroscopie de champ intégral couvrant l'optique et le proche infrarouge. Il ciblera jusqu'à 5 millions d'étoiles dans la galaxie, et jusqu'à 25 millions de spectres dans la Voie lactée et les galaxies voisines. De plus, il pointera vers les trous noirs dans le but d'en déduire les propriétés. L'ELT, d'un diamètre de 39 m et équipé d'une optique adaptative et de plusieurs instruments à bord, sera capable d'atteindre une haute résolution avec un faible bruit à la fois dans l'optique et dans le proche infrarouge. Par exemple, le spectrographe à haute résolution (HIRES) aura une résolution de R$\sim 100,000$ idéale pour mesurer des lignes très faibles comme dans les étoiles les plus pauvres en métal, et ses performances sont également optimales pour les exoplanètes et la science à haut décalage vers le rouge. Avec une résolution plus faible (jusqu'à R~ 15000), un autre instrument intéressant à l'ELT est le spectrographe multi-objets (MOSAIC). Bien que la résolution soit inférieure à celle de HIRES, MOSAIC sera idéal pour suivre simultanément par spectroscopie jusqu'à 200 cibles. MO-

SAIC cartographiera les étoiles dans la région intérieure de notre Galaxie et il tournera également son regard vers les galaxies à haut décalage horaire. Grâce à cette combinaison d'instruments, l'ELT sera idéal pour l'étude des objets situés dans la Voie lactée et à un redshift beaucoup plus élevé. Depuis l'espace, le JWST (Gardner et al., 2006), composé de miroirs hexagonaux d'un diamètre total de 6.6 m, permettra d'acquérir des données infrarouges. Il pourra explorer l'Univers lointain et naissant, et sonder directement les régions de formation des étoiles et l'assemblage des galaxies. Le dossier scientifique du JWST ne s'arrête pas à la physique des grands décalages vers le rouge, mais il comprend également les exoplanètes et les objets solaires, les régions de formation des étoiles dans le volume local. Le JWST tentera donc de répondre à des questions allant des origines de la vie à la fin des âges sombres et aux premières lumières.

Grâce à toutes ces installations et à ces études, ainsi qu'aux programmes WEAVE et 4MOST mentionnés ci-dessus, le ciel sera balayé du proche ultraviolet au proche infrarouge, couvrant à la fois la Voie lactée et les sources extragalactiques. Les futures études chimio-dynamiques bénéficieront largement de cette richesse de données créant une carte multidimensionnelle sans précédent de la Galaxie. D'autre part, cet énorme ensemble de données couvrira également les études à haut décalage vers le rouge et il sera possible de sonder directement l'Univers primitif. Tant les études de la Voie lactée avec ses satellites que celles des systèmes à haut-décalage permettront de répondre aux questions sur la formation des premières étoiles, la formation et l'évolution des galaxies, la nature et les propriétés de la matière noire et de l'énergie noire.

Comme la quantité de données va considérablement augmenter, de nouvelles techniques d'analyse rapides et efficaces doivent être développées. Par exemple, des méthodes basées sur l'apprentissage machine et le réseau de neurones peuvent apporter l'amélioration souhaitée. Dans mon prochain poste de post-doctorant, je prévois d'utiliser un réseau neuronal convolutif, appelé *StarNet* (Fabbro et al., 2018; Bialek et al., 2019; Venn et al., 2019) et développé à l'Université de Victoria, pour extraire des informations chimiques à partir de spectres à haute résolution et de données WEAVE+Pristine. Cet outil a été testé et formé sur les spectres stellaires observés et synthétiques. Je vais utiliser cet outil et l'améliorer en y incorporant mes méthodes d'inférence bayésiennes (Sestito et al., 2019) pour inférer en plus des paramètres stellaires précis avec la photométrie et l'astrométrie de la mission spatiale Gaia (DR3 à venir), et donc indépendamment des spectres eux-mêmes. Cette suite d'outils d'analyse de données sera non seulement extrêmement rapide, mais elle réduira également le budget d'erreurs de mes prochaines analyses chimio-dynamiques. De cette façon, je déduirai rapidement et efficacement les abondances chimiques et les propriétés cinématiques à partir des observations, avec pour objectif ultime de reconstruire une carte de haute précision et multidimensionnelle de la Voie lactée.

En conclusion, dans les années à venir, nos connaissances sur les débuts de l'Univers et sur tous les sujets liés à l'archéologie galactique ou à la paléontologie seront largement approfondies et elles bénéficieront d'un apport sans précédent de nouvelles données de haute qualité et de nouvelles méthodes d'analyse très performantes.

Federico Sestito

Galactic Archæology in the Gaia era: unveiling the formation of the Milky Way with extremely metal-poor stars

Résumé

L'étude des étoiles très pauvres en métaux ([Fe/H]< -2,0) est vraiment unique à notre Groupe Local, c'est seulement ici que nous pouvons résoudre des étoiles individuelles et étudier ces cibles rares. Ces étoiles sont également les plus anciennes parmi la population de la Voie lactée, et se sont formées au cours des premiers milliards d'années de l'Univers. Aujourd'hui, nous pouvons combiner les données astrométriques et photométriques exquises de Gaia DR2 avec les informations spectroscopiques des relevés au sol, afin de découvrir les propriétés physiques de la Voie lactée dans un espace à phases multidimensionnelles. Les résultats de ces investigations peuvent être comparés à des simulations entièrement cosmologiques pour en savoir plus sur la formation de la Galaxie. Dans ce travail, utilisant à la fois des observations et des simulations cosmologiques de pointe, j'ai découvert de façon surprenante qu'une fraction non négligeable des étoiles très pauvres en métaux est confinée au plan galactique. En particulier, la population planaire rétrograde renseigne sur la formation de la Galaxie, tandis que les étoiles planaires prograde échantillonnent tous les événements d'accrétion.

Mots-clés: Archéologie galactique, formation de la Voie Lactée, disque de la Voie Lactée, étoiles très pauvres en métal, Gaia DR2

Résumé en anglais

The study of the very metal-poor stars ([Fe/H]< -2.0) is truly unique to our Local Group, only here we can resolve individual stars and study these rare targets. These stars are also the oldest among the population of the Milky Way, and formed within the first few billions of years of the Universe. Nowadays, we can combine the exquisite astrometric and photometric data from Gaia DR2 with the spectroscopic information of ground-based surveys, in order to uncover the physical properties of the Milky Way in a multidimensional phase space. Results from such investigations can be compared to fully cosmological simulations to learn about the build-up of the Galaxy. In this work, using both observations and state-of-the-art cosmological simulations, I surprisingly found that a non-negligible fraction of the very metal-poor stars is confined to the Galactic plane. In particular, the retrograde planar population is informative on the formation of the Galaxy, while the prograde planar stars are sampling all the accretion events.

Keywords: Galactic Archaeology, Milky Way formation, Milky Way disk, Very metal-poor stars, Gaia DR2